UNIVERSIDADE FEDERAL DE MINAS GERAIS
Instituto de Ciências Exatas
Programa de Pós-Graduação em Química

EMILAY BAESSA TEIXEIRA DIOGO

ELECTROCHEMICAL SULFENYLATION AND PHOTOCATALYTIC TRANSFORMATIONS AS COMPLEMENTARY TOOLS FOR GREEN ORGANIC SYNTHESIS

BELO HORIZONTE
2025

UFMG/ICEX/DQ.1.684
T. 762

Emilay Baessa Teixeira Diogo

ELECTROCHEMICAL SULFENYLATION AND PHOTOCATALYTIC TRANSFORMATIONS AS COMPLEMENTARY TOOLS FOR GREEN ORGANIC SYNTHESIS

Thesis presented to the Graduate Program in Chemistry at the Federal University of Minas Gerais, as a partial requirement for the obtention of PhD degree in Chemistry.

Advisor: Prof. Dr. Eufrânio N. da Silva Júnior
Co-advisor: Prof. Dr. Cynthia L. M. Pereira

Belo Horizonte
2025

Ficha Catalográfica

D591e
2025
T

Diogo, Emilay Baessa Teixeira.
Electrochemical sulfenylation and photocatalytic transformations as complementary tools for green organic synthesis [manuscrito] / Emilay Baessa Teixeira Diogo. 2025.
266 f. : il., gráfs., tabs.

Orientador: Eufrânio Nunes da Silva Júnior.
Coorientadora: Cynthia Lopes Martins Pereira.

Tese (doutorado) – Universidade Federal de Minas Gerais – Departamento de Química.
Inclui bibliografias.
Apêndices: f. 181-266.

1. Química orgânica – Teses. 2. Quinona – Teses. 3. Eletroquímica – Teses. 4. Câncer – Teses. 5. Fotoquímica – Teses. 6. Química ambiental – Teses. 7. Fotoquímica orgânica – Teses. 8. Reação de oxidação-redução – Teses. I. Silva Júnior, Eufrânio Nunes da, Orientador. II. Pereira, Cynthia Lopes Martins, Coorientadora. III. Título.

CDU 043

Elaborada por Sérgio Ferreira da Silva – Bibliotecário – CRB6/2719.

UNIVERSIDADE FEDERAL DE MINAS GERAIS

UFMG
Programa de Pós-Graduação em Química
Departamento de Química - ICEx

química
pós-graduação-ufmg

"Electrochemical Sulfenylation And Photocatalytic Transformations As Complementary Tools For Green Organic Synthesis"

Emilay Baessa Teixeira Diogo

Tese aprovada pela banca examinadora constituída pelos Professores:

Prof. Eufrânio Nunes da Silva Júnior - Orientador
UFMG

Profa. Cynthia Lopes Martins Pereira - Coorientadora
UFMG

Profa. Adriana Akemi Okuma
CEFET-MG

Prof. Cassiano Lino dos Santos Costa
CDTN

Profa. Amanda Silva de Miranda
UFMG

Prof. Cleiton Moreira da Silva
UFMG

Belo Horizonte, 08 de outubro de 2025.

Documento assinado eletronicamente por **Eufranio Nunes da Silva Junior**, **Professor do Magistério Superior**, em 09/10/2025, às 00:13, conforme horário oficial de Brasília, com fundamento no art. 5º do Decreto nº 10.543, de 13 de novembro de 2020.

Documento assinado eletronicamente por **Cynthia Lopes Martins Pereira**, **Professora do Magistério Superior**, em 09/10/2025, às 10:12, conforme horário oficial de Brasília, com fundamento no art. 5º do Decreto nº 10.543, de 13 de novembro de 2020.

Documento assinado eletronicamente por **Cassiano Lino dos Santos Costa**, **Usuário Externo**, em 09/10/2025, às 12:17, conforme horário oficial de Brasília, com fundamento no art. 5º do Decreto nº 10.543, de 13 de novembro de 2020.

Documento assinado eletronicamente por **Amanda Silva de Miranda**, **Professora do Magistério Superior**, em 09/10/2025, às 15:01, conforme horário oficial de Brasília, com fundamento no art. 5º do Decreto nº 10.543, de 13 de novembro de 2020.

Documento assinado eletronicamente por **Cleiton Moreira da Silva**, **Professor do Magistério Superior**, em 11/10/2025, às 22:09, conforme horário oficial de Brasília, com fundamento no art. 5º do Decreto nº 10.543, de 13 de novembro de 2020.

Documento assinado eletronicamente por **Adriana Akemi Okuma**, **Usuário Externo**, em 17/10/2025, às 21:00, conforme horário oficial de Brasília, com fundamento no art. 5º do Decreto nº 10.543, de 13 de novembro de 2020.

A autenticidade deste documento pode ser conferida no site https://sei.ufmg.br/sei/controlador_externo.php?acao=documento_conferir&id_orgao_acesso_externo=0, informando o código verificador **4609894** e o código CRC **E9F7A522**.

Referência: Processo nº 23072.260958/2025-76 SEI nº 4609894

I dedicate this thesis to my parents, João Batista Diogo and Eliane Teixeira Diogo, whose unwavering support and encouragement gave me the courage to keep moving forward; to my brother, João Vitor Batista Diogo, for his constant presence in my life; and to God, my source of inspiration, for granting me this opportunity and guiding me throughout this journe.

ACKNOWLEDGMENTS

To God.

To my father, João Batista Diogo, my mother, Eliane Teixeira Diogo, and my brother, João Vitor Batista Diogo, I am profoundly grateful for your unconditional support and for always believing in me.

To my advisor and dear friend, Professor Eufrânio Nunes da Silva Júnior, whose guidance has been steadfast not only throughout my PhD but also long before it began. From the very start of my academic journey, Professor da Silva Júnior inspired me to love research and recognize the importance of always striving for excellence. His mentorship has shaped my scientific path, and his friendship has been an invaluable gift.

To my co-advisor, Professor Cynthia Lopes Martins Pereira, for her constant support and insightful guidance over the years. Her patience, encouragement, and generous contributions have been fundamental to my growth as a researcher. Thank you for always believing in me and for sharing knowledge in ways that made this journey lighter and more meaningful.

To Dr. Renata Gomes de Almeida, for the partnership and friendship we shared in the laboratory. Your collaboration, dedication, and good humor made our work together not only productive but also enjoyable.

To my colleagues from the Laboratory of Synthetic and Heterocyclic Chemistry, Ana Alves, Ana Luísa, Aristides, Breno Urcine, Dandara Borges, Eduardo Guimarães, Esther Paz, Gabriel Lopes, Henrique Guimarães, Ícaro Antônio, José Manuel, Joyce Cristina, Laura Patricia, Luana Machado, Nycolle Silva, and many others who were part of the lab, thank you for the companionship, teamwork, and support that made this path more pleasant and rewarding.

I would also like to acknowledge the dear friends I made during my stay in Paris, including Wilian Carvalho, Céline Demeese, Joel Tchuiteng, Mathilde Ponchelle, and Pothikumar Rajagopal, who made this experience truly special. I am especially grateful to Mateus Pena, whom I had already known before and whose companionship during this period became even more meaningful. Our friendship will never be forgotten.

To Dr. Edmond Gravel and Dr. Eric Doris, for warmly welcoming me to their laboratory in Paris and for all their valuable contributions.

To all the staff at the Commissariat à l'énergie atomique et aux énergies alternatives (CEA) who supported me in any way, my sincere thanks.

To Professor Cláudia Pessoa, from the Federal University of Ceará, Fortaleza, for her contribution to the anticancer assays.

To the staff of the Chemistry Department, especially those in the Graduate Program, for their continuous assistance and support.

To the Extension and Provision and Services Center (NEPS) at UFMG, for all the help with analytical analyses.

To the committee members who kindly accepted the invitation to evaluate and contribute to this work.

To all others who helped me, directly or indirectly, I will remain deeply grateful for your support.

This study was financed in part by the Coordenação de Aperfeiçoamento de Pessoal de Nível Superior - Brasil (CAPES) - COFECUB 88887.949766/2024-00.

To CNPq, CAPES, and FAPEMIG, for the financial support provided to this research.

"On ne fait jamais attention à ce qui a été fait; on ne voit que ce qui reste à faire."

"One never notices what has been done; one can only see what remains to be done."

Marie Curie

ABSTRACT

The development of electrochemical and photochemical methodologies provides complementary, sustainable approaches to modern organic synthesis. These approaches enable efficient molecular transformations with reduced environmental impact. Electrochemistry offers sustainable and efficient solutions for molecular functionalization, facilitating the development of environmentally friendly synthetic processes. This work first describes the use of an undivided electrochemical cell for the sulfenylation of quinoidal compounds. This process yielded fifteen sulfur-containing naphthoquinones with good to excellent yields, eliminating the need for chemical oxidants. Selected products were then oxidised to produce the corresponding sulfones, and the resulting derivatives were evaluated for their cytotoxic activity against various cancer cell lines, revealing promising anticancer potential. The second part of the work focuses on photochemistry, in which the organic photocatalyst *p*PCDA played a pivotal role in enabling seven distinct transformations under visible-light irradiation. Its unique photophysical properties promoted thioetherification, C–H arylation and coupling reactions efficiently, all of which were conducted under mild, environmentally friendly conditions. Together, these electrochemical and photochemical methodologies demonstrate complementary approaches to advancing sustainable organic synthesis, combining efficiency and versatility with reduced environmental impact.

Keywords: Quinones, electrochemistry, cancer, sulfenylation, photochemistry, green chemistry, organic photocatalyst

RESUMO

O desenvolvimento de metodologias eletroquímicas e fotoquímicas oferece abordagens complementares e sustentáveis para a síntese orgânica moderna. Essas abordagens possibilitam transformações moleculares eficientes com menor impacto ambiental. A eletroquímica fornece soluções sustentáveis e eficientes para a funcionalização molecular, facilitando o desenvolvimento de processos sintéticos ambientalmente amigáveis. Este trabalho descreve primeiramente o uso de uma célula eletroquímica não dividida para a sulfenilação de compostos quinoidais. Esse processo resultou em quinze naftoquinonas contendo enxofre, com rendimentos de bons a excelentes, eliminando a necessidade de oxidantes químicos. Produtos selecionados foram então oxidados para produzir as correspondentes sulfonas, e os derivados obtidos foram avaliados quanto à sua atividade citotóxica contra diversas linhagens de células cancerígenas, revelando potencial anticâncer promissor. A segunda parte do trabalho foca na fotoquímica, na qual o fotocatalisador orgânico *p*PCDA desempenhou um papel fundamental, possibilitando sete transformações distintas sob irradiação de luz visível. Suas propriedades fotofísicas únicas promoveram, de forma eficiente, reações de tioeterificação, arilação C–H e acoplamento, todas conduzidas sob condições brandas e ambientalmente amigáveis. Juntas, essas metodologias eletroquímicas e fotoquímicas demonstram abordagens complementares para o avanço da síntese orgânica sustentável, combinando eficiência e versatilidade com redução do impacto ambiental.

Palavras-chave: Quinonas, eletroquímica, câncer, sulfenilação, fotoquímica, química verde, fotocatalisador orgânico

FIGURES LIST

TABLES LIST

SCHEMES LIST

ABBREVIATIONS

A549	human lung carcinoma cell line
B16	murine melanoma
CCDC	Cambridge Crystallographic Data Centre
CE	counter electrode
CV	Cyclic voltammograms
DCM	dichloromethane
DEPT	distortionless enhancement by polarization transfer
DG	directing group
DMA	*N*,*N*-dimethylacetamide
DMAc	dimethylacetamide
DMF	*N*,*N*-dimethylformamide
DMSO	dimethyl sulfoxide
DMSO-d_6	deuterated dimethyl sulfoxide
DNA	deoxyribonucleic acid
DQ	Chemistry Department (*Departamento de Química*)
DU-145	human prostate cancer cell line
EDGs	electron donating groups
EI-MS	electronic ionization mass spectrometry
EnT	energy transfer
ESI-MS	electrospray ionization mass spectrometry
equiv.	equivalent(s)
EWGs	electron withdrawing groups
HCT-116	human colon cancer cell line
HepG2	human hepatocarcinoma cell line
HIV	human immunodeficiency virus
HL-60	human leukemia cell line
HMBC	heteronuclear multiple bond correlation
HRMS	high resolution mass spectrometry
IC_{50}	inhibitory concentration of 50% of the parasitary population
ICEx	Exact Sciences Institute (*Instituto de Ciências Exatas*)
IR	infrared spectroscopy

ISC	intersystem crossing
IUPAC	International Union of Pure and Applied Chemistry
J	coupling constant
K-562	human myelogenous leukemia
Lucena 1	myelogenous leukemia
L929	mouse fibroblast cell line
MCF-7	human breast cancer cell line
m-CPBA	*meta*-chloroperbenzoic acid
MDA-MB435	Melanoma cell lines
MeCN	acetonitrile
MeOH	methanol
MS	mass spectrometry
nBu$_4$NI	tetrabutylammonium iodide
nBu$_4$NBF$_4$	tetrabutylammonium tetrafluoroborate
nBu$_4$NPF$_6$	tetrabutylammonium hexafluorophosphate
NCI-H460	human lung cancer cell line
NMR	nuclear magnetic resonance
NMP	*N*-methylpyrrolidone
OVCAR-8	human ovarian cancer cell line
PC3	human prostatic cell line
PCDA	10,12-pentacosadiynoic acid
PDA	polydiacetylenes
RAJI	Burkitt lymphoma
RE	reference electrode
ROS	reactive oxygen species
SOD	superoxide dismutase
r.t.	room temperature
SET	single electron transfer
SF295	human glioblastoma cell line
SNB-19	human glioblastoma cell line
TLC	thin player chromatography
THF	tetrahydrofuran
TEM	transmission electron microscopy
TGA	thermogravimetric analysis

UFMG	Federal University of Minas Gerais (*Universidade Federal de Minas Gerais*)
UV	ultraviolet
UV-vis	ultraviolet-visible
WE	working electrode

INDEX

1. GENERAL INTRODUCTION

The advancement of efficient, selective, and sustainable chemical transformations remains a central objective in modern chemistry. Among the diverse strategies available, electrochemistry and photochemistry stand out as powerful and complementary approaches that harness clean and renewable energy inputs, namely electrical potential and light, to promote chemical reactions under mild conditions. These activation modes grant access to reactive intermediates and mechanistic pathways often inaccessible through conventional thermal or stoichiometric methods, thus enabling innovation in synthesis, catalysis, and materials science.

Electrochemical methodologies provide a precise and versatile means of inducing redox processes while eliminating or significantly reducing the need for stoichiometric oxidants and reductants. This not only improves atom economy but also reduces environmental impact. The fine modulation of the applied potential allows exceptional control over reaction selectivity and efficiency. In parallel, photochemical processes exploit the discrete energy states of photoexcited species to achieve selective bond activation via single-electron transfer, energy transfer, or radical-mediated pathways, expanding the scope of accessible chemical transformations.

By expansion of the synthetic repertoire, both approaches hold remarkable potential for applications in small-molecule activation, energy conversion, and environmentally benign synthesis. Their successful implementation, however, depends on a deep understanding of the fundamental interactions between light, electricity, and matter. Developing robust, reproducible, and scalable methodologies in these domains is therefore not merely an academic pursuit, but a decisive step toward addressing global challenges in sustainable synthesis, energy conversion, and environmental remediation.

In this context, the present study seeks to advance this field by developing and systematically evaluating innovative strategies grounded in electrochemical and photochemical principles. These strategies are expected to provide valuable mechanistic insights and demonstrate practical synthetic applicability.

Chapter 1:

Development of Electrochemical Methodologies

2. INTRODUCTION

2.1.1 Quinones

According to the IUPAC definition, "quinones are compounds having a fully conjugated cyclic dione structure, such as that of benzoquinones, derived from aromatic compounds by conversion of an even number of C–H= groups into –(C=O) groups with any necessary rearrangement of double bonds (polycyclic and heterocyclic analogues are included)".[1] Quinones are named according to the type of cyclic system from which they originate (**1-4**), such as benzoquinones (**5**), naphthoquinones (**6**), anthraquinones (**7**) and phenanthroquinones (**8**) (**Figure 1**).[2]

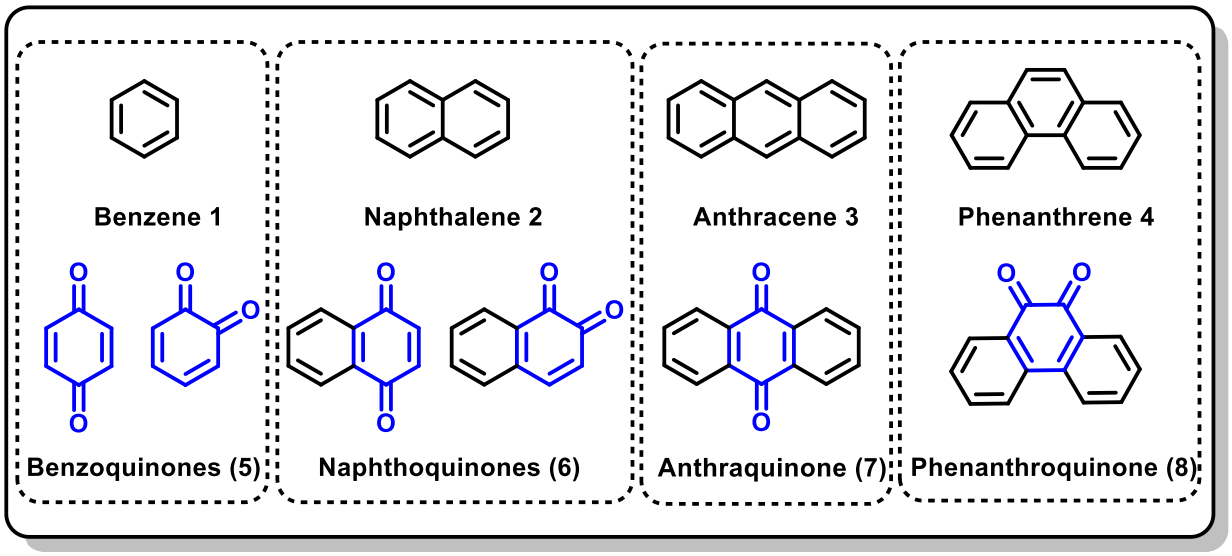

Figure 1: Nomenclature of quinones according to their hydrocarbon analog.

Quinones are of considerable importance due to their broad spectrum of biological activities, which are intrinsically linked to their chemical structure. They display pharmacological properties covering a wide range of bioactivities such as antitumor,[3]

[1] IUPAC. *Compendium of Chemical Terminology*. 2. ed. (the "Gold Book"). Versão online (2019-) criada por S. J. Chalk. ISBN 0-9678550-9-8

[2] a) WEAVER, M. G.; PETTUS, T. R. R. Synthesis of para- and ortho-quinones. 2014, ed. 2, v. 7, p. 373–410. b) SOUSA, E. T.; *et al*. Fontes, formação, reatividade e determinação de quinonas na atmosfera. **Química Nova**, 2016, v. 39, p. 486–495

[3] COELHO-CERQUEIRA, E.; NETZ, P. A.; do CANTO, V. P.; PINTO, A. C.; FOLLMER, C. Beyond topoisomerase inhibition: antitumor 1,4-naphthoquinones as potential inhibitors of human monoamine oxidase. **Chemical Biology & Drug Design**, 2014, v. 83, n. 4, p. 401–410.

antifungal,[4] antibacterial,[5] trypanocidal,[5] leishmanicidal,[6] anti-inflammatory[7] and anti-HIV.[8] Among these, naphthoquinones occupy a particularly prominent position, as highlighted in recent literature reviews, owing to their recognized biological potential.[9]

Naphthoquinoidal compounds exhibit a fundamentally planar structure derived from naphthalene (**Figure 1**) and are characterized by pronounced reactivity, making them of significant interest for their inherent synthetic versatility.[10] Naturally occurring naphthoquinone derivatives include isomers such as lawsone (**9**) and juglone (**10**), vitamin K_1 (**11**), lapachol (**12**), α-lapachone (**13**) and β-lapachone (**14**) (**Figure 2)**.[11]

2-Hydroxy-1,4-naphthoquinone, widely known as lawsone or hennotannic acid (**9**), can be obtained from the extract of dried powdered leaves of henna (*Lawsonia* spp., family Lythraceae). Lawsone (**9**) is responsible for the characteristic red dyeing properties of henna, traditionally used to stain hair, nails, and skin. Its applications extend to forensic science as a fingerprint reagent and to the development of novel bioactive compounds.[12]

An important regioisomer of lawsone is 5-hydroxy-1,4-naphthoquinone (**10**), commonly called juglone (**10**), found in several species of the *Juglandaceae* family. Juglone exhibits allelopathic activity, acting as a toxic agent that inhibits the growth of neighboring plants.[13] It is also a common natural colorant in the food industry, known as C.I. Natural Brown

---

[4] GAFNER, S.; *et al*. Antifungal and antibacterial naphthoquinones from Newbouldia laevis roots. **Phytochemistry**, 1996, v. 42, n. 5, p. 1315–1320.

[5] SILVA JÚNIOR, E. N. *et al*. Naphthoquinoidal [1,2,3]-triazole, a new structural moiety active against Trypanosoma cruzi. **European Journal of Medicinal Chemistry**, 2008, v. 43, n. 8, p. 1774–1780.

[6] GUIMARÃES, T. T. *et al.* Synthesis of novel α- and nor-α-lapachone-based 1,2,3-triazoles by copper-catalyzed azide–alkyne cycloaddition. **European Journal of Medicinal Chemistry**, 2013, v. 63, p. 523-530.

[7] ALMEIDA, E. R.; *et al*. Anti-inflammatory action of lapachol. **Journal of Ethnopharmacology**, 1990, v. 29, p. 239–241.

[8] STAGLIANO, K. W. *et al.* Regiocontrolled synthesis and HIV inhibitory activity of unsymmetrical binaphthoquinone and trimeric naphthoquinone derivatives of conocurvone. **Bioorganic & Medicinal Chemistry**, 2006, v. 14, n. 16, p. 5651–5665.

[9] a) RANI, R. *et al*. Natural naphthoquinones and their derivatives as potential drug molecules against trypanosome parasites. **Chemical Biology & Drug Design**, 2022, v. 100, p. 786–817.b) CORES, Á. et al. Quinones as neuroprotective agents. **Antioxidants**, 2023, v. 12, p. 1464. c) RAMOS-MILARÉ, Á. C. F. H. *et al.* The anti-Leishmania potential of bioactive compounds derived from naphthoquinones and their possible applications: a systematic review of animal studies. **Parasitology Research**, 2022, v. 121, p. 1247–1280.

[10] a) SILVA JÚNIOR, E. N. *et al.* Synthesis of quinones with highlighted biological applications: a critical update on the strategies towards bioactive compounds with emphasis on lapachones**. European Journal of Medicinal Chemistry,** 2019, v. 179, p. 863-915.b) DEVI, M. *et al*. A comprehensive review on synthesis, biological profile and photophysical studies of heterocyclic compounds derived from 2,3-diamino-1,4-naphthoquinone. **Journal of Molecular Structure**, 2022, v. 1269, p. 133786.

[11] LÓPEZ, L. I. *et al.* Naphthoquinones: biological properties and synthesis of lawsone and derivatives a structured review. **Vitae,** 2014, v. 21, p. 248-258.

[12] a) JELLY, R. *et al.* Lawsone: a novel reagent for the detection of latent fingermarks on paper surfaces. **Chemical Communications**, 2008, p. 3513. b) PRADHAN, R. *et al.* From body art to anticancer activities: perspectives on medicinal properties of henna. **Current Drug Targets**, 2012, v. 13, p. 1777-1798.

[13] SODERQUIST, C. J. Juglone and allelopathy. **Journal of Chemical Education**, 1973, v. 50, p. 782.

7.[14] The hydroxyl group position in these compounds is crucial, as it significantly influences their redox potential and prooxidant activity, thereby modulating their biological effects.[15]

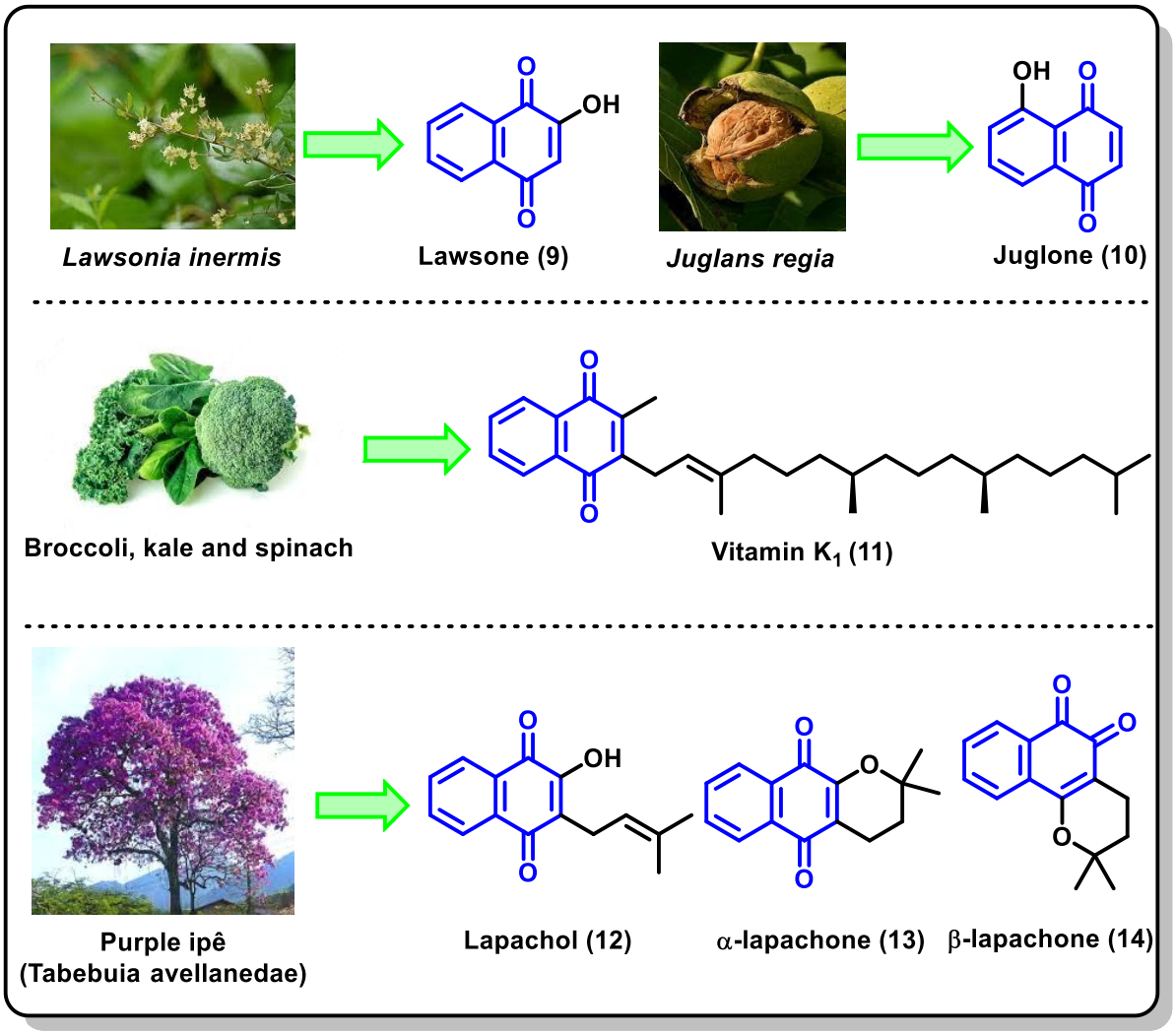

Figure 2: Examples of naturally occurring naphthoquinones: Lawsone (**9**), Juglone (**10**), Vitamin K_1 (**11**), Lapachol (**12**), α-lapachone (**13**) and *β*-lapachone (**14**).

Lapachol (**12**), *α*-lapachone (**13**), and *β*-lapachone (**14**) are important bioactive quinones that were initially isolated from the heartwood of trees belonging to the *Bignoniaceae* family (*Tabebuia sp*), for example, the Brazilian "Ipê" trees.[16] These compounds can also be found in other plant families, including *Verbenaceae*, *Proteaceae*, *Leguminosae*, *Sapotaceae*,

[14] BECHTOLD, T.; MUSSAK, R. *Handbook of Natural Colorants*. Chichester: John Wiley & Sons, 2009.
[15] a) MONKS, T. J. *et al.* Quinone chemistry and toxicity. **Toxicology and Applied Pharmacology**, 1992, v. 112, p. 2-16. b) MURAKAMI, K. *et al*. Effect of hydroxy substituent on the prooxidant action of naphthoquinone compounds. **Toxicology in Vitro**, 2010, v. 24, p. 905-909.
[16] BRITO, M. C. A. *et al*. Anti-inflammatory and cicatrizing properties of the Tabebuia genus: A review. **Research, Society and Development**, v. 10, n. 9, 2021.

Scrophulariaceae, and *Malvaceae*.[17] Additionally, *α*-lapachone (**13**) and *β*-lapachone (**14**) can be synthesized from lapachol.[18-19]

The chemistry of these compounds, referred to as "lapachones", was first explored in the early twentieth century by the chemist Samuel Hooker.[18] His research showed that *β*-lapachone (**14**) and *α*-lapachone (**13**) are present only in trace amounts in lapachol extraction. However, Hooker showed that a simple acid treatment of lapachol efficiently yields these molecules in good to excellent yields (**Scheme 1**).[19]

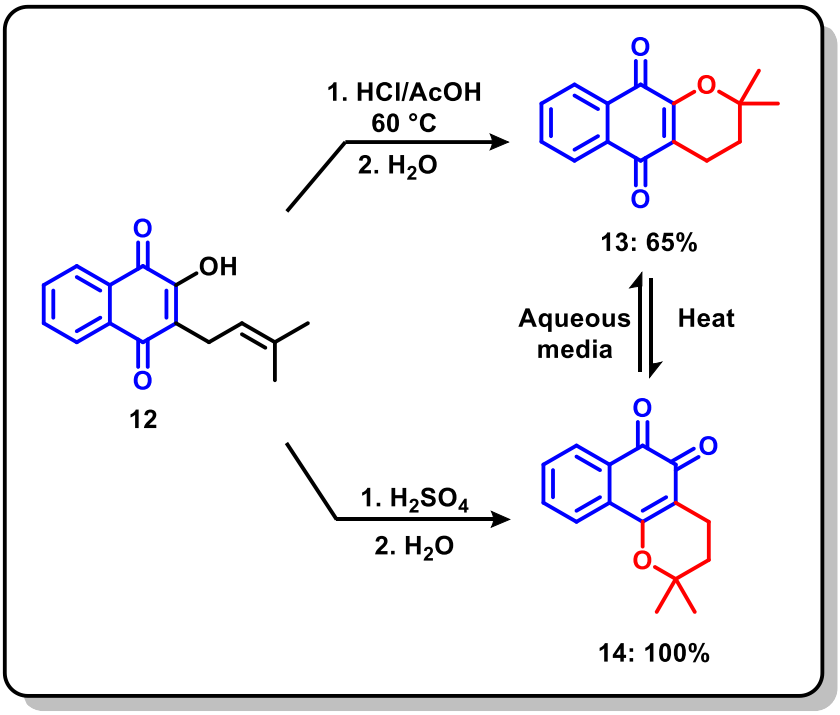

Scheme 1: Synthesis and conversion *α*-lapachone (**13**) and *β*-lapachone (**14**) from lapachol.

Lapachones exhibit a wide range of biological activities, including antitumor,[20] anti-inflammatory,[21] antimicrobial[22] and antifungal effects.[23] In particular, *β*-lapachone (**14**) has

[17] HIROTA, Y. Study on mechanism underlying metabolic biotransformation of vitamin K. **Vitamins**, 2017, v. 92, p. 63-72.
[18] HOOKER, S. C.; STEYERMARK, A. Conversion of ortho into para, and of para into ortho quinone derivatives. Part IV. Synthesis of furan derivatives of α- and β-naphthoquinones. Journal of the American Chemical Society, 1936, v. 58, p. 1202.**Pathophysiology of Haemostasis and Thrombosis**, 2000, v. 30, p. 298-307.
[19] PINTO, A. V.; CASTRO, S. L. The trypanocidal activity of naphthoquinones: a review. **Molecules**, 2009, v. 14, p. 4570.
[20] a) HUSSAIN, H. *et al.* Lapachol: an overview. **Arkivoc**, 2007, v. 2, p. 145.b) ARAÚJO, E. L.; *et al.* Lapachol: segurança e eficácia na terapêutica. Revista Brasileira de Farmacognosia, 2002, v. 12, p. 57-59
[21] MULLER, K.; *et al.* Potential antipsoriatic agents: lapachol compounds as potent inhibitors of HaCaT cell growth. **Journal of Natural Products**, 1999, v. 62, p. 1134-1136.
[22] EYONG, K. O. *et al.* Newbouldiaquinone A: a naphthoquinone–anthraquinone ether coupled pigment, as a potential antimicrobial and antimalarial agent from Newbouldia laevis. **Phytochemistry**, 2006, v. 67, p. 605-609.

attracted considerable attention for its pharmacological potential against various diseases, especially due to its potent antitumor properties.[23]

A key feature underpinning the pharmacological selectivity of β-lapachone (**14**) is its bioactivation by NAD(P)H quinone oxidoreductase-1 (NQO1), a cytosolic flavoprotein overexpressed in many solid tumors, including pancreatic, lung, breast, and prostate cancers, while being present at low levels in most normal tissues.[24] NQO1 catalyzes a two-electron reduction of β-lapachone (**14**) to the corresponding hydroquinone, which rapidly reoxidizes back to the parent quinone in a futile redox cycle. This cycle continuously generates reactive oxygen species (ROS), particularly superoxide ($O_2^{\bullet -}$) and hydrogen peroxide (H_2O_2), overwhelming the antioxidant capacity of tumor cells and driving them past the oxidative threshold that triggers apoptosis.[25]

This tumor-selective ROS generation mechanism has propelled β-lapachone (**14**) into clinical trials for pancreatic cancer therapy. Simultaneously, the search for structural analogues seeks to enhance pharmacokinetic properties, improve potency, and expand activity to other cancer types. Subtle structural modifications to the quinonoidal nucleus such as altering the position and electronic nature of substituents modulate the redox potential and influence the rate of NQO1-mediated reduction, thereby tuning ROS generation.[26]

Hydrogen peroxide, a reactive ROS, can further engage in various pathways to generate more reactive species, such as the hydroxyl radical (HO•).[27] These species are strongly associated with oxidative stress and are capable of damaging DNA, proteins, and lipids. The superoxide radical anion can also react with transition metal species, such as iron (Fe), either directly or in conjunction with hydrogen peroxide, leading to the formation of hydroxyl radicals via Fenton reaction. Hydroxyl radicals are among the most reactive species known and are capable of causing severe cellular damage in living organisms.[28-30]

---

[23] NETO, J. L. F. *et al.* Caracterização físico-química do potencial agente antineoplásico β-lapachona. **Revista de Ciências Farmacêuticas Básica e Aplicada**, 2012, v. 33, p. 545-553.
[24] QADIR, M. I.; IQBAL, M. S.; KHAN, R. β-lapachone: A promising anticancer agent with a unique NQO1 specific apoptosis in pancreatic cancer. **Current Cancer Drug Targets**, v. 22, n. 7, p. 537-540, 2022.
[25] ROSS, D.; SIEGEL, D. The diverse functionality of NQO1 and its roles in redox control. **Redox Biology**, v. 41, p. 101950, 2021.
[26] a) SILVA, M. N.; FERREIRA, V. F.; SOUZA, M. C. B. V. Um panorama atual da química e da farmacologia de naftoquinonas, com ênfase na beta-lapachona e derivados. **Química Nova**, 2003, v. 26, n. 3, p. 407-416.b) GERBER, D. E. *et al.* Phase 1 study of ARQ 761, a β-lapachone analogue that promotes NQO1-mediated programmed cancer cell necrosis. **British Journal of Cancer**, 2018, v. 119, p. 928-936.
[27] HAYES, J. D.; DINKOVA-KOSTOVA, A. T.; TEW, K. D. Oxidative stress in cancer. **Cancer Cell**, 2020, v. 38, n. 2, p. 167-197.

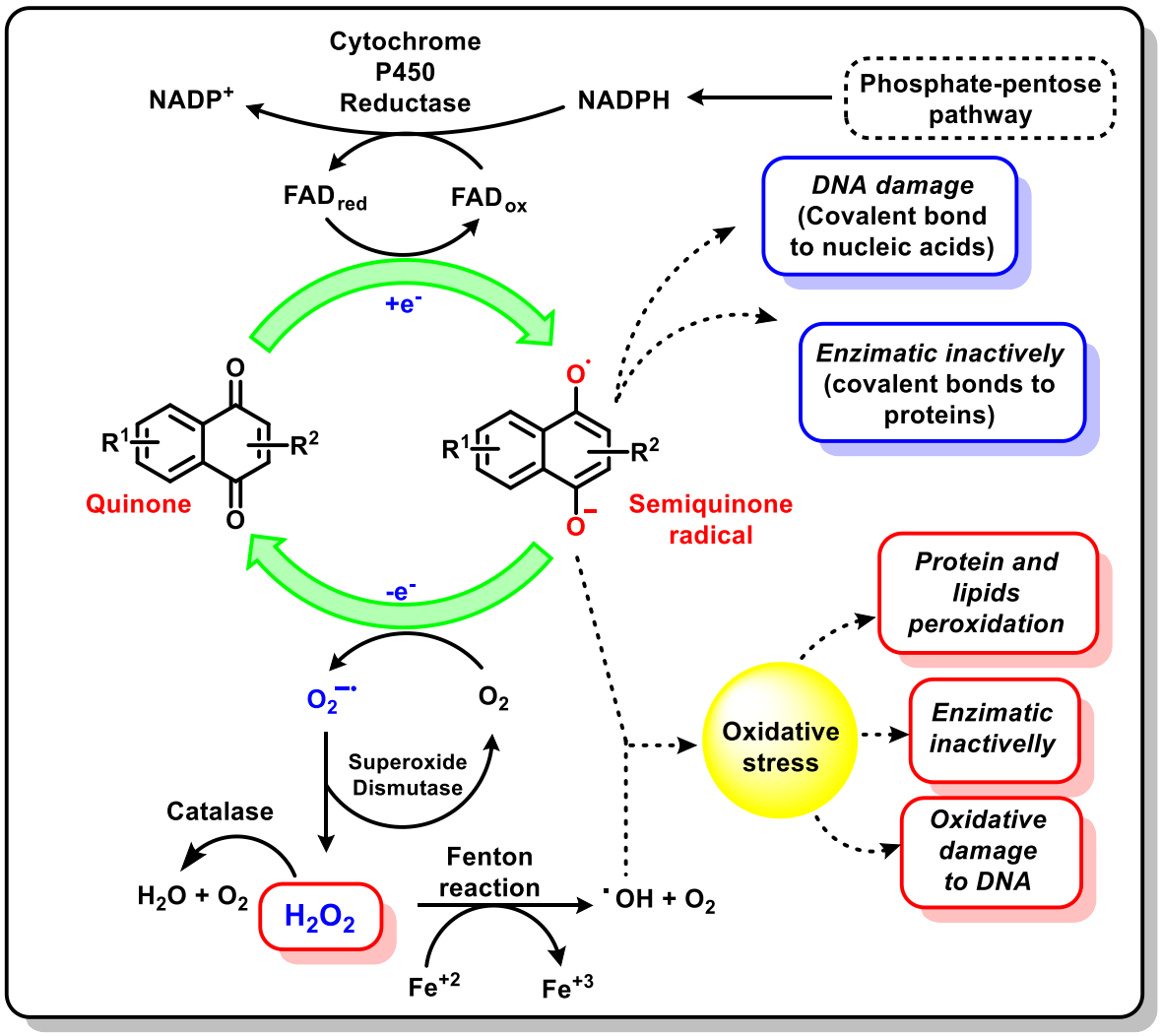

Scheme 2: The redox cycle of quinones and the subsequent generation of metabolites. (Adapted from reference 26).

Oxidative stress, defined as an imbalance between ROS production and antioxidant defenses, has been linked to neurodegenerative diseases, cardiovascular disorders, diabetes mellitus, and many other pathologies.[28] Tumor cells inherently exist in a state of elevated oxidative stress, maintaining ROS levels near the critical redox threshold that induces apoptosis.[29] Based on this understanding, numerous studies have sought novel drug candidates

[28] a) SIES, H. Oxidative stress: a concept in redox biology and medicine. **Redox Biology**, 2015, v. 4, p. 180-183.b) SIES, H.; JONES, D. P. Reactive oxygen species (ROS) as pleiotropic physiological signalling agents. **Nature Reviews Molecular Cell Biology**, 2020, v. 21, n. 7, p. 363-383.

[29] BANDYOPADHYAY, U.; DAS, D.; BANERJEE, R. K. Reactive oxygen species: oxidative damage and pathogenesis. **Current Science**, 1999, p. 658-666.

capable of selectively generating ROS within tumor cells, thereby inducing apoptosis while sparing healthy cells.[30]

Taken together, the unique combination of a tumor-selective activation pathway, potent ROS-mediated cytotoxicity, and structural tunability places β-lapachone (**14**) and its derivatives at the forefront of quinone-based anticancer drug development.

2.1.2 Sulfur-containing naphthoquinones

As discussed above, the naphthoquinone scaffold offers a versatile platform for structural modification, and its biological potential can be further enhanced by introducing a second redox-active center. In particular, the incorporation of sulfur into the quinonoidal framework has shown a significant impact on pharmacological activity.[31]

Sulfur-containing compounds have been recognized for their medicinal relevance for millennia. Historical records from ancient Egypt describe sulfur-based ointments with antibacterial properties, and in the 1920s, sulfur was administered to patients with rheumatoid arthritis.[32] Over the past decades, the clinical use of sulfur derivatives has expanded considerably, ranging from anti-antibacterial [33] and anti-inflammatory[34] agents in dermatological treatment, in addition to some compounds that show promising antitumor activity.[34,35]

Given their well-established biological importance, several research groups, including ours, have explored sulfur-linked quinones as candidates with high therapeutic potential, particularly against cancer. Almeida and coworkers[36] synthesized four *ortho*-quinones by

[30] GOMES, L. S.; *et al*. New chalcogen-functionalized naphthoquinones: Design, synthesis, and evaluation, in vitro and in silico, against squamous cell carcinoma. **ACS Omega**, v. 9, n. 20, p. 21948-21963, 2024.
[31] CRUZ, E. H. G. *et al.* Synthesis and antitumor activity of selenium-containing quinone-based triazoles possessing two redox centres, and their mechanistic insights. **European Journal of Medicinal Chemistry**, 2016, v. 122, p. 1-16.
[32] ILARDI, E. A.; VITAKU, E.; NJARDARSON, J. T. Data-mining for sulfur and fluorine: an evaluation of pharmaceuticals to reveal opportunities for drug design and discovery: miniperspective. **Journal of Medicinal Chemistry**, 2014, v. 57, p. 2832.
[33] a) WELD, J. T.; GUNTHER, A. The antibacterial properties of sulfur. **The Journal of Experimental Medicine**, 1947, 85(5), 531-542. b) KIM, S.; KUBEC, R.; MUSAH, R. A. Antibacterial and antifungal activity of sulfur-containing compounds from Petiveria alliacea L. **Journal of Ethnopharmacology**, 2006, 104, 188-192.
[34] a) LEE, D. Y. *et al.* Anti-inflammatory activity of sulfur-containing compounds from garlic. **Journal of Medicinal Food**, 2012, 15(11), 992-999. b) MULCHIN, B. J. *et al.* The anti-cancer, anti-inflammatory and tuberculostatic activities of a series of 6,7-substituted-5,8-quinolinequinones. **Bioorganic & Medicinal Chemistry**, 2010, 18, 3238-3251.
[35] DA CRUZ, E. H. *et al.* 1,2,3-Triazole-, arylamino- and thio-substituted 1,4-naphthoquinones: potent antitumor activity, electrochemical aspects, and bioisosteric replacement of C-ring-modified lapachones. **Bioorganic & Medicinal Chemistry**, 2014, 22(5), 1608-1619.
[36] ALMEIDA, R. G. *et al.* Synthesis of quinone imine and sulphur-containing compounds with antitumor and trypanocidal activities: redox and biological implications. **RSC Medicinal Chemistry**, 2020, 11, 1145-1160.

replacing the sodium sulfonate group with benzenethiol derivatives (**Scheme 3**). The yields achieved with the obtention of these four molecules were found to be between 30 and 40%. These compounds were evaluated against *Trypanosoma cruzi* and cancer cell lines HCT-116 (colon carcinoma), NCI-H460 (lung cancer), PC-3 (prostate), HL-60 (human promyelocytic leukemia), K-562 (human myelogenous leukemia) and Lucena 1 (myelogenous leukemia). The quinones showed promising IC_{50} values against *Trypanosoma cruzi* ranging from 24.3 to 112.0 μM, with the **16a** quinone showing the best activity. Against the HL-60 cancer cell line, the quinones showed good results ranging from 4.14 to 9.38 μM, with **16b** showing the best result.

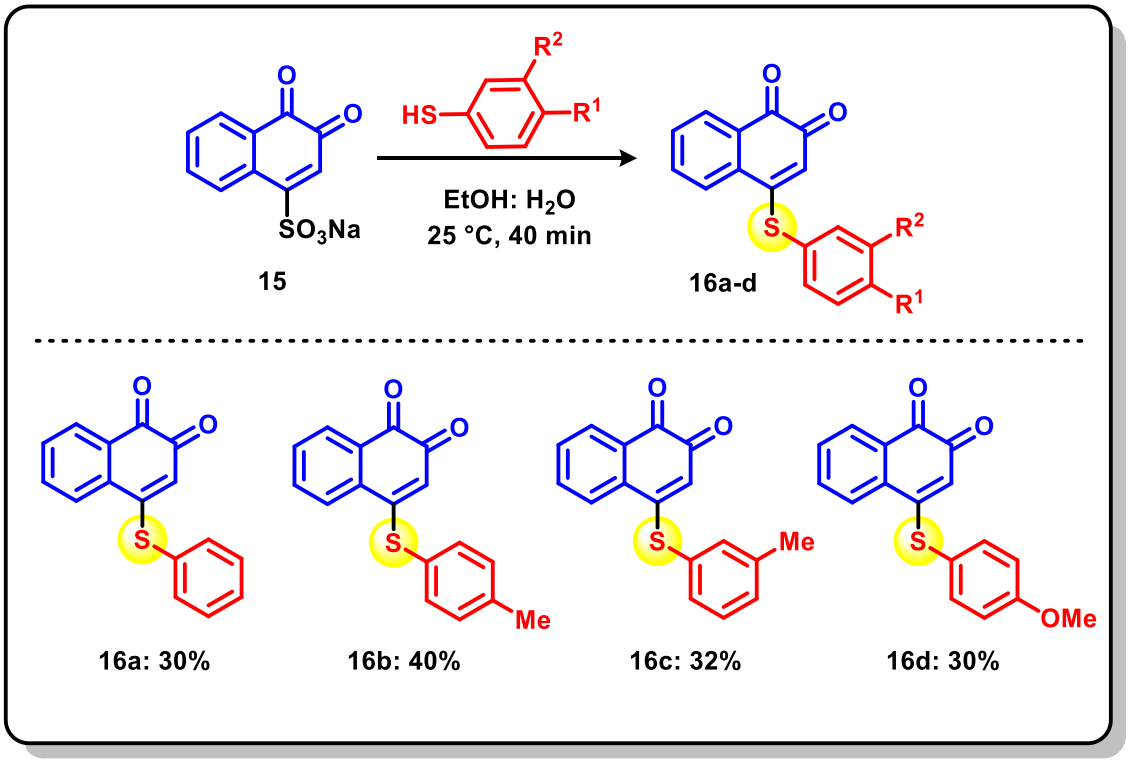

Scheme 3: Synthesis of sulfur aryl *ortho*-quinones **16a-d**.

In 2017, Valença and coworkers[37] developed a synthetic route for the synthesis of quinones containing the sulfonyl group *via* 1,3-dipolar cycloaddition reactions involving naphthoquinone-derived terminal alkynes and toluenesulfonyl azide. Several *N*-sulfonyl-1,2,3-triazoles containing the quinone nucleus were obtained in yields ranging from 32 to 98% and evaluated *in vitro* against tumor cell lines. Antitumor activity results showed that the triazole-based *para*-naphthoquinones were generally active against the tested tumor cell lines SF295 (human glioblastoma cell line), HCT-116, MDA-MB435 (Melanoma cell lines), MCF7 (human

[37] VALENÇA, W. O. *et al.* Synthesis of quinone-based N-sulfonyl-1,2,3-triazoles: chemical reactivity of Rh(II) azavinyl carbenes and antitumor activity. **ChemistrySelect**, 2017, 2(16), 4301-4308.

breast cancer cell line), NCI-H460, Jurkat (T lymphocyte lineage), OVCAR-8 (human ovarian cancer cell line) and DU-145 (human prostate cancer cell line) with IC_{50} values ranging from 0.28 to 3.63 µM.

To demonstrate that the methodology works with other naphthoquinones, Valença and coworkers[38] also synthesized *N*-sulfonyl-1,2,3-triazoles from lapachol (**12**), *nor*-lapachol (**21**) and lawsone (**9**) (**Scheme 4**). These derivatives also exhibited promising cytotoxicity against several tumor cell lines. The lapachol derivative (**20**) demonstrated the highest activity against the V79 cell line, with an IC_{50} of 0.31 µM, whereas the nor-lapachol (**23**) and lawsone (**25**) derivatives showed IC_{50} values of 0.21 and 2.07 µM, respectively, against the Jurkat cell line.

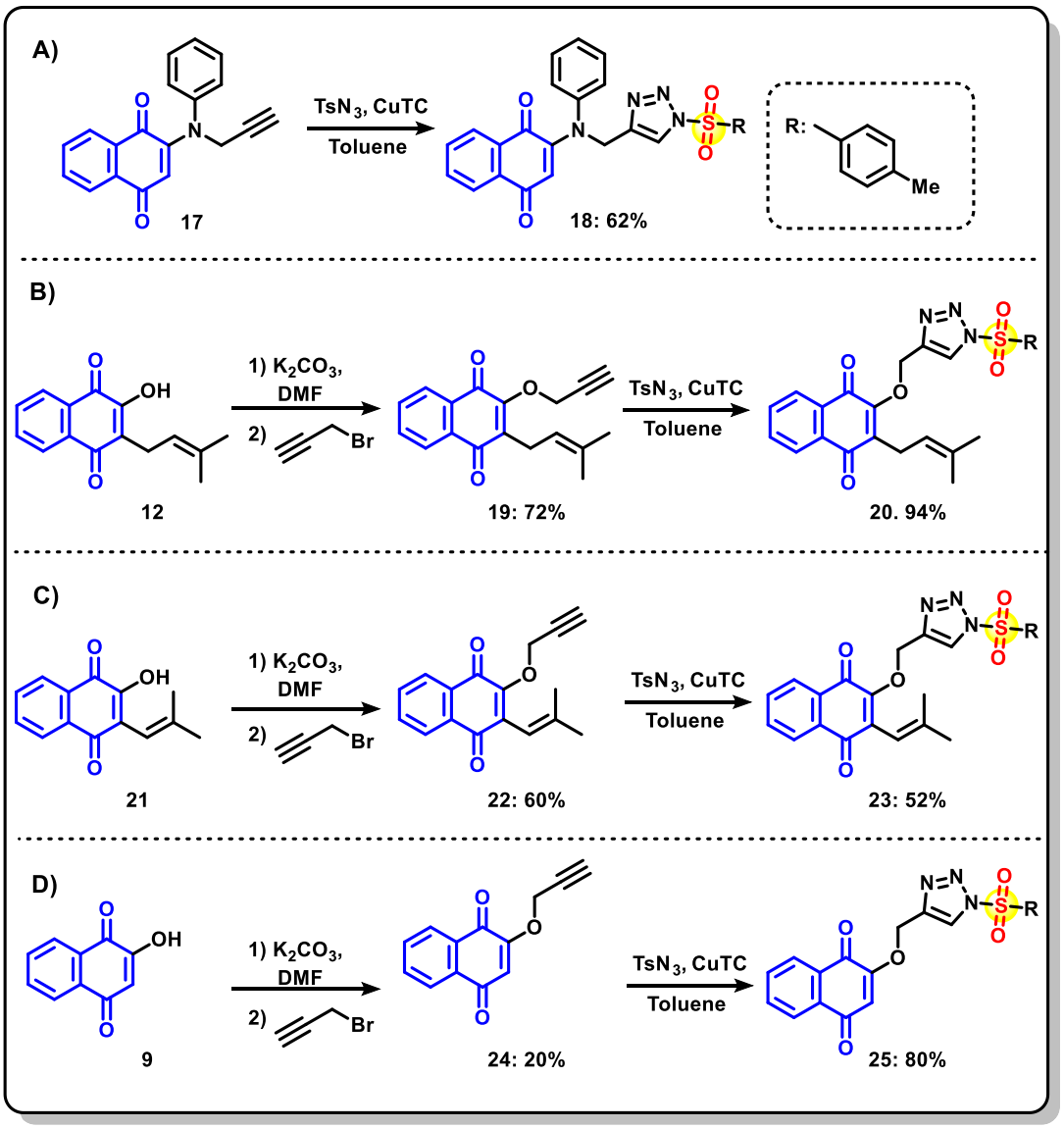

Scheme 4: Synthesis of sulfonyltriazole from: A) aminonaphthoquinones (**17**), B) lapachol (**12**), C) *nor*-lapachol (**21**), D) lawsone (**9**), with R = 4-MePh in all cases.

In 2013, Lee and coworkers[38] reported a methodology for the development of a new series of sulfur-coupled naphthoquinone compounds (**Scheme 5**). In this study, the authors performed the oxidation of sulfides to sulfones, which resulted in compounds with inhibitory activity against HepG2 cell lines (human hepatocarcinoma). Compounds containing 11, 12, and 15 carbon units exhibited significant inhibition, with the 12-carbon derivative displaying an IC_{50} value of 0.44 μM in the sulfone form and 1.66 μM in the sulfide form. Thus, the oxidation of sulfides to sulfones can be regarded as a useful transformation that broadens the scope of compounds available for biological evaluation.

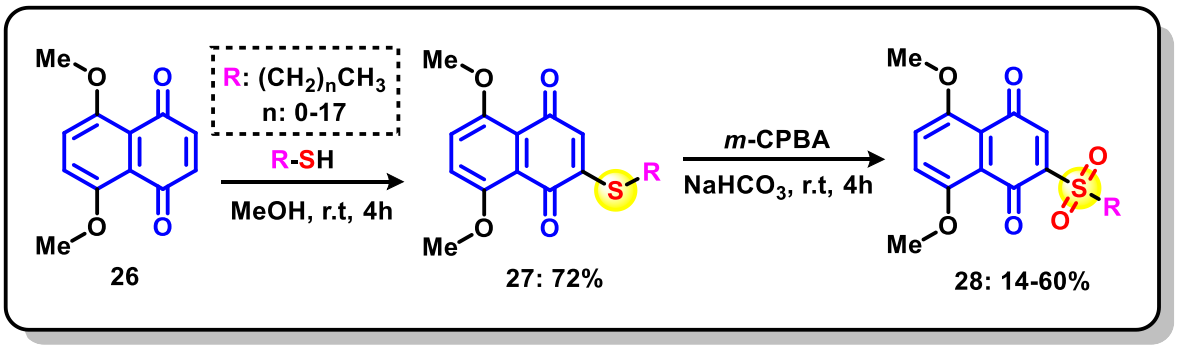

Scheme 5: Synthesis to obtain sulfur-containing naphthoquinone compounds.

The Brahmachari group[39] recently published a simple and efficient electrochemical approach for the regioselective C(sp^2)–H selenation and sulfenylation of 2-(arylamino)naphthoquinones (**29**) (**Scheme 6**). This work describes electrochemical methods to generate chalcogen-containing quinones but does not investigate their biological activity. However, it is a good example of how to obtain sulfur-containing naphthoquinones using a sustainable method, free of transition metal catalysts, oxidants, and high temperatures.

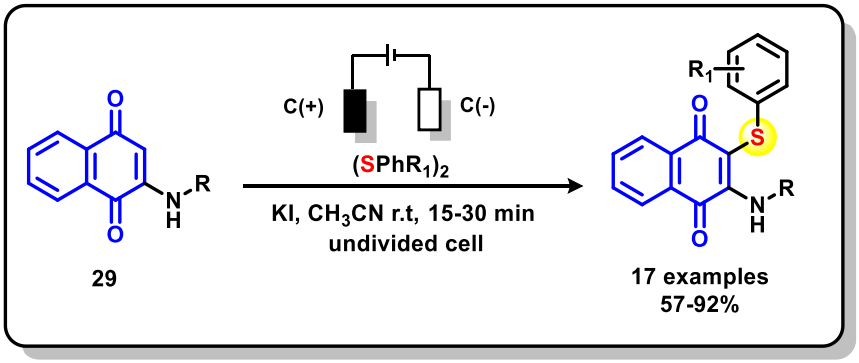

Scheme 6: Electrochemical Synthesis of Functionalized 2- (Arylamino)naphthoquinones

[38] LEE, K. *et al.* Synthesis of a novel series of 2-alkylthio substituted naphthoquinones as potent acyl-CoA: Cholesterol acyltransferase (ACAT) inhibitors. **European Journal of Medicinal Chemistry**, 2013, 62, 515-525
[39] KARMAKAR, P. *et al.* Electrochemical regioselective C(sp^2)–H selenylation and sulfenylation of substituted 2-amino-1,4-naphthoquinones. **The Journal of Organic Chemistry**, 2023, 88, 1049-1060.

2.1.3 Electrosynthesis: Definition and Application

Electrochemistry is a crucial branch of research dedicated to the study of redox processes. Electrolysis is a chemical process in which an electric current drives a nonspontaneous reaction.[40] The growing importance of electrochemistry in modern research is largely attributed to its environmentally friendly profile, which aligns with the current demand for sustainable methodologies. In particular, organic electrosynthesis has undergone a remarkable resurgence in recent years, offering innovative and greener synthetic strategies.[41]

The origins of electrochemistry can be traced back to the late 18th century, with Luigi Galvani's experiments on the contraction of frogs' legs under electrical stimulation, and to the early 19th century[42] with Alessandro Volta's invention of the first electric battery, the voltaic pile. In 1834, Michael Faraday defined the fundamental laws of electrolysis, setting the foundation for further advances in the field.[43]

Hermann Kolbe was a pioneer in the emergence of electrosynthesis, performing the first synthetic reactions driven by electricity. His radical decarboxylative dimerization of carboxylic acids represented a milestone in electro-organic chemistry. Later, other scientists, including Haber and Fiechter, made significant contributions to the development of electrosynthetic methodologies (**Scheme 7**).[44]

Another landmark reaction in the field of electrochemistry is the Shono oxidation, which involves the anodic removal of two electrons from compound **33** to generate the iminium intermediate **34**, a key reactive species that can undergo further transformations.[45]

In the twentieth century, Hickling proposed that electrochemical reactions could be conducted under potentiostatic control instead of the conventional constant-current (galvanostatic) electrolysis.[46] This innovation broadened the applicability of electrochemistry to industrial-scale processes and established it as an economically viable approach for producing commodity chemicals. Notable examples include the Simons fluorination process,

---

[40] MARKEN, F.; ATOBE, M. **Modern Electrosynthetic Methods in Organic Chemistry**. 1st ed. CRC Press, 2018.
[41] YUAN, Y.; LEI, A. Is electrosynthesis always green and advantageous compared to traditional methods? **Nature Communications**, 2020, 11, 802.
[42] ZHU, C. *et al.* Organic electrochemistry: molecular syntheses with potential. **ACS Central Science**, 2021, 7(3), 415-431
[43] FARADAY, M. Siebente Reihe von Experimental-Untersuchungen über Elektricitat. **Annalen der Physik**, 1834, 109, 433–451.
[44] KOLBE, H. Untersuchungen über die Elektrolyse organischer Verbindungen. **Annalen der Chemie und Pharmacie**, 1849, 69, 257.
[45] SHONO, T. Electroorganic chemistry in organic synthesis. **Tetrahedron**, 1984, 40, 811-850.
[46] HICKLING, A. Studies in electrode polarisation. Part IV. The automatic control of the potential of a working electrode. **Transactions of the Faraday Society**, 1942, 38, 27-33.

the Monsanto adiponitrile process, and the BASF lysmeral synthesis via anodic benzylic oxidation, all of which demonstrated the scalability of electroorganic synthesis.[47]

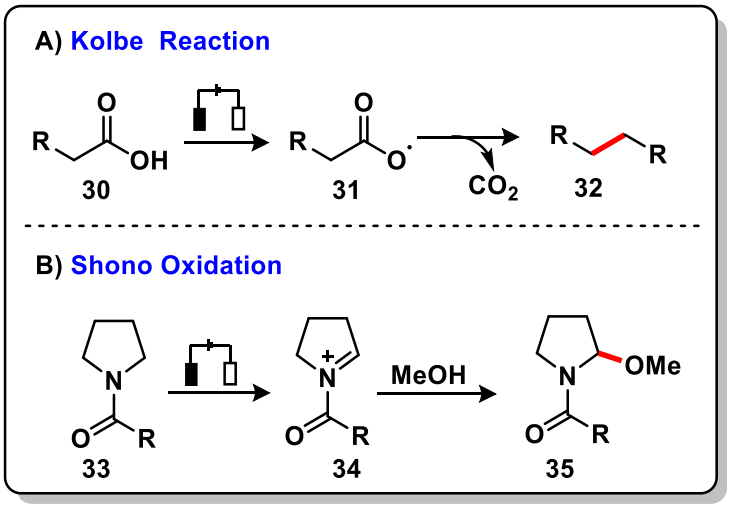

Scheme 7: A) Kolbe reaction and B) Shono oxidation.

Electrosynthesis has been recognized as a green methodology for chemical transformations because electrons are residue-free reactant and can be sustainably generated from renewable energy sources such as wind or solar power. Consequently, interest in this approach continues to grow. From a technical standpoint, effective electrochemical transformations require knowledge of suitable functionalities and operating modes, including instrumentation, electrodes, electrolytes, solvents, and the electrochemical cell design.[48]

Instrumentation determines whether electrolysis is performed under potentiostatic control (chronoamperometry) or galvanostatic control (chronopotentiometry). In potentiostatic electrolysis, a potentiostat applies a fixed potential to the working electrode (WE) relative to a reference electrode (RE), while current flows between the WE and the counter electrode (CE). In galvanostatic electrolysis, a galvanostat passes a constant current through the cell, allowing the WE potential to fluctuate. This mode typically requires only two electrodes. Each method presents distinct advantages and limitations in terms of control, performance, and reproducibility.

[47] MEYER, T. H. *et al.* Powering the future: how can electrochemistry make a difference in organic synthesis? **Chem**, 2020, 6, 2484-2496.
[48] KINGSTON, C. *et al.* A survival guide for the "electro-curious". **Accounts of Chemical Research**, 2020, 53(1), 72-83.

The choice of WE material is critical to optimizing product yield and selectivity in electrosynthesis. Ideal WEs should possess:[49]

- High conductivity;
- Wide usable potential range;
- Chemical inertness;
- Physical stability under varying conditions (temperature, pressure, solvents);
- Fast charge transfer;
- Low residual current.

Carbon-based electrodes are particularly popular due to their cost-effectiveness compared with noble metals such as platinum, as well as their advantageous combination of high surface area, good electrical conductivity, and chemical stability (**Figure 3**).[50]

A common example is glassy carbon, a dense, structurally robust form of carbon characterized by excellent mechanical strength, high chemical resistance, low background current, and a wide potential window that enables a broad range of redox reactions. Reticulated vitreous carbon (RVC) is another widely used material, composed of a foam-like network with an open, interconnected structure. Its high surface area enhances mass transfer, making it suitable for applications in electrocatalysis and electrochemical energy storage.[51,52]

Carbon felt electrodes, composed of randomly dispersed carbon fibers, offer high porosity, which facilitates efficient mass transport of reactants and products.[53] Graphite, another form of carbon, is inexpensive and highly conductive but less chemically stable than glassy carbon. It is thus preferred for applications in which chemical stability is not a primary requirement, such as certain analytical techniques or short-duration electrochemical experiments.[54]

---

[49] HEARD, D. M.; LENNOX, A. J. Electrode materials in modern organic electrochemistry. **Angewandte Chemie International Edition**, 2020, 59, 18866-18884
[50] KISSINGER, P.; HEINEMAN, W. R. **Laboratory Techniques in Electroanalytical Chemistry**. Revised and expanded. CRC Press, 2018.
[51] DE SOUZA VIEIRA, L. A review on the use of glassy carbon in advanced technological applications. **Carbon**, 2022, 186, 282-302.
[52] FRIEDRICH, J. M. *et al.* Reticulated vitreous carbon as an electrode material. **Journal of Electroanalytical Chemistry**, 2004, 561, 203-217.
[53] LE, T. X. H.; BECHELANy, M.; CRETIN, M. Carbon felt-based electrodes for energy and environmental applications: a review. **Carbon,** 2017, 122, 564-591.
[54] AKANDA, M. R. *et al.* Recent advances in nanomaterial-modified pencil graphite electrodes for electroanalysis. **Electroanalysis**, 2016, 28, 408-424.

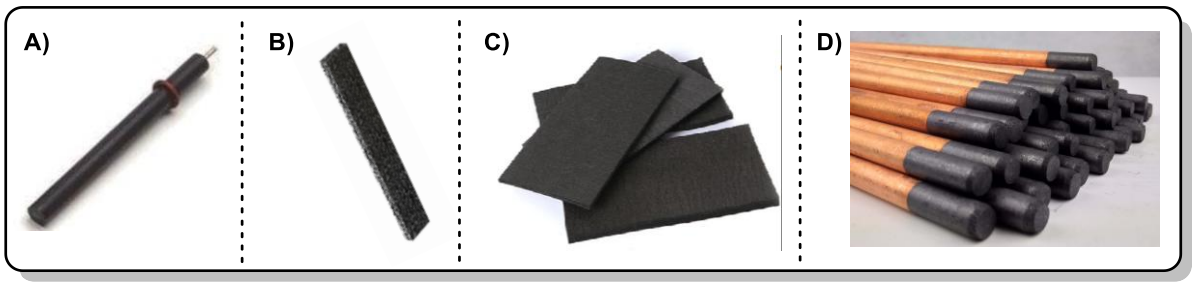

Figure 3: Different types of carbon electrodes, in A) the glassy carbon, B) the RVC, C) the carbon felt and D) graphite electrode.

Despite being more expensive than the carbon-based electrodes mentioned above, metal electrodes play a critical role in electrochemical cells by providing efficient platforms for electron-transfer reactions. They are generally characterized by fast electron-transfer kinetics and wide potential windows, enabling a broad range of redox transformations. Platinum and its alloys are widely used due to their mechanical strength, ease of cleaning, chemical stability, and corrosion resistance.[55] However, the high cost of platinum limits its large-scale use. Mercury is another historically important electrode material, valued for its reproducible surface and the ability to renew it easily. Nevertheless, its high toxicity and susceptibility to oxidation restrict its applicability in modern systems.[56]

The choice of solvent and supporting electrolyte is equally critical in electrochemical cells. Factors to consider when selecting a solvent–electrolyte system include:[57]

- The binding affinity or buffering capacity of the electrolyte;
- The influence of the electrolyte on the bilayer structure, that is, the organization of solvent and ions at the electrode–electrolyte interface;
- Possible reactions with electrogenerated intermediates;
- The potential range of the solvent;
- The ease of electrolyte recrystallization.

An ideal solvent should be chemically and electrochemically stable, have a high dielectric constant to dissolve sufficient amounts of supporting electrolyte, and be capable of dissolving the analyte of interest. These properties help maintain charge neutrality, minimize solution resistance, and facilitate mass transport to and from the working electrode.

---

[55] JERKIEWICZ, G. Applicability of platinum as a counter-electrode material in electrocatalysis research. **ACS Catalysis**, 2022, 12, 2661-2670.
[56] VYSKOČIL, V.; BAREK, J. Mercury electrodes – possibilities and limitations in environmental electroanalysis. **Critical Reviews in Analytical Chemistry**, 2009, 39, 173-188.
[57] MCKENZIE, E. C. R. *et al.* Versatile tools for understanding electrosynthetic mechanisms. **Chemical Reviews**, 2022, 122, 3292-3335.

The design of the electrochemical cell is another key parameter in electrosynthesis experiments. Two widely applied configurations are the undivided and divided cell (**Figure 4**).[58] Undivided cells have a simpler design and are easier to operate, but they are more prone to side reactions and the formation of undesired products. Divided cells offer greater selectivity because they employ porous separators or semi-permeable membranes that control ion movement and limit undesired cross-reactions. Careful cell design can therefore significantly enhance both the selectivity and efficiency of electrochemical processes.[59]

Electrochemical transformations offer several advantages over traditional chemical methods. They can often be performed under milder reaction conditions, avoiding the use of hazardous reagents and costly catalysts. This green synthetic approach provides high selectivity, broad functional group tolerance, high atom economy, access to novel reactivities, and the *in situ* generation of reactive species, making it an attractive and sustainable alternative to many conventional processes. [44,60] These advantages position electrosynthesis as a promising platform for the development of innovative methods in organic synthesis.

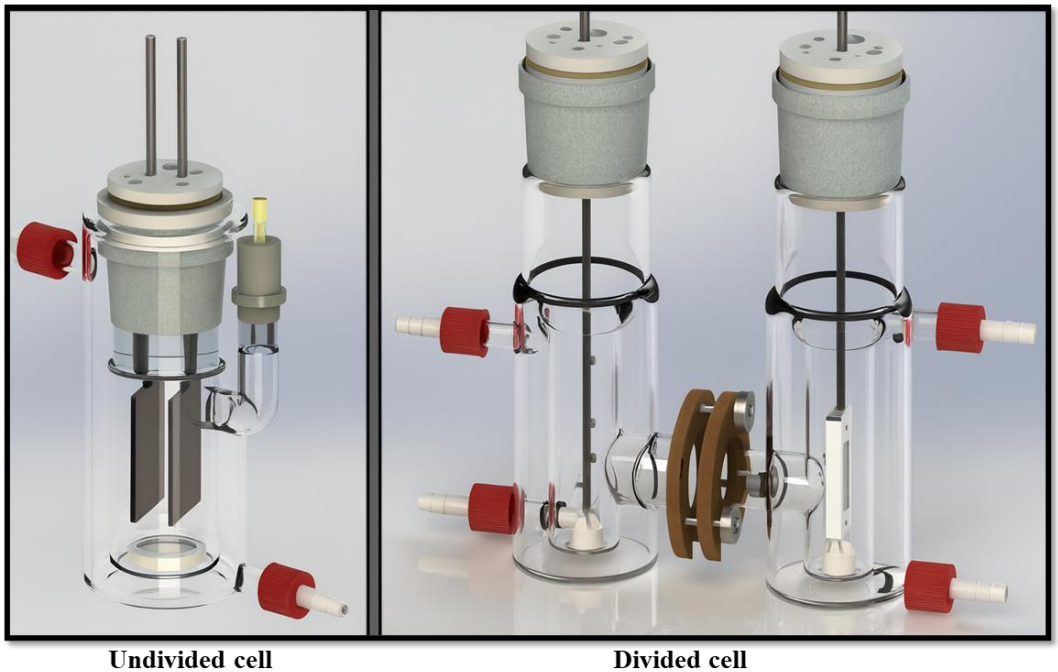

Figure 4: Representation of an undivided cell and of a divided cell. (Reproduced from ref. 60)

[58] WALDVOGEL, S. R. *et al.* Electrochemical arylation reaction. **Chemical Reviews**, 2018, 118(14), 6706-6765.
[59] POLLOK, D.; WALDVOGEL, S. R. Electro-organic synthesis – a 21st century technique. **Chemical Science**, 2020, 11(46), 12386-12400.
[60] SCHEIDE, M. R. *et al.* Electrohalogenation of organic compounds. **Organic & Biomolecular Chemistry**, 2021, 19, 2578.

Several research groups, including ours, have explored new reactions enabled by electrochemistry, leading to more accessible routes for the synthesis of valuable building blocks. As illustrated in **Scheme 6**, the Brahmachari group recently reported a straightforward and efficient electrochemical protocol for the selenization and sulfenylation of naphthoquinones.[39]

In 2020, our group developed an efficient electrochemical selenization–cyclization protocol employing platinum anodes and cathodes in undivided electrochemical cells for the preparation of naphthoquinones. Using lapachol or lawsone derivatives as starting materials, a diverse series of multifunctional selenium-containing quinonoid redox compounds was synthesized (**Scheme 8**).[61]

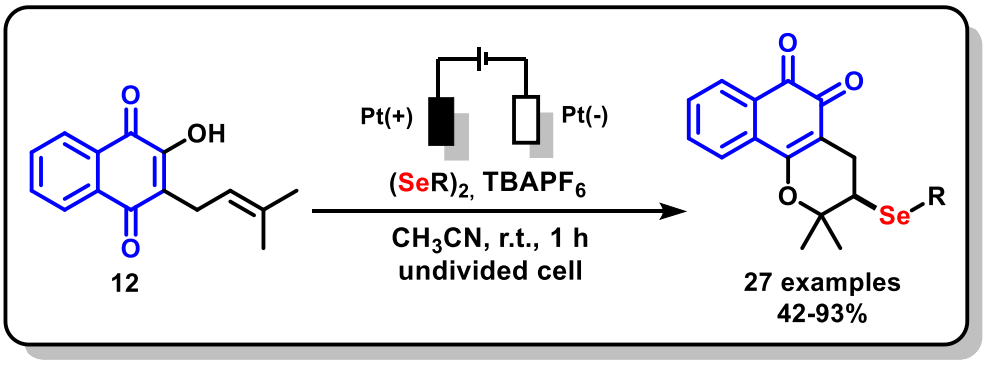

Scheme 8: Electrochemical selenization/cyclization.

[61] KHARMA, A. *et al.* Electrochemical selenation/cyclization of quinones: a rapid, green and efficient access to functionalized trypanocidal and antitumor compounds. **European Journal of Organic Chemistry**, 2020, 29, 4474-4486.

2.2 RESEARCH PURPOSE

The primary objective of this research is to develop a sustainable synthetic methodology for the preparation of naphthoquinones with potential antitumor activity. This will be achieved through the electrosynthesis of derivatives from lapachol (**12**) and lawsone (**9**), minimizing the use of hazardous reagents and reducing waste generation.

Beyond its environmental advantages, this approach highlights the potential of electrosynthesis to provide rapid and efficient access to structurally diverse naphthoquinone derivatives. Such versatility is particularly valuable in the early stages of drug discovery, where expanding the range of available compounds is essential for identifying promising bioactive scaffolds.

Overall, this work seeks to demonstrate that electrosynthesis can serve not only as a greener alternative to conventional methods but also as a powerful tool for generating chemical diversity, thereby contributing to the development of innovative molecules with applications in cancer research and beyond.

2.2.1 General Objective

Development of an electrosynthetic methodology for the sulfenylation/cyclization of naphthoquinones and exploration of the biological potential of these new derivatives in cancer treatment.

2.2.2 Specific Objectives

Step 1: Electrosynthetic Methodology for Sulfenylation/Cyclization of Lapachol (**12**).

- Design an electrosynthetic protocol to introduce sulfur (sulfenylation) and induce cyclization in lapachol;
- Optimize reaction parameters, including electrode material, applied potential, solvent, and temperature, to achieve high yields and selectivity;
- Investigate the reaction mechanism to elucidate the pathway.

Step 2: Scope expansion of the developed methodology and Oxidation of synthesized molecules.

- Apply the developed protocol to react lapachol (**12**) and C-allyl lawsone (**36**) with various disulfides, including both alkyl and aryl disulfides.
- Perform selective oxidation of the synthesized sulfides to the corresponding sulfones, given that sulfone derivatives are frequently associated with enhanced antitumor activity.

Step 3: Characterization

- Conduct comprehensive structural characterization of all synthesized compounds at each stage using appropriate analytical techniques, including NMR spectroscopy, mass spectrometry, IR spectroscopy, melting point determination, and, when feasible, single-crystal X-ray diffraction to confirm molecular structure and purity.

Step 4: Antitumor Activity Testing.

- Assess the antitumor activity of each compound using appropriate in vitro assays, enabling correlation between structural features and biological response.

Scheme 9 shows a general idea of the purpose of the work.

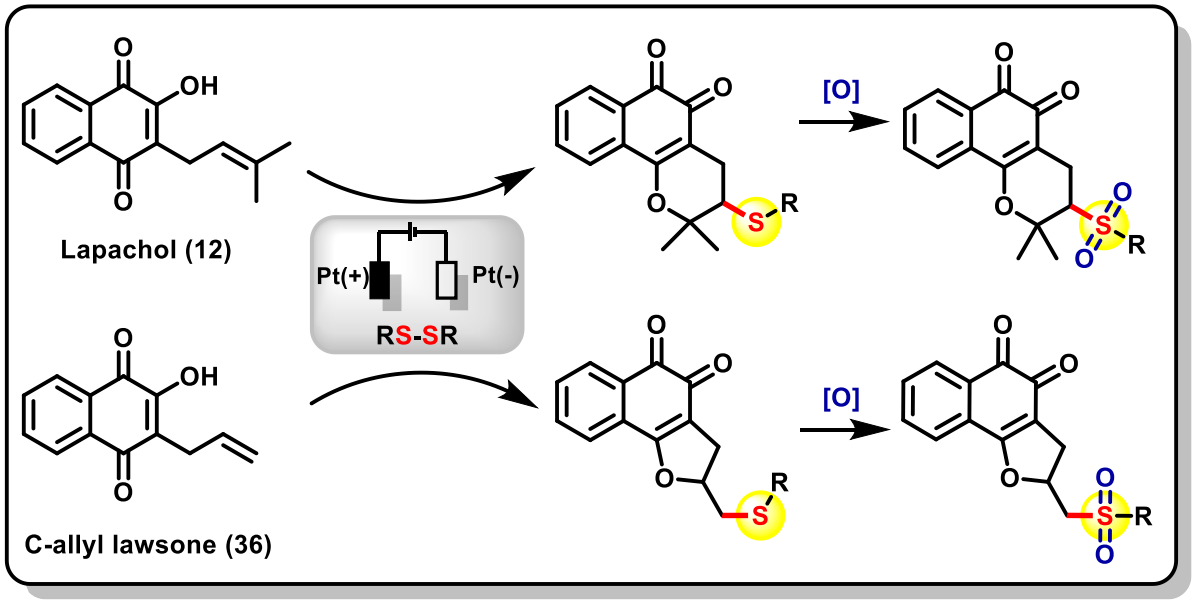

Scheme 9: General representation of the research objectives.

2.3 RESULTS AND DISCUSSION

2.3.1 Sulfur-containing cyclization of naphthoquinones: optimization and synthesis

Based on the electrochemical cyclization methodology for selenium incorporation previously developed by our group,[62] we initiated our studies on sulfur insertion into quinoidal systems via electrosynthesis, using lapachol (**12**) and diphenyl disulfide (**37**) as model substrates. The electrochemical setup consisted of two undivided platinum electrodes (Pt(+) | | Pt(-): 10 x 10 x 0.2 mm) fully immersed in the solution, which was subjected to a constant current of 10 mA and 20 V.

As an initial step toward achieving sulfenylation/cyclization of lapachol (**12**), we examined the influence of the supporting electrolyte on reaction performance. The first electrolyte tested was tetrabutylammonium iodide (nBu$_4$NI) (**Table 1**, entry1). After one hour, a complex mixture of products was obtained, suggesting that the iodide anion interfered with the desired product formation. To address this, tetrabutylammonium tetrafluoroborate (nBu$_4$NBF$_4$) was evaluated as an alternative (**Table 1**, entry 2), resulting in improved reaction control and affording the target product in 25% yield after 3 hours.

Further optimization led us to test tetrabutylammonium hexafluorophosphate (nBu$_4$NPF$_6$) as the electrolyte. This choice proved most effective, delivering the sulfenylation/cyclization product in 59% yield after 3 hours (**Table 1**, entry 3), thus underscoring the critical role of the electrolyte in the electrosynthesis process.

The influence of electrolyte loading was subsequently assessed. Reducing the amount of nBu$_4$NPF$_6$ led to a marked yield drop, with only 26% of product **38** being obtained (**Table 1**, entry 4). Conversely, increasing the electrolyte quantity resulted in lower yields of 46% and 40% (**Table 1**, entries 5 and 6, respectively). These findings indicate that an optimal concentration of 1 equivalent of nBu$_4$NPF$_6$ is necessary to achieve maximum efficiency.

With the electrolyte optimized, the effect of solution concentration on the reaction was investigated. Using acetonitrile (MeCN) as the solvent, a significant decrease in product formation was observed when the reaction mixture was diluted from 0.02 M to 0.01 M, yielding only trace amounts of the desired compound (**Table 1**, entry 7). This reduction in

[62] KHARMA, A. *et al.* Electrochemical selenation/cyclization of quinones: a rapid, green and efficient access to functionalized trypanocidal and antitumor compounds. **European Journal of Organic Chemistry**, 2020, 29, 4474-4486.

yield is attributed to the lower concentration of active species at the electrode surface, which slows the reaction rate in diffusion-controlled processes.[63]

Increasing the reaction concentration in MeCN resulted in a slight decrease in yield, with the target compound being obtained in 51% yield (**Table 1**, entry 8). Although the variation is small and may lie within the experimental error, this reduction can also be explained by mass-transfer limitations, which is an intrinsic factor in electrochemical systems. In highly concentrated solutions, the diffusion layer at the electrode interface can become saturated, restricting the replenishment of reactants at the electrode surface. This limitation is particularly detrimental when the reaction is under diffusion control, as it slows the overall electron-transfer rate and increases the probability of side reactions involving reactive intermediates.[64] These results reinforce the need for precise tuning of the reaction concentration: excessive dilution limits the number of active species available for electron transfer, while excessive concentration can hinder their mobility toward the electrode.

To further refine the methodology, the effect of solvent choice was systematically investigated. Solvents play a dual role in electrosynthesis: they act as the medium for solubilizing reactants and electrolytes, and they govern the ionic conductivity and stability of electrochemically generated intermediates. As shown in **Table 1**, MeCN)remained the most effective solvent, delivering the highest yields under the optimized conditions.

When acetone was employed, the desired product was obtained in only 30% yield (**Table 1**, entry 9), likely due to its lower dielectric constant and reduced ability to stabilize ionic intermediates. Methanol (MeOH) produced a complex mixture of products after 3 hours, which can be attributed to competitive side reactions, including direct solvent oxidation at the anode and nucleophilic trapping of cationic intermediates.

Polar aprotic solvents such as dimethylformamide (DMF), dimethyl sulfoxide (DMSO), and dimethylacetamide (DMAc) failed to produce significant amounts of the target compound (**Table 1**, entries 10–15). These solvents, despite their high dielectric constants, possess high viscosities that hinder ion mobility, reducing mass transfer to the electrode surface. In addition, DMF and DMAc are susceptible to anodic oxidation at the potentials required for the sulfenylation/cyclization process, leading to decomposition and loss of efficiency.

---

[63] a) FUCHIGAMI, T.; ATOBE, M.; INAGI, S. **Fundamentals and Applications of Organic Electrochemistry: Synthesis, Materials, Devices**. John Wiley & Sons, 2014.b) TANAKA, N. Solvent effects on mechanisms and characteristics of electrode reactions. **Electrochimica Acta**, 1976, 21, 701-710.

[64] FRY, A. J. Solvents and supporting electrolytes. In: **Laboratory Techniques in Electroanalytical Chemistry, Revised and Expanded**. CRC Press, 2018. p. 469-485.

In the case of dichloromethane (DCM) and tetrahydrofuran (THF), the absence of product can be rationalized by their relatively low dielectric constants, which result in poor electrolyte dissociation and consequently low ionic conductivity. Furthermore, both solvents have narrow electrochemical stability windows, which may cause solvent degradation under the applied potentials.[51]

Table 1: Results of the optimization for the electrolyte and solvent. Isolated yields after column chromatography.

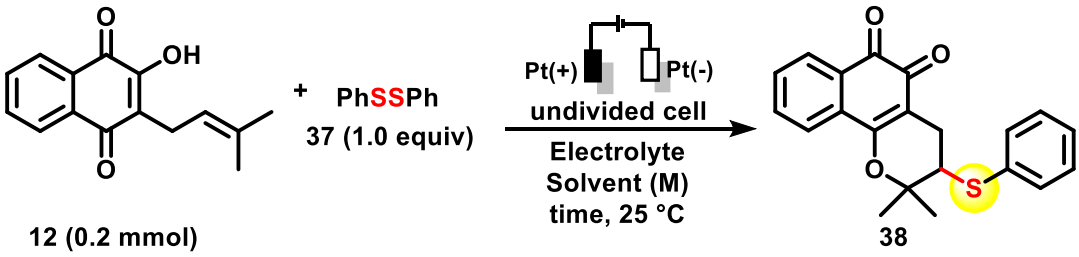

Entry	Solvent (M)	Electrolyte (equiv)	Current	time/h	Yield%
1	MeCN (0.02)	nBu$_4$NI (1.0)	10 mA	1.0	mixture
2	MeCN (0.02)	nBu$_4$NBF$_4$ (1.0)	10 mA	3.0	25
3	MeCN (0.02)	nBu$_4$NPF$_6$ (1.0)	10 mA	3.0	59
4	MeCN (0.02)	nBu$_4$NPF$_6$ (0.8)	10 mA	3.0	26
5	MeCN (0.02)	nBu$_4$NPF$_6$ (1.2)	10 mA	3.0	46
6	MeCN (0.02)	nBu$_4$NPF$_6$ (1.5)	10 mA	3.0	40
7	MeCN (0.01)	nBu$_4$NPF$_6$ (1.0)	10 mA	3.0	traces
8	MeCN (0.04)	nBu$_4$NPF$_6$ (1.0)	10 mA	3.0	51
9	Acetone (0.02)	nBu$_4$NPF$_6$ (1.0)	10 mA	3.0	30
10	DMF (0.02)	nBu$_4$NPF$_6$ (1.0)	10 mA	24	No Reaction
11	DMSO (0.02)	nBu$_4$NPF$_6$ (1.0)	10 mA	24	traces
12	DCM (0.02)	nBu$_4$NPF$_6$ (1.0)	10 mA	24	No Reaction
13	THF (0.02)	nBu$_4$NPF$_6$ (1.0)	10 mA	24	No Reaction
14	MeOH (0.02)	nBu$_4$NPF$_6$ (1.0)	10 mA	3.0	mixture
15	DMAc (0.02)	nBu$_4$NPF$_6$ (1.0)	10 mA	24	traces

After optimizing solvent and electrolyte, the influence of applied current on reaction performance was investigated. The applied current directly affects the potential at the working electrode, which in turn controls the rate of electron transfer to and from the reactants. A decrease from the optimized current value (**Table 2**, entry 1) led to a lower reaction rate, increasing the residence time of intermediates in solution and favoring side reactions or

reversion to starting materials. Conversely, increasing the applied current (**Table 2**, entries 2–3) can raise the electrode potential beyond the optimal window for selective substrate activation. This not only accelerates undesired oxidation or reduction pathways but can also promote competitive electrolyte degradation.

Overall, these findings highlight that the efficiency of the sulfenylation–cyclization process is governed by a delicate interplay between solvent properties, electrolyte composition, and current density. The optimized parameters ensure a balance between efficient mass transport, stability of reactive intermediates, and controlled electrode potentials, all of which are critical for achieving high selectivity and yield in electrochemical transformations.

As expected, when the reaction was performed without applying any current, no product formation was observed and lapachol (**12**) was fully recovered (**Table 2**, entry 4). This confirms that the transformation is purely electrochemically driven and that no significant background reactivity occurs under the reaction conditions in the absence of an external electron flow.

Subsequent experiments assessed the influence of electrode material and electrode configuration on the reaction outcome (**Table 2**, entries 5–7). In all cases where alternative electrode materials or asymmetric cathode/anode combinations were employed, the yields were markedly lower than the 59% obtained with the Pt(+)‖Pt(−) setup. This observation highlights the critical role of platinum as both anode and cathode in facilitating the sulfenylation/cyclization process. Platinum's unique combination of properties excellent electrical conductivity, broad electrochemical stability window, chemical inertness, and efficient electron-transfer kinetics likely contributes to its superior performance. Furthermore, platinum's resistance to surface passivation ensures a consistently active electrode surface, which is essential for sustaining the multi-electron processes involved in this reaction.

Temperature optimization revealed only marginal effects within the tested range. Conducting the reaction at lower temperatures resulted in a slight decrease in efficiency (**Table 2**, entries 8–9), likely due to reduced diffusion rates of reactants and intermediates in solution. Conversely, raising the temperature caused a sharp drop in yield (**Table 2**, entry 10). This detrimental effect at higher temperatures could be attributed to accelerated decomposition of electrochemically generated intermediates, increased rates of competing side reactions, or decreased selectivity in the redox steps.

The influence of reaction time was also evaluated while keeping all other parameters constant. Extending the reaction duration from the optimized value to 8 hours did not improve yield (**Table 2**, entry 11), suggesting that the reaction had reached completion or that the product was susceptible to degradation under prolonged electrolysis. This plateau in yield further suggests that the key electron-transfer and subsequent chemical steps proceed to completion within the optimized timeframe, and that extended electrolysis may only serve to overoxidize the product or consume it in secondary reactions.

Overall, these results emphasize that the optimal conditions for this sulfenylation/cyclization are highly dependent on maintaining both the appropriate electrode material and the precise electrolysis parameters. The choice of platinum electrodes, combined with controlled temperature, current, and reaction time, ensures a delicate balance between efficient conversion and preservation of product integrity.

Table 2: Results of the optimization for the electrode, current, temperature and time. Isolated yields after column chromatography.

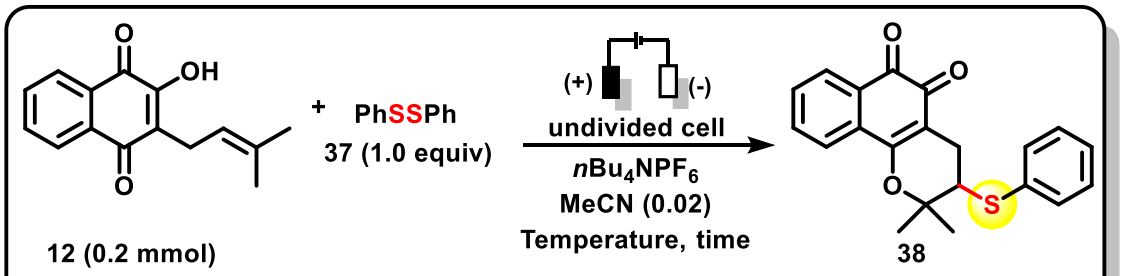

Entry	Electrode (+)	Electrode (-)	Current	Temperature/°C	time/h	Yield%
1	Pt	Pt	8 mA	25	3.0	35
2	Pt	Pt	12 mA	25	3.0	43
3	Pt	Pt	15 mA	25	3.0	41
4	Pt	Pt	-	25	3.0	No Reaction
5	Pt	RVC	10mA	25	3.0	12
6	RVC	Pt	10mA	25	3.0	18
7	RVC	RVC	10mA	25	3.0	19
8	Pt	Pt	10 mA	0	3.0	46
9	Pt	Pt	10 mA	10	3.0	46
10	Pt	Pt	10 mA	50	3.0	26
11	Pt	Pt	10 mA	25	8.0	59

In the final stage of optimization, the effect of the stoichiometric ratio between lapachol (**12**) and diphenyl disulfide (**37**) was investigated. Altering the equivalence of

diphenyl disulfide to either 0.8 or 1.2 relative to lapachol resulted in decreased yields of 22% and 48%, respectively (**Table 3**, entries 1–2). This outcome can be rationalized in terms of the delicate balance between chemical stoichiometry and mass transfer dynamics within the electrochemical cell. When the amount of disulfide is reduced, the balance shifts toward the starting materials, limiting product formation. Conversely, an excess of disulfide may increase solution viscosity and saturation effects at the electrode–solution interface, thereby impairing mass transport and decreasing the efficiency of electron transfer.

Once all variables were optimized, a scale-up experiment was performed using 0.5 mmol of lapachol (**12**). Under otherwise identical conditions, this modification resulted in a notable improvement of the isolated yield to 70% (**Table 3**, entry 3). This enhancement likely reflects a better match between the electrode surface area and the total amount of reactants, allowing more efficient utilization of the active electrode surface and improved local current distribution. Importantly, factors such as electrode geometry, surface roughness, and microscopic heterogeneity can significantly influence the local reaction environment, impacting both selectivity and yield.

With these parameters established, the methodology is now primed for extension to a broader substrate scope. The optimized conditions, providing a solid starting point for investigating the substrate scope, building upon the efficiency already demonstrated with the model substrate and extending it to more challenging disulfides.

Table 3: Results of the optimization for the lapachol (**12**) and diphenyl disulfide (**37**). Isolated yields after column chromatography.

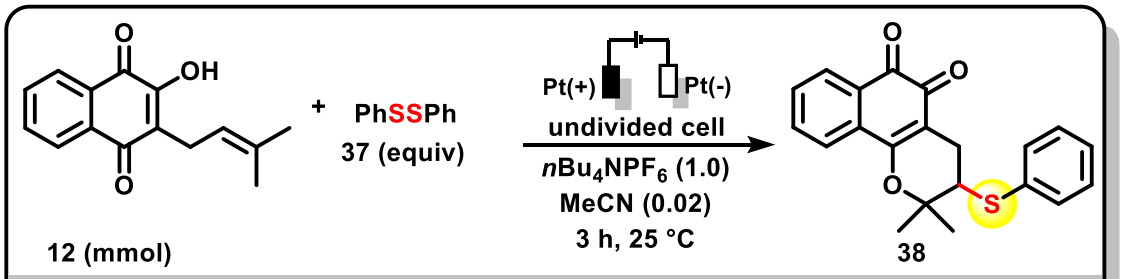

Entry	12 (mmol)	37 (equiv)	Current	Yield%
1	0.2	0.8	10 mA	22
2	0.2	1.2	10 mA	48
3	0.5	1.0	10 mA	70

After establishing the optimal conditions for the electrochemical sulfenylation/cyclization reaction, the scope and generality of the methodology were

systematically explored. Initially, the reaction of lapachol (**12**) with a series of structurally diverse disulfides was investigated, enabling the synthesis of products with varied substitution patterns and electronic properties.

As illustrated in **Scheme 10**, the methodology proved to be highly effective, furnishing nine distinct derivatives. The substrate set included disulfides bearing electron-donating groups (EDGs), electron-withdrawing groups (EWGs), as well as aliphatic disulfides. The influence of substituent electronic effects was particularly evident in the reaction outcomes. EDG-containing disulfides afforded the highest yields: for example, the para-methyl-substituted product **38b** was isolated in an exceptional 96% yield, and the para-methoxy derivative **38c** in 94% yield. These results suggest that electron-rich aromatic disulfides may enhance the electrophilicity of the intermediate species or facilitate a more favorable redox profile under the applied electrochemical conditions.

Conversely, EWG-containing disulfides, such as bromo (**38d**), chloro (**38e**), and fluoro (**38f**) derivatives, resulted in comparatively lower yields, ranging from 40% to 71%. This decrease is likely due to the electron-withdrawing nature of these substituents, which could diminish the reactivity of the disulfide toward the electrophilic intermediates in the proposed mechanism. The detailed mechanistic rationale for this behavior will be addressed later in the text.

The methodology also proved effective for substrates bearing meta-substituted methyl groups, exemplified by product **38g**, obtained in 53% yield, indicating that steric effects alone do not preclude product formation. In addition, the process was successfully applied to aliphatic disulfides, affording products **38h** and **38i** in 61% and 65% yield, respectively, thereby demonstrating the method's versatility beyond aromatic systems.

All synthesized compounds were fully characterized by ^{1}H and ^{13}C Nuclear Magnetic Resonance (NMR) spectroscopy, High-Resolution Mass Spectrometry (HRMS), and Infrared (IR) spectroscopy. Furthermore, single-crystal X-ray diffraction unequivocally confirmed the structures of **38b**, **38e**, **38f**, and **38h**, validating the success of the synthetic strategy. The complete characterization data and spectra are provided in the Appendix of this thesis.

In a subsequent phase, the methodology was applied to C-allyl-lawsone (**36**), a derivative prepared according to established literature procedures (described in the Experimental Section). In line with our earlier studies on electrochemical selenation/cyclization using C-allyl-lawsone as a substrate, the reactions predominantly yielded 5-membered heterocyclic products (**Scheme 11**).

When employing diphenyl disulfide (**37**), the sulfenylation/cyclization product **39a** was obtained in a modest 25% yield. Notably, the introduction of EDG substituents once again had a pronounced positive effect: para-methyl (**39b**) and para-methoxy (**39c**) derivatives were obtained in 50% and 63% yield, respectively. In contrast, products bearing EWG substituents such as chlorine (**39d**) and fluorine (**39e**) were isolated in moderate yields of 35% and 37%. Finally, an aliphatic disulfide-derived product (**39f**) was synthesized but only in 20% yield, suggesting that in the case of C-allyl-lawsone, the reaction is more sensitive to steric and electronic mismatches between the substrate and the disulfide partner.

These results collectively demonstrate that the developed electrochemical protocol exhibits broad applicability across structurally and electronically diverse disulfides, although the reaction efficiency is clearly modulated by the electronic nature of the substituents. This insight provides a foundation for rational substrate design in future applications, particularly toward the synthesis of bioactive sulfur-containing quinones.

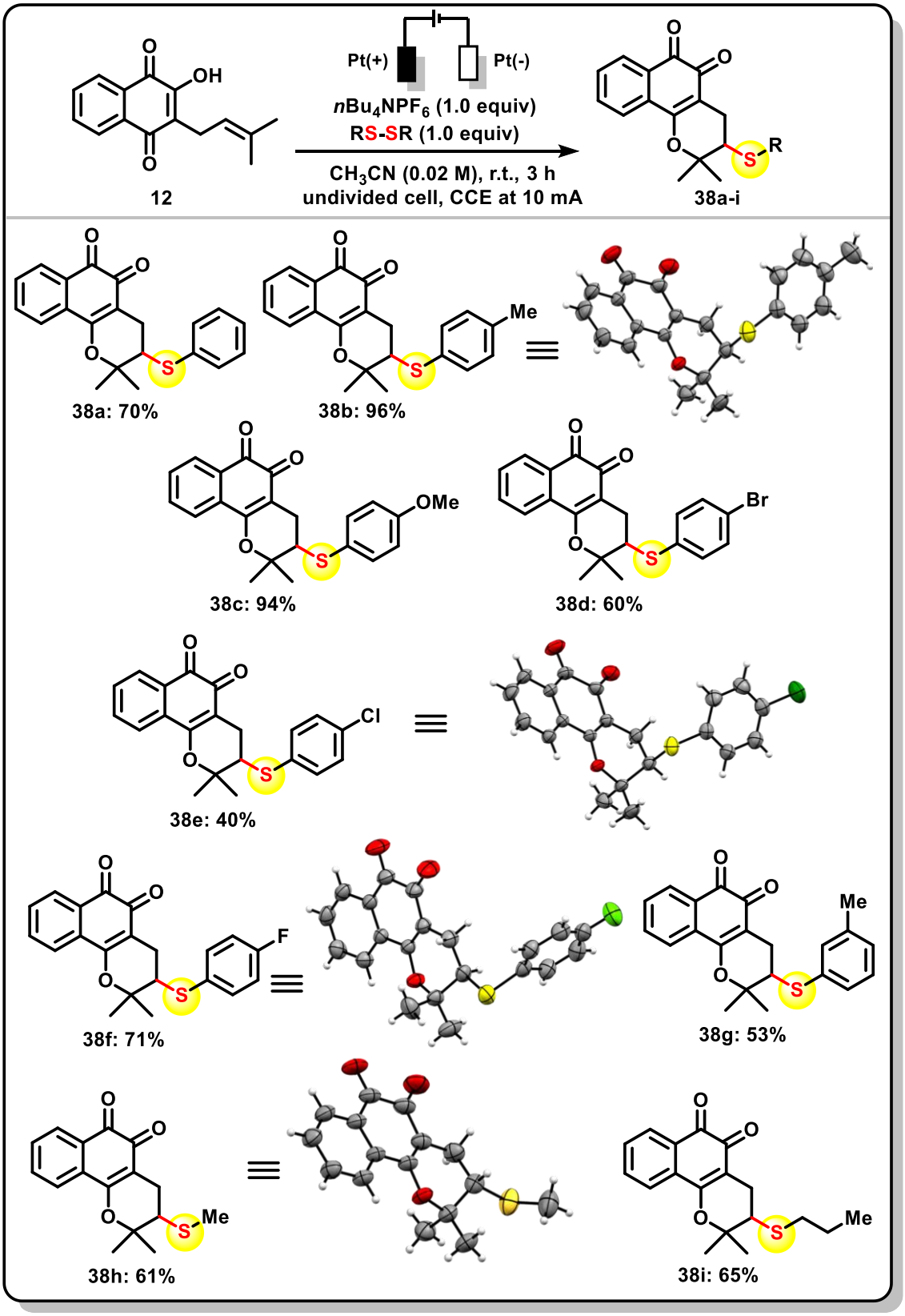

Scheme 10: Lapachol (**12**) derivatives synthesized using electrosynthesis. Crystal structures of compounds **38b**, **38e**, **38f** and **38h** are also represented here. Isolated yields after column chromatography.

For further validation, the structures of **39c**, **39d** and **39e** were elucidated using crystallographic methods. Together, these results provide insight into the reactivity of *C*-allyl-lawsone and its compatibility with various disulfides, both with EDG and EWG groups further extending the utility of this methodology in the synthesis of diverse compounds.

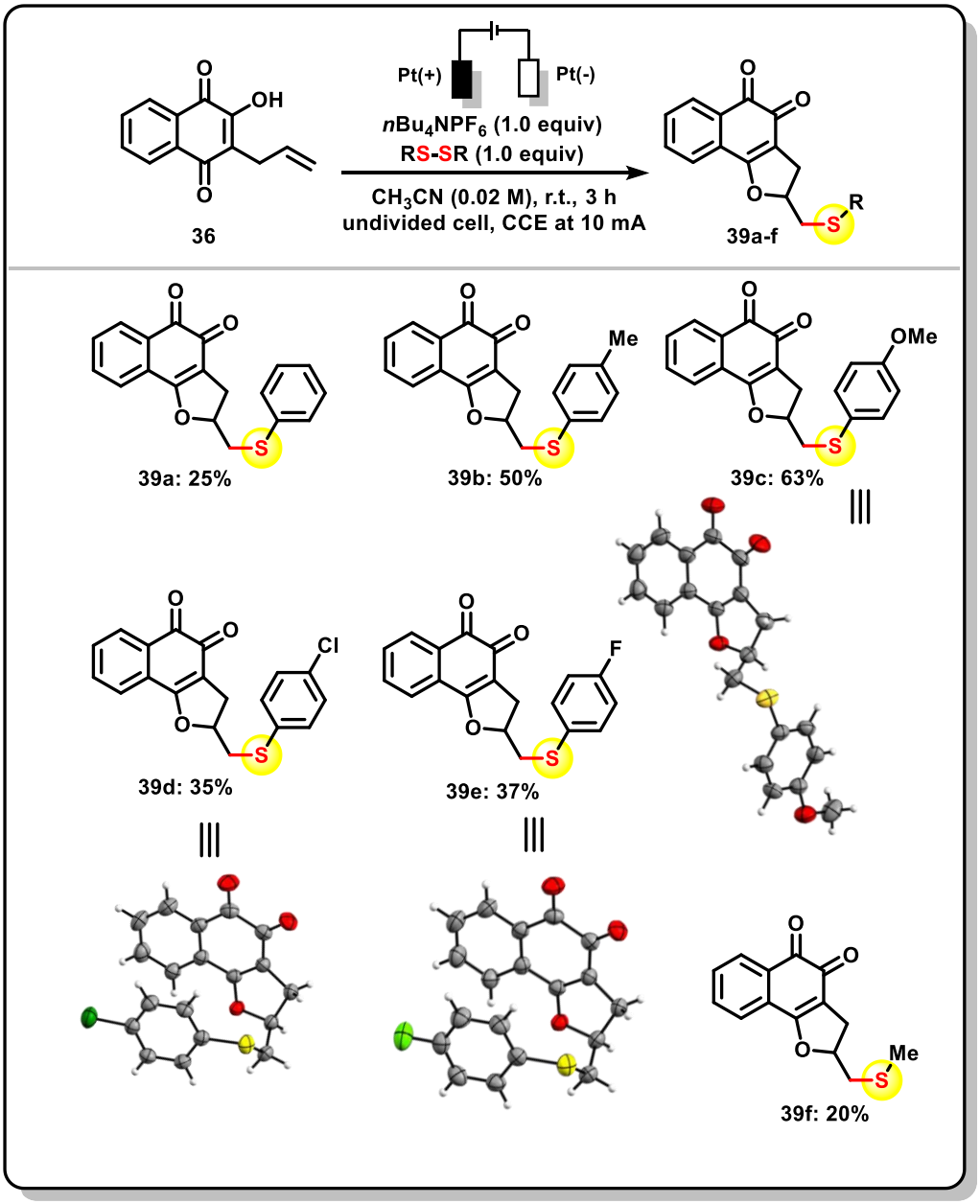

Scheme 11: C-allyl-lawsone (**36**) derivatives synthesized using electrosynthesis. Crystal structures of compounds **39c**, **39d and 39e** are also represented here. Isolated yields after column chromatography.

Another class of sulfur derivatives with remarkable biological activities, as previously discussed, are sulfones. In light of this, we performed the oxidation of selected sulfur-containing naphthoquinone derivatives obtained from lapachol (**12**) and C-allyl-lawsone (**36**) to their corresponding sulfone analogues using a classical oxidative protocol mediated by $RuCl_3 \cdot H_2O$ and $NaIO_4$ (**Scheme 12**).

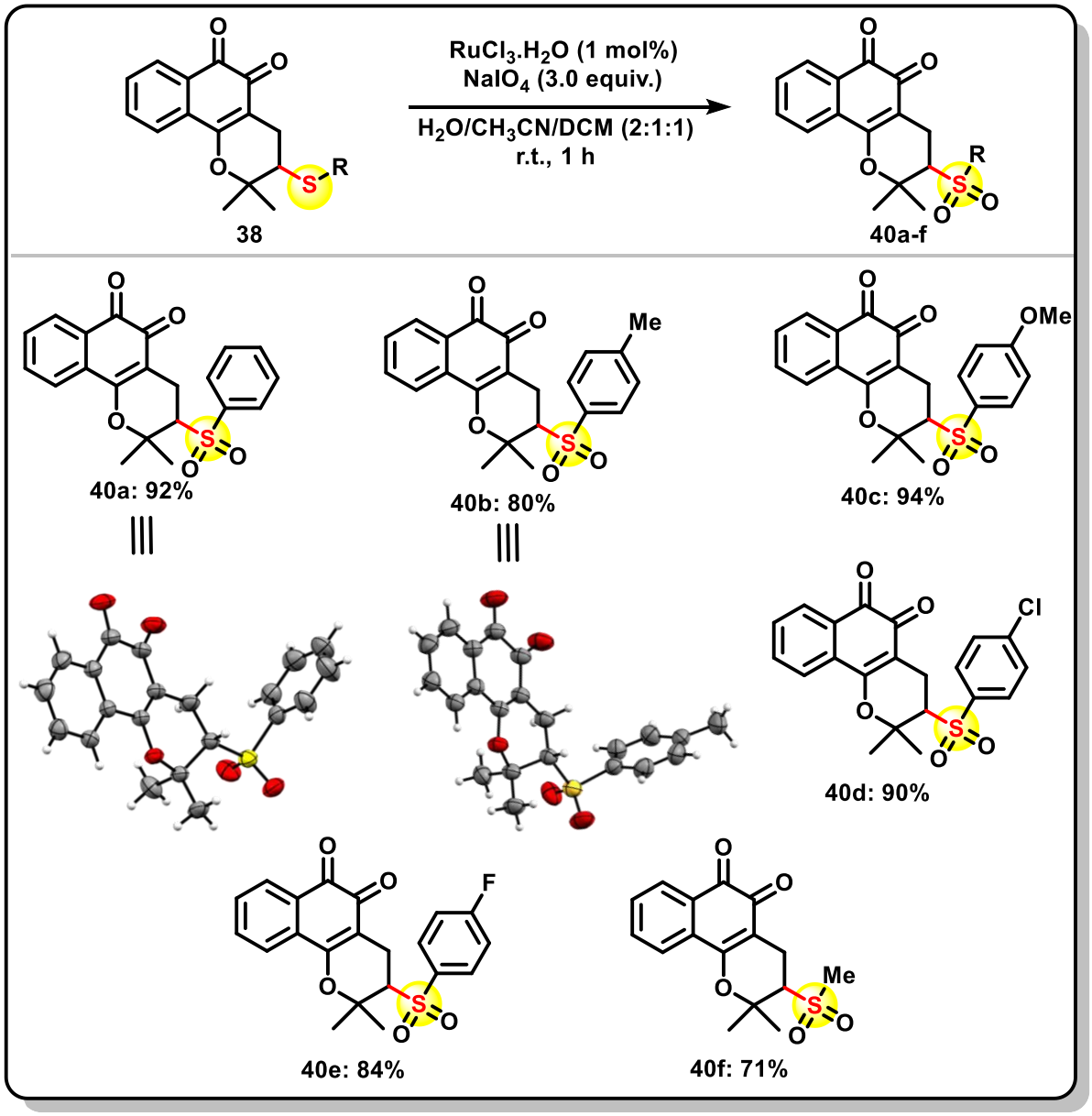

Scheme 12: Lapachol (**12**) derived sulfones synthesis. Crystal structures of compounds **40a,** and **40b** are also represented here. Isolated yields after column chromatography.

Derivatives originating from lapachol (**12**) were efficiently converted into the corresponding oxidized products (**40a–40f**) in excellent yields, ranging from 71% to 94%. The molecular structures of **40a** and **40b** were unequivocally confirmed by single-crystal X-

ray diffraction analysis, providing solid structural evidence for the identity of the synthesized lapachone-derived sulfones (**Scheme 12**).

As representative examples, compounds **41a**, **41b**, and **41c**, derived from C-allyl-lawsone (**36**), were also subjected to the oxidation protocol. The corresponding sulfone derivatives were obtained in moderate yields ranging from 65% to 80%. The molecular structure of **41b** was unambiguously determined by single-crystal X-ray diffraction analysis (**Scheme 13**).

These results confirm the successful conversion of sulfur-containing naphthoquinone derivatives into their sulfone analogues, thereby broadening the chemical diversity of the synthesized library. This expanded set of compounds offers valuable candidates for subsequent studies, particularly in the context of exploring their potential biological and pharmacological properties.

2.3.2 Characterization of Synthesized Products

All compounds synthesized in this study were thoroughly characterized using a comprehensive set of analytical techniques, including ^{1}H and ^{13}C nuclear magnetic resonance (NMR) spectroscopy, high resolution mass spectrometry (HRMS), infrared (IR) spectroscopy, melting point (m.p.) analysis and, when possible, single-crystal X-ray diffraction. The corresponding spectra and analytical data are provided in the Appendix and detailed in the Experimental Section.

To illustrate the characterization process, we selected as a representative example the compound with a para-methylphenyl sulfide group (-SPhMe). This substituent recurs across the different series investigated in this work, making it suitable for exemplifying the spectroscopic features of both the electrosynthetic product and its oxidized sulfone derivative. Notably, no additional signals are expected in the ^{1}H and ^{13}C NMR spectra of the sulfone relative to its sulfide precursor; rather, slight downfield shifts are anticipated, attributable to the electron-withdrawing effect of the sulfonyl group and the presence of two carbonyl moieties.

The ^{1}H NMR spectrum (400 MHz, $CDCl_3$) of compound **38b** displayed two doublets at δ 8.03 and 7.77 ppm, along with two triplets at δ 7.63 and 7.50 ppm, corresponding to the unsubstituted benzene hydrogens (H-5, H-6, H-7, H-8) of the β-lapachone framework. Two additional doublets at δ 7.35 and 7.10 ppm were assigned to the aromatic protons of the para-

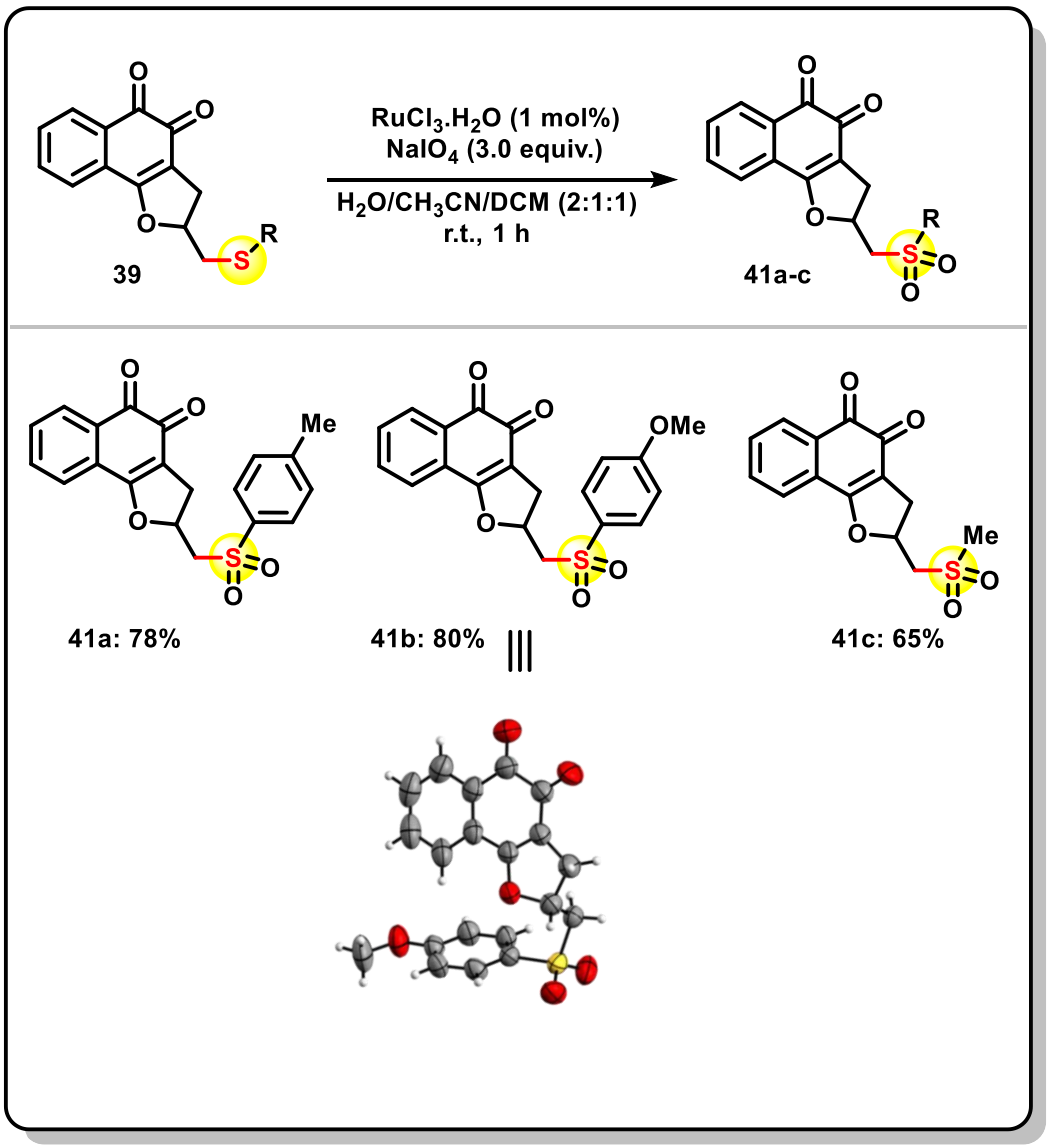

Scheme 13: C-allyl-lawsone (**36**) derived sulfones synthesis. Crystal structure of compound **41b** is also represented here. Isolated yields after column chromatography.

substituted phenyl ring (H-13, H-13′, H-14, H-14′).

Furthermore, three double doublets were identified: δ 3.26 ppm, corresponding to the methine hydrogens H-10 of the C-ring in β-lapachone; δ 2.97 and 2.58 ppm, corresponding to the diastereotopic methylene protons H-9, which couple both to each other and to H-10. Three singlets were also observed: δ 2.31 ppm, attributed to the methyl group on the para-substituted phenyl ring (H-16); and δ 1.65 and 1.50 ppm, corresponding to the diastereotopic methyl groups bound to the C-ring of β-lapachone (Figure 5). These data are in full agreement with

previously reported literature values for analogous compounds.[65]

In the ^{13}C-NMR spectrum, characteristic signals for the carbonyl carbons C-1 and C-2 appeared at δ 179.6 and 178.3 ppm, respectively, consistent with the β-lapachone core. Methine, methylene, and methyl carbons resonated at δ 50.8, 27.6, 24.7, 22.4, and 22.2 ppm, with DEPT 135 analysis confirming that the δ 22.4 ppm signal corresponds to C-9 (CH-2) due to its inverted phase. Vinyl carbons resonated in the expected δ 161.4–112.3 ppm range, confirming the integrity of the quinoidal system (**Figure 6**).

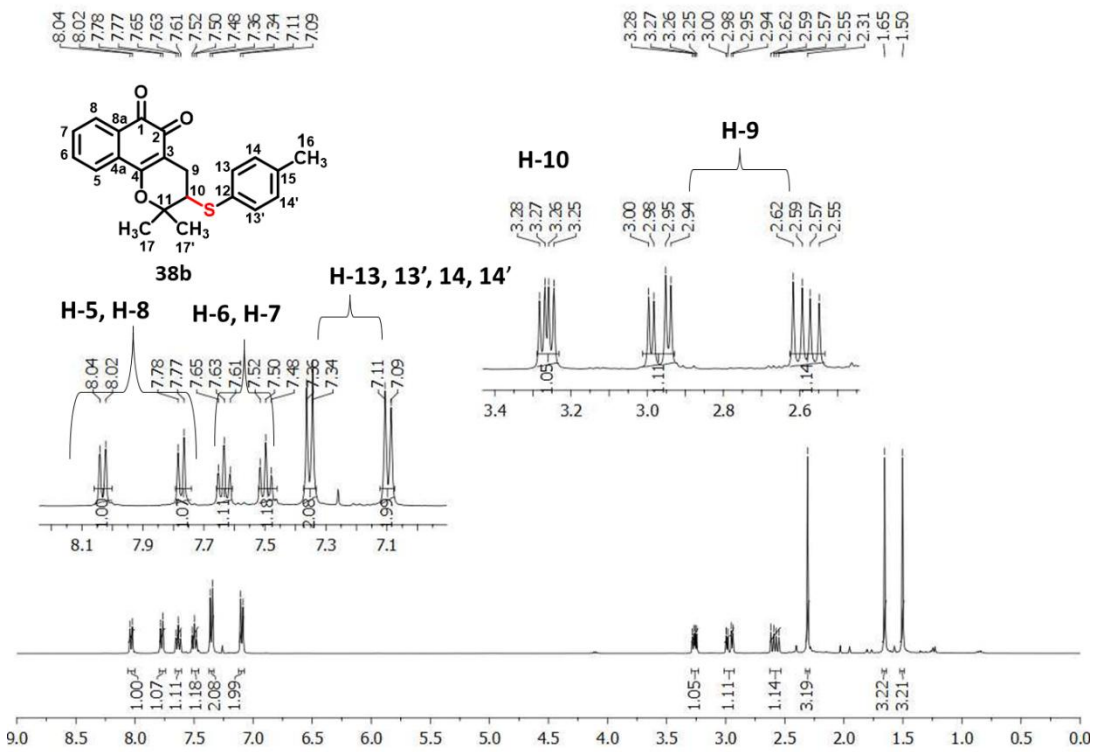

Figure 5: ^{1}H NMR spectrum of compound **38b** (400 MHz, $CDCl_3$).

[65] VIEIRA, A. A. *et al.* Hybrid compounds with two redox centres: modular synthesis of chalcogen-containing lapachones and studies on their antitumor activity. **European Journal of Medicinal Chemistry**, 2015, 101, 254-265.

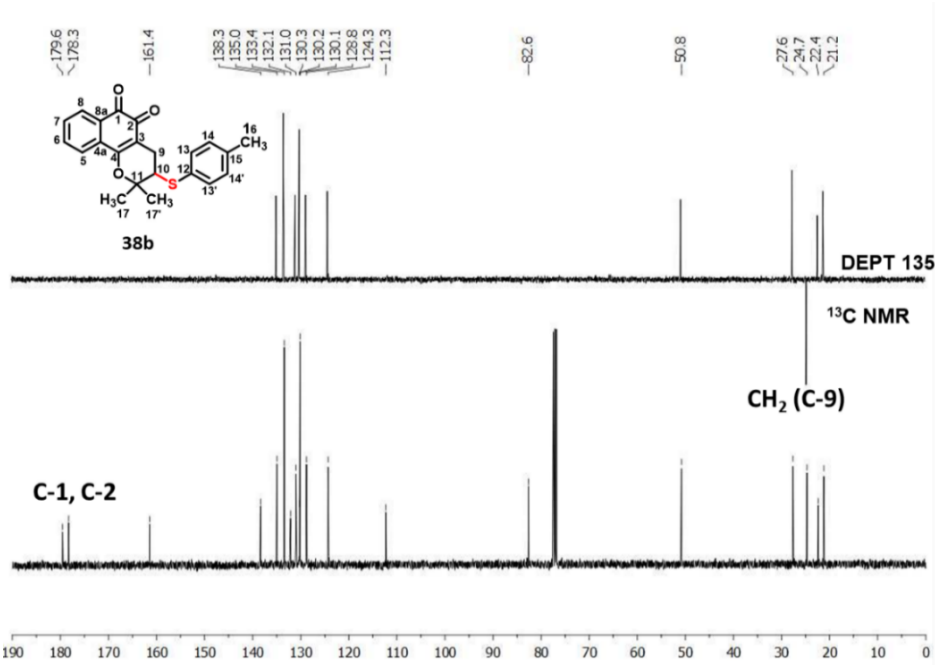

Figure 6: ^{13}C NMR and DEPT 135 spectrum of compound **38b** (101 MHz, $CDCl_3$).

A plausible crystal was successfully obtained from compound **38b,** and its structure was studied by X-ray diffraction crystallography, confirming the proposed structure. **Figure 7** shows the ORTEP-3 projection obtained for this compound.

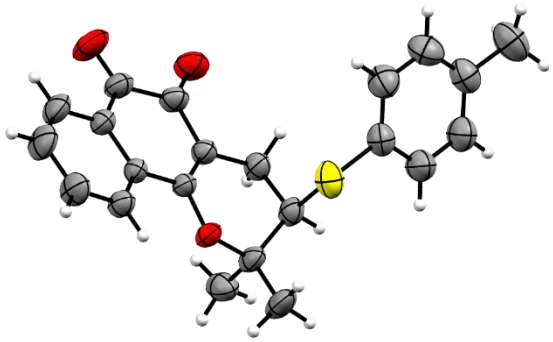

Figure 7: ORTEP-3 projection of compound **38b**. Color code: grey, carbon; red, oxygen; yellow, sulfur. White balls represent hydrogen atoms.

The characterization of compound **40c** is done by comparing it with product **38b**. By analyzing the ^{1}H NMR spectrum, we can observe the similarity between these compounds. It is possible to observe a slight shift in the signals, which can be attributed to the presence of the sulfone group (**Figure 8**).

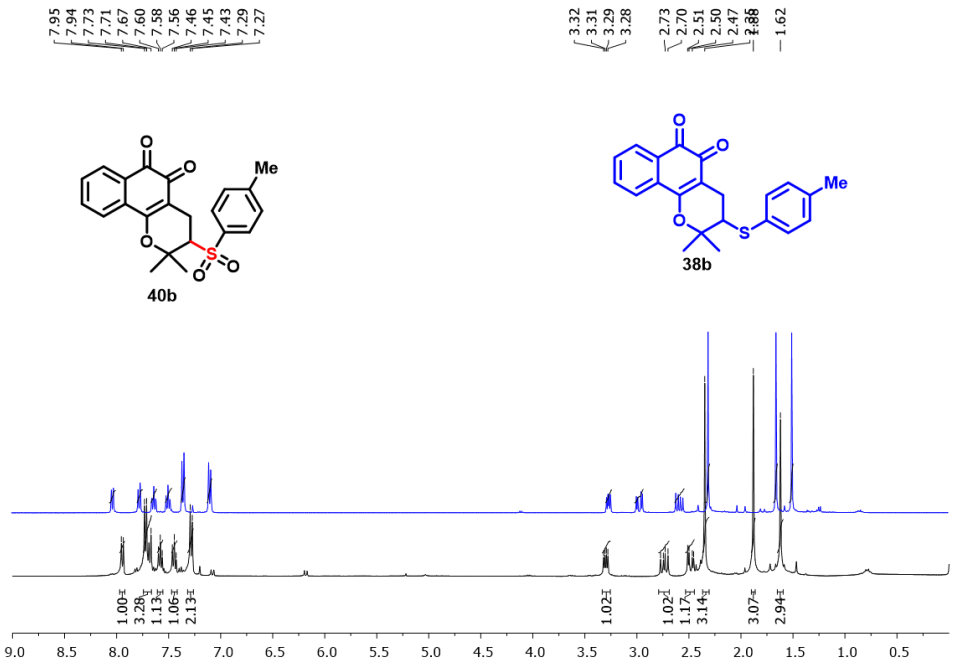

Figure 8: ^{1}H NMR spectrum of compound **40b** (black) and **38b** (blue) (400 MHz, $CDCl_3$).

In the ^{13}C NMR spectrum, we also observe a signal shift (**Figure 9**). In particular, the signal that was previously at 50.8 ppm has shifted to 64.3 ppm, indicating greater deshielding. This shift can be attributed to the methine carbon, which is directly bonded to the sulfone group and experiences more pronounced interference.

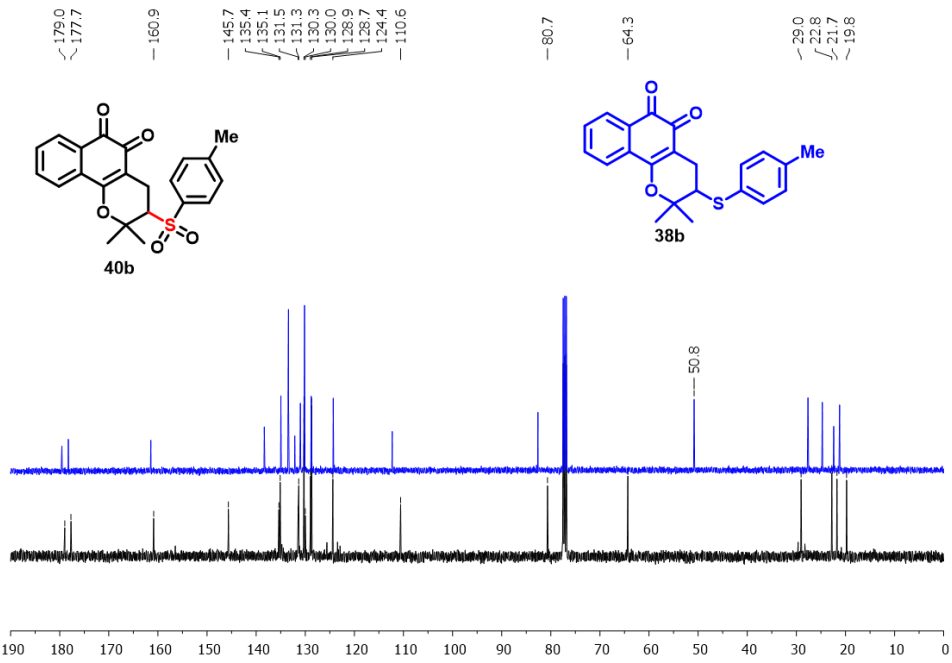

Figure 9: ^{13}C NMR spectrum of compound **40b** (black) and **38b** (blue) (101 MHz, $CDCl_3$).

When relying solely on ^{1}H and ^{13}C NMR spectroscopy for the characterization of compounds containing a sulfone group, it becomes evident that these techniques, while highly informative, are not sufficient to unambiguously confirm the product structure. This limitation underscores the necessity of employing complementary analytical methods. Therefore, the sulfone derivative was subjected to single-crystal X-ray diffraction, which unequivocally confirmed the proposed structure. The ORTEP-3 projection obtained from the crystallographic data is presented in **Figure 10**. Additional characterization was performed using high-resolution mass spectrometry (HRMS), infrared (IR) spectroscopy, and melting point determination, with the corresponding data provided in the Experimental Section.

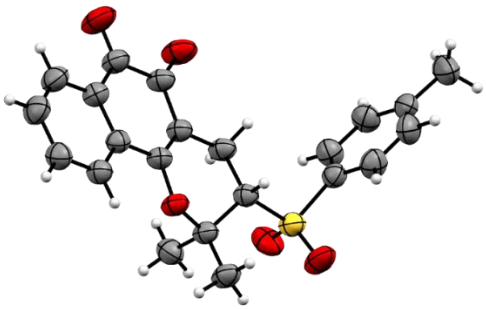

Figure 10: ORTEP-3 projection of compound **40b.** Color code: grey, carbon; red, oxygen; yellow, sulfur. White balls represent hydrogen atoms.

The second representative class of compounds selected for detailed characterization comprises the derivatives *C*-allyl lawsone (**36**). For compound **39b**, the ^{1}H NMR spectrum (400 MHz, $CDCl_3$) shows the signals of the unsubstituted benzylic ring between 7.05-8.04 ppm (H-5, H6, H-7, H-8) (**Figure 11**). Two doublets at 7.32 ppm and 7.06 ppm, were assigned to the aromatic hydrogens of the para-substituted phenyl ring (H-12, H-12′, H-13, H-13′). The methine hydrogens H-10 appeared as a multiplet at δ 5.17–5.24 ppm. The diastereotopic methylene hydrogens (H-9, H-10) were observed as a double doublet at δ 3.32 ppm, a multiplet at δ 3.26–3.17 ppm, and another double doublet at δ 3.00 ppm, each coupling both to one another and to the adjacent methine hydrogens. A singlet at δ 2.28 ppm was attributed to the methyl group attached to the *para*-substituted phenyl ring.

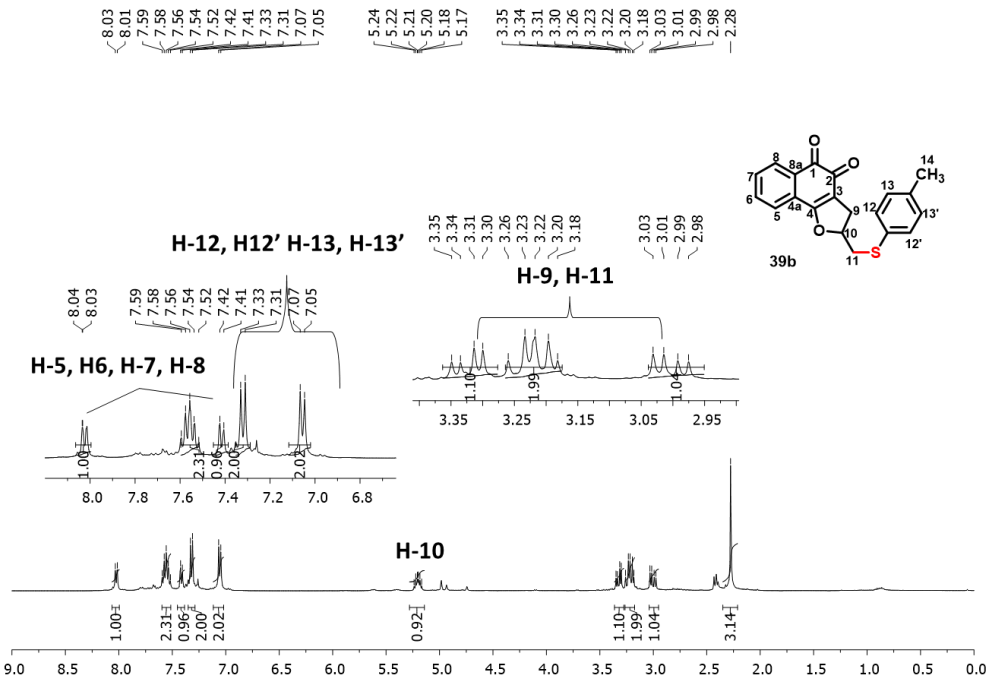

Figure 11: ^{1}H NMR spectrum of compound **39b** (400 MHz, $CDCl_3$)**.**

In the ^{13}C NMR spectrum, we have the carbonyls at 181.1 ppm and 175.4 ppm (C-1, C-2), we have the signals at 86.3 ppm, we have the methine carbon (C-10), and we can also notice the methylene carbons at 39.9 ppm and 31.4 ppm (C-9, C-11) confirmed with DEPT 135 and at 21.1 ppm we have the methylene carbon. The other signals from vinyl carbons are in the expected range between 169.6 and 111.9 ppm (**Figure 12**).

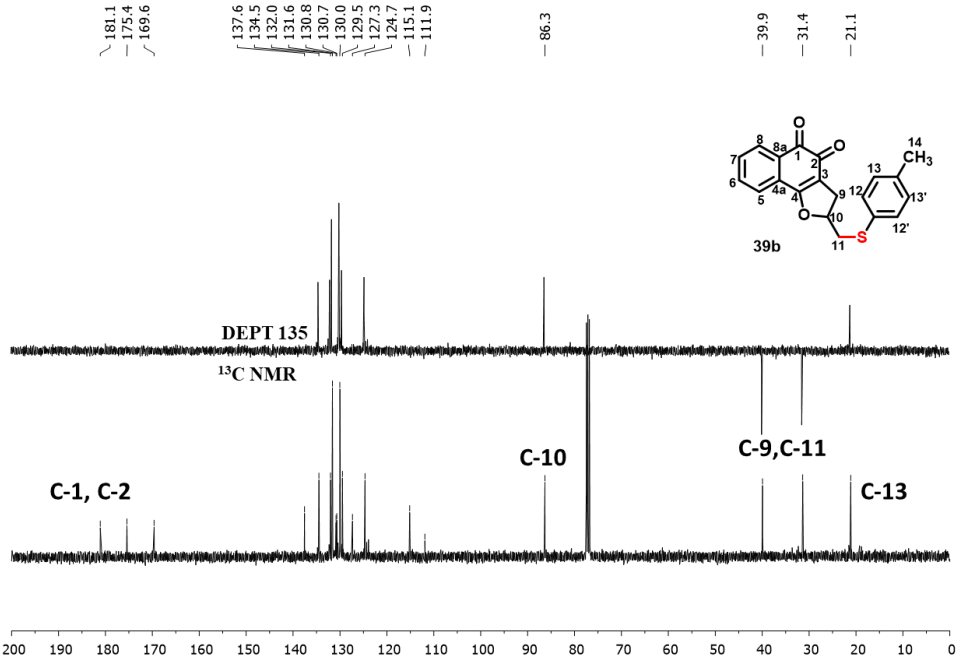

Figure 12: ^{13}C NMR and DEPT 135 spectrum of compound **39b** (101 MHz, $CDCl_3$).

Finally, a comprehensive characterization of compound **41a** was carried out, with a critical comparative analysis of its ^{1}H NMR spectrum against that of precursor **39b** (**Figure 13**). Careful examination revealed notable shifts in the positions of several signals, consistent with structural changes upon oxidation. A particularly striking observation concerns the transformation of the methylene proton resonances: in **39b**, these protons appear as typical diastereotopic signals, whereas in **41a** they are resolved into four distinct resonances, each integrating for 1H. This splitting pattern arises from the pronounced electronic influence of the adjacent sulfone group, which induces significant anisotropic and deshielding effects, thereby creating a more complex chemical environment for each proton.

Equally noteworthy changes were observed in the ^{13}C NMR spectrum (**Figure 14**). The methylene carbon, originally resonating at δ 39.9 ppm in **39b**, experienced a substantial downfield shift to δ 61.3 ppm in **41a**. This pronounced deshielding effect is directly attributable to the strong electron-withdrawing nature of the sulfone functionality, which alters the local electronic density around the carbon center. Such a shift serves as a clear spectroscopic signature for the presence of the sulfone group, complementing the evidence obtained from the ^{1}H NMR analysis.

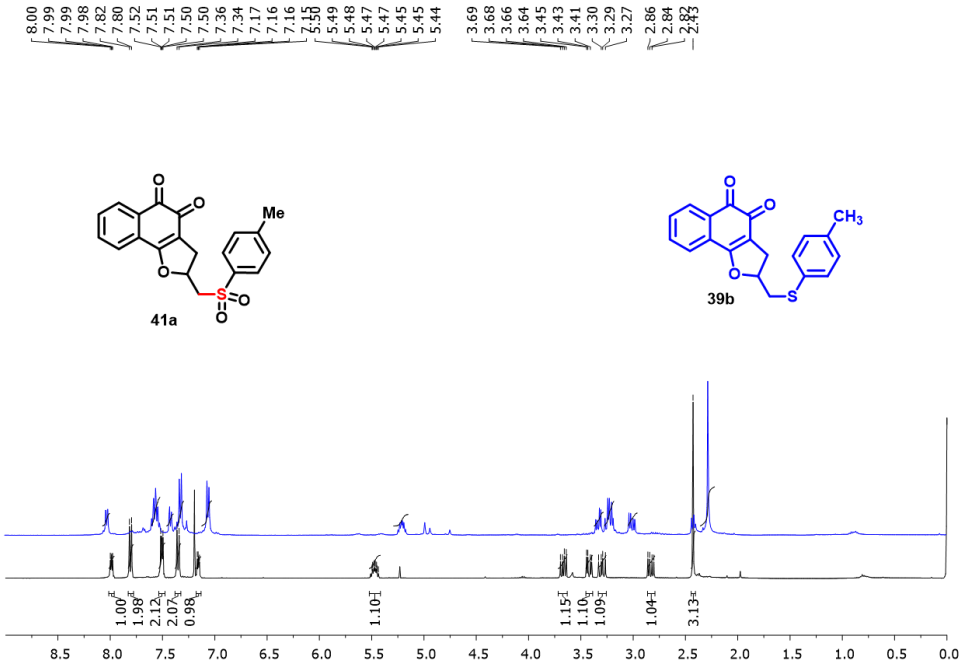

Figure 13: ^{1}H NMR spectrum of compound **41a** (black) and **39b** (blue) (400 MHz, $CDCl_3$).

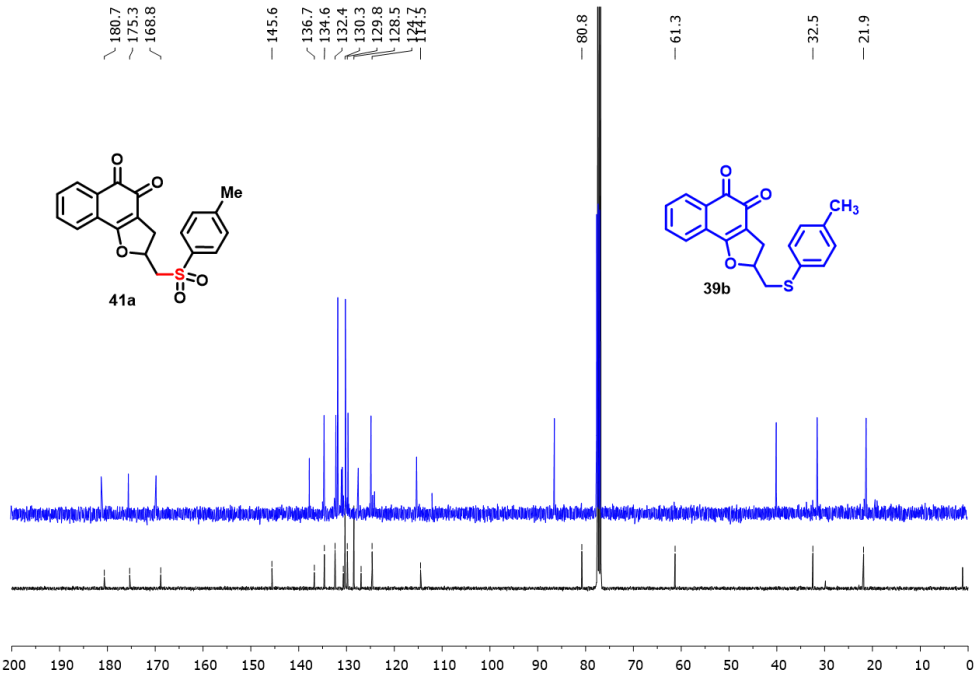

Figure 14: ^{13}C NMR spectrum of compound **41a** (black) and **39b** (blue) (101 MHz, $CDCl_3$).

2.3.3 Study of the electrochemical reaction mechanism

With the compounds synthesized and fully characterized, the mechanistic investigation was initiated. Given that the transformations were electrochemically driven, the study began with cyclic voltammetry (CV), a powerful technique for probing reaction pathways in organic electrosynthesis. CV enables the identification of redox-active intermediates, the determination of kinetic parameters, and the assessment of redox potentials relevant to the reaction under study.

To gain mechanistic insight, CV analyses were performed on selected compounds. Each compound was first evaluated individually to define the optimal potential window, carefully avoiding electrolytic degradation. The potential range for each scan was chosen based on the electrochemical behavior of the analyte, as observed in preliminary experiments. All recorded cyclic voltammograms are provided in the Appendix.

Figure 15 illustrates representative voltammograms for lapachol (**12**), disulfide (**37**) and the cyclized product **38a**. For disulfide (**37**), a semi-reversible process redox couple was observed, indicating partial chemical reversibility of the $[PhSSPh]^{0/+}$ process under the applied scan rates. The anodic peak at E = -0.41 V gives rise to the radical cation $[PhSSPh]^{+\cdot}$, which subsequently undergoes a reaction to form $[(PhS)_4]^{2+}$ (E = - 0.06 V). The resulting species exhibits a cathodic response at E = -1.22 V, which can be explained by the reduction of a $[(PhS)_3]^{+}$ cation, in agreement with previous literature findings.[66]

Lapachol (**12**) has an anodic peak at E = 0.70 V, probably related to its oxidation process. The cathodic peak at E = -0.88 V indicates the reduction of lapachol which may indicate a structural rearrangement that occurs during this electrochemical process.

When lapachol (**12**) and disulfide (**37**) are combined in solution, the CV profile more closely resembles that of lapachol, suggesting that the initial oxidation step is governed by the quinonoid substrate. This step triggers the formation of a cationic intermediate that undergoes intramolecular nucleophilic cyclization at the most substituted carbon atom. For lapachol (**12**), this leads to a six-membered ring (**38a**), whereas in C-allyl-lawsone (**36**), five-membered rings (**39a**) are obtained.

---

[66] a) LAM, K.; GEIGER, W. E. Anodic oxidation of disulfides: detection and reactions of disulfide radical cations. **The Journal of Organic Chemistry**, 2013, 78(16), 8020-8027. b) MATSUMOTO, K. *et al*. Addition of ArSSAr to dienes via intramolecular C–C bond formation initiated by a catalytic amount of ArS+. **Chemical Communications**, n. 36, p. 5448-5450, 2009.; c) MATSUMOTO, K.; SUGA, S.; YOSHIDA, J. Organic reactions mediated by electrochemically generated ArS+. **Organic & biomolecular chemistry**, v. 9, n. 8, p. 2586-2596, 2011.

The lower yields observed for C-allyl-lawsone (**36**) can be rationalized by the reduced nucleophilicity of its π-electron system, which is less substituted compared to lapachol (**12**). This electronic deficiency disfavors carbocation stabilization and slows the intramolecular nucleophilic attack necessary for ring closure (**Scheme 14**). Notably, the positive influence of electron-donating substituents in disulfides on reaction yield can be rationalized by their ability to stabilize the carbocationic intermediate, thereby facilitating the cyclization step.

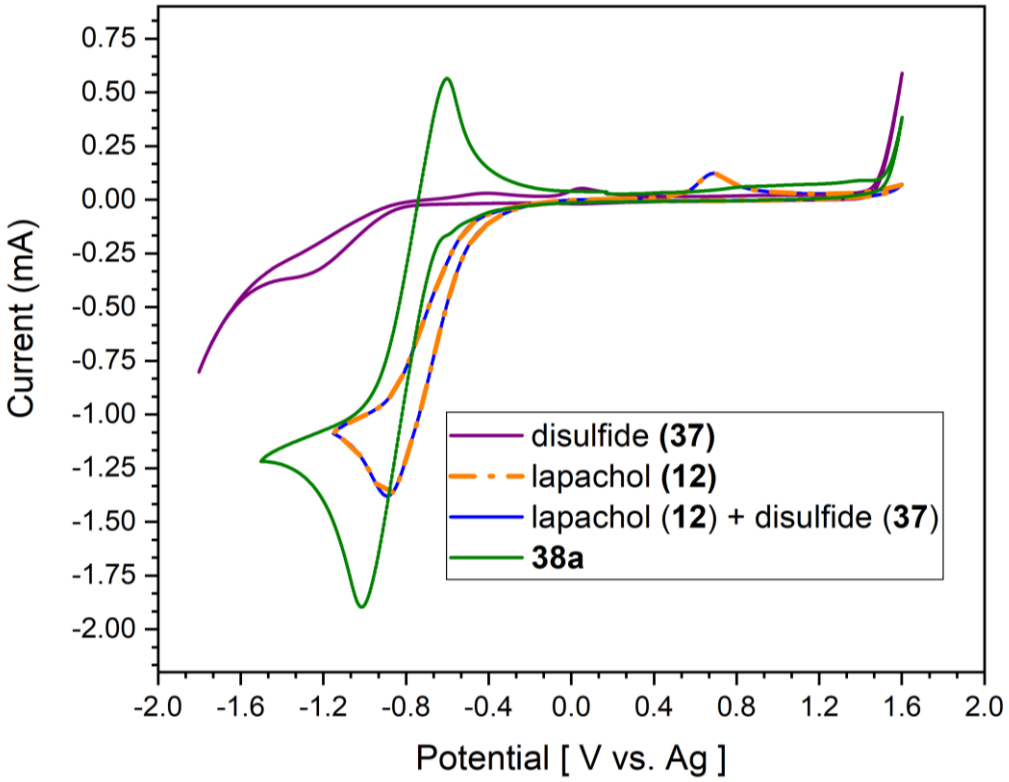

Figure 15: Cyclic voltammograms in MeCN at 200 mVs^{-1}. nBu$_4$NPF$_6$, lapachol (**12**), disulfide (**37**) 0.02 M in MeCN. disulfide (**37**) (purple); lapachol (**12**) (orange); lapachol (**12**) + disulfide (**37**) (blue); **38a** (green).

It is also noteworthy that, near the reversible oxidation peaks at E = -0.59 V and E = -1.01 V, product **38a** shows a reversible reduction with an $E_{1/2}$ value of -0.80 V. This electrochemical profile confirms that the quinone framework is obtained in its oxidized form after the electrolysis process, which is consistent with the oxidative character of the methodology and the stability of the product under the applied potential.

To further validate the proposed mechanism and assess the influence of alkene substitution on cyclization efficiency, a novel naphthoquinone derivative containing a single terminal methyl group was designed and synthesized. This compound serves as a model for a

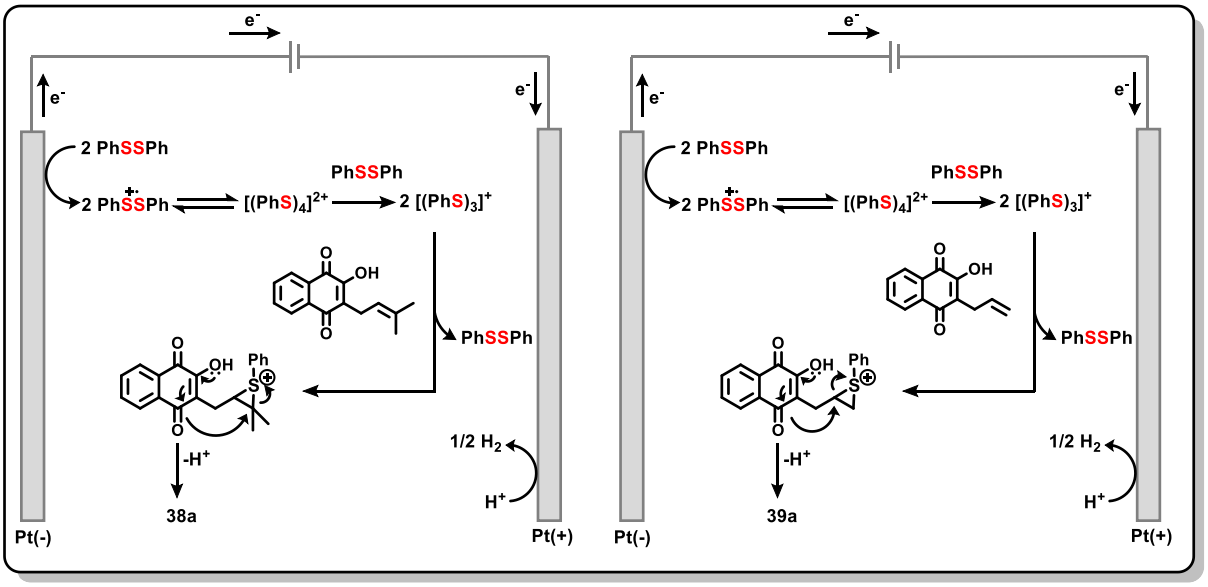

Scheme 14: Proposed mechanism for forming of 6-membered ring products from lapachol (**12**) and 5-membered ring products from C-allyl lawsone (**36**).

mono-substituted terminal alkene, enabling a direct comparison with lapachol (**12**), which bears a di-substituted terminal alkene, and C-allyl-lawsone (**36**), characterized by an unsubstituted terminal alkene. This systematic variation in substitution allows for a more precise evaluation of the electronic and steric effects that govern the cyclization step.

Under the optimized electrochemical conditions, the mono-substituted substrate afforded two distinct cyclization products: a six-membered ring derivative (**43**) in 27% yield and a five-membered ring derivative (**44**) in 21% yield (**Scheme 15**). The formation of both products demonstrates that the carbocationic intermediate generated after oxidation is sufficiently stabilized by the methyl substituent to undergo either cyclization pathway. The methyl group contributes to electronic stabilization through hyperconjugation, facilitating carbocation formation when compared to the unsubstituted system, while also introducing steric effects that influence the conformational arrangement required for intramolecular nucleophilic attack leading to ring closure.

In comparison to lapachol (**12**), the absence of a second substituent in the mono-substituted derivative reduces sulfonium cation stabilization, which correlates with the lower yield observed for the six-membered ring product. Conversely, when compared to C-allyl-lawsone (**36**), the presence of one substituent enhances carbocation stability and promotes the formation of the five-membered ring in higher yield than in the unsubstituted case. This intermediate reactivity profile supports the idea that the cyclization outcome is determined by

the delicate balance between carbocation stabilization and the conformational predisposition of the side chain to undergo intramolecular attack.

These observations provide consistent experimental evidence for the proposed mechanistic pathway and confirm that the substitution pattern at the terminal alkene directly influences the competition between five- and six-membered ring closure, allowing for predictable reactivity trends in structurally related naphthoquinone systems.

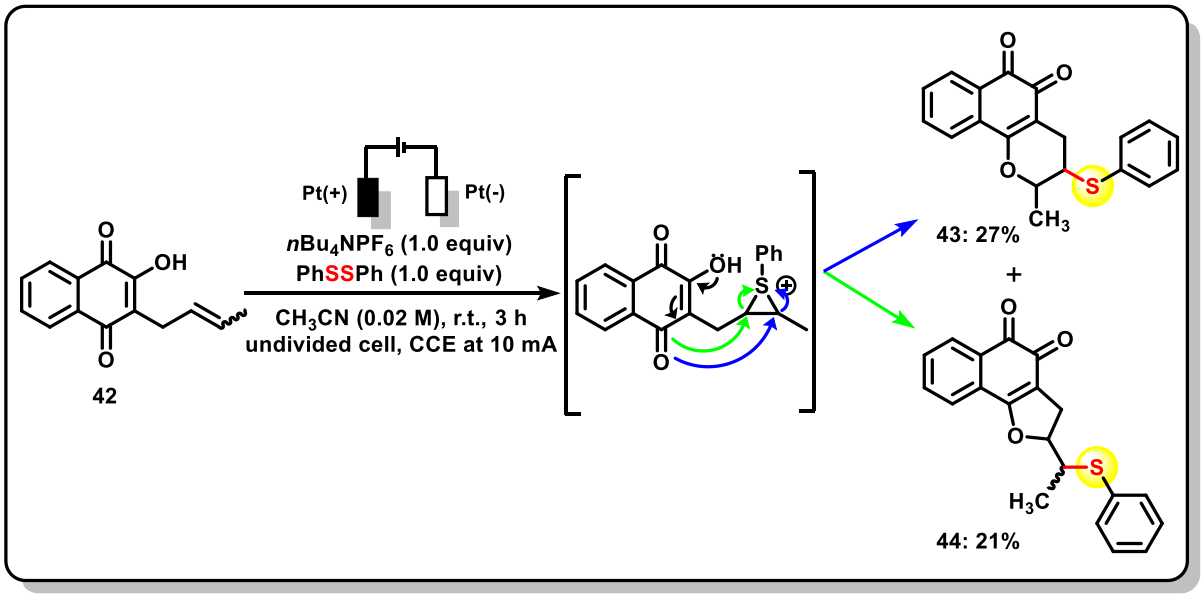

Scheme 15: Mono-substituted terminal alkene electrochemical cyclization.

2.3.4 Study of the oxidation reaction mechanism

To synthesize the sulfone derivatives, ruthenium tetroxide (RuO_4) was employed as a catalytic oxidant, a methodology extensively reported in the literature for its efficiency and selectivity in oxidizing sulfides to sulfones. A key advantage of this protocol is that RuO_4 does not need to be handled directly, as it can be generated in situ via the oxidation of Ru((III) chloride ($RuCl_3 \cdot H_2O$) with sodium periodate ($NaIO_4$) under mild conditions.

The reaction was carried out in a biphasic system consisting of a chlorinated solvent, acetonitrile, and water. The addition of acetonitrile proved essential for maintaining high catalytic activity, as it promotes the reactivation of deactivated ruthenium carboxylate complexes and enhances the solubility and transfer of RuO_4 between phases. This effect ensures continuous turnover of the catalyst and avoids premature deactivation.

From a mechanistic perspective, the catalytic cycle begins in the aqueous phase, where Ru(III) from $RuCl_3$ is oxidized by $NaIO_4$ to Ru(VIII) in the form of RuO_4, a volatile and

highly electrophilic oxidant. Due to its solubility in the organic phase, RuO_4 migrates into the solvent layer containing the sulfur-containing naphthoquinone substrate. In this phase, RuO_4 promotes a stepwise oxidation of the thioether moiety: first converting the sulfide to the sulfoxide intermediate, followed by a second oxygen transfer to yield the sulfone. Both oxidation steps occur through the formation of a transient Ru(VI) oxo-species, which is then reoxidized to Ru(VIII) in the aqueous phase. After each oxidation cycle, the reduced ruthenium species is transferred back into the aqueous layer, where $NaIO_4$ restores it to the active RuO_4 form, closing the catalytic cycle.

This biphasic mechanism provides excellent chemoselectivity for the S-oxidation without overoxidizing the quinone moiety, which remains unaltered under the optimized conditions. The process is illustrated in **Scheme 16**, exemplifying the transformation of a thioether intermediate into the corresponding sulfone derivative (compound **40**) with high yield and structural integrity preserved.

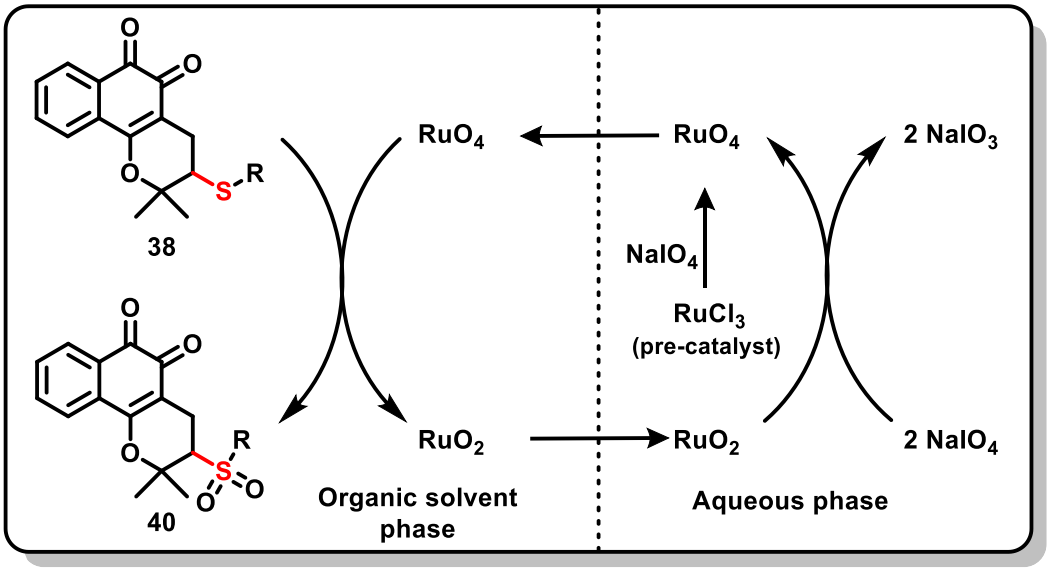

Scheme 16: Sulfide oxidation reaction mechanism.

2.3.5 Pharmacological evaluation against different tumor strains

Compounds **38a–38h**, **39a–39f**, and sulfones **40a–40f** were evaluated for their cytotoxic activity against eight human cancer cell lines and the normal murine fibroblast line L929, used as a reference for toxicity and selectivity. IC_{50} values, corresponding to the concentration required to inhibit 50% of cell growth, were determined after 72 h of incubation (**Table 4**). Biological assays were performed in collaboration with Professor Dr. Cláudia Pessoa's group at the Federal University of Ceará (UFC) using the MTT assay, which measures mitochondrial dehydrogenase activity. In this assay, the enzyme catalyzes the conversion of the yellow MTT reagent into purple formazan, allowing the quantification of cell viability.

The cancer cell panel comprised HCT-116 (colon carcinoma), PC3 (prostate carcinoma), HL-60 (human promyelocytic leukemia), B16 (murine melanoma), SNB-19 (human glioblastoma), K562 (human myelogenous leukemia), RAJI (Burkitt lymphoma), and A549 (human lung carcinoma), all provided by the National Cancer Institute (Bethesda, MD, USA). The L929 cell line (NCTC clone 929) was obtained from the American Type Culture Collection (Manassas, VA, USA) and used as a control.

Cytotoxicity was further assessed in terms of selectivity using the MTT method. The selectivity index (SI) was calculated as SI = IC_{50} normal cell / IC_{50} tumor cell. Compounds with SI > 2.0 were considered selectively toxic, capable of killing at least twice as many tumor cells as healthy cells at the same concentration. SI values below 2 indicate potential toxicity toward normal cells. This parameter is crucial to ensure preferential targeting of cancer cells, thereby increasing therapeutic efficacy and minimizing side effects. Conventional chemotherapeutic and radiotherapeutic approaches typically show low selectivity, which contributes to their extensive adverse effects.

Table 4: Cytotoxic activity was expressed as IC_{50} μM (95% CI) against cancer and normal cell lines after 72 h exposure. HCT-116 (colon carcinoma), PC3 (prostate carcinoma), B16 (murine melanoma), A549 (human lung carcinoma), HL-60 (human promyelocytic leukemia), SNB-19 (human glioblastoma), K562 (human myelogenous leukemia), RAJI (Burkitt lymphoma) and L929 (normal cell line).

Compound	HCT116	PC3	B16	A549	HL60	SNB19	K562	RAJI	L929
38a	3.27 ± 0.66	4.01 ± 0.21	3.97 ± 0.59	3.50 ± 0.17	1.21 ± 0.28	4.12 ± 0.39	4.00 ± 0.03	1.02 ± 0.05	3.28 ± 0.78
38b	10.34 ± 1.10	8.64 ± 0.75	6.97 ± 0.24	5.53 ± 1.00	2.29 ± 0.41	12.54 ± 1.31	7.39 ± 0.78	4.02 ± 0.90	4.72 ± 0.31
38c	4.93 ± 0.57	5.78 ± 0.09	4.26 ± 0.41	5.99 ± 0.63	2.15 ± 0.16	3.04 ± 0.11	2.29 ± 0.35	1.23 ± 0.13	4.29 ± 0.06
38d	9.30 ± 1.35	8.33 ± 0.31	8.07 ± 0.78	11.56 ± 0.09	6.06 ± 0.77	25.03 ± 1.45	10.21 ± 1.19	21.07 ± 1.15	11.51 ± 1.14
38e	4.43 ± 0.62	4.24 ± 0.67	3.14 ± 0.43	4.60 ± 0.79	2.73 ± 0.96	5.40 ± 0.42	3.71 ± 0.18	5.29 ± 1.69	5.05 ± 1.34
38f	6.80 ± 1.97	8.40 ± 1.18	4.85 ± 0.01	8.85 ± 0.13	2.17 ± 0.90	8.44 ± 0.27	6.00 ± 1.73	16.73 ± 1.25	6.41 ± 2.16
38g	3.52 ± 0.58	5.65 ± 0.15	5.98 ± 0.12	5.31 ± 0.42	2.41 ± 0.20	3.82 ± 0.64	2.65 ± 0.34	4.83 ± 0.19	5.04 ± 1.61
38h	1.39 ± 1.50	3.61 ± 0.44	3.05 ± 0.93	2.18 ± 1.12	1.63 ± 0.67	5.35 ± 1.24	3.82 ± 0.54	0.77 ± 0.15	1.54 ± 0.52
38i	1.75 ± 0.17	2.87 ± 0.38	6.50 ± 0.27	2.44 ± 0.10	1.29 ± 0.07	2.52 ± 0.23	2.70 ± 0.64	2.71 ± 0.21	4.85 ± 2.11
39a	2.30 ± 0.48	4.52 ± 0.06	2.03 ± 0.18	2.23 ± 0.71	1.26 ± 0.10	2.67 ± 1.18	2.55 ± 0.38	5.13 ± 0.91	1.19 ± 0.01
39b	3.76 ± 0.34	8.76 ± 0.22	5.41 ± 0.20	6.25 ± 0.77	3.23 ± 0.18	3.87 ± 0.01	3.48 ± 0.68	4.79 ± 0.16	7.88 ± 0.12
39c	2.52 ± 0.58	6.26 ± 0.60	2.71 ± 0.42	3.96 ± 0.99	2.04 ± 0.35	4.64 ± 0.33	3.51 ± 0.81	1.38 ± 0.04	3.62 ± 0.96
39d	3.32 ± 0.10	3.92 ± 0.16	2.40 ± 0.77	4.94 ± 0.29	1.10 ± 0.41	3.23 ± 0.33	2.28 ± 0.02	3.11 ± 0.15	3.99 ± 0.42
39e	1.87 ± 0.08	3.82 ± 0.01	3.30 ± 0.50	3.16 ± 0.10	1.23 ± 0.12	2.36 ± 0.03	3.00 ± 0.11	2.15 ± 0.12	4.32 ± 0.41
39f	4.20 ± 0.14	7.72 ± 0.09	4.29 ± 0.79	5.01 ± 0.13	3.46 ± 0.10	3.87 ± 0.29	2.90 ± 0.08	2.47 ± 0.05	4.77 ± 1.27
40a	3.23 ± 0.29	5.41 ± 0.47	3.25 ± 0.05	5.67 ± 0.38	1.67 ± 0.17	3.60 ± 0.68	2.04 ± 0.49	2.40 ± 0.32	3.23 ± 0.62
40b	3.44 ± 0.07	5.54 ± 0.93	3.65 ± 0.09	4.91 ± 0.49	1.71 ± 0.15	3.55 ± 0.54	2.15 ± 0.17	2.91 ± 0.01	3.54 ± 0.14
40c	6.41 ± 0.42	10.45 ± 1.85	6.19 ± 0.45	11.13 ± 0.96	2.44 ± 0.47	8.07 ± 0.56	9.81 ± 2.02	6.58 ± 0.17	6.97 ± 0.08
40d	2.65 ± 0.38	5.24 ± 1.21	2.14 ± 0.24	3.56 ± 0.23	1.23 ± 0.04	3.75 ± 0.19	1.85 ± 0.61	1.65 ± 0.02	2.47 ± 0.41
40e	2.71 ± 0.11	4.48 ± 0.57	2.64 ± 0.20	6.04 ± 0.23	1.40 ± 0.23	3.56 ± 0.02	1.89 ± 0.40	1.82 ± 0.11	2.82 ± 0.56
40f	4.14 ± 0.04	6.94 ± 0.91	5.23 ± 0.37	6.48 ± 0.15	1.85 ± 0.13	5.92 ± 0.41	2.60 ± 0.17	3.13 ± 0.11	6.08 ± 1.81
Doxorubicin	0.17 ± 0.11	0.02 ± 0.03	0.06 ± 0.01	0.57 ± 0.16	0.08 ± 0.01	1.20 ± 0.80	0.49 ± 0.28	2.33 ± 0.69	0.27 ± 0.29

Table 4 presents the complete cytotoxicity profiles of all synthesized compounds against a panel of tumor cell lines and the normal L929 fibroblast line. Within this dataset, the RAJI cell line derived from Burkitt's lymphoma, yielded particularly notable results. Seven derivatives (**38a**, **38c**, **38h**, **39c**, **39e**, **40d**, and **40**e) exhibited lower IC_{50} values compared with doxorubicin (**Figure 16**), indicating superior cytotoxic potency under identical conditions. These findings suggest that specific structural or physicochemical modifications in these molecules may enhance their molecular target interactions and/or improve cellular uptake, positioning them as promising lead candidates for anticancer drug development.

Figure 16: Comparative cytotoxic activity of the synthesized compounds against the RAJI cell line, highlighting differences in potency relative to the reference drug doxorubicin (Dox). IC_{50} values are shown in green and errors in orange.

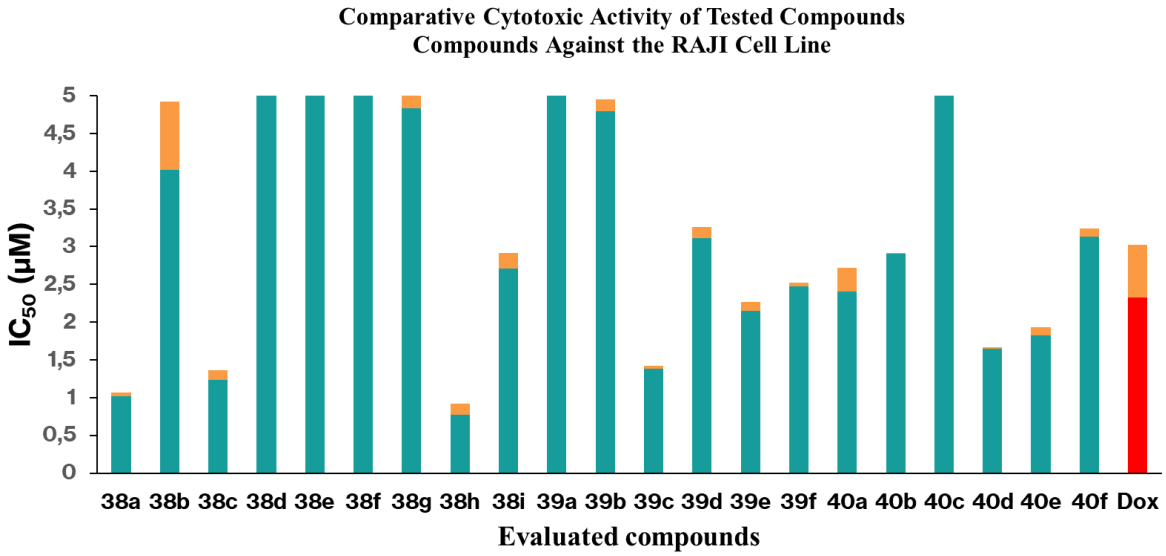

The HL-60 model, extensively employed for evaluating antitumor agents, provided additional insights. In this cell line, none of the derivatives surpassed doxorubicin (IC_{50} = 0.08 µM). The most active compound was **39d** (IC_{50} = 1.10 µM). However, when compared with *β*-lapachone (IC_{50} = 1.63 µM),[67] a reference quinone, derivatives **38a**, **38i**, **39a**, **39d**, **39e**, **40d**, and **40e** displayed improved potency (**Figure 17**), reinforcing that strategic structural modifications of β-lapachone (**14**) remain a valuable approach for developing active agents against hematologic cancers.

[67] JARDIM, G. A. M. *et al*. Naphthoquinone-based chalcone hybrids and derivatives: Synthesis and potent activity against cancer cell lines. **MedChemComm**, v. 6, n. 1, p. 120-130, 2015.

Figure 17: Comparative cytotoxic activity of the synthesized compounds against the HL60 cell line, highlighting differences in potency relative to the reference drug doxorubicin (Dox) and *β*-lapachone (*β*-lap)[67]. IC_{50} values are shown in green and errors in orange.

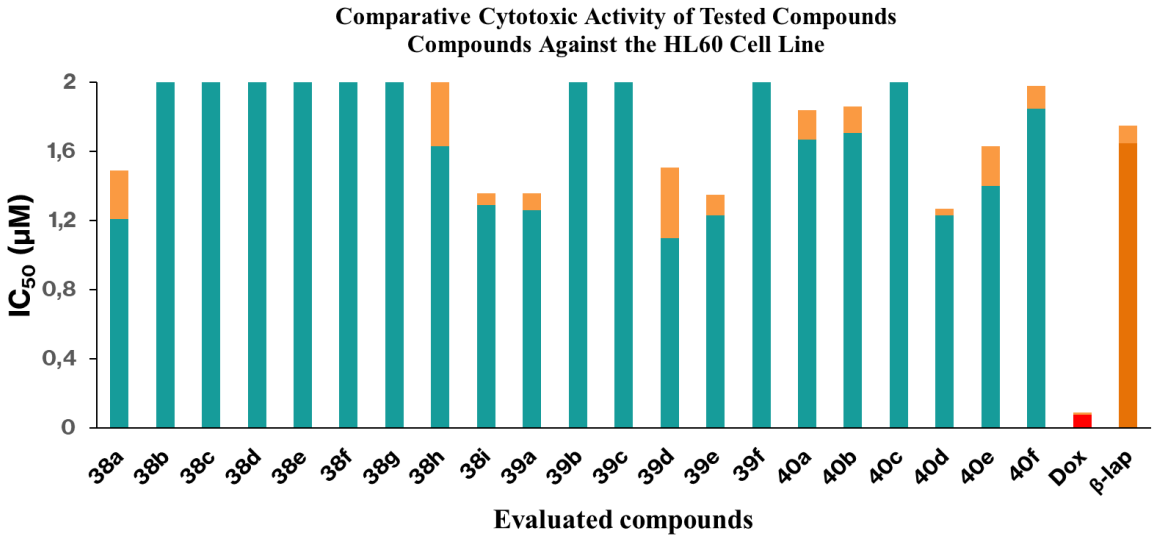

Among the tested derivatives, **38h** emerged as the most potent, exhibiting superior cytotoxicity both in absolute terms and relative to *β*-lapachone (**14**) (**Table 5**). In HCT116 cells, **38h** displayed an IC_{50} of 1.39 μM, while in A549 and HL-60 the values were 2.18 μM and 1.63 μM, respectively. Compared with *β*-lapachone (**14**) (0.97 μM for HCT116, 1.5 μM for A549, and 1.65 μM for HL-60),[67] **38h** maintained comparable or enhanced performance. The highest potency was recorded against RAJI cells, with an IC_{50} of 0.77 μM, indicating notable activity against lymphoid-derived cancers. In K562 cells (chronic myeloid leukemia), **38h** achieved an IC_{50} of 3.82 μM, which is comparable to that of *β*-lapachone (**14**) (IC_{50} 4.0 μM),[68] suggesting that the structural modifications in 38h may contribute to maintaining or slightly enhancing its cytotoxic potential.

[68] TALHI, O.*et al.* Bis (4-hydroxy-2H-chromen-2-one): Synthesis and effects on leukemic cell lines proliferation and NF-κB regulation. **Bioorganic & Medicinal Chemistry**, v. 22, n. 11, p. 3008-3015, 2014.

Table 5: Comparison of the cytotoxic activity (IC_{50}, µM) of compound **38h** and *β*-lapachone across selected tumor cell lines. Literature values are reported for *β*-lapachone.[67-68]

	IC_{50} µM (95% CI)			
Compound	HCT116	A549	HL-60	K562
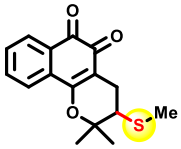 **38h**	1.39	2.18	1.63	3.82
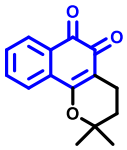 ***β*-lapachone (14)**	0.97	1.15	1.65	4.00

Table 6 summarizes the selectivity index (SI) for the synthesized compounds, calculated as the ratio between cytotoxicity in the normal L929 cell line and in each cancer cell line. An SI value above 2 indicates preferential cytotoxicity toward tumor cells relative to normal cells, a desirable property in anticancer drug candidates.

Overall, most derivatives exhibited SI values close to or slightly above 1 across the tumor panel, suggesting little to no selectivity. However, certain compounds stood out for specific cell lines. Notably, **38i** showed the highest SI against HL-60 (3.7), indicating strong tumor selectivity in this leukemia model. Similarly, **39d** and **39e** displayed SI values above 3.0 for HL-60, while **40f** also performed well (SI = 3.3).

The RAJI cell line, previously identified as a highlight for potency, again showed favorable selectivity for several derivatives. Compounds **38h** (SI = 2.1), 39c (SI = 2.6), **39e** (SI = 2.0), and **40f** (SI = 1.9) all demonstrated selective cytotoxicity against RAJI cells compared to L929, reinforcing their potential in targeting lymphoid malignancies.

In contrast, some potent compounds such as **39a** displayed low SI values (≤ 0.5 in multiple cell lines), indicating reduced selectivity despite strong cytotoxic activity. This underscores the importance of considering both potency and selectivity during lead optimization to minimize potential toxicity toward healthy cells.

Taken together, the SI data reinforce the cytotoxicity findings, highlighting compounds **38h**, **38i**, **39e**, and **40f** as promising candidates that combine potent antitumor activity with favorable selectivity profiles, particularly in hematologic cancer models such as HL-60 and RAJI. These results support the need for further studies aimed at elucidating their

mechanisms of action and conducting in vivo evaluations to confirm their therapeutic potential.

Among these, **38h** is particularly noteworthy for its activity against the RAJI cell line, where it combined potent cytotoxicity with favorable selectivity. This result highlights its potential relevance for lymphoid-derived cancers. Future studies should focus on mechanistic investigations and the evaluation of possible synergistic effects with established chemotherapeutics, aiming to advance **38h** as a viable anticancer candidate. Although preliminary, these findings provide valuable insights for the rational optimization of this derivative to further enhance its antitumor properties.

Table 6: Selectivity index [calculated by the ratio of cytotoxicity between L929 cell line and each cancer cell lines]. HCT-116 (colon carcinoma), PC3 (prostate carcinoma), B16 (murine melanoma), A549 (human lung carcinoma), HL-60 (human promyelocytic leukemia), SNB-19 (human glioblastoma), K562 (human myelogenous leukemia), RAJI (Burkitt lymphoma) and L929 (normal cell line).

Compounds	HCT116	PC3	SNB19	K562	B16	A549	HL60	RAJI
38a	0.7	0.7	0.9	0.7	0.9	1.0	1.6	1.7
38b	1.1	1.0	0.8	1.3	1.5	1.9	2.4	1.3
38c	0.9	0.7	0.7	0.9	1.0	0.7	2.0	1.7
38d	1.2	1.4	0.9	1.1	1.4	1.0	1.9	0.6
38e	1.1	1.2	0.9	1.4	1.6	1.1	1.8	1.0
38f	0.9	0.8	0.8	1.1	1.3	0.7	2.4	0.4
38g	1.4	0.9	1.3	2.0	0.8	0.9	2.1	1.0
38h	1.1	0.4	0.5	0.4	0.5	0.7	0.9	2.1
38i	2.0	1.6	1.9	1.7	0.9	1.9	3.7	1.7
39a	0.5	0.3	0.5	0.4	0.6	0.5	0.9	0.2
39b	2.1	0.9	2.0	2.2	1.5	1.3	2.4	1.6
39c	1.4	0.6	0.8	1.0	1.3	0.9	1.8	2.6
39d	1.2	1.0	1.2	1.7	1.7	0.8	3.6	1.3
39e	2.3	1.1	1.8	1.4	1.3	1.4	3.5	2.0
39f	1.1	0.6	1.2	1.7	1.1	1.0	1.4	1.9
40a	1.0	0.6	0.9	1.6	1.0	0.6	1.9	1.3
40b	1.0	0.6	1.0	1.7	1.0	0.7	2.1	1.2
40c	1.1	0.7	0.9	0.6	1.1	0.6	2.9	1.1
40d	0.9	0.5	0.7	1.4	1.2	0.7	2.0	1.5
40e	1.0	0.6	0.8	1.9	1.1	0.5	2.0	1.6
40f	1.5	0.9	1.0	2.4	1.2	0.9	3.3	1.9

2.4 CONCLUSIONS

In summary, this work has successfully introduced an electrochemically efficient approach for synthesizing a diverse array of redox-active sulfur-containing quinone compounds. This method utilizes the sulfenylation/cyclization of quinones and has proven to be a facile and versatile route, yielding our target products in consistently good to excellent yields. Notably, this work led to the successful synthesis of 15 distinct compounds, with 9 of them undergoing oxidation to sulfones.

Among the synthesized compounds, **38b** and **39b** exhibited excellent (96% and 94% yields, respectively). Moreover, all sulfones were obtained with yields exceeding 60%.

Particularly noteworthy, compounds **38i** and **39e** (IC_{50} 1.75 and 1.87, respectively) demonstrated good activity and selectivity against colon carcinoma cells (HCT-116), positioning them as promising candidates for future studies and potential applications in cancer treatment. Among the sulfones, **40d** and **40e** achieved activities of IC_{50} 1.65 and 1.82 against the RAJI cell line, surpassing the performance of doxorubicin (IC_{50} 2.33).

This research not only provides a practical, rapid, and environmentally friendly means of accessing sulfur-containing quinones but also underscores the potential as anticancer agents. Given the ease of use and efficiency of the electrochemical reactions employed in this study, this work has the potential to usher in a new era of opportunities for the synthesis of novel sulfur-containing molecules with prospective biological activities. This represents a significant step forward at the intersection of electrochemistry and organic synthesis, which promises exciting prospects for developing of biologically active compounds.

The results described in this work have been published in the *European Journal of Organic Chemistry* in the special edition: Hot Topic: Tumors and Cancer.

Emilay B. T. Diogo, Fábio G. Delolo, Gabriela A. P. Graça, Esther R. S. Paz, Ícaro A. O. Bozzi, Renata Diniz, Juliano P. Passos, Tulio Matencio, Liane K. Soares, Diego Alves, Pedro M. S. Costa, Claudia Pessoa, Cynthia L. M. Pereira, Lutz Ackermann* and Eufrânio N. da Silva Júnior*. Electrochemical Sulphenylation/Cyclization of Quinones: A Rapid, Green and Efficient Access to Cytotoxic Compounds. **2023**, e202300506. doi.org/10.1002/ejoc.202300506.

2.5 EXPERIMENTAL

2.5.1 General Remarks

Starting materials obtained from commercial suppliers were used as received unless otherw stated. Flash column chromatography (FCC) was performed using silica gel (Aldrich 40-63 μm, 230-400 mesh). Thin layer chromatography (TLC) was performed using aluminum-backed 60 F_{254} silica plates. Visualization was achieved by UV fluorescence. Proton nuclear magnetic resonance (NMR) spectra were recorded using a Avance III HD 400 and Avance NEO 600 instruments. ^{13}C NMR spectra were recorded at 101 MHz as stated. Chemical shifts (δ) are given in parts per million (ppm). Peaks are described as singlets (s), doublets (d), doublet of doublets (dd), triplets (t), doublet of triplets (dt), quartets (q), doublet of quartets (qt), and multiplets (m). The ^{1}H and ^{13}C NMR spectra were referenced to the appropriate residual solvent or TMS peak. Coupling constants (*J*) were quoted to the nearest 0.5 Hz. Mass spectra were obtained using high-resolution mass spectrometry (HRMS) and were recorded using a Thermo Scientific Exactive Plus Orbitrap MS system for atmospheric solids analysis probe (ASAP). Infrared spectra were recorded on a Perkin Elmer Spectrum One spectrometer using KBr plates. IR bands are described by the wavenumber ($\bar{\nu}$, cm^{-1}). Melting points were determined using the MQAPF - 302 melting point apparatus and were uncorrected. The anode and cathode are platinum plate electrodes (10 x 10 x 0.2 mm). Electrocatalysis was conducted using an AXIOMET AX-3003P potentiostat in constant current mode. The names of the compounds were generated using ChemDraw software.

2.5.2 C-allyl lawsone (36) synthesis and Characterization

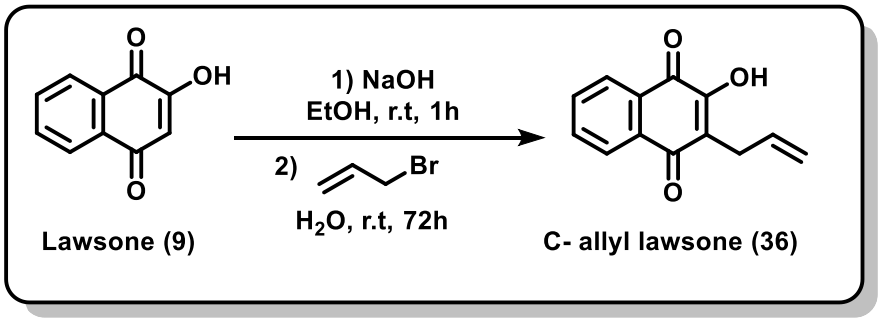

Scheme 17: C-allyl lawsone (**36**) synthesis

2-Hydroxy-1,4-naphthoquinone (lawsone) (**9**) (5 g, 29 mmol) was added to a 250 mL round bottom flask containing a mixture of 50 mL ethanol and NaOH (1.4 g, 35 mmol). The mixture was stirred for 1 hour, observing the appearance changing of the from an orange solution to a suspension containing a red solid. The red solid was vacuum filtered, washed with ethyl ether, and then dried in an oven at 70 ºC to obtain the solid in quantitative yield. The red solid (sodium lawsonate) was used in the next step without further purification.

Sodium lawsonate (3 g, 15 mmol) and allyl bromide (30 mL) were added to a 250 mL round bottom flask. The solution was stirred for 1 h, and then added 70 mL of distilled water. The mixture was stirred at room temperature for 72 hours, and the precipitate's color change from red to yellow was observed. The reaction was stopped, and 30 mL of distilled water was added to the mixture. The mixture was then separated with ethyl acetate (3 x 15 mL) and then dried over Na_2SO_4. The crude product was purified on a chromatographic column under the following conditions. Purification by column chromatography on silica gel (*n*-hexane/EtOAc 9:1) yielded **36** (1.80 g, 56 %) as a yellow solid. [66]

3-alil-2-hidroxinaftaleno-1,4-diona (36): ^{1}H NMR (400 MHz, $CDCl_3$) δ: 8.09 (dd, *J* = 18.5, 7.1 Hz, 2H), 7.71 (dt, *J* = 29.8, 7.5 Hz, 2H), 7.41 (s, 1H), 5.97-5.82 (m, 1H), 5.23-4.99 (m, 2H), 3.36 (d, *J* = 6.5 Hz, 2H). **^{13}C NMR (101 MHz, $CDCl_3$) δ:** 184.3, 181.6, 153.3, 135.1, 133.9, 133.1, 132.9, 129.5, 127.0, 126.3, 122.0, 116.6, 27.6.

2.5.3 General procedure for disulfide synthesis

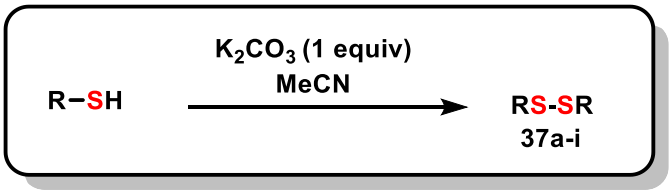

Scheme 18: Disulfide synthesis **37a-i.**

To a round bottle (50 mL) were added thiol derivative (5 mmol), potassium carbonate (0.69 g, 5 mmol), and MeCN (10 mL) sequentially, and the reaction was conducted at room temperature under air atmosphere for 1 hour. The desired disulfides were obtained quantitatively after filtration and concentration.[68]

Characterization Data: Products 37a-i

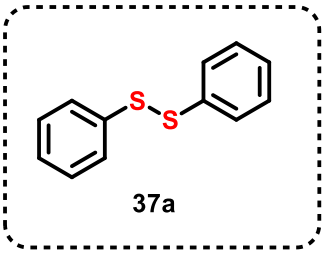

1,2-diphenyldisulfane (37a): ^{1}H NMR (400 MHz, $CDCl_3$) δ: 7.53- 7.56 (m, 2H), 7.37 – 7.32 (m, 2H), 7.24- 7.28 (m, 1H). **^{13}C NMR (101 MHz, $CDCl_3$) δ:** 137.2 (2xC), 129.2 (4xCH), 127.6 (4xCH), 127.3 (2xCH).

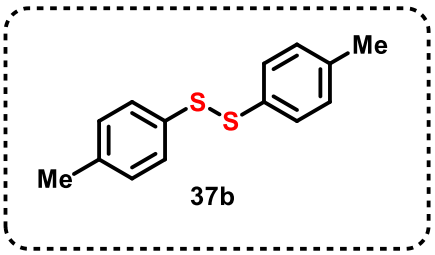

1,2-di-*p*-tolyldisulfane (37b): ^{1}H NMR (400 MHz, $CDCl_3$) δ: 7.41 (d, J = 8.2 Hz, 4H), 7.12 (d, J = 8.1 Hz, 4H), 2.34 (s, 6H). **^{13}C NMR (101 MHz, $CDCl_3$) δ:** 137.6 (2xC), 134.0 (2xC), 129.9 (4xCH), 128.7 (4xCH), 21.2 (2xCH_3).

[68] OUYANG, Wensen *et. al*. Sequential C–H activation enabled expedient delivery of polyfunctional arenes. **Chemical Communications**, v. 57, n. 65, p. 8075-8078, 2021.

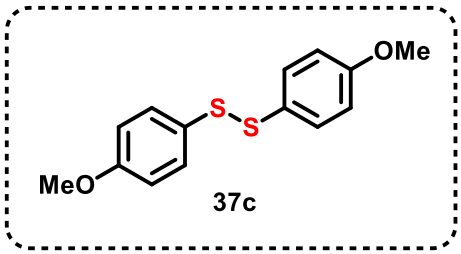

37c

1,2-bis(4-methoxyphenyl)disulfane (37c): ^{1}H NMR (400 MHz, $CDCl_3$) δ: 7.25 (d, *J* = 8.8 Hz, 4H), 6.66 (d, *J* = 8.8 Hz, 4H), 3.58 (s, 6H). **^{13}C NMR (101 MHz, $CDCl_3$) δ:** 159.9 (2xC), 132.5 (4xCH), 128.3 (2xC), 114.6 (4xCH), 55.2 (2xCH_3).

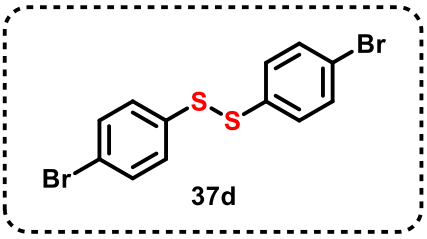

37d

1,2-bis(4-bromophenyl)disulfane (37d): ^{1}H NMR (600 MHz, $CDCl_3$) δ: 7.36 – 7.33 (m, 4H), 7.27 – 7.24 (m, 4H). **^{13}C NMR (151 MHz, $CDCl_3$) δ:** 135.9 (2xC), 132.4 (4xCH), 129.5 (4xCH), 121.7 (2xC).

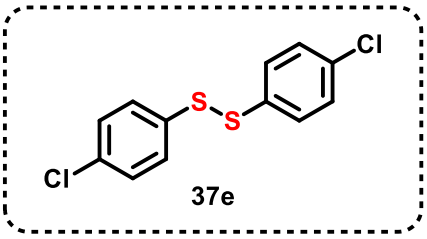

37e

1,2-bis(4-chlorophenyl)disulfane (37e): ^{1}H NMR (400 MHz, $CDCl_3$) δ: 7.34 – 7.29 (m, 4H), 7.21 – 7.17 (m, 4H). **^{13}C NMR (101 MHz, $CDCl_3$) δ:** 135.3 (2xC), 133.8 (2xC), 129.5 (4xCH), 129.4 (4xCH).

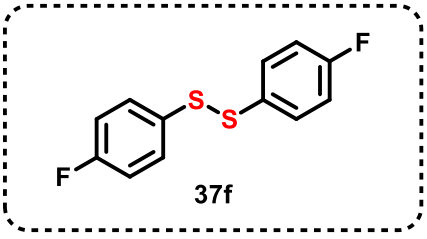

37f

1,2-bis(4-fluorophenyl)disulfane (37f): ^{1}H NMR (400 MHz, $CDCl_3$) δ: 7.49 – 7.43 (m, 4H), 7.05 – 6.98 (m, 4H). **^{13}C NMR (101 MHz, $CDCl_3$) δ:** 162.7 ($^{1}J_{C\text{-}F}$ = 249.1 Hz), 132.3 ($^{4}J_{C\text{-}F}$ = 3.3 Hz), 131.6 ($^{3}J_{C\text{-}F}$ = 8.3 Hz), 116.4 ($^{2}J_{C\text{-}F}$ = 22.2 Hz)

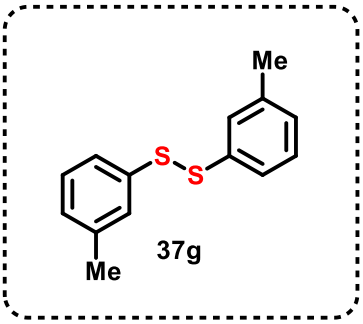

37g

1,2-di-*m*-tolyldisulfane (37g): ^{1}H NMR (400 MHz, $CDCl_3$) δ: 7.42 (d, *J* = 5.9 Hz, 4H), 7.31 – 7.25 (m, 2H), 7.12 (d, *J* = 7.4 Hz, 2H), 2.41 (s, 6H). **^{13}C NMR (101 MHz, $CDCl_3$) δ:** 138.9 (2xC), 137.0 (2xC) 129.0 (2xCH), 128.1 (2xCH), 124.6 (2xCH), 21.4 (2xCH_3).

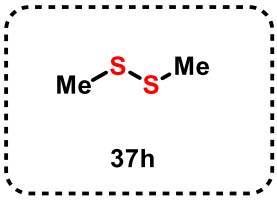

37h

1,2-dimethyldisulfane (37h): ^{1}H NMR (600 MHz, $CDCl_3$) δ: 2.36 (s, 6H). **^{13}C NMR (151 MHz, $CDCl_3$) δ:** 22.0 (2xCH_3).

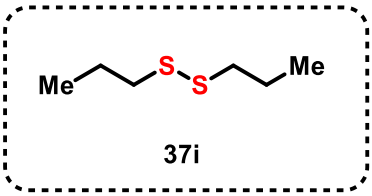

37i

1,2-dipropyldisulfane (37i): ^{1}H NMR (400 MHz, $CDCl_3$) δ: 2.63 – 2.55 (m, 4H), 1.69 – 1.59 (m, 4H), 0.93 (t, *J* = 7.3 Hz, 6H)**. ^{13}C NMR (101 MHz, $CDCl_3$) δ:** 41.3 (2xCH_2), 22.6 (2xCH_2), 13.2 (2xCH_3).

2.5.4 General Electrosynthesis Procedure

A 25 mL electrosynthesis reactor was charged with lapachol (**12**) or C-allyl lawsone (**36**) (0.5 mmol), the corresponding disulfide derivative (0.5 mmol, 1 equiv.), nBu$_4$NPF$_6$ (0.5 mmol, 1 equiv.), and acetonitrile (25 mL). The reactor was equipped with two platinum electrodes (Pt(+)||Pt(-): 10 x 10 x 0.2 mm) immersed in the solution, which was submitted to constant stirring. The continuous current was set to 10 mA and 20 V. The reaction was electrolyzed for 3 hours. The resulting mixture was transferred to a 100 mL round bottom flask and after solvent removal by reduced pressure, the crude product was purified by FCC, under the conditions noted.

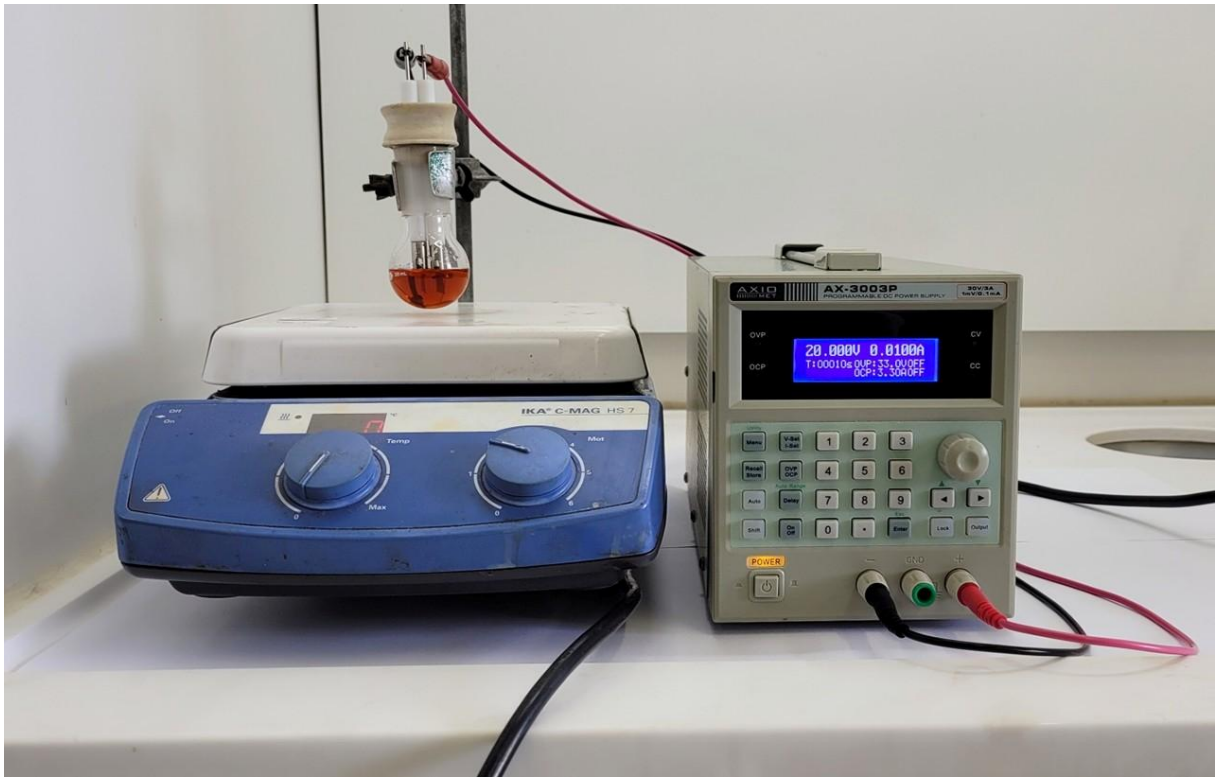

Figure 18: General apparatus for the electrosynthesis procedure.

2.5.5 Characterization Data: Products 38a-i

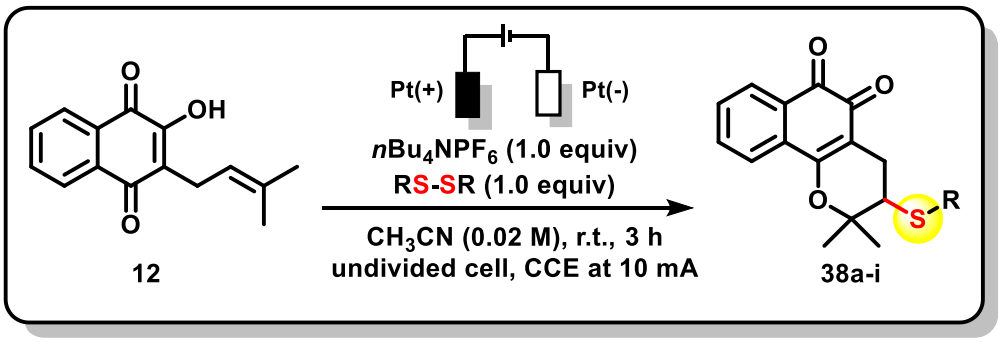

Scheme 19: Lapachol (**12**) derivatives electrochemical synthesis, compounds **38a-i.**

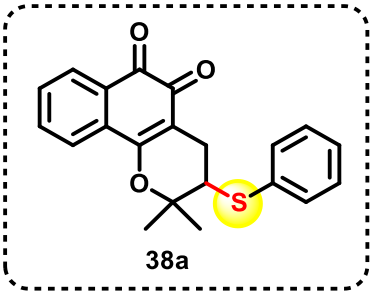

2,2-dimethyl-3-(phenylthio)-3,4-dihydro-2H-benzo[*h*]chromene-5,6-dione (38a): The product was obtained by the general electrosynthesis procedure described above. Lapachol (**12)** (121.1 mg, 0.5 mmol), 1,2-diphenyldisulfane (**37a)** (109.2 mg, 0.5 mmol), and *n*Bu_4NPF_6 (0.5 mmol) were used as starting materials. Purification by column chromatography on silica gel (*n*-hexane/EtOAc 4:1) yielded **38a** (122.5 mg, 70%) as a red solid. **^{1}H NMR (400 MHz, $CDCl_3$) *δ*:** 7.93 (d, *J* = 7.6 Hz, 1H), 7.69 (d, *J* = 7.7 Hz, 1H), 7.55 (t, *J* = 7.6 Hz, 1H), 7.39 (dd, *J* = 19.1, 7.1 Hz, 3H), 7.26-7.13 (m, 3H), 3.26 (dd, *J* = 9.5, 5.5 Hz, 1H), 2.91 (dd, *J* = 17.9, 5.5 Hz, 1H), 2.51 (dd, *J* = 17.8, 9.6 Hz, 1H), 1.57 (s, 3H), 1.42 (s, 3H).**^{13}C NMR (101 MHz, $CDCl_3$) *δ*:** 179.4 (C), 178.1 (C), 161.35 (C), 134.9 (CH), 134.0 (C), 132.6 (2xCH), 132.0 (C), 131.0 (CH), 130.1 (C), 129.3 (2xCH), 128.7 (CH), 127.9 (CH), 124.2 (CH), 112.1 (C), 82.5 (C), 50.3 (CH), 27.5 (CH_3), 24.7 (CH_2), 22.3 (CH_3). **HRMS (ESI^+):** 351.1041 $[M+H]^+$. Cald. for $[C_{21}H_{18}O_3S]^+$: 351.1055. **m.p. (°C)** = 123.0-124.2; **IR (KBr, cm^{-1}) *ν*:** 2979, 1605, 1385, 739.

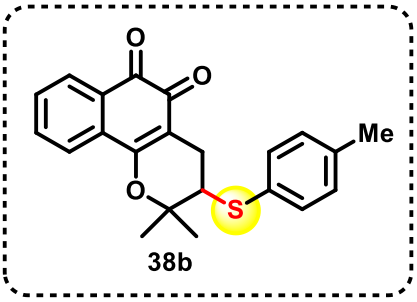

38b

2,2-dimethyl-3-(p-tolylthio)-3,4-dihydro-2H-benzo[*h*]chromene-5,6-dione (38b): The product was obtained by the general electrosynthesis procedure described above. Lapachol (**12**) (121.1 mg, 0.5 mmol), 1,2-di-*p*-tolyldisulfane (**37b**) (123.2 mg, 0.5 mmol), and nBu$_4$NPF$_6$ (0.5 mmol) were used as starting materials. Purification by column chromatography on silica gel (*n*-hexane/EtOAc 4:1) yielded **38b** (174.8 mg, 96%) as a red solid. **^{1}H NMR (400 MHz, CDCl$_3$) δ:** 8.03 (d, J = 7.5 Hz, 1H), 7.77 (d, J = 7.7 Hz, 1H), 7.63 (t, J = 7.6 Hz, 1H), 7.50 (t, J = 7.3 Hz, 1H), 7.35 (d, J = 8.1 Hz, 2H), 7.10 (d, J = 7.9 Hz, 2H), 3.26 (dd, J = 9.5, 5.5 Hz, 1H), 2.97 (dd, J = 17.9, 5.5 Hz, 1H), 2.58 (dd, J = 17.9, 9.5 Hz, 1H), 2.31 (s, 3H), 1.65 (s, 3H), 1.50 (s, 3H). **^{13}C NMR (101 MHz, CDCl$_3$) δ:** 179.6 (C), 178.3 (C), 161.4 (C), 138.3 (C),135.0 (CH), 133.4 (2xCH), 132.1 (C), 131.0 (CH), 130.3 (C), 130.2 (C), 130.1 (2xCH), 128.8 (CH), 124.3 (CH), 112.3 (CH), 82.6 (C), 50.8 (CH), 27.6 (CH_3), 24.7 (CH_2), 22.4 (CH_3) 22,2 (CH_3). **HRMS (ESI$^+$):** 365.1195 $[M+H]^+$. Cald. for $[C_{22}H_{20}O_3S]^+$: 365.1206. **m.p. (°C) =** 168.1-169.3; **IR (KBr, cm^{-1}) ν:** 2933, 1607, 1120, 815. The structure of the product was also confirmed by X-ray diffraction (CCDC number = 2233629).

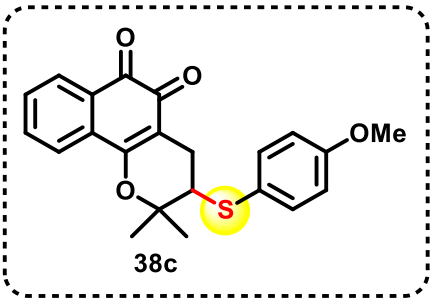

38c

3-((4-methoxyphenyl)thio)-2,2-dimethyl-3,4-dihydro-2H-benzo[*h*]chromene-5,6-dione (38c): The product was obtained by the general electrosynthesis procedure described above. Lapachol (**12**) (121.1 mg, 0.5 mmol), 1,2-bis(4-methoxyphenyl)disulfane (**37c**) (139,2 mg, 0.5 mmol), and nBu$_4$NPF$_6$ (0.5 mmol) were used as starting materials. Purification by column chromatography on silica gel (*n*-hexane/EtOAc 4:1) yielded **38c** (178.5 mg, 94%) as a red solid. **^{1}H NMR (600 MHz, CDCl$_3$) δ:** 7.97 (d, J = 7.6 Hz, 1H), 7.71 (d, J = 7.8 Hz, 1H), 7.56

(d, J = 7.6 Hz, 1H), 7.43 (t, J = 7.5 Hz, 1H), 7.35 (d, J = 8.7 Hz, 2H), 6.76 (d, J = 8.7 Hz, 2H), 3.71 (s, 3H), 3.11 (dd, J = 9.4, 5.5 Hz, 1H), 2.87 (dd, J = 17.8, 5.5 Hz, 1H), 2.51 (dd, J = 17.8, 9.4 Hz, 1H), 1.59 (s, 3H), 1.44 (s, 3H).**^{13}C NMR (151 MHz, $CDCl_3$) δ:** 179.6 (C), 178.3 (C), 161.5 (C), 160.1(C), 136.0 (2xCH), 135.0 (CH), 132.9 (C), 131,0 (CH), 130.2 (C), 128.8 (CH), 124.3 (CH), 124.1 (C), 115.0 (2xCH), 112.3 (C), 82.9 (C), 55.5 (CH), 51.4 (CH_3), 27.7 (CH_3), 24.6 (CH_2), 22.4 (CH_3). **HRMS (ESI$^+$):** 381.1144 $[M+H]^+$. Cald. for $[C_{22}H_{20}O_4S]^+$: 381.1161. **m.p. (°C) =** 154.0-155.3; **IR (KBr, cm^{-1}) ν:** 2932, 1605, 1291, 789.

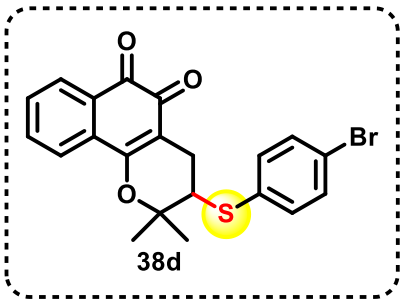

38d

3-((4-bromophenyl)thio)-2,2-dimethyl-3,4-dihydro-2H-benzo[*h*]chromene-5,6-dione (38d): The product was obtained by the general electrosynthesis procedure described above. Lapachol (**12**) (121.1 mg, 0.5 mmol), 1,2-bis(4-bromophenyl)disulfane (**37d**) (188,1 mg, 0.5 mmol), and nBu$_4$NPF$_6$ (0.5 mmol) were used as starting materials. Purification by column chromatography on silica gel (*n*-hexane/EtOAc 4:1) yielded **38d** (128.4 mg, 60%) as a red solid. **^{1}H NMR (400 MHz, $CDCl_3$) δ:** 8.06 (dd, J = 7.6, 1.1 Hz, 1H), 7.80-7.76 (m, 1H), 7.65 (td, J = 7.7, 1.3 Hz, 1H), 7.52 (td, J = 7.6, 1.1 Hz, 1H), 7.45-7.41 (m, 2H), 7.34-7.30 (m, 2H), 3.32 (dd, J = 9.4, 5.5 Hz, 1H), 2.99 (dd, J = 17.9, 5.5 Hz, 1H), 2.60 (dd, J = 17.9, 9.4 Hz, 1H), 1.65 (s, 3H), 1.51 (s, 3H).**^{13}C NMR (101 MHz, $CDCl_3$) δ:** 179.5 (C), 178.3 (C), 161.4 (C), 135.0 (CH), 134.3 (2 x CH), 133.3 (C), 132.6 (2xCH), 131.2 (CH), 130.3 (C), 129.0 (CH), 124.3 (CH), 122.3 (C), 112.1 (C), 82.4 (C), 50.7 (CH), 27.6(CH_3), 24.8 (CH_2), 22.5 (CH_3). **HRMS (ESI$^+$):** 429.0150 $[M+H]^+$. Cald. for $[C_{21}H_{17}BrO_3S]^+$: 429.0160. **m.p. (°C) =** 154.7-156.0; **IR (KBr cm^{-1}) ν:** 2979, 1607, 1292, 820.

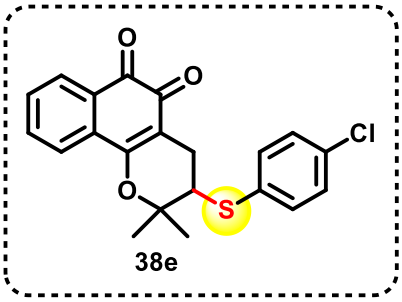

38e

3-((4-chlorophenyl)thio)-2,2-dimethyl-3,4-dihydro-2H-benzo[*h*]chromene-5,6-dione (38e): The product was obtained by the general electrosynthesis procedure described above. Lapachol (**12**) (121.1 mg, 0.5 mmol), 1,2-bis(4-chlorophenyl)disulfane *__37e)__ (143,6 mg, 0.5 mmol), and nBu$_4$NPF$_6$ (0.5 mmol) were used as starting materials. Purification by column chromatography on silica gel (*n*-hexane/EtOAc 4:1) yielded **38e** (76.8 mg, 40%) as a red solid. **^{1}H NMR (400 MHz, CDCl$_3$) δ:** 7.96 (dd, J = 7.6, 1.0 Hz, 1H), 7.71 (d, J = 7.3 Hz, 1H), 7.57 (td, J = 7.7, 1.3 Hz, 1H), 7.44 (td, J = 7.6, 1.0 Hz, 1H), 7.34-7.29 (m, 2H), 7.22-7.17 (m, 2H), 3.25 (dd, J = 9.4, 5.5 Hz, 1H), 2.91 (dd, J = 17.9, 5.5 Hz, 1H), 2.52 (dd, J = 17.9, 9.5 Hz, 1H), 1.58 (s, 3H), 1.44 (s, 3H).**^{13}C NMR (101 MHz, CDCl$_3$) δ:** 179.4 (C), 178.2 (C), 161.4 (C), 135.0 (CH), 134.2 (C), 134.1 (2xCH), 132.5 (C), 132.0 (C), 131.1 (CH), 130.1 (C), 129.5 (2xCH), 128.9 (CH), 124.3 (CH), 112.0 (C), 82.4 (C), 50.7 (CH), 27.6 (CH_3), 24.7 (CH_2), 24.0 (C), 22.4 (CH_3). **HRMS (ESI$^+$):** 385.0656 $[M+H]^+$. Cald. for $[C_{21}H_{17}ClO_3S]^+$: 385.0665. **m.p. (°C)** = 180.9-182.1; **IR (KBr, cm^{-1}) ν**: 2980, 1608, 1094, 821. The structure of the product was also confirmed by X-ray diffraction (CCDC number = 2233628).

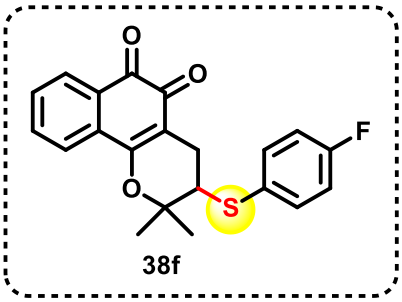

38f

3-((4-fluorophenyl)thio)-2,2-dimethyl-3,4-dihydro-2H-benzo[*h*]chromene-5,6-dione (38f): The product was obtained by the general electrosynthesis procedure described above. Lapachol (**12**) (121.1 mg, 0.5 mmol), 1,2-bis(4-fluorophenyl)disulfane **37f** (127,2 mg, 0.5 mmol), and nBu$_4$NPF$_6$ (0.5 mmol) were used as starting materials. Purification by column chromatography on silica gel (*n*-hexane/EtOAc 4:1) yielded **38f** (130.7 mg, 71%) as a red solid. **^{1}H NMR (400 MHz, CDCl$_3$) δ:** 8.05 (dd, J = 7.6, 1.1 Hz, 1H), 7.82-7.75 (m, 1H), 7.65

(td, *J* = 7.7, 1.3 Hz, 1H), 7.55-7.45 (m, 3H), 7.02 (t, *J* = 8.6 Hz, 2H), 3.26 (dd, *J* = 9.5, 5.5 Hz, 1H), 2.97 (dd, *J* = 17.8, 5.5 Hz, 1H), 2.60 (dd, *J* = 17.8, 9.5 Hz, 1H), 1.67 (s, 3H), 1.52 (s, 3H).**^{13}C NMR (101 MHz, $CDCl_3$) *δ*:** 179.5 (C), 178.3 (C), 164.1 (C), 161.5 (C), 135.7 (CH), 135.6 (CH), 135.0 (2xCH), 132.0 (C), 131.1 (CH), 130.2 (C), 129.0 (C), 129.0 (C), 128.9 (2xCH), 124.3(CH), 116.7 (CH), 116.5 (CH), 82.4, 51.3 (CH), 27.6(CH_3), 24.7 (CH_2), 22.4(CH_3). **HRMS (ESI$^+$):** 369.0949 $[M+H]^+$. Cald. for $[C_{21}H_{17}FO_3S]^+$: 369.0961. **m.p. (°C)** = 161.5-163.1; **IR (KBr, cm^{-1}) *ν*:** 2983, 1605, 1228, 823. The structure of the product was also confirmed by X-ray diffraction (CCDC number = 2233627).

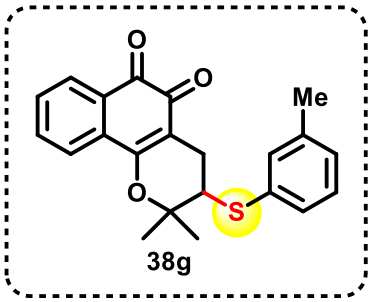

38g

2,2-dimethyl-3-(m-tolylthio)-3,4-dihydro-2H-benzo[*h*]chromene-5,6-dione (38g): The product was obtained by the general electrosynthesis procedure described above. Lapachol (**12**) (121.1 mg, 0.5 mmol), 1,2-di-m-tolyldisulfane (**37g**) (123.1 mg, 0.5 mmol), and *n*Bu_4NPF_6 (0.5 mmol) were used as starting materials. Purification by column chromatography on silica gel (*n*-hexane/EtOAc 4:1) yielded **38g** (96.5 mg, 53%) as a red solid. **^{1}H NMR (400 MHz, $CDCl_3$) *δ*:** 8.06 (dd, *J* = 7.6, 1.0 Hz, 1H), 7.81 (d, *J* = 7.3 Hz, 1H), 7.66 (td, *J* = 7.7, 1.3 Hz, 1H), 7.53 (td, *J* = 7.6, 1.0 Hz, 1H), 7.28 (d, *J* = 9.3 Hz, 2H), 7.20 (t, *J* = 7.5 Hz, 1H), 7.08 (d, *J* = 7.5 Hz, 1H), 3.36 (dd, *J* = 9.5, 5.5 Hz, 1H), 3.03 (dd, *J* = 17.9, 5.5 Hz, 1H), 2.63 (dd, *J* = 17.9, 9.5 Hz, 1H), 2.33 (s, 3H), 1.69 (s, 3H), 1.54 (s, 3H).**^{13}C NMR (101 MHz, $CDCl_3$) *δ*:** 179.5 (C), 178.3 (C), 161.4 (C), 139.2 (C), 135.0 (CH), 133.8 (C), 133.3 (CH), 132.1 (C), 131.0 (CH), 130.2 (C), 129.7 (CH), 129.2 (CH), 128.8 (CH), 128.8 (CH), 124.3 (CH), 112.3 (C), 82.6 (C), 50.4 (CH), 27.6 (CH_3), 24.8 (CH_2), 22.4 (CH_3), 21.4 (CH_3). **HRMS (ESI$^+$):** 365.1197 $[M+H]^+$. Cald. for $[C_{22}H_{20}O_3S]^+$: 365.1211. **m.p. (°C)** = 127.6-128.1; **IR (KBr, cm^{-1}) *ν*:** 2980, 1605, 1291, 783.

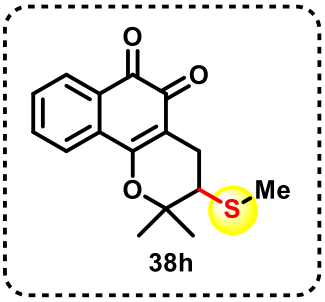

38h

2,2-dimethyl-3-(methylthio)-3,4-dihydro-2H-benzo[*h*]chromene-5,6-dione (38h): The product was obtained by the general electrosynthesis procedure described above. Lapachol (**12**) (121.1 mg, 0.5 mmol), 1,2-dimethyldisulfane (**37h**) (47.1 mg, 0.5 mmol), and nBu$_4$NPF$_6$ (0.5 mmol) were used as starting materials. Purification by column chromatography on silica gel (*n*-hexane/EtOAc 4:1) yielded **3h** (87.9 mg, 61%) as an orange solid. **^{1}H NMR (400 MHz, CDCl$_3$) δ:** 7.99 (dd, J = 7.6, 1.1 Hz, 1H), 7.73 (d, J = 7.7 Hz, 1H), 7.59 (td, J = 7.7, 1.3 Hz, 1H), 7.45 (td, J = 7.6, 1.0 Hz, 1H), 3.00 (dd, J = 17.6, 5.4 Hz, 1H), 2.78 (dd, J = 10.2, 5.4 Hz, 1H), 2.43 (dd, J = 17.6, 10.2 Hz, 1H), 2.18 (s, 3H), 1.62 (s, 3H), 1.36 (s, 3H). **^{13}C NMR (101 MHz, CDCl$_3$) δ:** 179.6 (C), 178.3 (C), 161.5 (C), 135.0 (CH), 132.2 (C), 131.1 (CH), 130.2 (C), 128.9 (CH), 124.3 (CH), 112.3 (C), 83.0 (C), 48.3 (CH), 27.6 (CH), 24.1 (CH_2), 21.8 (CH), 16.1 (CH). **HRMS (ESI$^+$):** 289.0882 $[M+H]^+$. Cald. for $[C_{16}H_{16}O_3S]^+$: 289.0898. **m.p. (°C) =** 134.6-135.9; **IR (KBr, cm^{-1}) ν:** 2981, 1603, 1292, 779.

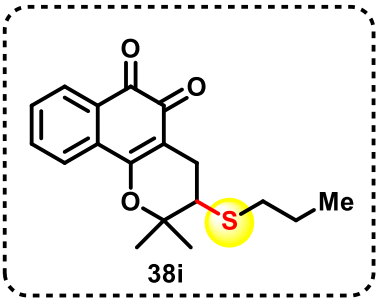

38i

2,2-dimethyl-3-(propylthio)-3,4-dihydro-2H-benzo[*h*]chromene-5,6-dione (38i): The product was obtained by the general electrosynthesis procedure described above. Lapachol (**12**) (121.1 mg, 0.5 mmol), 1,2-dimethyldisulfane (**37i**) (74.2 mg, 0.5 mmol), and nBu$_4$NPF$_6$ (0.5 mmol) were used as starting materials. Purification by column chromatography on silica gel (*n*-hexane/EtOAc 4:1) yielded **38i** (102.1 mg, 65%) as an orange solid. **^{1}H NMR (400 MHz, CDCl$_3$) δ:** 8.01 (d, J = 7.5 Hz, 1H), 7.76 (d, J = 7.7 Hz, 1H), 7.62 (t, J = 7.5 Hz, 1H), 7.48 (t, J = 7.4 Hz, 1H), 3.02 (dd, J = 17.5, 5.2 Hz, 1H), 2.85 (dd, J = 10.0, 5.5 Hz, 1H), 2.61 (t, J = 7.2 Hz, 2H), 2.48 (dd, J = 17.6, 10.4 Hz, 1H), 1.67 (s, 3H), 1.61 (dd, J = 14.5, 7.3 Hz,

2H), 1.38 (s, 3H), 0.98 (t, J = 7.2 Hz, 3H). **^{13}C NMR (101 MHz, $CDCl_3$) δ:** 179.6 (C), 178.2 (C), 161.5 (C), 134.9 (CH), 132.1 (C), 131.0 (CH), 130.1 (C), 128.7 (CH), 124.3 (CH), 112.5 (C), 83.1 (C), 46.3 (CH), 34.8 (CH_2), 27.5 (CH_3), 25.0 (CH_2), 23.1 (CH_2), 21.7 (CH_3), 13.4 (CH_3). **HRMS (ESI$^+$):** 317.1198 $[M+H]^+$. Cald. for $[C_{16}H_{16}O_3S]^+$: 317.1206. **m.p. (°C)** = 97.0-98.2; IR (**KBr**, cm^{-1}) ***v***: 2961, 1571,1294, 772.

2.5.6 Characterization Data: Products 39a-f

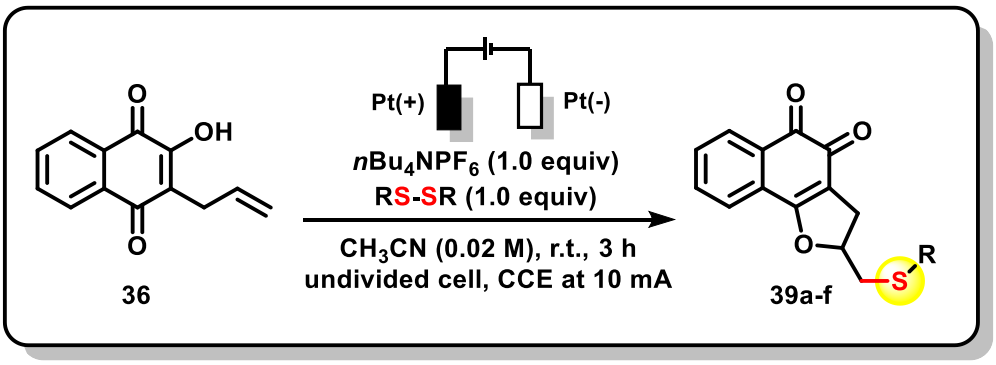

Scheme 20: C-allyl lawsone (**36**) derivatives electrochemical synthesis, compounds **39a-f**.

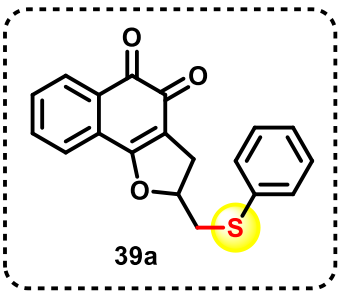

2-((phenylthio)methyl)-2,3-dihydronaphtho[1,2-*b*]furan-4,5-dione (39a): The product was obtained by the general electrosynthesis procedure described above. C-allyl lawsone (**36**) (107.0 mg, 0.5 mmol), 1,2-diphenyldisulfane (**37a**) (109.2 mg, 0.5 mmol), and nBu$_4$NPF$_6$ (0.5 mmol) were used as starting materials. Purification by column chromatography on silica gel (*n*-hexane/EtOAc 7:3) yielded **39a** (40.3 mg, 25%) as a red solid. **^{1}H NMR (400 MHz, $CDCl_3$) δ:** 8.02 (d, J = 7.0 Hz, 1H), 7.59-7.48 (m, 3H), 7.40 (d, J = 8.3 Hz, 3H), 7.22 (dd, J = 10.7, 7.6 Hz, 2H), 5.21 (dq, J = 12.4, 6.3 Hz, 1H), 3.36 (dd, J = 14.0, 5.6 Hz, 1H), 3.27-3.19 (m, 2H), 2.99 (dd, J = 15.6, 6.8 Hz, 1H).**^{13}C NMR (101 MHz, $CDCl_3$) δ:** 181.1 (C), 175.5 (C), 169.6 (C), 134.7 (C), 134.6 (CH), 132.1 (CH), 130.9 (2xCH), 130.7 (C), 129.6 (CH), 129.3 (2xCH), 127.4 (C), 127.3 (CH), 124.7 (CH), 115.2 (C), 86.2 (CH), 39.4 (CH_2), 31.5

(CH_2). **HRMS (ESI$^+$):** 323.0731 $[M+H]^+$. Cald. for $[C_{19}H_{14}O_3S]^+$: 323.0742. **m.p. (°C)** = 67.0-68.2; **IR (KBr, cm^{-1}) *v*:** 2921, 1614, 1246, 742.

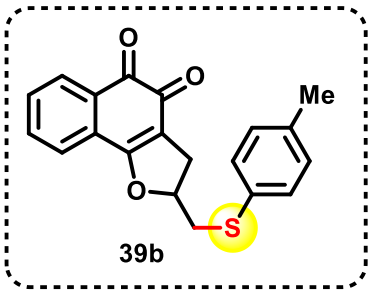

39b

2-((p-tolylthio)methyl)-2,3-dihydronaphtho[1,2-*b*]furan-4,5-dione (39b): The product was obtained by the general electrosynthesis procedure described above. C-allyl lawsone (**36**) (107.0 mg, 0.5 mmol), 1,2-di-*p*-tolyldisulfane (**37b**) (123.2 mg, 0.5 mmol), and *n*Bu_4NPF_6 (0.5 mmol) were used as starting materials. Purification by column chromatography on silica gel (*n*-hexane/EtOAc 7:3) yielded **5b** (84.0 mg, 50%) as a red solid. **^{1}H NMR (400 MHz, $CDCl_3$) *δ*:** 8.02 (d, *J* = 7.6 Hz, 1H), 7.52-7.59 (m, 2H), 7.41 (d, *J* = 7.1 Hz, 1H), 7.32 (d, *J* = 8.1 Hz, 2H), 7.06 (d, *J* = 7.9 Hz, 2H), 5.17-5.24 (m, 1H), 3.32 (dd, *J* = 14.1, 5.6 Hz, 1H), 3.26-3.17 (m, 2H), 3.00 (dd, *J* = 15.6, 6.8 Hz, 1H), 2.28 (s, 3H). **^{13}C NMR (101 MHz, $CDCl_3$) *δ*:** 181.1 (C), 175.4 (C), 169.6 (C), 137.6 (C), 134.5 (CH), 132.0 (CH), 131.6 (CH), 130.8 (C), 130.7 (C), 130.0 (CH), 129.5 (CH), 127.3 (C), 124.7 (CH), 115.1 (C), 111.9 (C), 86.3 (CH), 39.9 (CH_2), 31.4 (CH_2), 21.1 (CH_3). **HRMS (ESI$^+$):** 337.0887 $[M+H]^+$. Cald. for $[C_{20}H_{16}O_3S]^+$: 337.0898. **m.p. (°C)** = 69.0-70.1; **IR (KBr, cm^{-1}) *v*:** 2918, 1615, 1215, 805.

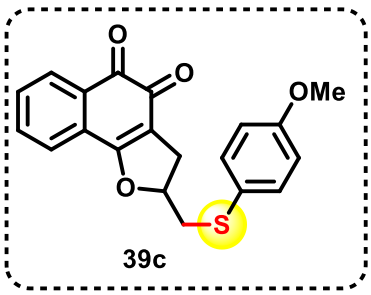

39c

2-(((4-methoxyphenyl)thio)methyl)-2,3-dihydronaphtho[1,2-*b*]furan-4,5-dione (39c): The product was obtained by the general electrosynthesis procedure described above. C-allyl lawsone (**36**) (107.0 mg, 0.5 mmol), 1,2-bis(4-methoxyphenyl)disulfane (**37c**) (139,2 mg, 0.5 mmol), and *n*Bu_4NPF_6 (0.5 mmol) were used as starting materials. Purification by column chromatography on silica gel (*n*-hexane/EtOAc 7:3) yielded **39c** (110.9 mg, 63%) as a red solid. **^{1}H NMR (400 MHz, $CDCl_3$) *δ*:** 8.03 (d, *J* = 7.2 Hz, 1H), 7.62-7.51 (m, 2H), 7.41 (dd, *J*

= 14.2, 8.0 Hz, 3H), 6.79 (d, *J* = 8.5 Hz, 2H), 5.18 (dq, *J* = 12.4, 6.3 Hz, 1H), 3.75 (s, 3H), 3.32-3.11 (m, 3H), 3.00 (dd, *J* = 15.6, 6.9 Hz, 1H). **^{13}C NMR (101 MHz, $CDCl_3$) *δ*:** 181.1 (C), 175.4 (C), 169.6 (C), 159.7 (C), 134.5 (CH), 134.4 (2xCH), 132.0 (CH), 130.7 (C), 129.5 (CH), 127.4 (C), 124.7 (C), 124.7 (CH), 115.1 (C), 114.9 (2xCH), 86.4 (CH), 55.4 (CH_3), 41.0 (CH_2), 31.3 (CH_2). **HRMS (ESI$^+$):** 353.0837 $[M+H]^+$. Cald. for $[C_{20}H_{16}O_4S]^+$: 353.0848. **m.p. (°C) =** 75.8-77.1; **IR (KBr, cm^{-1}) *ν*:** 2923, 1620, 1246, 831.

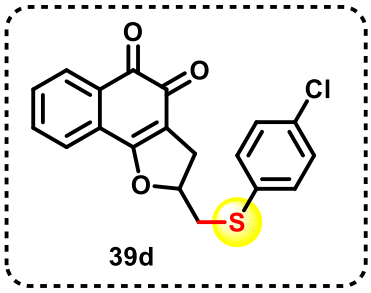

39d

2-(((4-chlorophenyl)thio)methyl)-2,3-dihydronaphtho[1,2-*b*]furan-4,5-dione (39d): The product was obtained by the general electrosynthesis procedure described above. C-allyl lawsone (**36**) (107.0 mg, 0.5 mmol), 1,2-bis(4-chlorophenyl)disulfane **(37d)** (143.6 mg, 0.5 mmol), and *n*Bu_4NPF_6 (0.5 mmol) were used as starting materials. Purification by column chromatography on silica gel (*n*-hexane/EtOAc 7:3) yielded **39d** (62.4 mg, 35%) as a red solid. **^{1}H NMR (400 MHz, $CDCl_3$) *δ*:** 7.99 (dd, *J* = 7.3, 1.4 Hz, 1H), 7.57-7.47 (m, 2H), 7.31-7.26 (m, 3H), 7.17-7.12 (m, 2H), 5.24-5.14 (m, 1H), 3.31-3.17 (m, 3H), 2.97 (dd, *J* = 15.6, 6.7 Hz, 1H). **^{13}C NMR (101 MHz, $CDCl_3$) *δ*:** 181.1 (C), 175.5 (C), 169.5 (C), 134.6 (CH), 133.4 (C), 133.4 (C), 132.3 (2xCH), 132.2 (CH), 130.7 (C), 129.6 (CH), 129.4 (2 x CH), 127.2 (C), 124.6 (CH), 115.1 (C), 86.2 (CH), 39.7 (CH_2), 31.5 (CH_2). **HRMS (ESI$^+$):** 357.0341 $[M+H]^+$. Cald. for $[C_{19}H_{13}ClO_3S]^+$: 357.0352. **m.p. (°C) =** 129.0-130.1; **IR (KBr, cm^{-1}) *ν*:** 2914, 1611, 1247, 811. The structure of the product was also confirmed by X-ray diffraction (CCDC number = 2233631).

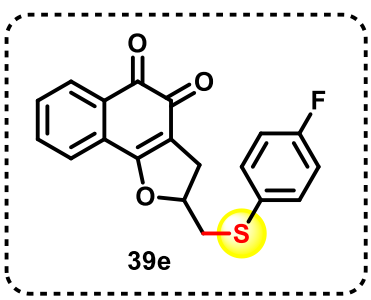

39e

2-(((4-fluorophenyl)thio)methyl)-2,3-dihydronaphtho[1,2-*b*]furan-4,5-dione (39e): The product was obtained by the general electrosynthesis procedure described above. C-allyl lawsone (**36**) (107.0 mg, 0.5 mmol), 1,2-bis(4-fluorophenyl)disulfane (**37f**) (127.2 mg, 0.5 mmol), and *n*Bu_4NPF_6 (0.5 mmol) were used as starting materials. Purification by column chromatography on silica gel (*n*-hexane/EtOAc 7:3) yielded **39e** (62.8 mg, 37%) as a red solid. **^{1}H NMR (600 MHz, $CDCl_3$) *δ*:** 8.00 (d, *J* = 7.2 Hz, 1H), 7.52 (dt, *J* = 21.6, 7.2 Hz, 2H), 7.43-7.30 (m, 3H), 6.90 (t, *J* = 8.3 Hz, 2H), 5.16 (dd, *J* = 9.6, 6.1 Hz, 1H), 3.29-3.14 (m, 3H), 2.96 (dd, *J* = 15.5, 6.7 Hz, 1H).**^{13}C NMR (151 MHz, $CDCl_3$) *δ*:** 181.1 (C), 175.5 (C), 169.6 (C), 162.5 ($^1J_{C\text{-}F}$ = 246,6 Hz), 134.6 (CH), 133.9 ($^2J_{C\text{-}F}$ = 8,0 Hz), 132.2 (CH), 130.8 (C), 129.7 ($^4J_{C\text{-}F}$ = 3,4 Hz), 129.7 (CH), 127.3 (C), 124.6 (CH), 116.5 ($^3J_{C\text{-}F}$ = 21,8 Hz), 115.2 (C), 86.2 (CH), 40.6 (CH_2), 31.5 (CH_2). **HRMS (ESI$^+$):** 341.0637 $[M+H]^+$. Cald. for $[C_{19}H_{13}FO_3S]^+$: 341.0648. **m.p. (°C)** = 163.7-167.9; **IR (KBr, cm^{-1}) *ν*:** 3058, 1611, 1217, 815. The structure of the product was also confirmed by X-ray diffraction (CCDC number = 2233630).

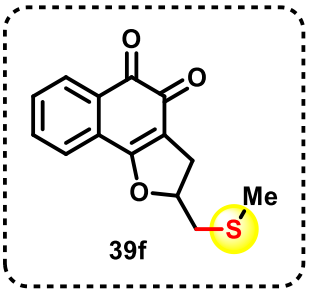

39f

2-((methylthio)methyl)-2,3-dihydronaphtho[1,2-*b*]furan-4,5-dione (39f): The product was obtained by the general electrosynthesis procedure described above. C-allyl lawsone (**36**) (107.0 mg, 0.5 mmol), 1,2-dimethyldisulfane (**37h**) (47.1 mg, 0.5 mmol), and *n*Bu_4NPF_6 (0.5 mmol) were used as starting materials. Purification by column chromatography on silica gel (*n*-hexane/EtOAc 4:1) yielded **39f** (26.0 mg, 20%) as an orange solid. **^{1}H NMR (400 MHz, $CDCl_3$) *δ*:** 8.01 (d, *J* = 7.5 Hz, 1H), 7.63-7.48 (m, 4H), 5.24 (dq, *J* = 10.0, 6.1 Hz, 1H), 3.23 (dd, *J* = 15.6, 9.9 Hz, 1H), 2.95-2.67 (m, 4H), 2.17 (s, 3H). **^{13}C NMR (101 MHz, $CDCl_3$) *δ*:** 181.1 (C), 175.5 (C), 169.6 (C), 134.7 (CH), 132.2 (CH), 130.8 (C), 129.7 (CH), 127.5 (C), 124.6 (CH), 115.3 (C), 87.0 (CH), 39.3 (CH_2), 31.8 (CH_2), 16.8 (CH_3). **HRMS (ESI$^+$):** 261.0575 $[M+H]^+$. Cald. for $[C_{14}H_{12}O_3S]^+$: 261.0585. **m.p. (°C)** = 149.8-151; **IR (KBr, cm^{-1}) *ν*:** 2914, 1610, 1213, 889.

2.5.7 General procedure for oxidation with $RuCl_3 \cdot H_2O/NaIO_4$

A round bottom flask was charged with the corresponding quinone (0.10 mmol), $NaIO_4$ (63.9 mg, 0.30 mmol), and $RuCl_3 \cdot H_2O$ (0.22 mg, 1 mol%) in $H_2O/CH_3CN/CH_2Cl_2$ (2:1:1, 4.0 mL) solution. The mixture was kept under vigorous for 1 hour, and analysis by TLC showed complete consumption of the starting material. The resulting mixture was EtOAc, and the organic phase was dried with Na_2SO_4 and submitted to purification by FCC under the conditions noted.

2.5.8 Characterization Data: Products 40a-f

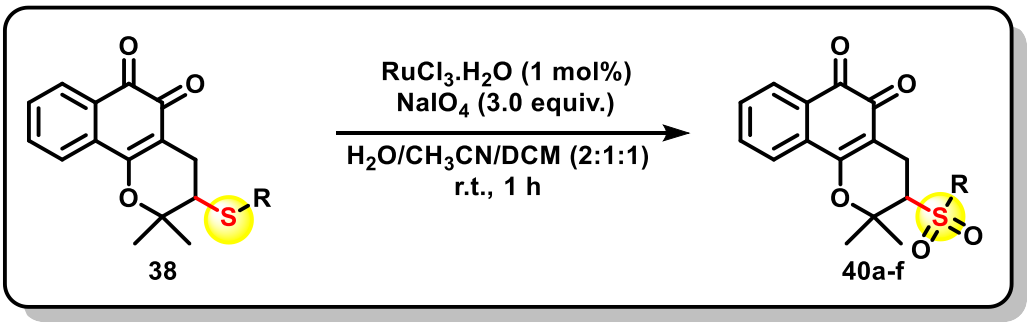

Scheme 21: Synthesis of sulfones **40a-f.**

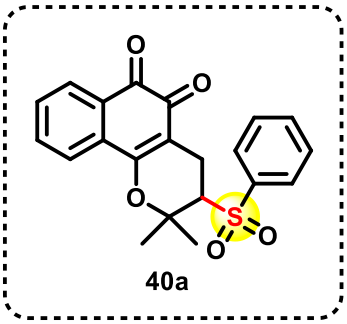

2,2-dimethyl-3-(phenylsulfonyl)-3,4-dihydro-2H-benzo[*h*]chromene-5,6-dione (40a): The product was obtained by the general procedure for oxidation described above. Quinone **38a** (35.0 mg, 0.1 mmol) was used as starting material. Purification by column chromatography on silica gel (*n*-hexane/EtOAc 1:1) yielded **40a** (35.2 mg, 92%) as an orange solid. **^{1}H NMR (400 MHz, $CDCl_3$) δ:** 7.97 (d, J = 7.5 Hz, 1H), 7.88 (s, 1H), 7.70 (s, 1H), 7.65-7.42 (m, 6H), 3.32 (dd, J = 11.3, 5.4 Hz, 1H), 2.76 (dd, J = 17.6, 11.3 Hz, 1H), 2.49 (dd, J = 17.6, 5.4 Hz, 1H), 1.92 (s, 3H), 1.64 (s, 3H). **^{13}C NMR (101 MHz, $CDCl_3$) δ:** 179.0 (C), 177.8 (C), 160.9

(C), 138.4 (C), 135.2 (CH), 134.5 (CH), 131.5 (C), 131.4 (CH), 130.1 (C), 129.7 (2 x CH), 129.1 (CH), 128.7 (2 x CH), 124.4 (CH), 110.6 (C), 80.7 (C), 64.4 (CH), 29.1 (CH_3), 22.8 (CH_3), 19.8 (CH_2). **HRMS (ESI$^+$):** 383.0941 $[M+H]^+$. Cald. for $[C_{21}H_{19}O_5S]^+$: 383.0948; **m.p. (°C) =** 198.1-199.3; **IR (KBr, cm^{-1}) *v*:** 2984, 1602, 1306, 1146, 603. The structure of the product was also confirmed by X-ray diffraction (CCDC number = 2233632).

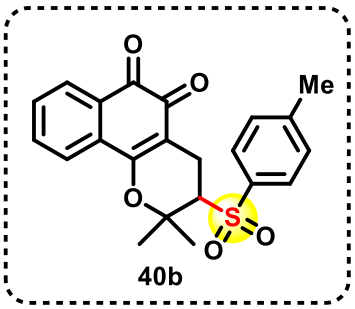

40b

2,2-dimethyl-3-tosyl-3,4-dihydro-2H-benzo[*h*]chromene-5,6-dione (40b): The product was obtained by the general procedure for oxidation described above. Quinone **38b** (36.4 mg, 0.1 mmol) was used as the starting material. Purification by column chromatography on silica gel (*n*-hexane/EtOAc 1:1) yielded **40b** (31.7 mg, 80%) as an orange solid. **^{1}H NMR (400 MHz, $CDCl_3$) *δ*:** 7.95 (d, *J* = 7.6 Hz, 1H), 7.74-7.67 (m, 3H), 7.58 (t, *J* = 7.6 Hz, 1H), 7.45 (t, *J* = 7.5 Hz, 1H), 7.28 (d, *J* = 8.1 Hz, 2H), 3.30 (dd, *J* = 11.0, 5.5 Hz, 1H), 2.74 (dd, *J* = 17.6, 11.1 Hz, 1H), 2.48 (dd, *J* = 17.7, 5.4 Hz, 1H), 29.35 (s, 3H), 1.88 (s, 3H), 1.62 (s, 3H).**^{13}C NMR (101 MHz, $CDCl_3$) *δ*:** 179.0 (C), 177.7 (C), 160.9 (C), 145.7 (C), 135.4 (C), 135.1 (CH), 131.5 (C), 131.3 (CH), 130.3 (2xCH), 130.0 (C), 128.9 (CH), 128.7 (2 x CH), 124.4 (CH), 110.6 (C), 80.7 (C), 64.3 (CH), 29.0 (CH_3), 22.8 (CH_3), 21.7 (CH_3), 19.8 (CH_2). **HRMS (ESI$^+$):** 397.1098 $[M+H]^+$. Cald. for $[C_{22}H_{21}O_5S]^+$: 397.1104. **m.p. (°C) =** 192.0-193.5; **IR (KBr, cm^{-1}) *v*:** 3063, 1602, 1291, 1145, 669.

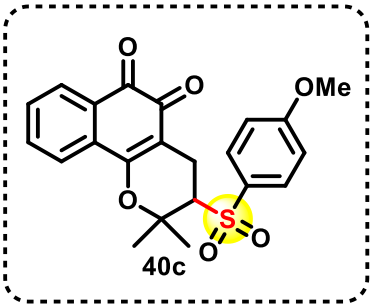

40c

3-((4-methoxyphenyl)sulfonyl)-2,2-dimethyl-3,4-dihydro-2H-benzo[*h*]chromene-5,6-dione (40c): The product was obtained by the general procedure for oxidation described

above. Quinone **38c** (38.0 mg, 0.1 mmol) was used as starting material. Purification by column chromatography on silica gel (*n*-hexane/EtOAc 1:1) yielded **40c** (38.7 mg, 94%) as an orange solid. **^{1}H NMR (400 MHz, $CDCl_3$) δ:** 7.97 (d, *J* = 7.6 Hz, 1H), 7.77 (d, *J* = 8.9 Hz, 2H), 7.69 (d, *J* = 7.6 Hz, 1H), 7.59 (t, *J* = 7.1 Hz, 1H), 7.46 (t, *J* = 7.5 Hz, 1H), 6.95 (d, *J* = 8.9 Hz, 2H), 3.80 (s, 3H), 3.28 (dd, *J* = 11.1, 5.5 Hz, 1H), 2.75 (dd, *J* = 17.6, 11.1 Hz, 1H), 2.50 (dd, *J* = 17.6, 5.5 Hz, 1H), 1.89 (s, 3H), 1.63 (s, 3H). **^{13}C NMR (101 MHz, $CDCl_3$) δ:** 179.1 (C), 177.8 (C), 164.4 (C), 161.0 (C), 135.1 (CH), 131.5 (C), 131.4 (CH), 131.0 (2 x CH), 130.1 (C), 129.7 (C), 129.0 (CH), 124.4 (CH), 114.9 (2xCH), 110.7 (C), 80.8 (C), 64.6 (CH), 55.9 (CH_3), 29.1 (CH_3), 22.8 (CH_3), 19.9 (CH_2). **HRMS (ESI^+):** 413.1046 $[M+H]^+$. Cald. for $[C_{22}H_{21}O_6S]^+$: 413.1053. **m.p. (°C)** = 76.1-77.8; **IR (KBr, cm^{-1}) *v*:** 2946, 1610,1296, 1143, 673.

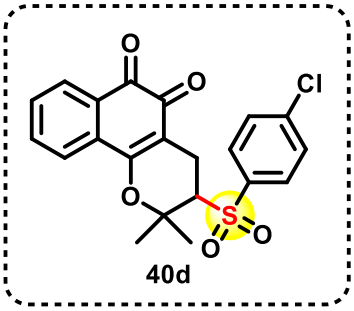

40d

3-((4-chlorophenyl)sulfonyl)-2,2-dimethyl-3,4-dihydro-2H-benzo[*h*]chromene-5,6-dione (40d): The product was obtained by the general procedure for oxidation described above. Quinone **38e** (38.5 mg, 0.1 mmol) was used as starting material. Purification by column chromatography on silica gel (*n*-hexane/EtOAc 1:1) yielded **40d** (37.4 mg, 90%) as an orange solid. **^{1}H NMR (400 MHz, $CDCl_3$) δ:** 8.04 (d, *J* = 7.6 Hz, 1H), 7.88 (d, *J* = 8.6 Hz, 2H), 7.76 (d, *J* = 7.5 Hz, 1H), 7.67 (td, *J* = 7.7, 1.2 Hz, 1H), 7.59-7.52 (m, 3H), 3.40 (dd, *J* = 11.1, 5.5 Hz, 1H), 2.83 (dd, *J* = 17.6, 11.1 Hz, 1H), 2.57 (dd, *J* = 17.6, 5.5 Hz, 1H), 1.97 (s, 3H), 1.71 (s, 3H). **^{13}C NMR (101 MHz, $CDCl_3$) δ:** 178.9 (C), 177.7 (C), 160.9 (C), 141.4 (C), 136.8 (C), 135.2 (CH), 131.5 (CH), 131.3 (C), 130.2 (2 x CH), 130.0 (2 x CH), 130.0 (C), 129.1 (CH), 124.4 (CH), 110.3 (C), 80.5 (C), 64.4 (CH), 29.1 (CH_3), 22.8 (CH_3), 19.8 (CH_2). **HRMS (ESI^+):** 417.0550 $[M+H]^+$. Cald. for $[C_{21}H_{18}ClO_5S]^+$: 417.0558. **m.p. (°C)** = 173.9-175.2; **IR (KBr, cm^{-1}) *v*:** 2934, 1602, 1295,1140, 756.

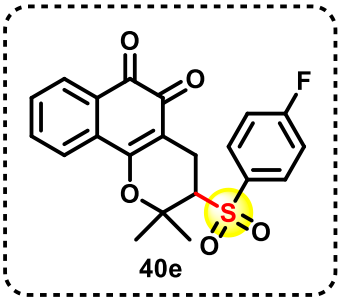

40e

3-((4-fluorophenyl)sulfonyl)-2,2-dimethyl-3,4-dihydro-2H-benzo[*h*]chromene-5,6-dione (40e): The product was obtained by the general procedure for oxidation described above. Quinone **38f** (36.8 mg, 0.1 mmol) was used as starting material. Purification by column chromatography on silica gel (*n*-hexane/EtOAc 1:1) yielded **40e** (33.6 mg, 84%) as an orange solid. **^{1}H NMR (400 MHz, $CDCl_3$) δ:** 8.05 (d, *J* = 6.7 Hz, 1H), 7.97 (dd, *J* = 8.8, 5.0 Hz, 2H), 7.77 (d, *J* = 7.8 Hz, 1H), 7.67 (t, *J* = 7.0 Hz, 1H), 7.55 (t, *J* = 8.0 Hz, 1H), 7.28 (dd, *J* = 9.2, 5.8 Hz, 2H), 3.38 (dd, *J* = 11.3, 5.4 Hz, 1H), 2.83 (dd, *J* = 17.6, 11.3 Hz, 1H), 2.56 (dd, *J* = 17.6, 5.4 Hz, 1H), 1.98 (s, 3H), 1.71 (s, 3H). **^{13}C NMR (101 MHz, $CDCl_3$) δ:** 178.9 (C), 177.7 (C),166,3 (C), 167.6 (C), 165.0 (C), 160.9 (C), 135.2 (CH), 134.5 (C), 134.5 (C), 131.7 (CH), 131.6 (CH), 131.5 (CH), 131.4 (C), 130.1 (C), 129.1 (CH), 124.4 (CH), 117.2 (CH), 117.0 (CH), 80.6 (CH), 64.6 (CH), 29.1 (CH_3), 22.8 (CH_3), 19.9 (CH_2). **HRMS (ESI$^+$):** 401.0846 $[M+H]^+$. Cald. for $[C_{21}H_{18}FO_5S]^+$: 401.0853. **m.p. (°C)** = 194.0-195.4; **IR (KBr, cm^{-1}) *v*:** 2976, 1619, 1289, 1149, 846.

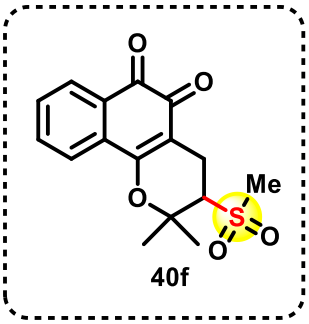

40f

2,2-dimethyl-3-(methylsulfonyl)-3,4-dihydro-2H-benzo[*h*]chromene-5,6-dione (40f): The product was obtained by the general procedure for oxidation described above. Quinone **38h** (28.8 mg, 0.1 mmol) was used as the starting material. Purification by column chromatography on silica gel (*n*-hexane/EtOAc 1:1) yielded **40f** (22.7 mg, 71%) as an orange solid. **^{1}H NMR (400 MHz, $CDCl_3$) δ:** 8.04 (d, *J* = 7.5 Hz, 1H), 7.75 (d, *J* = 7.7 Hz, 1H), 7.65 (t, *J* = 7.4 Hz, 1H), 7.53 (t, *J* = 7.5 Hz, 1H), 3.38 (dd, *J* = 11.4, 5.3 Hz, 1H), 3.10-3.02 (m, 4H), 2.93 (dd, *J* = 17.3, 11.6 Hz, 1H), 1.92 (s, 3H), 1.60 (s, 3H).**^{13}C NMR (101 MHz,**

CDCl$_3$) δ: 179.0 (C), 177.8 (C), 161.2 (C), 135.2 (CH), 131.6 (CH), 131.3 (C), 130.0 (C), 129.1 (CH), 124.5 (CH), 110.3 (C), 80.4 (C), 63.3 (CH), 41.7 (CH_3), 28.8 (CH_3), 22.5 (CH_3), 19.9 (CH_2). **HRMS (ESI$^+$):** 321.0782 $[M+H]^+$. Cald. for $[C_{16}H_{17}O_5S]^+$: 321.0791. **m.p. (°C)** = 190.6-191.8; **IR (KBr, cm^{-1}) ν:** 2980, 1617, 1149,1085, 618.

2.5.9 Characterization Data: Products 41a-c

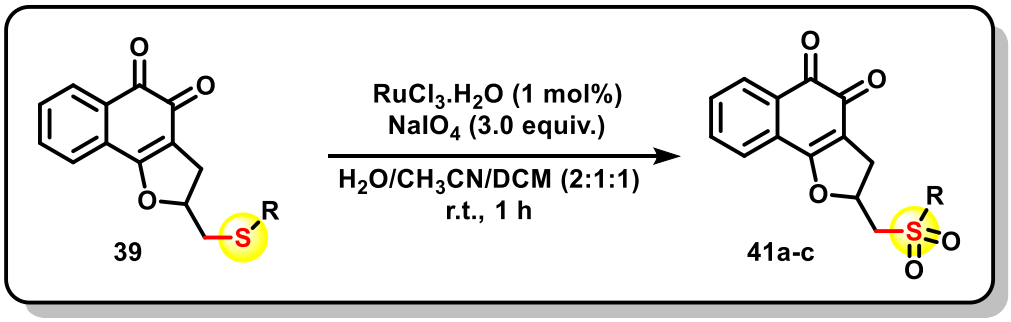

Scheme 22: Synthesis of sulfones **41a-c.**

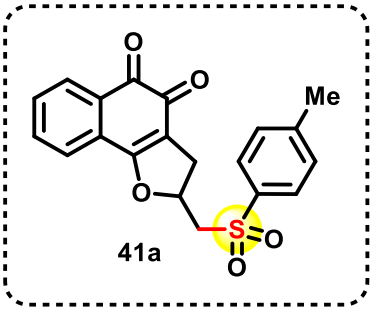

2-(tosylmethyl)-2,3-dihydronaphtho[1,2-*b*]furan-4,5-dione (41a): The product was obtained by the general procedure for oxidation described above. Quinone **39b** (33.6 mg, 0.1 mmol) was used as starting material. Purification by column chromatography on silica gel (*n*-hexane/EtOAc 1:1) yielded **41a** (28.8 mg, 78%) as an orange solid. ^{1}H NMR (400 MHz, $CDCl_3$) δ: 8.01 – 7.96 (m, 1H), 7.81 (d, J = 8.3 Hz, 2H), 7.54 – 7.48 (m, 2H), 7.35 (d, J = 8.1 Hz, 2H), 7.18 – 7.13 (m, 1H), 5.50-5.44 (m, 1H), 3.67 (dd, J = 14.6, 7.6 Hz, 1H), 3.42 (dd, J = 14.6, 4.9 Hz, 1H), 3.30 (dd, J = 15.8, 10.2 Hz, 1H), 2.83 (dd, J = 15.8, 7.1 Hz, 1H), 2.43 (s, 3H). **^{13}C NMR (101 MHz, CDCl$_3$) δ:** 180.7 (C), 175.3 (C), 168.8 (C), 145.6 (C), 136.7 (C), 134.6 (CH), 132.4 (CH), 130.7 (C), 130.3 (2xCH), 129.8 (CH), 128.5 (2xCH), 126.9 (C), 124.7 (CH), 114.5 (C), 80.8 (CH), 61.3 (CH_2), 32.5 (CH_2), 21.9 (CH_3). **HRMS (ESI$^+$):** 369.0797 $[M+H]^+$. Cald. for $[C_{20}H_{17}O_5S]^+$: 369.0791. **m.p. (°C)** = 91.3-93.0; **IR (KBr, cm^{-1}) ν:** 2925, 1618, 1294, 1135, 770.

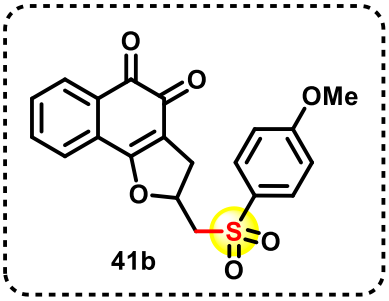

2-(((4-methoxyphenyl)sulfonyl)methyl)-2,3-dihydronaphtho[1,2-*b*]furan-4,5-dione (41b): The product was obtained by the general procedure for oxidation described above. Quinone **39c** (35.2 mg, 0.1 mmol) was used as starting material. Purification by column chromatography on silica gel (*n*-hexane/EtOAc 1:1) yielded **41b** (36.6 mg, 85%) as an orange solid. **^{1}H NMR (400 MHz, DMSO) *δ*:** 8.01 – 7.96 (m, 1H), 7.87 – 7.82 (m, 2H), 7.54 – 7.47 (m, 2H), 7.21 (dd, *J* = 4.1, 2.8 Hz, 1H), 7.03 – 6.97 (m, 2H), 5.51 – 5.41 (m, 1H), 3.85 (s, 3H), 3.66 (dd, *J* = 14.6, 7.5 Hz, 1H), 3.42 (dd, *J* = 14.6, 5.0 Hz, 1H), 3.30 (dd, *J* = 15.8, 10.2 Hz, 1H), 2.84 (dd, *J* = 15.8, 7.1 Hz, 1H). **^{13}C NMR (101 MHz, DMSO) *δ*:** 180.3 (C), 174.8 (C), 167.4 (C), 163.5 (C), 134.4 (CH), 132.2 (CH), 131.6 (C), 130.4 (C), 130.3 (2xCH), 128.7 (CH), 126.6 (C), 123.9 (CH), 114.8 (C), 114.6 (2xCH), 81.3 (CH), 59.7 (CH_2), 55.9 (CH_3), 31.4 (CH_2). **HRMS (ESI$^+$):** 385.0746 $[M+H]^+$. Cald. for $[C_{20}H_{17}O_8S]^+$: 385.0740. **m.p. (°C)** = 178.6 - 180.1; **IR (KBr, cm^{-1}) *ν*:** 2921, 1609, 1305, 1119, 785.

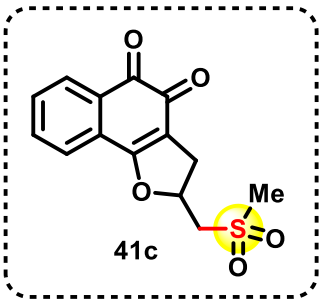

2-((methylsulfonyl)methyl)-2,3-dihydronaphtho[1,2-*b*]furan-4,5-dione (**41c**): The product was obtained by the general procedure for oxidation described above. Quinone **39f** (26.0 mg, 0.1 mmol) was used as starting material. Purification by column chromatography on silica gel (*n*-hexane/EtOAc 1:1) yielded **41c** (16.7 mg, 57%) as an orange solid. **^{1}H NMR (400 MHz, DMSO) *δ*:** 7.96 (d, *J* = 7.4 Hz, 1H), 7.79 (t, *J* = 7.3 Hz, 1H), 7.72–7.64 (m, 2H), 5.61-5.54 (m, 1H), 3.96 (dd, *J* = 15.0, 8.9 Hz, 1H), 3.66 (dd, *J* = 15.0, 2.7 Hz, 1H), 3.14 (s, 3H), 2.85 (dd, *J* = 15.5, 6.7 Hz, 2H). **^{13}C NMR (101 MHz, DMSO) *δ*:** 180.3 (C), 175.0 (C), 167.6 (C), 134.9 (CH), 132.2 (CH), 130.5 (C), 128.8 (CH), 126.8 (C), 124.3 (CH), 114.9 (C), 81.2 (CH), 58.2 (CH_2), 42.5 (CH_3), 31.6 (CH_2). **HRMS (ESI$^+$):** 293.0404 $[M+H]^+$. Cald. for

$[C_{14}H_{13}O_5S]^+$: 293.0478. **m.p. (°C)** = 217.0- 218.9; **IR (KBr, cm^{-1}) *v*:** 2925, 1613, 1304, 1124.

2.5.10 Synthesis and Characterization Products 42-44.

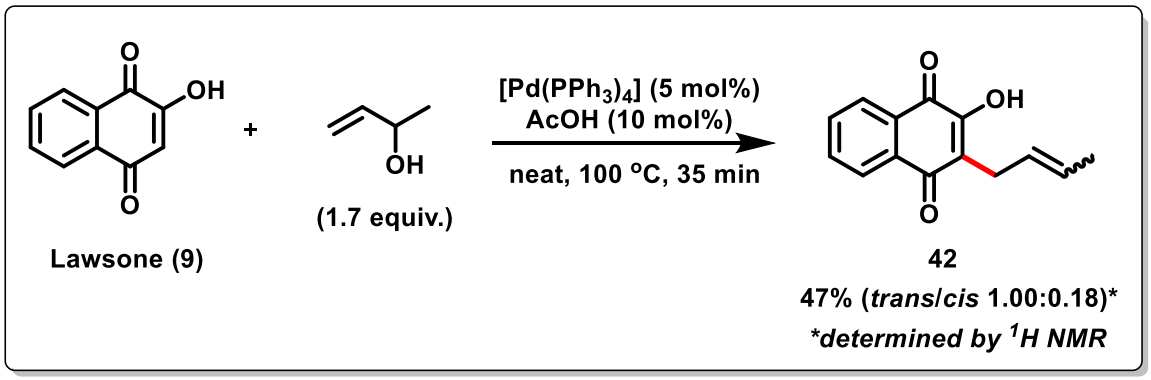

Scheme 23: Synthesis of compound **42**.

We also evaluated using 2-(but-2-en-1-yl)-3-hydroxy-1,4-naphthoquinone as substrate in the electrochemical sulfenylation/cyclization reaction. In this direction, we initially prepared the following derivative according to the method described by Spyroudis and co-workers.[69] A mixture of lawsone (470 mg, 2.7 mmol), $Pd(PPh_3)_4$ (156 mg, 0.135 mmol), AcOH (15.5 µL, 16.2 mg, 0.27 mmol) and 3-buten-2-ol (390 µL, 324 mg, 4.5 mmol) was thoroughly mixed and was put in a preheated oil bath at 100 °C. After 35 min the material was subjected to column chromatography (*n*-hexane/AcOEt 5:1) to afford the desired compound as a yellow solid composed of an inseparable mixture of the *trans* and *cis* isomers (290 mg, 47%, ***trans*** 1.00:0.18 ***cis***). *The achieved proportion was determined by ^{1}H-NMR and attribution of each isomer to its respective proportion was based on the literature.*

^{1}H NMR (400 MHz, $CDCl_3$) *δ*: 8.09 (d, *J* = 7.6 Hz, 1.18 H, 1 × H-*trans* + 1 × H-*cis*), 8.04 (d, *J* = 7.6 Hz, 1.18 H, 1 × H-*trans* + 1 × H-*cis*), 7.72 (td, *J* = 7.5, 0.7 Hz, 1.18 H, 1 × H-*trans* + 1 × H-*cis*), 7.65 (td, *J* = 7.5, 0.7 Hz, 1.18 H, 1 × H-*trans* + 1 × H-*cis*), 7.41 (s, 1.18 H, 1 × H-*trans* + 1 × H-*cis*), 5.63-5.43 (m, 2.36 H, 2 × H-*trans* + 2 × H-*cis*), 3.35 (d, *J* = 7.1 Hz, 0.36 H, 2 × H-*cis*), 3.27 (d, *J* = 6.4 Hz, 2.00 H, 2 × H-*trans*), 1.77 (d, *J* = 6.4 Hz, 0.54 H, 3 × H-*cis*), 1.62 (dd, *J* = 6.1, 0.8 Hz, 3.00 H, 3 × H-*trans*). **^{13}C NMR (101 MHz, $CDCl_3$) *δ*:** 184.4 (C-*trans* + C-*cis*), 181.7 (C-*trans* + C-*cis*), 153.0 (C-*trans* + C-*cis*), 135.0 (CH-*trans* + CH-*cis*), 133.0 (CH-*trans* + CH-*cis*), 132.9 (C-*trans* + C-*cis*), 129.5 (C-*trans* + C-*cis*), 127.4 (CH-*trans* + CH-*cis*), 126.9 (CH-*trans*), 126.9 (CH-*cis*), 126.3 (CH-*trans*), 126.2 (CH-*trans*),

[69]. Kazantzi, G.; Malamidou-Xenikaki; E.; Spyroudis, S. *Synlett*, **2007**, 03, 0427-0430.

126.1 (CH-*cis*), 125.8 (CH-*cis*), 123.1 (C-*cis*), 122.8 (C-*trans*), 26.4 (CH_2-*trans*), 21.6 (CH_2-*cis*), 18.0 (CH_3-*trans*), 13.0 (CH_3-*cis*). **HRMS (ESI$^+$):** 229.0866 $[M+H]^+$. Cald. for $[C_{14}H_{13}O_3]^+$: 229.0865; **IR (KBr, cm^{-1}) *v*:** 3340, 1640, 1588, 1344, 1271, 1217, 1099.

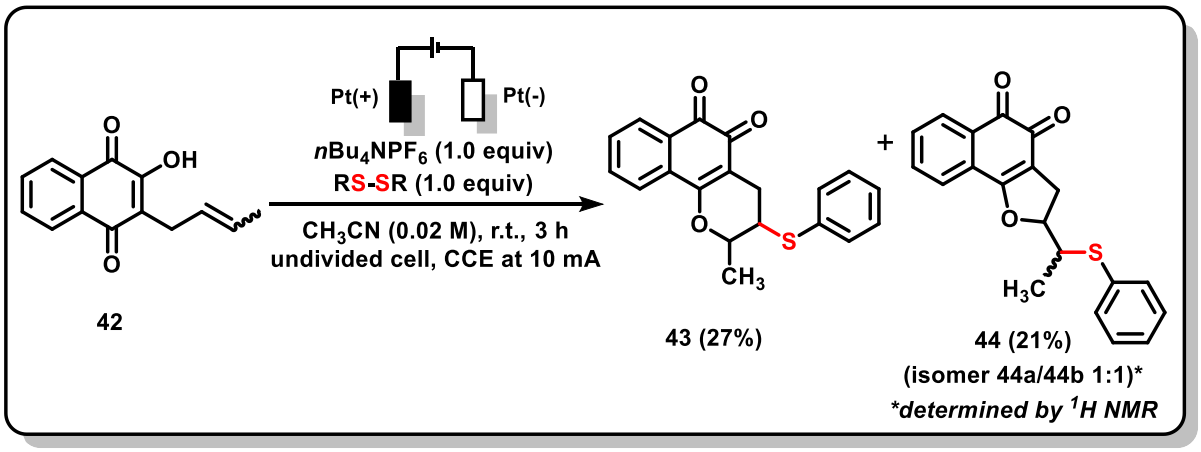

Scheme 24: Synthesis of compounds **43** and **44**.

The general electrosynthesis procedure described above was also proceeded using 2-(but-2-en-1-yl)-3-hydroxynaphthalene-1,4-dione **42** (114.0 mg, 0.5 mmol) as substrate, along with 1,2-diphenyldisulfane **37a** (109.2 mg, 0.5 mmol), and *n*Bu_4NPF_6 (0.5 mmol). Purification by column chromatography on silica gel (*n*-hexane/EtOAc 7:3) yielded the products **43** as a yellow solid (45 mg, 27%) and **44** (35 mg, 21%) as an orange solid.

2-methyl-3-(phenylthio)-3,4-dihydro-2*H*-benzo[*h*]chromene-5,6-dione (43)

^{1}H NMR (400 MHz, $CDCl_3$) *δ*: 8.05 (ddd, *J* = 7.7, 1.4, 0.4 Hz, 1H), 7.79 (dd, *J* = 7.8, 0.8 Hz, 1H), 7.64 (td, *J* = 7.6, 1.5 Hz, 1H), 7.55-7.51 (m, 1H), 7.49-7.47 (m, 2H), 7.34-7.30 (m, 3H), 4.40 (quint, *J* = 6.4 Hz, 1H), 3.30-3.24 (m, 1H), 2.97 (dd, *J* = 17.7, 5.4 Hz, 1H), 2.55 (dd, *J* = 17.7, 8.2 Hz, 1H), 1.62 (d, *J* = 6.44 Hz, 3H). **^{13}C NMR (101 MHz, $CDCl_3$) *δ*:** 179.5 (C), 178.4 (C), 161.8 (C), 135.0 (CH), 133.7 (2xCH), 132.3 (C), 131.9 (C), 131.1 (CH), 130.1 (C), 129.4 (2xCH), 128.9 (CH), 128.4 (CH), 124.3 (CH), 112.4 (C), 77.8 (CH), 45.2 (CH), 24.3 (CH_2), 19.6 (CH_3). **HRMS (ESI$^+$):** 337.0880 $[M+H]^+$. Cald. for $[C_{20}H_{17}O_3S]^+$: 337.0898. **m.p. (°C) =** 109-112; **IR (KBr, cm^{-1}) *v*:** 3070, 2926, 1698, 1602, 1572, 1342, 1253, 690.

2-(1-(phenylthio)ethyl)-2,3-dihydronaphtho[1,2-*b*]furan-4,5-dione (44)

*The desired compound **44** was obtained as an inseparable mixture of diastereoisomers **44a** and **44b**, which could not be separately assigned by NMR analyses*. **^{1}H NMR (400 MHz, $CDCl_3$) *δ*:** 8.07-8.03 (m, 1H), 7.63-7.54 (m, 2H), 7.49-7.42 (m, 2H), 7.39-7.32 (m, 1H), 7.31-7.28 (m, 1H), 7.27-7.19 (m 2H), 5.15-5.09 (m, 1H), 3.67-3.55 (m, 1H), 3.25-3.08 (2H), 1.43-

1.35 (m, 3H). **^{13}C NMR (101 MHz, $CDCl_3$) δ:** 181.2/181.1 (C-44a and C-44b), 175.4/175.4 (C-44a and C-44b), 169.8/169.8 (C-44a and C-44b), 134.6/134.5 (CH-44a and CH-44b), 133.6/133.4 (C-44a and C-44b), 133.3/132.8 (2xCH-44a and 2xCH-44b), 132.1/132.0 (CH-44a and CH-44b), 130.8/130.8 (C-44a and C-44b), 129.6/129.5 (CH-44a and CH-44b), 129.3/129.1 (2xCH-44a and 2xCH-44b), 127.9/127.9 (CH-44a and CH-44b), 127.4/127. (C-44a and C-44b), 124.6/124.6 (CH-44a and CH-44b), 115.6/115.6 (C-44a and C-44b), 90.2/89.6 (CH-44a and CH-44b), 47.9/46.4 (CH-44a and CH-44b), 29.8/28.6 (CH_2-44a and CH_2-44b), 17.0/15.3 (CH_3-44a and CH_3-44b). **HRMS (ESI^+):** 337.0879 $[M+H]^+$. Cald. for $[C_{20}H_{17}O_3S]^+$: 337.0898. **m.p. (°C) =** 85-86; **IR (KBr, cm^{-1}) ν:** 3059, 2928, 1614, 1570, 1406, 887, 723.

Chapter 2:

Development of Photochemical Methodologies

This chapter of the thesis was developed during a ten-month sandwich Ph.D. program, in collaboration with Professors Dr. Edmond Gravel and Dr. Eric Doris at the Commissariat à l'Énergie Atomique et aux Énergies Alternatives (CEA), Paris-Saclay, from September 2024 to June 2025, as part of the CAPES/COFECUB Project, Call No. 08/2023, Grant No. 88887.949766/2024-00.

3.1 INTRODUCTION

3.1.1 Photochemistry – Background

According to IUPAC, photochemistry is the branch of chemistry concerned with the chemical effects of light, spanning from ultraviolet (UV) to infrared (IR) radiation. A photochemical reaction refers to a chemical transformation initiated by the absorption of ultraviolet, visible, or infrared light.[70]

Unlike conventional thermal reactions, in which activation energy is supplied as heat, photochemical processes acquire this energy from light, typically in the UV or visible region.

Historically, photochemistry has played a central role in advancing the understanding of light–matter interactions. Foundational studies by Grotthuss and Draper established key laws regarding light absorption and its efficiency in inducing chemical changes.[71] The development of spectroscopy in the 20th century, and more recently supramolecular photochemistry and organic photocatalysis, has greatly expanded the range of viable transformations.[72]

Today, photochemistry serves as a versatile tool across multiple scientific disciplines. In organic synthesis,[73] it enables selective reactions under mild conditions. In materials science, it supports the design of functional of polymers[74] and in energy research, it contributes to the development of solar cells and solar-driven chemical energy storage systems.[75]

Beyond synthetic applications, photochemistry also offers promising strategies to address environmental challenges. Many photochemical processes operate under ambient conditions, reducing the need for high temperatures or hazardous reagents, thus aligning with the principles of green chemistry.[76] Furthermore, the use of sunlight as a clean and abundant energy source enhances the sustainability of these methods.[77] Applications include pollutant

---

[70] *IUPAC Compendium of Chemical Terminology*, 5th ed. International Union of Pure and Applied Chemistry; 2025.
[71] PERSICO, M.; Granucci, G. *Photochemistry. Theoretical Chemistry and Computational Modelling*. Springer International Publishing AG, part of Springer Nature 2018.
[72] BHATTACHARYYA, A.; DE SARKAR, S.; DAS, A. Supramolecular engineering and self-assembly strategies in photoredox catalysis. **ACS Catalysis**, v. 11, n. 2, p. 710-733, 2020.
[73] LIU, Jinjian *et al.* New redox strategies in organic synthesis by means of electrochemistry and photochemistry. **ACS Central Science**, v. 6, n. 8, p. 1317-1340, 2020.
[74] WEERASINGHE, M.A. *et al*. Polymers and light: a love–hate relationship. **Chemical Science**, v. 16, n. 13, p. 5326-5352, 2025.
[75] SAHU, P. K. *et al.* Design and development of nanostructured photocatalysts for large-scale solar green hydrogen generation. **Sustainable Energy & Fuels**, v. 8, n. 9, p. 1872-1917, 2024.
[76] QUINTAVALLA, A.; CARBONI, D.; LOMBARDO, M. Green Metrics and Sustainability in Photocatalysis. **ChemCatChem**, v. 16, n. 14, p. e202301225, 2024.
[77] MAKA, A. O.M; ALABID, J. M. Solar energy technology and its roles in sustainable development. **Clean Energy**, v. 6, n. 3, p. 476-483, 2022.

degradation,[78] water purification,[79] and the conversion of carbon dioxide into value-added chemicals.[80] By minimizing waste and energy consumption, photochemistry plays a pivotal role in advancing environmentally friendly technologies.

3.1.2 Fundamental Principles

The foundation of photochemical reactions lies in the interaction between electromagnetic radiation and molecules. When a light beam encounters a substance, it may be reflected, transmitted, or absorbed. Absorption occurs when the energy of the incident photon matches the energy gap between two electronic states of the absorbing species. The energy of radiation depends on its wavelength or frequency, as defined by the electromagnetic spectrum, which spans from low-energy radio waves to high-energy gamma rays (**Figure 19**).[81]

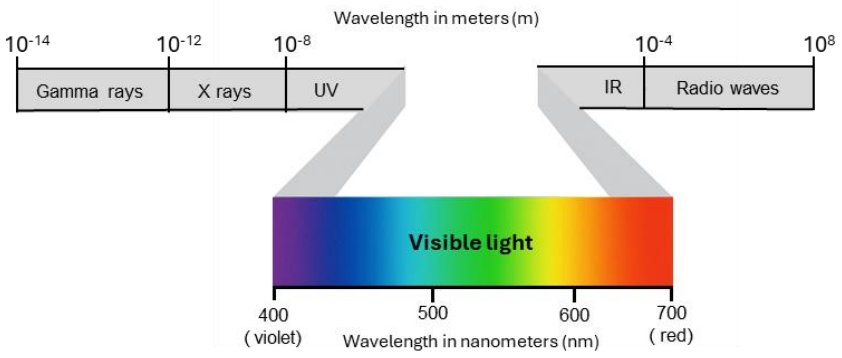

Figure 19: The electromagnetic spectrum, showing the range of wavelengths from gamma rays to radio waves.

Photon absorption promotes an electron from the ground state (S_0) to a higher-energy excited state, typically the first singlet excited state (S_1). This electronic transition is extremely fast (10^{-15} to 10^{-14} s) and governed by quantum mechanical principles, particularly by electronic selection rules.[82]

---

[78] SWAMINAATHAN, P. *et al*. Recent advances in photocatalytic degradation of persistent organic pollutants: Mechanisms, challenges, and modification strategies. **Sustainable Chemistry for the Environment**, p. 100171, 2024.
[79] BERRUTI, I. *et al*. Recent advances in solar photochemical processes for water and wastewater disinfection. **Chemical Engineering Journal Advances**, v. 10, p. 100248, 2022.
[80] YAASHIKAA, P. R. *et al*. A review on photochemical, biochemical and electrochemical transformation of CO2 into value-added products. **Journal of CO_2 Utilization**, v. 33, p. 131-147, 2019.
[81] GEORGE, C. *et al*. Interfacial photochemistry. In: **Physical Chemistry of Gas-Liquid Interfaces**. Elsevier, 2018. p. 435-457.
[82] ROHATGI-MUKHERJEE, K. K. **Fundamentals of photochemistry**. New Age International, 1978.

Once excited, the molecule exists in an electronically excited state. In a singlet state, the electron spins remain paired, as in the ground state. However, through processes such as intersystem crossing (ISC), the molecule may transition to a triplet state (T_1), where the spins are parallel. Triplet states are typically more stable and longer-lived than singlet excited states, and they exhibit distinct reactivity due to their different spin configurations and lifetimes.[83]

The photophysical behavior of a molecule can be illustrated by a Jablonski diagram (**Scheme 25**), which depicts the electronic states involved in excitation and the possible relaxation pathways. Upon photon absorption, a molecule is promoted from the ground state (S_0) to an excited singlet state (S_n). From there, it may relax to lower singlet levels through internal conversion and return non-radiatively to the ground state. Alternatively, it may emit a photon via fluorescence, typically a rapid process occurring from S_1 to S_0 on the nanosecond timescale. Intersystem crossing can also populate the triplet state (T_1), which, due to its spin-forbidden nature, decays more slowly. This decay can occur radiatively through phosphorescence, often observed on microsecond to millisecond timescales or through non-radiative pathways such as vibrational relaxation. These competing processes determine whether the excitation energy is dissipated or retained for photochemical transformations.[12-14]

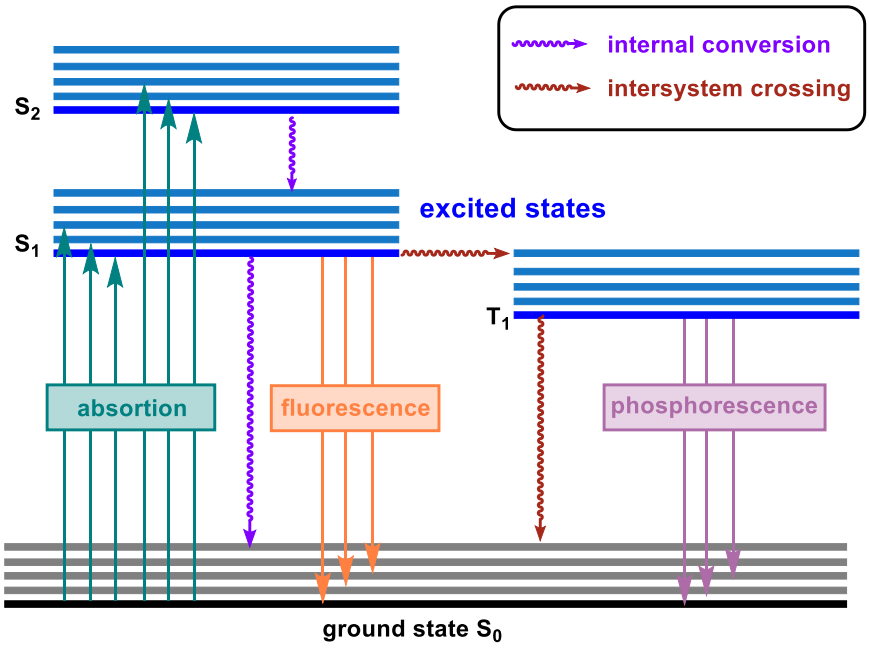

Scheme 25: Jablonski diagram showing basic photophysical processes; S for singlet state and T for triplet state.

[83] HEINE, J.; MÜLLER-BUSCHBAUM, K. Engineering metal-based luminescence in coordination polymers and metal–organic frameworks. **Chemical Society Reviews**, v. 42, n. 24, p. 9232-9242, 2013.

If the excited species is sufficiently stable and reactive, it can participate in specific chemical reactions. One major pathway is single electron transfer (SET), in which the excited molecule acts as either an oxidant or reductant, initiating redox processes with other species. [84] Another pathway is energy transfer (EnT), in which the excitation energy is transferred to a second molecule without electron exchange, as in triplet–triplet sensitization (**Scheme 26**).[85]

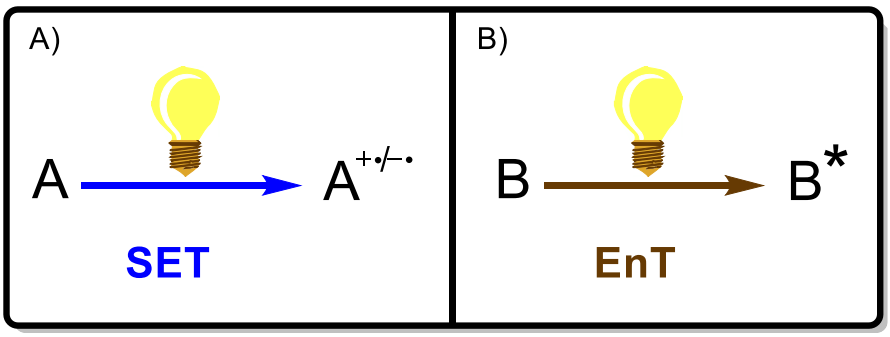

Scheme 26: Schematic representation of photochemical mechanisms: (A) Single-electron transfer (SET), in which a donor (A) transfers an electron to an acceptor, forming radical ions ($A^{+\cdot}/A^{-\cdot}$), and (B) Energy transfer (EnT), in which a donor (B) transfers its excitation energy to an acceptor (B*), with no electron movement.

These pathways are particularly significant in photosensitizer mediated systems, such as redox photocatalysis, where the excited species often serves as a photochemical mediator. After transferring electrons or energy, the photosensitizer is regenerated, thus closing the catalytic cycle. This regeneration can occur spontaneously through a sacrificial donor or acceptor, or it may be coupled to another reaction step, such as a redox coupling with an intermediate generated elsewhere in the system.[86] Such catalytic turnover is essential for enabling photochemical reactions to proceed efficiently with catalytic amounts of the sensitizer, thereby enhancing both the practicality and the sustainability of the process.

Having outlined the fundamental mechanisms that govern photochemical processes, it is essential to consider the practical aspects of how these reactions are driven specifically, the choice of light source.

---

[84] YOSHIDA, J.; PATUREAU, F. W. **Organic Redox Chemistry**. Wiley-VCH, 2021.
[85] STRIETH-KALTHOFF, F.; GLORIUS, F. Triplet energy transfer photocatalysis: unlocking the next level. **Chem**, v. 6, n. 8, p. 1888-1903, 2020.
[86] LOWE, G. A. Enabling artificial photosynthesis systems with molecular recycling: A review of photo-and electrochemical methods for regenerating organic sacrificial electron donors. **Beilstein Journal of Organic Chemistry**, v. 19, n. 1, p. 1198-1215, 2023. b) COSTANTINO, F.; KAMAT, P. V. Do sacrificial donors donate H_2 in photocatalysis?. **ACS Energy Letters**, v. 7, n. 1, p. 242-246, 2021.

3.1.3 Sources of Light

The proper selection of a light source is a critical factor in the planning and execution of photochemical reactions, as it determines which electronic transitions can be accessed by the reacting molecules. In photochemistry, light serves as source of energy, and its intensity, wavelength, and emission efficiency are key parameters that influence both the performance and the selectivity of the process. Irradiation sources available in the laboratory whether artificial or natural vary widely in terms of technology, cost, stability, emission spectrum, and compatibility with different experimental setups. Recent technological developments have expanded the range of available light sources, from traditional mercury and halogen lamps to modern LEDs, lasers, and even sunlight, each offering distinct advantages for specific photochemical applications.[87]

Mercury lamps (Hg): High-intensity lamps provide strong and efficient ultraviolet radiation, which can promote a wide range of photochemical reactions. They exhibit well-defined emissions with strong and characteristic spectral lines, commonly at wavelengths of 254, 313, and 365 nm, which facilitate selective processes and enable monochromatic irradiation. In addition, these lamps are highly versatile, as they are available in different pressure configurations to cover various spectral ranges and meet different experimental requirements.[88] This is a well-established technology, widely studied and described in literature, with clearly defined protocols for practical use.

However, these lamps also have several important disadvantages. They can generate significant heat, particularly in the high and medium-pressure types, which requires appropriate cooling systems. They also pose a chemical hazard because they contain mercury, a toxic metal that demands special precautions during handling and disposal. Furthermore, the emission spectrum of these lamps is fixed, although their spectral lines are intense, the emission range cannot be adjusted, which makes it necessary to use filters or monochromators to select specific wavelengths. Their operating cost should also be considered, as their service life is limited and

[87] DINDA, B. **Essentials of pericyclic and photochemical reactions**. Cham, Switzerland: Springer International Publishing, 2017.
[88] SHANKAR, R. *et al*. A practical review on photooxidation of crude oil: Laboratory lamp setup and factors affecting it. **Water Research**, v. 68, p. 304-315, 2015. b) SCHENCK, G. O. Light sources and light filters in preparative organic photochemistry. In: **Preparative Organic Photochemistry**. Berlin, Heidelberg: Springer Berlin Heidelberg, 1968. p. 472-494.

periodic replacement is necessary. Finally, because they emit high-energy ultraviolet radiation, strict protective measures are required to ensure safe operation and prevent harm.[89]

Halogen lamps: Halogen lamps are widely used in photochemistry because they provide intense and stable light with a broad emission spectrum that covers the visible region and part of the infrared. They operate through incandescent filaments and have a color temperature of approximately 3200–3400 K, which ensures good color reproduction and a constant luminous flux, supporting experimental reproducibility. Although they are less energy-efficient than modern sources such as high-power LEDs or high-intensity discharge lamps, and they emit a considerable amount of heat that requires careful thermal management, these characteristics can be advantageous in reactions that benefit from simultaneous heating. In organic synthesis, for example, they are employed in photoinduced processes such as the photocatalytic oxidation of aromatic derivatives, where visible light activates the photocatalyst while the heat assists the reaction. These features make halogen lamps a versatile and accessible light source for a wide range of photochemical applications.[90]

LEDs (Light-Emitting Diodes): have become essential light sources in photochemistry applied to organic synthesis, replacing traditional broad-spectrum lamps. By emitting light in narrow and controllable bands, they can selectively excite molecules or intermediates, which enhances both the efficiency and the selectivity of reactions. Their main characteristics include high energy efficiency, low power consumption, and a long operational lifetime that often exceeds 50.000 hours.[91] In addition, their robustness and compact size allow easy integration into portable reactors and continuous-flow systems, supporting the design of modern experiments on both laboratory and industrial scales. Recent advances, such as the development of UV-A LEDs and progress in UV-B and UV-C technologies, have expanded the scope of photochemistry by enabling the excitation of substrates that require higher energy and creating opportunities for direct reactions and innovative synthetic methodologies.[92] Despite some

[89] KADAM, A. R.; NAIR, G. B.; DHOBLE, S. J. Insights into the extraction of mercury from fluorescent lamps: A review. **Journal of Environmental Chemical Engineering**, v. 7, n. 4, p. 103279, 2019.
[90] KOVALENKO, O. *et al*. Analysis of Tungsten Halogen Lamps Characteristics. **Light & Engineering**, v. 29, n. 5-2, p. 79, 2021. b) ESEN, V.; SAĞLAM, Ş.; ORAL, B. Light sources of solar simulators for photovoltaic devices: A review. **Renewable and Sustainable Energy Reviews**, v. 77, p. 1240-1250, 2017.
[91] KHAN, N.; ABAS, N. Comparative study of energy saving light sources. **Renewable and sustainable energy reviews**, v. 15, n. 1, p. 296-309, 2011.
[92] GOTI, G. *et al.* The impact of UV light on synthetic photochemistry and photocatalysis. **Nature chemistry**, v. 16, n. 5, p. 684-692, 2024.

limitations such as reduced light penetration in dense media, higher costs for certain wavelengths, and the need for careful adjustment of intensity and distance LEDs are now firmly established as versatile and efficient tools for advancing photochemical methodologies in organic synthesis.[93]

Lasers (light amplification by stimulated emission of radiation): is a light source that generates an intense, coherent, and highly directional beam at well-defined wavelengths. Unlike lamps or LEDs, which emit light in multiple directions and across a broad range of wavelengths, lasers produce virtually monochromatic radiation composed of aligned, in-phase photons. This results in high power density, strong spectral selectivity, and excellent coherence.[94] These characteristics allow the selective excitation of molecules at specific wavelengths and enable precise control over the energy delivered to the system. Despite their high cost and greater operational complexity, lasers are indispensable in experiments that require high temporal and spatial resolution, greatly expanding the scope and efficiency of photochemical investigations.[95]

Sunlight: Sunlight is the most abundant and sustainable natural source of radiation, covering a broad spectrum from ultraviolet to infrared. Its continuous profile and high energy flux make it a promising alternative for photochemical processes in line with green chemistry principles. Recent advances, such as continuous-flow reactors coupled with luminescent solar concentrators or parabolic trough collectors, enable the efficient capture and concentration of solar photons, including the diffuse fraction.[96] These systems ensure more uniform irradiation, improved thermal control, and automatic compensation for intensity variations. However, the direct use of sunlight has limitations: its intensity depends on latitude, weather conditions, and time of day, and its power density is reduced in certain spectral regions, which can hinder highly selective or sensitive reactions.[97] Artificial sources, by contrast, provide rigorous control of wavelength, intensity, and exposure time, ensuring greater reproducibility and selectivity.

---

[93] HASAN, M. *et al.* An overview of LEDs' effects on the production of bioactive compounds and crop quality. **Molecules**, v. 22, n. 9, p. 1420, 2017.
[94] TRÄGER, F. (Ed.). **Springer handbook of lasers and optics**. Springer Science & Business Media, 2012.
[95] SEEBER, F. Light sources and laser safety. **Fundamentals of photonics**, v. 1, n. 2, p. 3, 2007.
[96] CAMBIÉ, D.; NOËL, T.. Solar photochemistry in flow. **Accounts on Sustainable Flow Chemistry**, p. 1-27, 2018.
[97] CAMBIÉ, D. *et al*. Energy-efficient solar photochemistry with luminescent solar concentrator based photomicroreactors. **Angewandte chemie**, v. 131, n. 40, p. 14512-14516, 2019.

The choice between sunlight and artificial sources must therefore balance sustainability, experimental control, and energy efficiency. With current technologies, sunlight is already a viable and efficient option, capable of driving photochemical reactions in a clean and sustainable manner.

3.1.4 Photochemistry: Mediators

In many photochemical reactions, light is not absorbed directly by the target reactant but by a photochemical mediator, also referred to as a photosensitizer. These species play a crucial role in converting light energy into a chemically useful form through energy, electron, or proton transfer thereby extending the applicability of light, particularly visible light, in synthetic and catalytic processes.

Classical photochemical mediators include both transition-metal complexes and purely organic molecules.[98] Organic mediators, such as acetophenone (**45**), benzophenone (**46**) Mes-acr^{+} (**47**), chrysazin (**48**), eosin Y (**49**) and rose bengal (**50**) are effective in aqueous and metal-free environments. Many of these compounds enable mild and selective oxidation reactions, which are especially valuable for green and sustainable synthesis. Transition-metal complexes, such as those based on iridium (**51**) and ruthenium (**52**), have been extensively studied because of their high stability, strong emission, and tunable redox properties. They typically show high quantum yields and efficient absorption in the visible region. **Figure 2** shows the structures of these compounds.

More recent efforts have explored supramolecular materials and conducting polymers as next-generation mediators, and among them a particularly promising class is polydiacetylene (PDA). This material is notable for its thermal stability, high electronic conductivity, and distinctive photophysical properties.[99] In this context, PDA has emerged as a versatile platform capable of mediating photooxidation and photoreduction, although it remains only marginally explored for this specific purpose. Given these unique features, PDA will be the central focus of this work.

---

[98] SKUBI, K. L.; BLUM, T. R.; YOON, T. P. Dual catalysis strategies in photochemical synthesis. **Chemical reviews**, v. 116, n. 17, p. 10035-10074, 2016.
[99] JANG, H. *et al.* Polydiacetylene (PDA) Embedded Polymer-Based Network Structure for Biosensor Applications. **Gels**, v. 11, n. 1, p. 66, 2025.

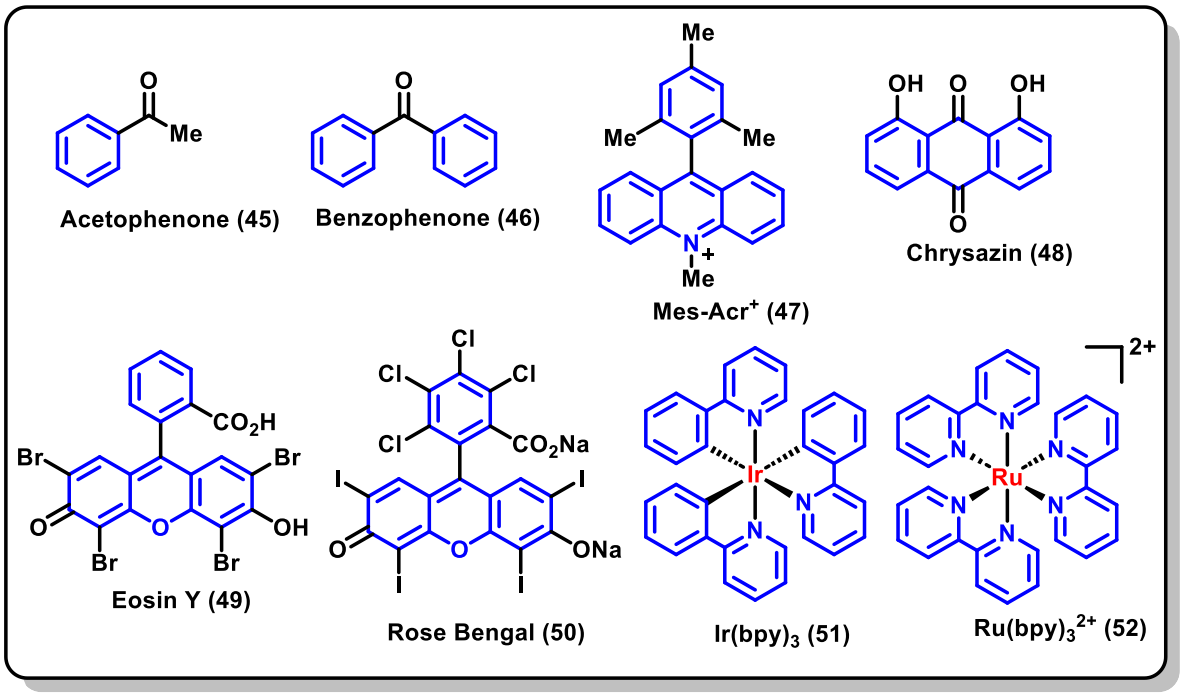

Figure 20: Chemical structures of common photocatalysts

3.1.5 Photochemistry: Mediator: PDA

Polydiacetylenes (PDAs) are a distinctive class of conjugated polymers that have attracted considerable attention because of their unique optical properties and their potential applications in functional devices, particularly as chemical and biological sensors. They are produced through a 1,4 addition polymerization of diacetylene monomers, which are characterized by two triple bonds separated by a single bond (–C≡C–C≡C–).[100] When these monomers are organized in highly ordered structures such as thin films, crystals, or self assembled bilayers exposure to ultraviolet light induces the formation of new conjugated double bonds along the backbone, resulting in a long, linear polymer chain. This process yields PDAs with an extended electronic structure that imparts a characteristic deep blue color.[101]

Importantly, one of the most notable features of PDAs is their sensitivity to external stimuli. Variations in temperature or pH, interactions with specific molecules, or mechanical stress can induce conformational changes along the π conjugated backbone. Under such stimuli, torsion within the backbone may occur, leading to the formation of red colored PDA. These

[100] CUI, H.; WEBBER, M. J.; STUPP, S. I. Self-assembly of peptide amphiphiles: From molecules to nanostructures to biomaterials. **Peptide Science: Original Research on Biomolecules**, v. 94, n. 1, p. 1-18, 2010.
[101] KIM, Y.; IIMURA, K.; TAMAOKI, N. Mechanoresponsive diacetylenes and polydiacetylenes: Novel polymerization and chromatic functions. **Bulletin of the Chemical Society of Japan**, v. 97, n. 4, p. uoae034, 2024.

structural modifications often manifest as reversible color transitions, typically shifting from blue to red (**Scheme 3**).[101-102] This dynamic behavior has been widely exploited in real time sensing and monitoring applications. For these reasons, PDAs are emerging as versatile platforms for the development of optical sensors and smart materials, [103] attracting growing interest at the interface of photochemistry, materials science, and nanotechnology.[104]

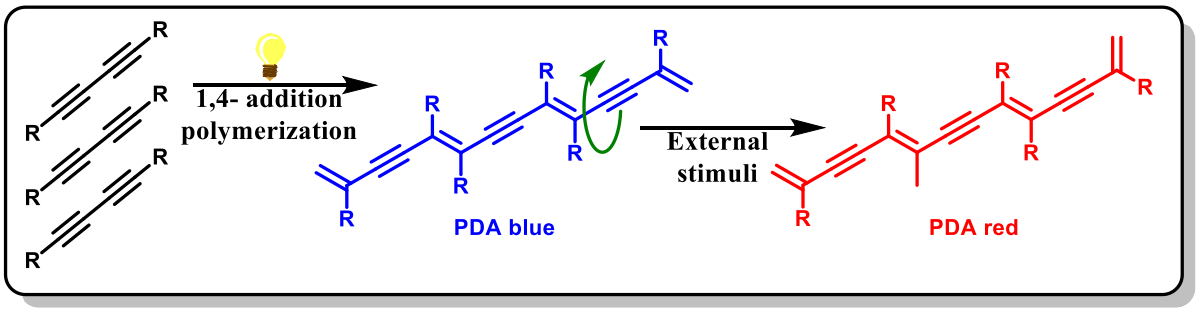

Scheme 27: Alignment of diacetylene monomers for topochemical 1,4-polymerization, leading to the formation of blue-colored PDA. Subsequent application of external stimuli induces torsion of the π-conjugated backbone, resulting in red-colored PDA.

In the present work, the potential of polydiacetylenes as photoactive materials was investigated within the context of organic synthesis, exploring their capacity to efficiently capture and utilize light energy to drive chemical transformations. The highly ordered π-conjugated framework of these polymers provides an ideal platform for facilitating photochemical processes, offering unique opportunities to design innovative reaction pathways under mild conditions. Employing PDAs in this context represents a distinctive strategy that bridges functional material design with synthetic methodology development, demonstrating how their photophysical attributes can be leveraged to expand the toolbox of modern photochemistry and contribute to more sustainable approaches in organic synthesis.

[102] GATEBE, E. *et al.* Synthesis and characterization of polydiacetylene films and nanotubes. **Langmuir**, v. 24, n. 20, p. 11947-11954, 2008
[103] PARK, C. H. *et al.* A direct, multiplex biosensor platform for pathogen detection based on cross-linked polydiacetylene (PDA) supramolecules. **Advanced Functional Materials**, v. 19, n. 23, p. 3703-3710, 2009.
[104] MACKIEWICZ, N. *et al.* Tumor-Targeted Polydiacetylene Micelles for In Vivo Imaging and Drug Delivery. **Small**, v. 7, n. 19, p. 2786-2792, 2011.

3.2 RESEARCH PURPOSE

This research focuses on the development of new photochemical methodologies employing a supramolecular mediator, polydiacetylene (PDA). By harnessing light as a clean and abundant energy source, photocatalytic strategies enable milder reaction conditions, lower energy consumption, and reduced formation of hazardous byproducts. Within this context, the design of innovative supramolecular catalytic systems, such as PDA-based materials, offers unique opportunities to drive selective transformations in line with the principles of green chemistry. The advancement and application of these methodologies not only expand the toolkit of modern synthetic chemistry but also foster environmentally responsible and resource-efficient practices.

3.2.1 General Objective

To develop and investigate new photocatalyzed reactions using supramolecular catalysts based on 10,12-pentacosadiynoic acid (PCDA) polymers. This includes the preparation and functionalization of *p*PCDA materials, as well as the synthesis and comprehensive characterization of the resulting products, with the goal of broadening the scope and applications of photochemistry.

3.2.2 Specific Objectives

- Preparation and characterization of *p*PCDA:

To develop and characterize *p*PCDA materials with improved photocatalytic properties.

- Develop new *p*PCDA-mediated photocatalytic reactions

Design and implement novel light-driven synthetic methodologies employing *p*PCDA to construct C–C, C–S, and C–N bonds, with emphasis on developing efficient, selective,

- Synthesis and characterization of products:

To isolate and analyze the products using advanced spectroscopic and analytical techniques

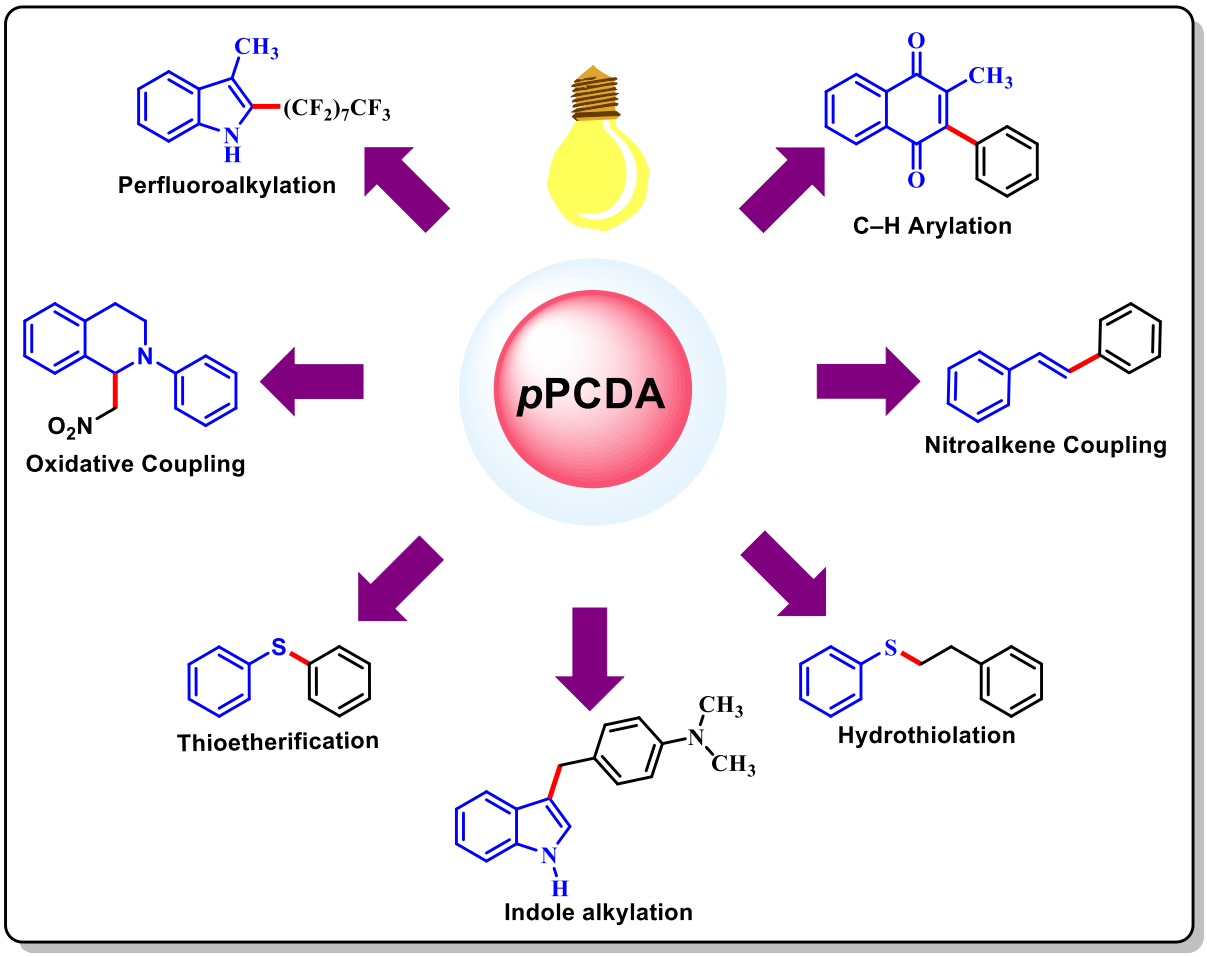

Scheme 28: Scope of photocatalytic transformations mediated by *p*PCDA with representative products.

3.3. RESULTS AND DISCUSSION

3.3.1 *p*PCDA preparation and characterization

The investigation began with the synthesis of a nanoribbon-shaped photocatalyst based on polymerized 10,12-pentacosadiynoic acid (PCDA), referred to as *p*PCDA (**Scheme 29**). The preparation protocol was adapted from a method previously described by SAYMUNG 2021,[105] with complete experimental details provided in the Experimental Section of this thesis.

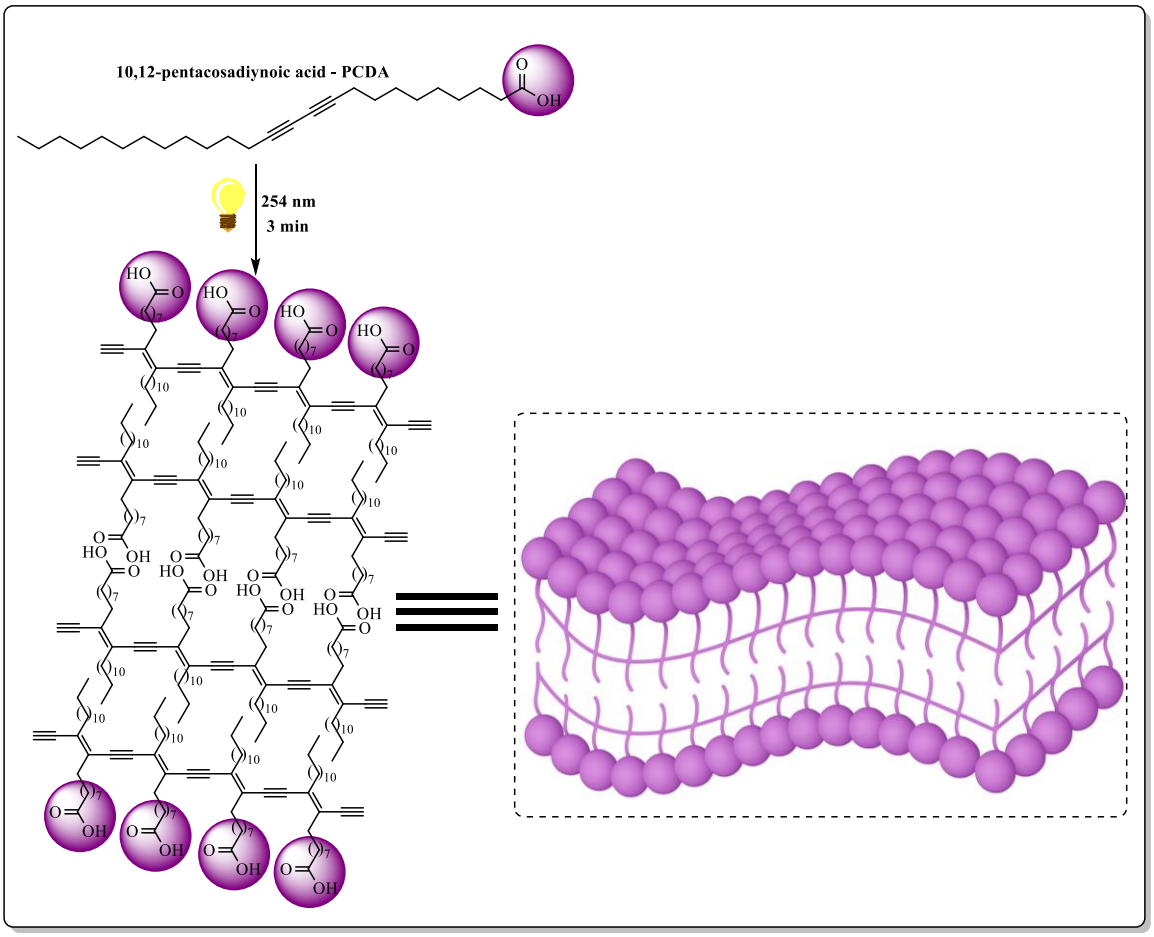

Scheme 29: Schematic representation of the *p*PCDA reaction pathway. Adapted from SAYMUNG.[105]

[105] SAYMUNG, R.; TRAIPHOL, N.; TRAIPHOL, R. Promoting self-assembly and synthesis of color-responsive polydiacetylenes using mixed water-organic solvents: Effects of solvent composition, structure, and incubation temperature. **Colloids and Surfaces A: Physicochemical and Engineering Aspects**, v. 626, p. 127046, 2021.

Following synthesis, the *p*PCDA photocatalyst was characterized using a combination of analytical techniques to evaluate its structural, optical, and thermal properties. Ultraviolet-visible (UV–Vis) spectroscopy revealed two distinct absorption maxima at 512 and 557 nm. These bands are characteristic of the red-phase polydiacetylene backbone and indicate a partially disrupted π-conjugated system, reflecting both successful polymerization and conformational reorganization[106] (**Figura 21**).

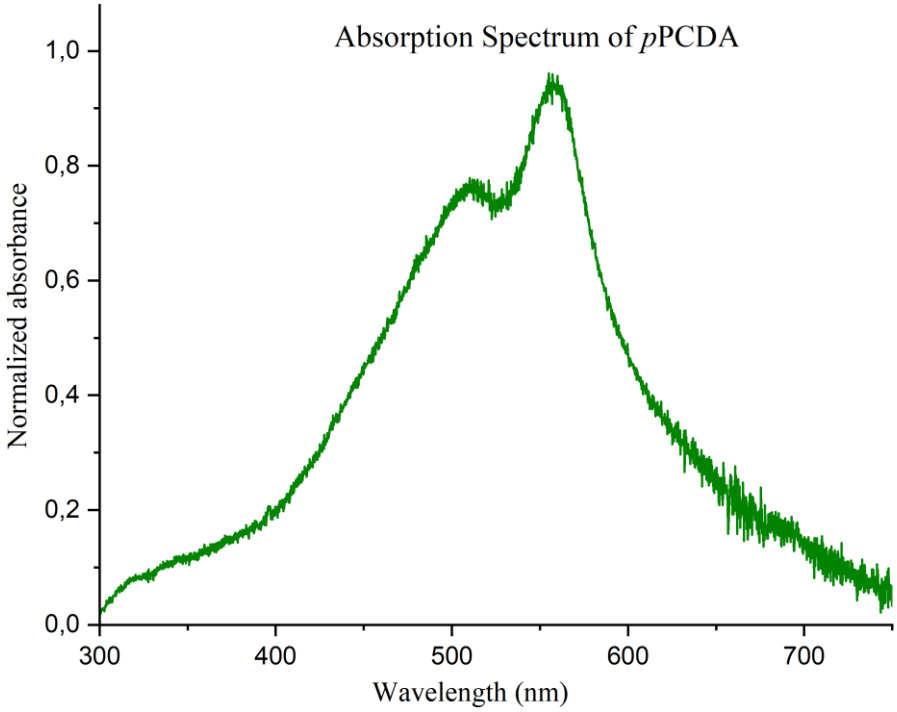

Figure 21: UV-Vis absorption spectrum of *p*PCDA, showing two absorption maxima at 512 and 557 nm.

Fluorescence spectroscopy further confirmed the emissive properties of the red phase. Upon excitation at 450 nm, the material exhibited a strong emission band centered at 645 nm, consistent with the photophysical profile of red-phase PDA and demonstrating the optical activation of the photocatalyst (**Figure 22**).

[106] JOUNG, J. F. *et al*. Electronic relaxation dynamics of PCDA-PDA studied by transient absorption spectroscopy. **Physical Chemistry Chemical Physics**, v. 18, n. 33, p. 23096-23104, 2016.

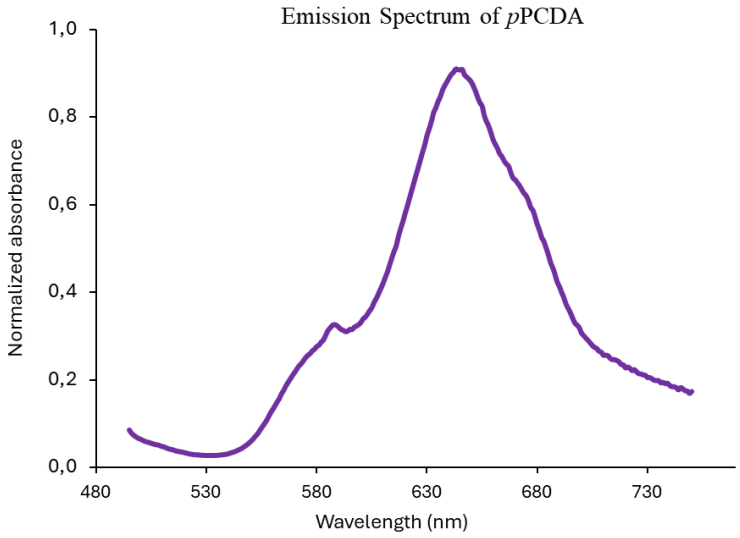

Figure 22: Fluorescence emission spectrum of *p*PCDA recorded at $\lambda_{ex}c$ = 450 nm.

Transmission electron microscopy (TEM) was employed to investigate the supramolecular organization of the nanoribbon assemblies. The micrographs revealed stacked bilayer structures with periodic spacing and sharply defined edges — hallmarks of highly ordered architectures typically derived from PCDA monomers. Although some liposome-like assemblies[107] were also detected a morphology commonly encountered under similar self-assembly conditions the TEM images clearly indicate that the bilayer arrangement predominates in this system (**Figure 23**). This morphological profile reflects efficient self-assembly and suggests a high degree of structural uniformity throughout the material.

[107] MAURELLI, A.M. *et al*. In depth study of the polydopamine coating of liposomes as a potential alternative to PEGylation for the stabilization of nanocarriers in biological fluids. **Materials Today Chemistry**, v. 37, p. 101994, 2024. b) KIM, C.; LEE, K. Polydiacetylene (PDA) liposome-based immunosensor for the detection of exosomes. **Biomacromolecules**, v. 20, n. 9, p. 3392-3398, 2019.

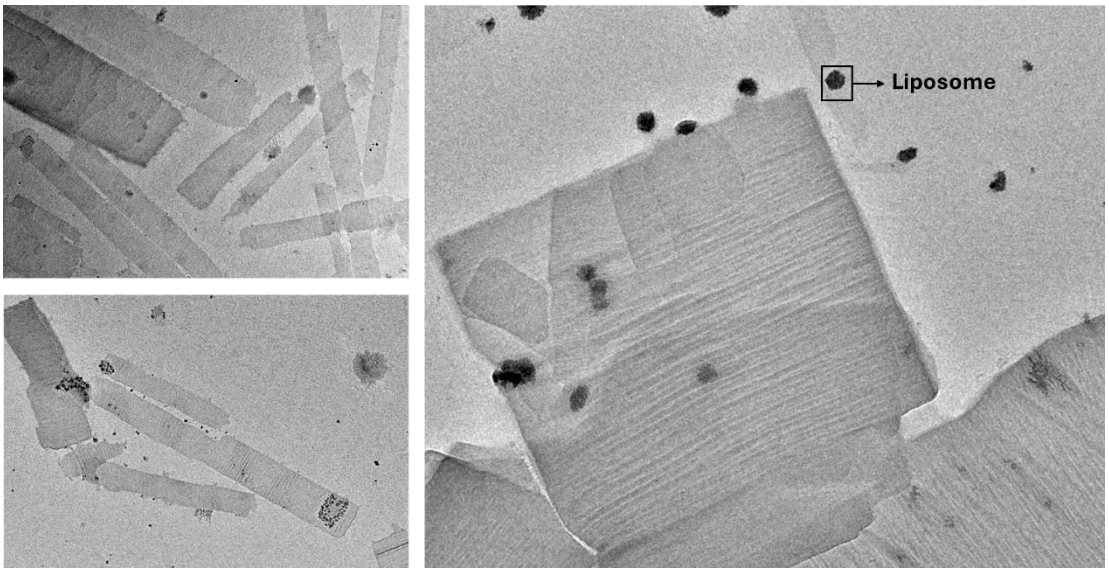

Figure 23: Transmission electron microscopy (TEM) image of *p*PCDA monomers.

Thermogravimetric analysis (TGA) was employed to assess thermal stability. Two major weight loss events were observed at approximately 220 °C and 430 °C, corresponding to the thermal degradation of the polymerized diacetylene framework and confirming the robustness of the structure (**Figure 24**).

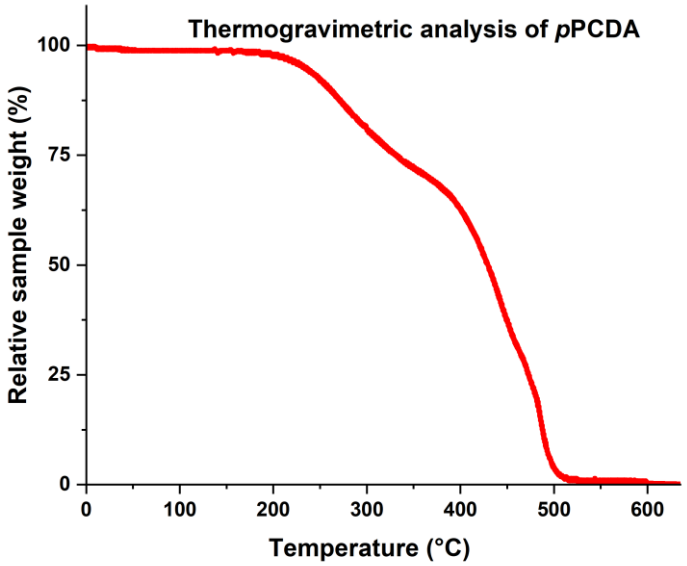

Figure 24: Thermogravimetric analysis (TGA) curve of *p*PCDA.

Collectively, these analytical results validate the successful synthesis of *p*PCDA, its transition to the optically active red phase, and the formation of a well-defined, thermally

stable supramolecular architecture. These characteristics underscore its potential for application in visible-light-driven photocatalysis.

The photocatalytic potential of red-phase *p*PCDA nanoribbon assemblies was systematically evaluated by investigating their ability to generate singlet oxygen ($^1O_2$) under visible-light irradiation, specifically with green light. To monitor $^1O_2$ production, the chemical probe 1,3-diphenylisobenzofuran (DPBF) was employed a well-established method for detecting reactive oxygen species. DPBF reacts selectively with singlet oxygen, leading to disruption of its conjugated π-system and a progressive decrease in its characteristic absorbance at 420 nm.

Upon irradiation of a solution containing DPBF and red-phase *p*PCDA with green light, a pronounced and time-dependent decrease in DPBF absorbance was observed. Notably, after just 30 seconds of exposure, the absorbance at 420 nm dropped to less than 25% of its initial value, indicating rapid and efficient generation of singlet oxygen by the polymerized *p*PCDA assemblies (**Figure 25a**). These results strongly suggest that the nanostructured PDA functions as an effective photosensitizer, promoting energy transfer necessary for $^1O_2$ production.

By contrast, a control experiment performed under identical conditions but in the absence of *p*PCDA showed minimal DPBF degradation, with 85% of the initial absorbance retained after 30 seconds of irradiation (**Figure 25b**). This stark difference highlights the essential role of polymerized *p*PCDA in mediating the photogeneration of singlet oxygen.

These findings confirm the photocatalytic activity of red-phase *p*PCDA and highlight its potential as a visible-light-responsive mediator, a property of particular relevance for applications in light-driven organic synthesis. Against this background, the transformations described below were conceived as exploratory studies to assess the capabilities of *p*PCDA as a supramolecular mediator. Rather than pursuing extensive optimization, the focus was to establish proof-of-concept reactivity across different bond-forming processes.

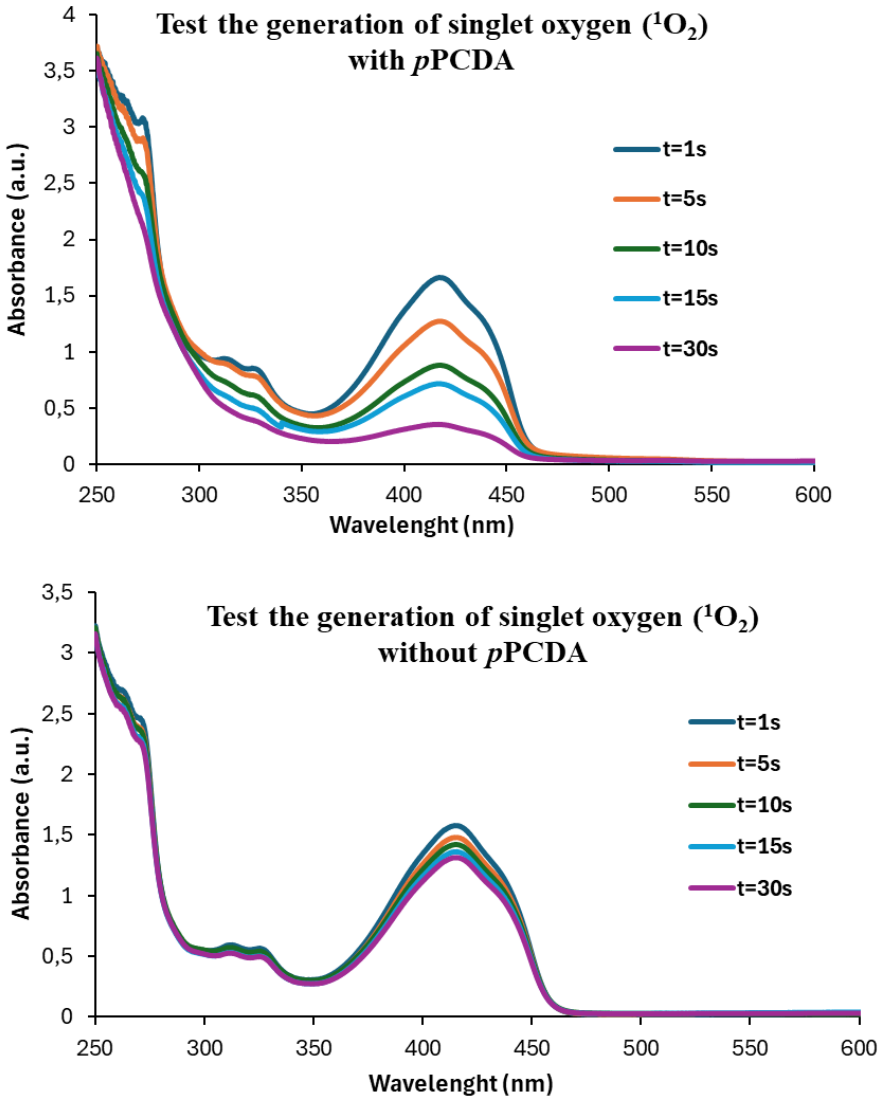

Figure 25: Singlet oxygen ($^1O_2$) generation test: A) with *p*PCDA and B) without *p*PCDA.

3.3.2 Thioetherification of aryldiazonium salts

With the *p*PCDA photocatalyst synthesized and fully characterized, its capacity to mediate photoredox transformations was evaluated. The first transformation selected was the formation of carbon–sulfur (C–S) bonds via coupling between aryl diazonium salts and thiols under mild, metal-free conditions.

Thioethers are key structural motifs present in various bioactive compounds with pharmacological relevance, including antitumor,[108] anti-HIV,[109], antidepressant[110] and anti-inflammatory.[111] Their synthesis typically relies on metal-catalyzed cross-coupling reactions using Pd,[112] Cu,[113] Ni,[114] Co,[115] Fe,[116] or In[117] complexes. However, these methods often entail challenges such as the use of toxic or expensive metals, high temperatures, and stoichiometric amounts of base, which limit their sustainability and functional group tolerance.

In this context, the use of *p*PCDA as a metal-free organic photocatalyst provides a valuable alternative. It enables efficient C–S bond formation under ambient conditions, using visible light and avoiding harsh reagents an approach aligned with green chemistry principles.

The catalytic performance of the polydiacetylene-based system was examined in the thioetherification of aryl diazonium salts, employing 1-(4-methoxyphenyl)-2-(tetrafluoro-λ^5-boraneyl)diazene (**54**) as the electrophilic partner and thiol (**53**) as the nucleophile. Under green-light irradiation at room temperature, and in the presence of 5 mol% catalyst, the corresponding thioether product (**55a**) was obtained in excellent yield (88%) after 5 hours.

By contrast, control reactions conducted in the absence of one of the essential components, either the *p*PCDA photocatalyst or the light source, resulted in drastically reduced yields. When the reaction was performed without the photocatalyst while maintaining all other conditions, the corresponding thioether was obtained with a yield of just 35%. On the

---

[108] LLAUGER, L. *et al*. Evaluation of 8-arylsulfanyl, 8-arylsulfoxyl, and 8-arylsulfonyl adenine derivatives as inhibitors of the heat shock protein 90. **Journal of medicinal chemistry**, v. 48, n. 8, p. 2892-2905, 2005.

[109] SINHA, A. K. *et al*. An Overview on Indole Aryl Sulfide/Sulfone (IAS) as Anti-HIV Non-Nucleoside Reverse Transcriptase Inhibitors (NNRTIs). **Asian Journal of Organic Chemistry**, v. 11, n. 4, p. e202100744, 2022.

[110] MARTINS, P.; ROMEIRO, G.; RIBEIRO, C. 4-thio derivatives of dibenzosuberone: potential antidepressant compounds. **Letters in Organic Chemistry**, v. 7, n. 5, p. 383-387, 2010.

[111] MARCINCAL-LEFEBVRE, A. *et al*. (Phenylthio) phenylamine derivatives as potential antiinflammatory compounds. **Journal of Medicinal Chemistry**, v. 24, n. 7, p. 889-893, 1981.

[112] TEVEROVSKIY, G.; SURRY, D. S.; BUCHWALD, S. L. Pd-Catalyzed Synthesis of Ar SCF3 Compounds under Mild Conditions. **Angewandte Chemie International Edition**, v. 50, n. 32, p. 7312-7314, 2011.

[113] MA, D. *et al*. Domino Condensation/S-Arylation/Heterocyclization Reactions: Copper-Catalyzed Three-Component Synthesis of 2-N-Substituted Benzothiazoles. **Angewandte Chemie**, v. 123, n. 5, p. 1150-1153, 2011.

[114] JAMMI, S. *et al*. Efficient ligand-free nickel-catalyzed C–S cross-coupling of thiols with aryl iodides. **Tetrahedron letters**, v. 49, n. 9, p. 1484-1487, 2008.

[115] WONG, Y.; JAYANTH, T. T.; CHENG, C. Cobalt-catalyzed aryl− sulfur bond formation. **Organic letters**, v. 8, n. 24, p. 5613-5616, 2006.

[116] CORREA, A.; CARRIL, M.; BOLM, C. Iron-Catalyzed S-Arylation of Thiols with Aryl Iodides. **ChemInform**, v. 39, n. 30, p. no-no, 2008.

[117] REDDY, V. P. *et al*. Indium-catalyzed C− S cross-coupling of aryl halides with thiols. **The Journal of organic chemistry**, v. 74, n. 8, p. 3189-3191, 2009.

other hand, when the reaction was carried out in the dark with *p*PCDA and all other reagents present, but without light, the yield dropped further to just 12%.

These results clearly demonstrate that both light and photocatalyst are indispensable for efficiently activating the system. Product formation does not significantly proceed through thermal pathways or non-photocatalytic mechanisms under the mild conditions employed.

To further assess the scope of the photocatalytic system, four additional thioether derivatives were synthesized, affording yields ranging from low to moderate (35–60%). As shown in **Scheme 30**, the introduction of a nitro group, a strong electron-withdrawing substituent, on either the thiol or the diazonium salt led to comparable yields of 60%. This observation suggests that both partners can tolerate electron-deficient functional groups within the redox window of the system, without significantly impairing the overall reaction efficiency.

In the case of the naphthyl-substituted thiol, the corresponding product (**55d**) was obtained in a moderate yield of 50% was obtained, which is lower than that observed for the *p*-methylated aromatic thiol (**55a**). This reduced yield may be attributed to enhanced electronic delocalization in the naphthalene ring system, which could overly stabilize the thiol radical intermediate, thereby diminishing its reactivity in the radical–radical coupling step. This outcome underscores the role of resonance effects in modulating the efficiency of the transformation.

Finally, when an aliphatic thiol was employed, the desired product was obtained in 35% yield. Although modest, this result is noteworthy given the limited exploration of aliphatic substrates in this class of reactions, as most literature examples predominantly focus on aromatic thiols.

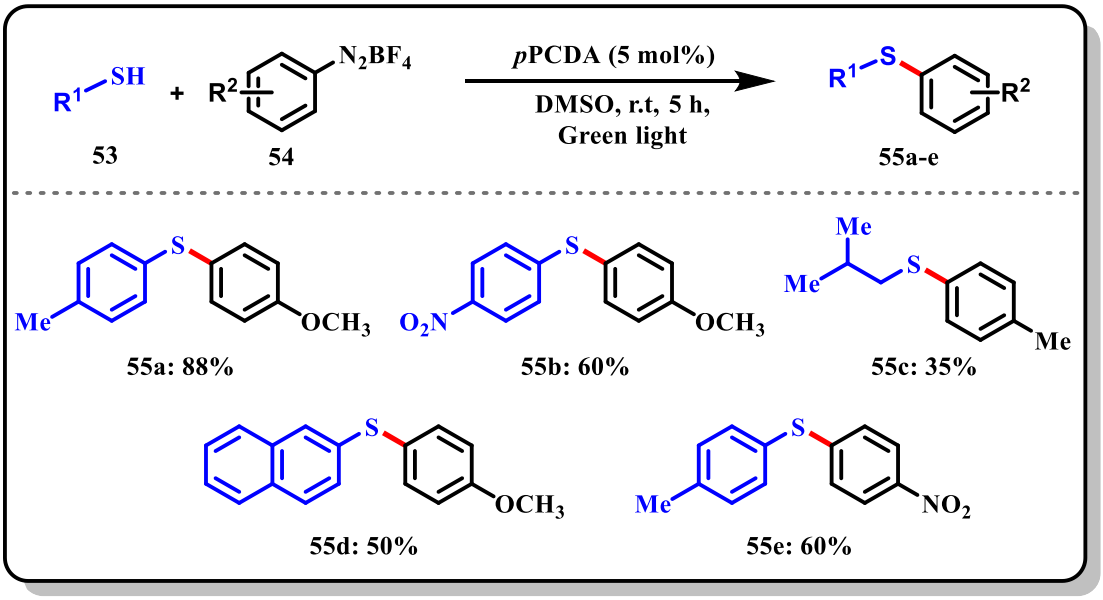

Scheme 30: Light-driven *p*PCDA-catalyzed thioetherification of aryl diazonium salts, yielding products **55a**–**55f**. Isolated yields after column chromatography.

Based on the experimental results and prior literature reports,[118,119] a plausible mechanism for this photoreaction is proposed (**Scheme 31**). Upon green light irradiation, the *p*PCDA photocatalyst is excited state (*p*PCDA*). In this activated state, *p*PCDA* acts as a reductant, transferring an electron to the aryl diazonium salt to generate the corresponding aryl radical (**54-I**) and the oxidized form of the catalyst, *p*PCDA^{+}•.

Subsequently, the oxidized *p*PCDA^{+}• species functions as an oxidant, abstracting an electron from the aryl thiol to form the thiol radical cation (**53-I**) and thereby simultaneously regenerating the ground-state *p*PCDA and completing the catalytic cycle. The thiol radical cation undergoes deprotonation to yield the neutral thiyl radical (**53-II**), which then undergoes radical–radical coupling with the aryl radical (**54-I**) to furnish the aryl sulfide (**55**) as the final product.

[118] HONG, B.; LEE, J.; LEE, A. Visible-light-promoted synthesis of diaryl sulfides under air. **Tetrahedron Letters**, v. 58, n. 29, p. 2809-2812, 2017.
[119] LI, J. *et al.* Metal-Free Cercosporin-Photocatalyzed C-S Coupling for the Selective Synthesis of Aryl Sulfides under Mild Conditions. **European Journal of Organic Chemistry**, v. 2019, n. 42, p. 7175-7178, 2019.

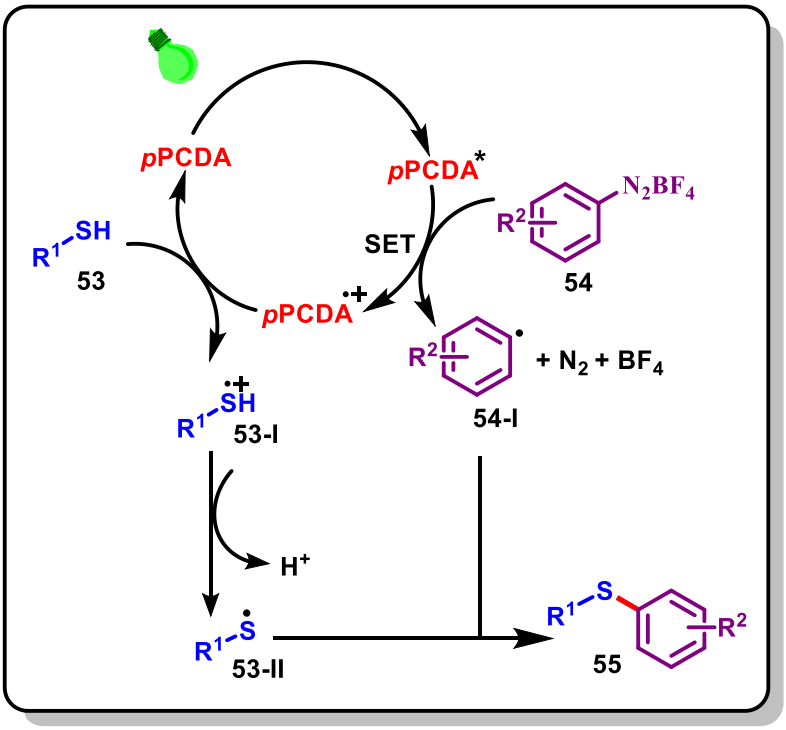

Scheme 31: Plausible mechanism for the thioetherification of aryldiazonium salts.

Following the success of this reaction, the same methodology was applied to a diazonium salt in combination with various thiol substrates. Additionally, both a 1,4-naphthoquinones and nitrostyrene were successfully employed under similar conditions.

3.3.3 C–H Arylation of Naphthoquinones with Aryldiazonium Salts

1,4-Naphthoquinones are highly reactive molecules due to their quinonoid structure, which, upon light irradiation, can access excited states that further enhance their chemical reactivity.[120] This intrinsic photoreactivity enables their participation in a variety of light-driven processes. Consequently, 1,4-naphthoquinones have been extensively investigated as key intermediates in photoinduced organic transformations.[121] In addition to their synthetic utility, they exhibit significant biological activities, such as antitumor and antimicrobial

[120] JANG, J.; LEE, G.; CHO, E. Visible light induced reactions of quinones. **Bulletin of the Korean Chemical Society**, v. 45, n. 12, p. 966-976, 2024.
[121] NUROHMAH, B. A. *et al*. Photorelease Reaction of Alcohol from 1, 4-Naphthoquinone-Based Photodegradable Molecules. **ACS omega**, v. 10, n. 16, p. 16892-16899, 2025. B) ANDO, Y.; SUZUKI, K. Photoredox reactions of quinones. **Chemistry–A European Journal**, v. 24, n. 60, p. 15955-15964, 2018.

effects[122] (as discussed in Chapter 1) and have also been applied in the design of functional materials with redox-active properties.[123]

Two naphthoquinone derivatives were successfully synthesized using the proposed methodology. In the first case, the reaction of 1,4-naphthoquinone (**56**) with two equivalents of the diazonium salt afforded the bis-arylated product (**57a**) in 54% yield. This result indicates that both reactive positions on the quinonoid core were efficiently functionalized under the applied conditions. In contrast, when menadione, a 1,4-naphthoquinone derivative bearing a methyl group at the 2-position, was used as the substrate, only monoarylation (**57b**) was observed, leading to a slightly higher yield of 62% (**Scheme 32**). These outcomes demonstrate that the methodology is compatible with both unsubstituted and substituted naphthoquinones, enabling selective functionalization depending on the substitution pattern of the starting material.

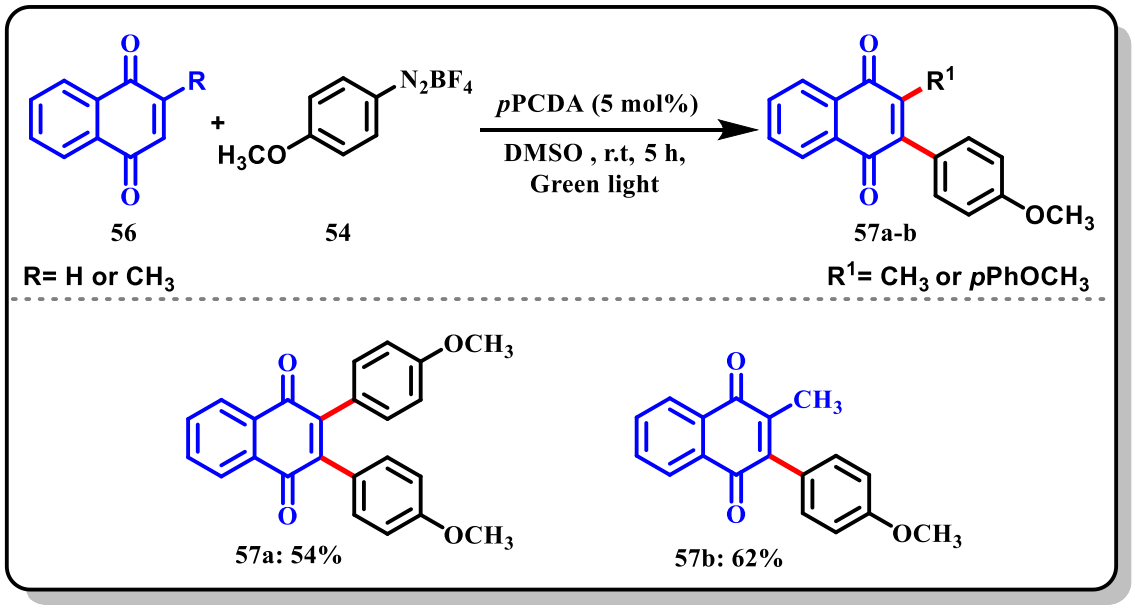

Scheme 32: Light-driven *p*PCDA-catalyzed C–H arylation of naphthoquinones with aryl diazonium salts, affording products **57a**–**57b**. Isolated yields after column chromatography

[122] XIANG, S. *et al.* Exploiting the Anticancer, Antimicrobial and Antiviral Potential of Naphthoquinone Derivatives: Recent Advances and Future Prospects. **Pharmaceuticals**, v. 18, n. 3, p. 350, 2025.
[123] MIYATAKE, K. *et al*. All-Solid-State Rechargeable Air Batteries with Naphthoquinone-Based Negative Electrodes: Improved Performance and Cyclability. **Energy & Environmental Materials**, p. e12887, 2025.b) GUO, L. *et al*. Enhanced Performance of All-Solid-State Rechargeable Air Batteries with Redox-Active Naphthoquinone-Based Polymer Electrode. **Sustainable Energy & Fuels**, 2025.

According to literature precedents,[124] the reaction mechanism involved in this process differs slightly from that proposed for the thioetherification reaction discussed previously, particularly in the final steps related to rearomatization and stabilization of the radical intermediate. Initially, a SET occurs from the photoexcited state of the organic photocatalyst (*p*PCDA) to the diazonium salt, generating an aryl radical (**54-I**) with concomitant release of nitrogen gas.

The resulting aryl radical (**54-I**) is highly reactive and rapidly adds to the naphthoquinone ring, forming a semiquinone-type radical intermediate (**56-I**). This intermediate subsequently undergoes electron transfer to the oxidized form of the catalyst (*p*PCDA^{+}•), thereby regenerating the photocatalyst in its ground state and completing the catalytic cycle. Finally, deprotonation of the arylated intermediate(**56-II**), facilitated by the tetrafluoroborate counterion (BF_4^-), restores aromaticity to the quinonoid system, yielding the monoarylated product (**Scheme 33**).

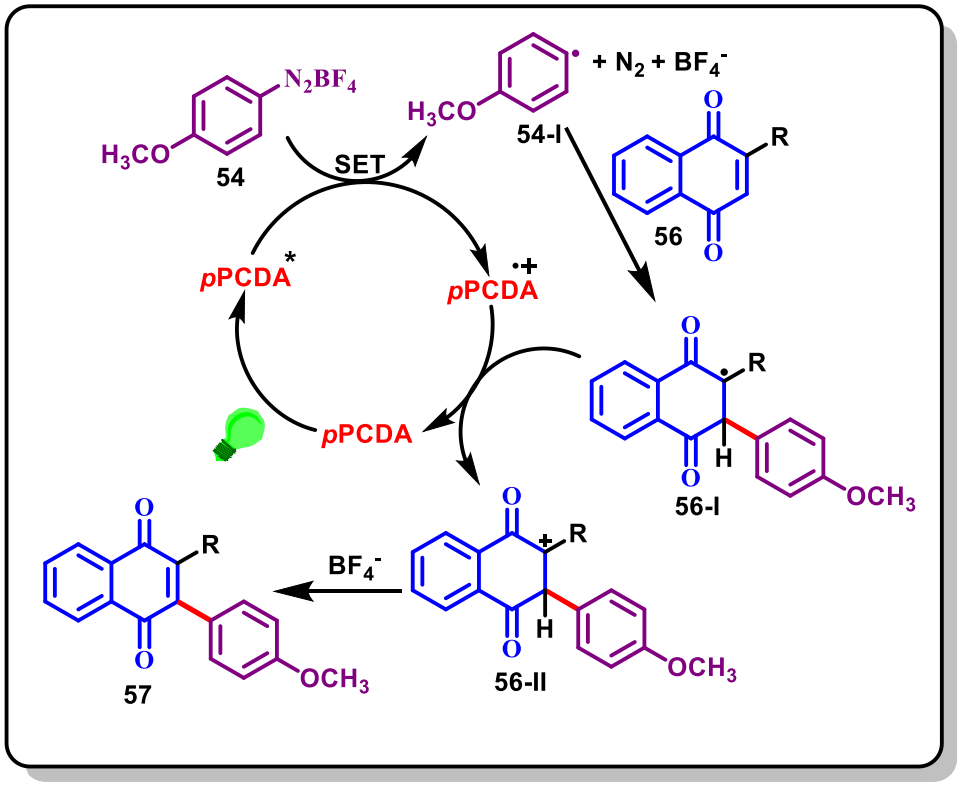

Scheme 33: Plausible mechanism for the C–H arylation of naphthoquinones with aryl diazonium salts.

[124] NAGAR, B.; DHAR, B. B. Photochemical C–H Arylation of Napthoquinones Using Eosin Y. **ACS omega**, v. 7, n. 36, p. 32615-32619, 2022. B) NAGAR, B.; DHAR, B. B. Visible light-mediated thiolation of substituted 1, 4-naphthoquinones using eosin Y as a photoredox catalyst. **The Journal of Organic Chemistry**, v. 87, n. 5, p. 3195-3201, 2022.

In the case of the bis-arylated compound, the reaction proceeds through a second ring undergoes arylation via an analogous sequence of radical formation, addition, electron transfer, and deprotonation.

3.3.4 Cross-Coupling of Aryldiazonium Salts with Nitroalkenes

The reaction employing nitrostyrenes is particularly noteworthy due to their high reactivity toward radical addition and the facile elimination of NO_2, which facilitates the formation of stilbene derivatives. Stilbenes are structurally significant compounds with broad applications in photochemistry,[125] pharmaceuticals,[126] functional materials,[127] and natural products.[128]

Under the previously optimized conditions, the aryl–alkene coupling product was obtained in 38% yield (**59**). Although this value is considered moderate, it confirms the viability of the methodology under visible-light irradiation and highlights its effectiveness even when applied to electronically activated and potentially sensitive substrates. This result underscores both the robustness and versatility of the protocol, while, in line with the exploratory nature of this study, it also opens new avenues for the synthesis of functionalized derivatives of interest across various domains of chemistry.

According to literature,[129] the reaction mechanism may proceed through two distinct pathways. In the initial step, an aryl radical (**54-I**) is generated via SET from the photoexcited state of the organic photocatalyst *p*PCDA$^{+\bullet}$ to the aryldiazonium salt. This aryl radical is then rapidly intercepted by the nitroalkene (**58**), resulting in the formation of a *β*-nitro radical intermediate (**58-I**).

From this point, intermediate **58-I** may evolve into the final coupling product through one of two mechanistically plausible routes:

---

[125] VILLARÓN, D.; WEZENBERG, S. J. Stiff-stilbene photoswitches: from fundamental studies to emergent applications. **Angewandte Chemie**, v. 132, n. 32, p. 13292-13302, 2020.
[126] KAUR, G. *et al*. Stilbenes: a journey from folklore to pharmaceutical innovation. **Archives of Microbiology**, v. 206, n. 5, p. 229, 2024.
[127] MARTÍNEZ-ABADÍA, M.; GIMÉNEZ, R.; ROS, M. Self-assembled α-cyanostilbenes for advanced functional materials. **Advanced Materials**, v. 30, n. 5, p. 1704161, 2018.
[128] SHEN, T.; WANG, X.; LOU, H. Natural stilbenes: an overview. **Natural product reports**, v. 26, n. 7, p. 916-935, 2009.
[129] ZHANG, N. *et al*. Synthesis of stilbene derivatives via visible-light-induced cross-coupling of aryl diazonium salts with nitroalkenes using–NO 2 as a leaving group. **Chemical Communications**, v. 52, n. 99, p. 14234-14237, 2016.b) MA, J.J. *et al*. Decarboxylative and Denitrative Trifluoromethylation for the Synthesis of Cvinyl CF_3 Compounds with Togni (II) Reagent. **Advanced Synthesis & Catalysis**, v. 357, n. 16-17, p. 3447-3452, 2015.

(a) oxidation of the β-nitro radical by the radical cation of the photocatalyst (*p*PCDA^{+}•), leading to the formation of intermediate **58-I** and subsequent elimination of the nitro group (NO_2); or

(b) a radical chain propagation mechanism, in which **54** is oxidized by another equivalent of the aryldiazonium salt, thereby regenerating the aryl radical **54-I** and sustaining the reaction via a chain-transfer process.

Both pathways are consistent with known reactivity patterns of nitroalkenes and diazonium salts under photoredox conditions and support the efficient formation of substituted stilbene derivatives in this system.

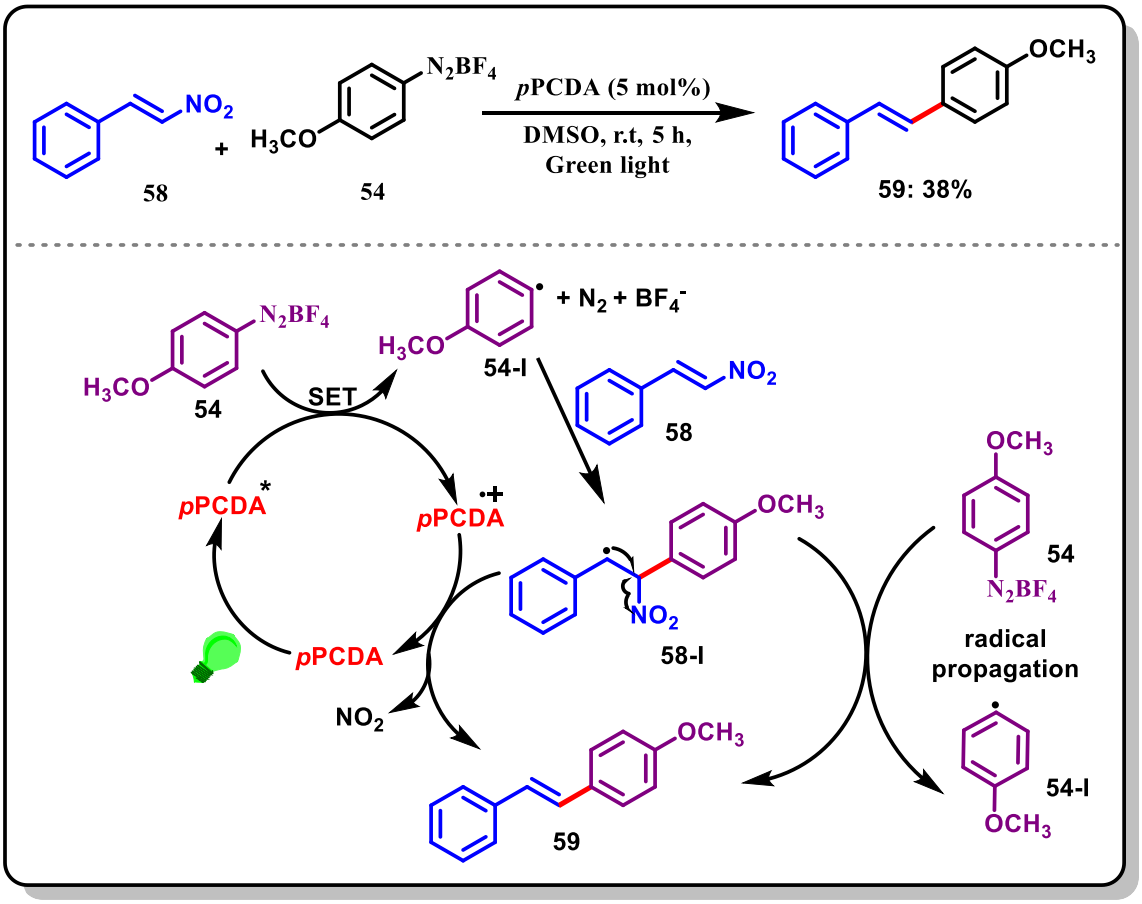

Scheme 34: Light-driven *p*PCDA-catalyzed cross-coupling of aryl diazonium salts with nitroalkenes, along with the proposed reaction mechanism. Isolated yields after column chromatography

3.3.5 Oxidative C–C Bond Coupling

A new methodology was tested for the oxidative C–C bond coupling between *N*-phenyl tetrahydroisoquinoline and nitromethane, representing a valuable contribution to the field of visible-light photoredox catalysis. The development of oxidative C–C bond formation

has emerged as an important strategy in modern organic synthesis,[130] enabling the direct construction of carbon–carbon bonds from simple and readily available precursors without the need for pre-functionalized substrates.

With this approach, the photocatalyst *p*PCDA was employed in the development of this novel reaction protocol. Under the reaction conditions, irradiation with green LEDs, 2 mol% of *p*PCDA, and an oxygen atmosphere, the desired product **62** was obtained in 60% yield after 24 hours.

Control experiments highlighted the critical importance of both the photocatalyst and light: in the absence of irradiation, the yield dropped to 10%, and without the catalyst, only 15% of the product was obtained. These results confirm that both photoactivation and the presence of *p*PCDA are indispensable for efficient reaction progress under the tested conditions.

A plausible mechanism, according to the literature,[131] (**Scheme 35**) involves the excitation of *p*PCDA to excited state (*p*PCDA*) upon visible-light absorption. This excited species undergoes reductive quenching via SET with *N*-phenyl tetrahydroisoquinoline, generating a radical cation intermediate (**60-I**) and the reduced form of the catalyst (***p*PCDA**$^{\bullet-}$). The latter subsequently transfers an electron to molecular oxygen, regenerating the ground-state catalyst and forming the superoxide radical anion ($\mathbf{O_2^{\bullet-}}$).

In parallel, the radical cation (**60-I**) is converted into the corresponding iminium ion (**60-II**) through hydrogen atom abstraction by $\mathbf{O_2^{\bullet-}}$. Finally, this iminium intermediate undergoes nucleophilic attack by nitromethane, affording the oxidative C–C coupling product **62**.

[130] VELASCO-RUBIO, Á. *et al*. C–C bond formation via photocatalytic direct functionalization of simple alkanes. **Chemical Communications**, v. 59, n. 62, p. 9424-9444, 2023.b) HUANG, Z.; TANG, S.; LEI, A. Oxidative cross-coupling: an alternative way for C–C bond formations. **Science Bulletin**, v. 60, n. 16, p. 1391-1394, 2015.

[131] HARI, D. P.; KÖNIG, B. Eosin Y catalyzed visible light oxidative C–C and C–P bond formation. **Organic letters**, v. 13, n. 15, p. 3852-3855, 2011. B) GUADALUPE M. M. *et al*. Immobilized Eosin Y on Modified Silica Nanoparticles and their Applications in Organic Synthesis. **European Journal of Organic Chemistry**, v. 28, n. 1, p. e202401003, 2025.

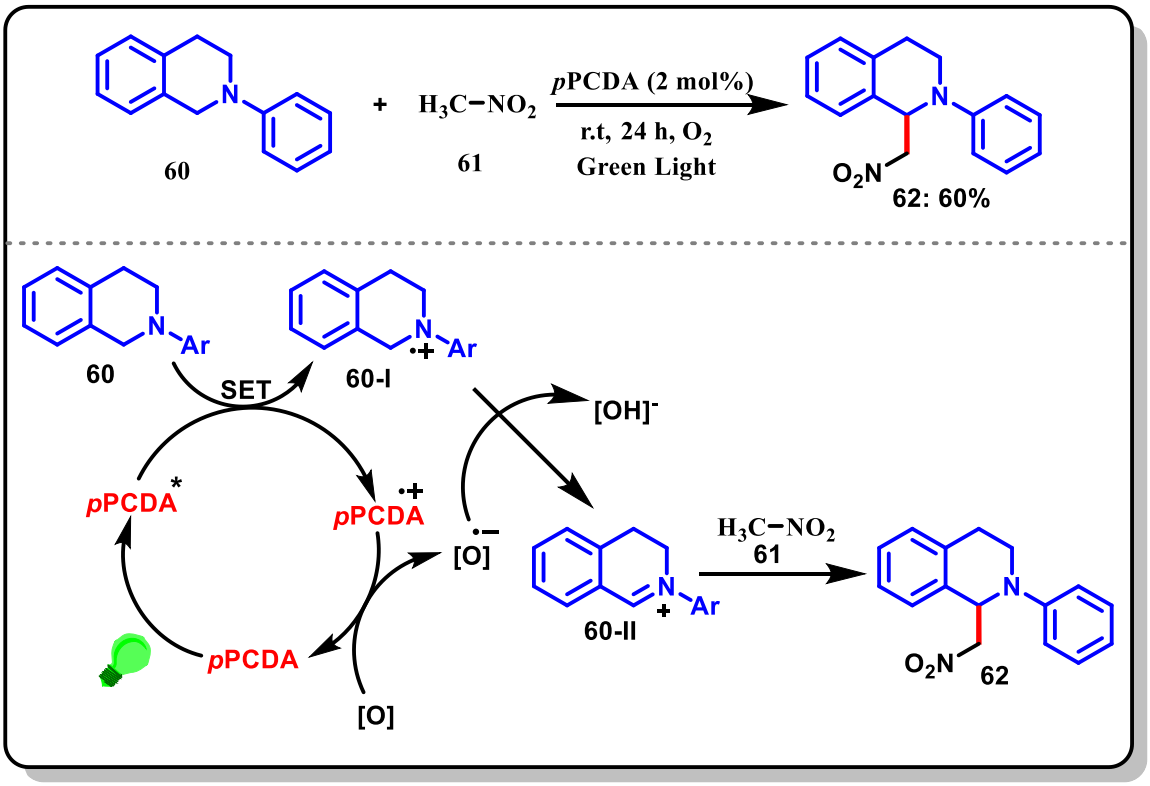

Scheme 35: Light-driven *p*PCDA-catalyzed oxidative C–C bond coupling of aryl diazonium salts with nitroalkenes, together with the proposed reaction mechanism. Isolated yields after column chromatography.

3.3.6 Perfluoroalkylation of indoles

Continuing the investigation into the catalytic potential of *p*PCDA, its application in the perfluoroalkylation of indoles was evaluated, an important transformation for the introduction of perfluoroalkyl groups, which enhance molecular stability, lipophilicity, and biological activity.[132] The direct functionalization of the indole nucleus, a structural motif present in numerous natural products and pharmaceutical agents, further underscores the versatility of *p*PCDA in promoting selective transformations under visible-light irradiation.

The reaction between 3-methylindole (**63**) and perfluorooctyl iodide (**64**), carried out in the presence of 5 mol% of *p*PCDA and irradiated with green light at room temperature, furnished the perfluoroalkylated product (**65**) in 41% yield after overnight stirring. Control experiments confirmed the photocatalytic nature of the process: no product formation was

[132] LEROUX, F.; JESCHKE, P.; SCHLOSSER, M. α-Fluorinated ethers, thioethers, and amines: anomerically biased species. **Chemical reviews**, v. 105, n. 3, p. 827-856, 2005.b) GRGAS, D. *et al*. A review: per-and polyfluoroalkyl substances—biological degradation. **Toxics**, v. 11, n. 5, p. 446, 2023.

observed in the absence of either light or catalyst, highlighting the essential roles of both components in enabling the transformation.

Based on experimental evidence and precedents in the literature,[133] a plausible reaction mechanism is proposed (**Scheme 36**). Upon absorption of visible light, *p*PCDA is promoted to its photoexcited state (*p*PCDA*), which undergoes oxidative quenching via SET to perfluorooctyl iodide. This step generates the corresponding perfluoroalkyl radical (**64-I**) and an iodide anion.

The radical (**64-1**) then selectively adds to the electron-rich 2-position of the indole nucleus (adjacent to the nitrogen atom), forming a resonance-stabilized radical intermediate (**63-I**). This intermediate is subsequently oxidized by another equivalent of perfluorooctyl iodide, generating the corresponding species (**63-II**) and regenerating the radical suggesting the involvement of a radical chain propagation process.

Finally, deprotonation of the intermediate (**63-II**) restores aromaticity to the indole core, affording the perfluoroalkylated product (**65**).

[133] HE, X.W. *et al*. Visible light-induced perfluoroalkylation reaction of indoles in the presence of Na2-eosin Y. **Tetrahedron Letters**, v. 162, p. 155571, 2025. b) YAJIMA, T.; IKEGAMI, M. Metal-Free Visible-Light Radical Iodoperfluoroalkylation of Terminal Alkenes and Alkynes. **European Journal of Organic Chemistry**, v. 2017, n. 15, p. 2126-2129, 2017.

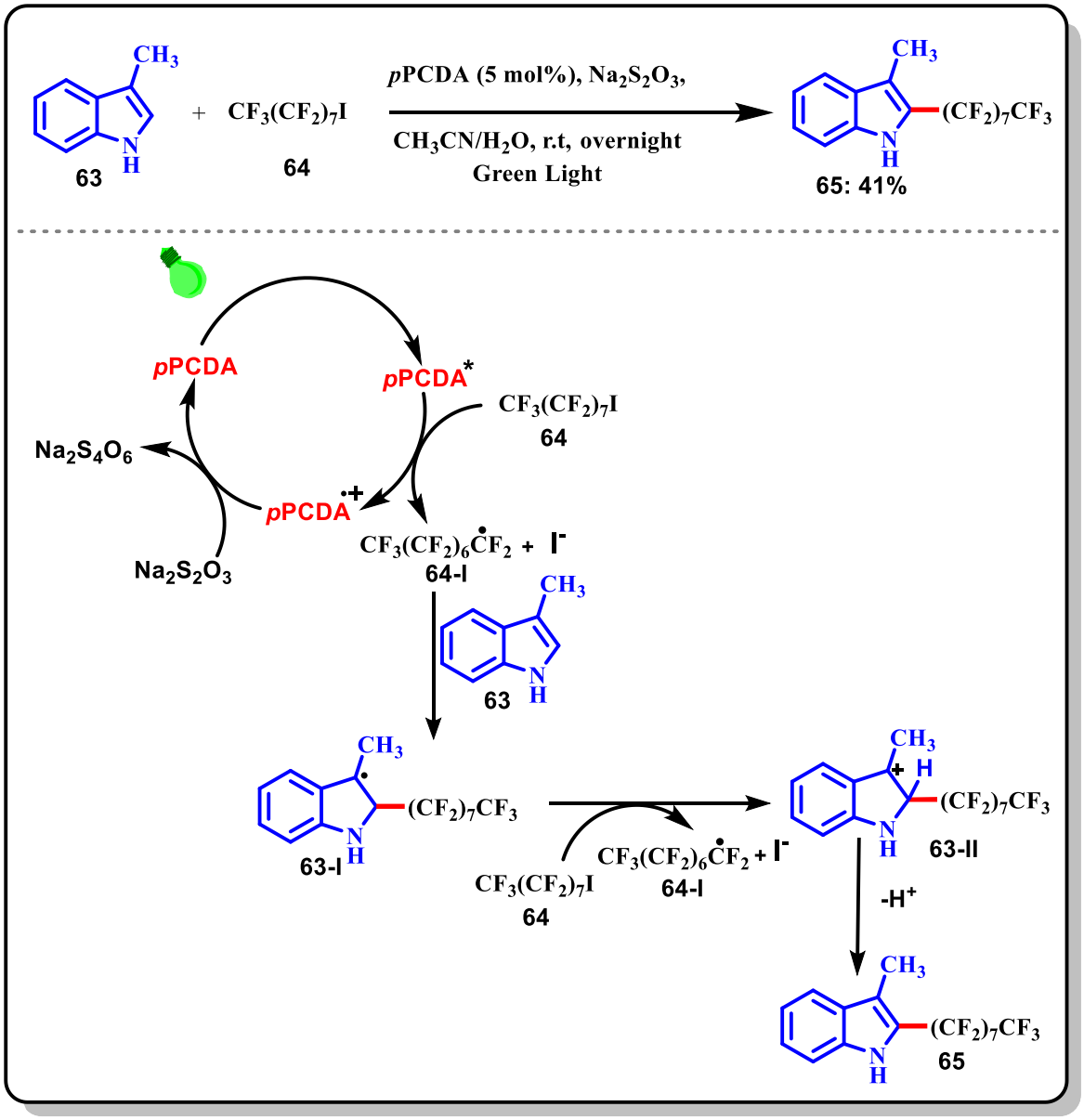

Scheme 36: Light-driven *p*PCDA-catalyzed perfluoroalkylation of indoles, along with the proposed reaction mechanism. Isolated yields after column chromatography

3.3.7 Alkylation of indoles with tertiary amines

In this study, a photoinduced alkylation strategy was investigated, employing tertiary amines as alkyl radical precursors under blue light irradiation. Indole is a well-known heterocyclic scaffold with a broad spectrum of biological activities.[134] Among its derivatives, 3-alkylated indoles are of particular interest due to their presence in numerous natural

[134] KUMAR, S.; RITIK, A. A brief review of the biological potential of indole derivatives. **Future Journal of Pharmaceutical Sciences**, v. 6, n. 1, p. 121, 2020. B) PRAVIN, N. J. *et al*. Indoles as promising therapeutics: a review of recent drug discovery efforts. **Bioorganic Chemistry**, v. 154, p. 108092, 2025.

products[135] and bioactive compounds.[136] Given their structural relevance, the development of efficient and selective methods for their synthesis remains a key objective in organic synthesis.

Two products were successfully obtained using this protocol, which involved 10 equivalents of *N,N*-dimethylaniline relative to indole, 10 mol% *p*PCDA, and DMF as the solvent, under blue-light irradiation with stirring for 24 h. The free N–H indole derivative (**67a**) was isolated in 61% yield, while the N-methylated indole (**67b**) was obtained in 30% yield (**Scheme 37**). These results highlight both the efficiency of the transformation and its compatibility with unsubstituted and N-substituted indole substrates. Control experiments further underscored the essential role of the photocatalyst: in the absence of light, no product was detected, whereas omission of *p*PCDA afforded the N–H indole derivative in only 12% yield. Collectively, these findings confirm that both photoactivation and the presence of *p*PCDA are indispensable for the efficient progression of the reaction.

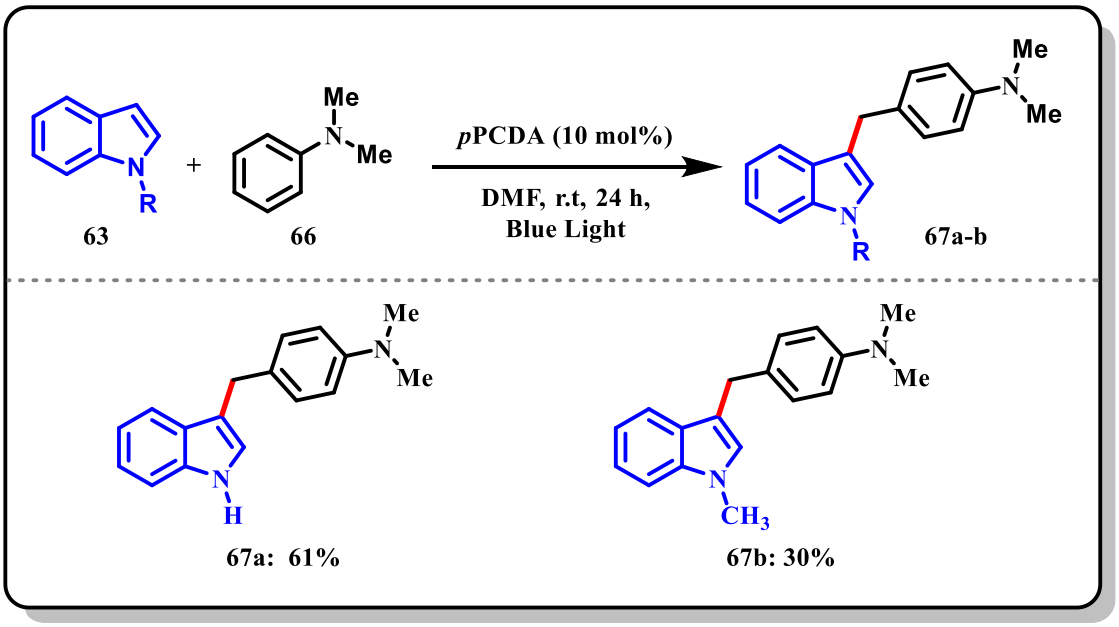

Scheme 37: Light-driven *p*PCDA-catalyzed alkylation of indoles with tertiary amines, affording products **67a–67b**. Isolated yields after column chromatography

Based on literature precedents,[137-138] a plausible reaction mechanism was proposed (**Scheme 38**). Upon exposure to visible light, the organic photocatalyst *p*PCDA is promoted to

[135] SALEH, E. A. M. *et al*. Recent advances in catalytic approaches for the synthesis of 3-substituted indoles: mechanisms and strategies. **RSC advances**, v. 15, n. 16, p. 12255-12290, 2025.
[136] MAZZOTTA, S. *et al*. 3-Amino-alkylated indoles: Unexplored green products acting as anti-inflammatory agents. **Future Medicinal Chemistry**, v. 12, n. 1, p. 5-17, 2020.

its excited state *p*PCDA*. From this photoexcited state, a SET occurs from *N,N*-dimethylaniline (**66**) to *p*PCDA*, affording the corresponding amine radical cation (**66-I**) and the reduced form of the photocatalyst, the radical anion *p*PCDA•⁻.

Simultaneously, molecular oxygen (O_2) present in the reaction medium serves as the terminal oxidant, reoxidizing *p*PCDA•⁻ back to its ground-state neutral form, thereby completing the photocatalytic cycle.

The amine radical cation (**66-I**) subsequently undergoes deprotonation, mediated by the superoxide anion (O_2•⁻), formed during the regeneration of *p*PCDA, yielding the α-aminoalkyl radical (**66-II**). This intermediate is then further oxidized, either by molecular oxygen or by other oxidizing species present in the system, to afford the reactive iminium ion (**66-III**), a highly electrophilic species prone to nucleophilic attack.

Indole then acts as a nucleophile, attacking iminium (**66-III**) at the C3 position, leading to the formation of intermediate (**66-IV**), a 3-alkylated indole derivative. Protonation of the tertiary amine moiety in this intermediate facilitates the elimination of N-methylaniline (**66**), resulting in the generation of a conjugated azafulvalene-type intermediate (**63-I**). This intermediate subsequently undergoes nucleophilic addition with another molecule of *N,N*-dimethylaniline (**66**), affording intermediate (**67-I**). Final deprotonation of this species furnishes the target functionalized product (**67**).

---

[137] DING, X. *et al*. Visible-Light-Promoted Alkylation of Indoles with Tertiary Amines by the Oxidation of a sp^3 C-H Bond. **Advanced Synthesis & Catalysis**, v. 360, n. 4, p. 762-767, 2018.
[138] DAI, X. Q. *et al*. Metal and acid-free visible light-mediated Friedel-Crafts alkylation reactions of indole with anilines. **Tetrahedron Letters**, v. 59, n. 30, p. 2945-2949, 2018.

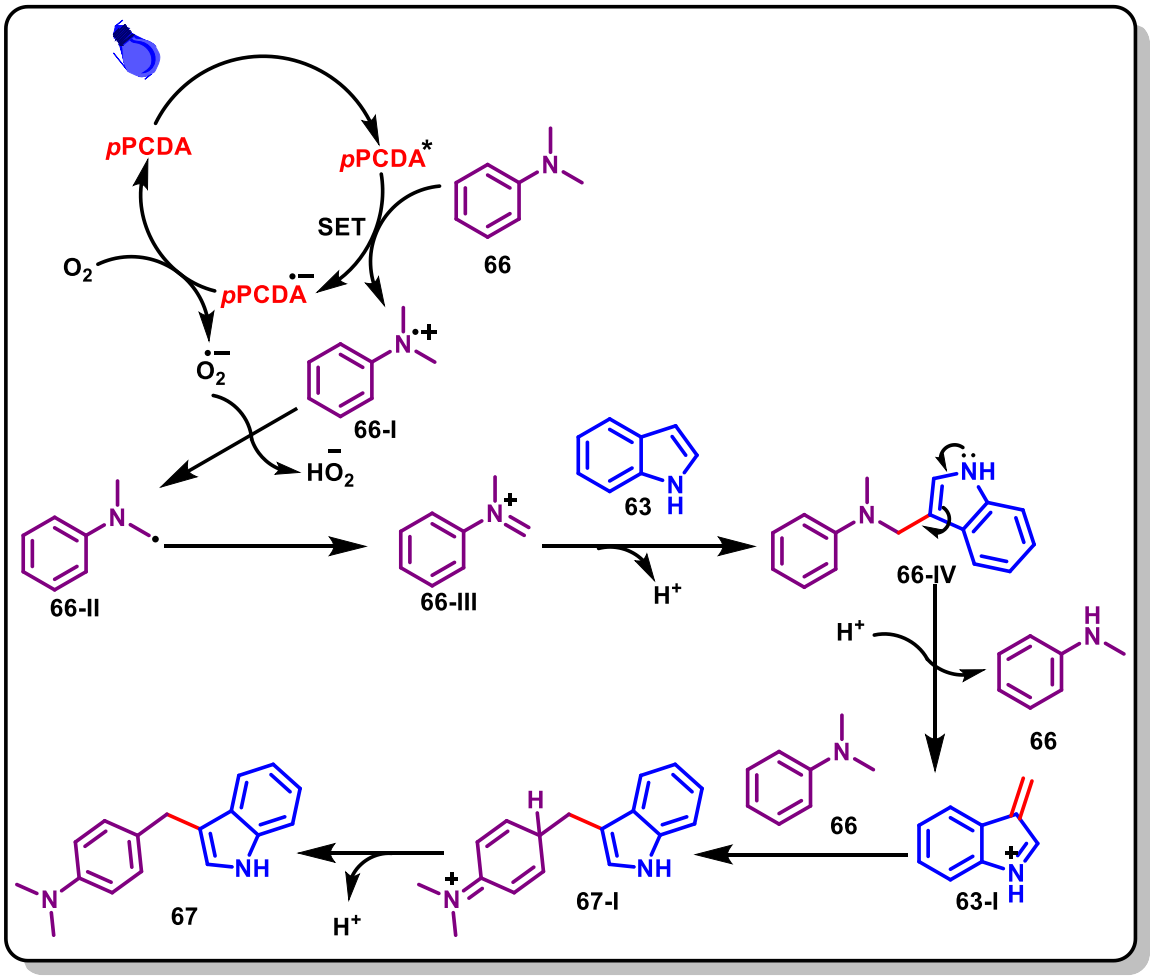

Scheme 38: Plausible mechanism for the alkylation of indoles with tertiary amines.

3.3.8 Hydrothiolation of Styrene

The final transformation investigated was the hydrothiolation of styrene. Photocatalytic thiol–ene click reactions have emerged as a versatile and valuable synthetic strategy in medicinal chemistry, enabling the efficient synthesis of thioethers, key structural motifs present in a wide range of biologically active compounds. In this study, twelve examples were obtained under green-light irradiation, with isolated yields ranging from low to excellent (**Scheme 39**). The optimal conditions 1 mol% *p*PCDA, two equivalents of thiol relative to the alkene, acetonitrile as the solvent, and an air atmosphere at room temperature were applied to the synthesis of products **69a–l**. Under these conditions, the desired thioether (**69a**) was obtained in 90% yield after 5 h of stirring. Control experiments revealed that the transformation can also proceed without *p*PCDA, affording a relatively high yield of 61%, and even in the absence of light, the product was still obtained in 35% yield at 20 °C. These

findings indicate that both non-catalyzed and non-photoactivated pathways are operative under the reaction conditions, raising a legitimate question: if significant conversion is possible without either the photocatalyst or irradiation, to what extent is the use of *p*PCDA justified? The answer lies in the broader perspective of synthetic applicability. Incorporation of *p*PCDA not only raises the yield from 61% to 90% but also improves selectivity and reproducibility, ensuring more consistent outcomes across diverse substrates. From an industrial standpoint, such gains are far from trivial, as higher and more reliable yields directly translate into reduced costs and better resource efficiency. Thus, while the baseline reactivity of the system already demonstrates promise, the use of *pP*CDA as a supramolecular mediator provides a clear advantage that may extend the methodology's scope and practical relevance. Ultimately, whether its inclusion is warranted will depend on the specific goals of the synthetic route and the context of application.

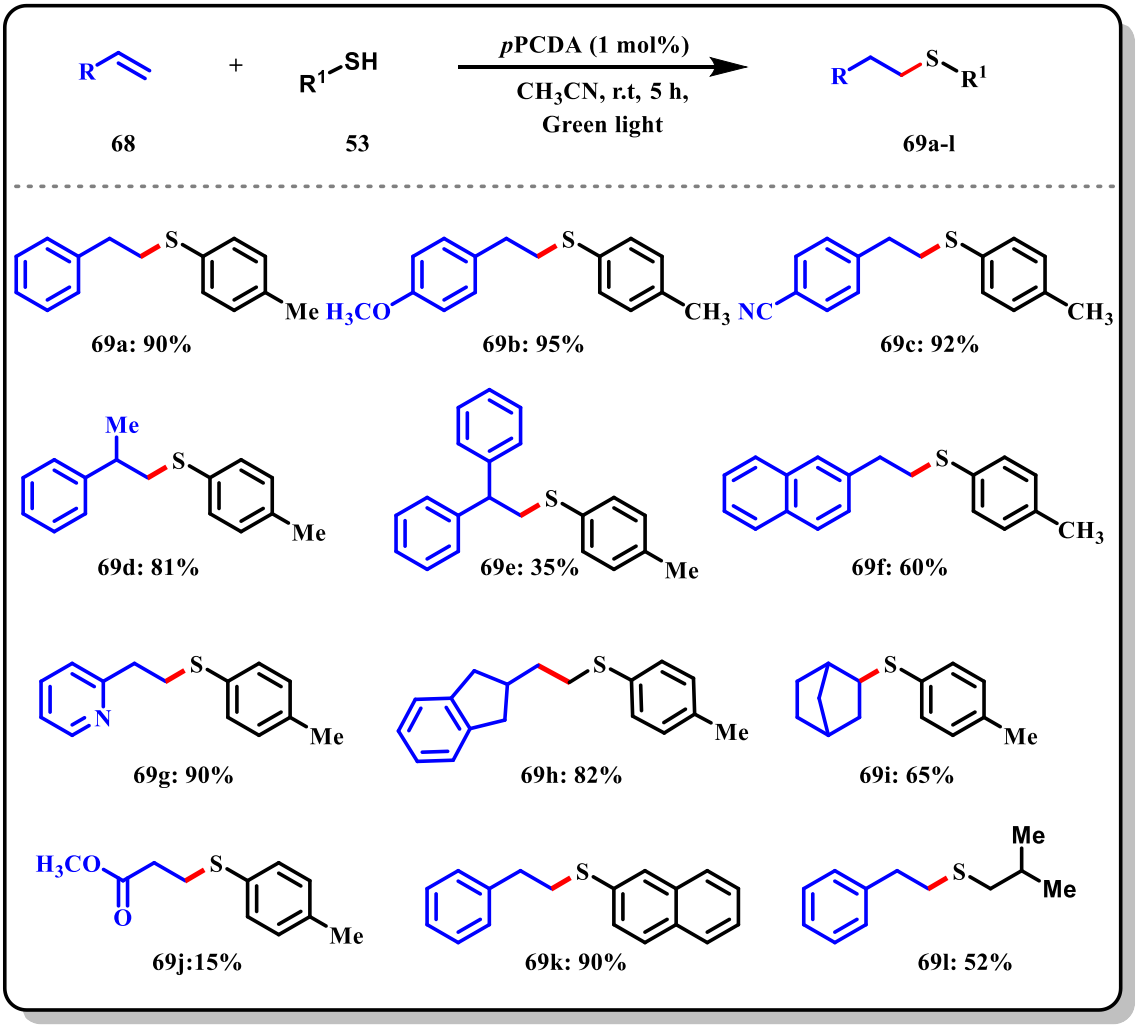

Scheme 39: Light-driven *p*PCDA-catalyzed hydrothiolation of Styrene, affording products **67a–l**. Isolated yields after column chromatography

The substrate scope was first examined by varying the alkene while keeping p-thiocresol constant as the thiol component. Simple styrene, *p*-methoxystyrene bearing an electron-donating group, and *p*-cyanostyrene bearing an electron-withdrawing group all delivered the corresponding thioethers in excellent yields of 95% (**69b**) and 92% (**69c**), respectively. In contrast, *α*-methylstyrene gave thioether (**69d**) in 81% yield, while 1,1-diphenylethylene afforded only 35% of product (**69e**). The reaction of 2-vinylnaphthalene with *p*-thiocresol yielded thioether (**69f**) in 60%, whereas the heteroaromatic 2-vinylpyridine afforded product (**69g**) in 90% yield.

The alkene scope was further extended to dihydroindene, norbornene, and methyl acrylate. Under the optimized conditions, products (**69h**) and (**69i**) were obtained in 82% and 65% yields, respectively. In contrast, methyl acrylate furnished thioether (**69j**) in only 15% yield. Despite the modest value, this example is noteworthy, as unsaturated aliphatic esters are rarely explored in photocatalytic hydrothiolations.

Variation of the thiol partner while maintaining styrene as the alkene afforded thioethers **69k** and **69l**. Naphthalene-2-thiol delivered product **69k** in 90% yield, whereas 2-methylpropanethiol gave product **69l** in 52% yield.

These results demonstrate the broad applicability of the methodology to structurally diverse alkenes and thiols, further reinforcing the high synthetic potential of *p*PCDA as an organic photocatalyst. To assess catalyst reusability, the hydrothiolation leading to product **69b** was selected as a model reaction. Five consecutive cycles were performed, affording yields between 89% and 95% (**Figure 26**). The consistent efficiency across all runs highlights the robustness and stability of *p*PCDA under the applied conditions, confirming its suitability for sustainable synthetic applications. The ability to reuse the catalyst without significant loss of activity is of considerable practical importance, as it reduces operational costs, minimizes waste, and underscores the potential of *p*PCDA as an efficient and environmentally benign photocatalyst for visible-light-mediated organic transformations.

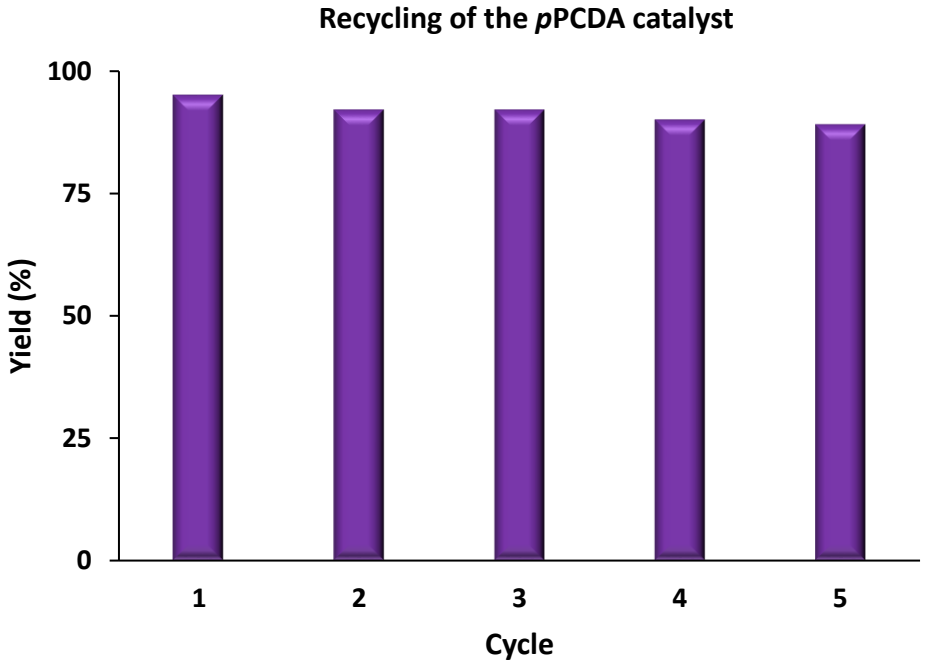

Figure 26: Recycling of the *p*PCDA photocatalyst over five consecutive runs for the synthesis of product **69b**.

Based on literature precedents,[139] the reaction is proposed to proceed as depicted in **Scheme 40**. Upon irradiation with green light, *p*PCDA is promoted to its excited state (*p*PCDA*). A single-electron transfer (SET) from the thiol (**53**) to *p*PCDA* generates the corresponding radical cation (**53-I**) together with the reduced form of the photocatalyst (*p*PCDA•⁻). The radical cation then undergoes deprotonation to afford the thiyl radical (**53-II**), which subsequently adds to the alkene (**68**) to yield the alkyl radical (**68-I**). Finally, a hydrogen atom transfer (HAT) from a thiol molecule to intermediate (**68-I**) produces the thioether product (**69**) and regenerates the thiyl radical (**53-II**), thereby sustaining the radical chain process.

[139] ALI, H. *et al*. Visible light-driven photocatalytic thiol–ene/yne reactions using anisotropic 1D Bi 2 S 3 nanorods: A green synthetic approach. **Nanoscale**, v. 15, n. 35, p. 14551-14563, 2023. b) CUI, H. *et al*. Visible-light-induced selective synthesis of sulfoxides from alkenes and thiols using air as the oxidant. **Green Chemistry**, v. 19, n. 15, p. 3520-3524, 2017.

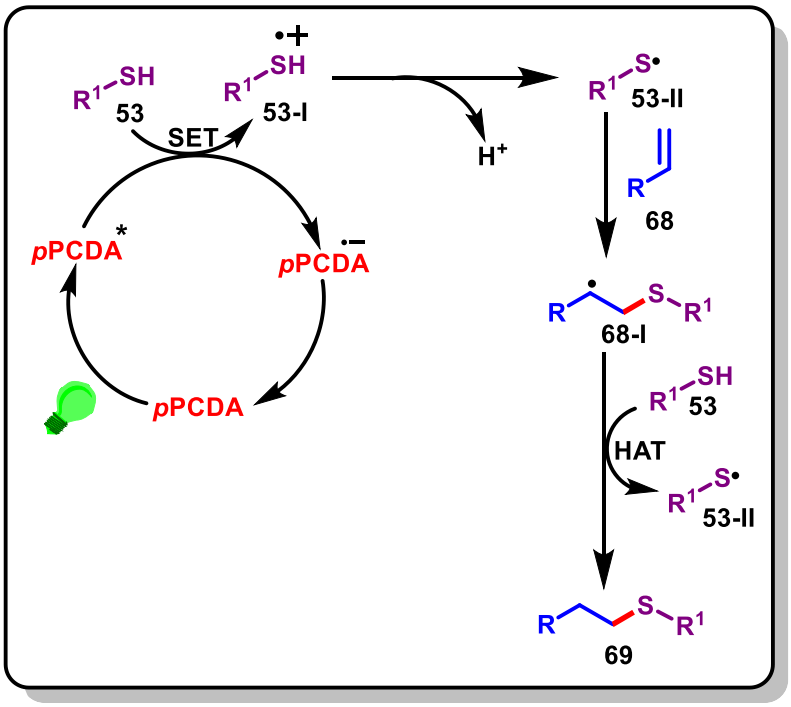

Scheme 40: Plausible mechanism for the hydrothiolation of styrene.

3.3.9 Characterization of Synthesized Products

All synthesized compounds were characterized by ^{1}H and ^{13}C NMR spectroscopy. Since none of the compounds are novel, detailed discussion is limited to selected representative examples, given the structural and spectral similarities among the products. Complete experimental procedures, along with the full set of NMR spectra, are provided in the Experimental Section and in the Appendix of this thesis.

The ^{1}H NMR spectrum of compound (**55a**) exhibits eight aromatic hydrogens resonances between δ 6.8 and 7.3 ppm, appearing as multiplets and consistent with a substituted aryl unit. Singlets at δ ~3.7 ppm and δ ~2.2 ppm are assigned to the methoxy and methyl groups, respectively.

The ^{13}C NMR spectrum shows eight signals in the aromatic region instead of twelve, consistent with the presence of symmetry-equivalent aromatic CH carbons. Additional resonances at δ ~55 ppm and δ ~21 ppm are attributed to the methoxy and methyl carbons, respectively. The number of signals, their chemical shift distribution, fully corroborate the proposed molecular structure.

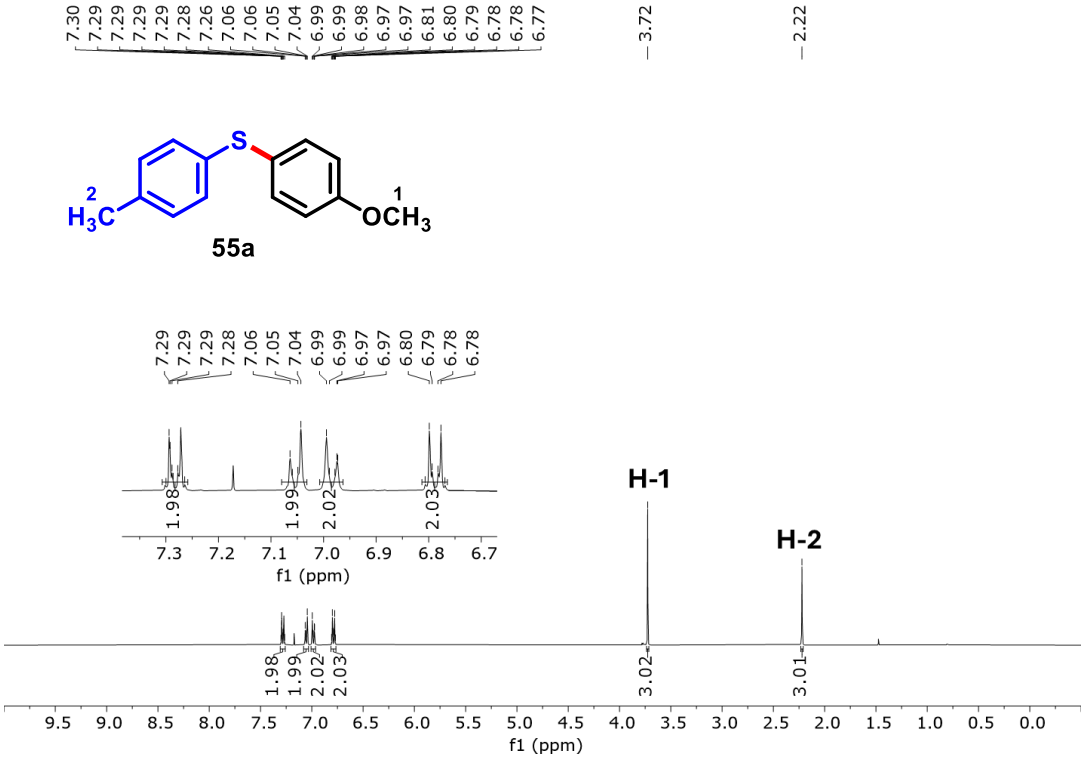

Figure 27: ^{1}H NMR spectrum of compound **55a** (400 MHz, $CDCl_3$).

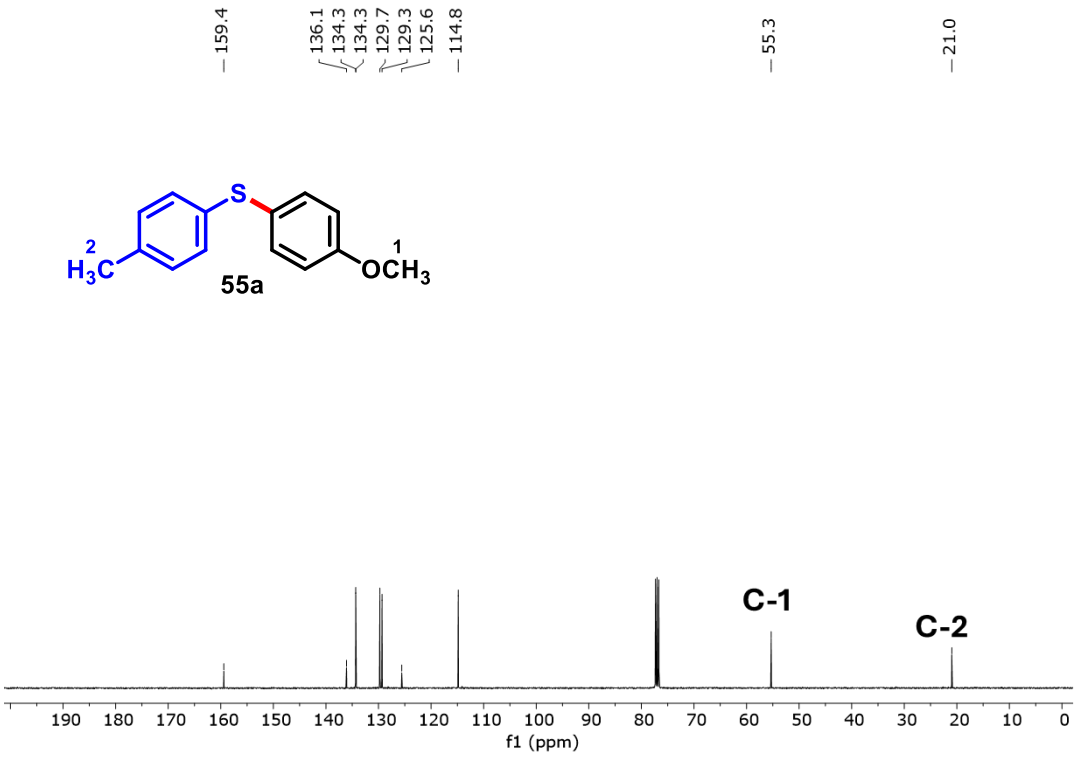

Figure 28: ^{13}C NMR spectrum of compound **55a** (101 MHz, $CDCl_3$).

The ^{1}H and ^{13}C NMR spectra of compound **62** are fully consistent with the proposed structure and agree with literature data. They exhibit the high level of complexity characteristic of molecules with low symmetry. The aromatic region of the ^{1}H NMR spectrum (δ ~6.7–7.2 ppm) contains nine distinct resonances, corresponding to the hydrogens of the two aromatic rings. The absence of molecular symmetry, combined with the electronic influence of the nitromethyl and nitrogen substituents, creates a unique chemical environment for each aromatic hydrogen. This results in multiple, non-overlapping multiplets.

The aliphatic region displays resonances attributable to three CH_2 groups, all located in asymmetric environments. In each case, the protons are diastereotopic due to the rigid molecular framework and the presence of a chiral carbon center, leading to separate signals or complex multiplets rather than simple first-order patterns. The chiral center disrupts the equivalence of otherwise similar protons, making each proton in a CH_2 group magnetically distinct and thereby increasing the number of observable signals in the ^{1}H NMR spectrum.

The resonance at δ 78.9 ppm in the ^{13}C NMR spectrum is assigned to the carbon directly bonded to the nitro group, further supporting the successful nitromethylation of the tetrahydroisoquinoline core.

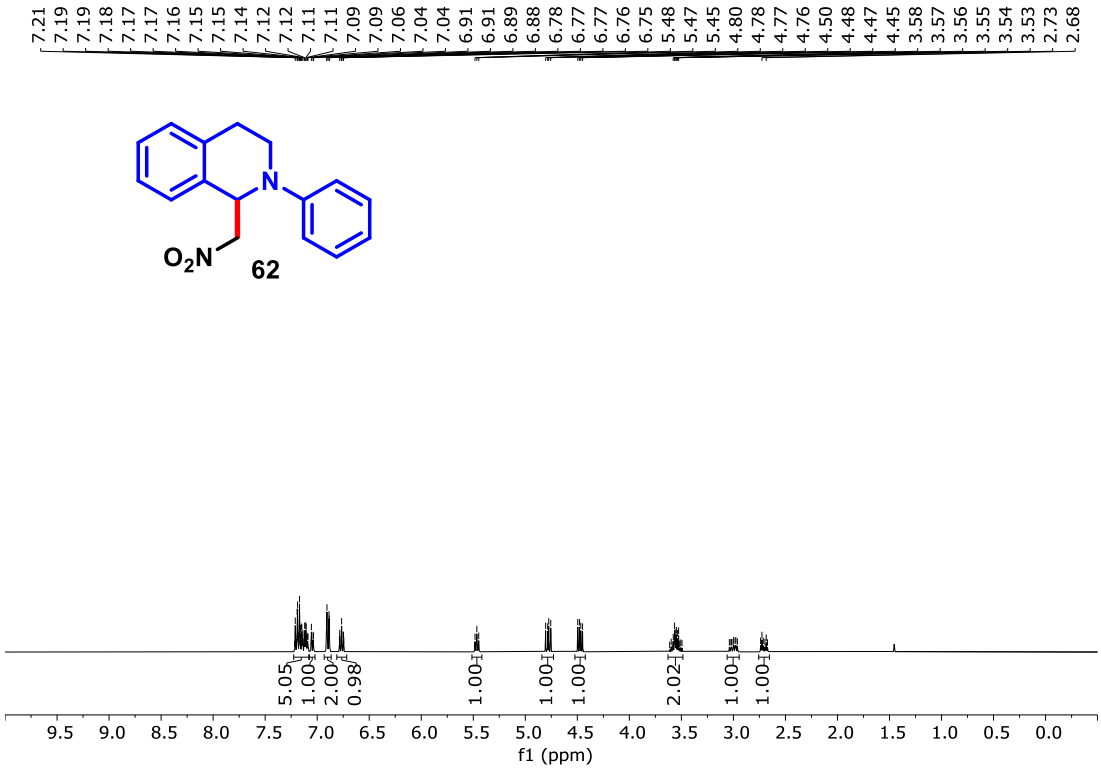

Figure 29: ^{1}H NMR spectrum of compound **62** (400 MHz, $CDCl_3$).

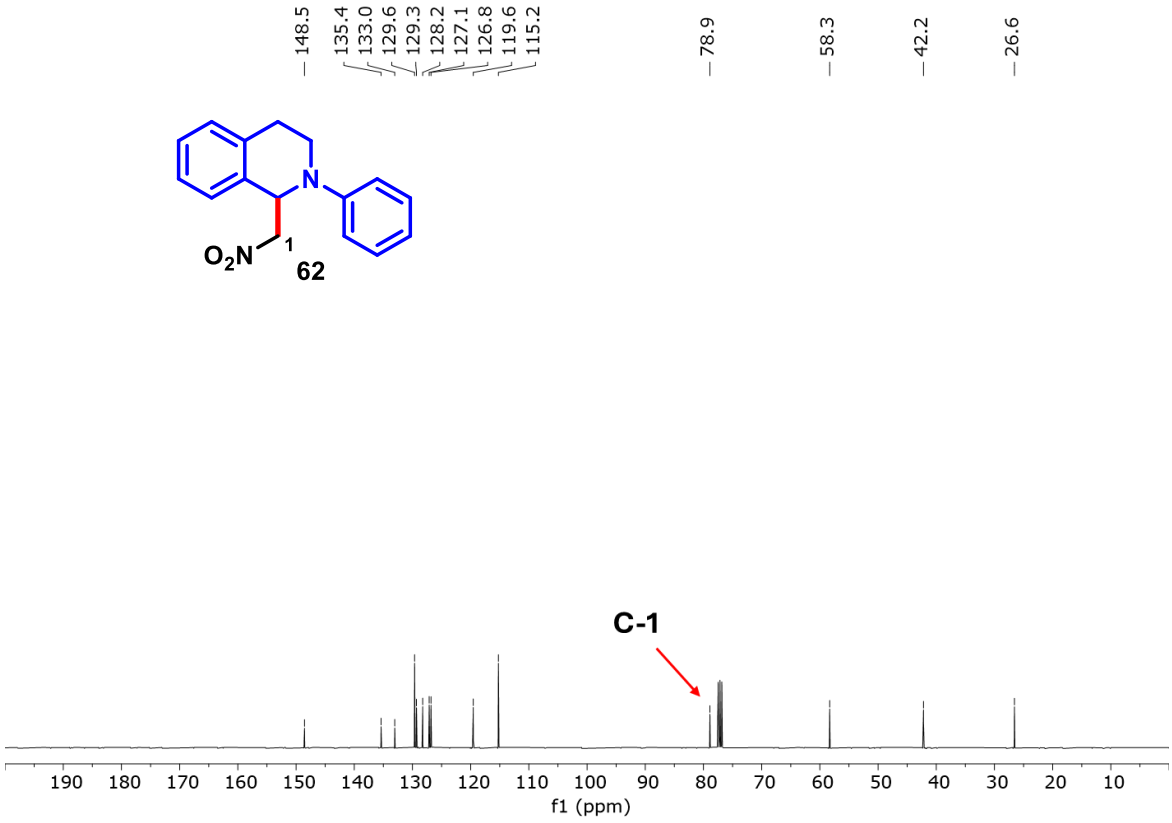

Figure 30: ^{13}C NMR spectrum of compound **62** (101 MHz, $CDCl_3$).

In compound (**65**), the ^{1}H NMR spectrum notably lacks the resonance for the proton at position 2, consistent with substitution by the perfluoroalkyl group. Additional evidence comes from the methyl resonance at δ ~2.35 ppm, which appears as a triplet due to ^{1}H–^{19}F spin–spin coupling. In such interactions, the magnetic moment of a hydrogen nucleus is influenced by the magnetic moments of neighboring fluorine atoms, resulting in signal splitting. Coupling to a single fluorine atom typically produces a doublet, whereas coupling to two equivalent fluorines yields a triplet, as observed here, thus reinforcing the successful incorporation of the perfluoroalkyl moiety.

Further confirmation is provided by the ^{19}F NMR spectrum, which displays the characteristic resonances of the fluorinated fragment. The absence of a detectable ^{13}C signal for the fluorinated carbon is expected, as direct attachment to multiple fluorine atoms leads to strong ^{13}C–^{19}F coupling and rapid relaxation, causing severe line broadening and attenuation. Under standard acquisition conditions, these effects often render such carbons undetectable.

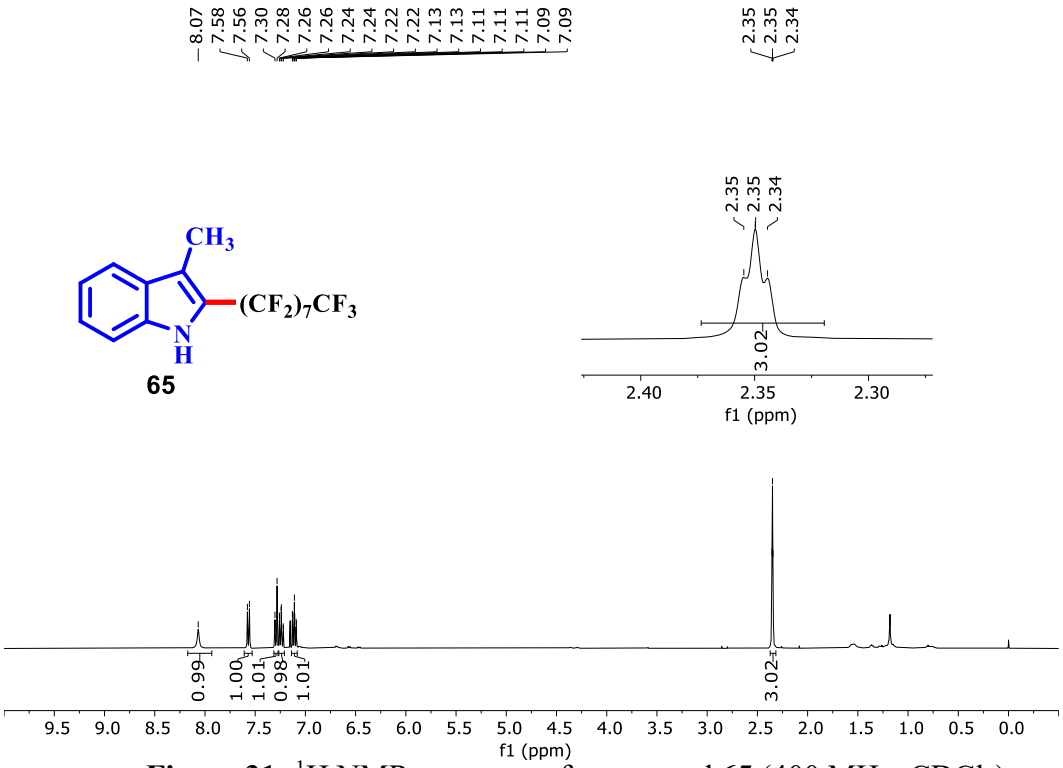

Figure 31: ^{1}H NMR spectrum of compound **65** (400 MHz, $CDCl_3$).

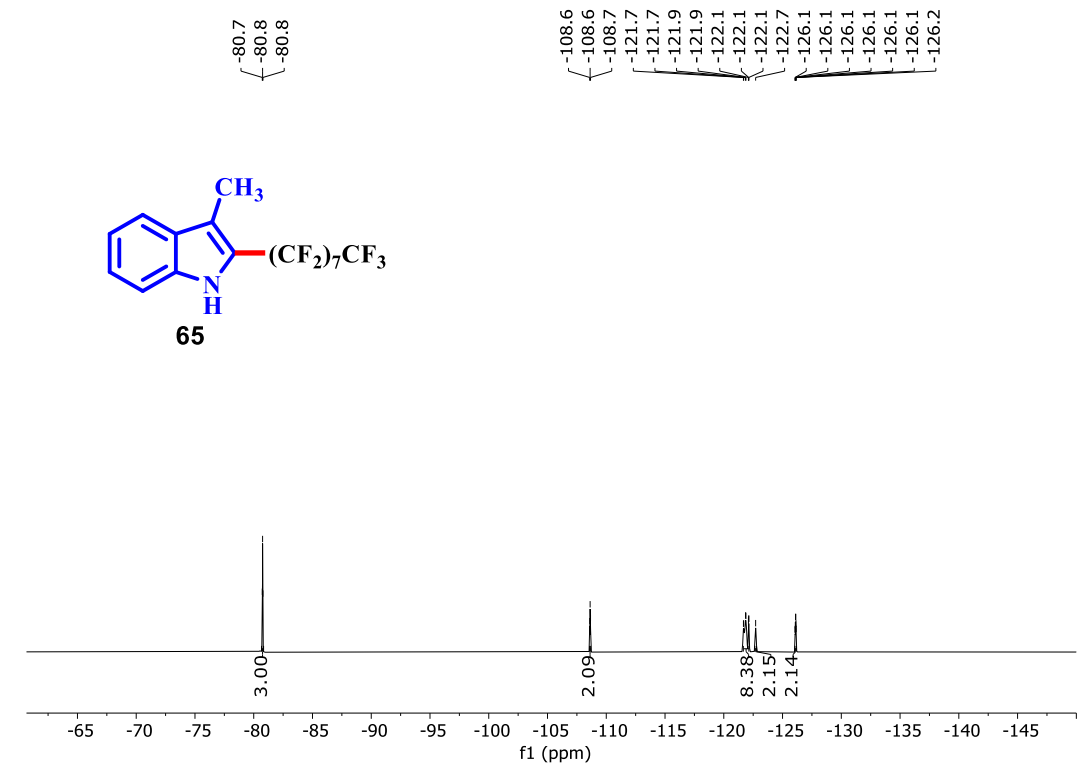

Figure 32: ^{19}F NMR spectrum of compound **65** (376 MHz, $CDCl_3$).

The ^{1}H NMR spectrum of compound **67a** displays nine aromatic hydrogens resonances between δ ~6.6 and 7.5 ppm, which is consistent with the substitution pattern of a

monosubstituted indole skeleton. A broad signal at δ ~7.8 ppm is assigned to the N–H hydrogens of the indole ring. A singlet at δ 3.95 ppm corresponds to the newly formed CH_2 group, confirming the successful synthesis of the target compound. Additionally, a singlet at δ 2.83 ppm, integrating for six protons, is attributed to two equivalent N-methyl groups. These methyl groups appear as a single resonance because they are chemically and magnetically equivalent; both are bonded to the same nitrogen atom, which is also connected to the aromatic ring, creating a symmetric electronic environment. Rapid rotation about the N–C bonds on the NMR timescale averages the electronic environments of both methyl groups, producing a single, sharp singlet.

The same symmetry effect is reflected in the ^{13}C NMR spectrum, in which the two methyl carbons give rise to a single resonance at δ 41 ppm, which is consistent with literature data for N,N-dimethylaniline.[140] The CH_2 carbon appears at δ 30.5 ppm. The chemical shift values and the overall spectral pattern are consistent with both the proposed structure and literature reports, thus confirming the formation of the desired product.

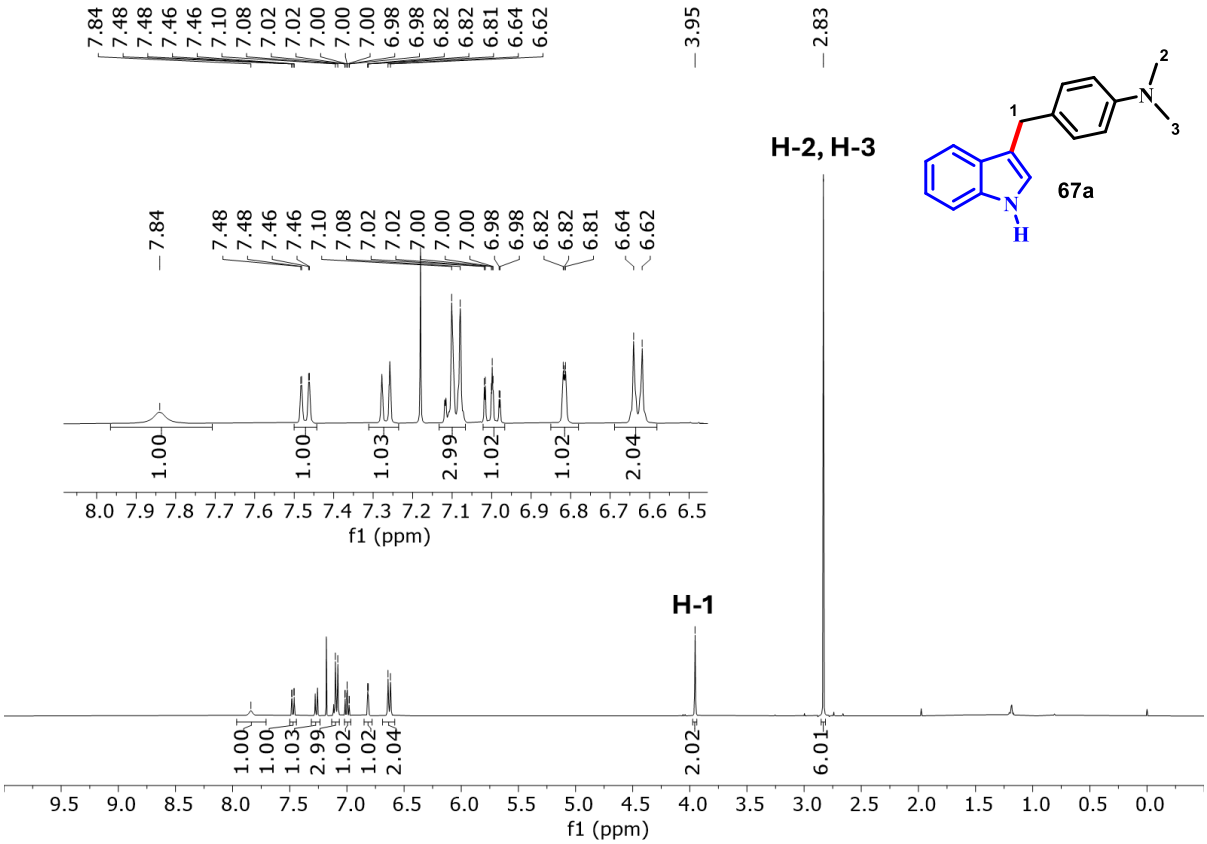

Figure 33: ^{1}H NMR spectrum of compound **67a** (400 MHz, $CDCl_3$).

[140] KE, Zhengang *et al*. Alcohol promoted N-methylation of anilines with CO_2/H_2 over a cobalt catalyst under mild conditions. **Green Chemistry**, v. 23, n. 22, p. 9147-9153, 2021.

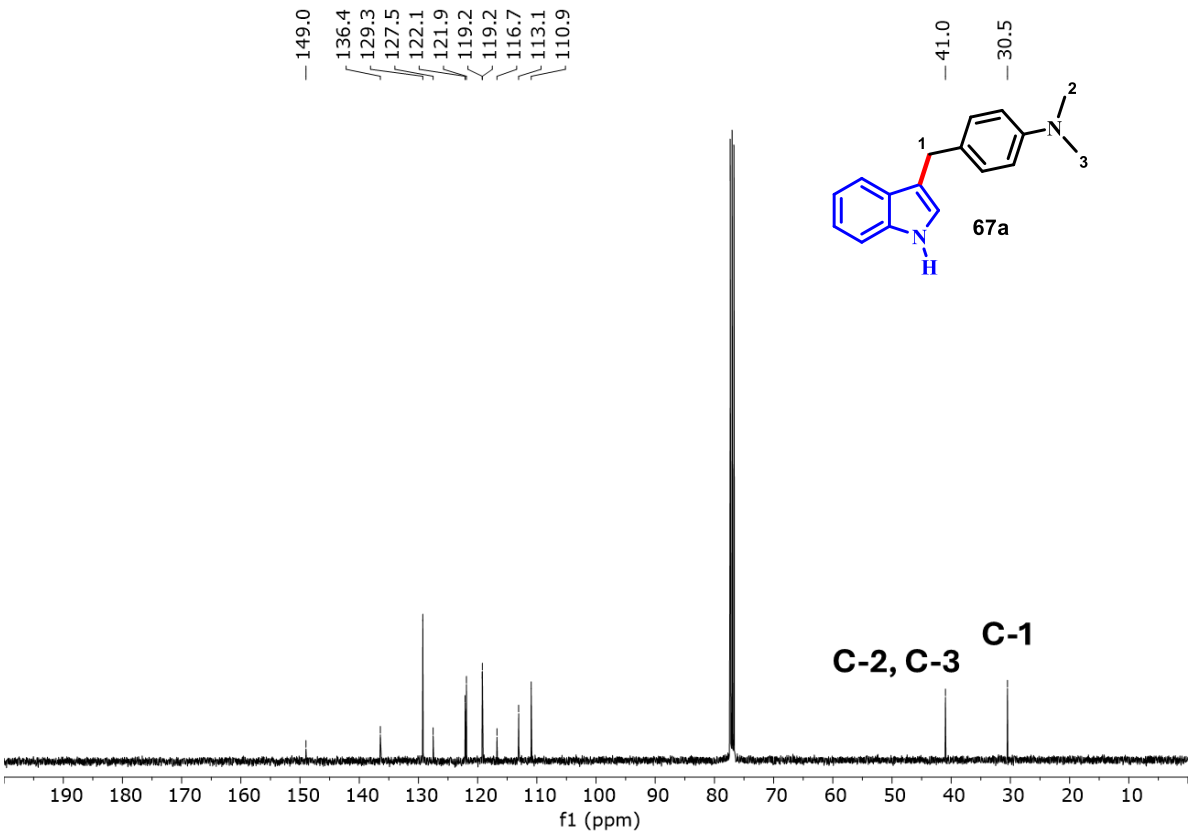

Figure 34: ^{13}C NMR spectrum of compound **67a** (101 MHz, $CDCl_3$).

The ^{1}H NMR spectrum of methyl 3-(p-tolylthio)propanoate (**69j**) exhibits four aromatic hydrogen resonances between δ 7.00 and 7.20 ppm, consistent with the substitution pattern of a para-substituted aromatic ring. Two singlets are observed at δ 3.60 and 2.20 ppm, each integrating for three hydrogens; the signal at δ 3.60 ppm is assigned to the methoxy group of the ester, whereas the signal at δ 2.20 ppm corresponds to the methyl substituent on the aromatic ring. Additionally, two triplets are centered at δ 3.04 and 2.53 ppm, each integrating for two protons, which are attributed to the methylene groups of the propanoate chain.

The ^{13}C NMR spectrum shows a signal at δ ~172 ppm, characteristic of the ester carbonyl carbon. The methoxy carbon appears at δ 51.8 ppm, while the methyl carbon of the p-tolyl group resonates at δ 21.0 ppm. The remaining resonances correspond to the aromatic carbons and the two aliphatic methylene carbons. The chemical shifts and signal distribution are in full agreement with the proposed structure and with the literature, confirming the successful synthesis of methyl 3-(p-tolylthio)propanoate.

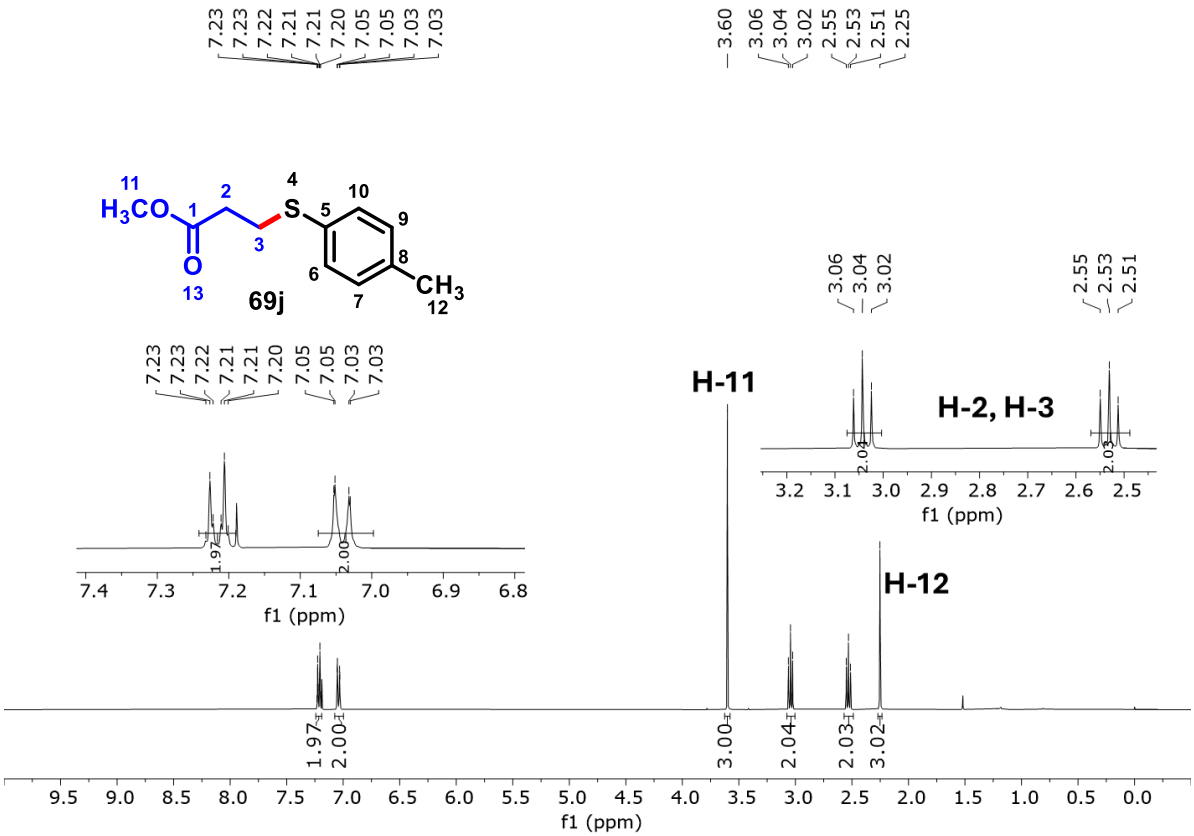

Figure 35: ^{1}H NMR spectrum of compound **69j** (400 MHz, $CDCl_3$).

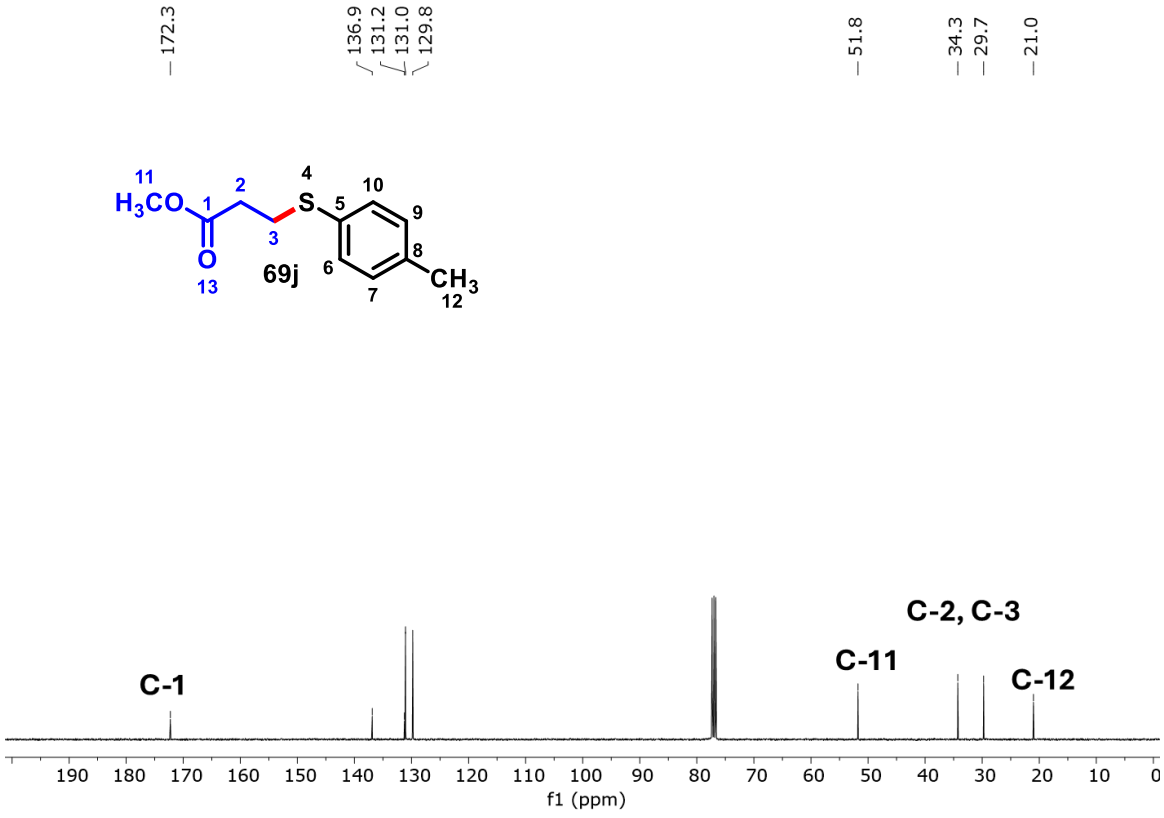

Figure 36: ^{13}C NMR spectrum of compound **69j** (101 MHz, $CDCl_3$).

3.4 CONCLUSIONS

The successful application of the organic photocatalyst *p*PCDA in seven distinct light-driven transformations thioetherification of aryldiazonium salts, C–H arylation of naphthoquinones with aryldiazonium salts, cross-coupling of aryldiazonium salts with nitroalkenes, oxidative C–C bond coupling, perfluoroalkylation of indoles, alkylation of indoles with tertiary amines, and hydrothiolation of styrene represents a significant advance in the field of organic synthesis. These initial studies not only demonstrate the broad applicability of *p*PCDA but also highlight its high efficiency under mild conditions. Such performance reinforces its potential as a versatile platform for synthetic applications, particularly in scenarios where conventional methods depend on harsh reagents or energy-intensive processes.

Notably, *p*PCDA exhibited both high selectivity and sustained catalytic activity across multiple cycles, enhancing the sustainability and cost-effectiveness of the methodology. This durability aligns closely with the principles of green chemistry, reducing waste generation and minimizing the demand for fresh catalyst inputs.

Building on these findings, future work will focus on expanding the reaction scope to a broader range of substrates and refining operational parameters. This optimization stage, currently being pursued by other members of the research group, is expected to further consolidate the synthetic utility of the catalyst, strengthen its relevance within the field, and generate new scientific contributions.

Overall, the work presented here represents a strategic first step, mapping key reactivity patterns and establishing reliable parameters for subsequent investigations. The transformations were deliberately designed as exploratory studies to validate the feasibility of *p*PCDA as a new photocatalytic mediator. This initial mapping of reactivity provides the foundation for more systematic investigations. By offering a solid experimental framework, these findings open the way for advances toward greener, more efficient, and broadly applicable synthetic methodologies.

3.5 EXPERIMENTAL

3.5.1 GENERAL REMARKS

Unless otherwise stated, all reactions were carried out under air. Starting materials, when not synthesized, were purchased from commercial suppliers (Merck, Sigma Aldrich) and used as received unless otherwise stated. Yields refer to isolated compounds estimated to be > 95% pure as determined by ^{1}H-NMR. Thin layer chromatography analyses (TLC) were performed on Merck TLC Silica Gel 60 F254 revealed under UV light or by treatment with a solution of potassium permanganate in ethanol followed by heating. Chromatographic separations were carried out on Aldrich brand silica gel 60 (230-240 mesh). Centrifugations were carried out on PowerSpin™ BX C885 Centrifuge for 5 minutes at 5000 rpm. NMR spectra were recorded on a Bruker Avance DRX 400 spectrometer at 400 MHz (^{1}H) and at 100 MHz (^{13}C) and Avance NEO 600 spectrometer at 600 MHz (^{1}H) and at 150 MHz (^{13}C), employing $CDCl_3$. For the ^{1}H NMR, tetramethylsilane (TMS) was used as a reference while for the ^{13}C spectra the residual non-deuterated solvent signal was used. Chemical shifts (δ) are reported in ppm and coupling constants (J) in Hertz (Hz). The following abbreviations were used to note signal multiplicities: s - singlet; sl - singlet large; d - doublet; t - triplet; q - quartet; dd - doublet of doublets; ddd - doublet of doublet of doublets; dt - doublet of triplets; ddt - doublet of doublet of triplets; dq - doublet of quartets; m - multiplet; p - pentet; sept - septet; td - triplet of doublets; tt - triplet of triplets. Unless otherwise specified, ultrasonic mixing was achieved using a Branson sonifier 550 equipped with a 3 mm tapered microtip (300 ms/s pulses, Output power 40%). Photo-polymerization were carried out using a 40 W low-pressure mercury UV lamp (Heraeus) emitting at a wavelength of 254 nm. ChemDraw Professional 22.2 was used to generate the IUPAC names of the compounds.

3.5.2 Self-assembling of *p*PCDA

A flask containing 100 mg of 10,12-pentacosadiynoic acid (PCDA), a blue powder, was charged with 10 mL of dichloromethane (DCM), in which the contents were fully dissolved. Pink filaments, corresponding to polymerized molecules, were observed at the surface. These polymerized species, present in negligible amounts and incapable of further assembly, were removed by filtration. The solvent was subsequently evaporated, yielding a white powder.

A crystallizer containing 150 mL of Milli-Q water was prepared, into which the solubilized PCDA was slowly introduced, followed by the addition of 100 mL of isopropanol. Immediate self-assembly occurred, producing a white suspension. The self-assembled material was polymerized under UV irradiation (254 nm) for three minutes, resulting in a color change to brown. The samples were freeze-dried for five days, affording *p*PCDA, which was then dissolved in methanol and heated with a heat blower until the solution turned red. Finally, the solvent was removed by rotary evaporation, yielding the red solid product.[142]

3.5.3 General apparatus for photochemical reactions

All photochemical reactions were carried out using the apparatus shown in **Figure 37**.

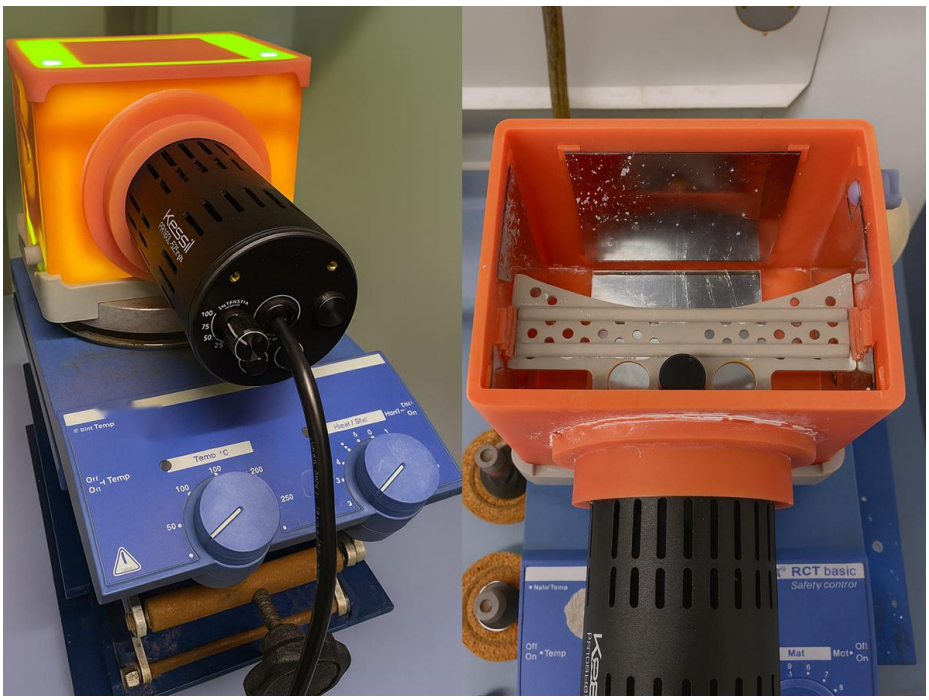

Figure 37. Apparatus used for all photochemical reactions.

[142] SAYMUNG, Rungarune; TRAIPHOL, Nisanart; TRAIPHOL, Rakchart. Promoting self-assembly and synthesis of color-responsive polydiacetylenes using mixed water-organic solvents: Effects of solvent composition, structure, and incubation temperature. **Colloids and Surfaces A: Physicochemical and Engineering Aspects**, v. 626, p. 127046, 2021.

3.5.4 General procedure for Thioetherification of aryldiazonium salts

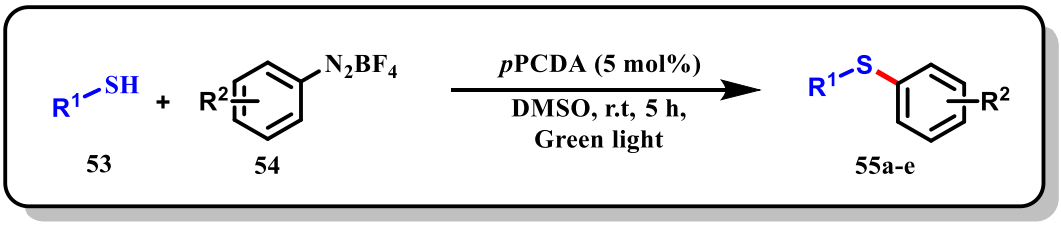

Scheme 41: Thioetherification of aryldiazonium salts synthesis

A mixture of the selected thiol (0.5 mmol), the diazonium salt (1 mmol), and *p*PCDA (5 mol %, 9.3 mg) in DMSO (2 mL) was irradiated with green LEDs at room temperature under an air atmosphere for 5 h. After irradiation, the reaction mixture was extracted with DCM and the combined organic layers were dried over anhydrous Na_2SO_4. The crude product was then purified by column chromatography on silica gel using a cyclohexane/ ethyl acetate gradient as the eluent.

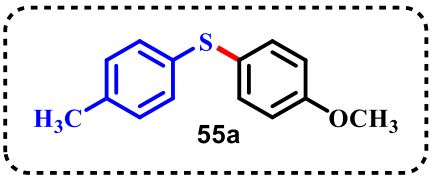

(4-methoxyphenyl)(p-tolyl)sulfane (55a): The general procedure was followed by using 4-methylbenzenethiol (0.5 mmol, 62.1 mg) and 4-methoxybenzenediazonium tetrafluoroborate (1 mmol, 221.9 mg). Purification by column chromatography on silica gel (cyclohexane /ethyl acetate 5%) afforded **55a** (101.1 mg, 88% yield) as a white solid. **^{1}H NMR (400 MHz, $CDCl_3$) δ:** 7.28 (d, J = 8.9 Hz, 2H), 7.05 (d, J = 8.2 Hz, 2H), 6.98 (d, J = 8.0 Hz, 2H), 6.79 (d, J = 8.9 Hz, 2H), 3.72 (s, 3H), 2.22 (s, 3H). **^{13}C NMR (101 MHz, $CDCl_3$) δ:** 159.4, 136.1, 134.3, 134.3, 129.7, 129.3, 125.6, 114.8, 55.3, 21.0. The spectroscopic data are consistent with those reported in the literature.[143]

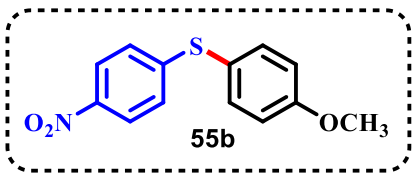

(4-methoxyphenyl)(4-nitrophenyl)sulfane (55b): The general procedure was followed by using 4-nitrobenzenethiol (0.5 mmol, 77.5 mg) and 4-methoxybenzenediazonium

[143] HONG, B.; LEE, J.; LEE, A. Visible-light-promoted synthesis of diaryl sulfides under air. **Tetrahedron Letters**, v. 58, n. 29, p. 2809-2812, 2017.

tetrafluoroborate (1 mmol, 221.9 mg). Purification by column chromatography on silica gel (cyclohexane/ethyl acetate 5%) afforded **55b** (78.3 mg, 60% yield) as a white solid. ^{1}H NMR (400 MHz, $CDCl_3$) δ: 7.97 (d, J = 9.1 Hz, 2H), 7.42 (d, J = 8.9 Hz, 2H), 7.02 (d, J = 9.1 Hz, 2H), 6.92 (d, J = 8.9 Hz, 2H), 3.80 (s, 3H). ^{13}C NMR (101 MHz, $CDCl_3$) δ: 161.1, 150.0, 145.0, 137.1, 125.6, 123.9, 120.2, 115.7, 55.5. The spectroscopic data are consistent with those reported in the literature.[144]

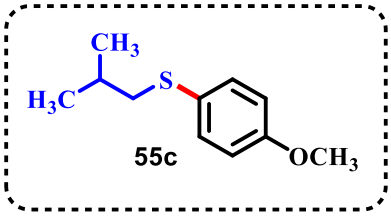

55c

Isobutyl(4-methoxyphenyl)sulfane (55c): The general procedure was followed by using 2-methylpropane-1-thiol (0.5 mmol, 45.1 mg) and 4-methoxybenzenediazonium tetrafluoroborate (1 mmol, 221.9 mg). Purification by column chromatography on silica gel (cyclohexane/ethyl acetate 1%) afforded **55c** (34 mg, 35% yield) as a colorless oil. **^{1}H NMR (400 MHz, $CDCl_3$) δ:** 7.25 (d, J = 8.9 Hz, 2H), 6.75 (d, J = 8.9 Hz, 2H), 3.71 (s, 3H), 2.63 (d, J = 6.9 Hz, 2H), 1.70 (dp, J = 13.4, 6.7 Hz, 1H), 0.93 (s, 3H), 0.91 (s, 3H). **^{13}C NMR (101 MHz, $CDCl_3$) δ:** 158.6, 132.7, 127.4, 114.4, 55.3, 44.9, 28.2, 21.9. The spectroscopic data are consistent with those reported in the literature.[145]

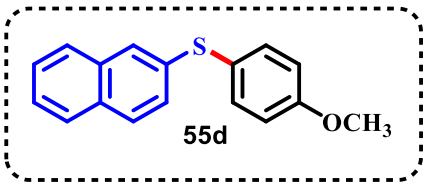

55d

(4-methoxyphenyl)(naphthalen-2-yl)sulfane (55d): The general procedure was followed by using naphthalene-2-thiol (0.5 mmol, 80.1 mg) and 4-methoxybenzenediazonium tetrafluoroborate (1 mmol, 221.9 mg). Purification by column chromatography on silica gel (cyclohexane/ethyl acetate 5%) afforded **55d** (66.5 mg, 50% yield) as a white solid. **^{1}H NMR (400 MHz, $CDCl_3$) δ:** 7.65 (d, J = 8.9 Hz, 1H), 7.60 (d, J = 8.7 Hz, 1H), 7.56 (d, J = 7.3 Hz, 1H), 7.50 (d, J = 1.4 Hz, 1H), 7.38-7.27 (m, 3H), 7.20 (dd, J = 8.6, 1.9 Hz, 1H), 6.81 (d, J =

[144] JIANG, M. *et al*. Room-temperature arylation of thiols: breakthrough with aryl chlorides. **Angewandte Chemie International Edition**, v. 56, n. 3, p. 874-879, 2017.
[145] ZHANG,.F. *et al*. Electrochemical Deoxygenative Thiolation of Preactivated Alcohols and Ketones. **Organic Letters**, v. 23, n. 19, p. 7524-7528, 2021.

8.9 Hz, 2H), 3.72 (s, 3H). **^{13}C NMR (101 MHz, $CDCl_3$) δ:** 159.8, 135.9, 135.2, 133.7, 131.7, 128.5, 127.6, 127.1, 126.6, 126.5, 126.4, 125.6, 124.3, 115.0, 55.3. The spectroscopic data are consistent with those reported in the literature.[146]

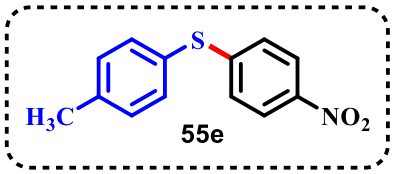

(4-nitrophenyl)(p-tolyl)sulfane (55e): The general procedure was followed by using 4-methylbenzenethiol (0.5 mmol, 62.1 mg) and 4-nitrobenzenediazonium tetrafluoroborate (1 mmol, 236.9 mg). Purification by column chromatography on silica gel (cyclohexane/ethyl acetate 5%) afforded **55e** (73.6 mg, 60% yield) as a white solid. **^{1}H NMR (400 MHz, $CDCl_3$) δ:** 7.96 (d, J = 9.1 Hz, 2H), 7.36 (d, J = 8.1 Hz, 2H), 7.19 (d, J = 8.3 Hz, 2H), 7.05 (d, J = 9.1 Hz, 2H), 2.34 (s, 3H). **^{13}C NMR (101 MHz, $CDCl_3$) δ:** 149.32, 145.08, 140.21, 135.06, 130.83, 126.42, 126.07, 123.94, 21.31. The spectroscopic data are consistent with those reported in the literature.[5]

3.5.5 General procedure for Arylation of Naphthoquinones with Aryldiazonium Salts

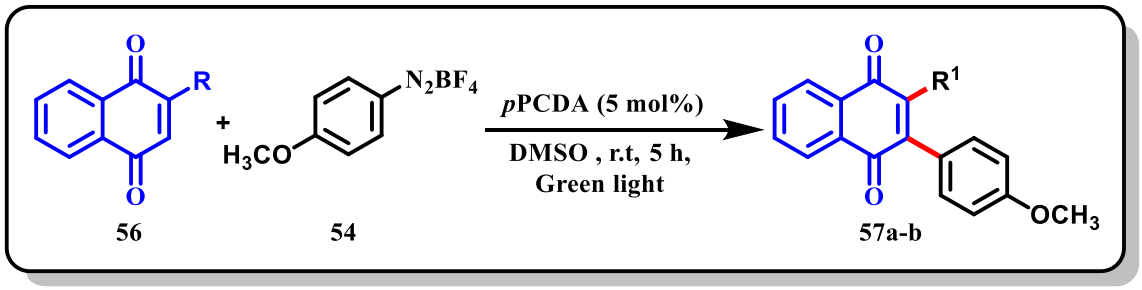

Scheme 42. Synthesis of Arylated Naphthoquinones via Reaction with Aryldiazonium Salts.

A mixture of the selected quinone (0.5 mmol), the diazonium salt (1 mmol), and *p*PCDA (5 mol %, 9.3 mg) in DMSO (2 mL) was irradiated with green LEDs at room temperature under an air atmosphere for 5 h. After irradiation, the reaction mixture was extracted with DCM and the combined organic layers were dried over anhydrous Na_2SO_4. The crude product was then purified by column chromatography on silica gel using a cyclohexane/ ethyl acetate gradient as the eluent.

[146] JIANG, Z. *et al*. Visible-light-promoted thioetherification of aryl diazonium salts with thiols via electron donor-acceptor complexes. **Molecular Catalysis**, v. 572, p. 114801, 2025.

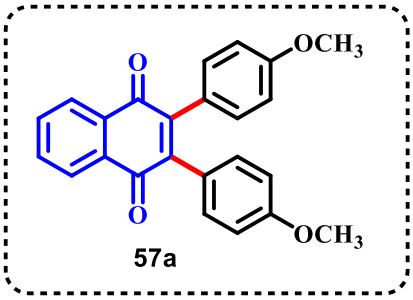

57a

2,3-bis(4-methoxyphenyl)naphthalene-1,4-dione (57a): The general procedure was followed by using naphthalene-1,4-dione (0.5 mmol, 79.1 mg) and 4-methoxybenzenediazonium tetrafluoroborate (1 mmol, 221.9 mg). Purification by column chromatography on silica gel (cyclohexane/ethyl acetate 15%) afforded **57a** (99.9 mg, 54% yield) as orange solid. **^{1}H NMR (400 MHz, $CDCl_3$) δ:** 8.13–8.08 (m, 1H), 7.72–7.67 (m, 1H), 6.96 (d, *J* = 8.9 Hz, 2H), 6.71 (d, *J* = 8.9 Hz, 2H), 3.71 (s, 3H). **^{13}C NMR (101 MHz, $CDCl_3$) δ:** 185.0, 159.4, 144.7, 133.7, 132.2, 132.2, 126.5, 125.7, 113.2, 55.2. The spectroscopic data are consistent with those reported in the literature.[6]

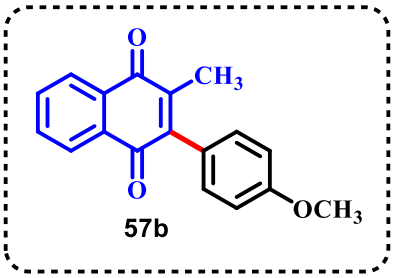

57b

2-(4-methoxyphenyl)-3-methylnaphthalene-1,4-dione (57b): The general procedure was followed by using 2-methylnaphthalene-1,4-dione (0.5 mmol, 86.1 mg) and 4-methoxybenzenediazonium tetrafluoroborate (1 mmol, 221.9 mg). Purification by column chromatography on silica gel (cyclohexane/ethyl acetate 15%) afforded **57b** (86.2 mg, 62% yield) as yellow solid. **^{1}H NMR (400 MHz, $CDCl_3$) δ:** 8.10-8.02 (m, 2H), 7.69-7.64 (m, 2H), 7.11 (d, *J* = 8.8 Hz, 2H), 6.93 (d, *J* = 8.8 Hz, 2H), 3.80 (s, 3H), 2.05 (s, 3H). **^{13}C NMR (101 MHz, $CDCl_3$) δ:** 185.88, 184.43, 159.76, 145.79, 143.81, 133.58, 133.49, 132.19, 132.16, 131.00, 126.61, 126.16, 125.65, 113.60, 55.30, 14.79. The spectroscopic data are consistent with those reported in the literature.[147]

[147] NAGAR, B.; DHAR, B. B. Photochemical C–H Arylation of Napthoquinones Using Eosin Y. **ACS omega**, v. 7, n. 36, p. 32615-32619, 2022.

3.5.6 General procedure Cross-Coupling of Aryldiazonium Salts with Nitroalkenes

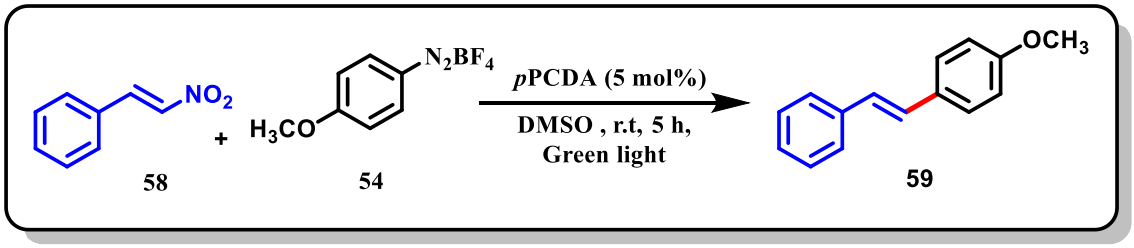

Scheme 43: Synthesis of Cross-Coupling of Aryldiazonium Salts with Nitroalkenes

1-methoxy-4-styrylbenzene (59): A mixture of the (2-nitrovinyl)benzene (0.5 mmol), the diazonium salt (1 mmol), and *p*PCDA (5 mol %, 9.3 mg) in DMSO (2 mL) was irradiated with green LEDs at room temperature under an air atmosphere for 5 h. After irradiation, the reaction mixture was extracted with DCM and the combined organic layers were dried over anhydrous Na_2SO_4. The crude product was then purified by column chromatography on silica gel Purification on silica gel chromatography (cyclohexane 100%) afforded XX (4**2.9** mg, **38**% yield) as white solid. **^{1}H NMR (400 MHz, $CDCl_3$) δ**: 7.45-7.36 (m, 4H), 7.27 (t, *J* = 7.6 Hz, 2H), 7.15 (d, *J* = 7.3 Hz, 1H), 7.00 (d, *J* = 16.3 Hz, 1H), 6.90 (d, *J* = 16.3 Hz, 1H), 6.86 - 6.79 (m, 2H), 3.76 (s, 3H). **^{13}C NMR (101 MHz, $CDCl_3$) δ:** 159.43, 137.78, 130.28, 128.78, 128.34, 127.85, 127.35, 126.74, 126.39, 114.27, 55.47. The spectroscopic data are consistent with those reported in the literature.[148]

3.5.7 General procedure Oxidative C–C Bond Coupling

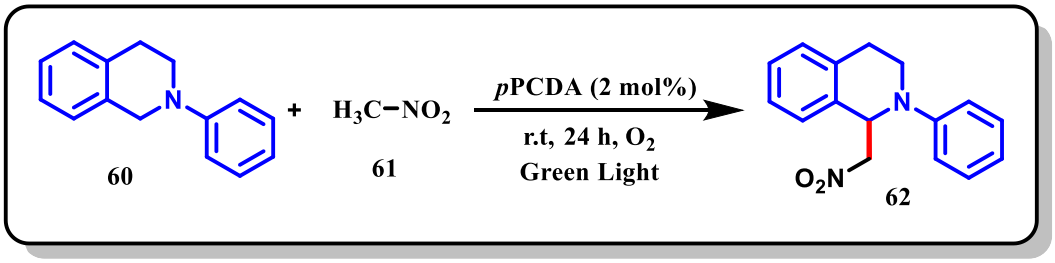

Scheme 44: Synthesis Oxidative C–C Bond Coupling.

[148] ZHANG, N. *et al.* Synthesis of stilbene derivatives via visible-light-induced cross-coupling of aryl diazonium salts with nitroalkenes using–NO 2 as a leaving group. **Chemical Communications**, v. 52, n. 99, p. 14234-14237, 2016

1-(nitromethyl)-2-phenyl-1,2,3,4-tetrahydroisoquinoline (62): In a 5 mL vial equipped with a septum and a magnetic stirring bar, 2-phenyl-1,2,3,4-tetrahydroisoquinoline (0.25 mmol) and *p*PCDA (0.02 equiv., 2 mol %, 2 mg) were dissolved in nitromethane (3 mL). The solution was bubbled with oxygen for 15 minutes and then kept under an oxygen balloon while being irradiated with green LEDs. After 24 hours, the reaction mixture was filtered and concentrated under reduced pressure. The residue was purified by flash chromatography on silica gel using a cyclohexane/ethyl acetate mixture as the eluent, affording compound **62** as a yellow solid (40.2 mg, 60% yield). **^{1}H NMR (400 MHz, $CDCl_3$) δ:** 7.23-7.08 (m, 5H), 7.08-7.02 (m, 1H), 6.90 (dd, *J* = 8.8, 1.1 Hz, 2H), 6.77 (tt, *J* = 7.2, 1.0 Hz, 1H), 5.47 (t, *J* = 7.2 Hz, 1H), 4.78 (dd, *J* = 11.8, 7.8 Hz, 1H), 4.47 (dd, *J* = 11.8, 6.6 Hz, 1H), 3.63-3.49 (m, 2H), 3.04-2.96 (m, 1H), 2.71 (dt, *J* = 16.3, 4.9 Hz, 1H). **^{13}C NMR (101 MHz, $CDCl_3$) δ:** 148.5, 135.4, 133.0, 129.6, 129.3, 128.2, 127.1, 126.8, 119.6, 115.2, 78.9, 58.3, 42.2, 26.6. The spectroscopic data are consistent with those reported in the literature.[149]

3.5.8 General procedure for Perfluoroalkylation of indoles

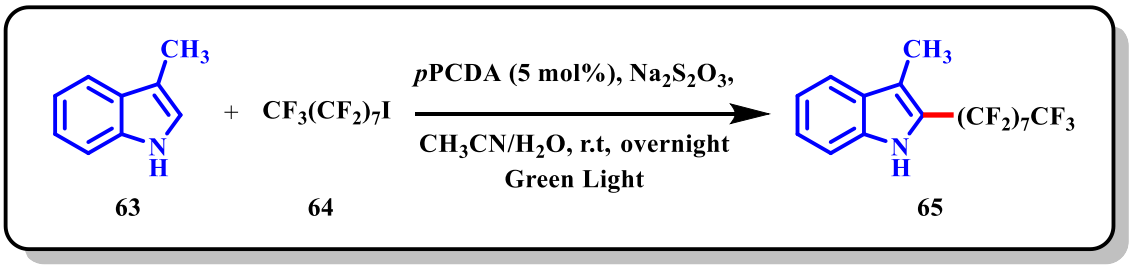

Scheme 45: Synthesis Perfluoroalkylation of indoles

3-methyl-2-(perfluorooctyl)-1H-indole (65): A mixture of 3-methylindole (0.2 mmol), 1-iodoperfluorooctane (0.3 mmol), $Na_2S_2O_3$ (1.0 mmol), and PDA (5 mol %, 3.7 mg) in CH_3CN (2.5 mL) was irradiated with green LEDs under an air atmosphere overnight. After completion of the reaction, the mixture was extracted with DCM, and the combined organic layers were dried over anhydrous Na_2SO_4, filtered, and concentrated under vacuum. The crude product was then purified by column chromatography on silica gel using a (cyclohexane/ethyl acetate 2%) as the eluent. afforded **65** (45.0 mg, 41% yield) as white solid. **^{1}H NMR (400 MHz, $CDCl_3$) δ**: 8.07 (s, 1H), 7.57 (d, *J* = 8.0 Hz, 1H), 7.29 (d, *J* = 8.2 Hz, 1H), 7.27-7.20

[149] HARI, D. P.; KÖNIG, B. Eosin Y catalyzed visible light oxidative C–C and C–P bond formation. **Organic letters**, v. 13, n. 15, p. 3852-3855, 2011

(m, 1H), 7.14-7.08 (m, 1H), 2.35 (t, *J* = 2.1 Hz, 3H). **^{13}C NMR (101 MHz, $CDCl_3$) δ:** 135.95, 128.34, 124.94, 120.37, 120.06, 119.52, 116.71, 111.50, 8.50. **^{19}F NMR (376 MHz, $CDCl_3$) δ:** -80.75 (t, *J* = 9.9 Hz), -108.63 (t, *J* = 13.0 Hz), -121.56-122.27 (m), -122.71 (s), -125.95-126.36 (m). The spectroscopic data are consistent with those reported in the literature.[150]

3.5.9 General procedure Alkylation of indoles with tertiary amines

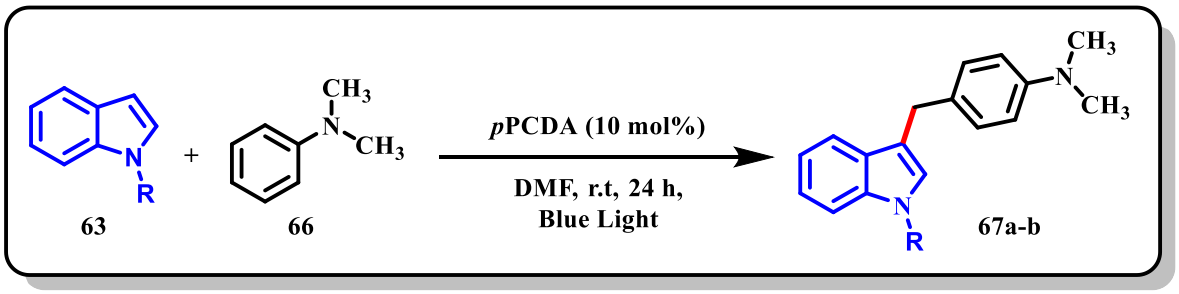

Scheme 46: Synthesis Alkylation of indoles with tertiary amines

A mixture of indole (0.5 mmol), N,N-dimethylaniline (5 mmol), and *p*PCDA (10 mol %, 18.7 mg) in DMF (4 mL) was irradiated with blue LEDs at room temperature under an air atmosphere for 24 h. After irradiation, the reaction mixture was extracted with DCM, and the combined organic layers were dried over anhydrous Na_2SO_4. The crude product was then purified by column chromatography on silica gel using a cyclohexane/ethyl acetate gradient as the eluent.

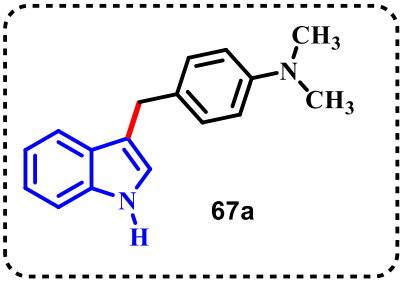

4-((1*H*-indol-3-yl)methyl)-*N*,*N*-dimethylaniline (67a): The general procedure was followed by using 1*H*-indole (0.5 mmol, 58.5 mg) and *N*,*N*-dimethylaniline (5 mmol, 605.9 mg). Purification by column chromatography on silica gel (cyclohexane/ethyl acetate 5%) afforded **67a** (76.2 mg, 61% yield) as white solid. **^{1}H NMR (400 MHz, $CDCl_3$) δ:** 7.84 (s, 1H), 7.47 (dd, *J* = 7.9, 0.8 Hz, 1H), 7.27 (dd, *J* = 8.1, 0.8 Hz, 1H), 7.09 (d, *J* = 8.7 Hz, 3H), 7.00 (ddd, *J*

[150] HE, Xiang-Wu et al. Visible light-induced perfluoroalkylation reaction of indoles in the presence of Na_2-eosin Y. **Tetrahedron Letters**, v. 162, p. 155571, 2025.

= 8.0, 7.1, 1.0 Hz, 1H), 6.84–6.79 (m, 1H), 6.63 (d, *J* = 8.7 Hz, 2H), 3.95 (s, 2H), 2.83 (s, 6H). **^{13}C NMR (101 MHz, $CDCl_3$) δ**: 149.01, 136.44, 129.26, 127.52, 122.11, 121.88, 119.22, 119.20, 116.73, 113.07, 110.95, 40.98, 30.49. The spectroscopic data are consistent with those reported in the literature.[151]

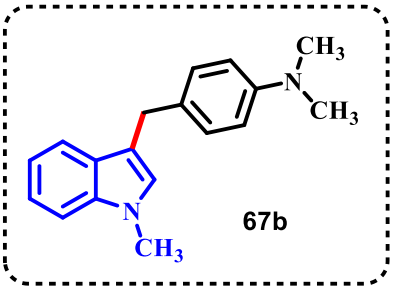

***N*,*N*-dimethyl-4-((1-methyl-1*H*-indol-3-yl)methyl)aniline (67b):** The general procedure was followed by using 1-methyl-1*H*-indole (0.5 mmol, 65.5 mg) and *N*,*N*-dimethylaniline (5 mmol, 605.9 mg). Purification by column chromatography on silica gel (hexane/ethyl acetate 5%) afforded **67b** (79.2 mg, 30% yield) as white solid. **^{1}H NMR (400 MHz, $CDCl_3$) δ**: 7.48-7.44 (m, 1H), 7.22–7.17 (m, 1H), 7.16-7.11 (m, 1H), 7.11–7.05 (m, 2H), 6.98 (ddd, *J* = 8.0, 6.9, 1.1 Hz, 1H), 6.66-6.59 (m, 3H), 3.93 (s, 2H), 3.62 (s, 3H), 2.82 (s, 6H). **^{13}C NMR (101 MHz, $CDCl_3$) δ:** 149.02, 137.12, 129.62, 129.25, 127.86, 126.93, 121.40, 119.24, 118.59, 115.20, 113.00, 109.01, 40.92, 32.52, 30.40. The spectroscopic data are consistent with those reported in the literature.[8]

3.5.10 General procedure for the synthesis hydrothiolation of styrene

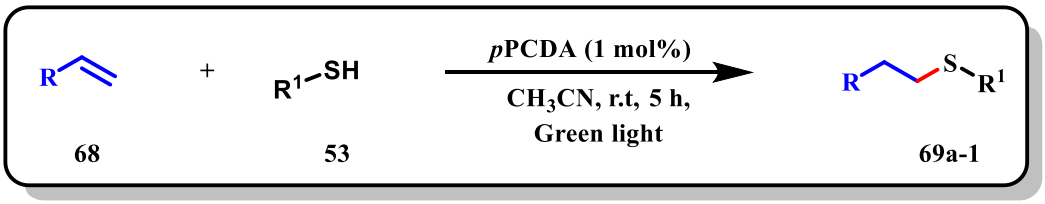

Scheme 47: Synthesis of styrene hydrothiolation

A mixture of alkene (1 mmol), thiol (2 mmol), and *p*PCDA (1 mol %, 3.7 mg) in CH_3CN (3 mL) was irradiated with green LEDs at room temperature for 5 hours. After completion of the reaction, the solvent was removed under reduced pressure. The crude product was then

[151] DING, Xuan et al. Visible-Light-Promoted Alkylation of Indoles with Tertiary Amines by the Oxidation of a sp3 C-H Bond. **Advanced Synthesis & Catalysis**, v. 360, n. 4, p. 762-767, 2018.

purified by column chromatography on silica gel using a cyclohexane/ethyl acetate gradient as the eluent.

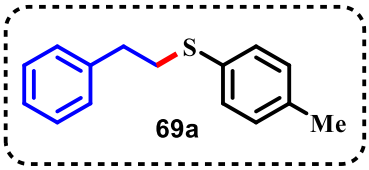

Phenethyl(*p*-tolyl)sulfane (69a): The general procedure was followed by using styrene (1 mmol, 104.1 mg) and 4-methylbenzenethiol (2 mmol, 248.4). Purification by column chromatography on silica gel (Cyclohexane) afforded **69a** (205 mg, 95% yield) as a colorless oil. **^{1}H NMR (400 MHz, $CDCl_3$) δ:** 7.24-7.18 (m, 4H), 7.16-7.08 (m, 3H), 7.06-7.01 (m, 2H), 3.07-3.01 (m, 2H), 2.85-2.78 (m, 2H), 2.24 (s, 3H). **^{13}C NMR (101 MHz, $CDCl_3$) δ**: 140.3, 136.2, 132.4, 130.1, 129.7, 128.5, 128.4, 126.4, 35.8, 35.7, 21.0 ppm. The spectroscopic data are consistent with those reported in the literature.

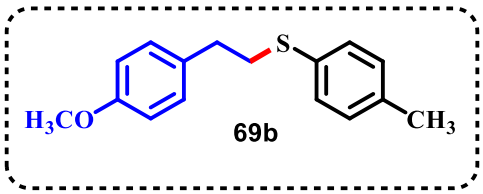

(4-methoxyphenethyl)(*p*-tolyl)sulfane (69b): The general procedure was followed by using 4-methoxystyrene (1 mmol, 134.1 mg) and 4-methylbenzenethiol (2 mmol, 248.4). Purification by column chromatography on silica gel (Cyclohexane) afforded **69b** (245 mg, 95% yield) as a colorless oil. **^{1}H NMR (400 MHz, $CDCl_3$) δ:** 7.22-7.17 (m, 2H), 7.06-7.00 (m, 4H), 6.78-6.73 (m, 2H), 3.71 (s, 3H), 3.05–2.98 (m, 2H), 2.80-2.73 (m, 2H), 2.25 (s, 3H). **^{13}C NMR (101 MHz, $CDCl_3$) δ:** 158.1, 136.1, 132.5, 132.4, 130.0, 129.7, 129.4, 113.8, 55.2, 36.0, 34.8, 21.0. The spectroscopic data are consistent with those reported in the literature.

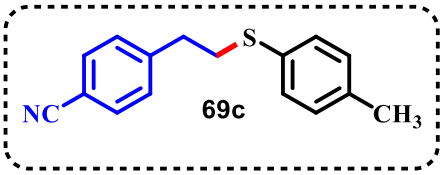

4-(2-(*p*-tolylthio)ethyl)benzonitrile (69c): The general procedure was followed by using 4-vinylbenzonitrile (1 mmol, 129.1 mg) and 4-methylbenzenethiol (2 mmol, 248.4). Purification by column chromatography on silica gel (Cyclohexane) afforded **69c** (232 mg, 92% yield) as a colorless oil. **^{1}H NMR (400 MHz, $CDCl_3$) δ:** 7.52-7.48 (m, 2H), 7.22-7.17 (m, 4H), 7.05

(d, *J* = 7.9 Hz, 2H), 3.07-3.02 (m, 2H), 2.87 (t, *J* = 7.6 Hz, 2H), 2.26 (s, 3H). **^{13}C NMR (101 MHz, $CDCl_3$) *δ*:** 145.7, 136.7, 132.2, 131.6, 130.6, 129.8, 129.4, 118.9, 110.3, 35.7, 35.4, 21.0. The spectroscopic data are consistent with those reported in the literature.

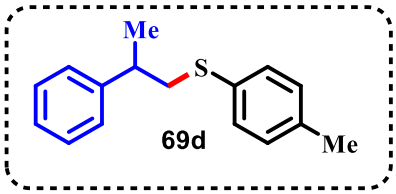

(2-phenylpropyl)(*p*-tolyl)sulfane (69d): The general procedure was followed by using α-methylstyrene (1 mmol, 118.1 mg) and 4-methylbenzenethiol (2 mmol, 248.4). Purification by column chromatography on silica gel (Cyclohexane) afforded **69d** (193 mg, 80% yield) as a colorless oil. **^{1}H NMR (400 MHz, $CDCl_3$) *δ*:** 7.26-7.20 (m, 2H), 7.18-7.09 (m, 5H), 7.03-6.99 (m, 2H), 3.10 (dd, *J* = 12.5, 6.1 Hz, 1H), 2.97-2.81 (m, 2H), 2.24 (s, 3H), 1.31 (d, *J* = 6.8 Hz, 3H). **^{13}C NMR (101 MHz, $CDCl_3$) *δ*:** 145.6, 136.0, 132.9, 129.9, 129.6, 128.5, 126.9, 126.5, 42.7, 39.4, 21.0, 20.9. The spectroscopic data are consistent with those reported in the literature.

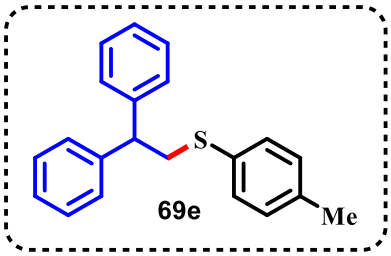

(2,2-diphenylethyl)(*p*-tolyl)sulfane (69e): The general procedure was followed by using 1,1-diphenylethylene (1 mmol, 180.2 mg) and 4-methylbenzenethiol (2 mmol, 248.4). Purification by column chromatography on silica gel (Cyclohexane) afforded **69e** (106 mg, 35% yield) as a colorless oil. **^{1}H NMR (400 MHz, $CDCl_3$) *δ*:** 7.22-7.16 (m, 4H), 7.15-7.07 (m, 8H), 7.01-6.97 (m, 2H), 4.09 (t, *J* = 7.9 Hz, 1H), 3.46 (d, *J* = 7.9 Hz, 2H), 2.21 (s, 3H).**^{13}C NMR (101 MHz, $CDCl_3$) *δ*:** 143.1, 136.2, 132.6, 130.3, 129.7, 128.5, 127.9, 126.6, 50.5, 40.3, 21.0. The spectroscopic data are consistent with those reported in the literature.

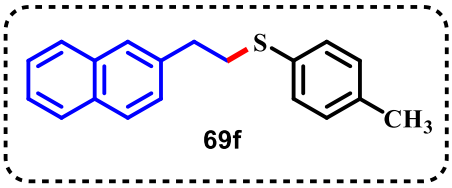

69f

(2-(naphthalen-2-yl)ethyl)(*p*-tolyl)sulfane (69f): The general procedure was followed by using 2-vinylnaphthalene (1 mmol, 154.2 mg) and 4-methylbenzenethiol (2 mmol, 248.4). Purification by column chromatography on silica gel (Cyclohexane) afforded **69f** (166 mg, 60% yield) as a colorless oil. **^{1}H NMR (400 MHz, $CDCl_3$) δ:** 7.74-7.64 (m, 3H), 7.52 (s, 1H), 7.40-7.29 (m, 2H), 7.22 (d, J = 8.0 Hz, 3H), 7.03 (d, J = 8.0 Hz, 2H), 3.15-3.08 (m, 2H), 3.00-2.92 (m, 2H), 2.23 (s, 3H). **^{13}C NMR (101 MHz, $CDCl_3$) δ:** 137.7, 136.2, 133.5, 132.4, 132.2, 130.2, 129.7, 128.0, 127.6, 127.5, 127.0, 126.7, 125.9, 125.4, 77.3, 77.0, 76.7, 35.9, 35.7, 20.9. The spectroscopic data are consistent with those reported in the literature.

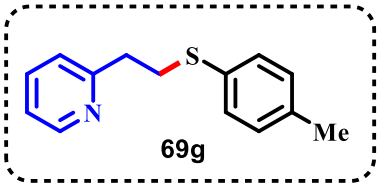

69g

2-(2-(*p*-tolylthio)ethyl)pyridine (69g): The general procedure was followed by using vinylpyridine (1 mmol, 105.1 mg) and 4-methylbenzenethiol (2 mmol, 248.4). Purification by column chromatography on silica gel (Cyclohexane) afforded **69g** (206 mg, 90% yield) as a colorless oil. **^{1}H NMR (400 MHz, $CDCl_3$) δ:** 8.48-8.45 (m, 1H), 7.51 (td, J = 7.7, 1.8 Hz, 1H), 7.25-7.19 (m, 2H), 7.09-6.98 (m, 4H), 3.22 (t, J = 7.5 Hz, 2H), 3.07–2.94 (m, 2H), 2.24 (s, 3H).**^{13}C NMR (101 MHz, $CDCl_3$) δ:** 159.8, 149.4, 136.3, 136.2, 132.3, 130.2, 129.7, 123.2, 121.4, 33.9, 21.0. The spectroscopic data are consistent with those reported in the literature.

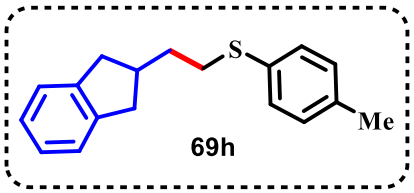

69h

(2,3-dihydro-1*H*-inden-2-yl)(*p*-tolyl)sulfane (69h): The general procedure was followed by using 1*H*-indene (1 mmol, 116.1 mg) and 4-methylbenzenethiol (2 mmol, 248.4). Purification by column chromatography on silica gel (Cyclohexane) afforded **69h** (196 mg, 82% yield) as

a colorless oil. **^{1}H NMR (400 MHz, $CDCl_3$) δ:** 7.25 (d, *J* = 7.9 Hz, 2H), 7.13-7.02 (m, 6H), 3.97 (p, *J* = 6.7 Hz, 1H), 3.25 (dd, *J* = 16.2, 7.5 Hz, 2H), 2.90 (dd, *J* = 16.2, 6.0 Hz, 2H), 2.26 (s, 3H).**^{13}C NMR (101 MHz, $CDCl_3$) δ:** 141.6, 136.7, 132.1, 131.5, 129.7, 126.6, 124.5, 45.9, 40.1, 21.1.

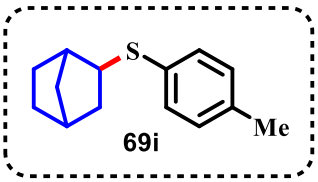

bicyclo[2.2.1]heptan-2-yl(*p*-tolyl)sulfane (69i): The general procedure was followed by using 2-norbornene (1 mmol, 94.1 mg) and 4-methylbenzenethiol (2 mmol, 248.4). Purification by column chromatography on silica gel (Cyclohexane) afforded **69i** (141 mg, 65% yield) as a colorless oil. **^{1}H NMR (400 MHz, $CDCl_3$) δ:** 7.17 (dt, *J* = 3.9, 2.2 Hz, 2H), 7.03-6.99 (m, 2H), 3.06 (ddd, *J* = 8.3, 4.5, 1.7 Hz, 1H), 2.24 (s, 3H), 2.23-2.16 (m, 2H), 1.70 (ddd, *J* = 13.0, 8.3, 2.3 Hz, 1H), 1.65-1.59 (m, 1H), 1.56-1.38 (m, 2H), 1.33 (dtd, *J* = 13.0, 4.4, 2.7 Hz, 1H), 1.14–1.08 (m, 3H). **^{13}C NMR (101 MHz, $CDCl_3$) δ:** 135.7, 133.8, 130.0, 129.5, 48.9, 42.2, 38.5, 36.5, 35.4, 28.9, 28.7, 21.0.

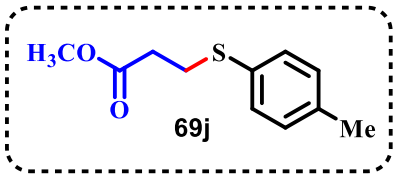

Methyl 3-(*p*-tolylthio)propanoate (69j): The general procedure was followed by using methyl acrylate (1 mmol, 86.1 mg) and 4-methylbenzenethiol (2 mmol, 248.4). Purification by column chromatography on silica gel (Cyclohexane) afforded **69j** (31.5 mg, 15% yield) as a colorless oil. **^{1}H NMR (400 MHz, $CDCl_3$) δ:** 7.24-7.20 (m, 1H), 7.04 (dd, *J* = 8.5, 0.6 Hz, 1H), 3.60 (s, 2H), 3.04 (t, *J* = 7.4 Hz, 1H), 2.53 (t, *J* = 7.4 Hz, 1H), 2.25 (s, 2H). **^{13}C NMR (101 MHz, $CDCl_3$) δ:** 172.3, 136.9, 131.2, 131.0, 129.8, 51.8, 34.3, 29.7, 21.0.

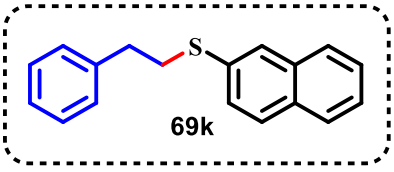

naphthalen-2-yl(phenethyl)sulfane (69k): The general procedure was followed by using styrene (1 mmol, 104.1 mg) and naphthalene-2-thiol (2 mmol, 320 mg). Purification by column chromatography on silica gel (Cyclohexane) afforded **69k** (237 mg, 90% yield) as a

colorless oil. **^{1}H NMR (400 MHz, $CDCl_3$) δ:** 7.72-7.62 (m, 4H), 7.42-7.31 (m, 3H), 7.26-7.18 (m, 2H), 7.17-7.10 (m, 3H), 3.21-3.15 (m, 2H), 2.92-2.85 (m, 2H). **^{13}C NMR (101 MHz, $CDCl_3$) δ:** 140.2, 133.9, 133.8, 131.7, 128.5, 128.4, 127.7, 127.3, 127.0, 126.8, 126.5, 126.5, 125.6, 35.5, 34.9.

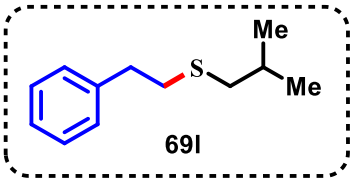

69l

Isobutyl(phenethyl)sulfane (69l): The general procedure was followed by using styrene (1 mmol, 104.1 mg) and 2-methylpropane-1-thiol (2 mmol, 180 mg). Purification by column chromatography on silica gel (Cyclohexane) afforded **69l** (100 mg, 52% yield) as a colorless oil. **^{1}H NMR (400 MHz, $CDCl_3$) δ:** 7.25-7.19 (m, 2H), 7.16-7.11 (m, 3H), 2.85-2.77 (m, 2H), 2.71-2.64 (m, 2H), 2.34 (d, J = 6.9 Hz, 2H), 1.73 (dp, J = 13.4, 6.7 Hz, 1H), 0.92 (s, 3H), 0.90 (s, 3H). **^{13}C NMR (101 MHz, $CDCl_3$) δ:** 140.7, 128.4, 128.4, 126.2, 41.6, 36.5, 34.3, 28.6, 22.0

REFERENCES

AKANDA, M. R. *et al.* Recent advances in nanomaterial-modified pencil graphite electrodes for electroanalysis. **Electroanalysis**, 2016, 28, 408-424.

ALI, H. *et al*. Visible light-driven photocatalytic thiol–ene/yne reactions using anisotropic 1D Bi 2 S 3 nanorods: A green synthetic approach. **Nanoscale**, v. 15, n. 35, p. 14551-14563, 2023.

ALMEIDA, E. R.; *et al*. Anti-inflammatory action of lapachol. **Journal of Ethnopharmacology**, 1990, v. 29, p. 239–241.

ALMEIDA, R. G. *et al.* Synthesis of quinone imine and sulphur-containing compounds with antitumor and trypanocidal activities: redox and biological implications. **RSC Medicinal Chemistry**, 2020, 11, 1145-1160.

ANDO, Y.; SUZUKI, K. Photoredox reactions of quinones. **Chemistry–A European Journal**, v. 24, n. 60, p. 15955-15964, 2018.

ARAÚJO, E. L.; *et al.* Lapachol: segurança e eficácia na terapêutica. Revista Brasileira de Farmacognosia, 2002, v. 12, p. 57-59

BANDYOPADHYAY, U.; DAS, D.; BANERJEE, R. K. Reactive oxygen species: oxidative damage and pathogenesis. **Current Science**, 1999, p. 658-666.

BECHTOLD, T.; MUSSAK, R. *Handbook of Natural Colorants*. Chichester: John Wiley & Sons, 2009.

BERRUTI, I. *et al*. Recent advances in solar photochemical processes for water and wastewater disinfection. **Chemical Engineering Journal Advances**, v. 10, p. 100248, 2022.

BHATTACHARYYA, A.; DE SARKAR, S.; DAS, A. Supramolecular engineering and self-assembly strategies in photoredox catalysis. **ACS Catalysis**, v. 11, n. 2, p. 710-733, 2020.

BRITO, M. C. A. *et al*. Anti-inflammatory and cicatrizing properties of the Tabebuia genus: A review. **Research, Society and Development**, v. 10, n. 9, 2021.

CAMBIÉ, D. *et al*. Energy-efficient solar photochemistry with luminescent solar concentrator based photomicroreactors. **Angewandte chemie**, v. 131, n. 40, p. 14512-14516, 2019.

CAMBIÉ, D.; NOËL, T.. Solar photochemistry in flow. **Accounts on Sustainable Flow Chemistry**, p. 1-27, 2018.

COELHO-CERQUEIRA, E.; NETZ, P. A.; do CANTO, V. P.; PINTO, A. C.; FOLLMER, C. Beyond topoisomerase inhibition: antitumor 1,4-naphthoquinones as potential inhibitors of human monoamine oxidase. **Chemical Biology & Drug Design**, 2014, v. 83, n. 4, p. 401–410.

CORES, Á. et al. Quinones as neuroprotective agents. **Antioxidants**, 2023, v. 12, p. 1464.

CORREA, A.; CARRIL, M.; BOLM, C. Iron-Catalyzed S-Arylation of Thiols with Aryl Iodides. **ChemInform**, v. 39, n. 30, p. no-no, 2008.
COSTANTINO, F.; KAMAT, P. V. Do sacrificial donors donate H2 in photocatalysis? **ACS Energy Letters**, v. 7, n. 1, p. 242-246, 2021.

CRUZ, E. H. G. *et al.* Synthesis and antitumor activity of selenium-containing quinone-based triazoles possessing two redox centres, and their mechanistic insights. **European Journal of Medicinal Chemistry**, 2016, v. 122, p. 1-16.

CUI, H. *et al*. Visible-light-induced selective synthesis of sulfoxides from alkenes and thiols using air as the oxidant. **Green Chemistry**, v. 19, n. 15, p. 3520-3524, 2017.

CUI, H.; WEBBER, M. J.; STUPP, S. I. Self-assembly of peptide amphiphiles: From molecules to nanostructures to biomaterials. **Peptide Science: Original Research on Biomolecules**, v. 94, n. 1, p. 1-18, 2010.

DA CRUZ, E. H. *et al.* 1,2,3-Triazole-, arylamino- and thio-substituted 1,4-naphthoquinones: potent antitumor activity, electrochemical aspects, and bioisosteric replacement of C-ring-modified lapachones. **Bioorganic & Medicinal Chemistry**, 2014, 22(5), 1608-1619.

DAI, X. Q. *et al*. Metal and acid-free visible light-mediated Friedel-Crafts alkylation reactions of indole with anilines. **Tetrahedron Letters**, v. 59, n. 30, p. 2945-2949, 2018.

DE SOUZA VIEIRA, L. A review on the use of glassy carbon in advanced technological applications. **Carbon**, 2022, 186, 282-302.

DEVI, M. *et al*. A comprehensive review on synthesis, biological profile and photophysical studies of heterocyclic compounds derived from 2,3-diamino-1,4-naphthoquinone. **Journal of Molecular Structure**, 2022, v. 1269, p. 133786.

DINDA, B. **Essentials of pericyclic and photochemical reactions**. Cham, Switzerland: Springer International Publishing, 2017.

DING, X. *et al*. Visible-Light-Promoted Alkylation of Indoles with Tertiary Amines by the Oxidation of a sp3 C-H Bond. **Advanced Synthesis & Catalysis**, v. 360, n. 4, p. 762-767, 2018.

ESEN, V.; SAĞLAM, Ş.; ORAL, B. Light sources of solar simulators for photovoltaic devices: A review. **Renewable and Sustainable Energy Reviews**, v. 77, p. 1240-1250, 2017.

EYONG, K. O. *et al.* Newbouldiaquinone A: a naphthoquinone–anthraquinone ether coupled pigment, as a potential antimicrobial and antimalarial agent from Newbouldia laevis. **Phytochemistry**, 2006, v. 67, p. 605-609.

FARADAY, M. Siebente Reihe von Experimental-Untersuchungen über Elektricitat. **Annalen der Physik**, 1834, 109, 433–451.

FRIEDRICH, J. M. *et al.* Reticulated vitreous carbon as an electrode material. **Journal of Electroanalytical Chemistry**, 2004, 561, 203-217.

FRY, A. J. Solvents and supporting electrolytes. In: **Laboratory Techniques in Electroanalytical Chemistry, Revised and Expanded**. CRC Press, 2018. p. 469-485.

FUCHIGAMI, T.; ATOBE, M.; INAGI, S. **Fundamentals and Applications of Organic Electrochemistry: Synthesis, Materials, Devices**. John Wiley & Sons, 2014.

GAFNER, S.; *et al*. Antifungal and antibacterial naphthoquinones from Newbouldia laevis roots. **Phytochemistry**, 1996, v. 42, n. 5, p. 1315–1320.

GATEBE, E. *et al.* Synthesis and characterization of polydiacetylene films and nanotubes. **Langmuir**, v. 24, n. 20, p. 11947-11954, 2008

GEORGE, C. *et al*. Interfacial photochemistry. In: **Physical Chemistry of Gas-Liquid Interfaces**. Elsevier, 2018. p. 435-457.

GERBER, D. E. *et al.* Phase 1 study of ARQ 761, a β-lapachone analogue that promotes NQO1-mediated programmed cancer cell necrosis. **British Journal of Cancer**, 2018, v. 119, p. 928-936.

GOMES, L. S.; *et al*. New chalcogen-functionalized naphthoquinones: Design, synthesis, and evaluation, in vitro and in silico, against squamous cell carcinoma. **ACS Omega**, v. 9, n. 20, p. 21948-21963, 2024.

GOTI, G. *et al.* The impact of UV light on synthetic photochemistry and photocatalysis. **Nature chemistry**, v. 16, n. 5, p. 684-692, 2024.

GUADALUPE M. M. *et al*. Immobilized Eosin Y on Modified Silica Nanoparticles and their Applications in Organic Synthesis. **European Journal of Organic Chemistry**, v. 28, n. 1, p. e202401003, 2025.

GUIMARÃES, T. T. *et al.* Synthesis of novel α- and nor-α-lapachone-based 1,2,3-triazoles by copper-catalyzed azide–alkyne cycloaddition. **European Journal of Medicinal Chemistry**, 2013, v. 63, p. 523-530.

GUO, L. *et al*. Enhanced Performance of All-Solid-State Rechargeable Air Batteries with Redox-Active Naphthoquinone-Based Polymer Electrode. **Sustainable Energy & Fuels**, 2025.

HARI, D. P.; KÖNIG, B. Eosin Y catalyzed visible light oxidative C–C and C–P bond formation. **Organic letters**, v. 13, n. 15, p. 3852-3855, 2011.

HASAN, M. *et al.* An overview of LEDs' effects on the production of bioactive compounds and crop quality. **Molecules**, v. 22, n. 9, p. 1420, 2017.

HAYES, J. D.; DINKOVA-KOSTOVA, A. T.; TEW, K. D. Oxidative stress in cancer. **Cancer Cell**, 2020, v. 38, n. 2, p. 167-197.

HE, X.W. *et al*. Visible light-induced perfluoroalkylation reaction of indoles in the presence of Na2-eosin Y. **Tetrahedron Letters**, v. 162, p. 155571, 2025.

HEARD, D. M.; LENNOX, A. J. Electrode materials in modern organic electrochemistry. **Angewandte Chemie International Edition**, 2020, 59, 18866-18884.

HEINE, J.; MÜLLER-BUSCHBAUM, K. Engineering metal-based luminescence in coordination polymers and metal–organic frameworks. **Chemical Society Reviews**, v. 42, n. 24, p. 9232-9242, 2013.

HICKLING, A. Studies in electrode polarisation. Part IV.—The automatic control of the potential of a working electrode. **Transactions of the Faraday Society**, 1942, 38, 27-33.

HIROTA, Y. Study on mechanism underlying metabolic biotransformation of vitamin K. **Vitamins**, 2017, v. 92, p. 63-72.

HUANG, Z.; TANG, S.; LEI, A. Oxidative cross-coupling: an alternative way for C–C bond formations. **Science Bulletin**, v. 60, n. 16, p. 1391-1394, 2015.

HUSSAIN, H. *et al.* Lapachol: an overview. **Arkivoc**, 2007, v. 2, p. 145.

ILARDI, E. A.; VITAKU, E.; NJARDARSON, J. T. Data-mining for sulfur and fluorine: an evaluation of pharmaceuticals to reveal opportunities for drug design and discovery: miniperspective. **Journal of Medicinal Chemistry**, 2014, v. 57, p. 2832.

IUPAC Compendium of Chemical Terminology, 5th ed. International Union of Pure and Applied Chemistry; 2025.

IUPAC. *Compendium of Chemical Terminology*. 2. ed. (the "Gold Book"). Versão online (2019-) criada por S. J. Chalk. ISBN 0-9678550-9-8

JAMMI, S. *et al*. Efficient ligand-free nickel-catalyzed C–S cross-coupling of thiols with aryl iodides. **Tetrahedron letters**, v. 49, n. 9, p. 1484-1487, 2008.

JANG, H. *et al.* Polydiacetylene (PDA) Embedded Polymer-Based Network Structure for Biosensor Applications. **Gels**, v. 11, n. 1, p. 66, 2025.

JANG, J.; LEE, G.; CHO, E. Visible light induced reactions of quinones. **Bulletin of the Korean Chemical Society**, v. 45, n. 12, p. 966-976, 2024.

JARDIM, G. A. M. *et al*. Naphthoquinone-based chalcone hybrids and derivatives: Synthesis and potent activity against cancer cell lines. **MedChemComm**, v. 6, n. 1, p. 120-130, 2015.

JELLY, R. *et al.* Lawsone: a novel reagent for the detection of latent fingermarks on paper surfaces. **Chemical Communications**, 2008, p. 3513.

JERKIEWICZ, G. Applicability of platinum as a counter-electrode material in electrocatalysis research. **ACS Catalysis**, 2022, 12, 2661-2670.

JOUNG, J. F. *et al*. Electronic relaxation dynamics of PCDA-PDA studied by transient absorption spectroscopy. **Physical Chemistry Chemical Physics**, v. 18, n. 33, p. 23096-23104, 2016.

KADAM, A. R.; NAIR, G. B.; DHOBLE, S. J. Insights into the extraction of mercury from fluorescent lamps: A review. **Journal of Environmental Chemical Engineering**, v. 7, n. 4, p. 103279, 2019.

KARMAKAR, P. *et al.* Electrochemical regioselective C(sp^2)–H selenylation and sulfenylation of substituted 2-amino-1,4-naphthoquinones. **The Journal of Organic Chemistry**, 2023, 88, 1049-1060.

KAUR, G. *et al*. Stilbenes: a journey from folklore to pharmaceutical innovation. **Archives of Microbiology**, v. 206, n. 5, p. 229, 2024.

KE, Zhengang *et al*. Alcohol promoted N-methylation of anilines with CO2/H2 over a cobalt catalyst under mild conditions. **Green Chemistry**, v. 23, n. 22, p. 9147-9153, 2021.

KHAN, N.; ABAS, N. Comparative study of energy saving light sources. **Renewable and sustainable energy reviews**, v. 15, n. 1, p. 296-309, 2011.

KHARMA, A. *et al.* Electrochemical selenation/cyclization of quinones: a rapid, green and efficient access to functionalized trypanocidal and antitumor compounds. **European Journal of Organic Chemistry**, 2020, 29, 4474-4486.

KIM, C.; LEE, K. Polydiacetylene (PDA) liposome-based immunosensor for the detection of exosomes. **Biomacromolecules**, v. 20, n. 9, p. 3392-3398, 2019.

KIM, S.; KUBEC, R.; MUSAH, R. A. Antibacterial and antifungal activity of sulfur-containing compounds from Petiveria alliacea L. **Journal of Ethnopharmacology**, 2006, 104, 188-192.

KIM, Y.; IIMURA, K.; TAMAOKI, N. Mechanoresponsive diacetylenes and polydiacetylenes: Novel polymerization and chromatic functions. **Bulletin of the Chemical Society of Japan**, v. 97, n. 4, p. uoae034, 2024.

KINGSTON, C. *et al.* A survival guide for the “electro-curious”. **Accounts of Chemical Research**, 2020, 53(1), 72-83.

KISSINGER, P.; HEINEMAN, W. R. **Laboratory Techniques in Electroanalytical Chemistry**. Revised and expanded. CRC Press, 2018.

KOLBE, H. Untersuchungen über die Elektrolyse organischer Verbindungen. **Annalen der Chemie und Pharmacie**, 1849, 69, 257.

KOVALENKO, O. *et al*. Analysis of Tungsten Halogen Lamps Characteristics. **Light & Engineering**, v. 29, n. 5-2, p. 79, 2021.

KUMAR, S.; RITIK, A. A brief review of the biological potential of indole derivatives. **Future Journal of Pharmaceutical Sciences**, v. 6, n. 1, p. 121, 2020.

LAM, K.; GEIGER, W. E. Anodic oxidation of disulfides: detection and reactions of disulfide radical cations. **The Journal of Organic Chemistry**, 2013, 78(16), 8020-8027.

LE, T. X. H.; BECHELANy, M.; CRETIN, M. Carbon felt-based electrodes for energy and environmental applications: a review. **Carbon,** 2017, 122, 564-591.

LEE, D. Y. *et al.* Anti-inflammatory activity of sulfur-containing compounds from garlic. **Journal of Medicinal Food**, 2012, 15(11), 992-999.

LEE, K. *et al.* Synthesis of a novel series of 2-alkylthio substituted naphthoquinones as potent acyl-CoA: Cholesterol acyltransferase (ACAT) inhibitors. **European Journal of Medicinal Chemistry**, 2013, 62, 515-525

LEROUX, F.; JESCHKE, P.; SCHLOSSER, M. α-Fluorinated ethers, thioethers, and amines: anomerically biased species. **Chemical reviews**, v. 105, n. 3, p. 827-856, 2005.b) GRGAS, D. *et al*. A review: per-and polyfluoroalkyl substances—biological degradation. **Toxics**, v. 11, n. 5, p. 446, 2023.

LIU, Jinjian *et al.* New redox strategies in organic synthesis by means of electrochemistry and photochemistry. **ACS Central Science**, v. 6, n. 8, p. 1317-1340, 2020.

LLAUGER, L. *et al*. Evaluation of 8-arylsulfanyl, 8-arylsulfoxyl, and 8-arylsulfonyl adenine derivatives as inhibitors of the heat shock protein 90. **Journal of medicinal chemistry**, v. 48, n. 8, p. 2892-2905, 2005.

LÓPEZ, L. I. *et al.* Naphthoquinones: biological properties and synthesis of lawsone and derivatives a structured review. **Vitae,** 2014, v. 21, p. 248-258.

LOWE, G. A. Enabling artificial photosynthesis systems with molecular recycling: A review of photo-and electrochemical methods for regenerating organic sacrificial electron donors. **Beilstein Journal of Organic Chemistry**, v. 19, n. 1, p. 1198-1215, 2023.

MA, D. *et al*. Domino Condensation/S-Arylation/Heterocyclization Reactions: Copper-Catalyzed Three-Component Synthesis of 2-N-Substituted Benzothiazoles. **Angewandte Chemie**, v. 123, n. 5, p. 1150-1153, 2011.

MA, J.J. *et al*. Decarboxylative and Denitrative Trifluoromethylation for the Synthesis of Cvinyl CF3 Compounds with Togni (II) Reagent. **Advanced Synthesis & Catalysis**, v. 357, n. 16-17, p. 3447-3452, 2015.

MACKIEWICZ, N. *et al*. Tumor-Targeted Polydiacetylene Micelles for In Vivo Imaging and Drug Delivery. **Small**, v. 7, n. 19, p. 2786-2792, 2011.

MAKA, A. O.M; ALABID, J. M. Solar energy technology and its roles in sustainable development. **Clean Energy**, v. 6, n. 3, p. 476-483, 2022.

MARCINCAL-LEFEBVRE, A. *et al*. (Phenylthio) phenylamine derivatives as potential antiinflammatory compounds. **Journal of Medicinal Chemistry**, v. 24, n. 7, p. 889-893, 1981.

MARKEN, F.; ATOBE, M. **Modern Electrosynthetic Methods in Organic Chemistry**. 1st ed. CRC Press, 2018.

MARTÍNEZ-ABADÍA, M.; GIMÉNEZ, R.; ROS, M. Self-assembled α-cyanostilbenes for advanced functional materials. **Advanced Materials**, v. 30, n. 5, p. 1704161, 2018.

MARTINS, P.; ROMEIRO, G.; RIBEIRO, C. 4-thio derivatives of dibenzosuberone: potential antidepressant compounds. **Letters in Organic Chemistry**, v. 7, n. 5, p. 383-387, 2010.

MATSUMOTO, K. *et al*. Addition of ArSSAr to dienes via intramolecular C–C bond formation initiated by a catalytic amount of ArS+. **Chemical Communications**, n. 36, p. 5448-5450, 2009.

MATSUMOTO, K.; SUGA, S.; YOSHIDA, J. Organic reactions mediated by electrochemically generated ArS+. **Organic & biomolecular chemistry**, v. 9, n. 8, p. 2586-2596, 2011.

MAURELLI, A.M. *et al*. In depth study of the polydopamine coating of liposomes as a potential alternative to PEGylation for the stabilization of nanocarriers in biological fluids. **Materials Today Chemistry**, v. 37, p. 101994, 2024.

MAZZOTTA, S. *et al*. 3-Amino-alkylated indoles: Unexplored green products acting as anti-inflammatory agents. **Future Medicinal Chemistry**, v. 12, n. 1, p. 5-17, 2020.

MCKENZIE, E. C. R. *et al.* Versatile tools for understanding electrosynthetic mechanisms. **Chemical Reviews**, 2022, 122, 3292-3335.

MEYER, T. H. *et al.* Powering the future: how can electrochemistry make a difference in organic synthesis? **Chem**, 2020, 6, 2484-2496.

MIYATAKE, K. *et al*. All-Solid-State Rechargeable Air Batteries with Naphthoquinone-Based Negative Electrodes: Improved Performance and Cyclability. **Energy & Environmental Materials**, p. e12887, 2025.

MONKS, T. J. *et al.* Quinone chemistry and toxicity. **Toxicology and Applied Pharmacology**, 1992, v. 112, p. 2-16.

MULCHIN, B. J. *et al.* The anti-cancer, anti-inflammatory and tuberculostatic activities of a series of 6,7-substituted-5,8-quinolinequinones. **Bioorganic & Medicinal Chemistry**, 2010, 18, 3238-3251.

MULLER, K.; *et al.* Potential antipsoriatic agents: lapachol compounds as potent inhibitors of HaCaT cell growth. **Journal of Natural Products**, 1999, v. 62, p. 1134-1136.

MURAKAMI, K. *et al*. Effect of hydroxy substituent on the prooxidant action of naphthoquinone compounds. **Toxicology in Vitro**, 2010, v. 24, p. 905-909.

NAGAR, B.; DHAR, B. B. Photochemical C–H Arylation of Napthoquinones Using Eosin Y. **ACS omega**, v. 7, n. 36, p. 32615-32619, 2022.

NAGAR, B.; DHAR, B. B. Visible light-mediated thiolation of substituted 1, 4-naphthoquinones using eosin Y as a photoredox catalyst. **The Journal of Organic Chemistry**, v. 87, n. 5, p. 3195-3201, 2022.

NETO, J. L. F. *et al.* Caracterização físico-química do potencial agente antineoplásico β-lapachona. **Revista de Ciências Farmacêuticas Básica e Aplicada**, 2012, v. 33, p. 545-553.

NUROHMAH, B. A. *et al*. Photorelease Reaction of Alcohol from 1, 4-Naphthoquinone-Based Photodegradable Molecules. **ACS omega**, v. 10, n. 16, p. 16892-16899, 2025.

PARK, C. H. *et al*. A direct, multiplex biosensor platform for pathogen detection based on cross-linked polydiacetylene (PDA) supramolecules. **Advanced Functional Materials**, v. 19, n. 23, p. 3703-3710, 2009.

PERSICO, M.; Granucci, G. *Photochemistry. Theoretical Chemistry and Computational Modelling*. Springer International Publishing AG, part of Springer Nature 2018.

PINTO, A. V.; CASTRO, S. L. The trypanocidal activity of naphthoquinones: a review. **Molecules**, 2009, v. 14, p. 4570.

POLLOK, D.; WALDVOGEL, S. R. Electro-organic synthesis – a 21st century technique. **Chemical Science**, 2020, 11(46), 12386-12400.

PRADHAN, R. *et al.* From body art to anticancer activities: perspectives on medicinal properties of henna. **Current Drug Targets**, 2012, v. 13, p. 1777-1798.

PRAVIN, N. J. *et al*. Indoles as promising therapeutics: a review of recent drug discovery efforts. **Bioorganic Chemistry**, v. 154, p. 108092, 2025.

QADIR, M. I.; IQBAL, M. S.; KHAN, R. β-lapachone: A promising anticancer agent with a unique NQO1 specific apoptosis in pancreatic cancer. **Current Cancer Drug Targets**, v. 22, n. 7, p. 537-540, 2022.

QUINTAVALLA, A.; CARBONI, D.; LOMBARDO, M. Green Metrics and Sustainability in Photocatalysis. **ChemCatChem**, v. 16, n. 14, p. e202301225, 2024.

RAMOS-MILARÉ, Á. C. F. H. *et al.* The anti-Leishmania potential of bioactive compounds derived from naphthoquinones and their possible applications: a systematic review of animal studies. **Parasitology Research**, 2022, v. 121, p. 1247–1280.

RANI, R. *et al*. Natural naphthoquinones and their derivatives as potential drug molecules against trypanosome parasites. **Chemical Biology & Drug Design**, 2022, v. 100, p. 786–817.

REDDY, V. P. *et al*. Indium-catalyzed C− S cross-coupling of aryl halides with thiols. **The Journal of organic chemistry**, v. 74, n. 8, p. 3189-3191, 2009.

ROHATGI-MUKHERJEE, K. K. **Fundamentals of photochemistry**. New Age International, 1978.

ROSS, D.; SIEGEL, D. The diverse functionality of NQO1 and its roles in redox control. **Redox Biology**, v. 41, p. 101950, 2021.

SAHU, P. K. *et al.* Design and development of nanostructured photocatalysts for large-scale solar green hydrogen generation. **Sustainable Energy & Fuels**, v. 8, n. 9, p. 1872-1917, 2024.

SALEH, E. A. M. *et al*. Recent advances in catalytic approaches for the synthesis of 3-substituted indoles: mechanisms and strategies. **RSC advances**, v. 15, n. 16, p. 12255-12290, 2025.

SAYMUNG, R.; TRAIPHOL, N.; TRAIPHOL, R. Promoting self-assembly and synthesis of color-responsive polydiacetylenes using mixed water-organic solvents: Effects of solvent composition, structure, and incubation temperature. **Colloids and Surfaces A: Physicochemical and Engineering Aspects**, v. 626, p. 127046, 2021.

SCHEIDE, M. R. *et al.* Electrohalogenation of organic compounds. **Organic & Biomolecular Chemistry**, 2021, 19, 2578.

SCHENCK, G. O. Light sources and light filters in preparative organic photochemistry. In: **Preparative Organic Photochemistry**. Berlin, Heidelberg: Springer Berlin Heidelberg, 1968. p. 472-494.

SEEBER, F. Light sources and laser safety. **Fundamentals of photonics**, v. 1, n. 2, p. 3, 2007.

SHANKAR, R. *et al*. A practical review on photooxidation of crude oil: Laboratory lamp setup and factors affecting it. **Water Research**, v. 68, p. 304-315, 2015.

SHEN, T.; WANG, X.; LOU, H. Natural stilbenes: an overview. **Natural product reports**, v. 26, n. 7, p. 916-935, 2009.

SHONO, T. Electroorganic chemistry in organic synthesis. **Tetrahedron**, 1984, 40, 811-850.

SIES, H. Oxidative stress: a concept in redox biology and medicine. **Redox Biology**, 2015, v. 4, p. 180- 183.

SIES, H.; JONES, D. P. Reactive oxygen species (ROS) as pleiotropic physiological signalling agents. **Nature Reviews Molecular Cell Biology**, 2020, v. 21, n. 7, p. 363-383.

SILVA JÚNIOR, E. N. *et al*. Naphthoquinoidal [1,2,3]-triazole, a new structural moiety active against Trypanosoma cruzi. **European Journal of Medicinal Chemistry**, 2008, v. 43, n. 8, p. 1774–1780.

SILVA JÚNIOR, E. N. *et al.* Synthesis of quinones with highlighted biological applications: a critical update on the strategies towards bioactive compounds with emphasis on lapachones**.** **European Journal of Medicinal Chemistry,** 2019, v. 179, p. 863-915.

SILVA, M. N.; FERREIRA, V. F.; SOUZA, M. C. B. V. Um panorama atual da química e da farmacologia de naftoquinonas, com ênfase na beta-lapachona e derivados. **Química Nova**, 2003, v. 26, n. 3, p. 407-416.

SINHA, A. K. *et al*. An Overview on Indole Aryl Sulfide/Sulfone (IAS) as Anti-HIV Non-Nucleoside Reverse Transcriptase Inhibitors (NNRTIs). **Asian Journal of Organic Chemistry**, v. 11, n. 4, p. e202100744, 2022.

SKUBI, K. L.; BLUM, T. R.; YOON, T. P. Dual catalysis strategies in photochemical synthesis. **Chemical reviews**, v. 116, n. 17, p. 10035-10074, 2016.

SODERQUIST, C. J. Juglone and allelopathy. **Journal of Chemical Education**, 1973, v. 50, p. 782.

SOUSA, E. T.; *et al*. Fontes, formação, reatividade e determinação de quinonas na atmosfera. **Química Nova**, 2016, v. 39, p. 486–495

STAGLIANO, K. W. *et al.* Regiocontrolled synthesis and HIV inhibitory activity of unsymmetrical binaphthoquinone and trimeric naphthoquinone derivatives of conocurvone. **Bioorganic & Medicinal Chemistry**, 2006, v. 14, n. 16, p. 5651–5665.

STRIETH-KALTHOFF, F.; GLORIUS, F. Triplet energy transfer photocatalysis: unlocking the next level. **Chem**, v. 6, n. 8, p. 1888-1903, 2020.

SWAMINAATHAN, P. *et al*. Recent advances in photocatalytic degradation of persistent organic pollutants: Mechanisms, challenges, and modification strategies. **Sustainable Chemistry for the Environment**, p. 100171, 2024.

TALHI, O.*et al.* Bis (4-hydroxy-2H-chromen-2-one): Synthesis and effects on leukemic cell lines proliferation and NF-κB regulation. **Bioorganic & Medicinal Chemistry**, v. 22, n. 11, p. 3008-3015, 2014.

TANAKA, N. Solvent effects on mechanisms and characteristics of electrode reactions. **Electrochimica Acta**, 1976, 21, 701-710.

TEVEROVSKIY, G.; SURRY, D. S.; BUCHWALD, S. L. Pd-Catalyzed Synthesis of Ar SCF3 Compounds under Mild Conditions. **Angewandte Chemie International Edition**, v. 50, n. 32, p. 7312-7314, 2011.

TRÄGER, F. (Ed.). **Springer handbook of lasers and optics**. Springer Science & Business Media, 2012.

VALENÇA, W. O. *et al.* Synthesis of quinone-based N-sulfonyl-1,2,3-triazoles: chemical reactivity of Rh(II) azavinyl carbenes and antitumor activity. **ChemistrySelect**, 2017, 2(16), 4301-4308.

VELASCO-RUBIO, Á. *et al*. C–C bond formation via photocatalytic direct functionalization of simple alkanes. **Chemical Communications**, v. 59, n. 62, p. 9424-9444, 2023.

VIEIRA, A. A. *et al.* Hybrid compounds with two redox centres: modular synthesis of chalcogen-containing lapachones and studies on their antitumor activity. **European Journal of Medicinal Chemistry**, 2015, 101, 254-265.

VILLARÓN, D.; WEZENBERG, S. J. Stiff-stilbene photoswitches: from fundamental studies to emergent applications. **Angewandte Chemie**, v. 132, n. 32, p. 13292-13302, 2020.

VYSKOČIL, V.; BAREK, J. Mercury electrodes – possibilities and limitations in environmental electroanalysis. **Critical Reviews in Analytical Chemistry**, 2009, 39, 173-188.

WALDVOGEL, S. R. *et al.* Electrochemical arylation reaction. **Chemical Reviews**, 2018, 118(14), 6706-6765.

WEAVER, M. G.; PETTUS, T. R. R. Synthesis of para- and ortho-quinones. 2014, ed. 2, v. 7, p. 373–410.

WEERASINGHE, M.A. *et al*. Polymers and light: a love–hate relationship. **Chemical Science**, v. 16, n. 13, p. 5326-5352, 2025.

WELD, J. T.; GUNTHER, A. The antibacterial properties of sulfur. **The Journal of Experimental Medicine**, 1947, 85(5), 531-542.

WONG, Y.; JAYANTH, T. T.; CHENG, C. Cobalt-catalyzed aryl− sulfur bond formation. **Organic letters**, v. 8, n. 24, p. 5613-5616, 2006.

XIANG, S. *et al.* Exploiting the Anticancer, Antimicrobial and Antiviral Potential of Naphthoquinone Derivatives: Recent Advances and Future Prospects. **Pharmaceuticals**, v. 18, n. 3, p. 350, 2025.

YAASHIKAA, P. R. *et al*. A review on photochemical, biochemical and electrochemical transformation of CO2 into value-added products. **Journal of CO2 Utilization**, v. 33, p. 131-147, 2019.

YAJIMA, T.; IKEGAMI, M. Metal-Free Visible-Light Radical Iodoperfluoroalkylation of Terminal Alkenes and Alkynes. **European Journal of Organic Chemistry**, v. 2017, n. 15, p. 2126-2129, 2017.

YOSHIDA, J.; PATUREAU, F. W. **Organic Redox Chemistry**. Wiley-VCH, 2021.

YUAN, Y.; LEI, A. Is electrosynthesis always green and advantageous compared to traditional methods? **Nature Communications**, 2020, 11, 802.

ZHANG, N. *et al*. Synthesis of stilbene derivatives via visible-light-induced cross-coupling of aryl diazonium salts with nitroalkenes using–NO_2 as a leaving group. **Chemical Communications**, v. 52, n. 99, p. 14234-14237, 2016.

ZHU, C. *et al.* Organic electrochemistry: molecular syntheses with potential. **ACS Central Science**, 2021, 7(3), 415-431

APPENDICES A - Characterization of the compounds

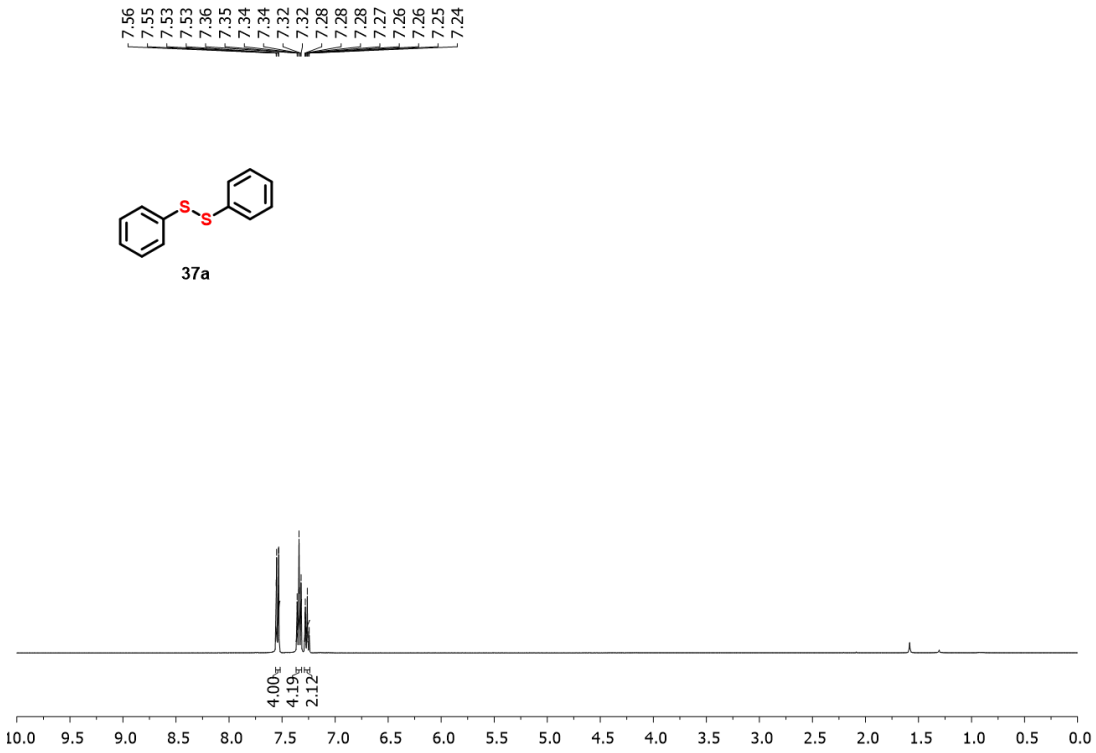

Figure A1: ^{1}H NMR spectrum of compound **37a** (400 MHz, $CDCl_3$).

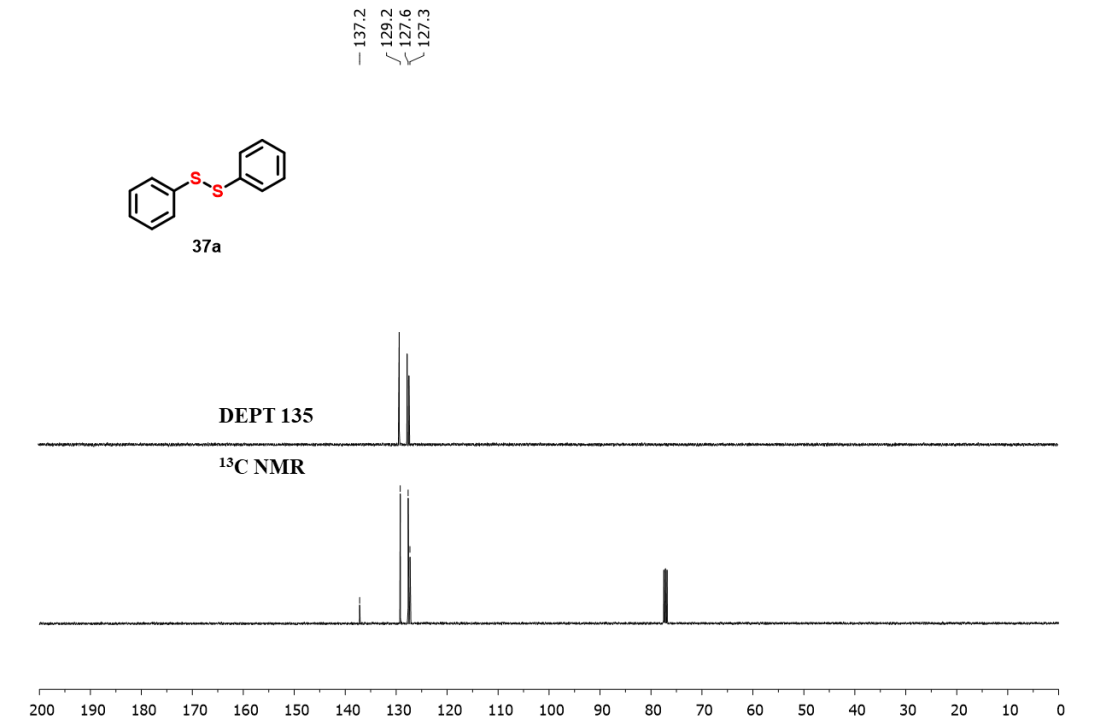

Figure A2: ^{13}C NMR and DEPT 135 spectrum of compound **37a** (101 MHz, $CDCl_3$).

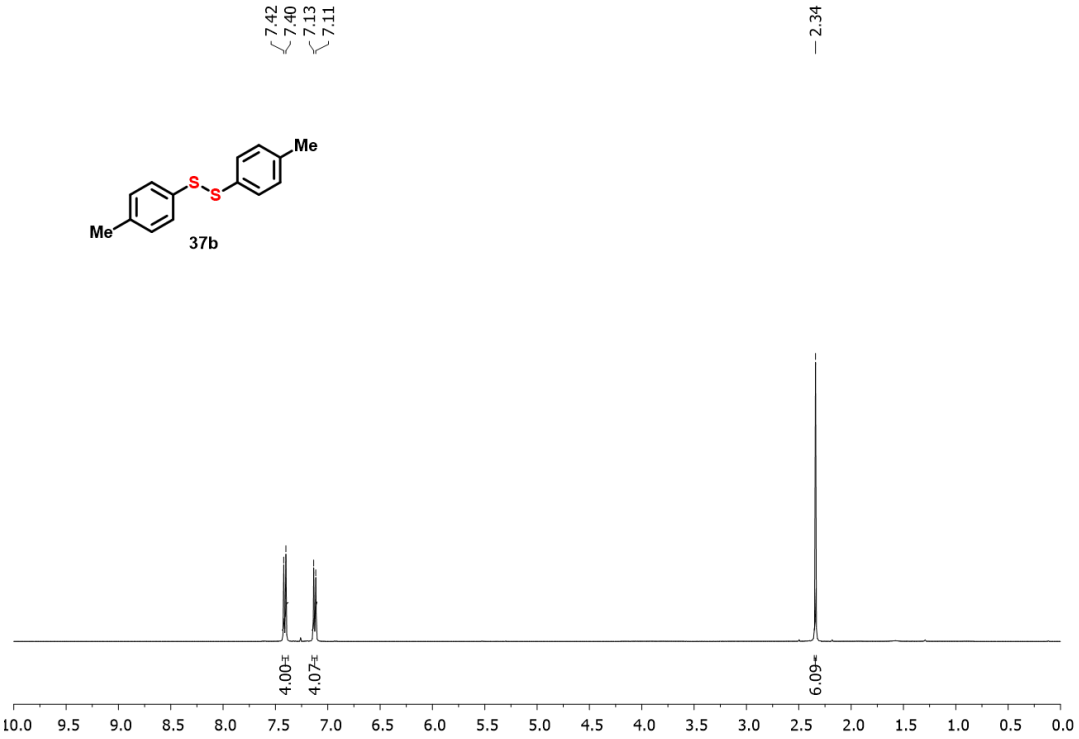

Figure A3: ^{1}H NMR spectrum of compound **37b** (400 MHz, $CDCl_3$).

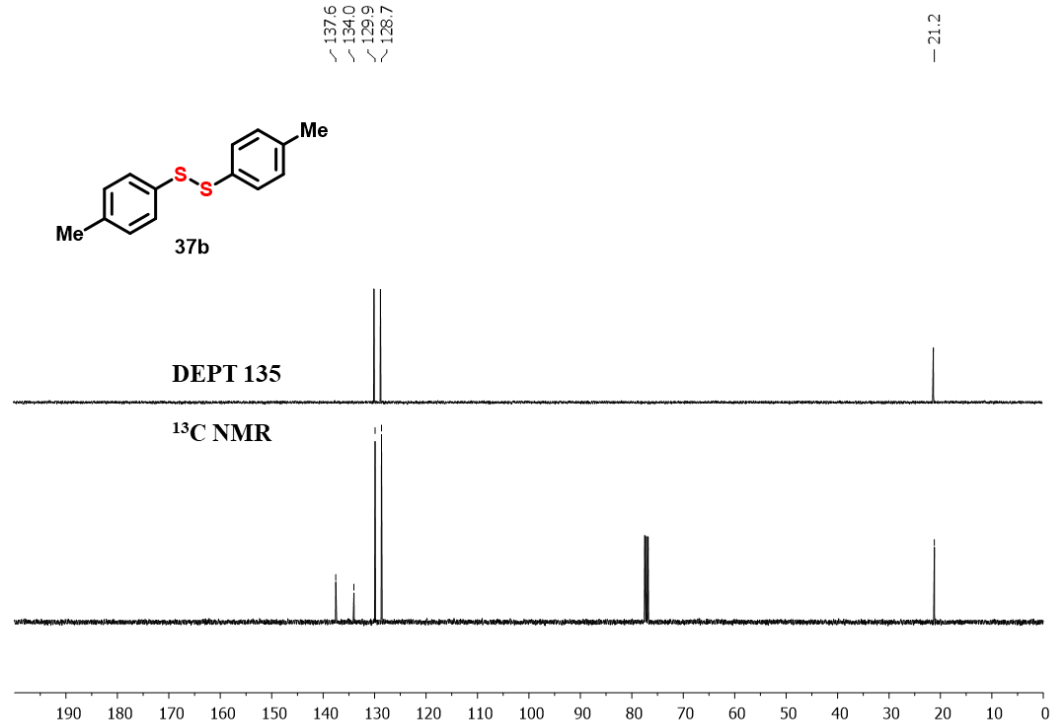

Figure A4: ^{13}C NMR and DEPT 135 spectrum of compound **37b** (101 MHz, $CDCl_3$).

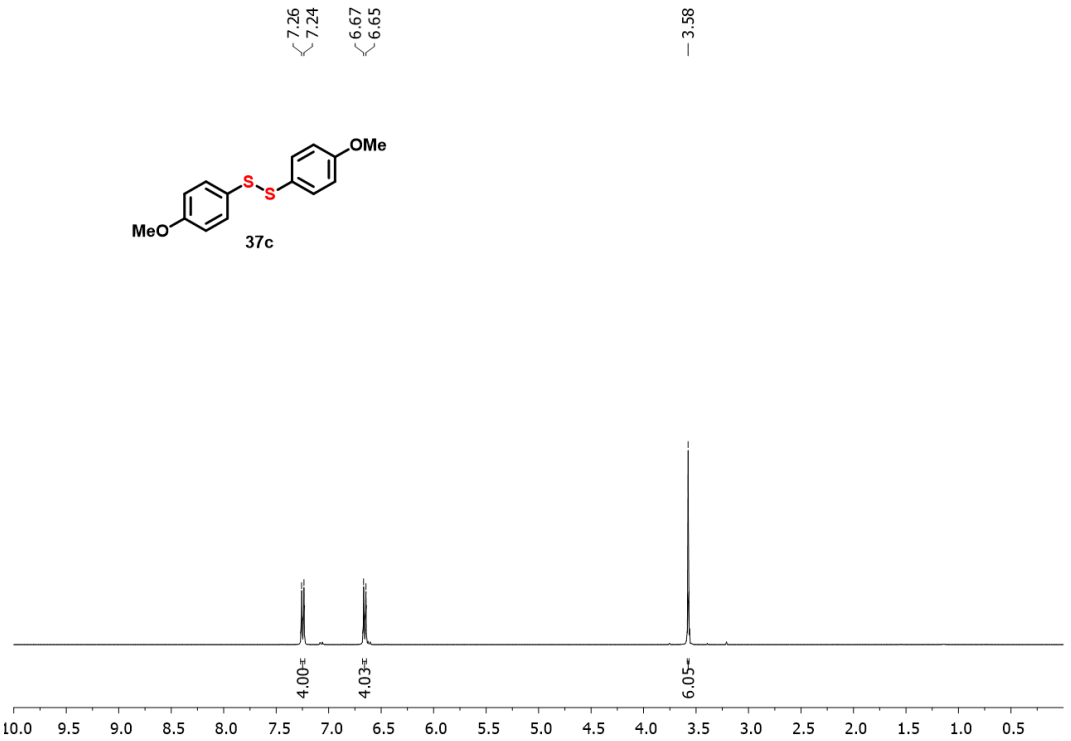

Figure A5: ^{1}H NMR spectrum of compound **37c** (400 MHz, $CDCl_3$).

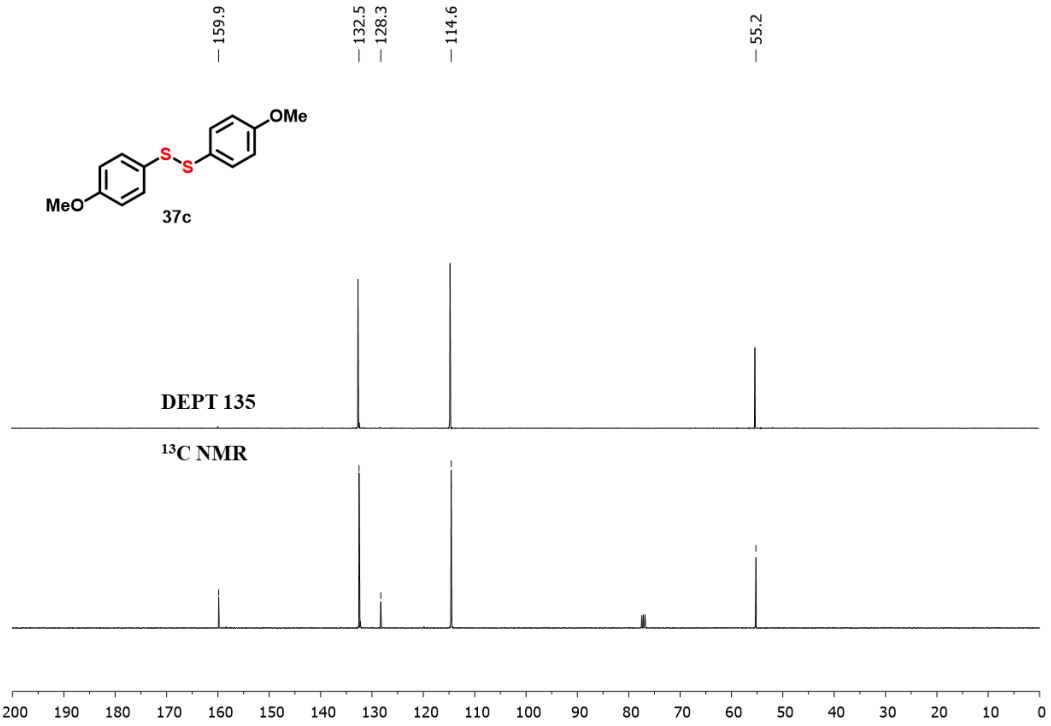

Figure A6: ^{13}C NMR and DEPT 135 spectrum of compound **37c** (101 MHz, $CDCl_3$).

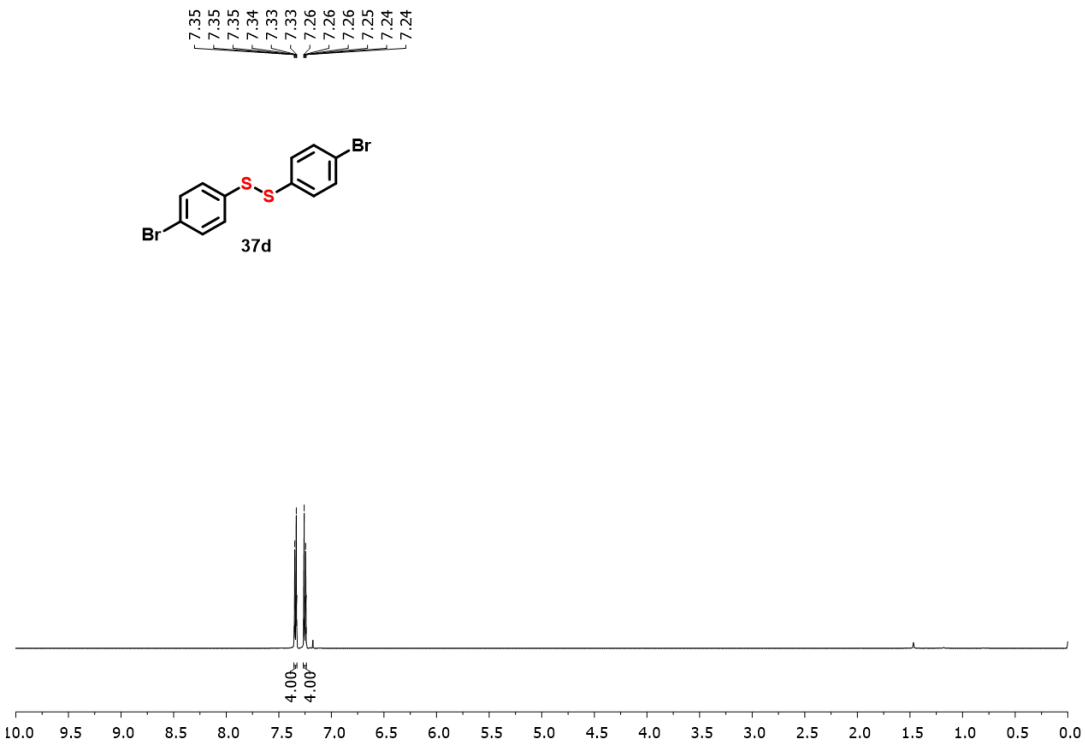

Figure A7: ^{1}H NMR spectrum of compound **37d** (400 MHz, $CDCl_3$).

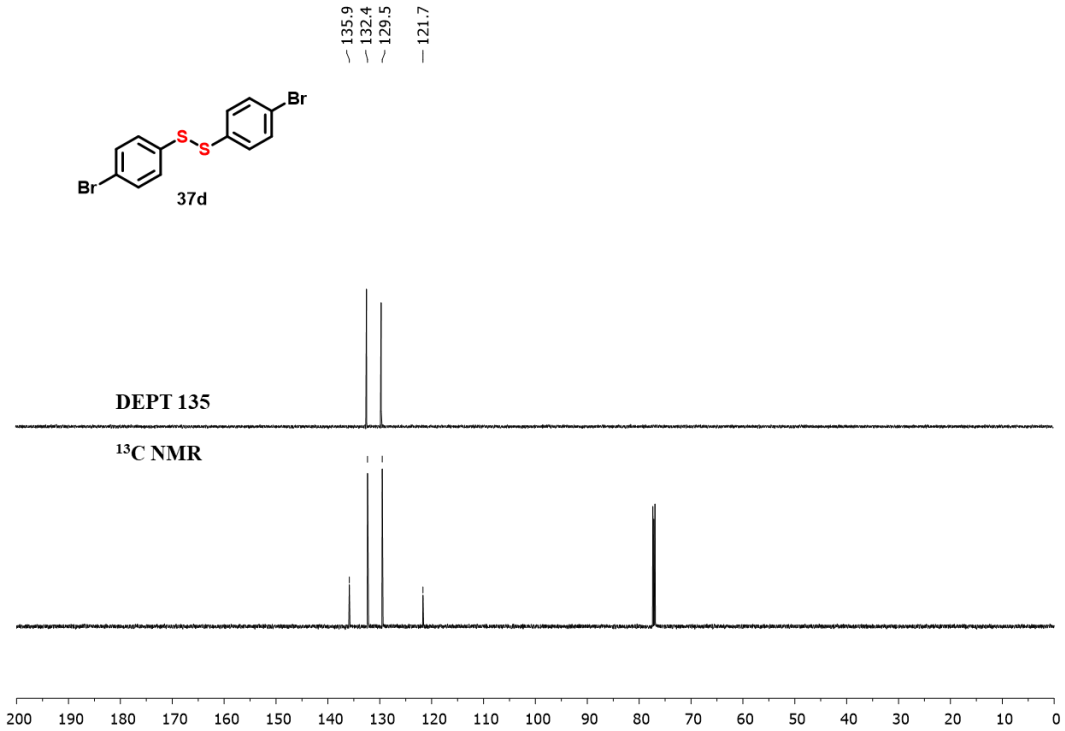

Figure A8: ^{13}C NMR and DEPT 135 spectrum of compound **37d** (101 MHz, $CDCl_3$).

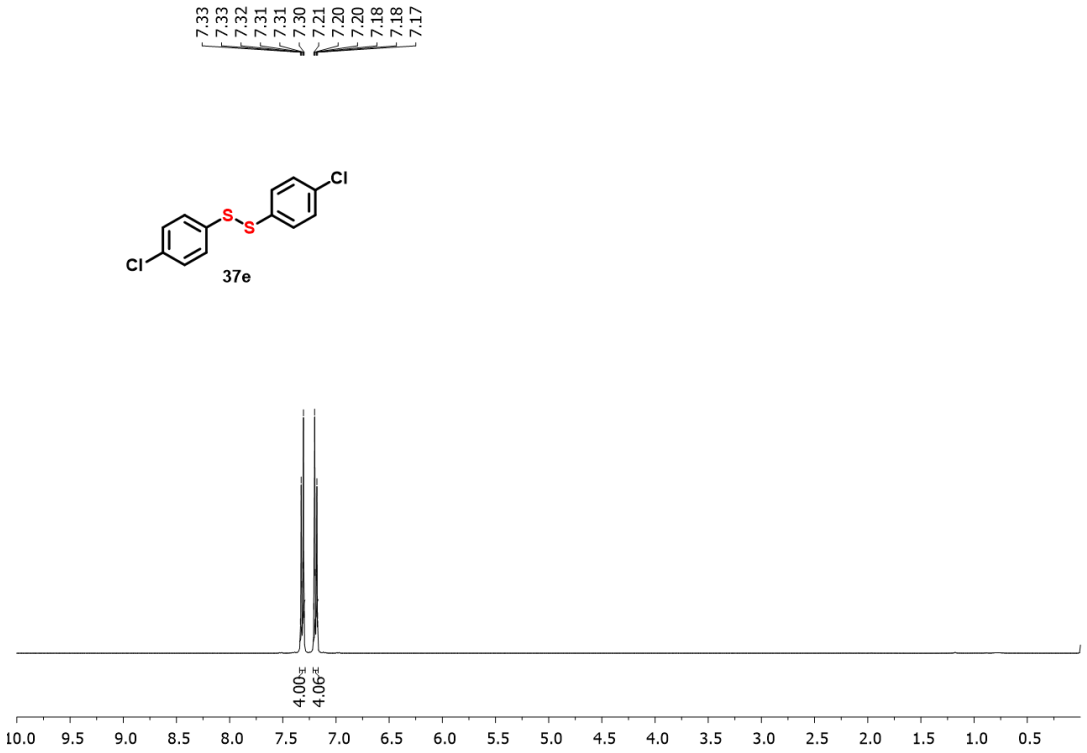

Figure A9: ^{1}H NMR spectrum of compound **37e** (400 MHz, $CDCl_3$).

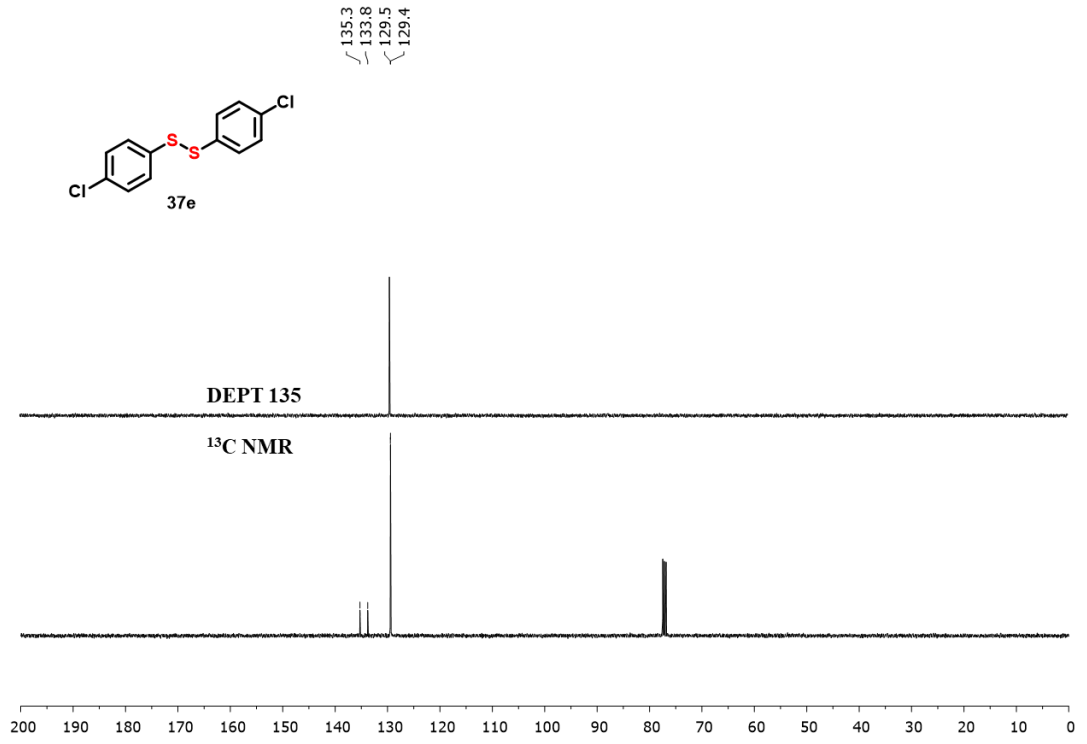

Figure A10: ^{13}C NMR and DEPT 135 spectrum of compound **37e** (101 MHz, $CDCl_3$).

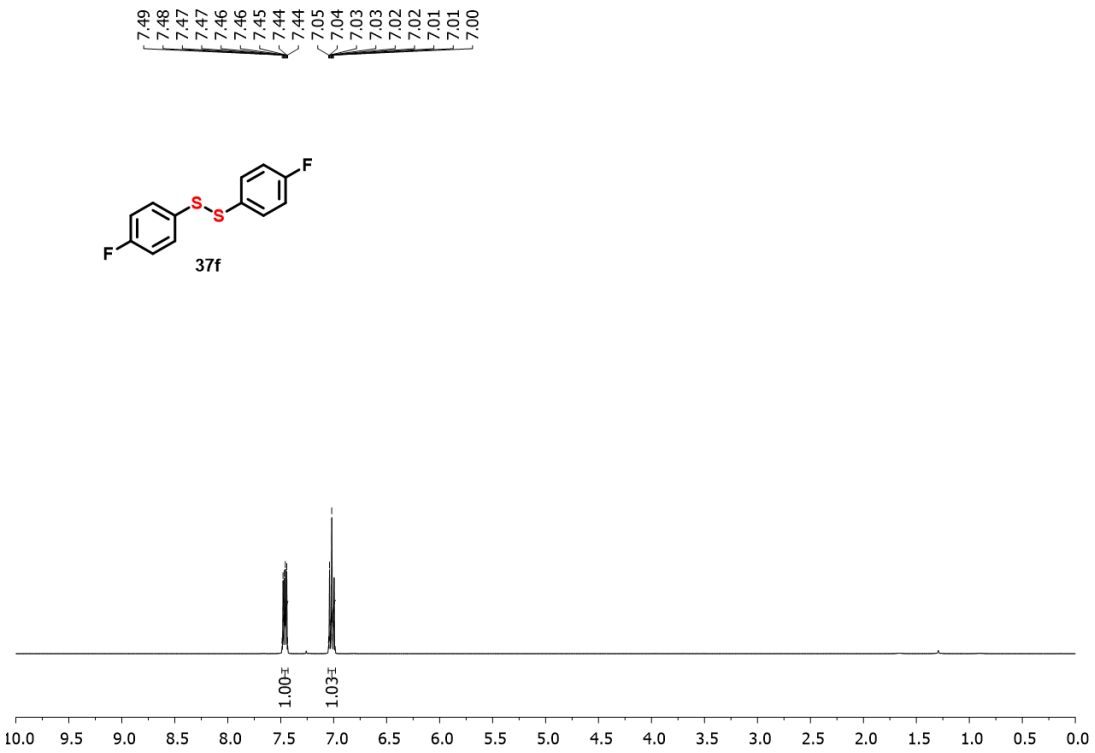

Figure A11: ^{1}H NMR spectrum of compound **37f** (400 MHz, $CDCl_3$).

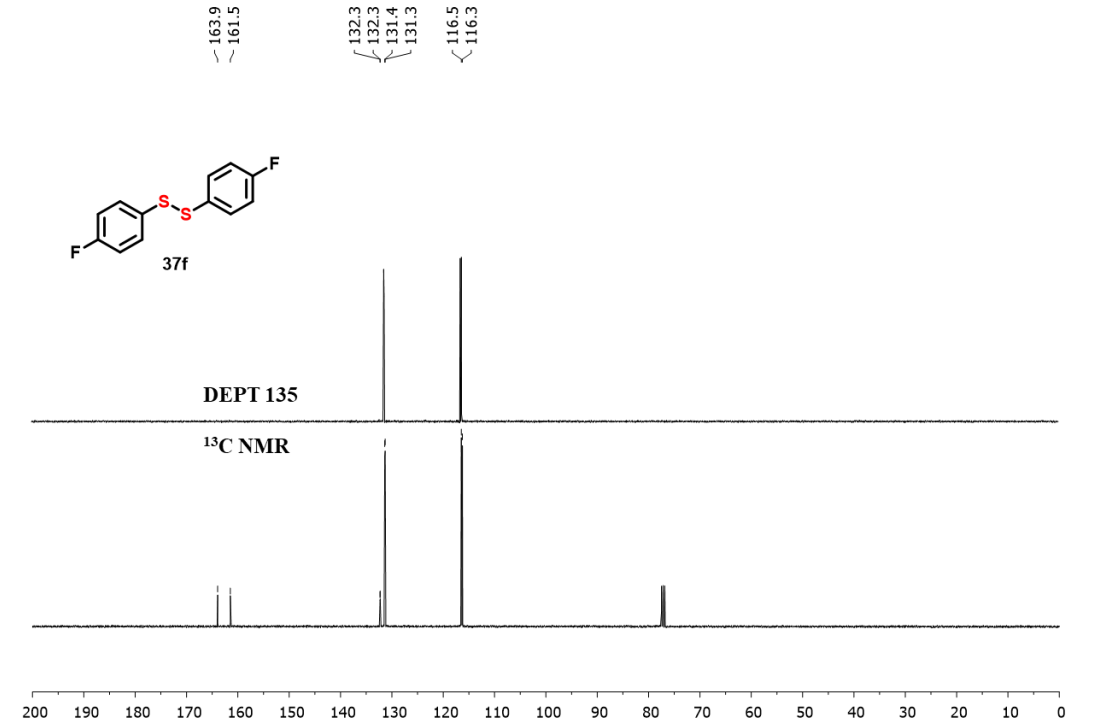

Figure A12: ^{13}C NMR and DEPT 135 spectrum of compound **37f** (101 MHz, $CDCl_3$).

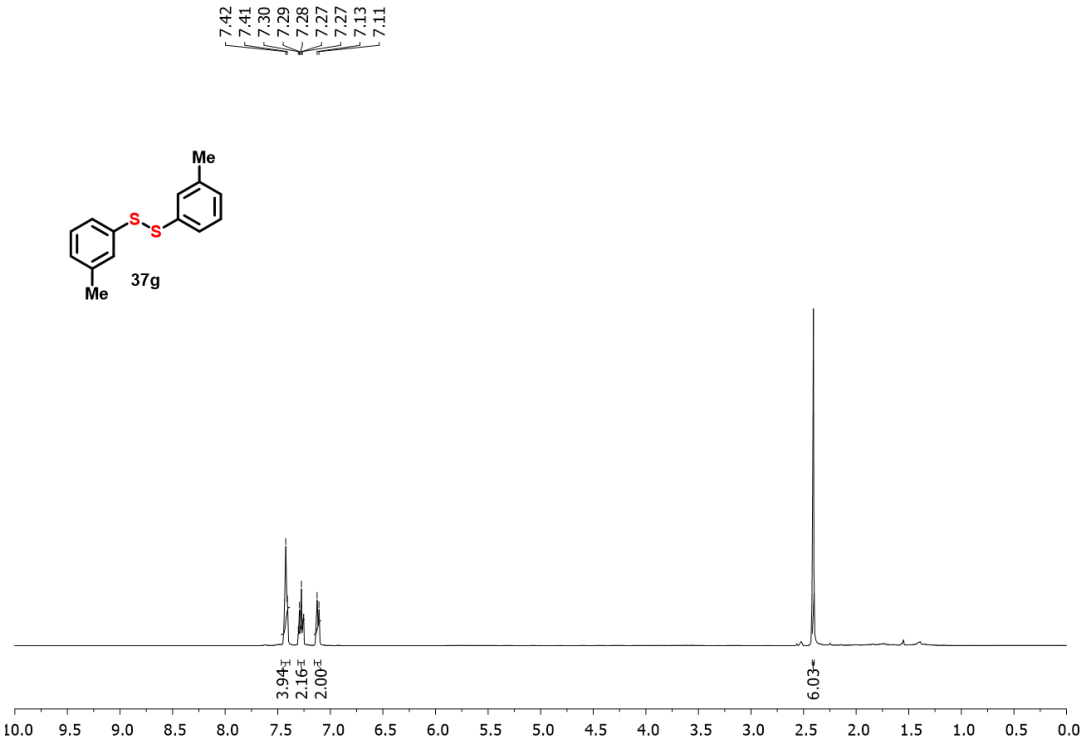

Figure A13: ^{1}H NMR spectrum of compound **37g** (400 MHz, $CDCl_3$).

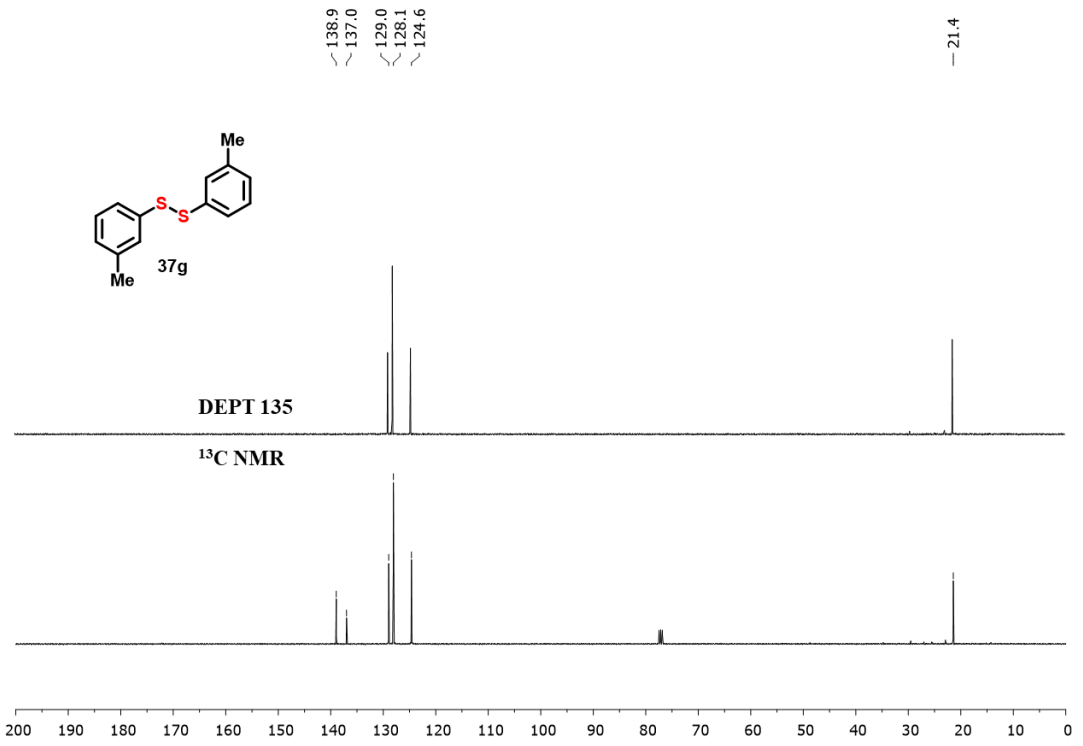

Figure A14: ^{13}C NMR and DEPT 135 spectrum of compound **37g** (101 MHz, $CDCl_3$).

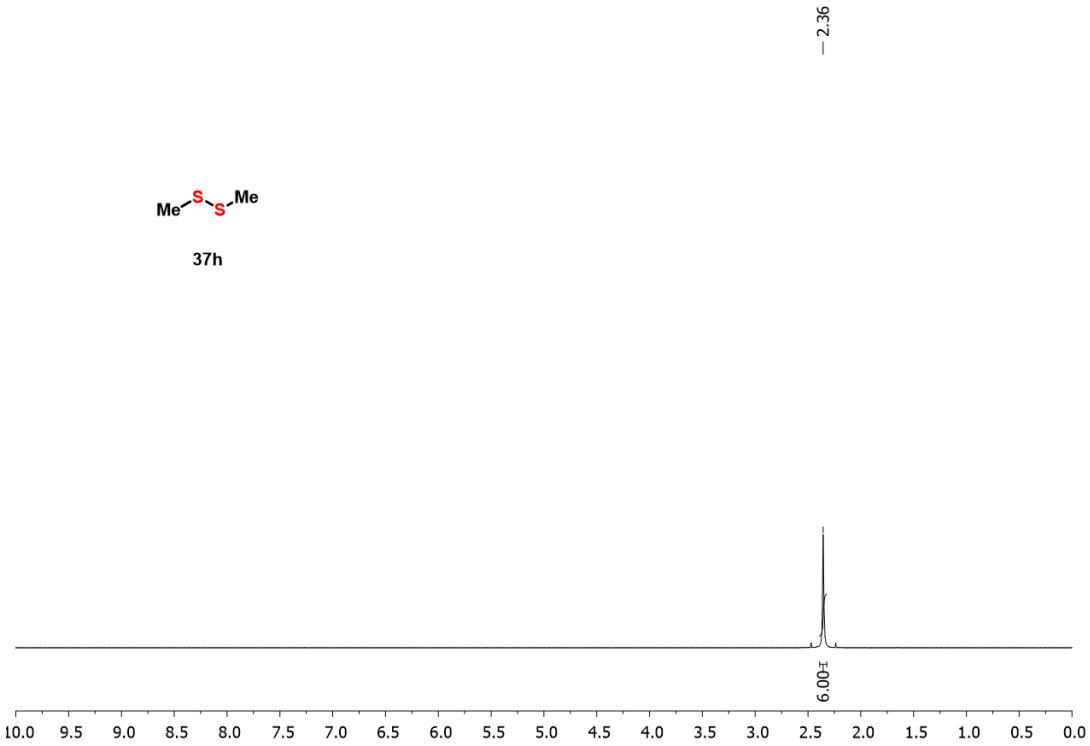

Figure A15: ^{1}H NMR spectrum of compound **37h** (400 MHz, $CDCl_3$).

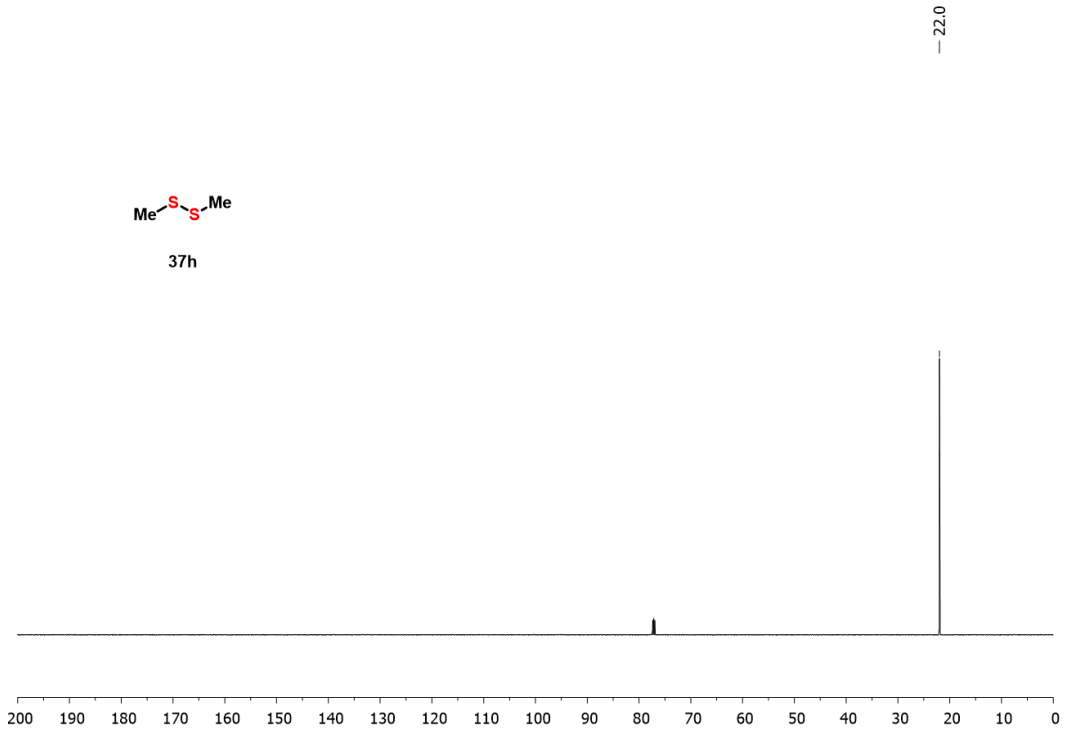

Figure A16: ^{13}C NMR spectrum of compound **37h** (101 MHz, $CDCl_3$).

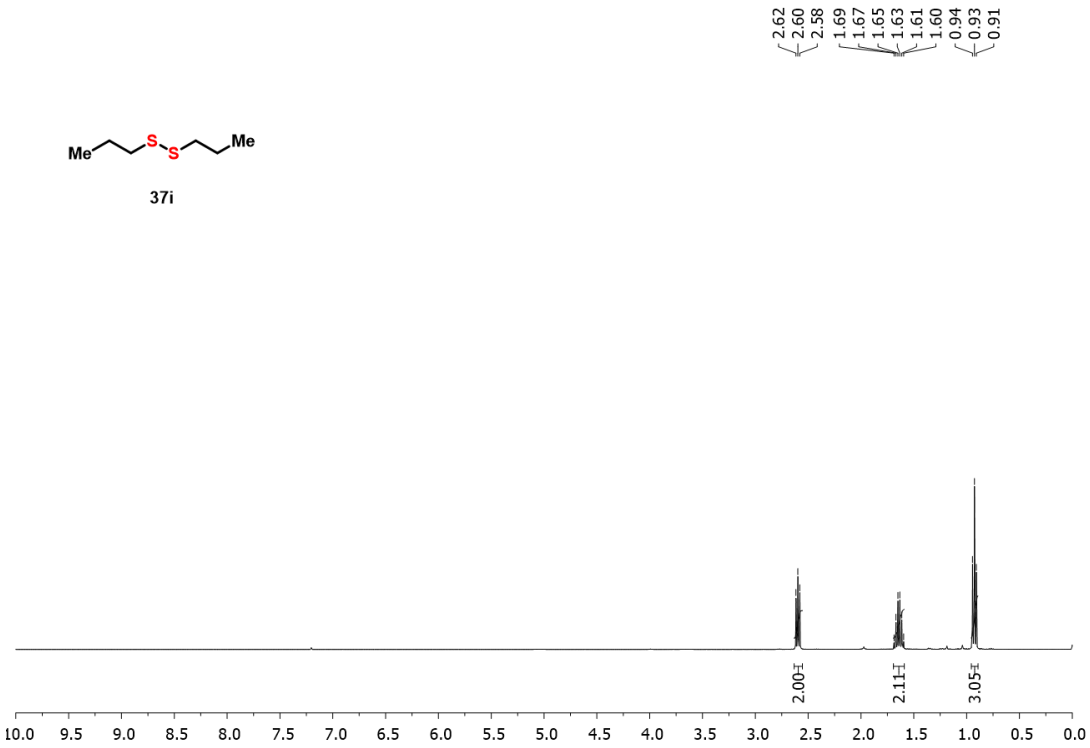

Figure A17: ^{1}H NMR spectrum of compound **37i** (400 MHz, $CDCl_3$).

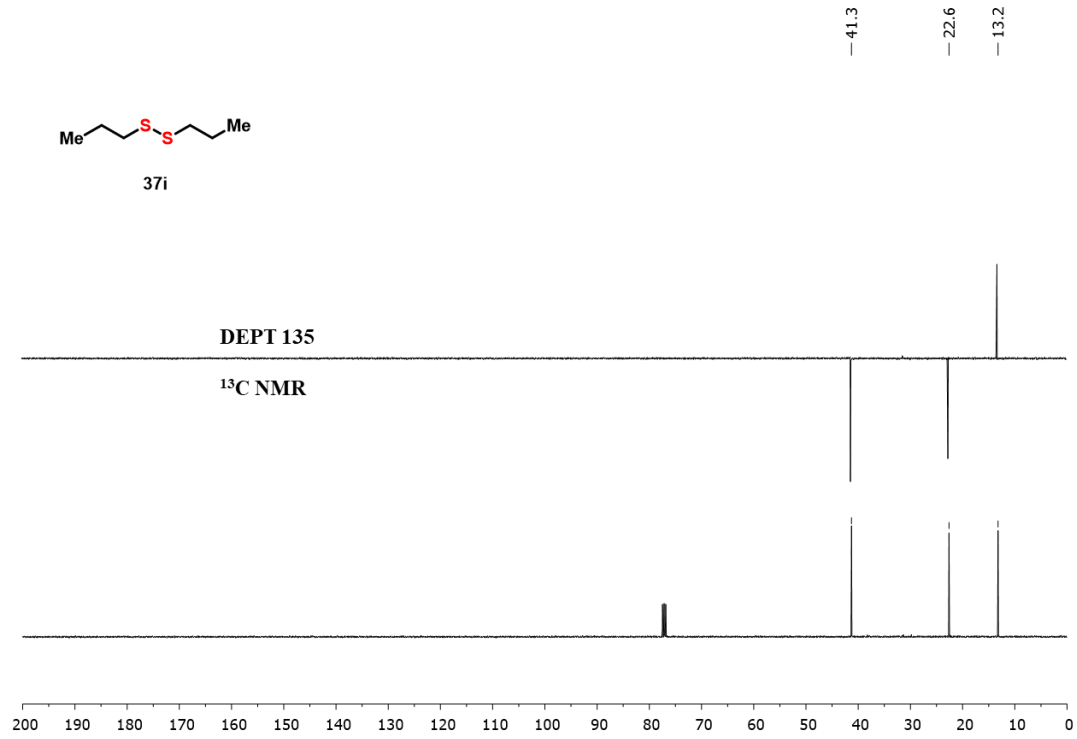

Figure A18: ^{13}C NMR and DEPT 135 spectrum of compound **37i** (101 MHz, $CDCl_3$).

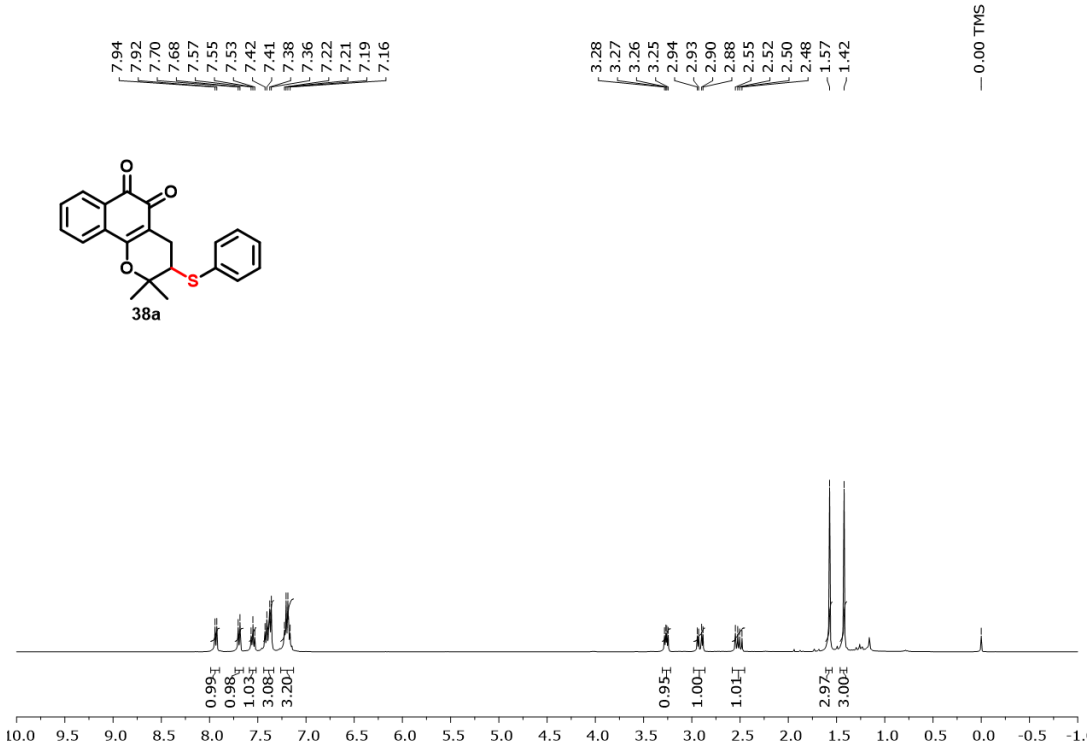

Figure A19: ^{1}H NMR spectrum of compound **38a** (400 MHz, $CDCl_3$).

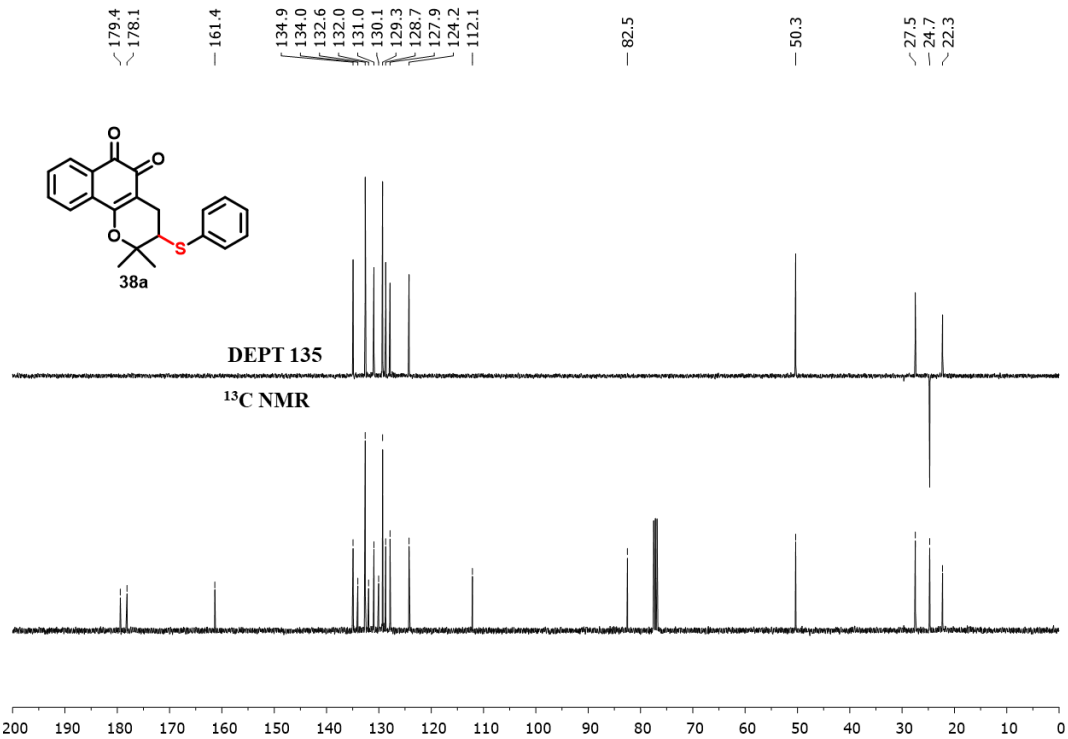

Figure A20: ^{13}C NMR and DEPT 135 spectrum of compound **38a** (101 MHz, $CDCl_3$).

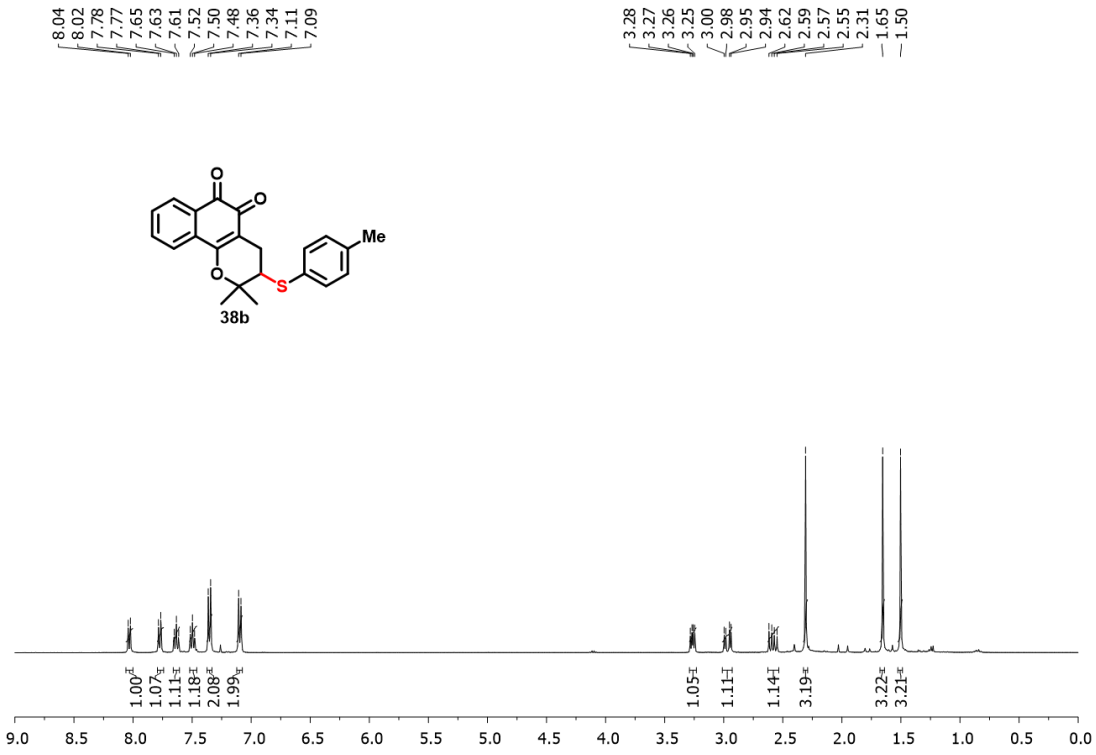

Figure A21: ^{1}H NMR spectrum of compound **38b** (400 MHz, $CDCl_3$).

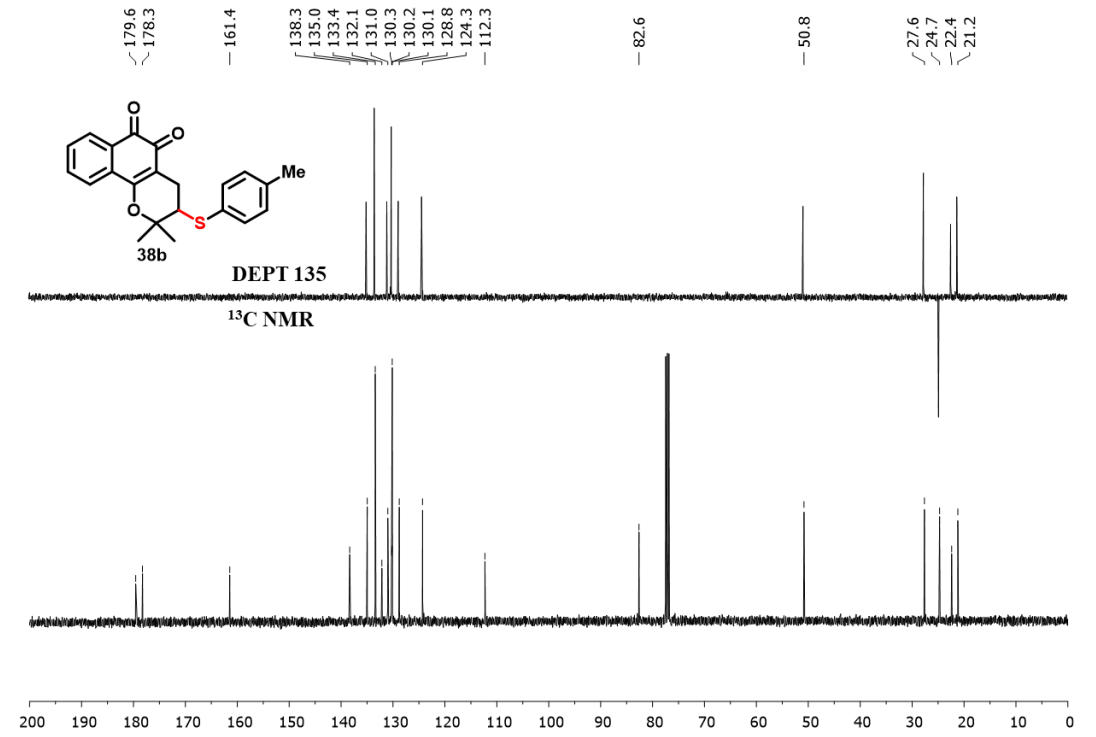

Figure A22: ^{13}C NMR and DEPT 135 spectrum of compound **38b** (101 MHz, $CDCl_3$).

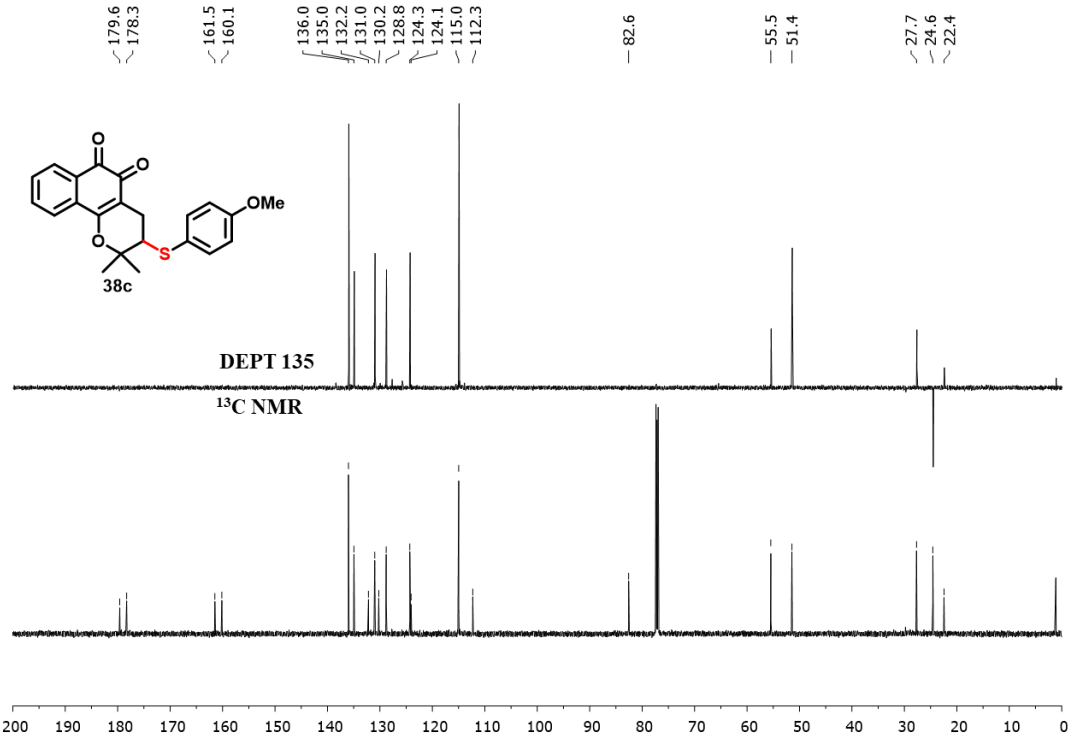

Figure A23: ^{1}H NMR spectrum of compound **38c** (400 MHz, $CDCl_3$).

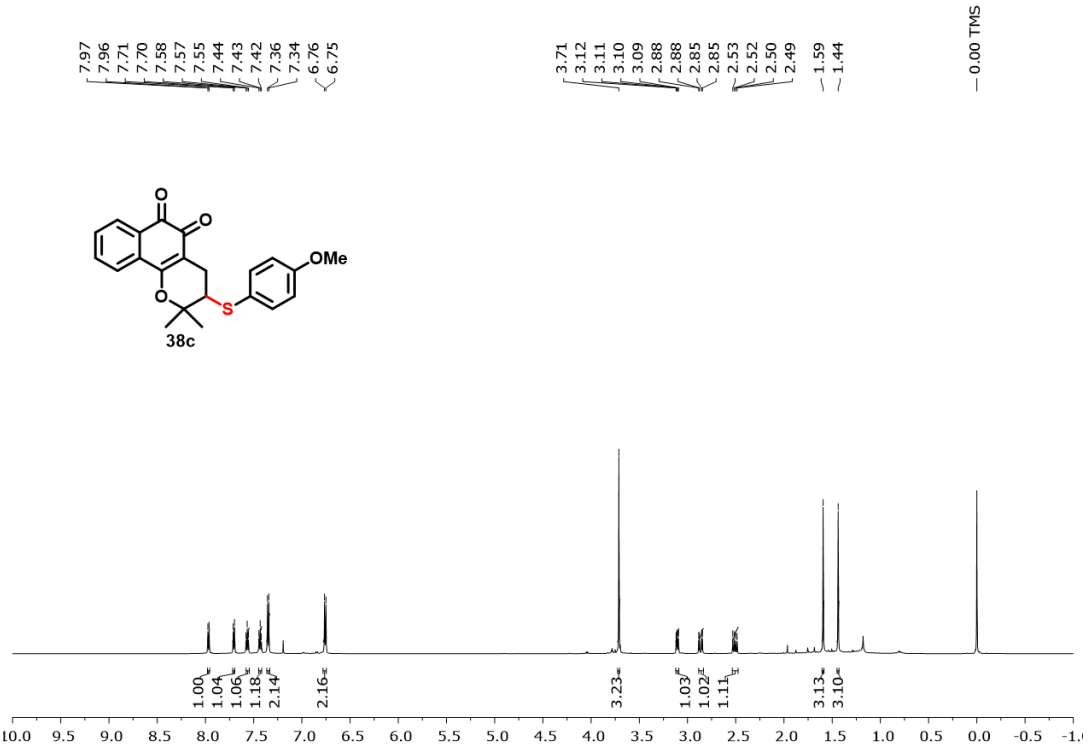

Figure A24: ^{13}C NMR and DEPT 135 spectrum of compound **38c** (101 MHz, $CDCl_3$).

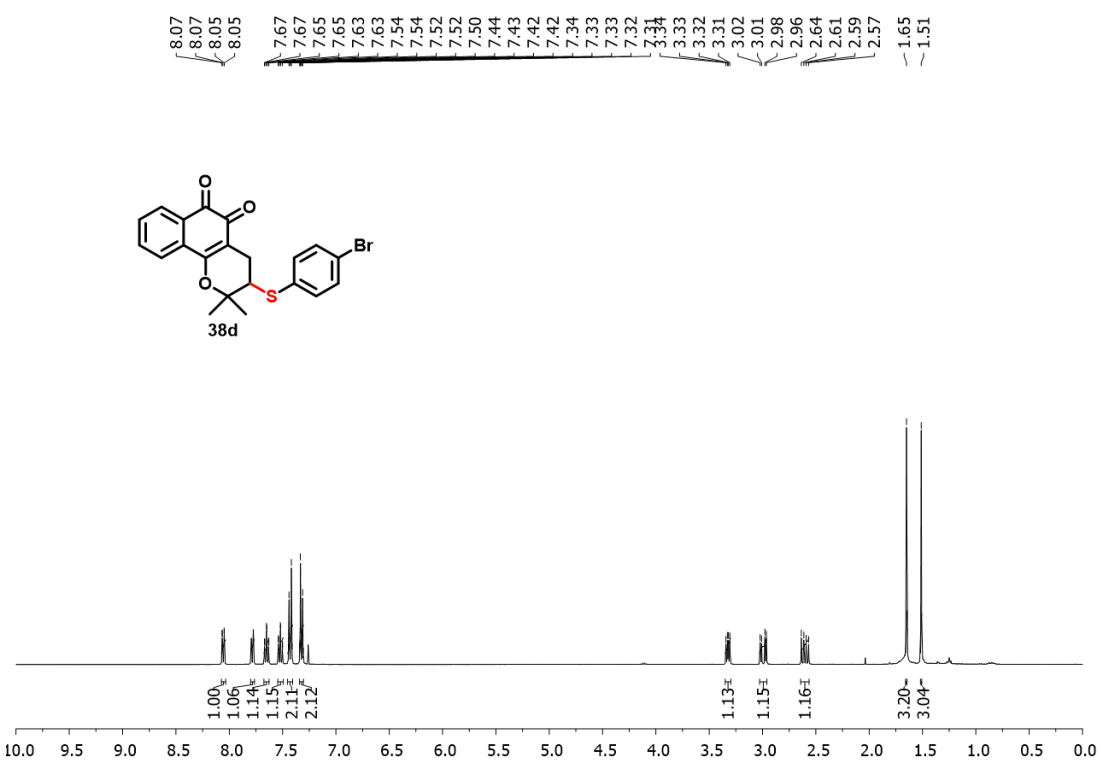

Figure A25: ^{1}H NMR spectrum of compound **38d** (400 MHz, $CDCl_3$).

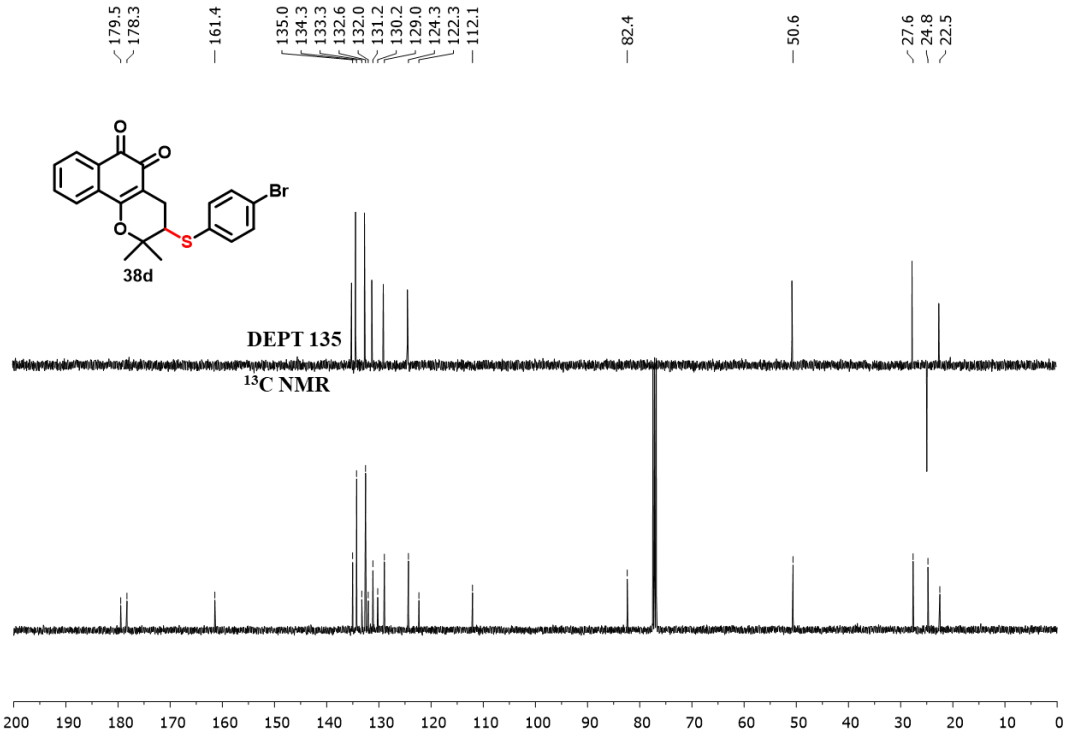

Figure A26: ^{13}C NMR and DEPT 135 spectrum of compound **38d** (101 MHz, $CDCl_3$).

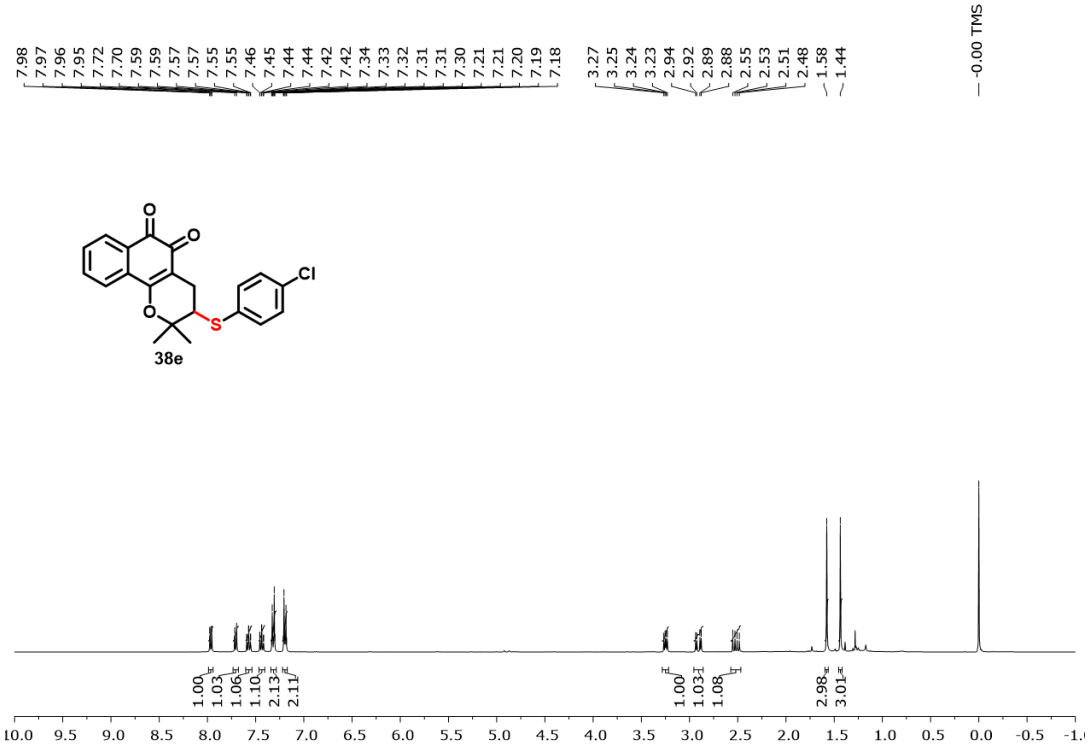

Figure A27: ^{1}H NMR spectrum of compound **38e** (400 MHz, $CDCl_3$).

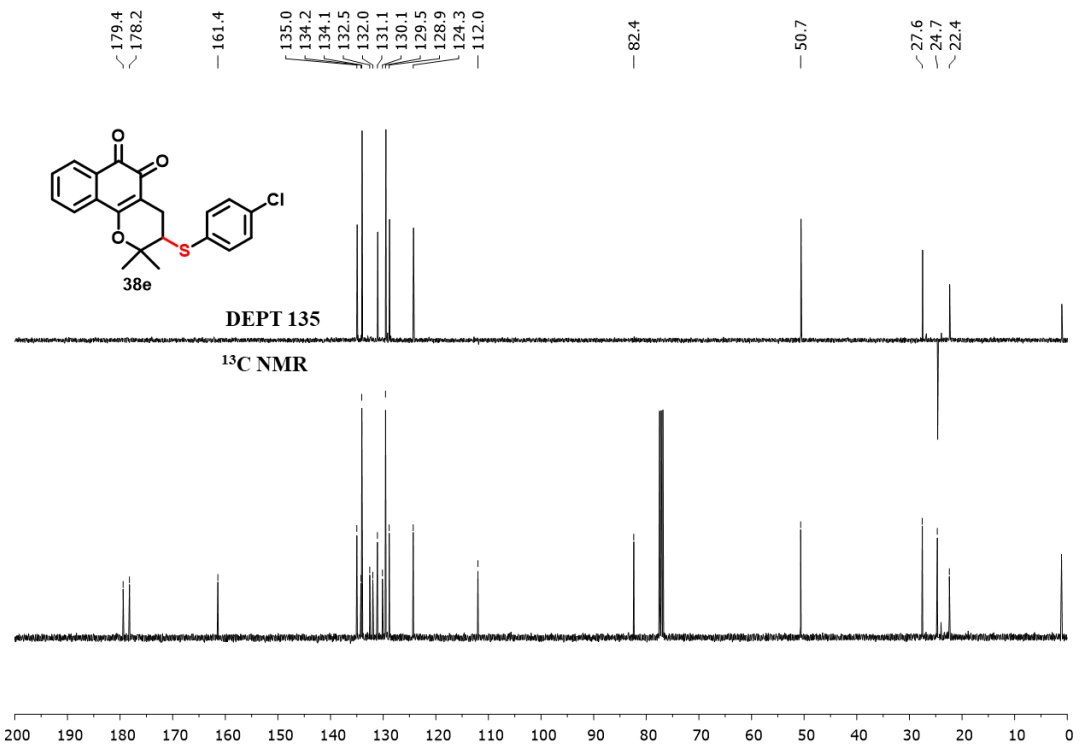

Figure A28: ^{13}C NMR and DEPT 135 spectrum of compound **38e** (101 MHz, $CDCl_3$).

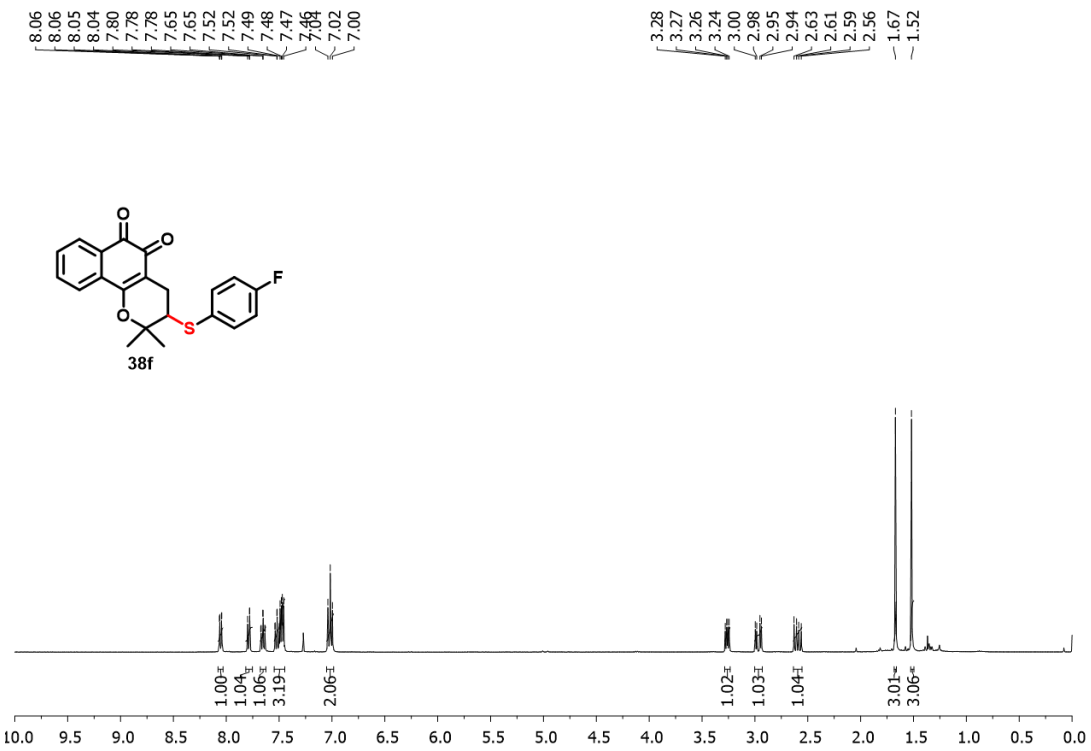

Figure A29: ^{1}H NMR spectrum of compound **38f** (400 MHz, $CDCl_3$).

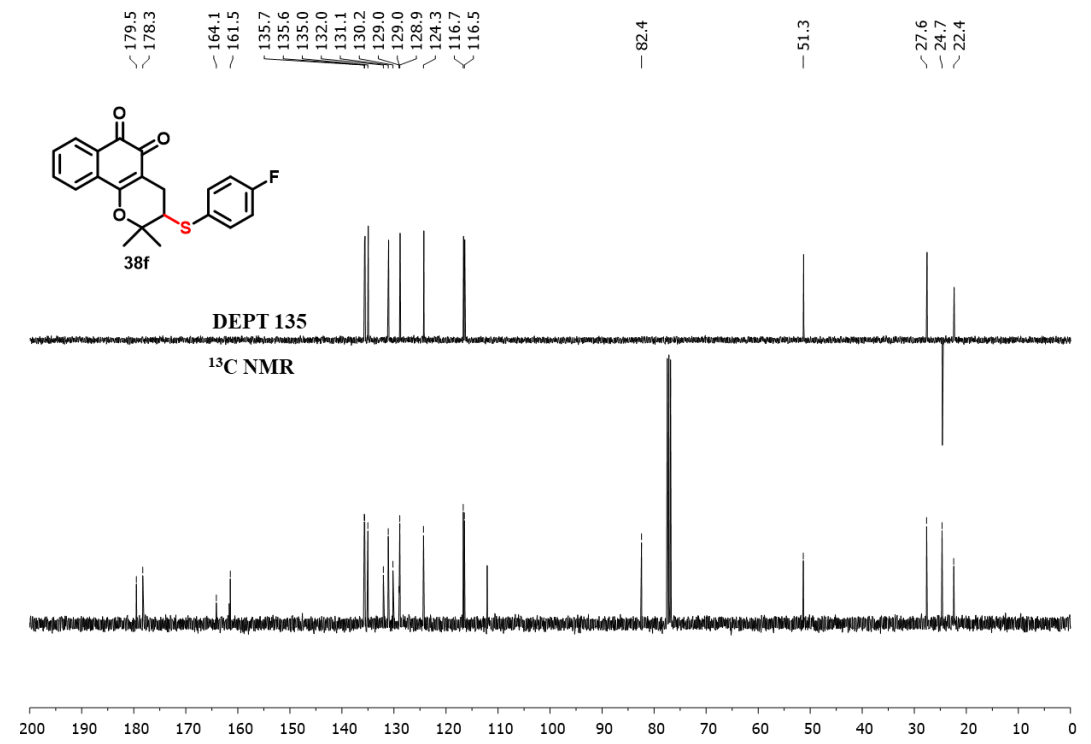

Figure A30: ^{13}C NMR and DEPT 135 spectrum of compound **38f** (101 MHz, $CDCl_3$).

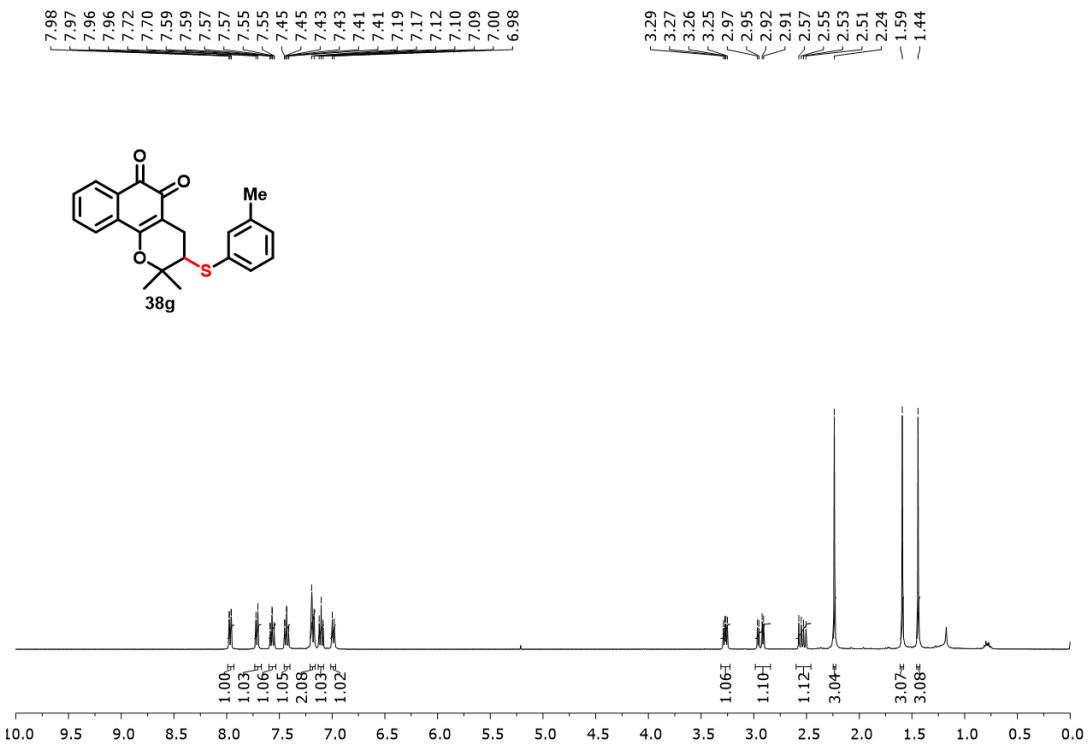

Figure A31: ^{1}H NMR spectrum of compound **38g** (400 MHz, $CDCl_3$).

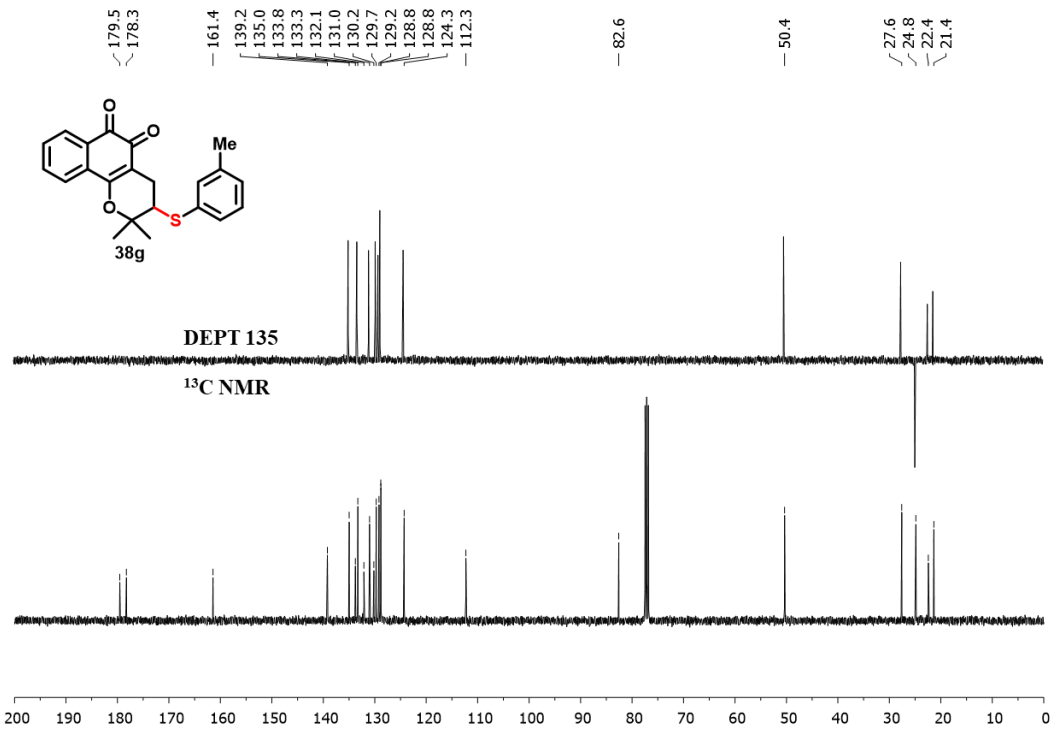

Figure A32: ^{13}C NMR and DEPT 135 spectrum of compound **38g** (101 MHz, $CDCl_3$).

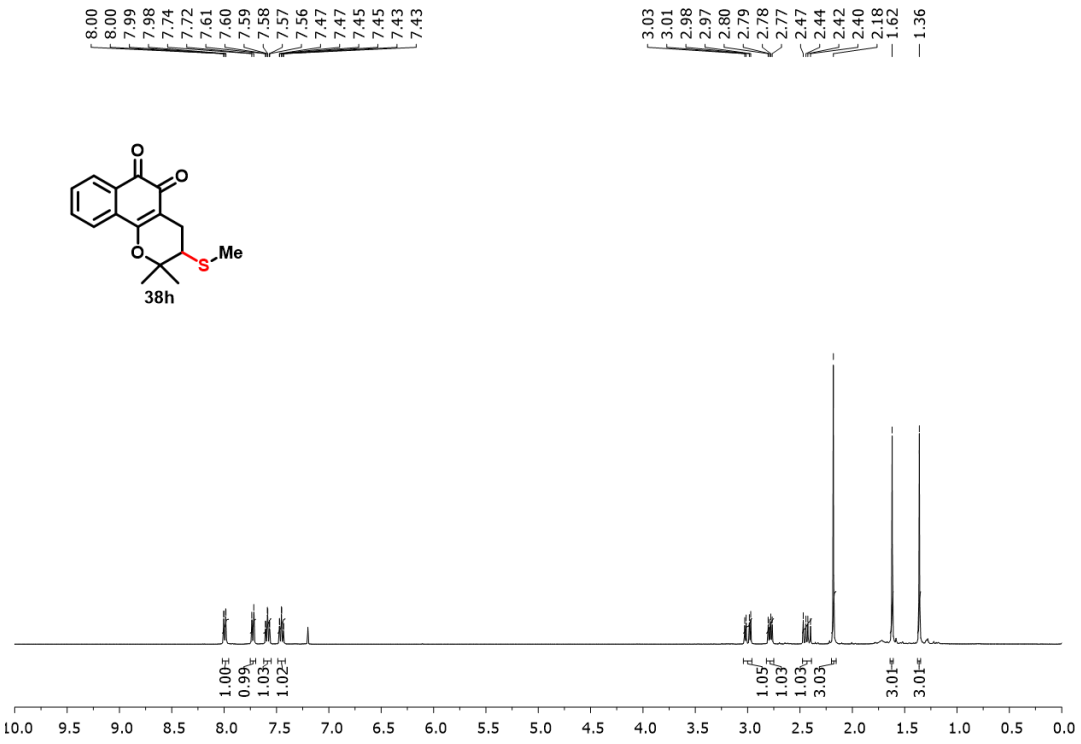

Figure A33: ^{1}H NMR spectrum of compound **38h** (400 MHz, $CDCl_3$).

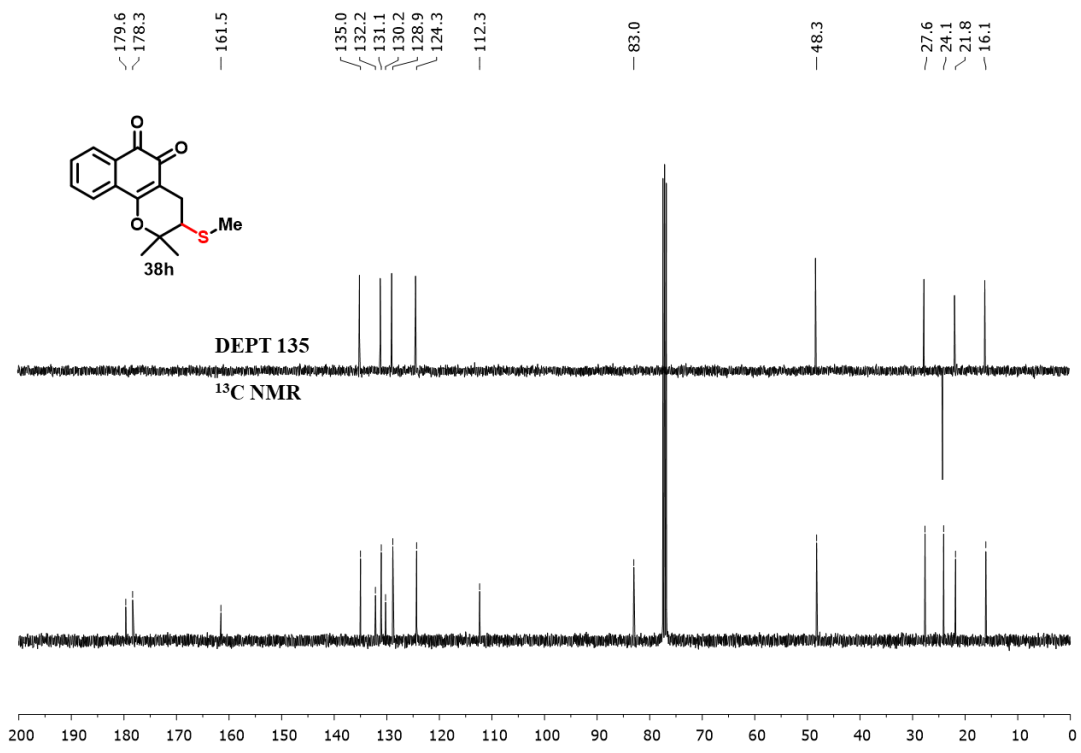

Figure A34: ^{13}C NMR and DEPT 135 spectrum of compound **38h** (101 MHz, $CDCl_3$).

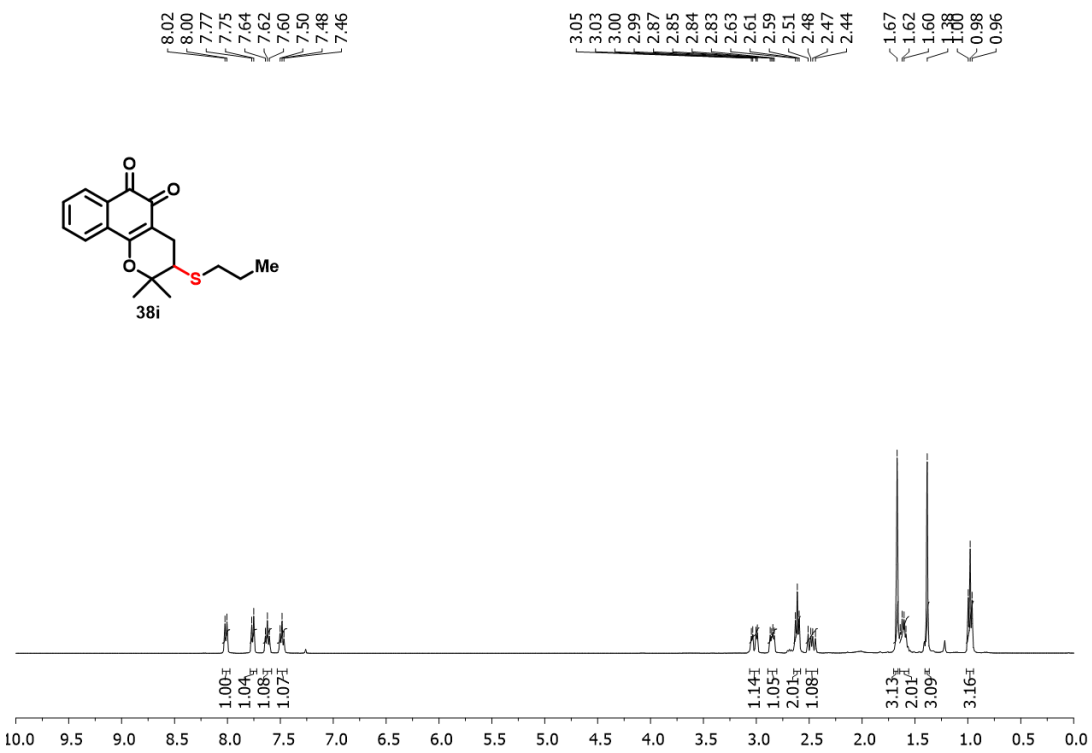

Figure A35: ^{1}H NMR spectrum of compound **38i** (400 MHz, $CDCl_3$).

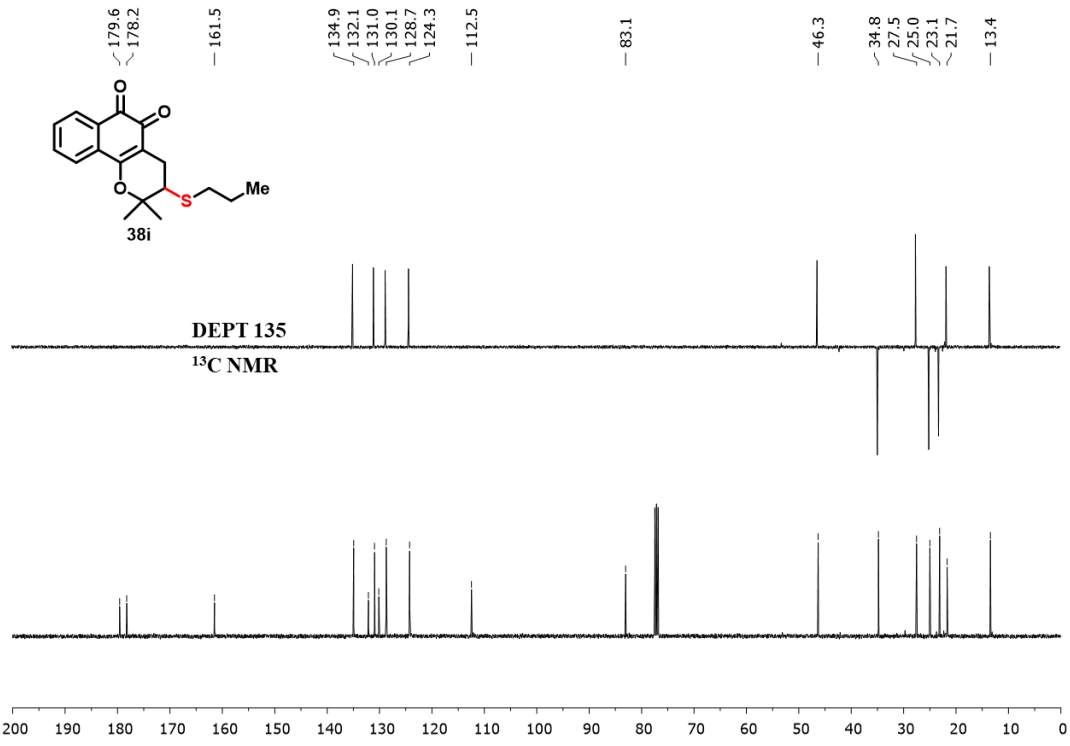

Figure A36: ^{13}C NMR and DEPT 135 spectrum of compound **38i** (101 MHz, $CDCl_3$).

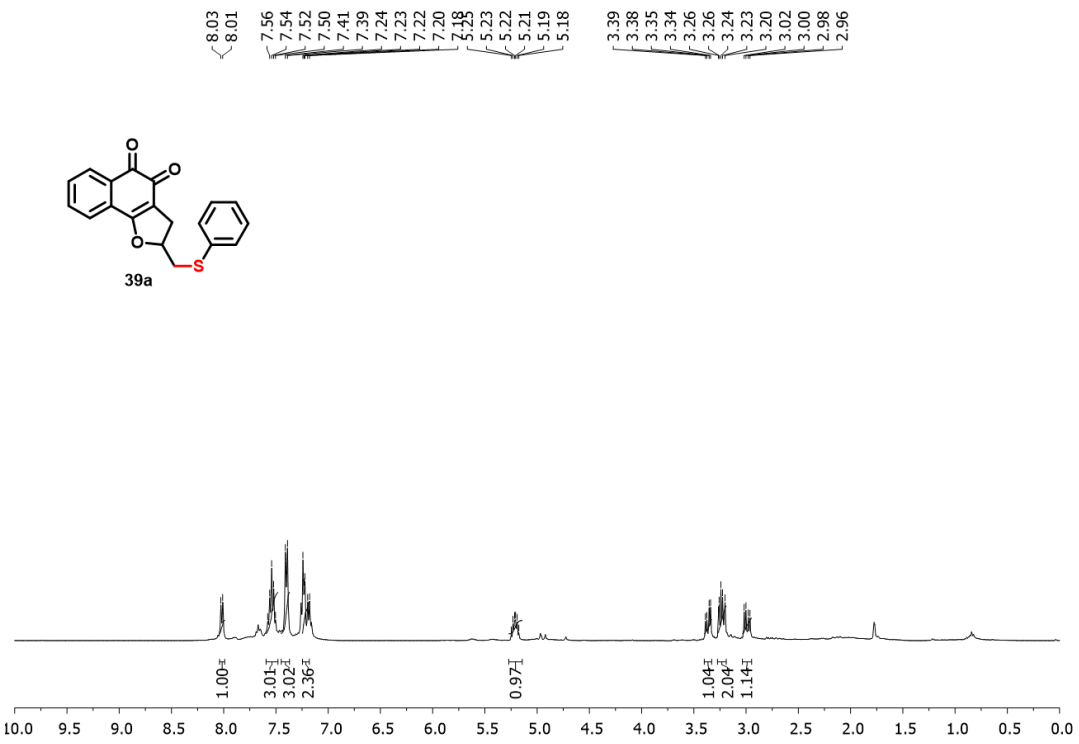

Figure A37: ^{1}H NMR spectrum of compound **39a** (400 MHz, $CDCl_3$).

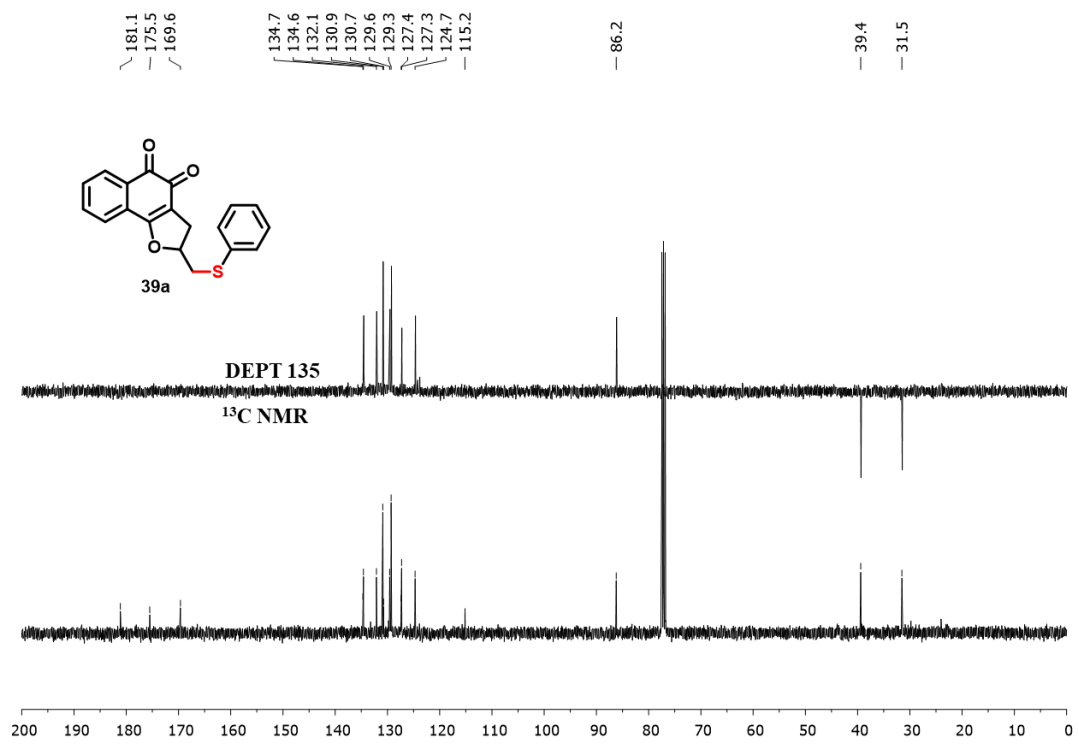

Figure A38: ^{13}C NMR and DEPT 135 spectrum of compound **39a** (101 MHz, $CDCl_3$).

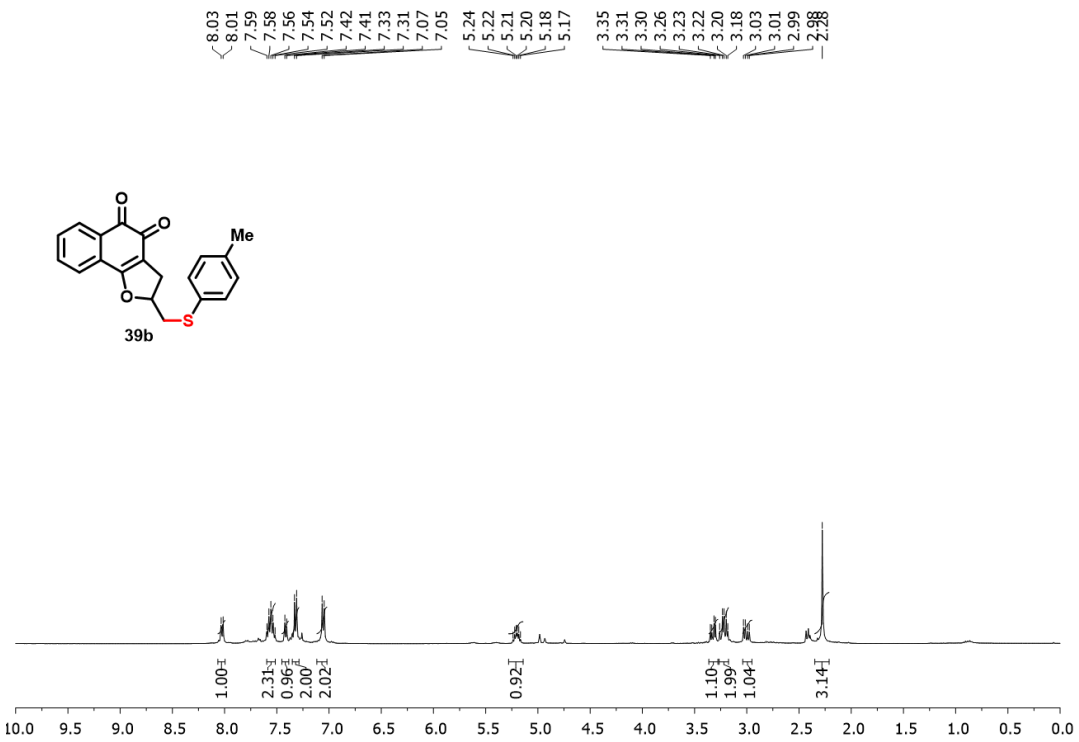

Figure A39: ^{1}H NMR spectrum of compound **39b** (400 MHz, $CDCl_3$).

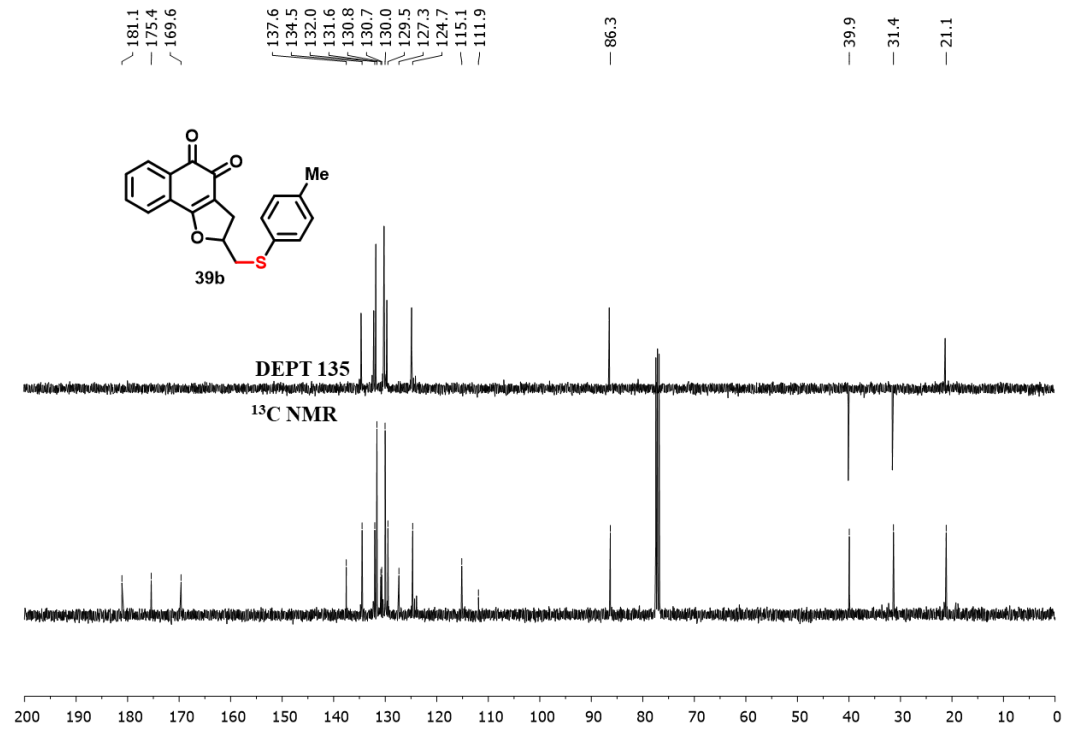

Figure A40: ^{13}C NMR and DEPT 135 spectrum of compound **39b** (101 MHz, $CDCl_3$).

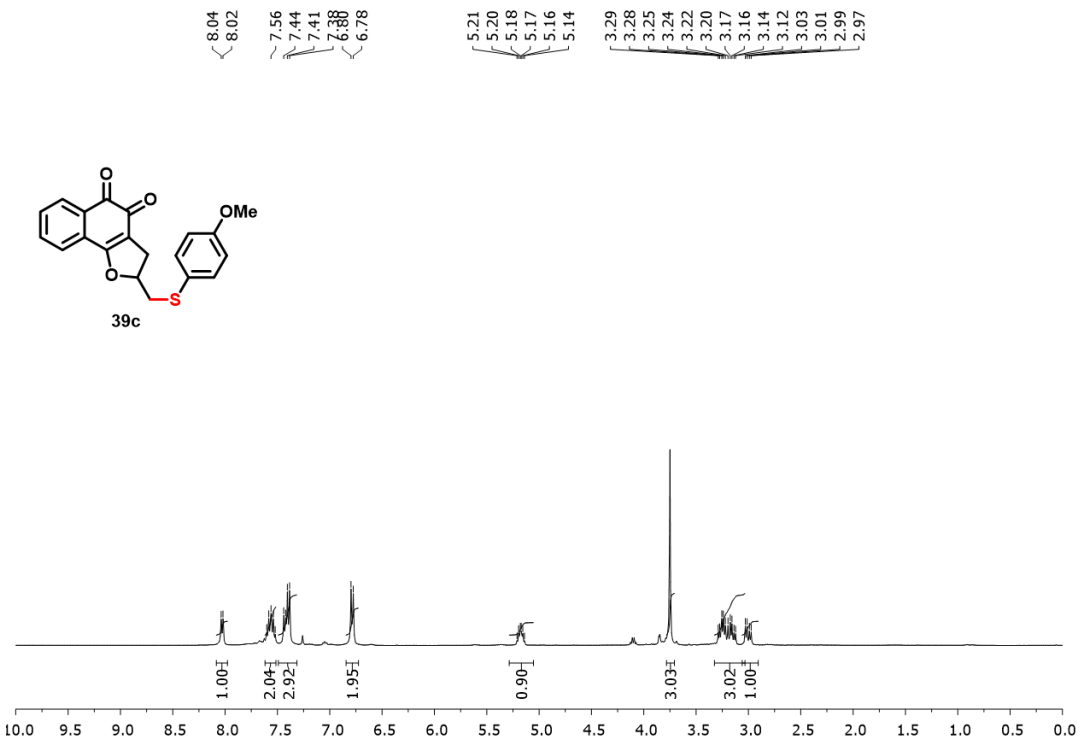

Figure A41: ^{1}H NMR spectrum of compound **39c** (400 MHz, $CDCl_3$).

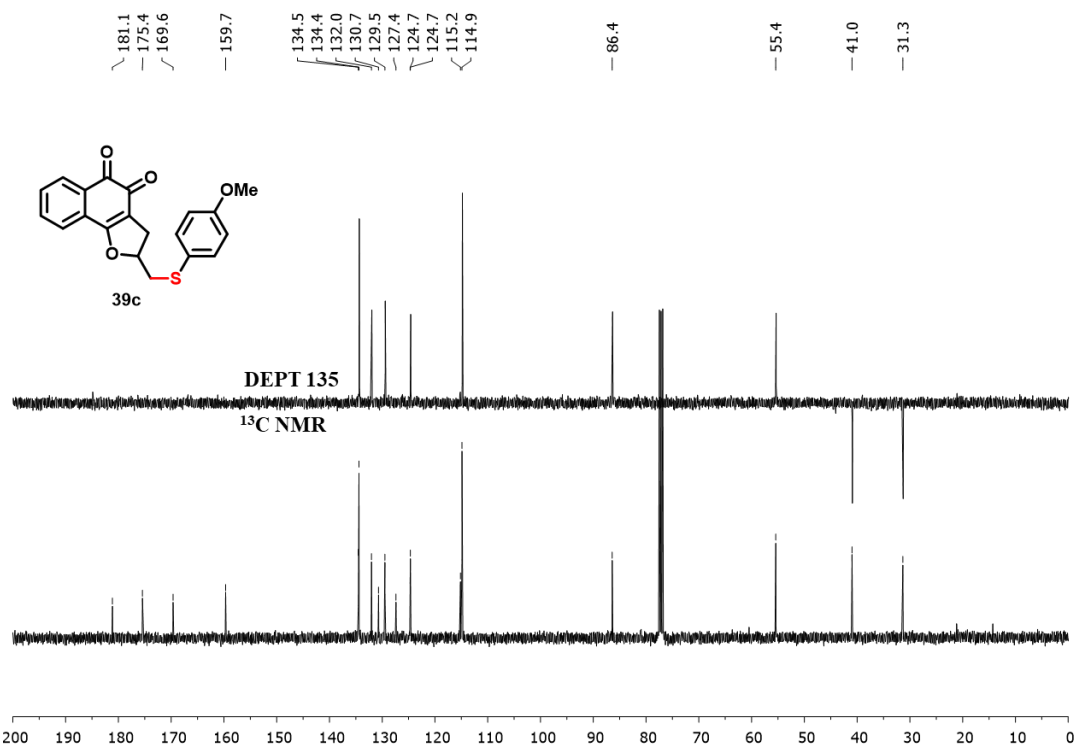

Figure A42: ^{13}C NMR and DEPT 135 spectrum of compound **39c** (101 MHz, $CDCl_3$).

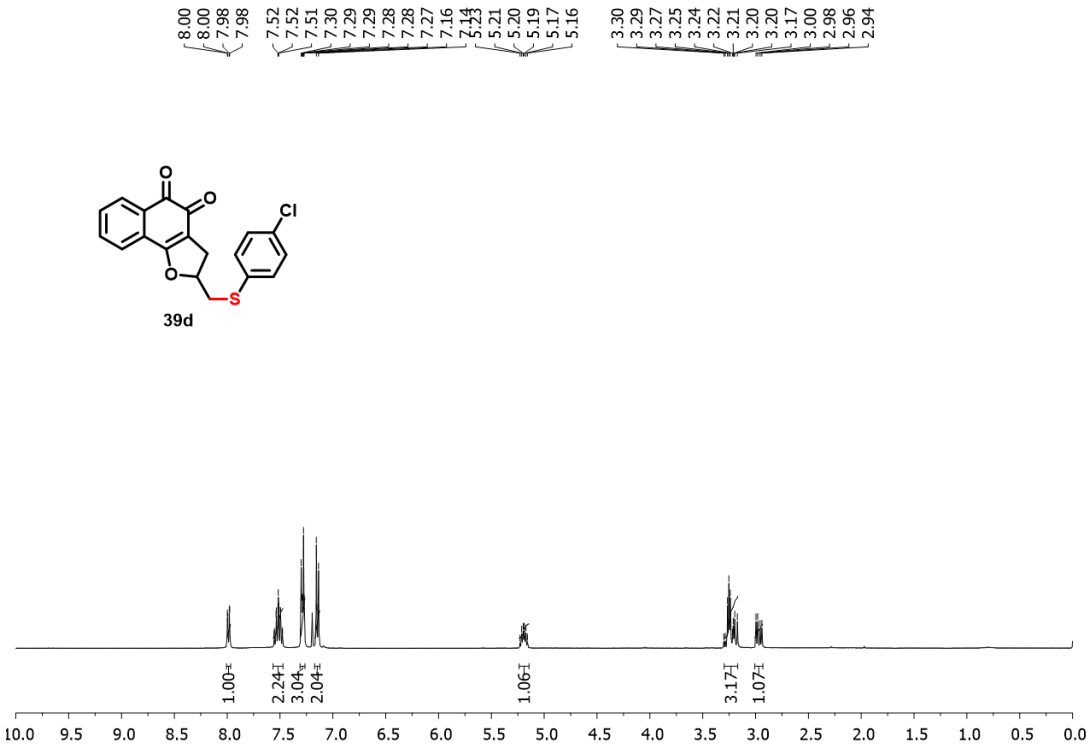

Figure A43: ^{1}H NMR spectrum of compound **39d** (400 MHz, $CDCl_3$).

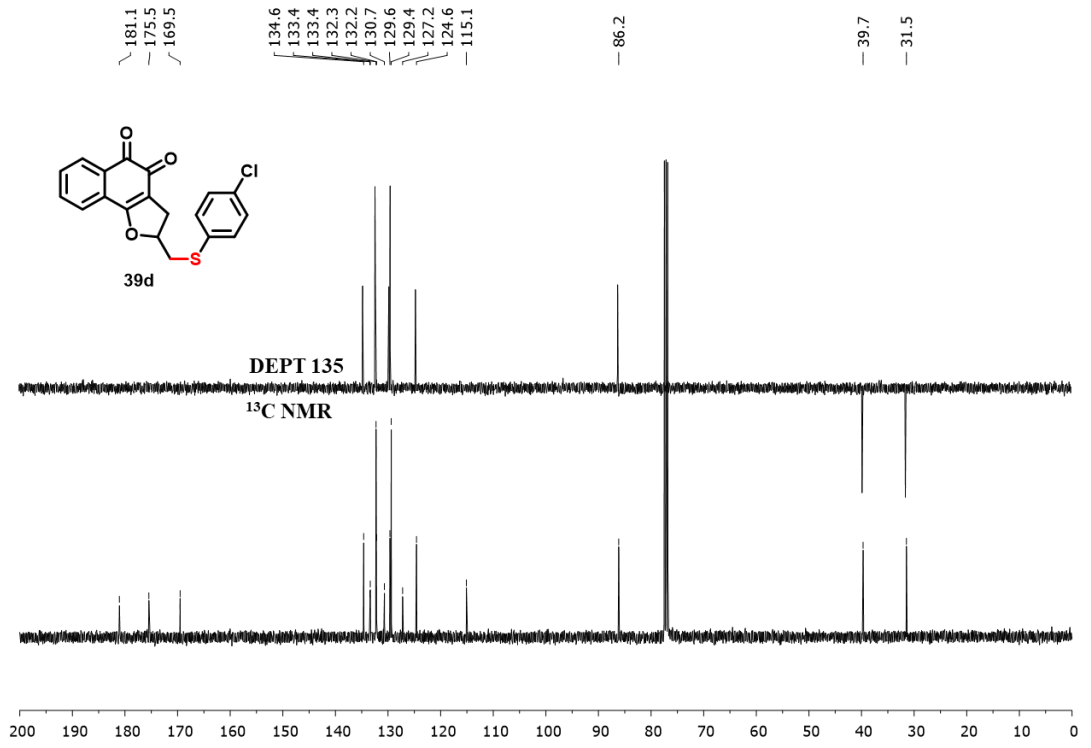

Figure A44: ^{13}C NMR and DEPT 135 spectrum of compound **39d** (101 MHz, $CDCl_3$).

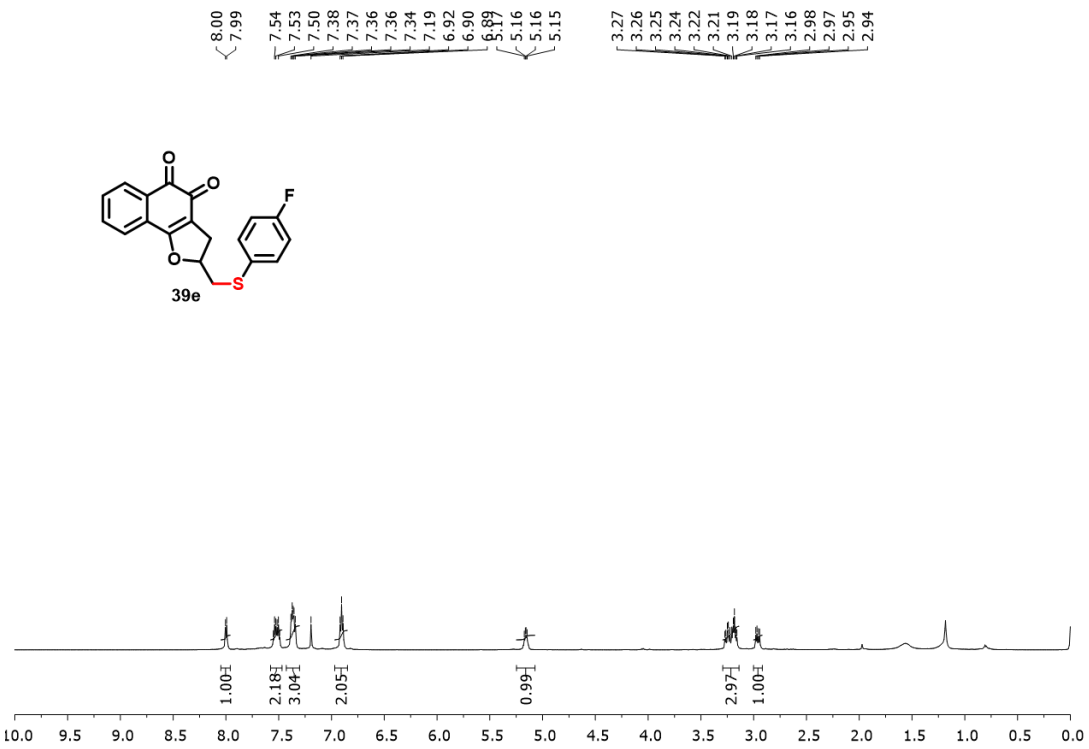

Figure A45: ^{1}H NMR spectrum of compound **39e** (400 MHz, $CDCl_3$).

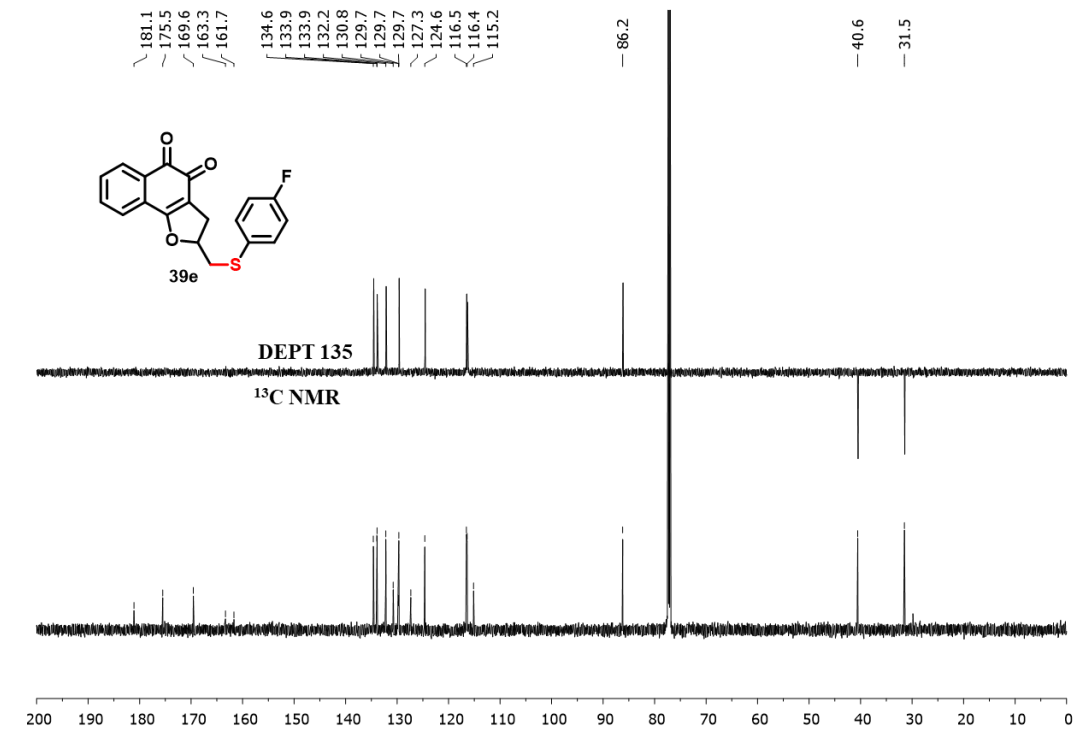

Figure A46: ^{13}C NMR and DEPT 135 spectrum of compound **39e** (101 MHz, $CDCl_3$).

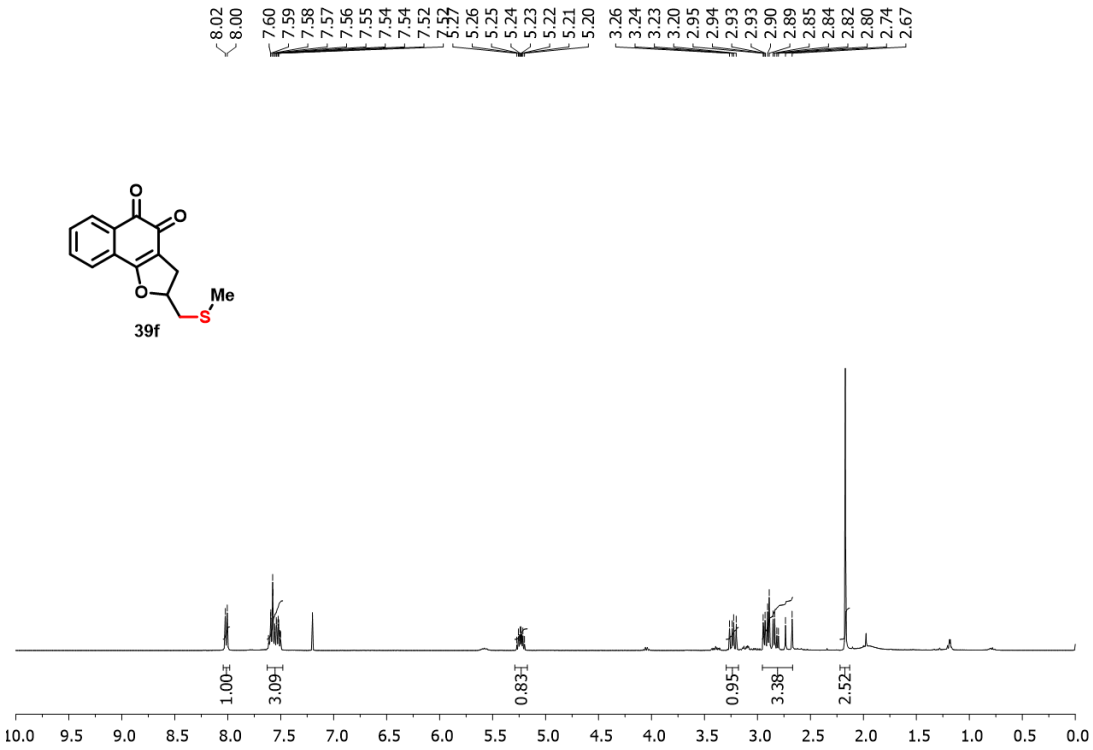

Figure A47: ^{1}H NMR spectrum of compound **39f** (400 MHz, $CDCl_3$).

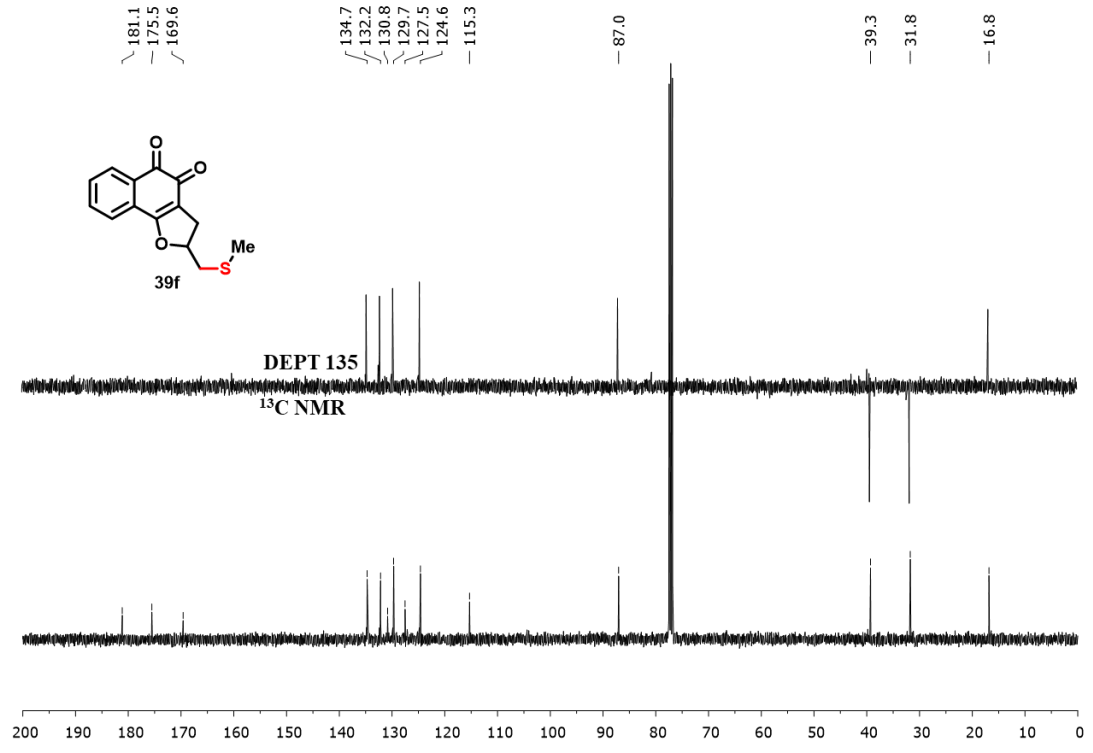

Figure A48: ^{13}C NMR and DEPT 135 spectrum of compound **39f** (101 MHz, $CDCl_3$).

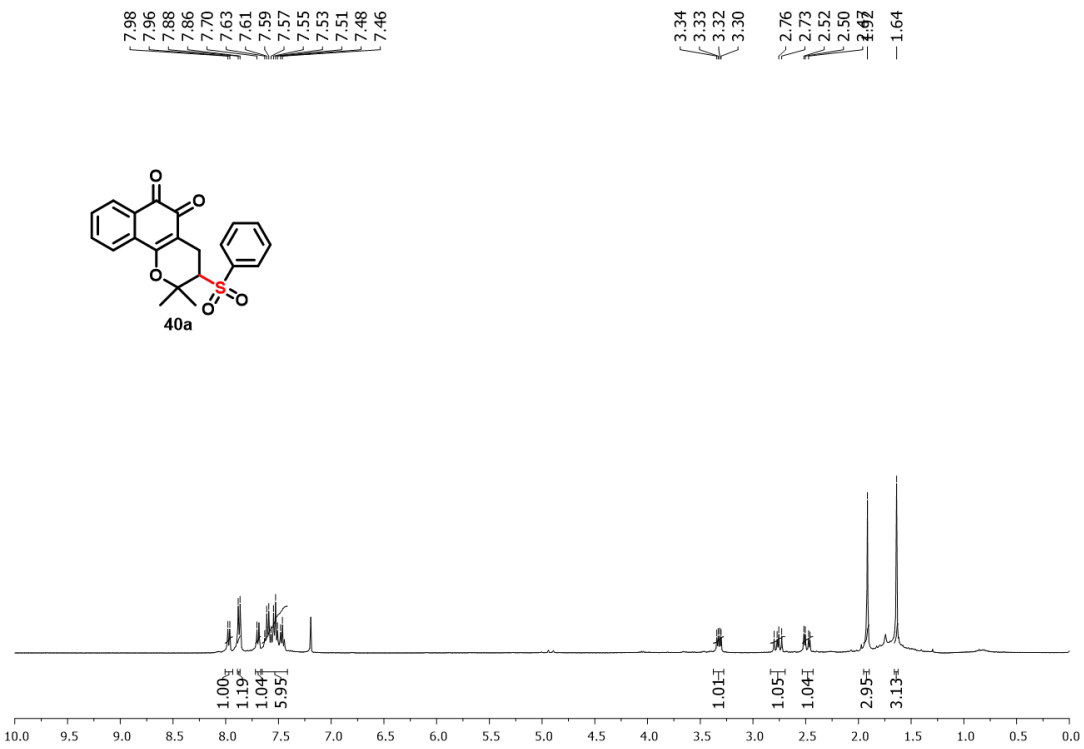

Figure A49: ^{1}H NMR spectrum of compound **40a** (400 MHz, $CDCl_3$).

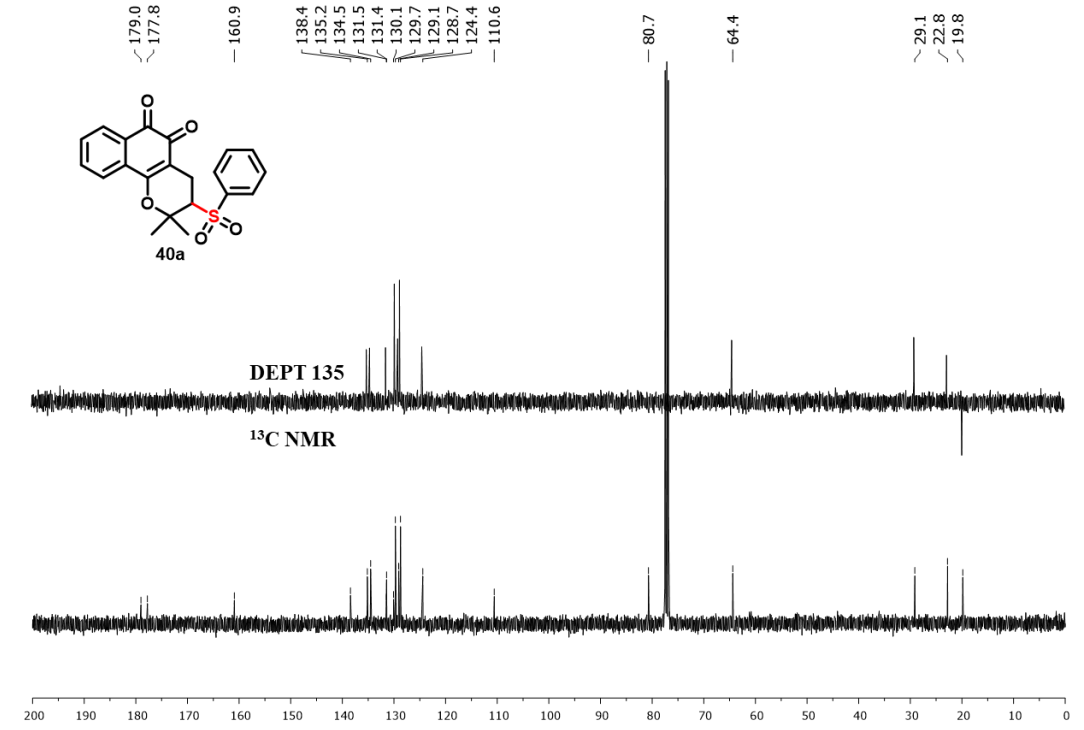

Figure A50: ^{13}C NMR and DEPT 135 spectrum of compound **40a** (101 MHz, $CDCl_3$).

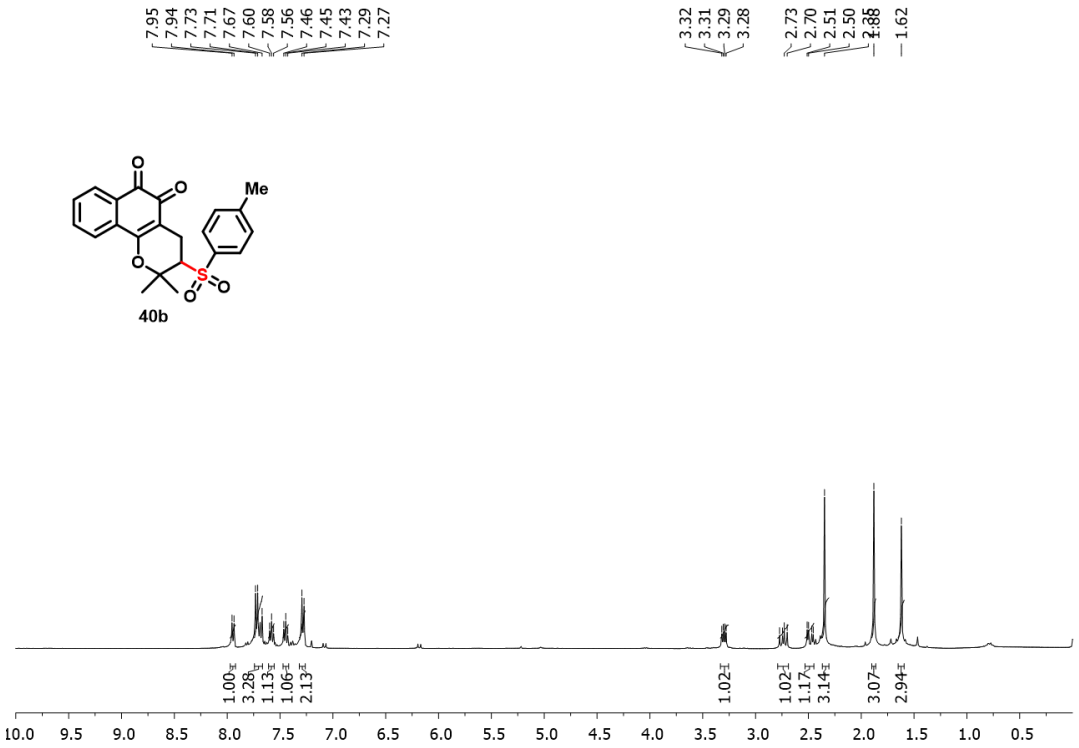

Figure A51: ^{1}H NMR spectrum of compound **40b** (400 MHz, $CDCl_3$).

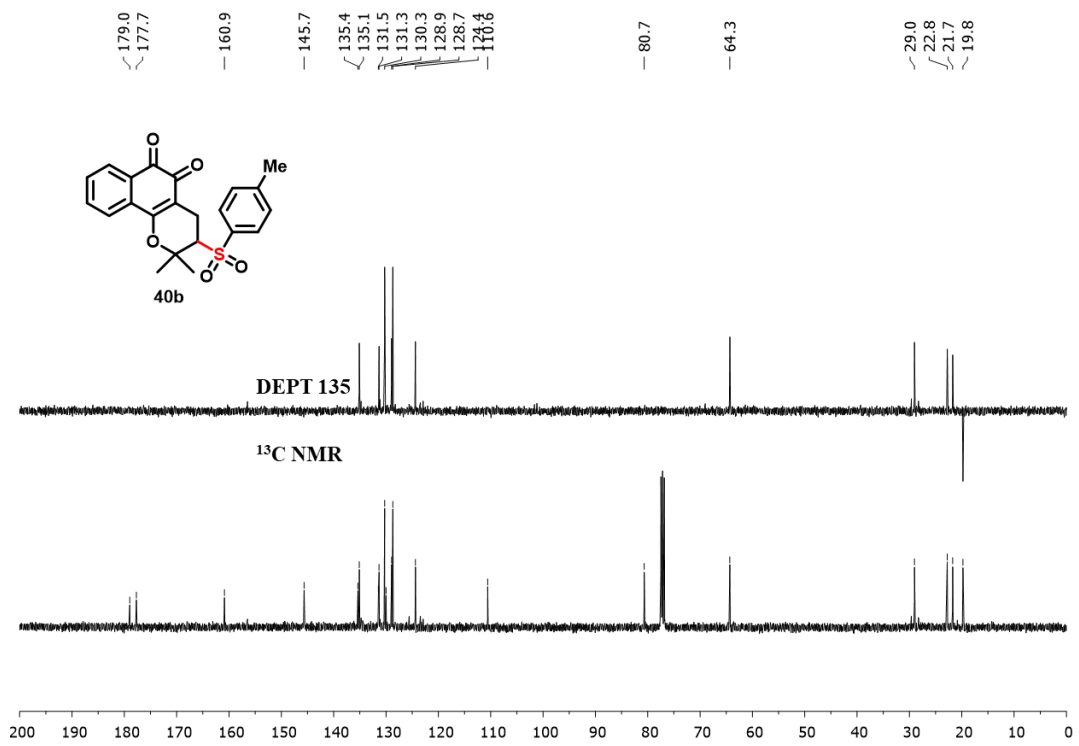

Figure A52: ^{13}C NMR and DEPT 135 spectrum of compound **40b** (101 MHz, $CDCl_3$).

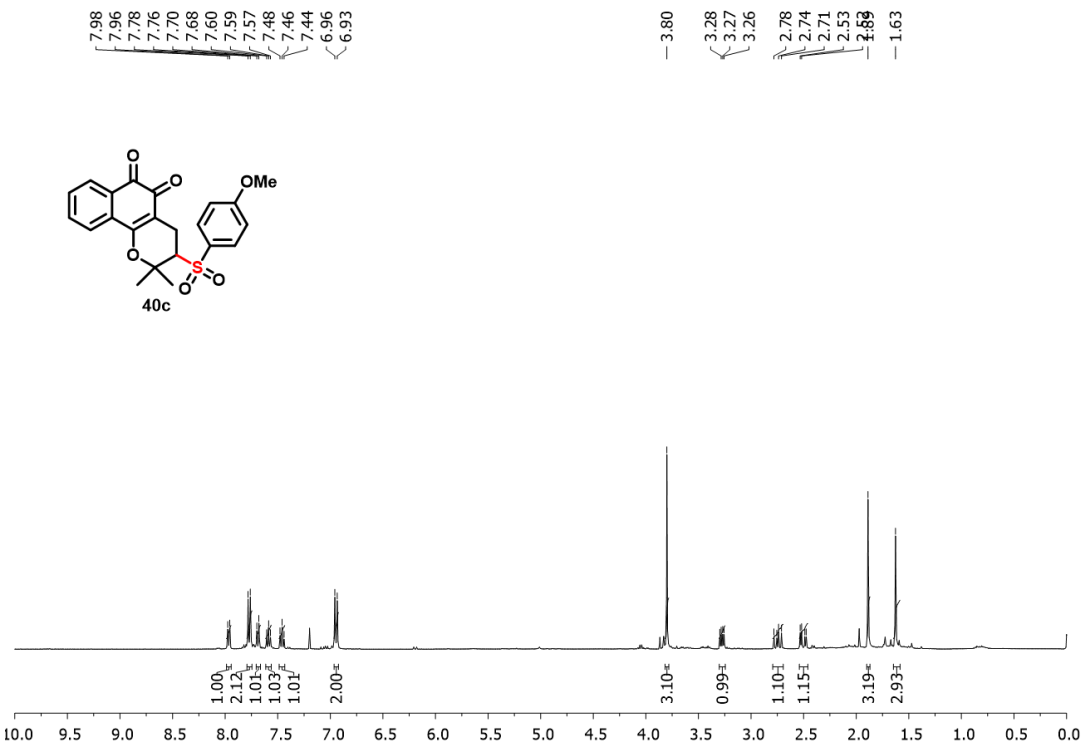

Figure A53: ^{1}H NMR spectrum of compound **40c** (400 MHz, $CDCl_3$).

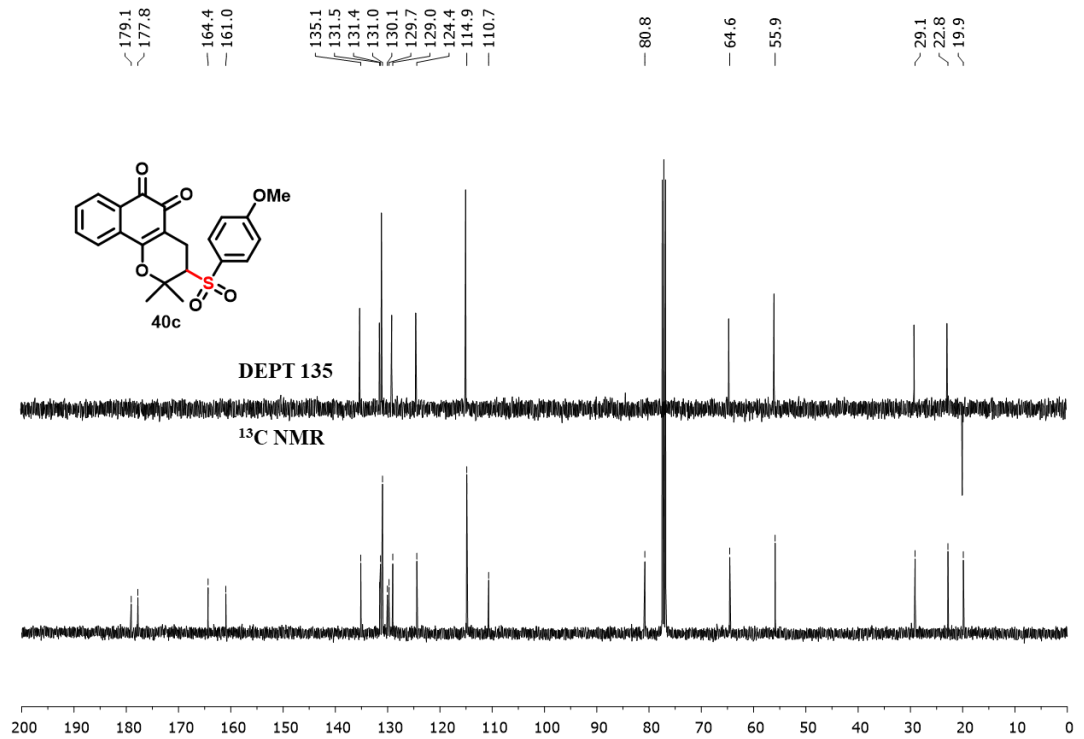

Figure A54: ^{13}C NMR and DEPT 135 spectrum of compound **40c** (101 MHz, $CDCl_3$).

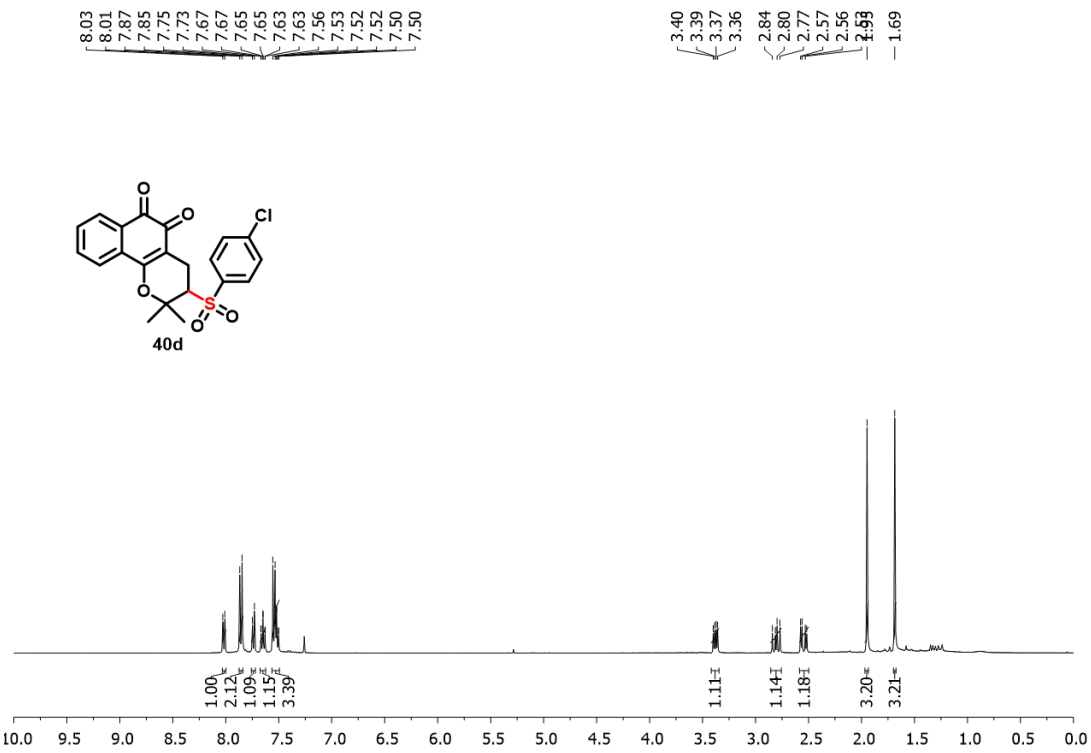

Figure A55: ^{1}H NMR spectrum of compound **40d** (400 MHz, $CDCl_3$).

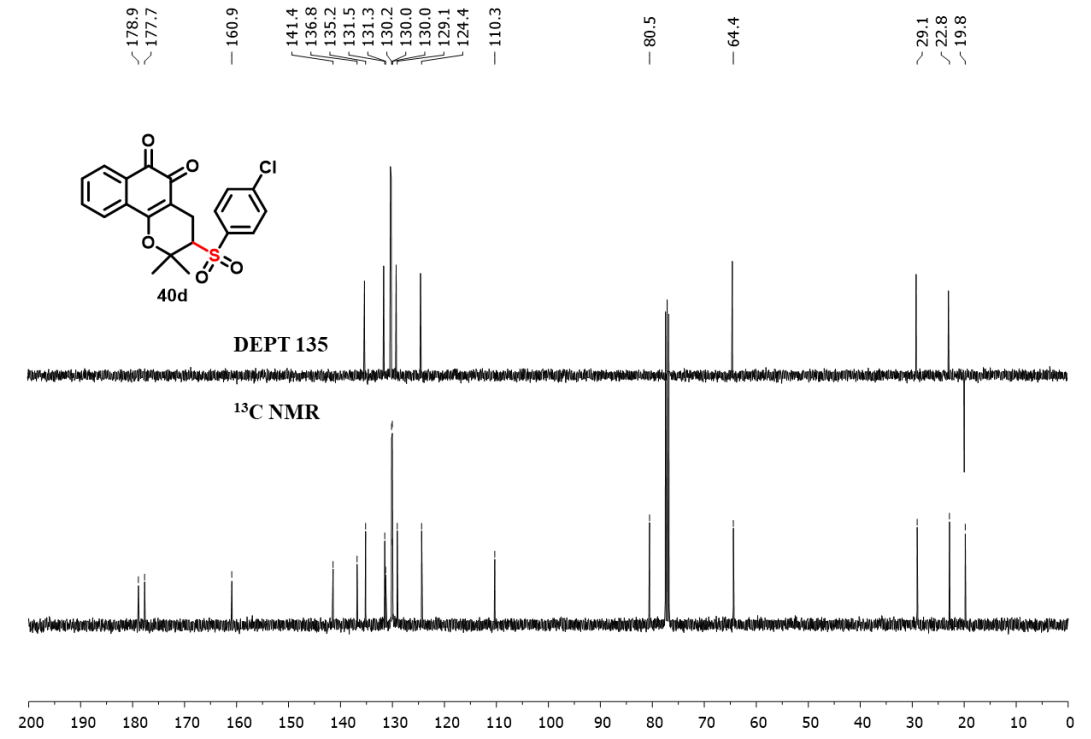

Figure A56: ^{13}C NMR and DEPT 135 spectrum of compound **40d** (101 MHz, $CDCl_3$).

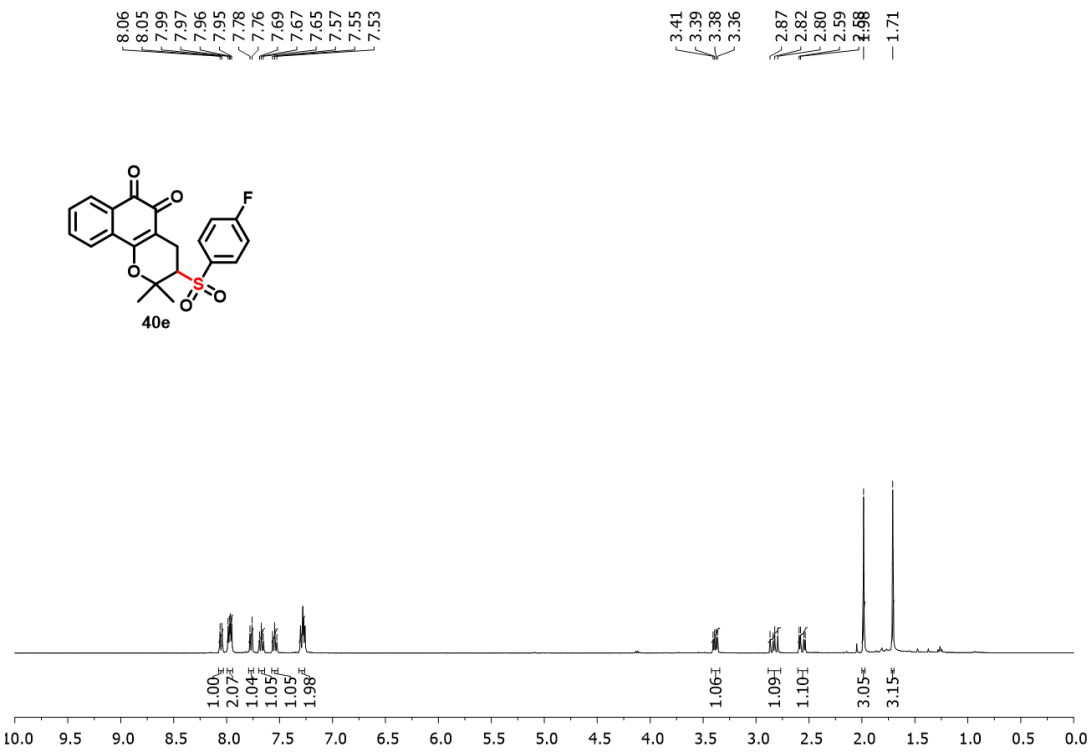

Figure A57: ^{1}H NMR spectrum of compound **40e** (400 MHz, $CDCl_3$).

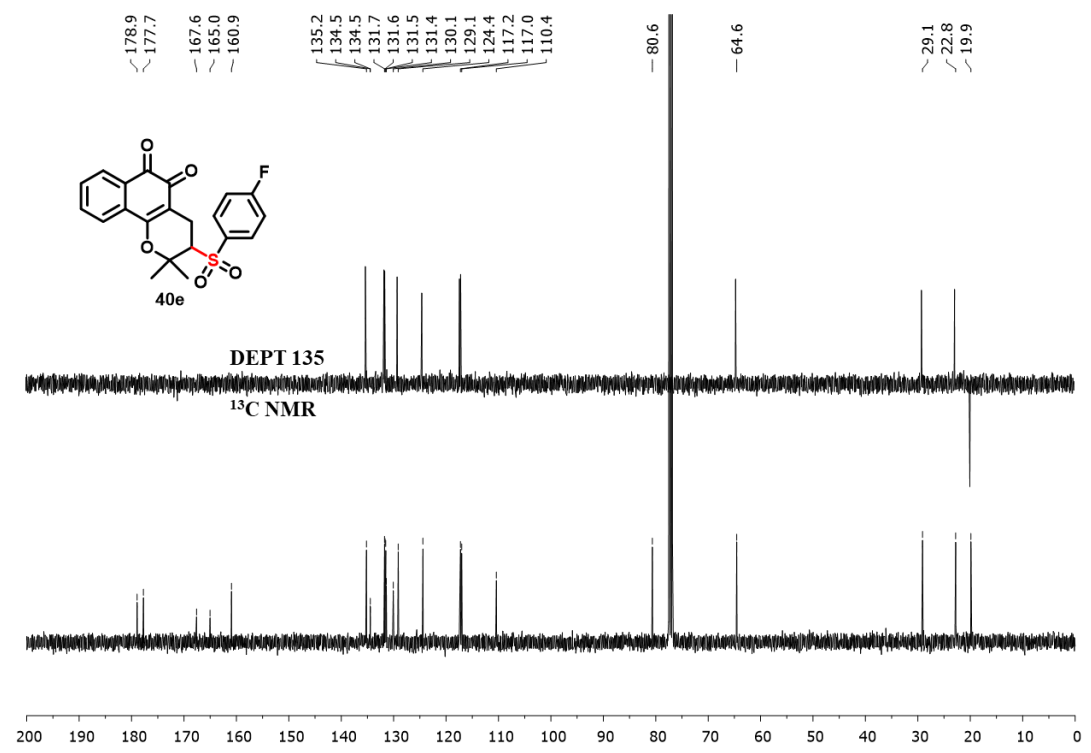

Figure A58: ^{13}C NMR and DEPT 135 spectrum of compound **40e** (101 MHz, $CDCl_3$).

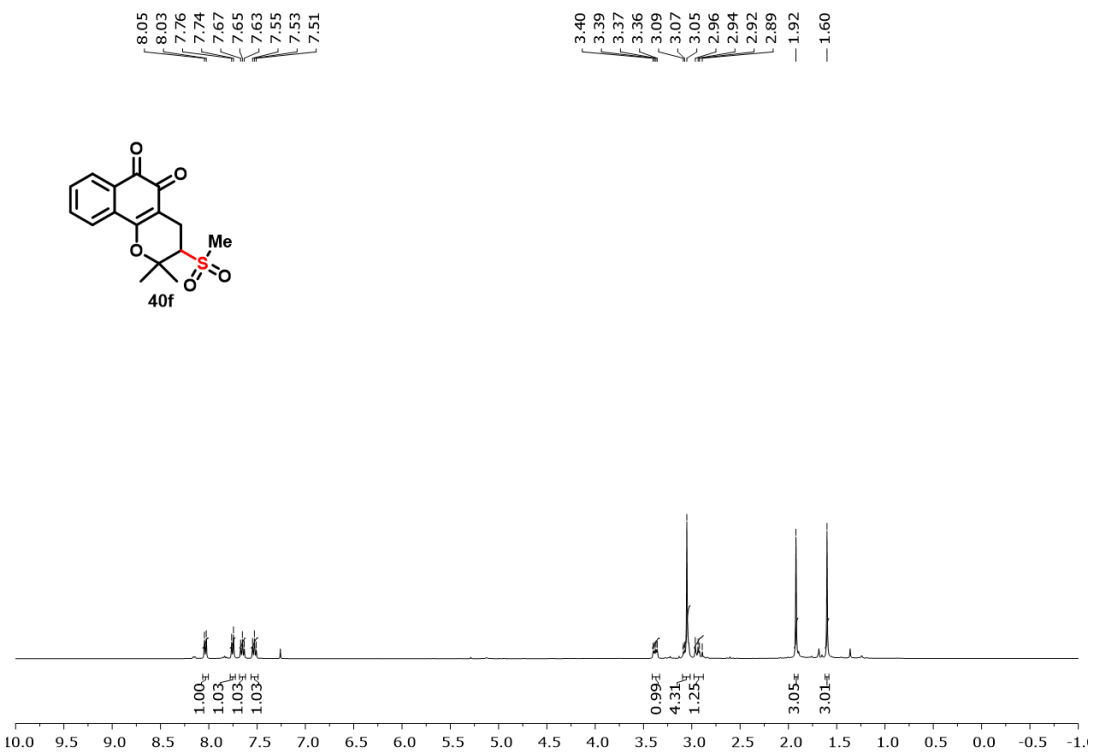

Figure A59: ^{1}H NMR spectrum of compound **40f** (400 MHz, $CDCl_3$).

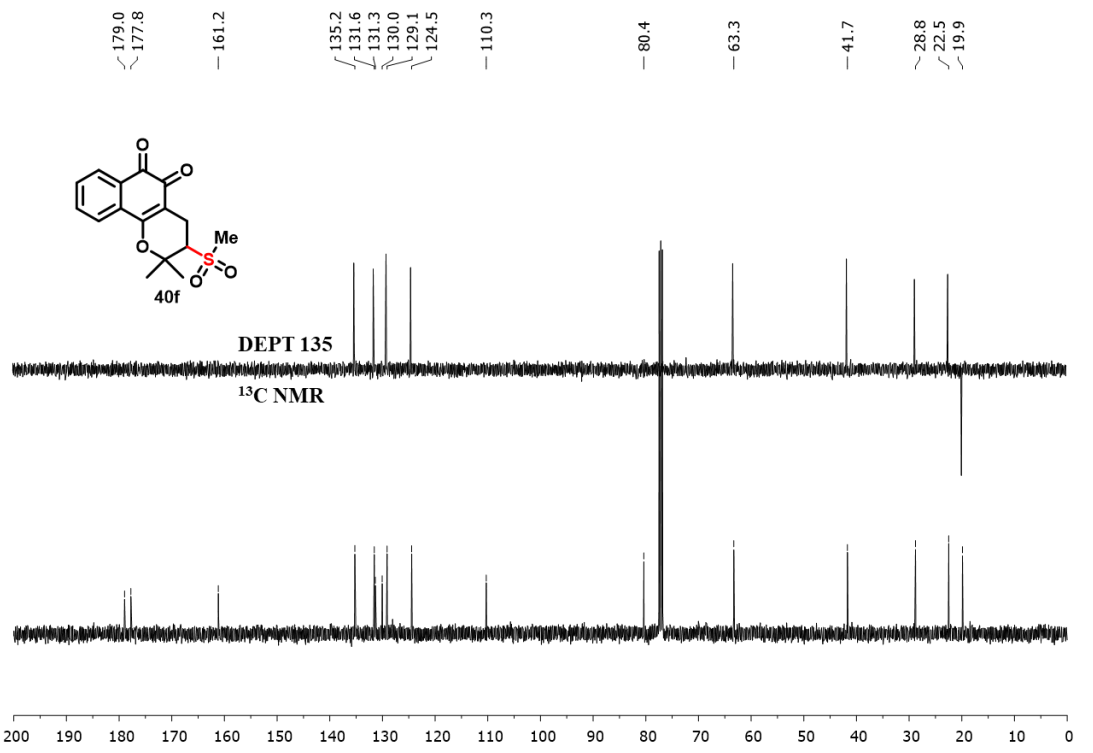

Figure A60: ^{13}C NMR and DEPT 135 spectrum of compound **40f** (101 MHz, $CDCl_3$).

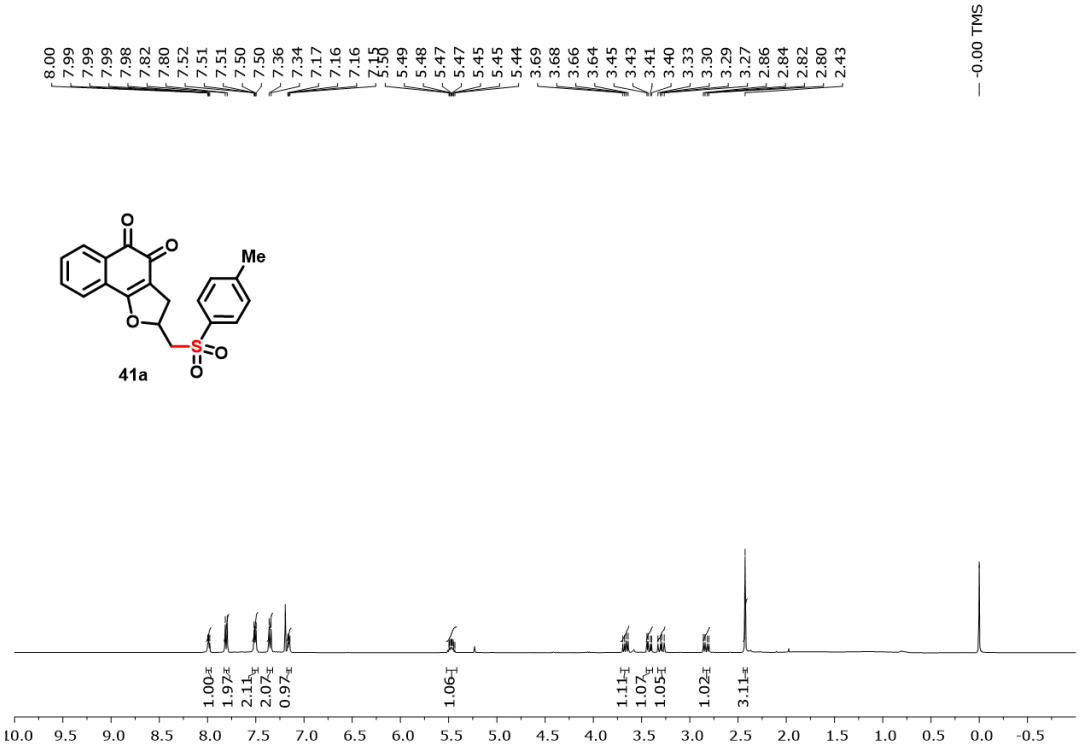

Figure A61: ^{1}H NMR spectrum of compound **41a** (400 MHz, $CDCl_3$).

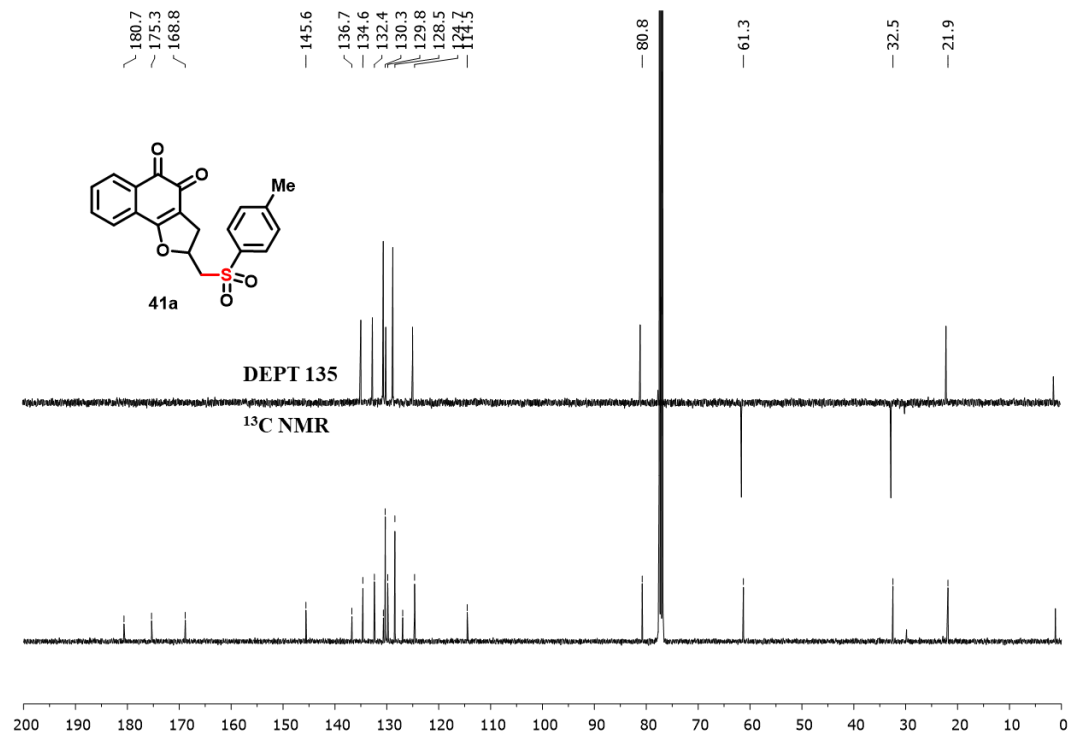

Figure A62: ^{13}C NMR and DEPT 135 spectrum of compound **41a** (101 MHz, $CDCl_3$).

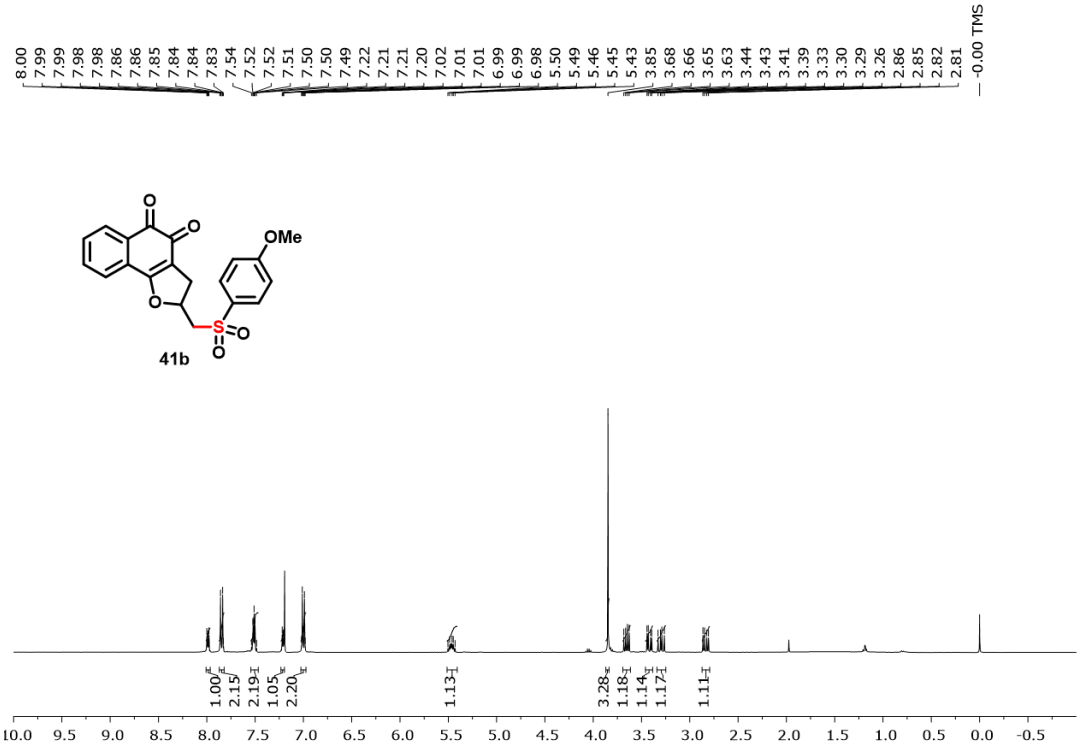

Figure A63: ^{1}H NMR spectrum of compound **41b** (400 MHz, DMSO-d_6).

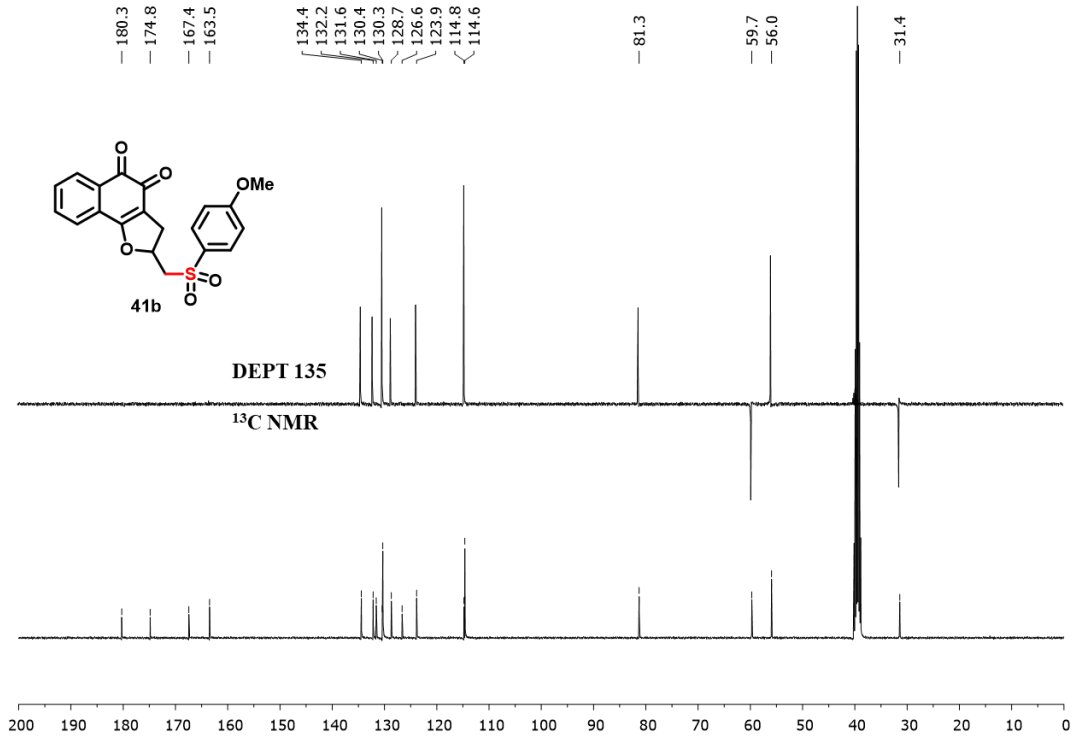

Figure A64: ^{13}C NMR and DEPT 135 spectrum of compound **41b** (101 MHz, DMSO-d_6).

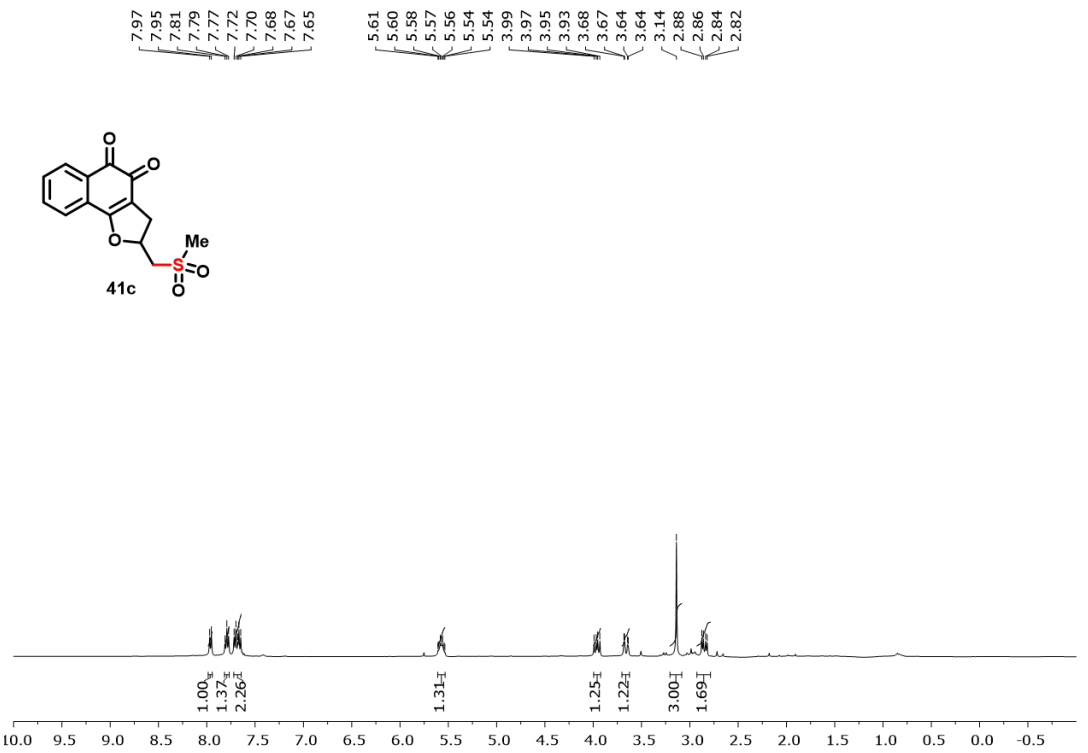

Figure A65: ^{1}H NMR spectrum of compound **41c** (400 MHz, DMSO-d_6).

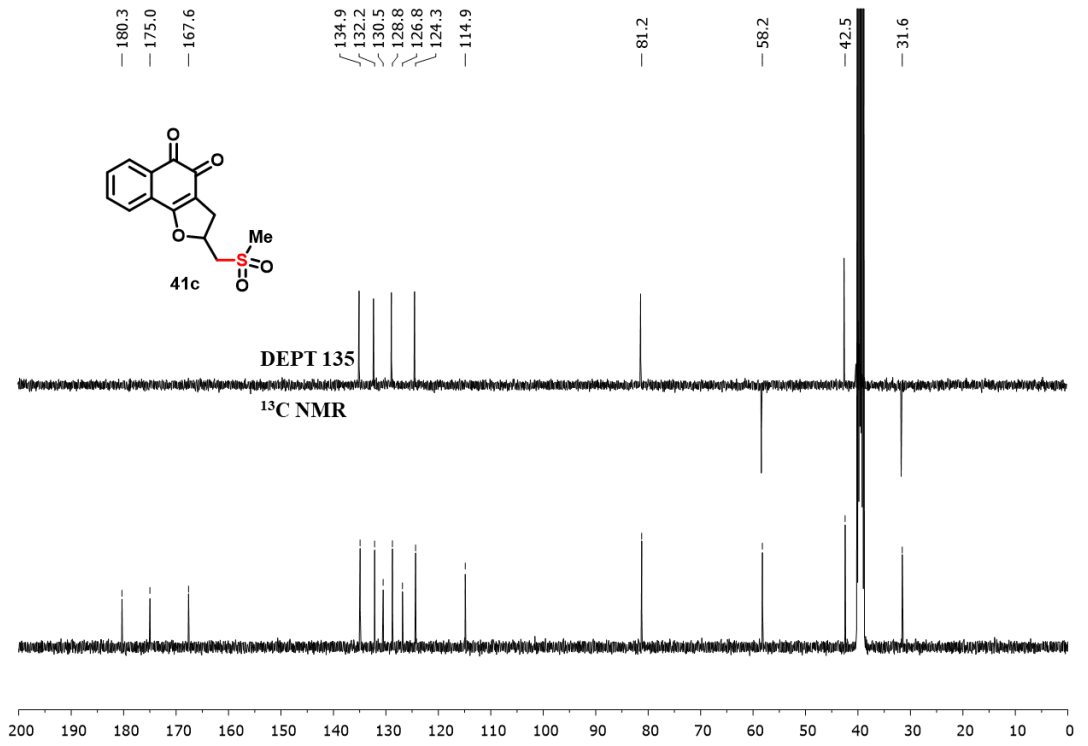

Figure A66: ^{13}C NMR and DEPT 135 spectrum of compound **41c** (101 MHz, DMSO-d_6).

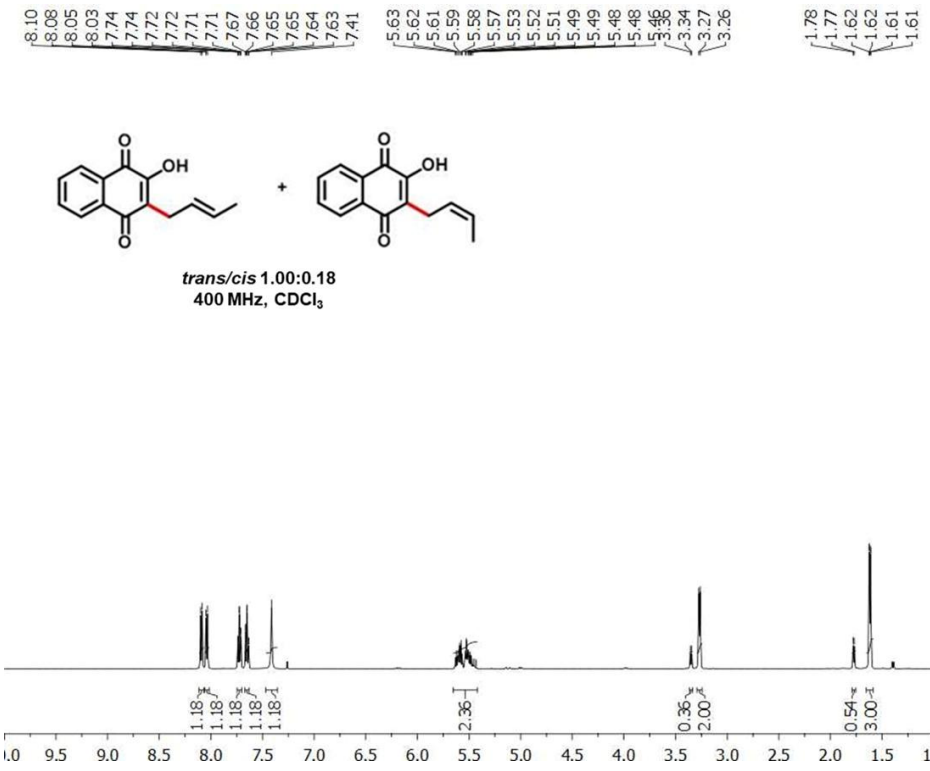

Figure A67: ^{1}H NMR spectrum of compound **42** (400 MHz, $CDCl_3$).

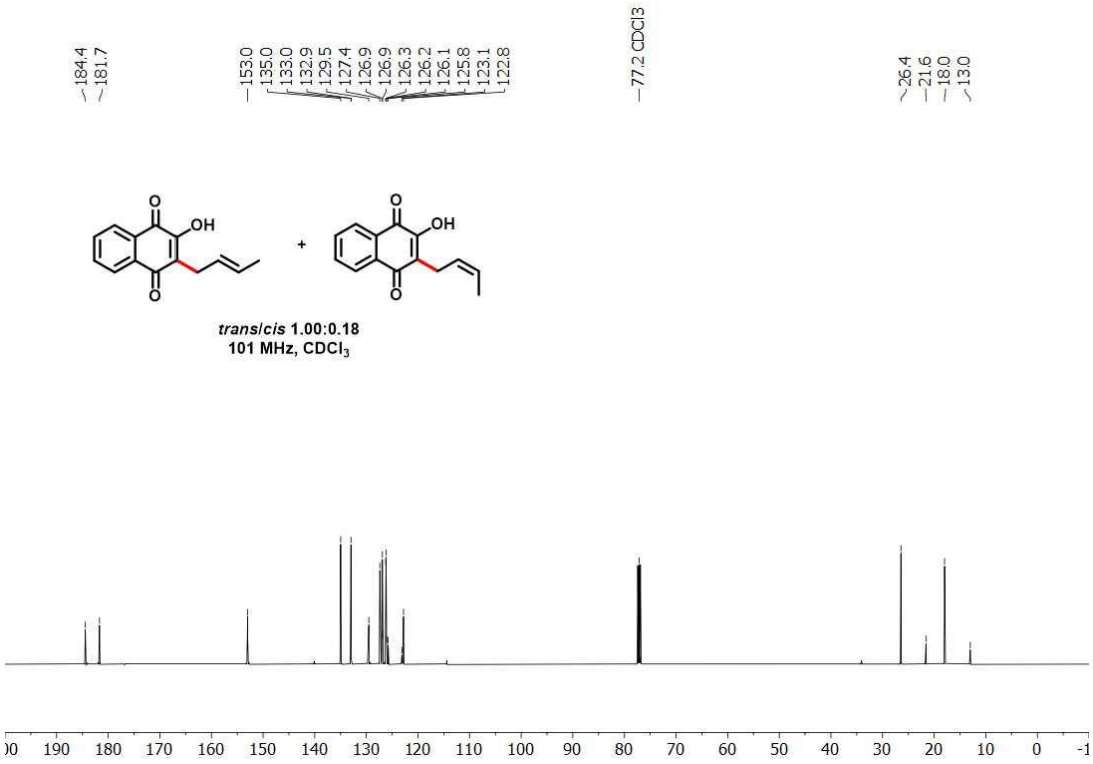

Figure A68: ^{13}C NMR and DEPT 135 spectrum of compound **42** (101 MHz, $CDCl_3$).

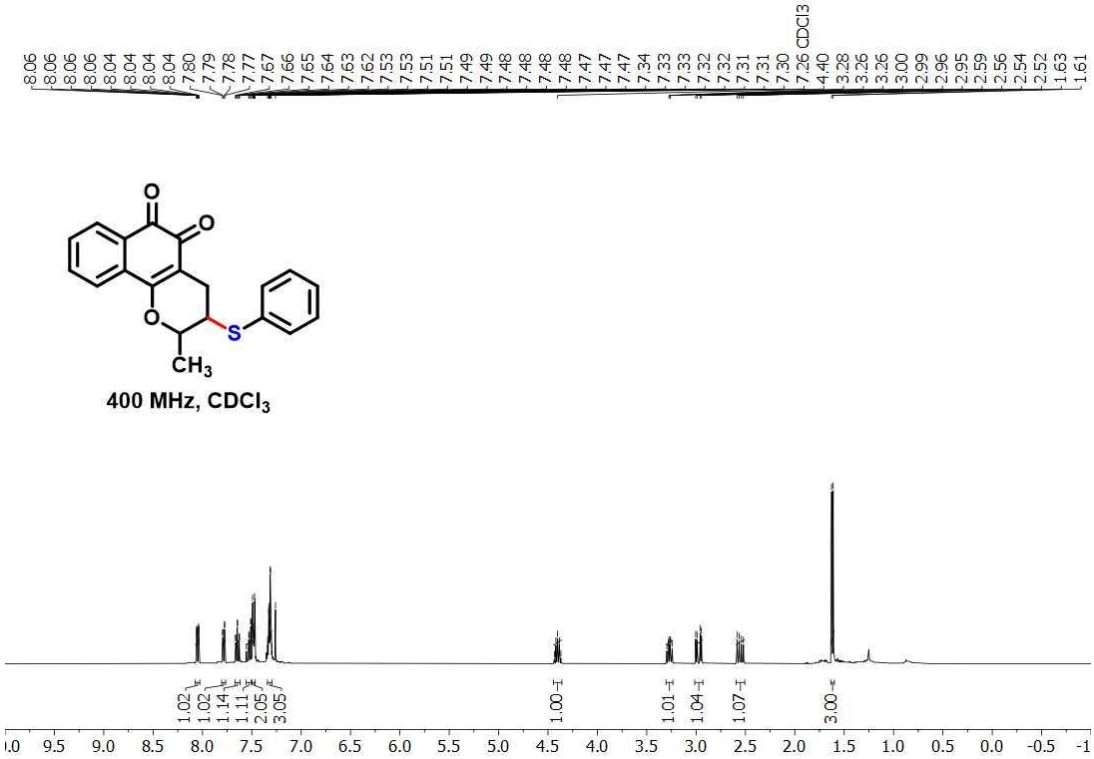

Figure A69: ^{1}H NMR spectrum of compound **43** (400 MHz, $CDCl_3$).

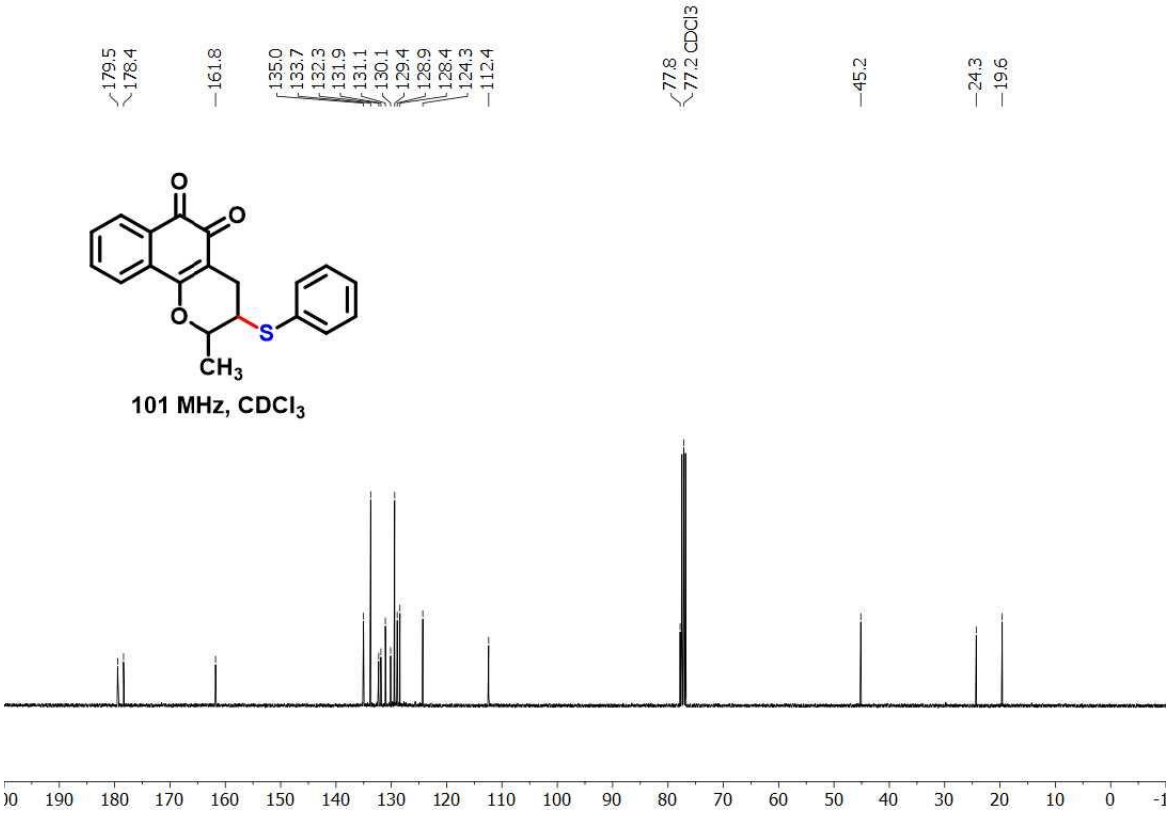

Figure A70: ^{13}C NMR spectrum of compound **43** (101 MHz, $CDCl_3$).

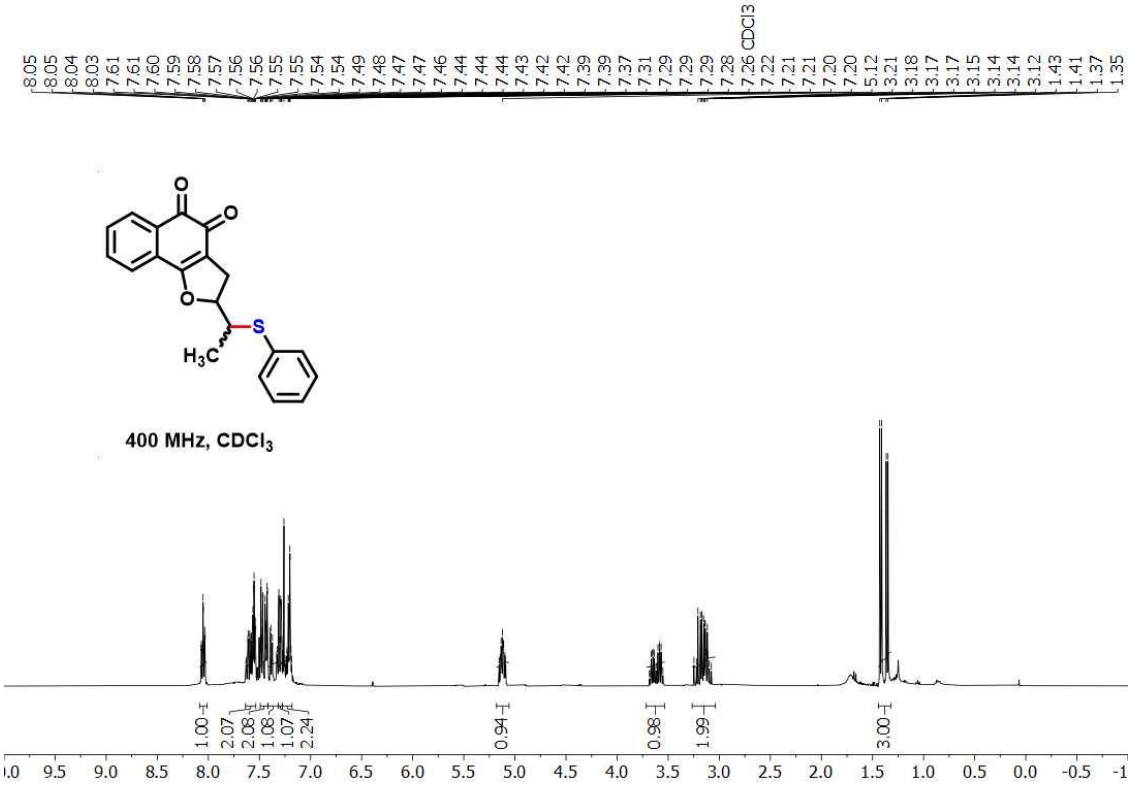

Figure A71: ^{1}H NMR spectrum of compound **44** (400 MHz, $CDCl_3$).

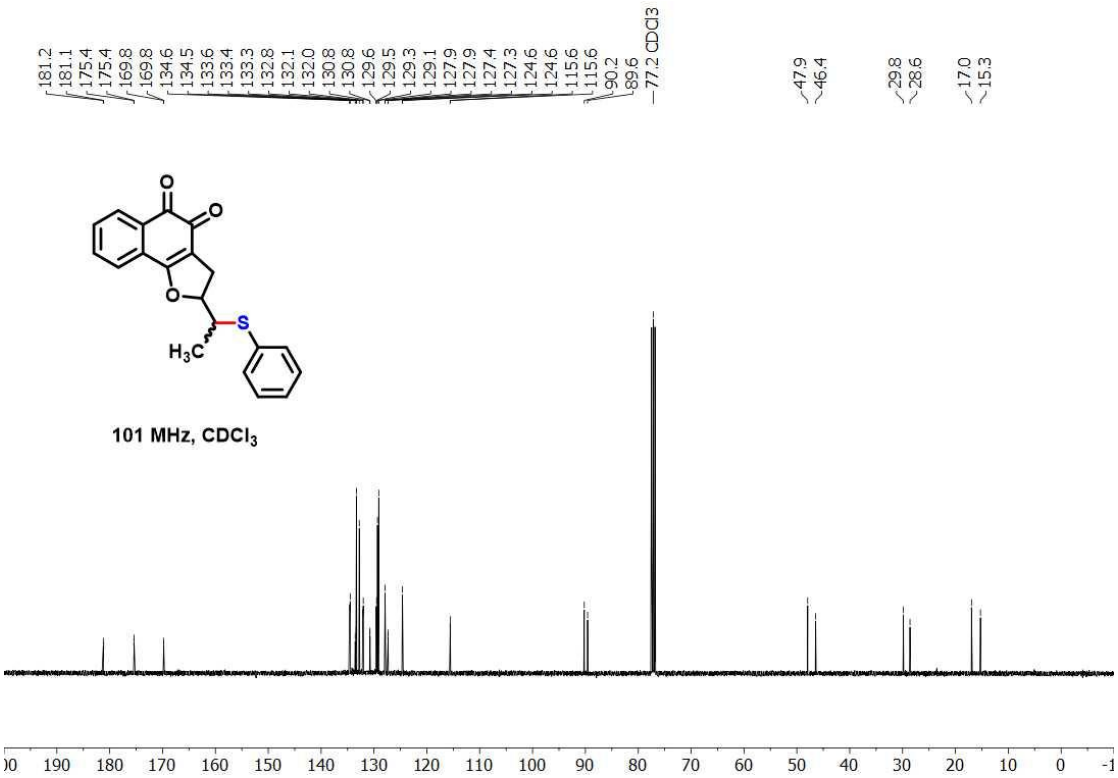

Figure A72: ^{13}C NMR spectrum of compound **44** (101 MHz, $CDCl_3$).

Table A1: Crystallographic data and refinement compound **38b.**

Compound 38b (CCDC: 2233629)		
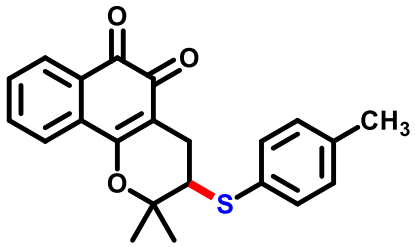		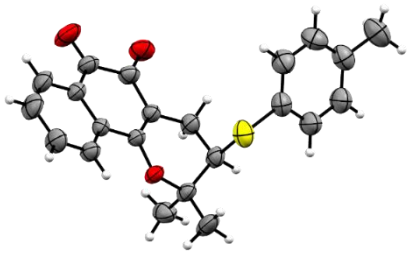
Empirical formula		$C_{22}H_{20}O_3S$
Formula weight ($g.mol^{-1}$)		364.44
Crystal system		Orthorhombic
Space group		Pbca
Z		8
λ (Å)		1.54184
T (K)		299 (10)
Unit cell dimensions	*a* (Å)	9.46985(5)
	b (Å)	18.46861(10)
	c (Å)	20.49433(10)
	α (º)	90
	β (º)	90
	γ (º)	90
V ($Å^3$)		3584.36(3)
Density (calculated) (g/cm^{-3})		1.351
Crystal size (mm^3)		0.15 x 0.19 x 0.37
Absorption coefficient (mm^{-1})		1.757
T_{min}/T_{max}		0.369/1.000
θ range for data collection (º)		4.315 to 79.685
Reflections collected		70725
	h	-12 to 12
Index ranges	*k*	-23 to 23
	l	-25 to16
Unique reflections		3877
Unique reflections with $I>2\sigma(I)$		3773
Independent/observed reflections		3877/3773
Symmetry factor (R_{int})		0.022
Completeness to $\theta = 79.685°$		0.994
F (000)		1536.0
Number os parameters		239
Goodnes-of-fit no F^2		1.125
Final *R* indexes for $I>2\sigma(I)$		$R_1 = 0.0498$; $wR_2 = 0.1518$
Final *R* indexes for all data		$R_1 = 0.0504$; $wR_2 = 0.1523$
$\Delta\rho_{max.}$ and $\Delta\rho_{min.}$		0.7 and -0.4

Table A2: Crystallographic data and refinement compound **38e.**

Compound 38e (CCDC: 2233628)		
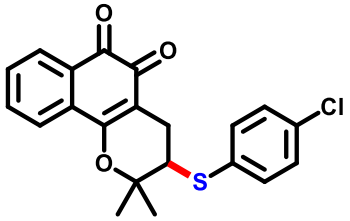		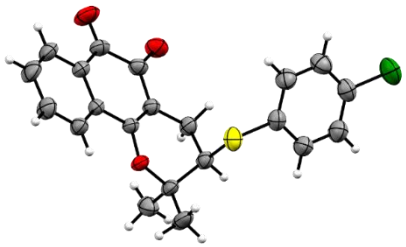
Empirical formula		$C_{21}H_{17}ClO_3S$
Formula weight (g.mol^{-1})		384.86
Crystal system		Orthorhombic
Space group		Pbca
Z		8
λ (Å)		1.54184
T (K)		299 (10)
Unit cell dimensions	*a* (Å)	9.43382(5)
	b (Å)	18.40996(11)
	c (Å)	20.29788(14)
	α (º)	90
	β (º)	90
	γ (º)	90
V (Å^3)		3525.26(4)
Density (calculated) (g/cm^{-3})		1.450
Crystal size (mm^3)		0.11 x 0.19 x 0.31
Absorption coefficient (mm^{-1})		3.182
T_{min}/T_{max}		0.398/1.000
θ range for data collection (º)		4.356 to 79.617
Reflections collected		70654
	h	-12 to 9
Index ranges	*k*	-23 to 23
	l	-25 to25
Unique reflections		3819
Unique reflections with $I>2\sigma(I)$		3713
Independent/observed reflections		3819/3713
Symmetry factor (R_{int})		0.0367
Completeness to θ = 79.617°		0.997
F (000)		1600.0
Number os parameters		238
Goodnes-of-fit no F^2		1.067
Final *R* indexes for $I>2\sigma(I)$		R_1 = 0.0352; wR_2 = 0.1021
Final *R* indexes for all data		R_1 = 0.0358; wR_2 = 0.1028
$\Delta\rho_{max}$. and $\Delta\rho_{min}$.		0.3 and -0.3

Table A3: Crystallographic data and refinement compound **38f.**

Compound 38f (CCDC: 2233627)		
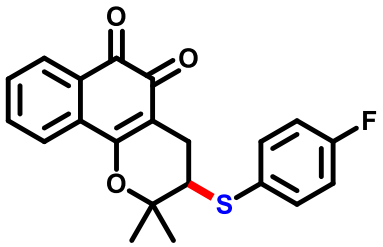		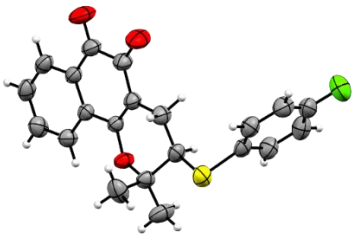
Empirical formula		$C_{21}H_{17}FO_3S$
Formula weight ($g.mol^{-1}$)		368.40
Crystal system		Triclinic
Space group		P-1
Z		2
λ (Å)		1.54184
T (K)		299 (10)
Unit cell dimensions	*a* (Å)	7.73101(9)
	b (Å)	9.04169(15)
	c (Å)	13.61467(19)
	α (º)	76.7250(13)
	β (º)	80.9117(11)
	γ (º)	73.2359(12)
V ($Å^3$)		882.58(2)
Density (calculated) (g/cm^{-3})		1.386
Crystal size (mm^3)		0.08 x 0.20 x 0.24
Absorption coefficient (mm^{-1})		1.876
T_{min}/T_{max}		0.513/1.000
θ range for data collection (º)		3.316 to 78.573
Reflections collected		18748
	h	-9 to 8
Index ranges	*k*	-11 to 11
	l	-17 to16
Unique reflections		3773
Unique reflections with $I>2\sigma(I)$		3425
Independent/observed reflections		3773/3425
Symmetry factor (R_{int})		0.026
Completeness to $\theta = 78.573°$		0.983
F (000)		384.0
Number os parameters		238
Goodnes-of-fit no F^2		1.074
Final *R* indexes for $I>2\sigma(I)$		$R_1 = 0.0360$; $wR_2 = 0.0991$
Final *R* indexes for all data		$R_1 = 0.0386$; $wR_2 = 0.1012$
$\Delta\rho_{max.}$ and $\Delta\rho_{min.}$		0.2 and -0.2

Table A4: Crystallographic data and refinement compound **38h.**

Compound 38h (CCDC: 2244270)		
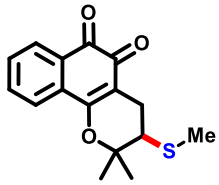		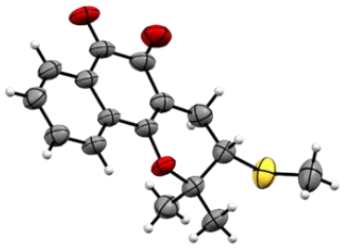
Empirical formula		$C_{16}H_{16}O_3S$
Formula weight (g.mol^{-1})		288.35
Crystal system		Monoclinic
Space group		$P2_1/n$
Z		4
λ (Å)		1.54184
T (K)		299 (10)
Unit cell dimensions	*a* (Å)	11.95852(19)
	b (Å)	8.12382(9)
	c (Å)	15.5966(3)
	α (º)	90
	β (º)	111.2439(19)
	γ (º)	90
V (Å^3)		1412.23(4)
Density (calculated) (g/cm^{-3})		1.356
Crystal size (mm^3)		0.09 x 0.17 x 0.38
Absorption coefficient (mm^{-1})		2.076
T_{min}/T_{max}		0.569/1.000
θ range for data collection (º)		4.030 to 79.543
Reflections collected		23495
	h	-15 to 15
Index ranges	*k*	-10 to 7
	l	-19 to 19
Unique reflections		3033
Unique reflections with $I>2\sigma(I)$		2694
Independent/observed reflections		3033/2694
Symmetry factor (R_{int})		0.047
Completeness to θ = 79.543°		0.987
F (000)		608.00
Number os parameters		185
Goodnes-of-fit no F^2		1.064
Final *R* indexes for $I>2\sigma(I)$		R_1 = 0.0407; wR_2 = 0.1111
Final *R* indexes for all data		R_1 = 0.0449; wR_2 = 0.1143
$\Delta\rho_{max.}$ and $\Delta\rho_{min.}$		0.5 and -0.3

Table A5: Crystallographic data and refinement compound **39c.**

Compound 39c (CCDC: 2244272)		
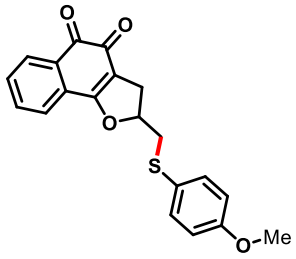		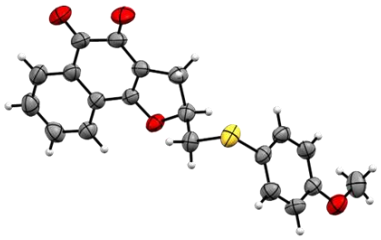
Empirical formula		$C_{20}H_{16}O_4S$
Formula weight (g.mol^{-1})		352.39
Crystal system		Monoclinic
Space group		$P2_1/n$
Z		4
λ (Å)		1.54184
T (K)		299 (10)
Unit cell dimensions	*a* (Å)	17.2794(4)
	b (Å)	4.99850(10)
	c (Å)	19.2728(4)
	α (º)	90
	β (º)	94.613(2)
	γ (º)	90
V (Å^3)		1659.22(6)
Density (calculated) (g/cm^{-3})		1.411
Crystal size (mm^3)		0.02 x 0.13 x 0.44
Absorption coefficient (mm^{-1})		1.927
T_{min}/T_{max}		0.586/1.000
θ range for data collection (º)		3.306 to 79.652
Reflections collected		32736
	h	-21 to 21
Index ranges	*k*	-6 to 6
	l	-24 to 24
Unique reflections		6432
Unique reflections with $I>2\sigma(I)$		5488
Independent/observed reflections		5488/6432
Symmetry factor (R_{int})		0.0498
Completeness to θ = 79.652°		0.989
F (000)		736.0
Number os parameters		228
Goodnes-of-fit no F^2		1.034
Final *R* indexes for $I>2\sigma(I)$		R_1 = 0.0471; wR_2 = 0.1343
Final *R* indexes for all data		R_1 = 0.0545; wR_2 = 0.1407
$\Delta\rho_{max}$. and $\Delta\rho_{min}$.		0.2 and -0.3

Table A6: Crystallographic data and refinement compound **39d.**

Compound 39d (CCDC: 2233631)		
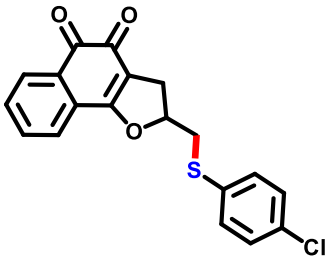		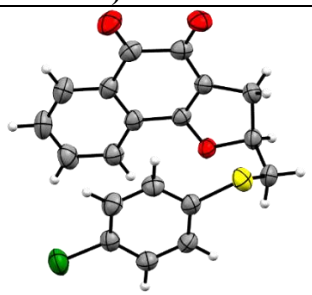
Empirical formula		$C_{19}H_{13}ClO_3S$
Formula weight (g.mol^{-1})		356.80
Crystal system		Orthorhombic
Space group		$P2_12_12_1$
Z		4
λ (Å)		1.54184
T (K)		299 (10)
Unit cell dimensions	a (Å)	5.53116(6)
	b (Å)	8.82081(9)
	c (Å)	32.2421(3)
	α (º)	90
	β (º)	90
	γ (º)	90
V (Å^3)		1573.07(3)
Density (calculated) (g/cm^{-3})		1.507
Crystal size (mm^3)		0.02 x 0.04 x 0.24
Absorption coefficient (mm^{-1})		3.519
T_{min} /T_{max}		0.665/1.000
θ range for data collection (º)		2.741 to 79.681
Reflections collected		32374
	h	-7 to 6
Index ranges	k	-11 to 11
	l	-40 to 33
Unique reflections		3387
Unique reflections with $I>2\sigma(I)$		3214
Independent/observed reflections		3387/3214
Symmetry factor (R_{int})		0.045
Completeness to θ = 79.681°		0.997
F (000)		736.0
Number os parameters		218
Goodnes-of-fit no F^2		1.063
Final R indexes for $I>2\sigma(I)$		R_1 = 0.0278; wR_2 = 0.0689
Final R indexes for all data		R_1 = 0.0297; wR_2 = 0.0698
$\Delta\rho_{max.}$ and $\Delta\rho_{min.}$		0.1 and -0.2

Table A7: Crystallographic data and refinement compound **39e.**

Compound 39e (CCDC: 2233630)		
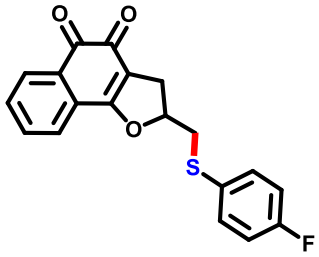		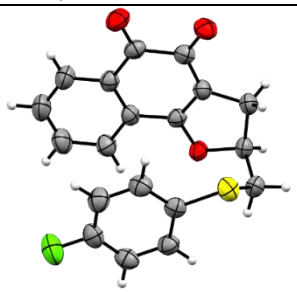
Empirical formula		$C_{19}H_{13}FO_3S$
Formula weight (g.mol^{-1})		340.35
Crystal system		Orthorhombic
Space group		$P2_12_12_1$
Z		4
λ (Å)		1.54184
T (K)		299 (10)
Unit cell dimensions	*a* (Å)	5.50050(4)
	b (Å)	8.86820(5)
	c (Å)	31.04540(16)
	α (º)	90
	β (º)	90
	γ (º)	90
V (Å^3)		1514.382(15)
Density (calculated) (g/cm^{-3})		1.493
Crystal size (mm^3)		0.19 x 0.34 x 0.35
Absorption coefficient (mm^{-1})		2.139
T_{min} /T_{max}		0.635/1.000
θ range for data collection (º)		2.784 to 78.581
Reflections collected		63543
	h	-6 to 6
Index ranges	*k*	-11 to 11
	l	-39 to 39
Unique reflections		3259
Unique reflections with $I>2\sigma(I)$		3216
Independent/observed reflections		3259/3216
Symmetry factor (R_{int})		0.054
Completeness to θ = 78.581°		0.996
F (000)		704.0
Number os parameters		217
Goodnes-of-fit no F^2		1.069
Final *R* indexes for $I>2\sigma(I)$		R_1 = 0.0301; wR_2 = 0.0841
Final *R* indexes for all data		R_1 = 0.0304; wR_2 = 0.0844
$\Delta\rho_{max.}$ and $\Delta\rho_{min.}$		0.2 and -0.2

Table A8: Crystallographic data and refinement compound **40a.**

Compound 40a (CCDC: 2233728)		
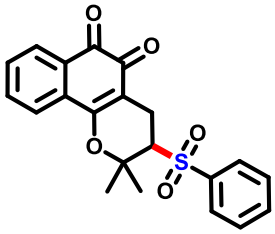		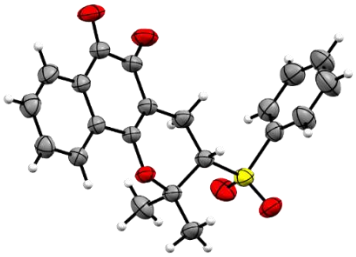
Empirical formula		$C_{21}H_{18}O_5S$
Formula weight (g.mol^{-1})		382.41
Crystal system		Monoclinic
Space group		$P2_1/n$
Z		4
λ (Å)		1.54184
T (K)		299 (10)
Unit cell dimensions	*a* (Å)	9.35252(9)
	b (Å)	16.05685(11)
	c (Å)	12.55825(11)
	α (º)	90
	β (º)	103.6553(9)
	γ (º)	90
V (Å^3)		1832.59(3)
Density (calculated) (g/cm^{-3})		1.386
Crystal size (mm^3)		0.16 x 0.39 x 0.51
Absorption coefficient (mm^{-1})		1.831
T_{min}/T_{max}		0.160/1.000
θ range for data collection (º)		4.551 to 79.779
Reflections collected		38340
	h	-11 to 11
Index ranges	*k*	-20 to 17
	l	-15 to 15
Unique reflections		3947
Unique reflections with $I>2\sigma(I)$		3685
Independent/observed reflections		3947/3685
Symmetry factor (R_{int})		0.042
Completeness to θ = 79.779°		0.991
F (000)		800.0
Number os parameters		247
Goodnes-of-fit no F^2		1.044
Final *R* indexes for $I>2\sigma(I)$		R_1 = 0.0370; wR_2 = 0.1007
Final *R* indexes for all data		R_1 = 0.0387; wR_2 = 0.1020
$\Delta\rho_{max}$. and $\Delta\rho_{min}$.		0.3 and -0.3

Table A9: Crystallographic data and refinement compound **40b.**

Compound 6b (CCDC: 2244273)		
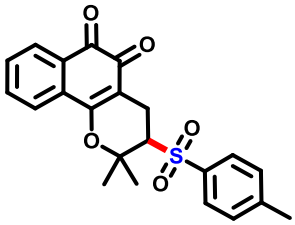		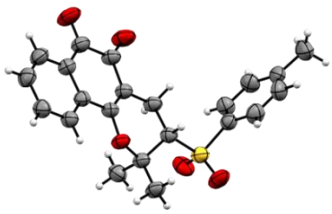
Empirical formula		$C_{22}H_{20}O_5S$
Formula weight (g.mol^{-1})		396.44
Crystal system		Triclinic
Space group		P-1
Z		2
λ (Å)		1.54184
T (K)		299 (10)
Unit cell dimensions	*a* (Å)	8.08875(10)
	b (Å)	9.36581(15)
	c (Å)	12.64120(19)
	α (º)	94.5958(13)
	β (º)	92.7529(11)
	γ (º)	95.4115(11)
V (Å^3)		948.84(2)
Density (calculated) (g/cm^{-3})		1.388
Crystal size (mm^3)		0.04 x 0.15 x 0.23
Absorption coefficient (mm^{-1})		1.788
T_{min}/T_{max}		0.648/1.000
θ range for data collection (º)		3.513 to 79.650
Reflections collected		15990
	h	-8 to 10
Index ranges	*k*	-11 to 11
	l	-15 to 16
Unique reflections		4013
Unique reflections with $I>2\sigma(I)$		3509
Independent/observed reflections		3509/4013
Symmetry factor (R_{int})		0.032
Completeness to $\theta = 79.779°$		0.973
F (000)		416.0
Number os parameters		257
Goodnes-of-fit no F^2		1.082
Final *R* indexes for $I>2\sigma(I)$		$R_1 = 0.0374$; $wR_2 = 0.1021$
Final *R* indexes for all data		$R_1 = 0.0424$; $wR_2 = 0.1055$
$\Delta\rho_{max.}$ and $\Delta\rho_{min.}$		0.2 and -0.3

Table A10: Crystallographic data and refinement compound **41b.**

Compound 41b (CCDC: 2278374)		
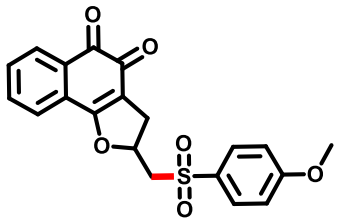		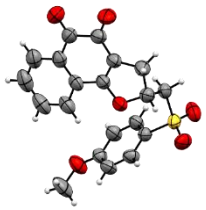
Empirical formula		$C_{22}H_{16}O_6S$
Formula weight (g.mol^{-1})		384.39
Crystal system		Monoclinic
Space group		$P2_1/c$
Z		4
λ (Å)		1.54184
T (K)		299 (10)
Unit cell dimensions	a (Å)	5.59340(10)
	b (Å)	16.6363(2)
	c (Å)	18.9290(2)
	α (º)	90
	β (º)	91.3440(10)
	γ (º)	90
V (Å^3)		1760.92(4)
Density (calculated) (g/cm^{-3})		1.450
Crystal size (mm^3)		0.11 x 0.24 x 0.27
Absorption coefficient (mm^{-1})		1.954
T_{min}/T_{max}		0.316/1.000
θ range for data collection (º)		3.537 to 79.766
Reflections collected		43839
	h	-7 to 7
Index ranges	k	-21 to 21
	l	-24 to 20
Unique reflections		3792
Unique reflections with $I>2\sigma(I)$		3360
Independent/observed reflections		3792/3360
Symmetry factor (R_{int})		0.043
Completeness to θ = 79.685°		0.990
F (000)		800.0
Number os parameters		245
Goodnes-of-fit no F^2		1.075
Final R indexes for $I>2\sigma(I)$		R_1 = 0.0516; wR_2 = 0.1477
Final R indexes for all data		R_1 = 0.0560; wR_2 = 0.1516
$\Delta\rho_{max.}$ and $\Delta\rho_{min.}$		0.5 and -0.3

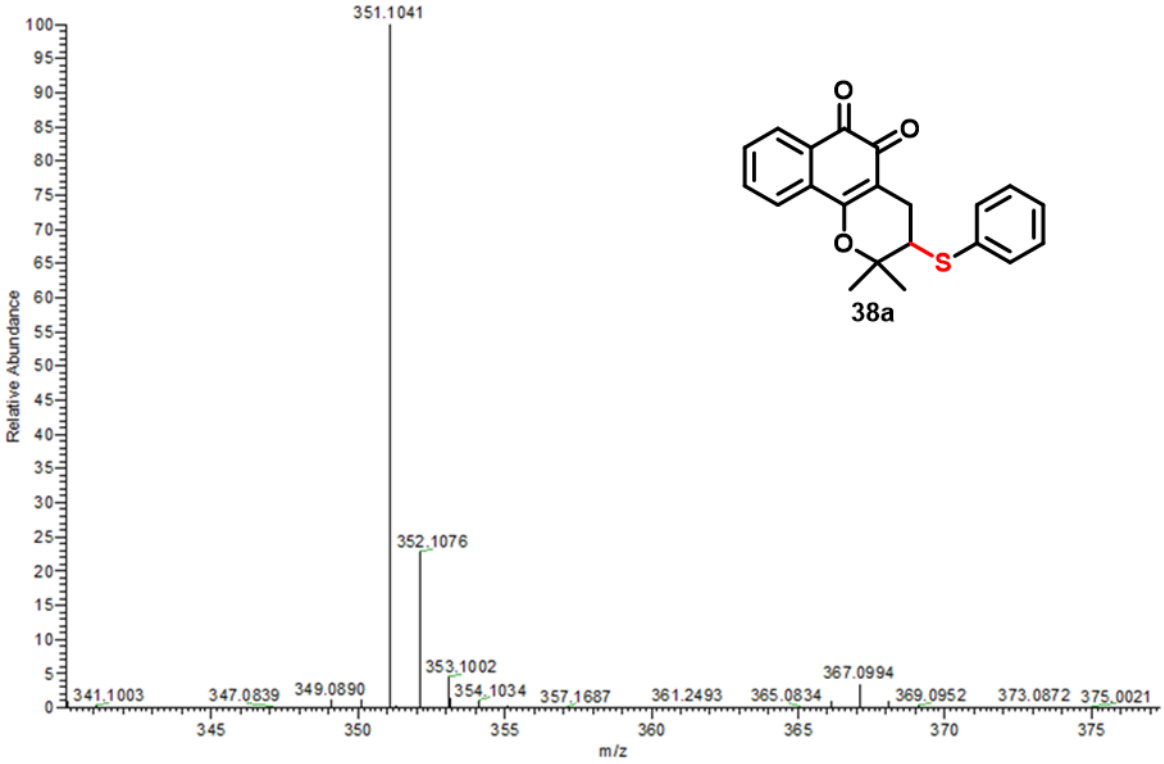

Figure A73: HRMS (ESI$^+$) of compound **38a**.

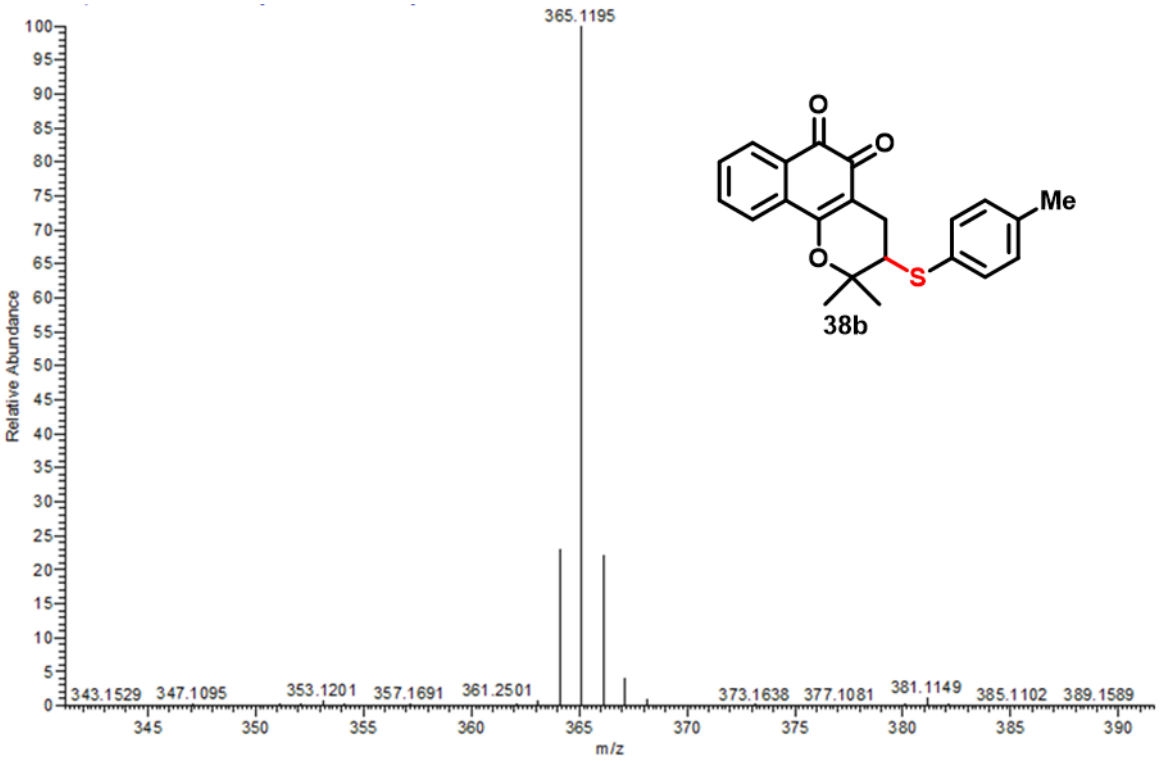

Figure A74: HRMS (ESI$^+$) of compound **38b.**

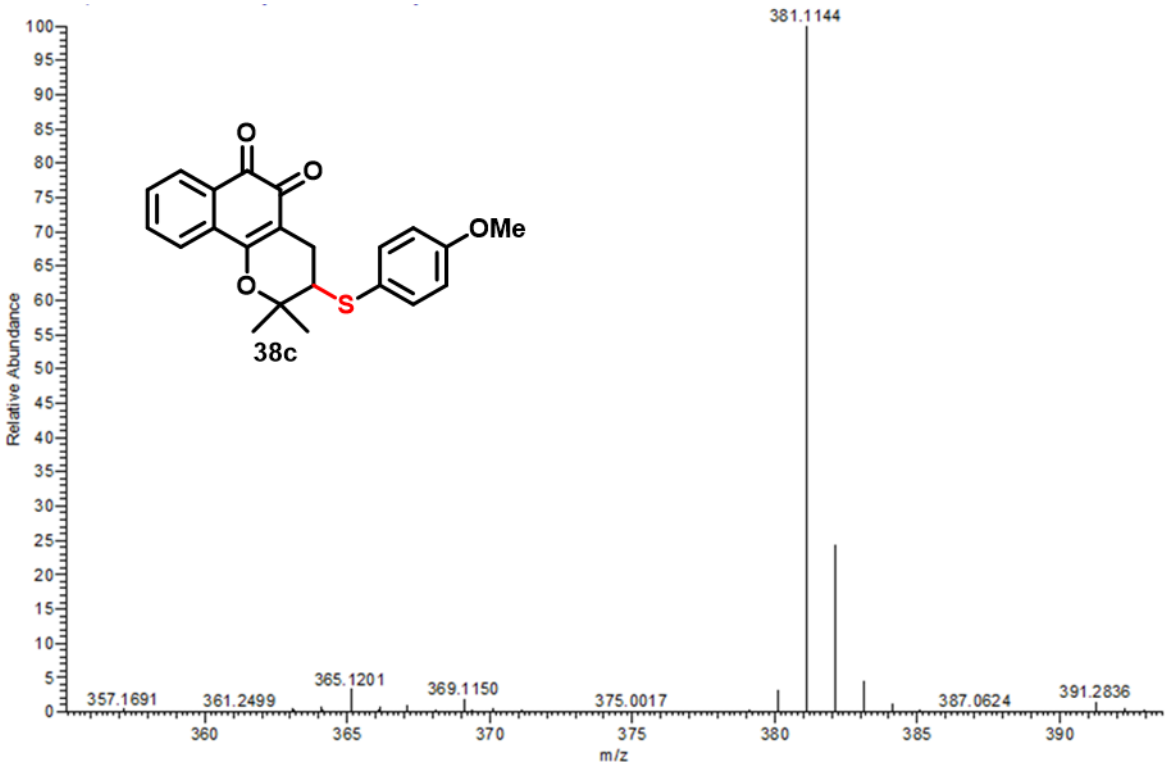

Figure A75: HRMS (ESI$^+$) of compound **38c.**

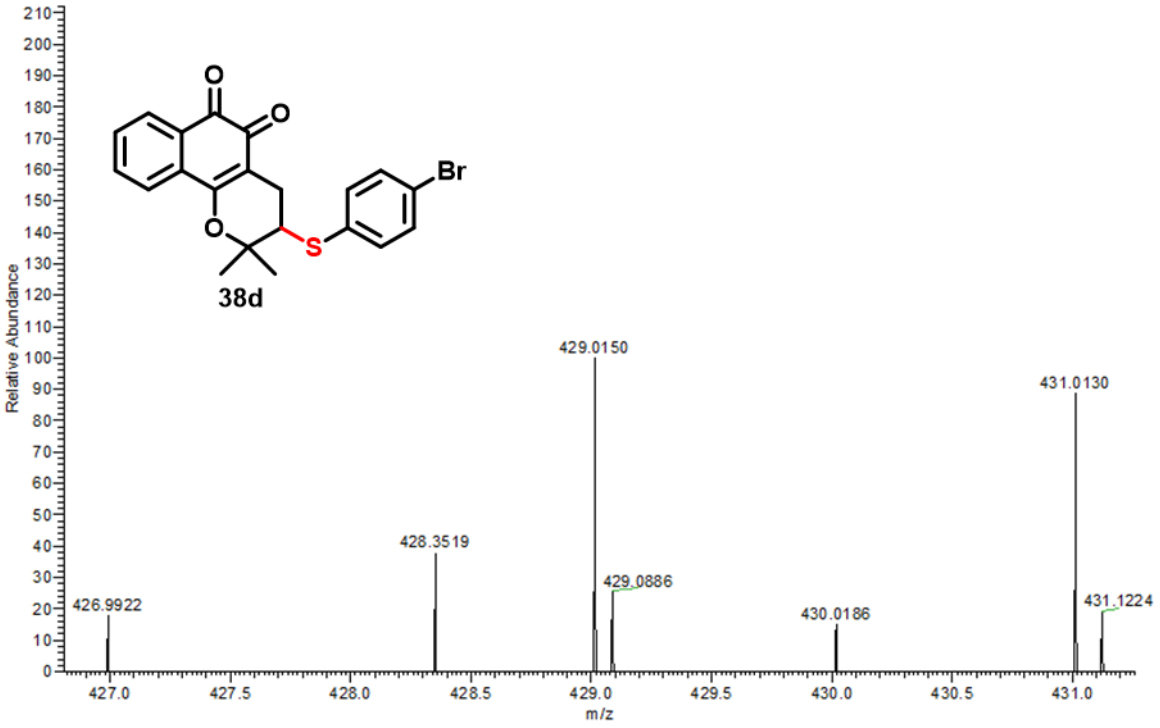

Figure A76: HRMS (ESI$^+$) of compound **38d.**

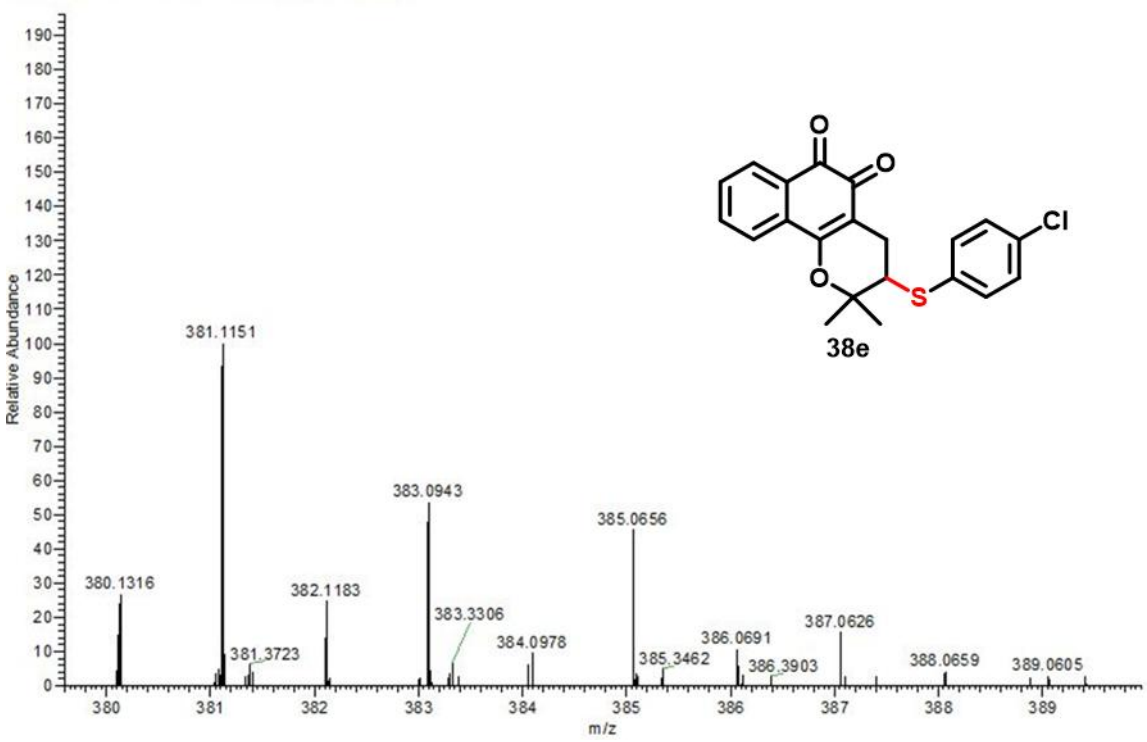

Figure A77: HRMS (ESI$^+$) of compound **38e.**

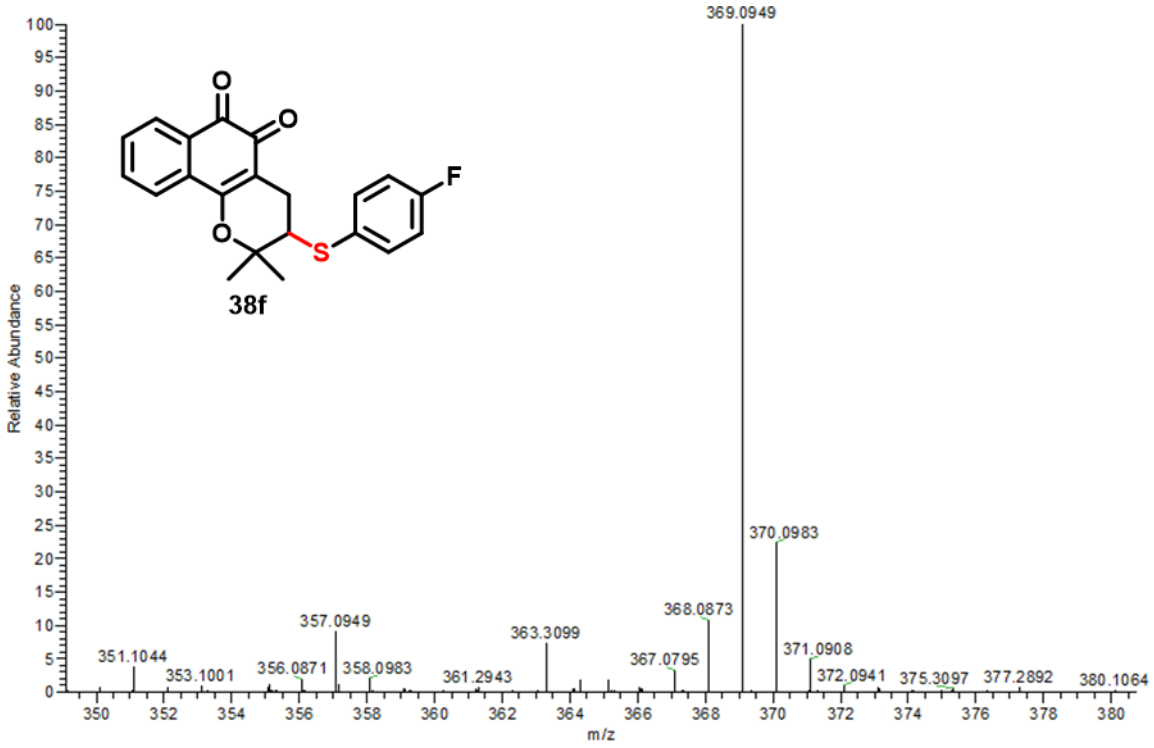

Figure A78: HRMS (ESI$^+$) of compound **38f.**

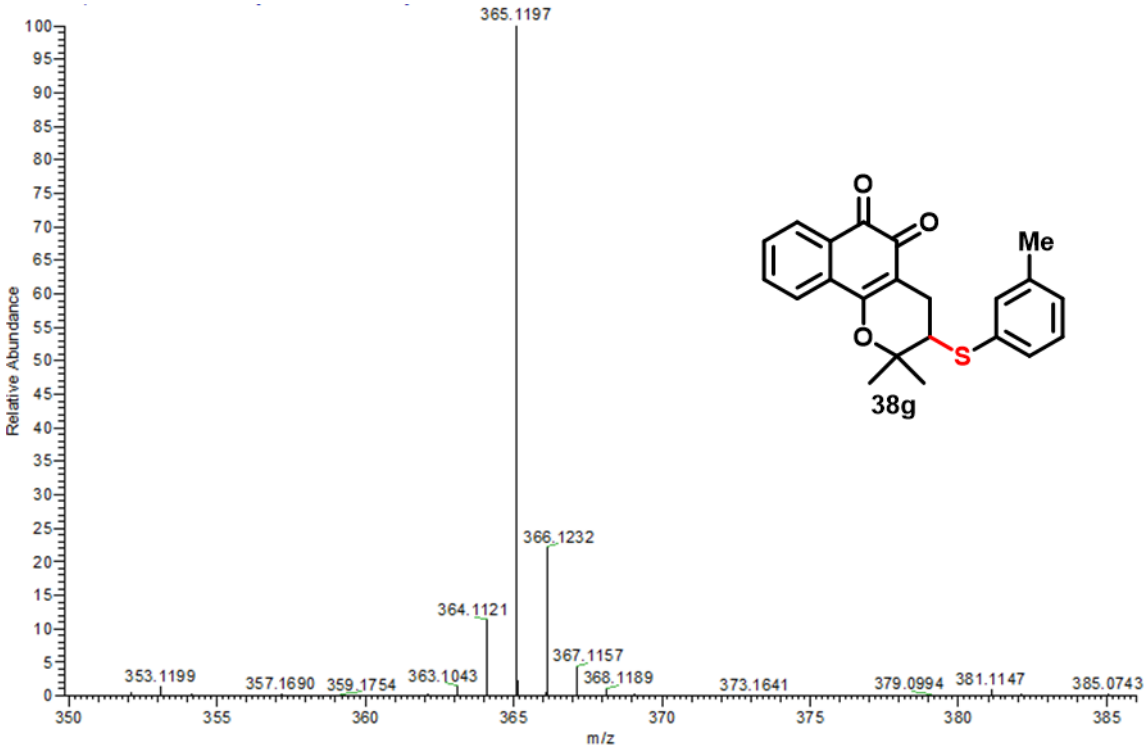

Figure A79: HRMS (ESI$^+$) of compound **38g.**

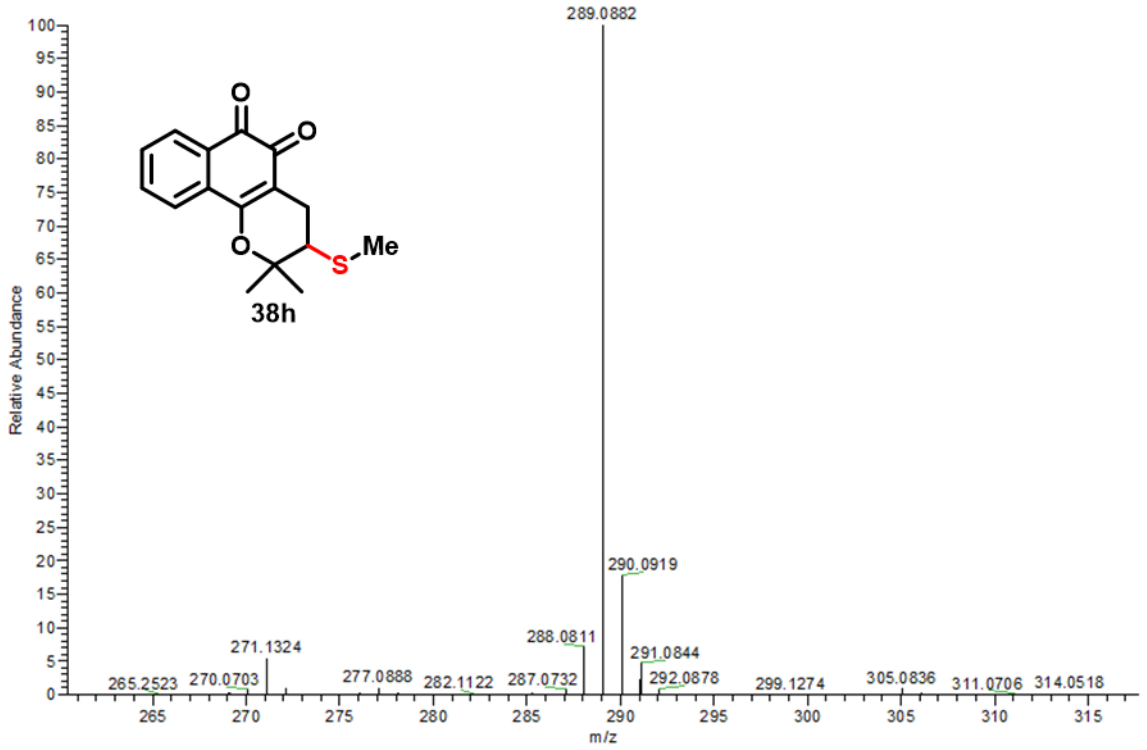

Figure A80: HRMS (ESI$^+$) of compound **38h.**

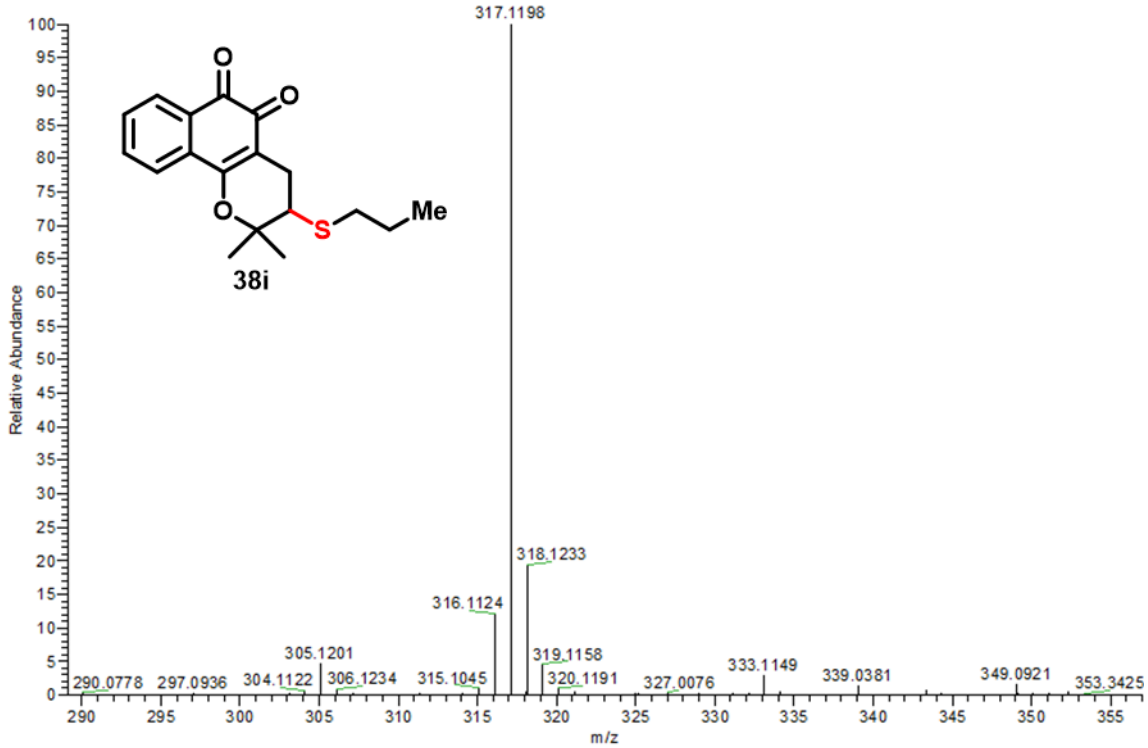

Figure A81: HRMS (ESI$^+$) of compound **38i.**

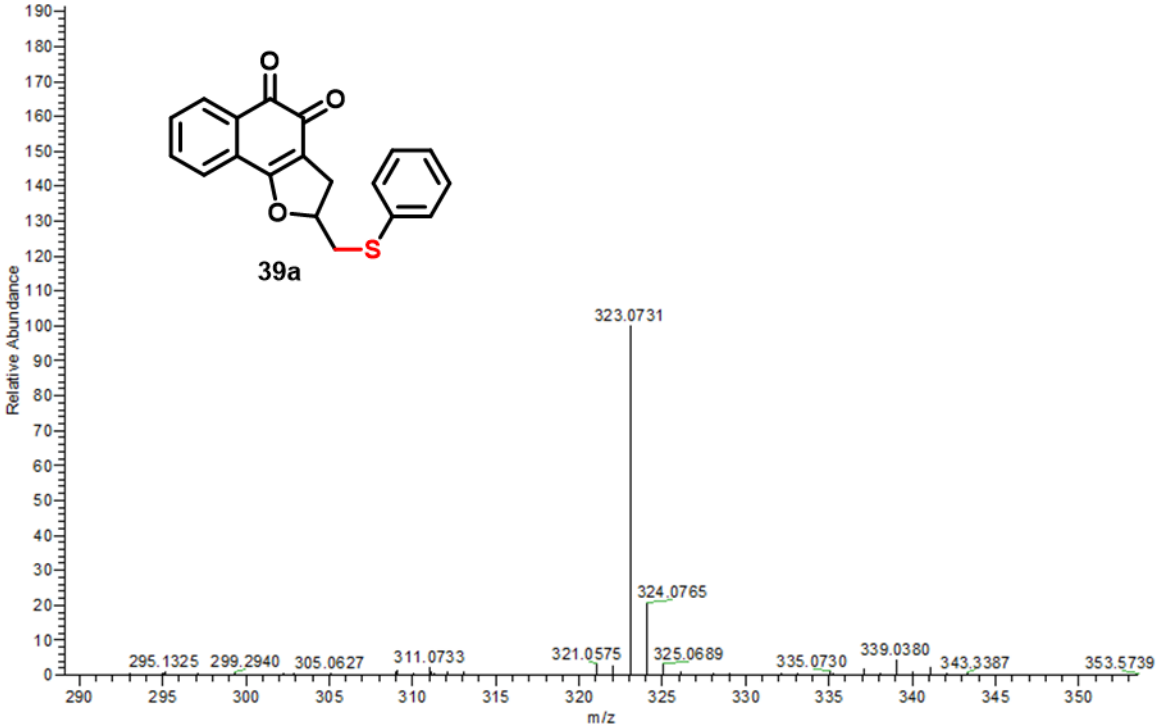

Figure A82: HRMS (ESI$^+$) of compound **39a.**

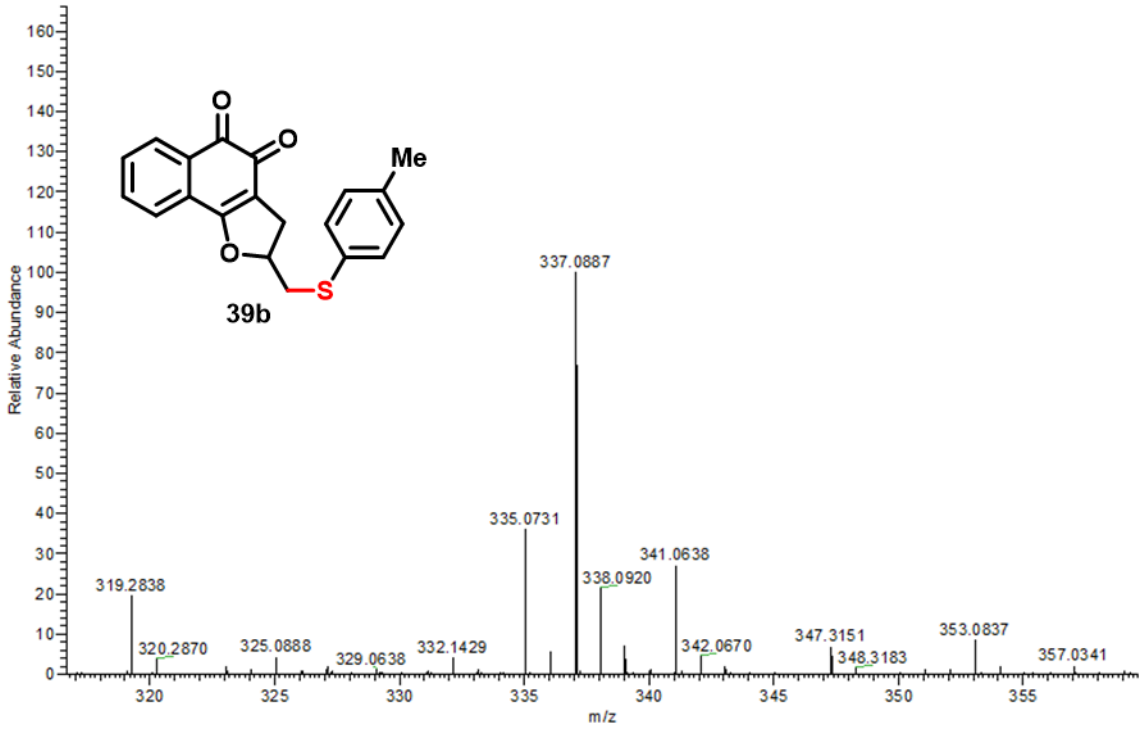

Figure A83: HRMS (ESI$^+$) of compound **39b.**

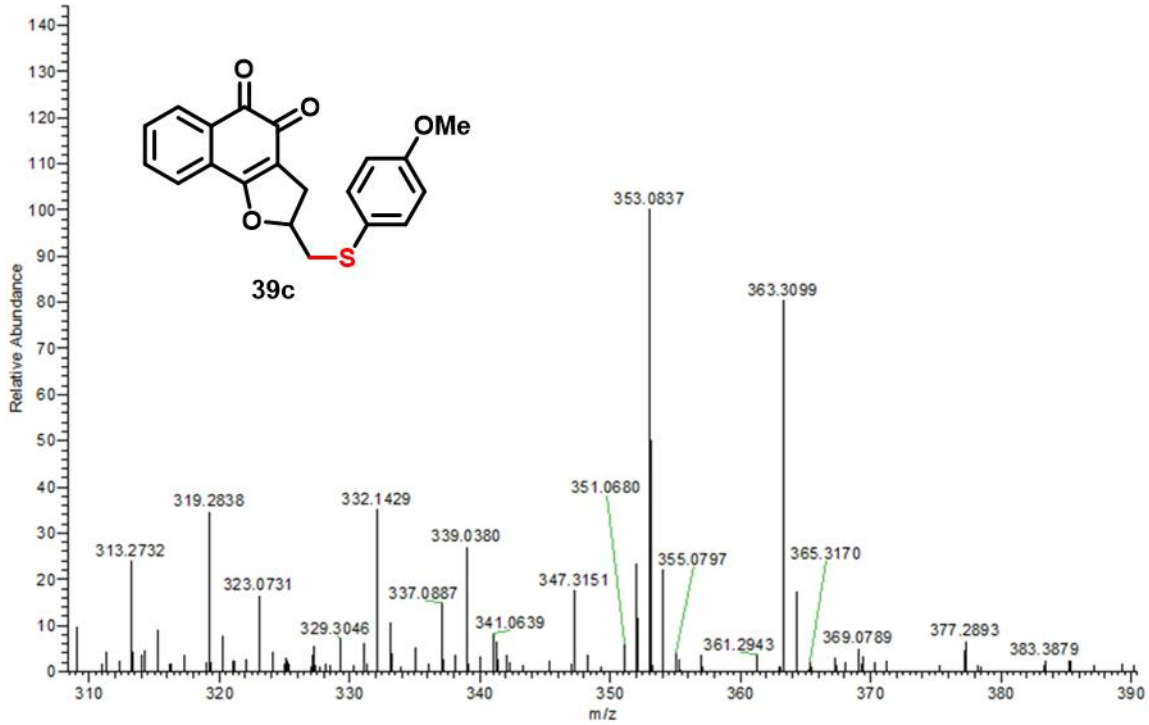

Figure A84: HRMS (ESI$^+$) of compound **39c.**

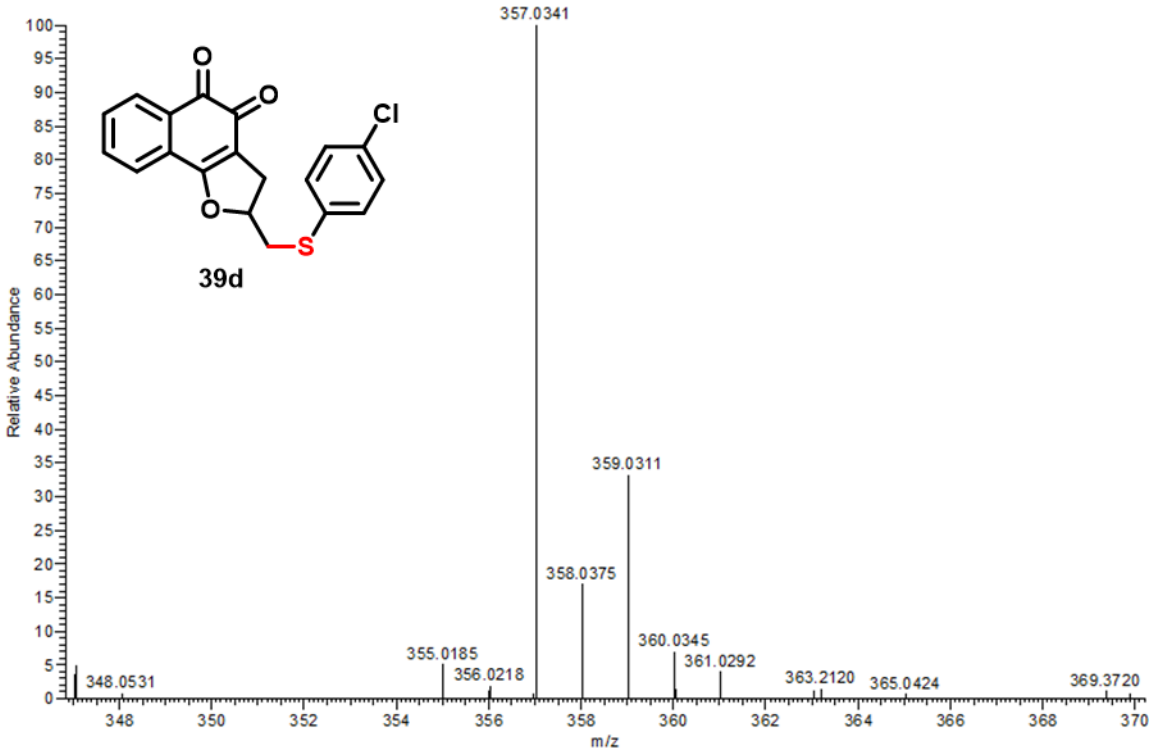

Figure A85: HRMS (ESI$^+$) of compound **39d.**

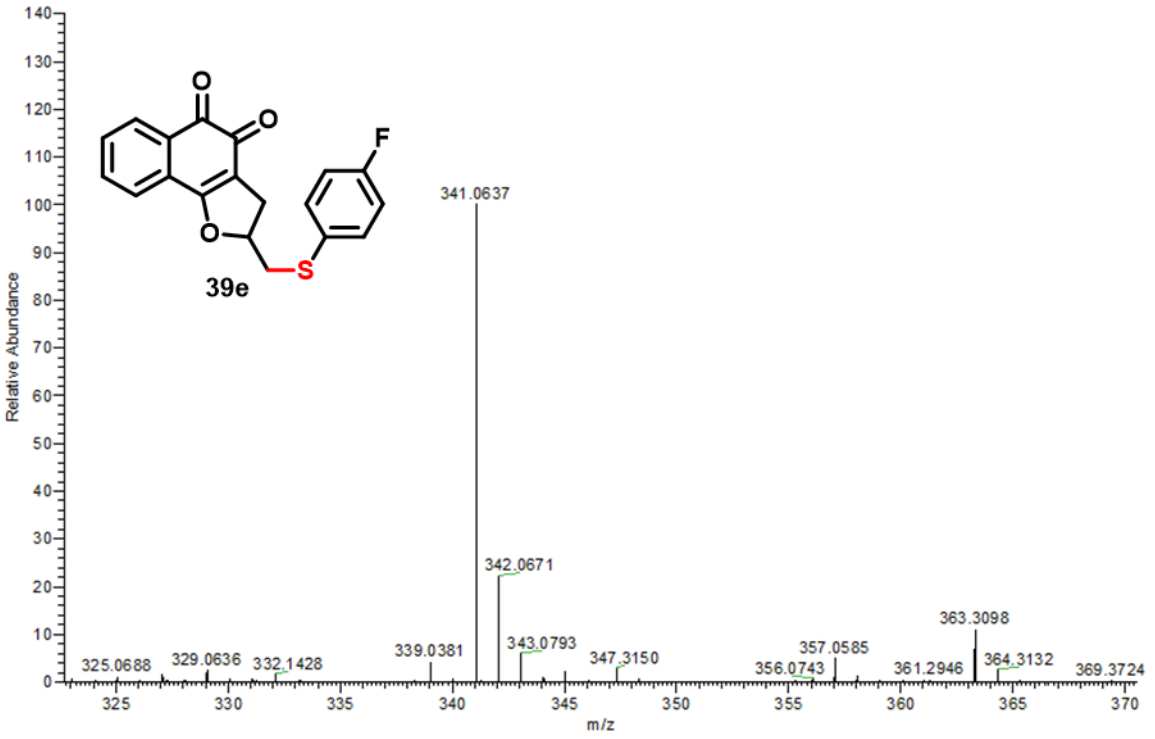

Figure A86: HRMS (ESI$^+$) of compound **39e.**

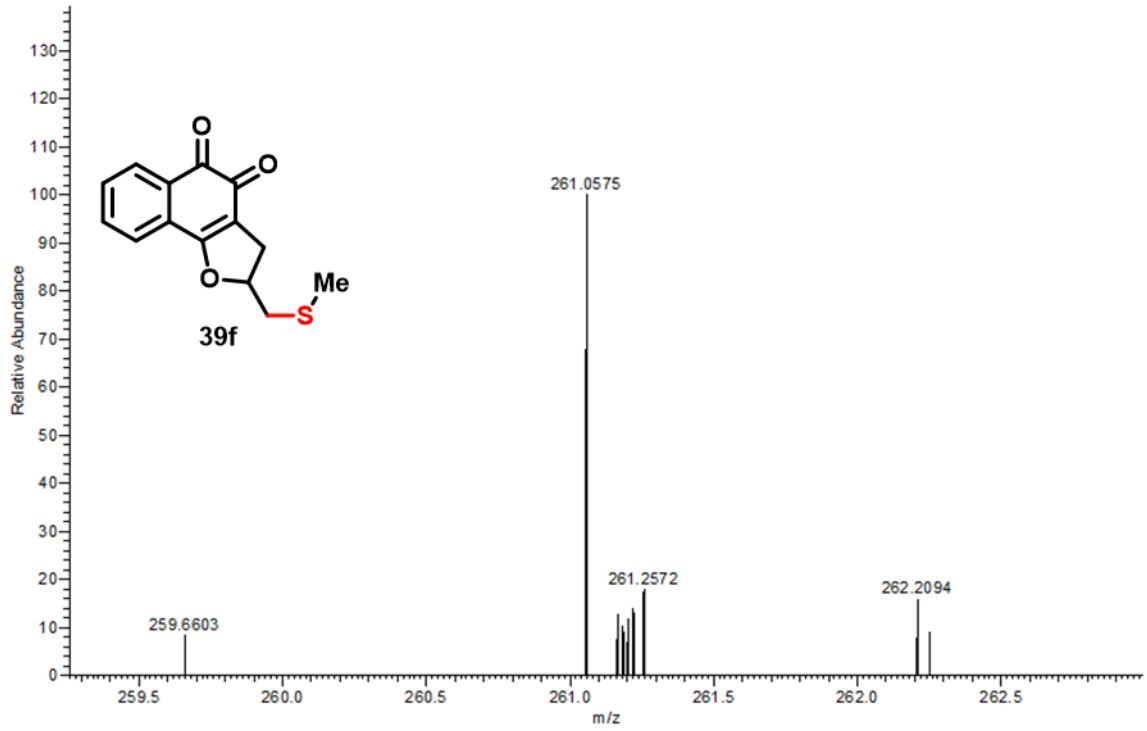

Figure A87: HRMS (ESI$^+$) of compound **39f.**

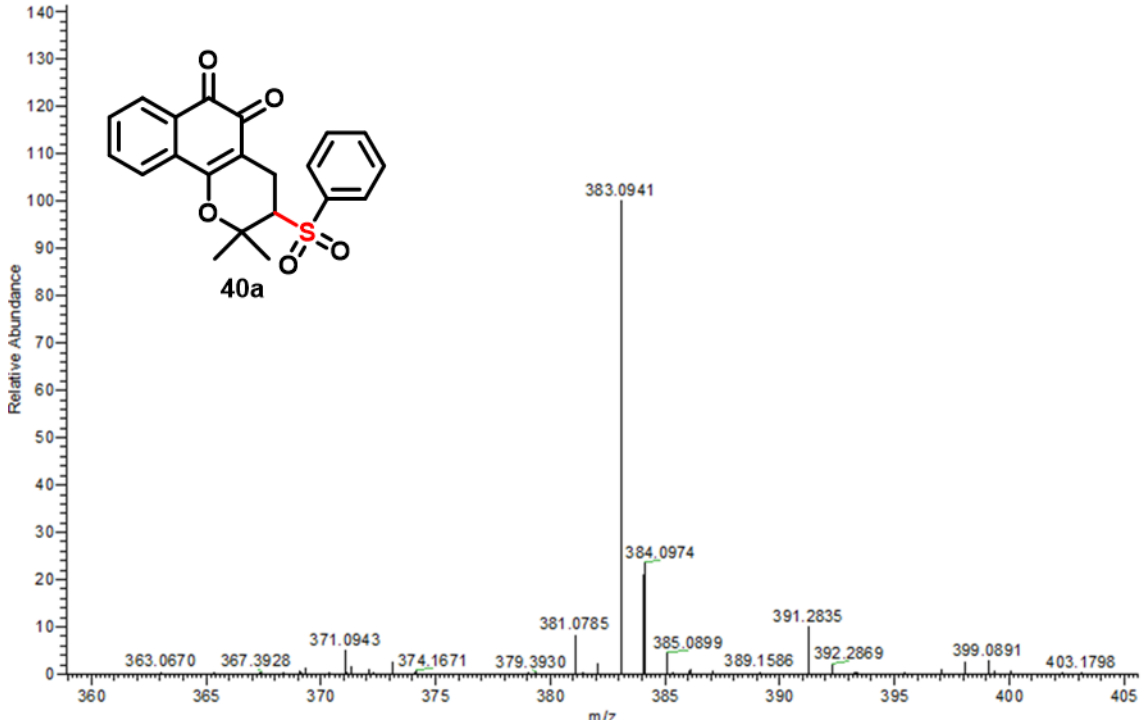

Figure A88: HRMS (ESI$^+$) of compound **40a.**

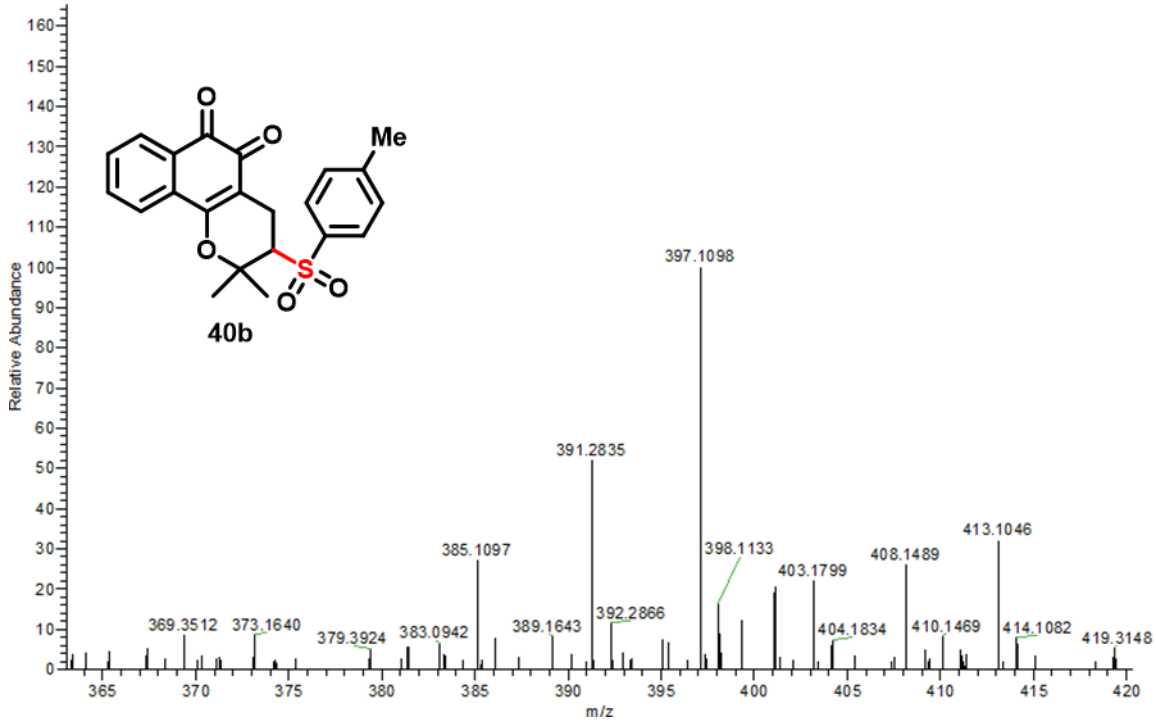

Figure A89: HRMS (ESI$^+$) of compound **40b.**

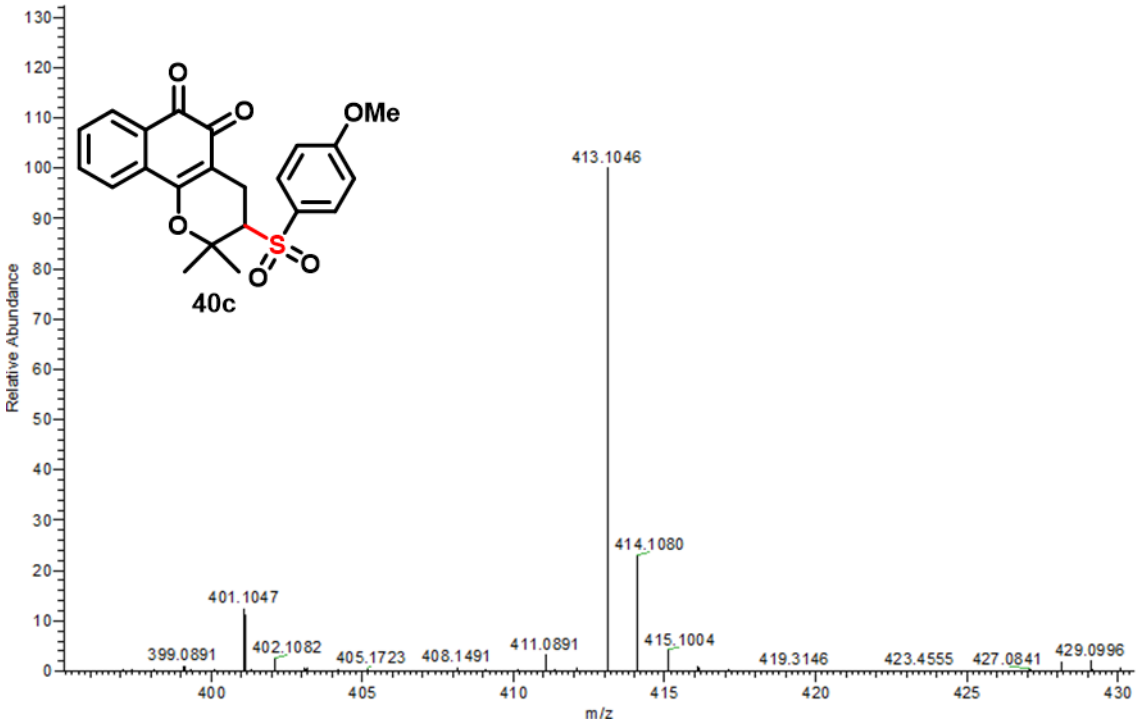

Figure A90: HRMS (ESI$^+$) of compound **40c.**

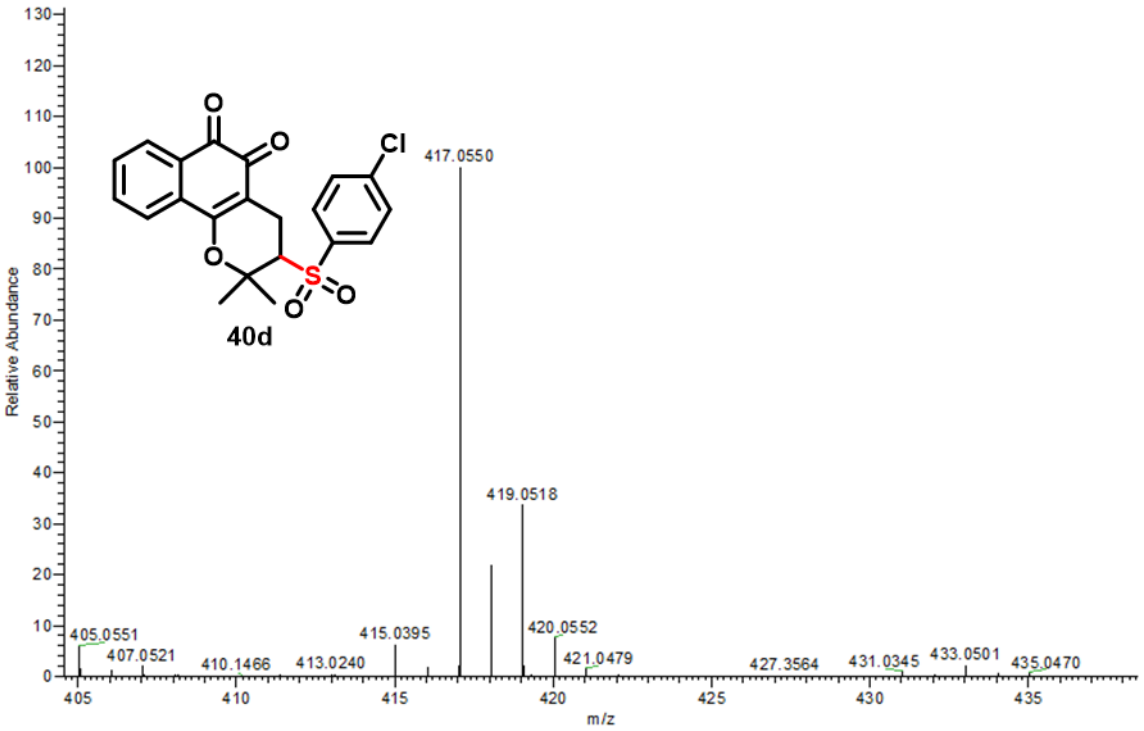

Figure A91: HRMS (ESI$^+$) of compound **40d.**

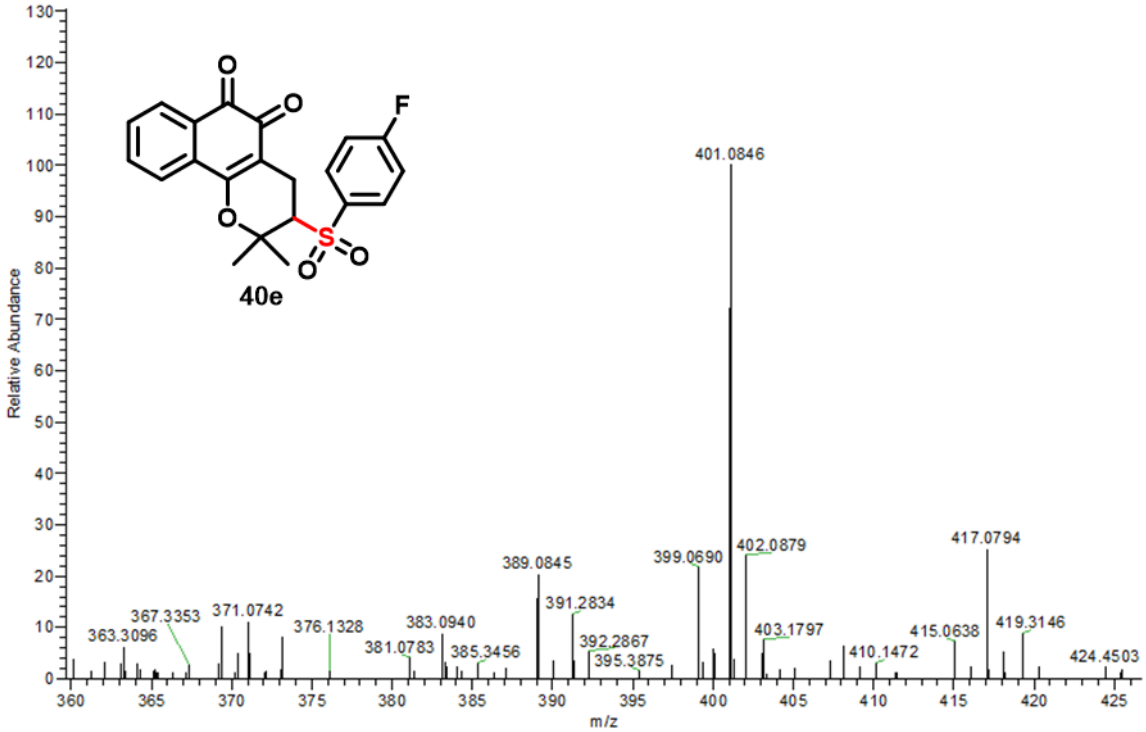

Figure A92: HRMS (ESI$^+$) of compound **40e.**

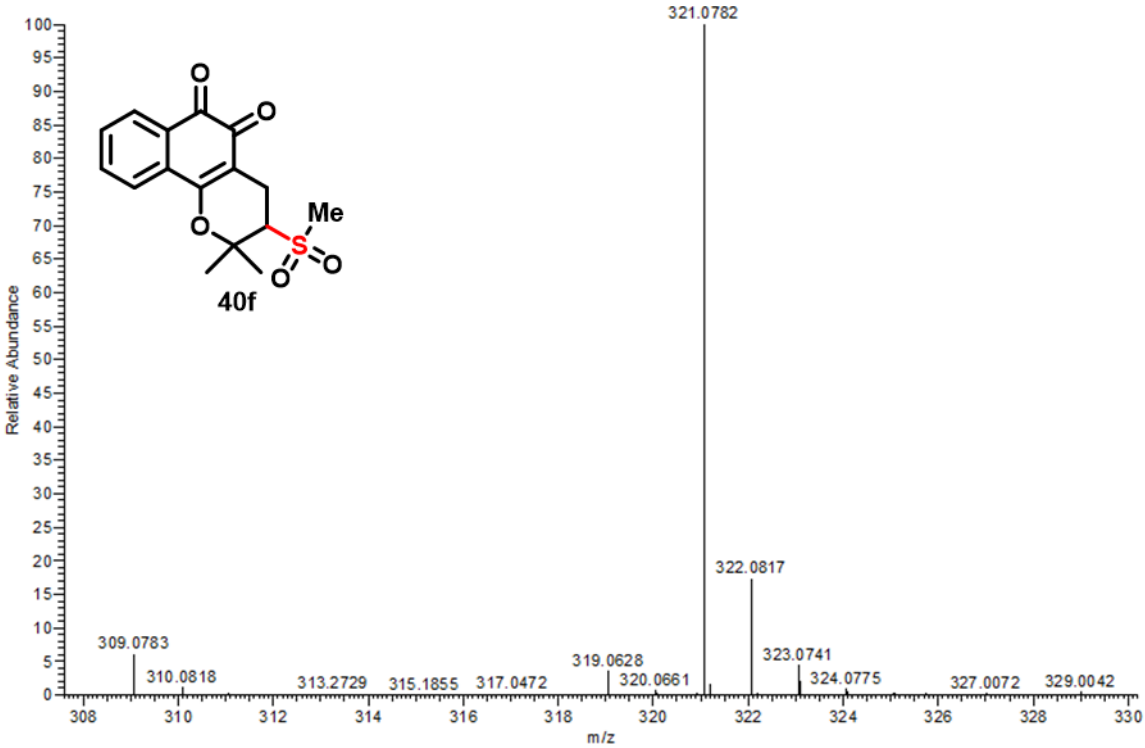

Figure A93: HRMS (ESI$^+$) of compound **40f.**

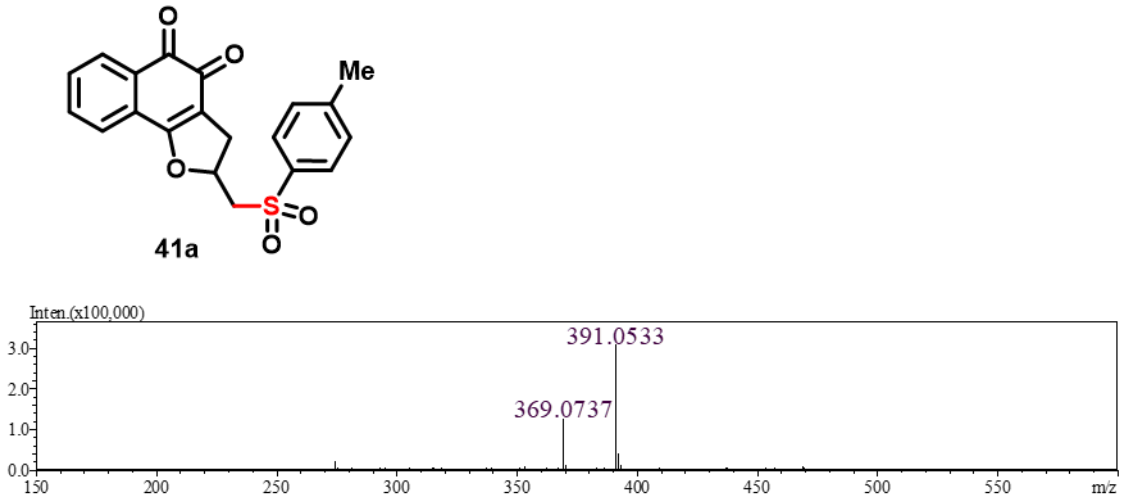

Figure A94: HRMS (ESI$^+$) of compound **41a.**

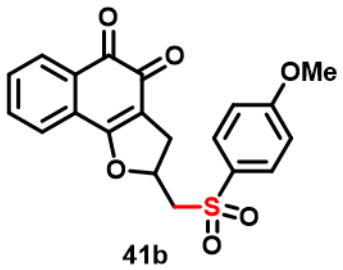

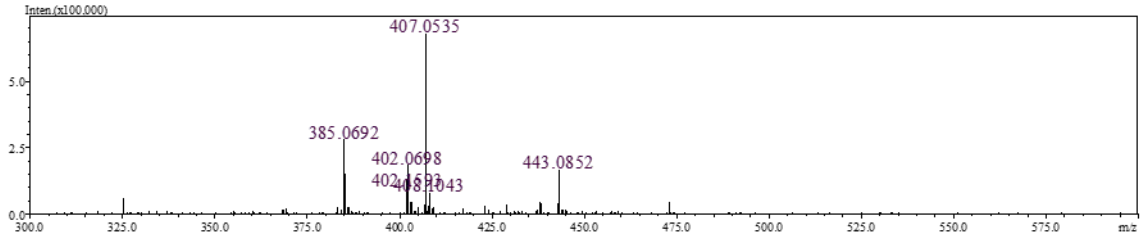

Figure A95: HRMS (ESI$^+$) of compound **41b.**

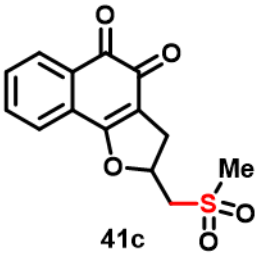

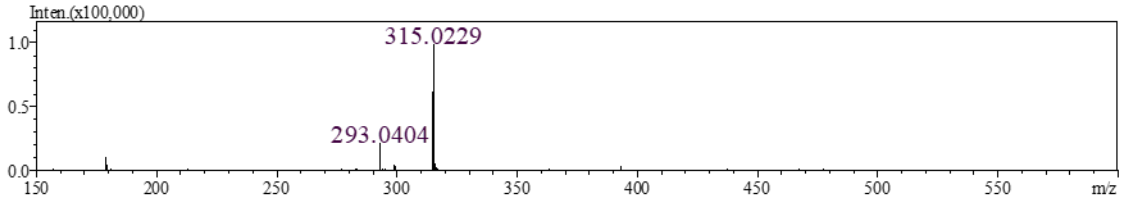

Figure A96: HRMS (ESI$^+$) of compound **41c.**

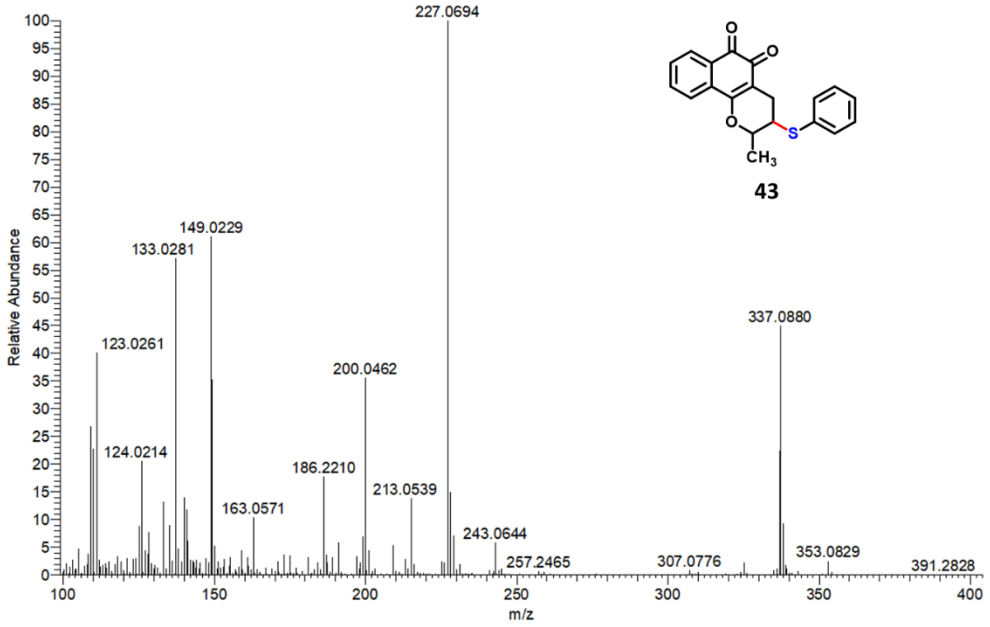

Figure A97: HRMS (ESI$^+$) of compound **43.**

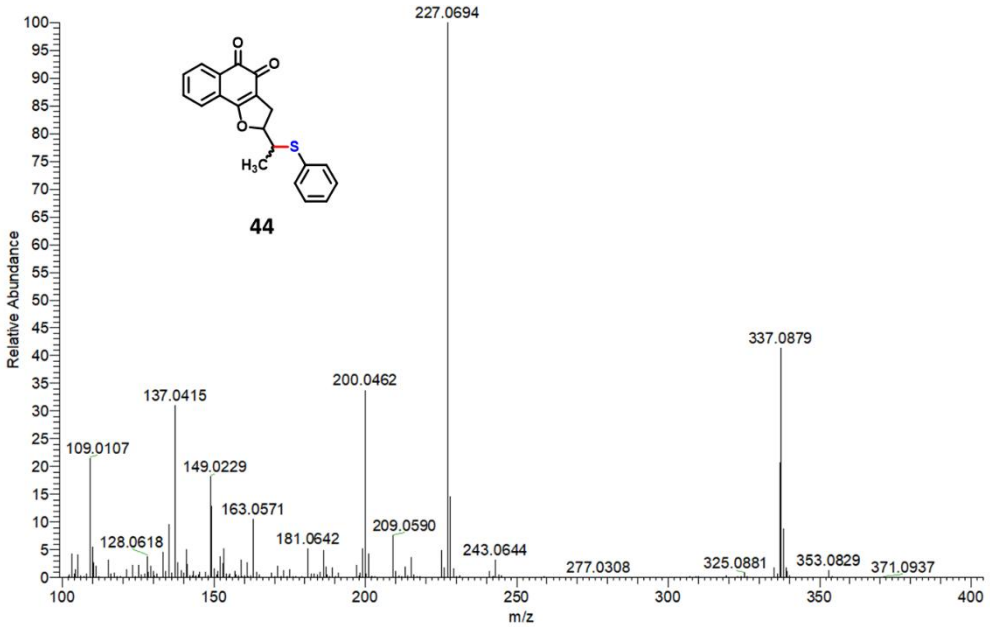

Figure A98: HRMS (ESI$^+$) of compound **44.**

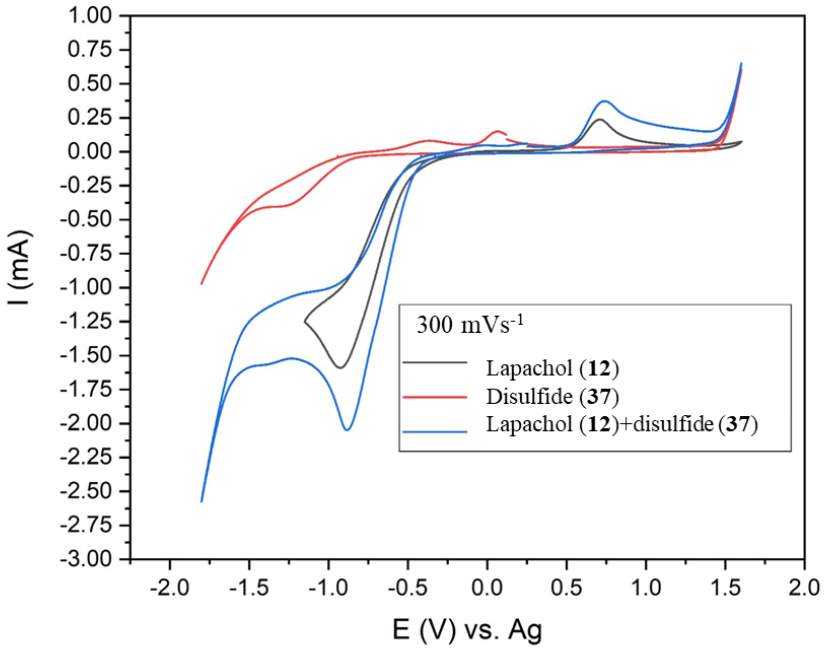

Figure A99: Cyclic voltammograms in MeCN at 300 mVs^{-1}. Concentration of nBu$_4$NPF$_6$, lapachol (**12**) (black), disulfide (**37**) (red), and lapachol (**12**) + disulfide (**37**) (blue) 0.02 M in MeCN.

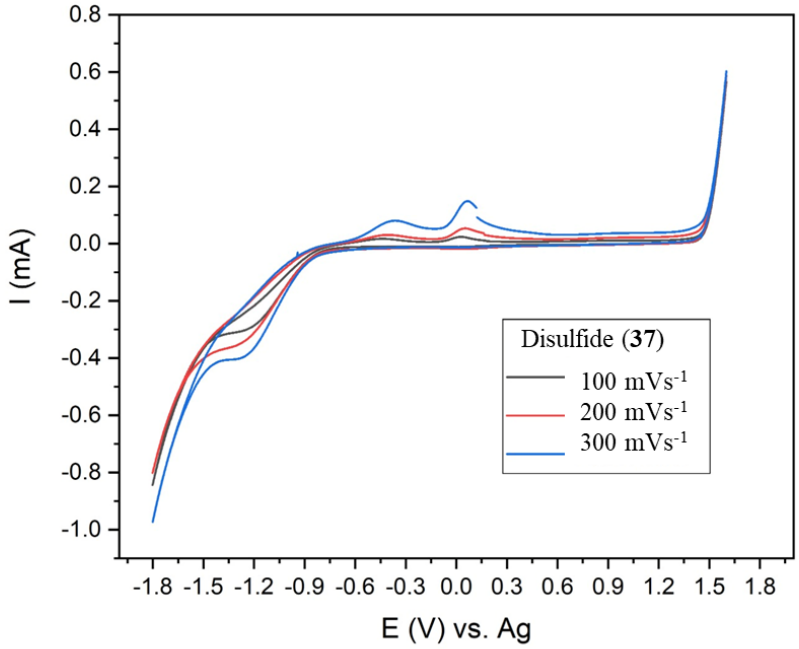

Figure A100: Cyclic voltammograms in MeCN. Concentration nBu$_4$NPF$_6$ and disulfide (**37**) 0.02 M in MeCN. 100 mVs^{-1} (black); 200 mVs^{-1} (red); 300 mVs^{-1} (blue).

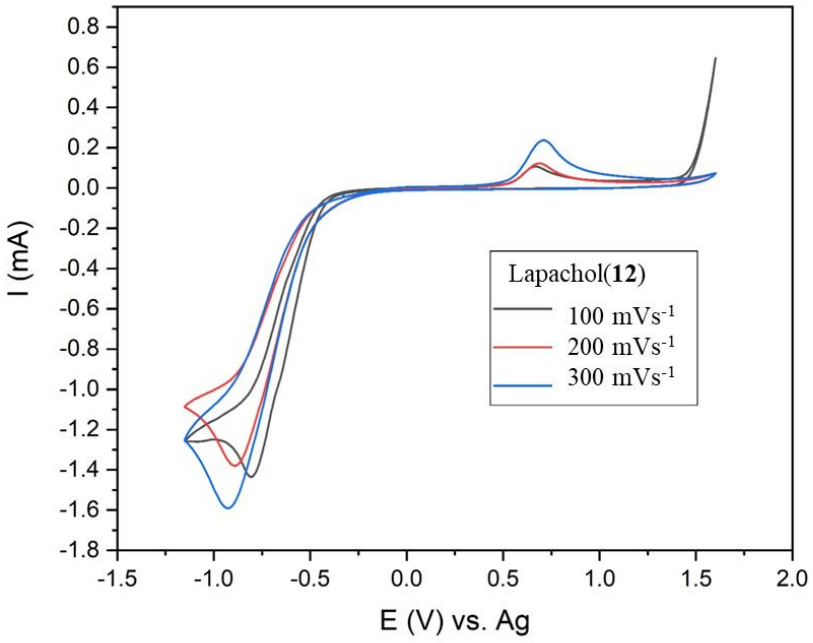

Figure A101: Cyclic voltammograms in MeCN. Concentration nBu$_4$NPF$_6$ and lapachol (**12**) 0.02 M in MeCN. 100 mVs^{-1} (black); 200 mVs^{-1} (red); 300 mVs^{-1} (blue).

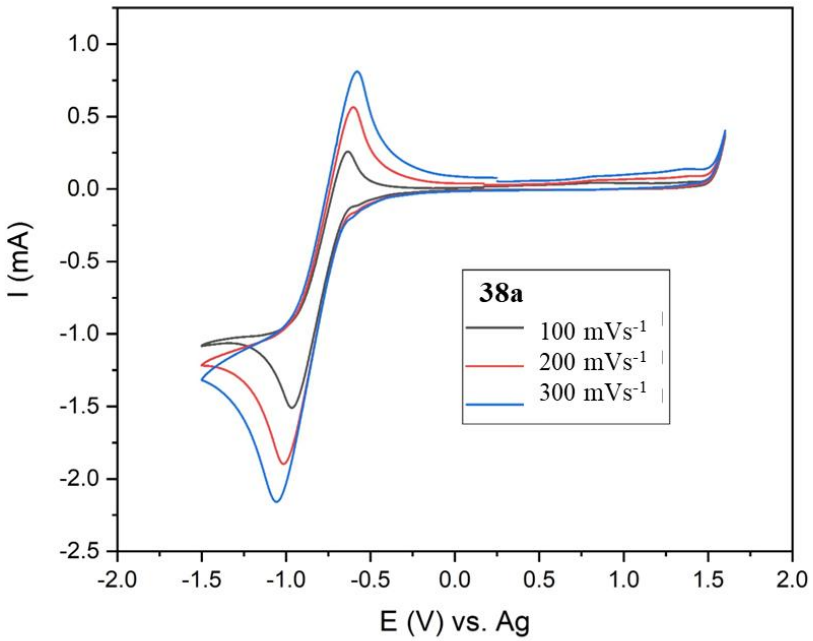

Figure A102: Cyclic voltammograms in MeCN. Concentration nBu$_4$NPF$_6$ and **38a** 0.02 M in MeCN. 100 mVs^{-1} (black); 200 mVs^{-1} (red); 300 mVs^{-1} (blue).

APPENDICES B - Characterization of the compounds

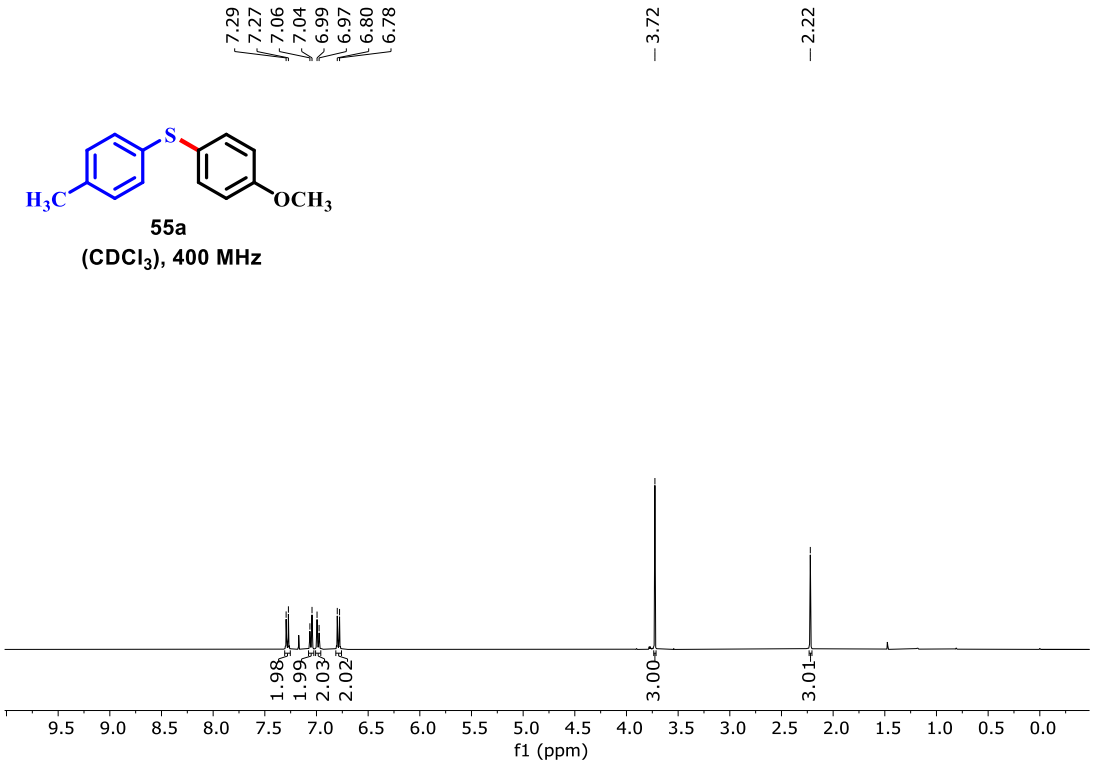

Figure B1: ^{1}H NMR spectrum of compound **55a** (400 MHz, $CDCl_3$).

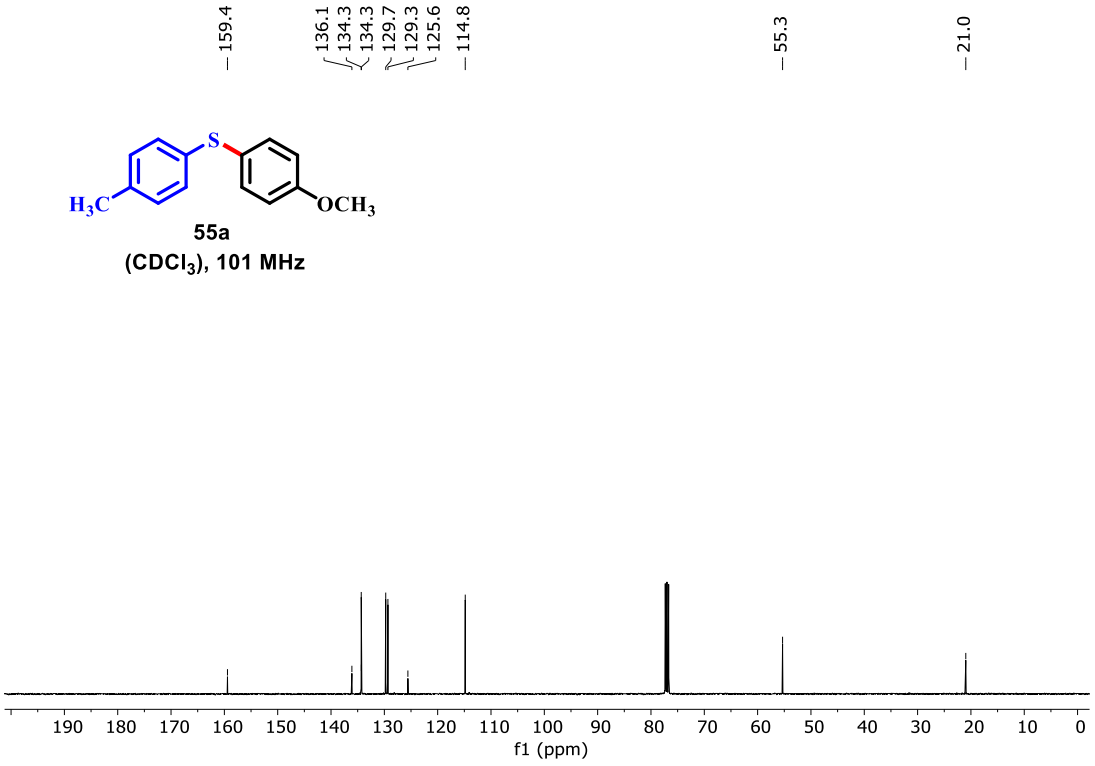

Figure B2: ^{13}C NMR spectrum of compound **55a** (101 MHz, $CDCl_3$).

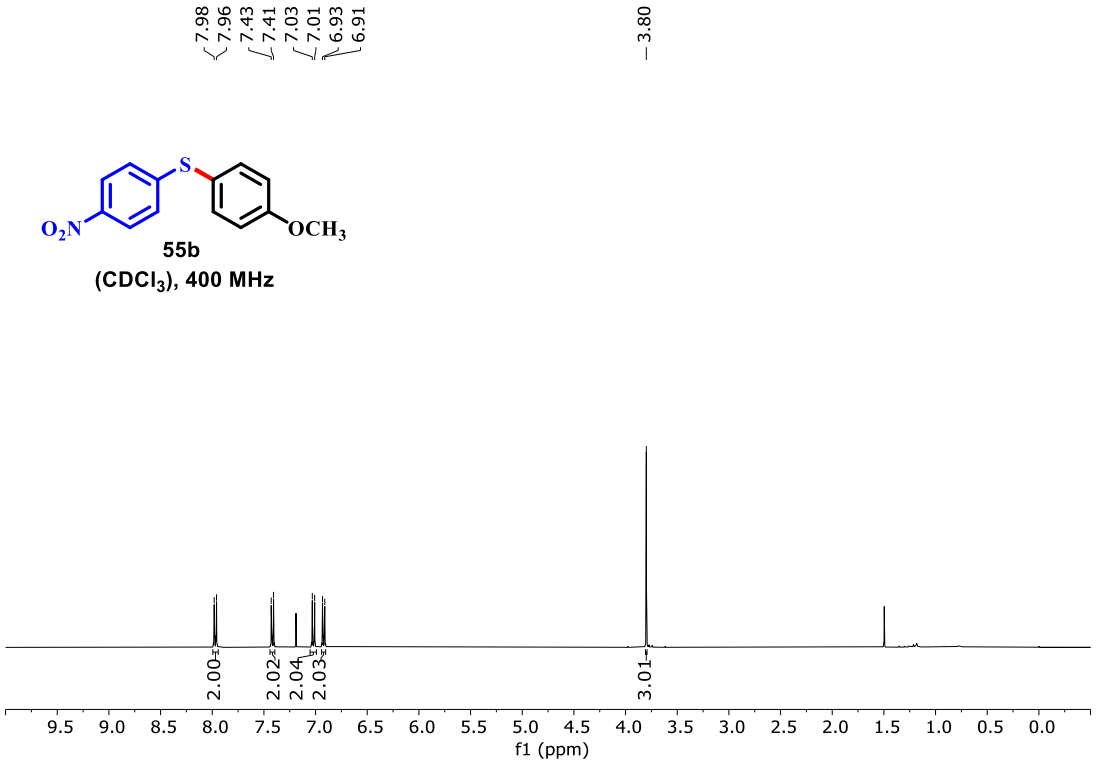

Figure B3: ^{1}H NMR spectrum of compound **55b** (400 MHz, $CDCl_3$).

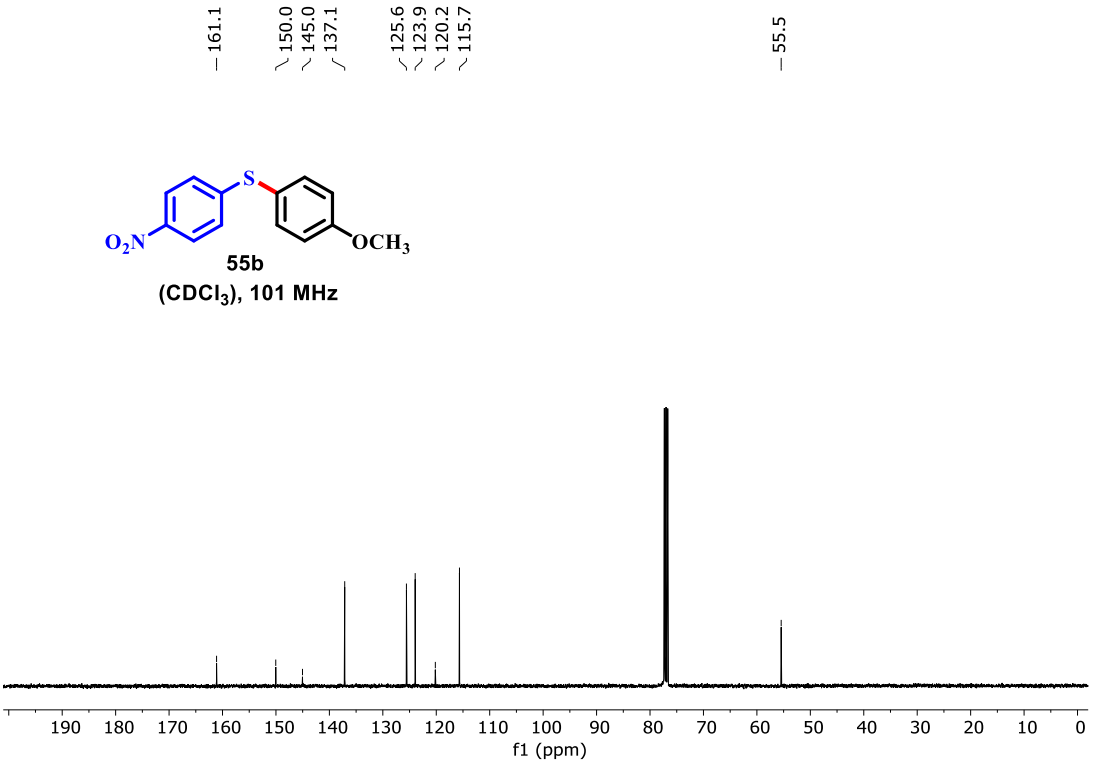

Figure B4: ^{13}C NMR spectrum of compound **55b** (101 MHz, $CDCl_3$).

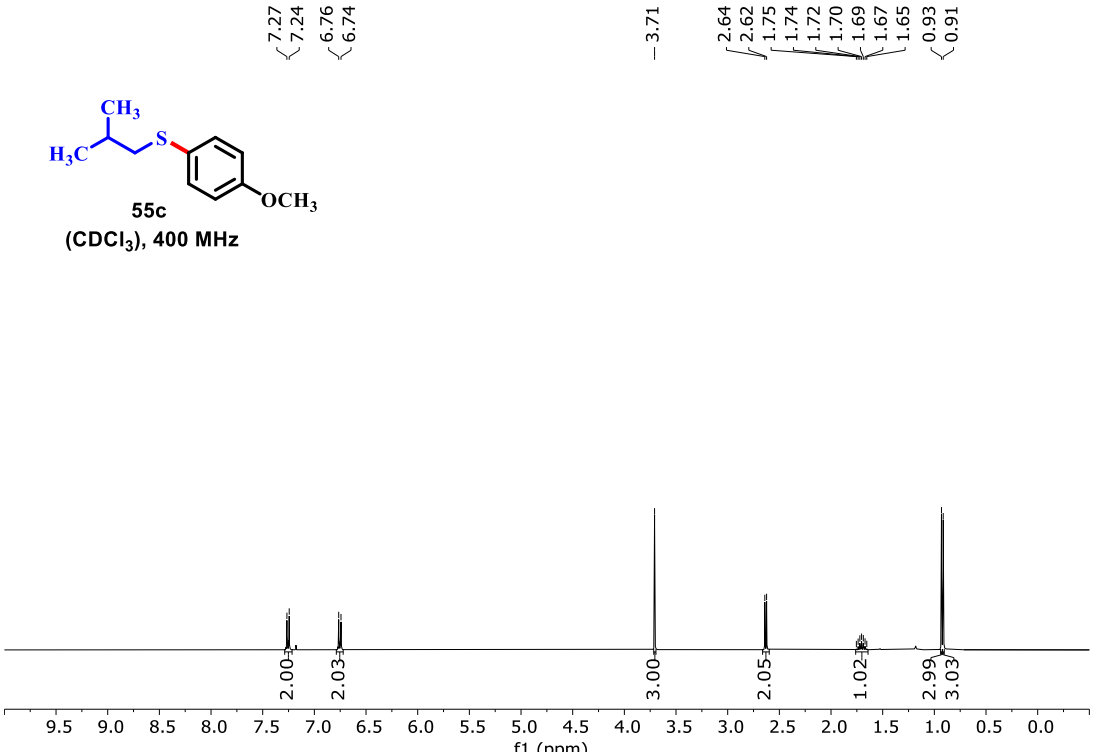

Figure B5: ^{1}H NMR spectrum of compound **55c** (400 MHz, $CDCl_3$).

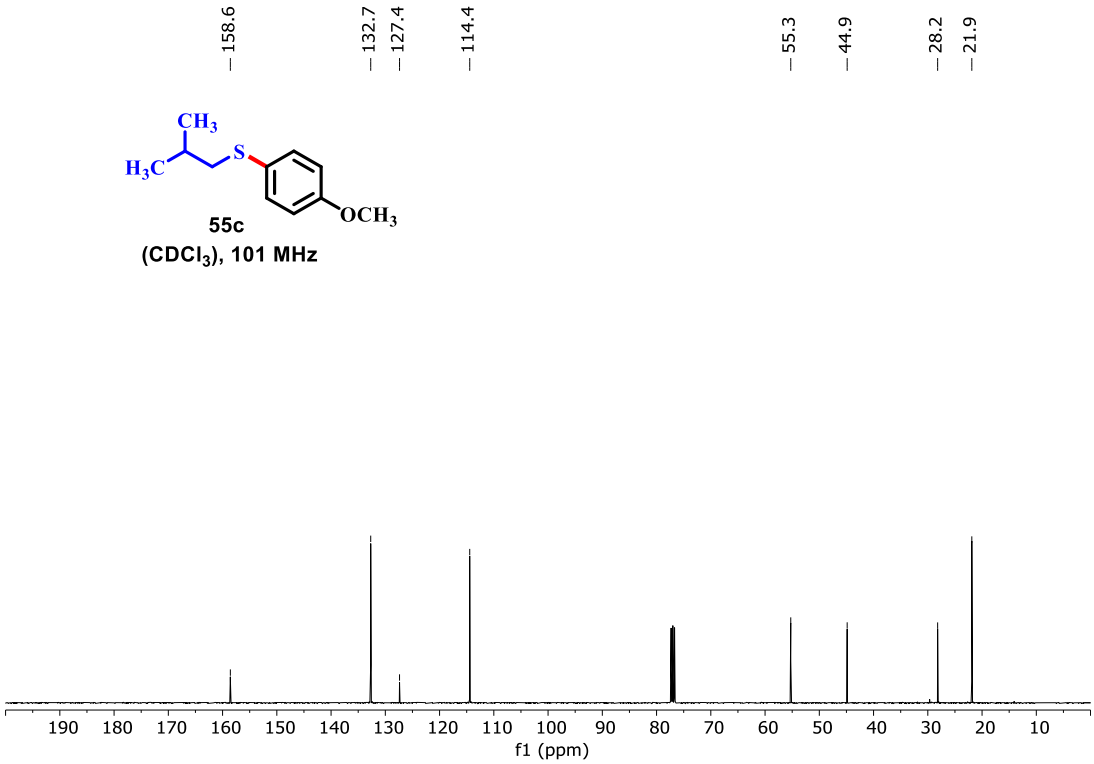

Figure B6: ^{13}C NMR spectrum of compound **55c** (101 MHz, $CDCl_3$).

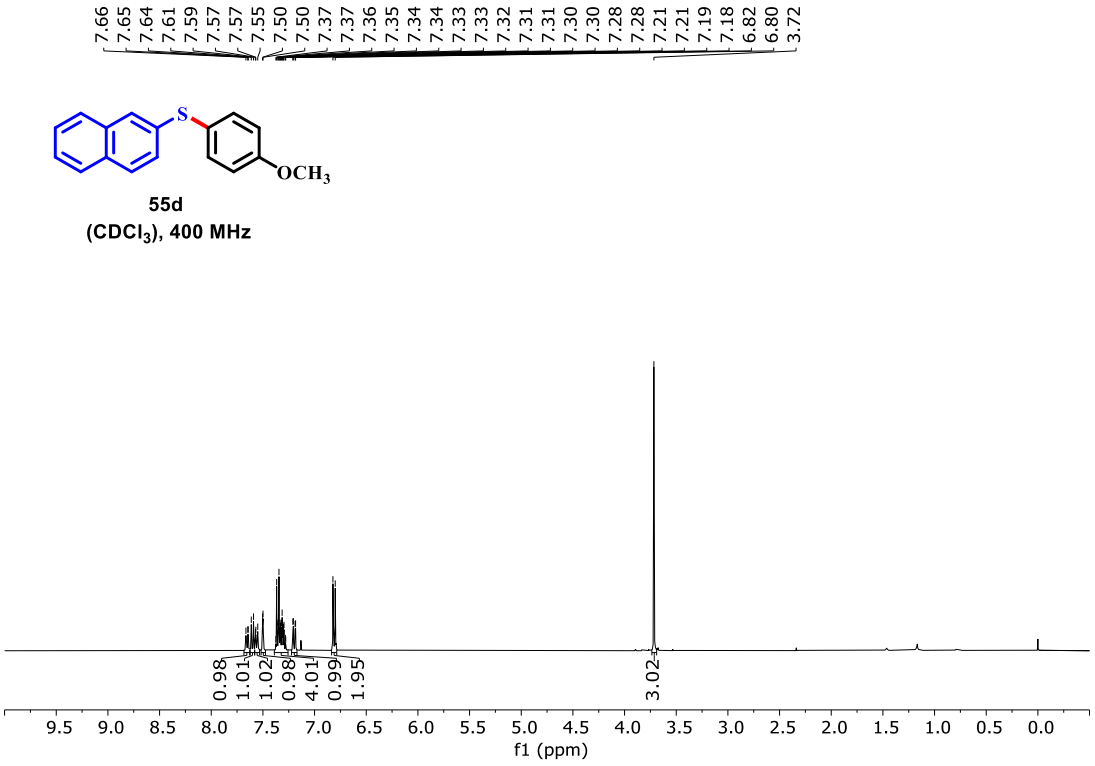

Figure B7: ^{1}H NMR spectrum of compound **55d** (400 MHz, $CDCl_3$).

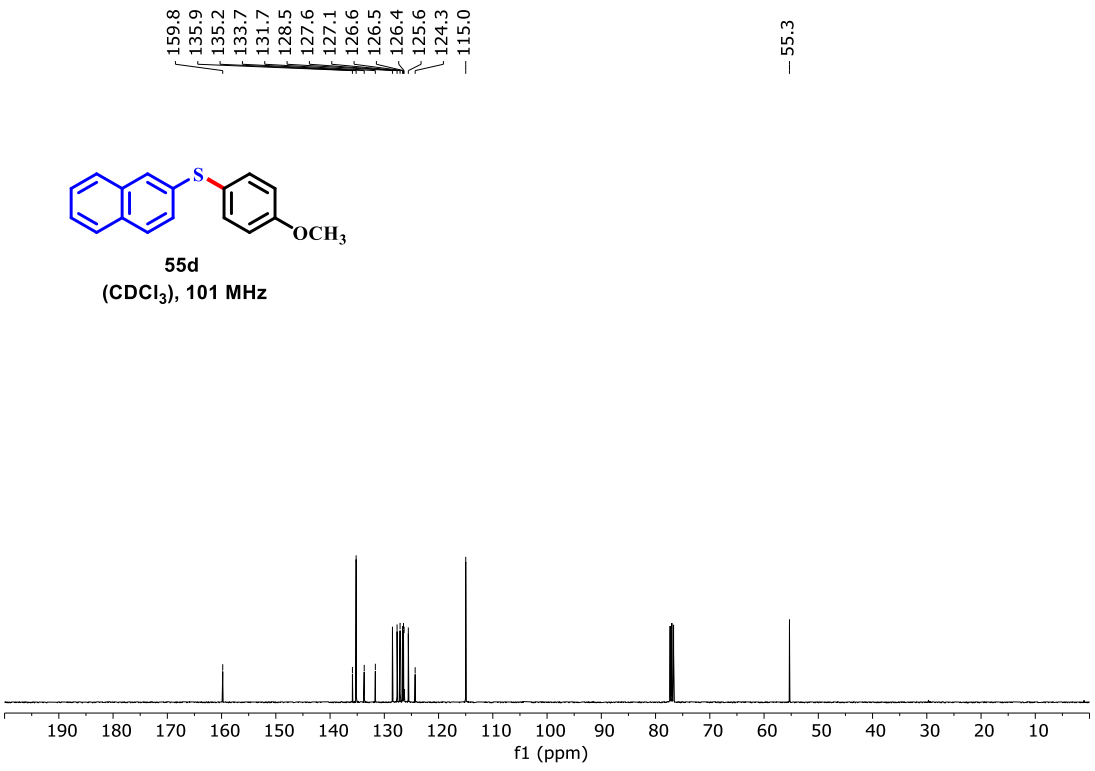

Figure B8: ^{13}C NMR spectrum of compound **55d** (101 MHz, $CDCl_3$).

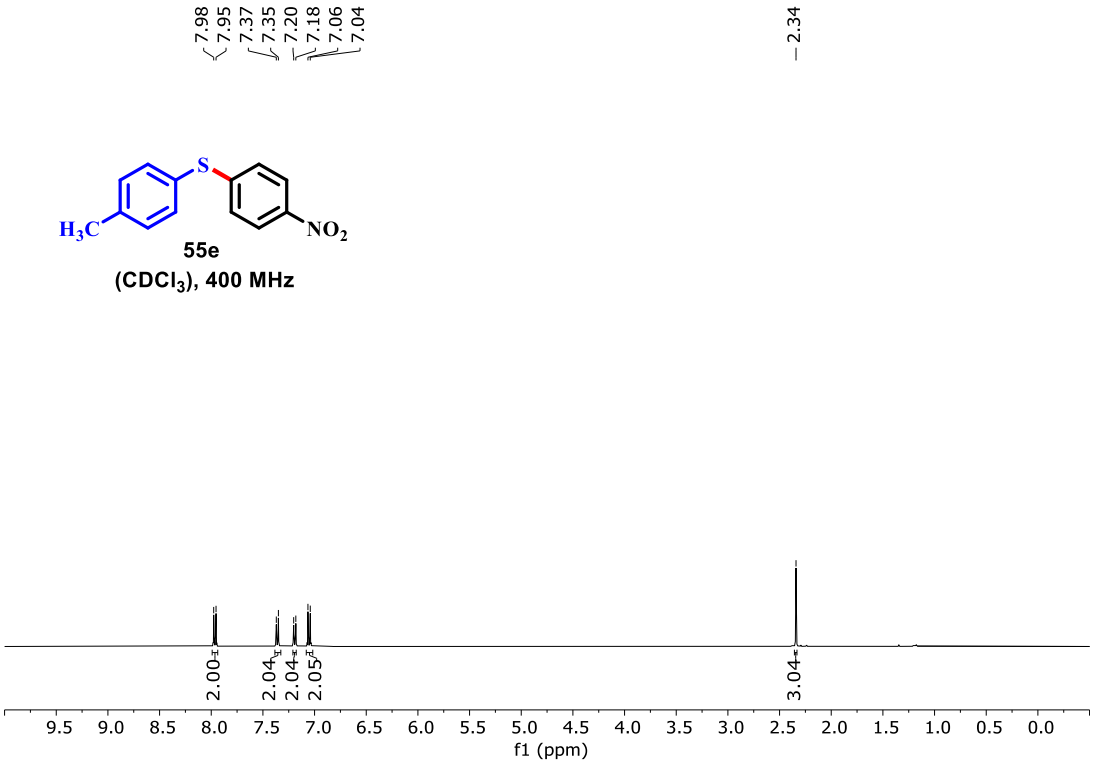

Figure B9: ^{1}H NMR spectrum of compound **55e** (400 MHz, $CDCl_3$).

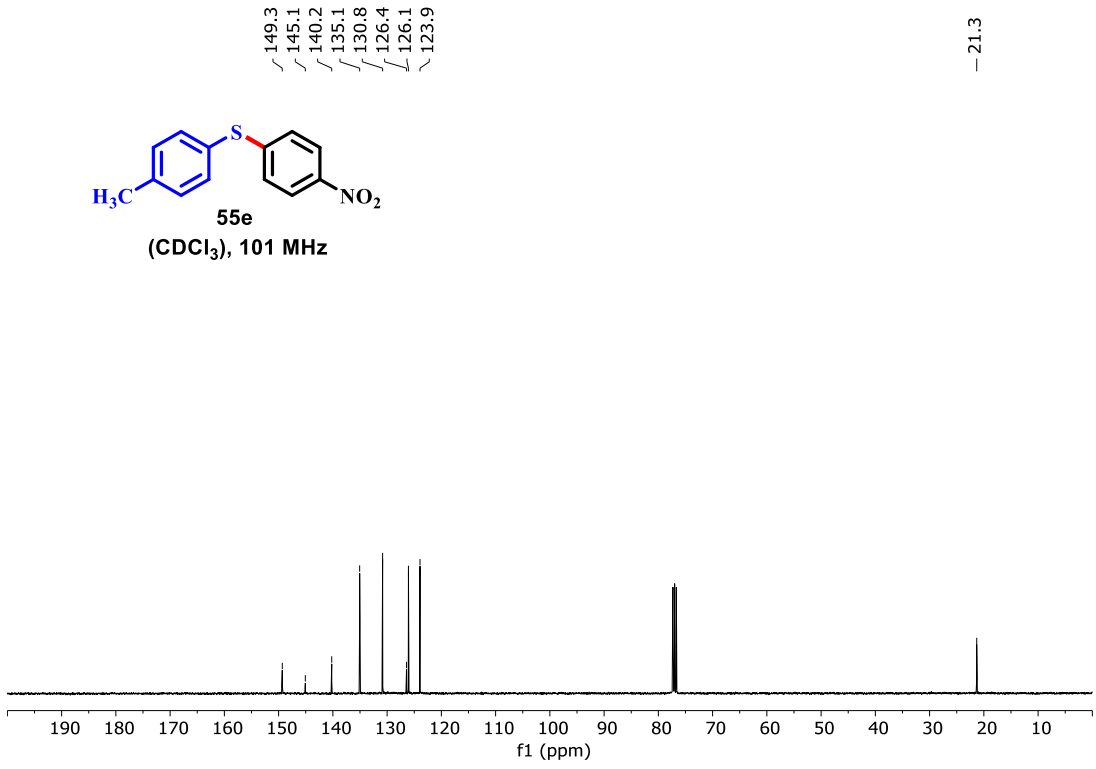

Figure B10: ^{13}C NMR spectrum of compound **55e** (101 MHz, $CDCl_3$).

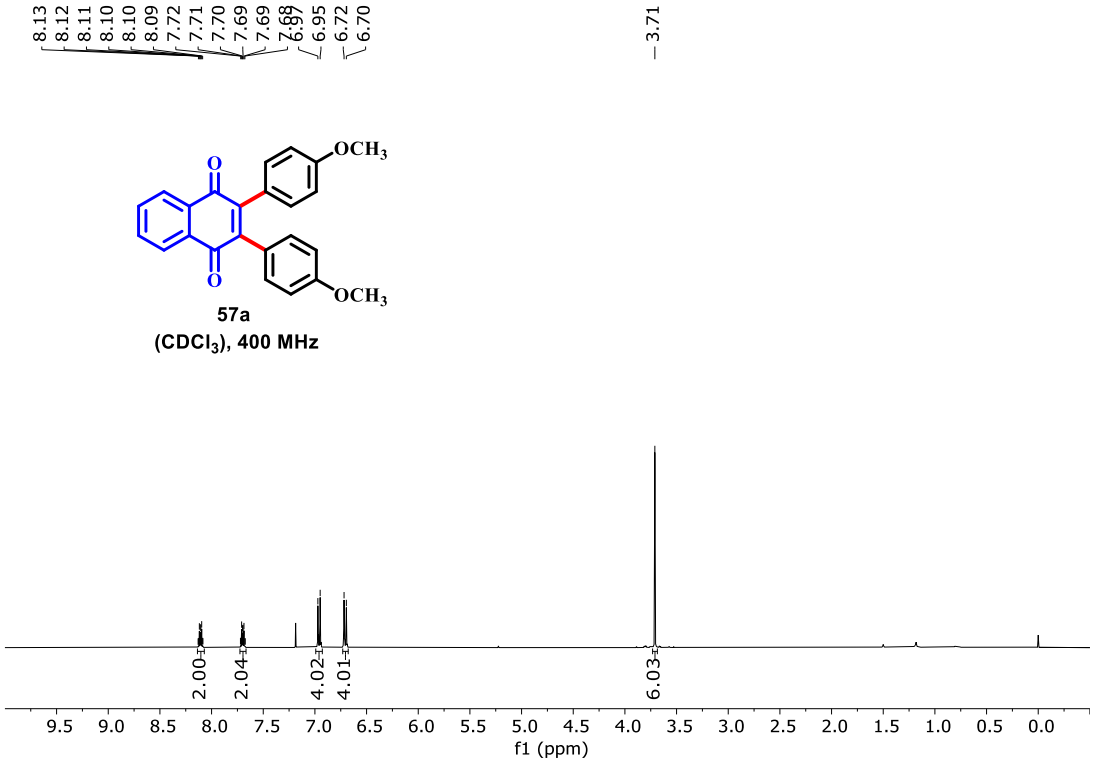

Figure B11: ^{1}H NMR spectrum of compound **57a** (400 MHz, $CDCl_3$).

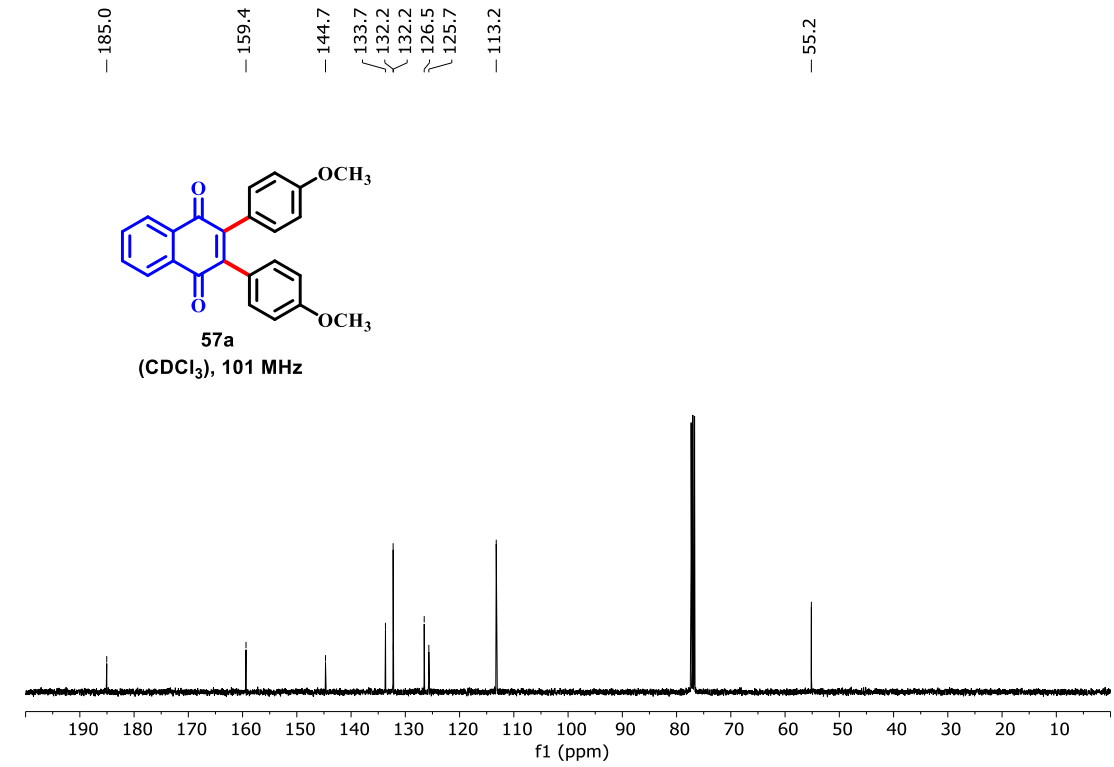

Figure B12: ^{13}C NMR spectrum of compound **57a** (101 MHz, $CDCl_3$).

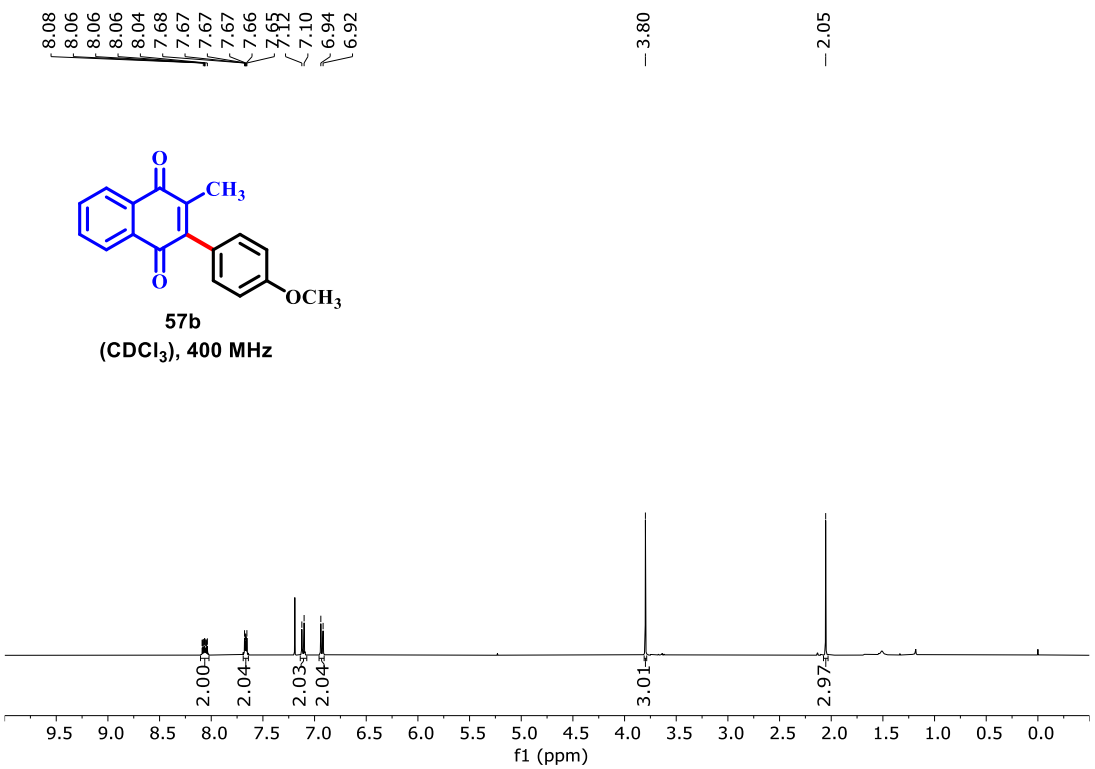

Figure B13: ^{1}H NMR spectrum of compound **57b** (400 MHz, $CDCl_3$).

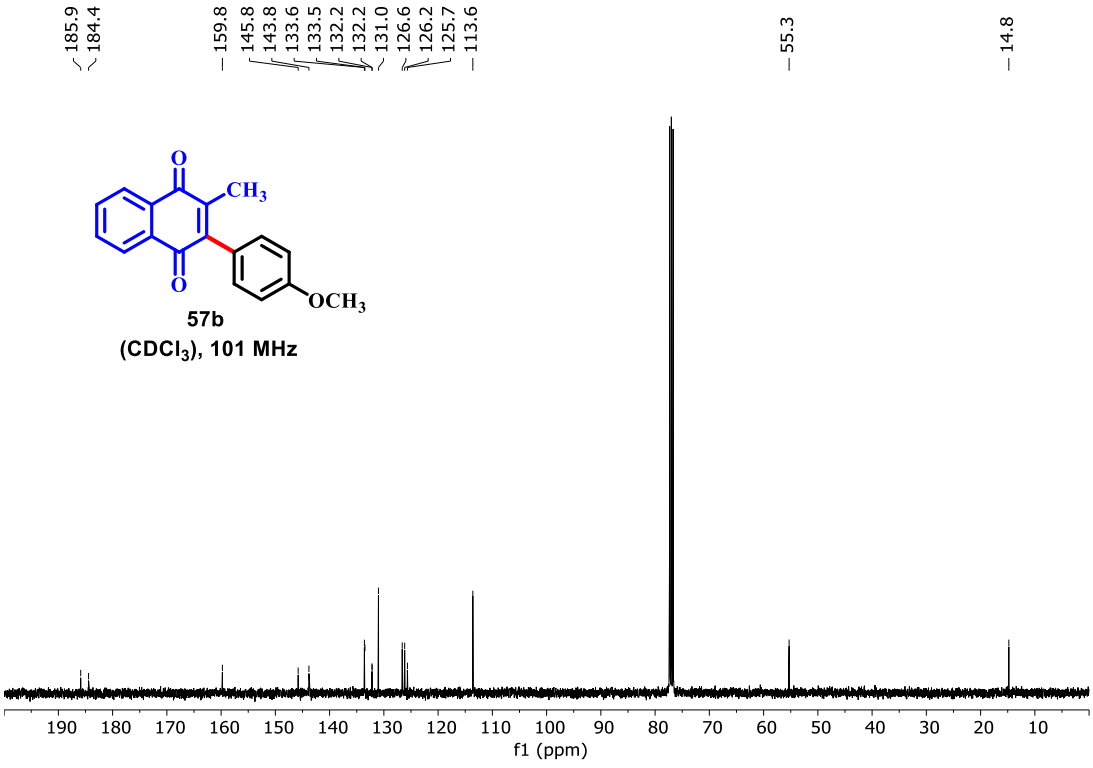

Figure B14: ^{13}C NMR spectrum of compound **57b** (101 MHz, $CDCl_3$).

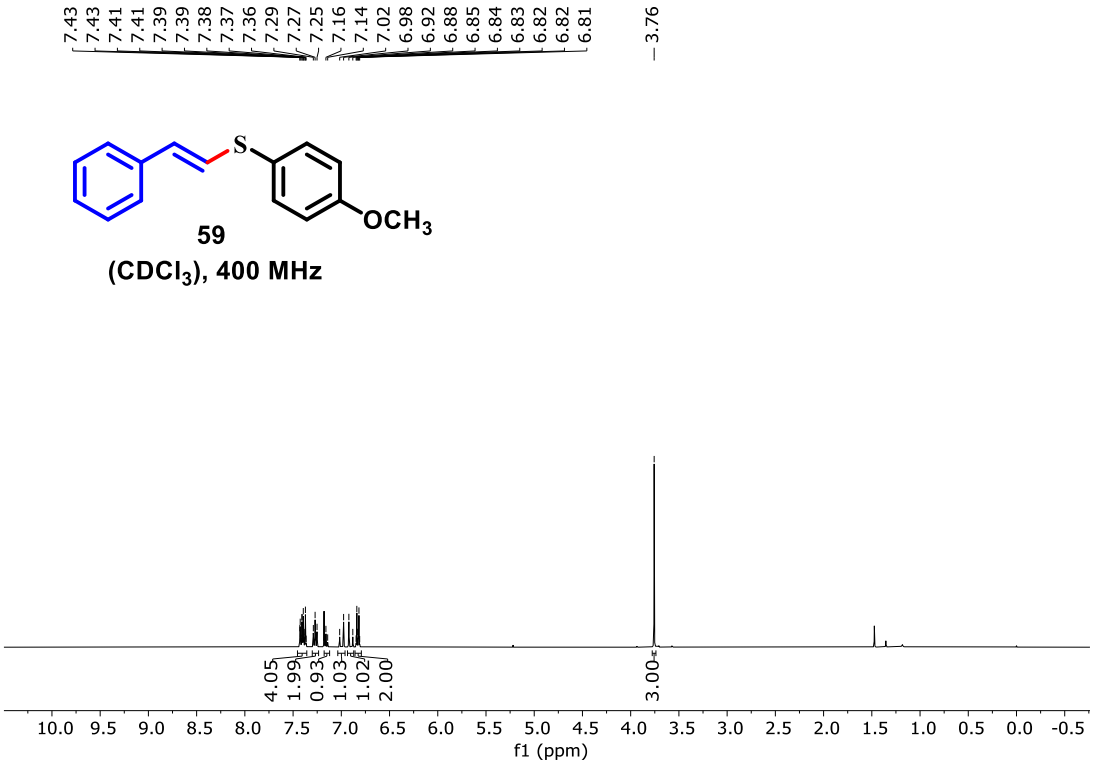

Figure B15: ^{1}H NMR spectrum of compound **59** (400 MHz, $CDCl_3$).

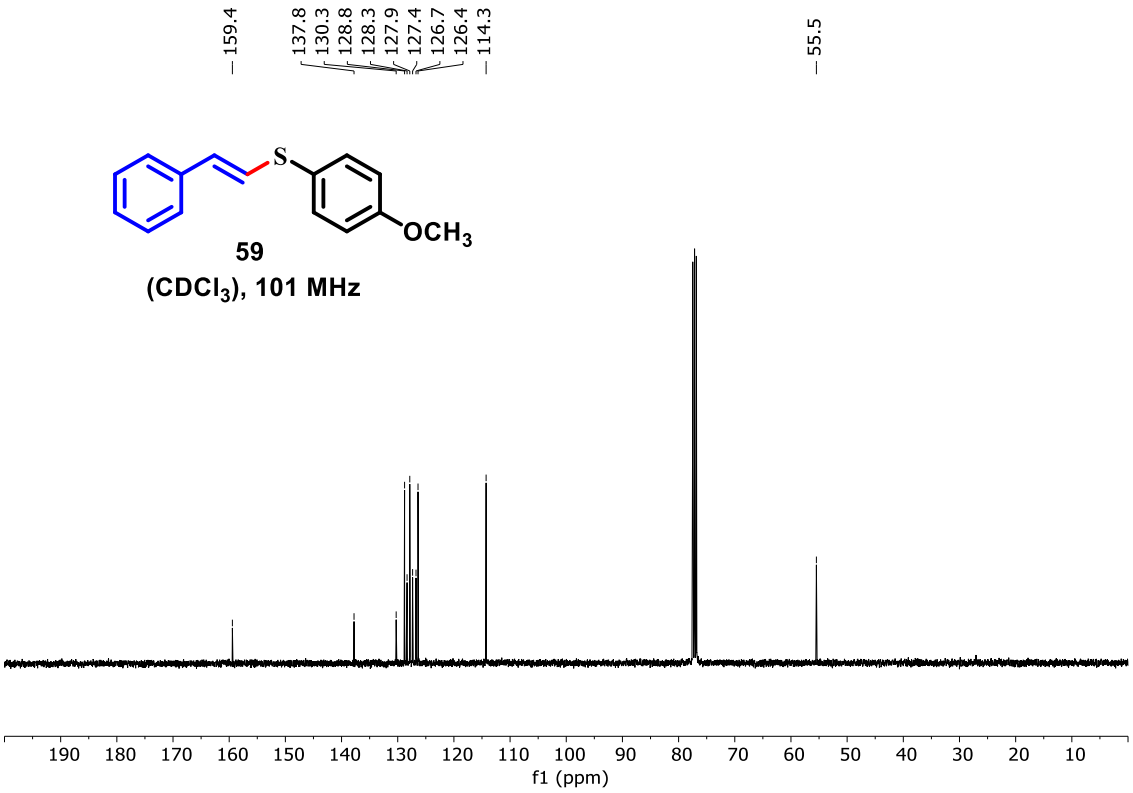

Figure B16: ^{13}C NMR spectrum of compound **59** (101 MHz, $CDCl_3$).

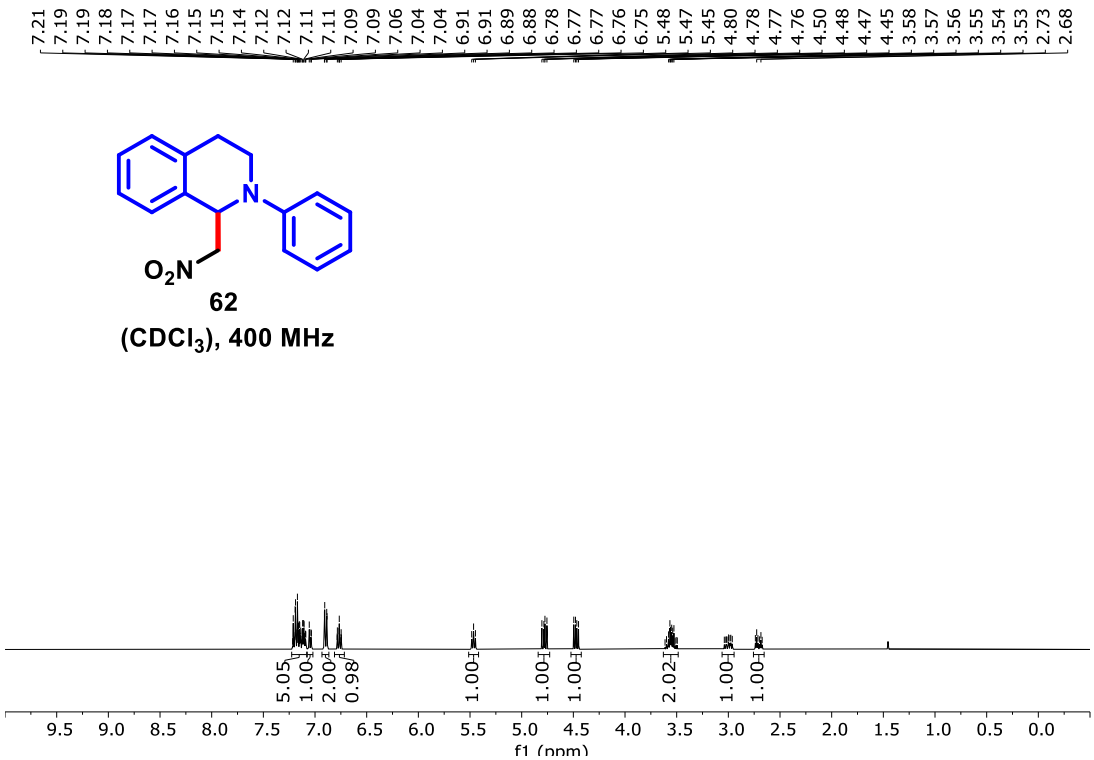

Figure B17: ^{1}H NMR spectrum of compound **62** (400 MHz, $CDCl_3$).

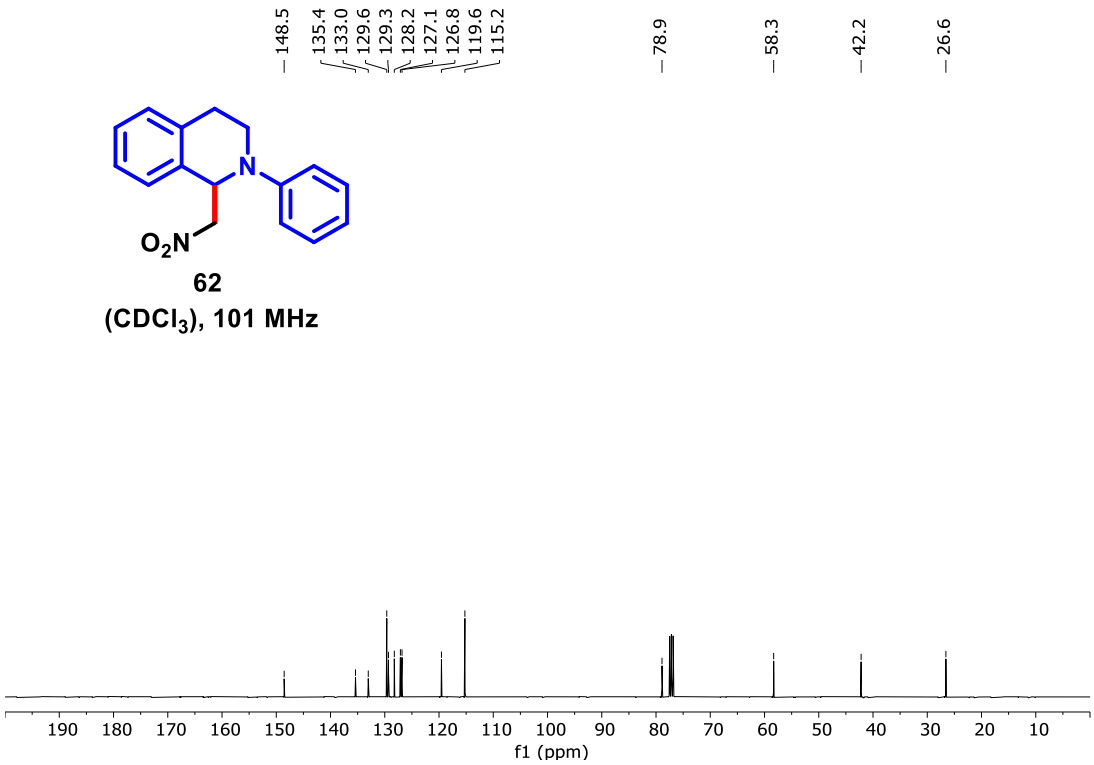

Figure B18: ^{13}C NMR spectrum of compound **62** (101 MHz, $CDCl_3$).

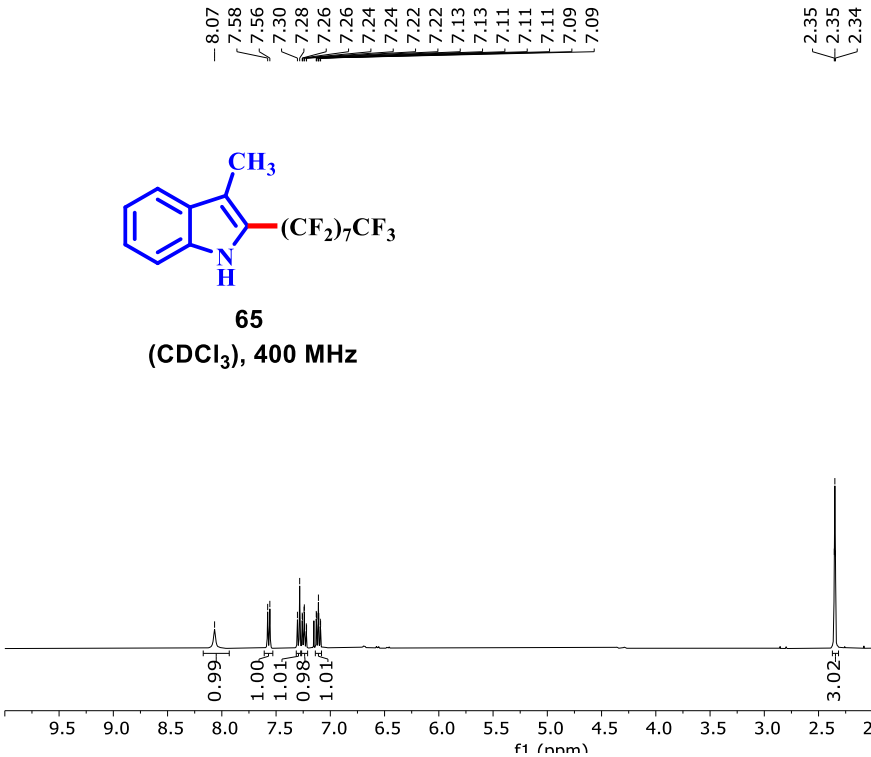

Figure B19: ^{1}H NMR spectrum of compound **65** (400 MHz, $CDCl_3$).

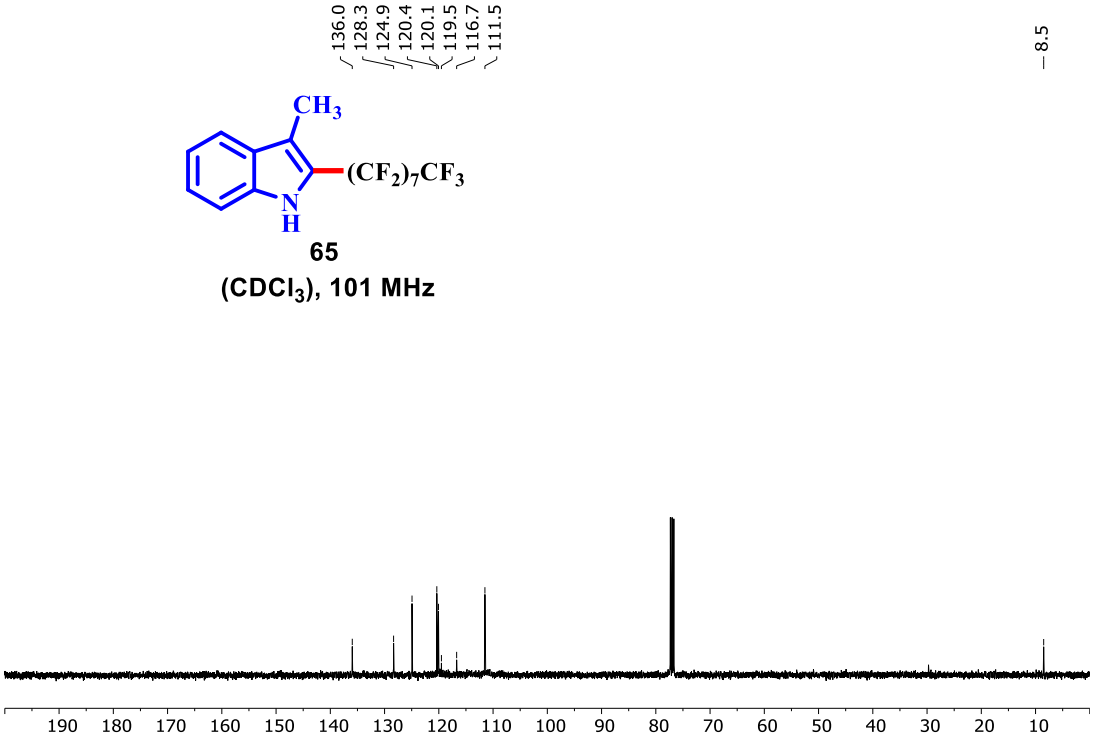

Figure B20: ^{13}C NMR spectrum of compound **XX** (101 MHz, $CDCl_3$).

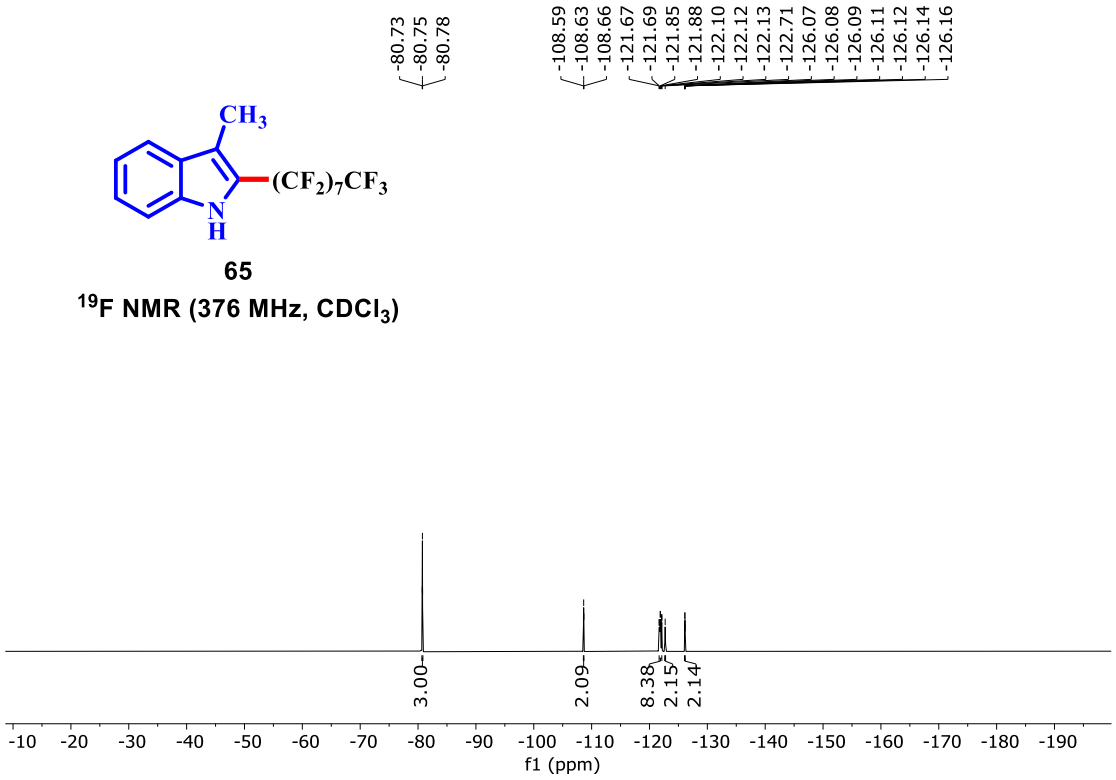

Figure B21: ^{19}F NMR spectrum of compound **65** (376 MHz, $CDCl_3$)

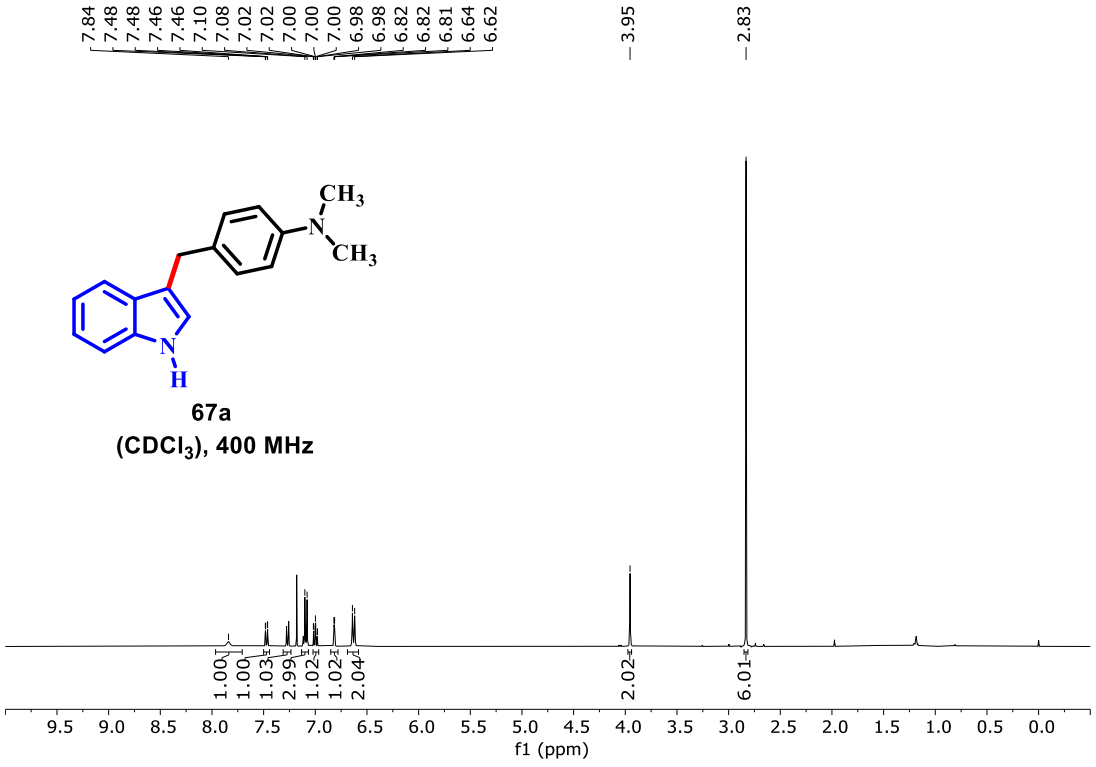

Figure B22: ^{1}H NMR spectrum of compound **67a** (400 MHz, $CDCl_3$).

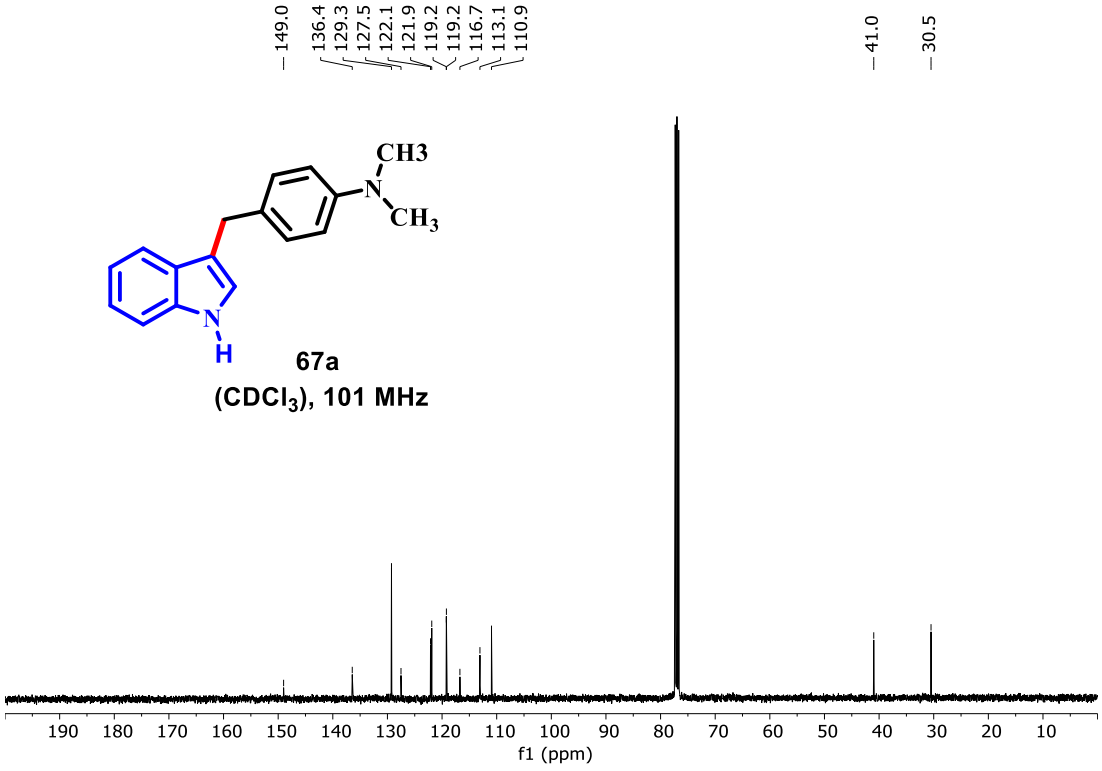

Figure B23: ^{13}C NMR spectrum of compound **67a** (101 MHz, $CDCl_3$).

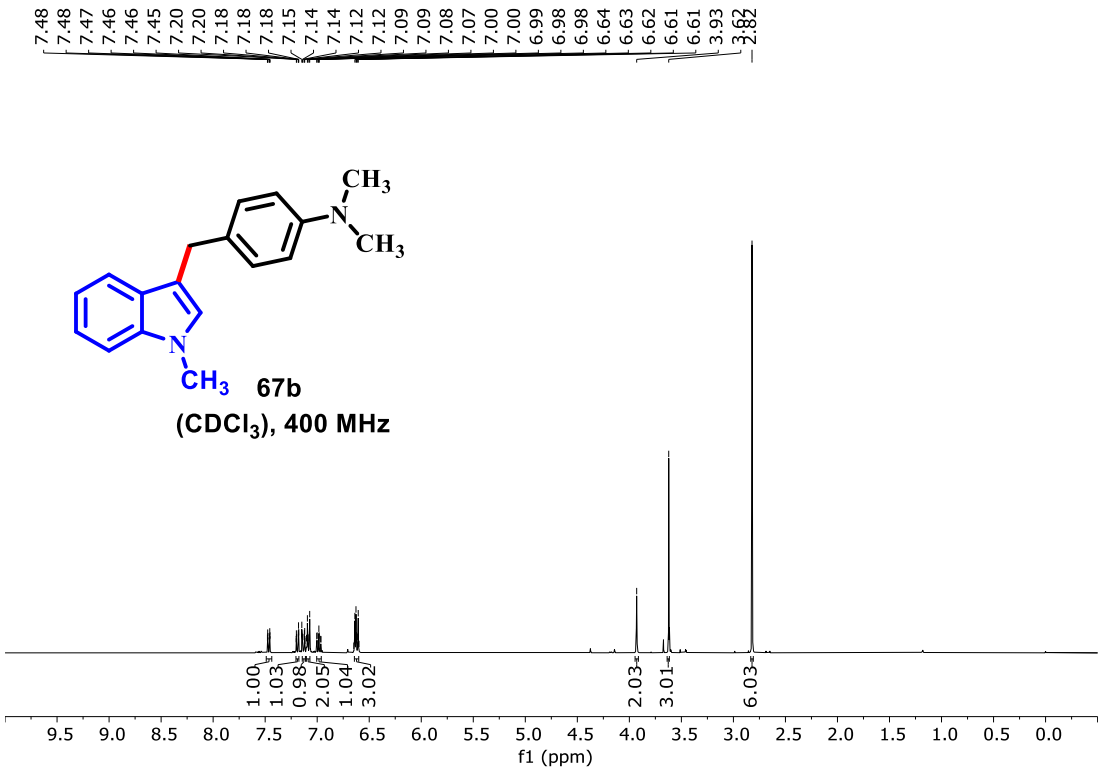

Figure B24: ^{1}H NMR spectrum of compound **67b** (400 MHz, $CDCl_3$).

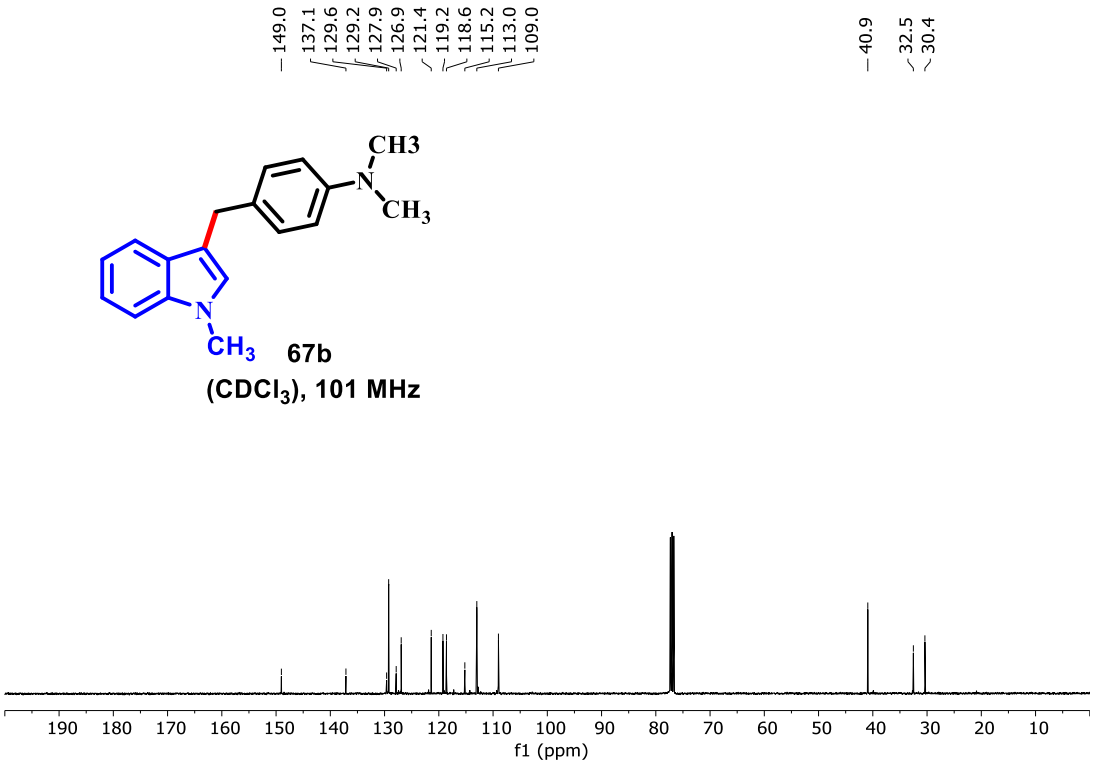

Figure B25: ^{13}C NMR spectrum of compound **67b** (101 MHz, $CDCl_3$).

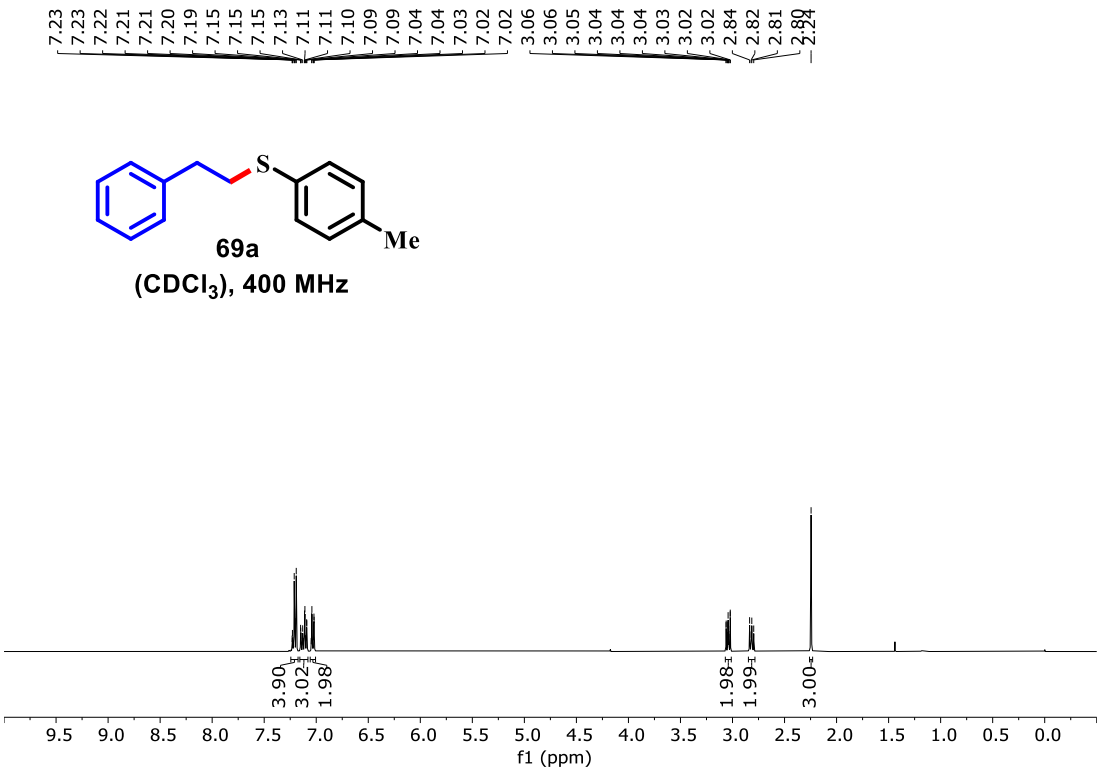

Figure B26: ^{1}H NMR spectrum of compound **69a** (400 MHz, $CDCl_3$).

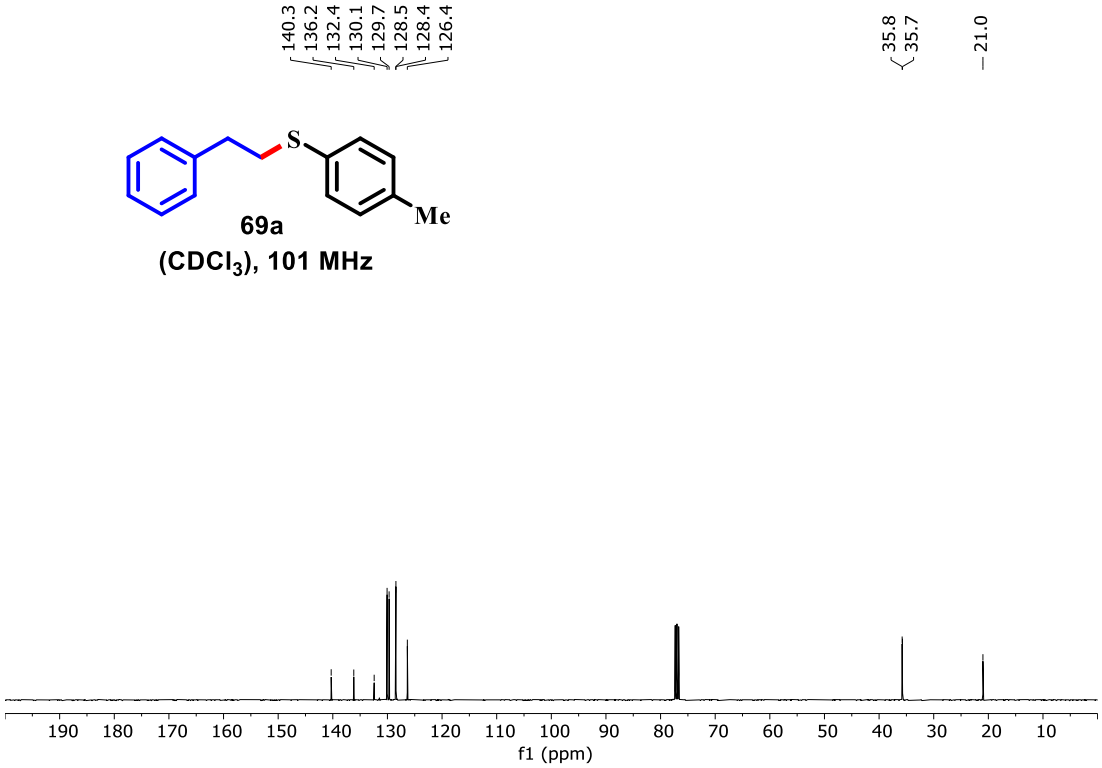

Figure B27: ^{13}C NMR spectrum of compound **69a** (101 MHz, $CDCl_3$).

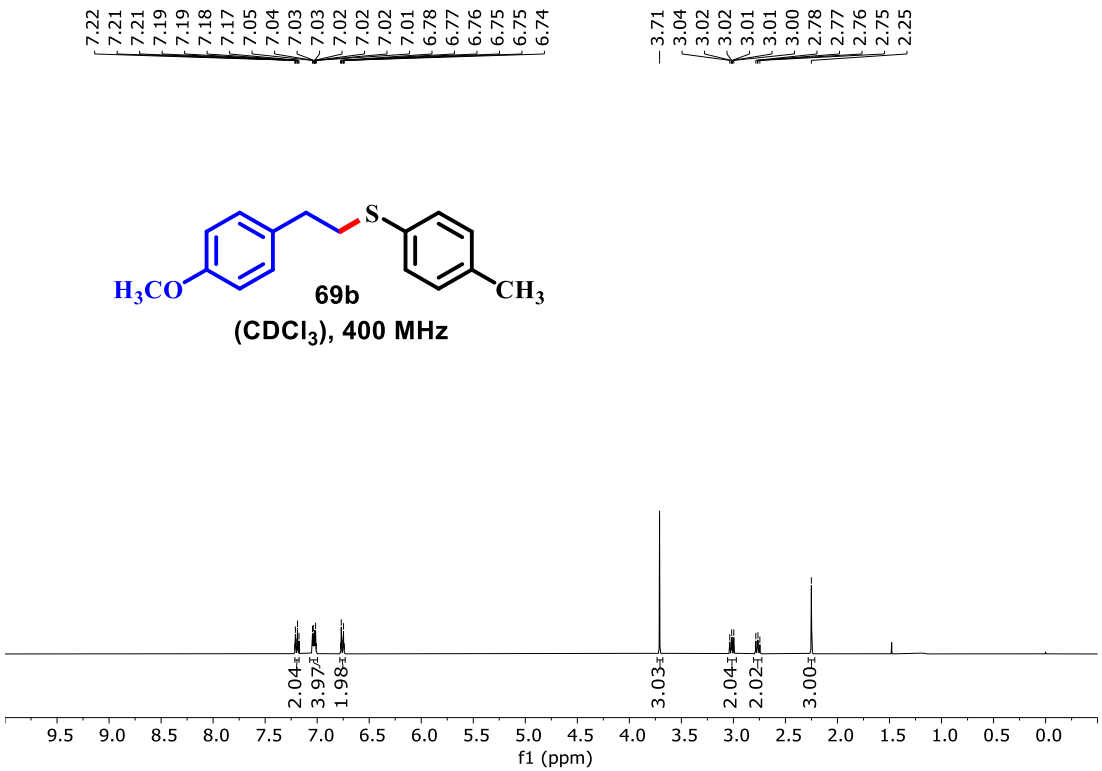

Figure B28: ^{1}H NMR spectrum of compound **69b** (400 MHz, $CDCl_3$).

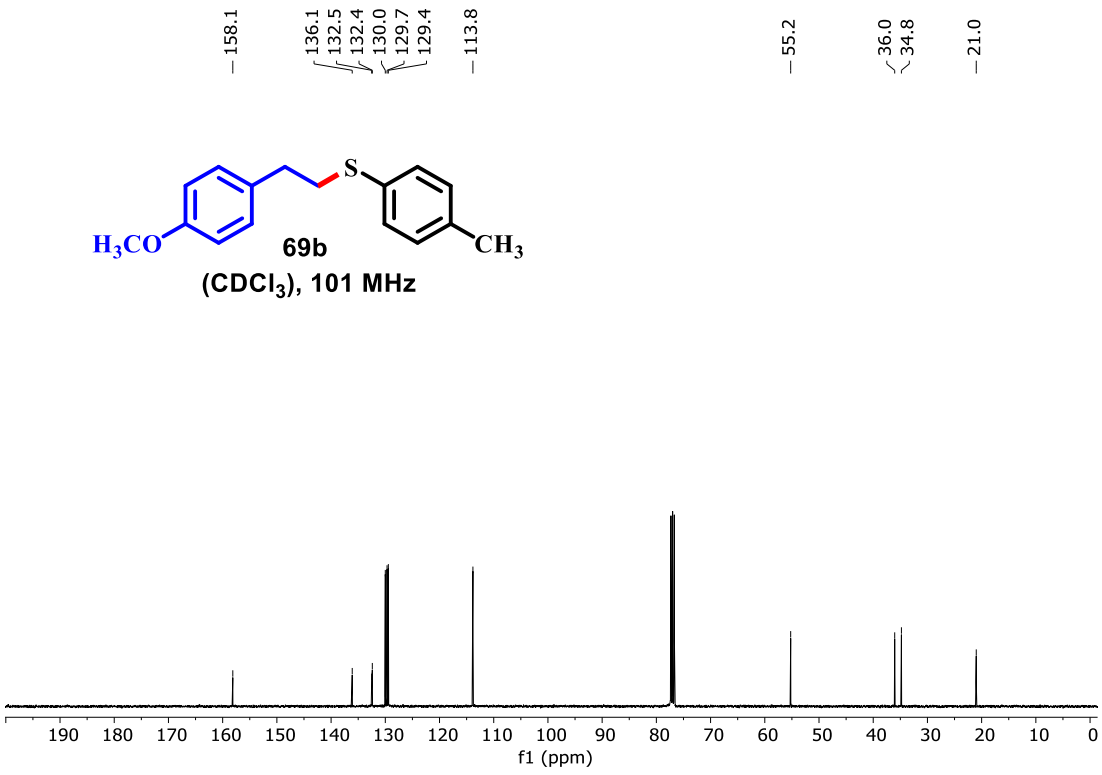

Figure B29: ^{13}C NMR spectrum of compound **69b** (101 MHz, $CDCl_3$).

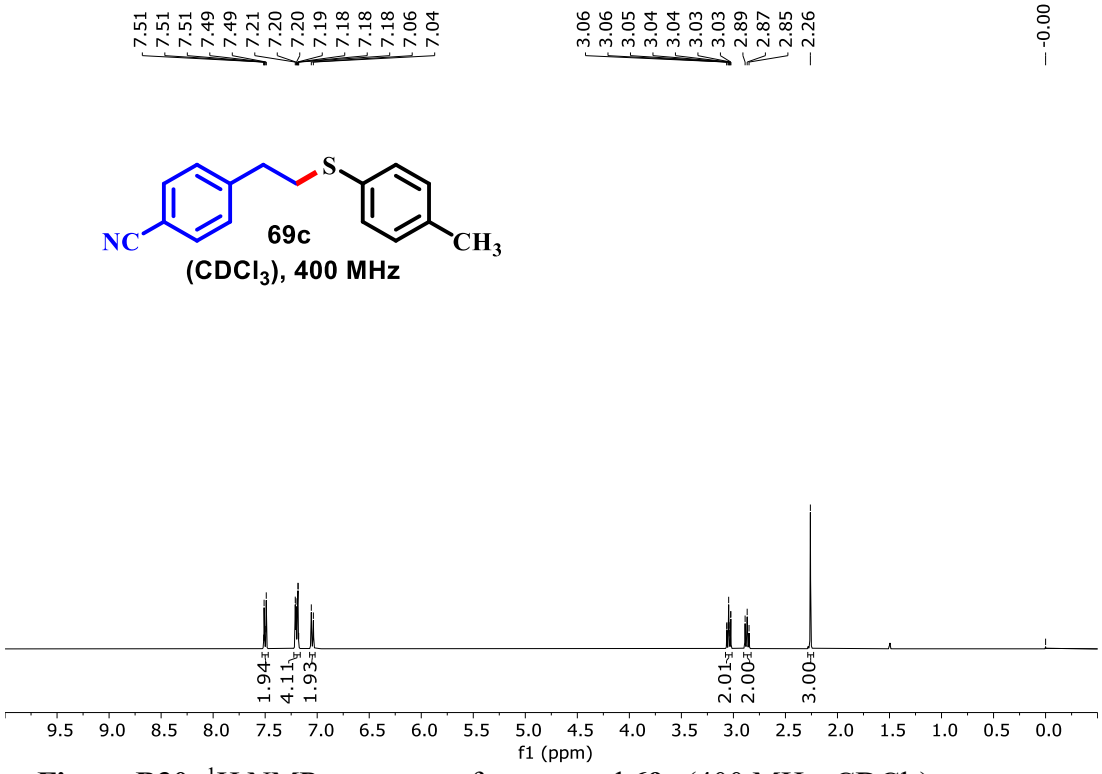

Figure B30: ^{1}H NMR spectrum of compound **69c** (400 MHz, $CDCl_3$).

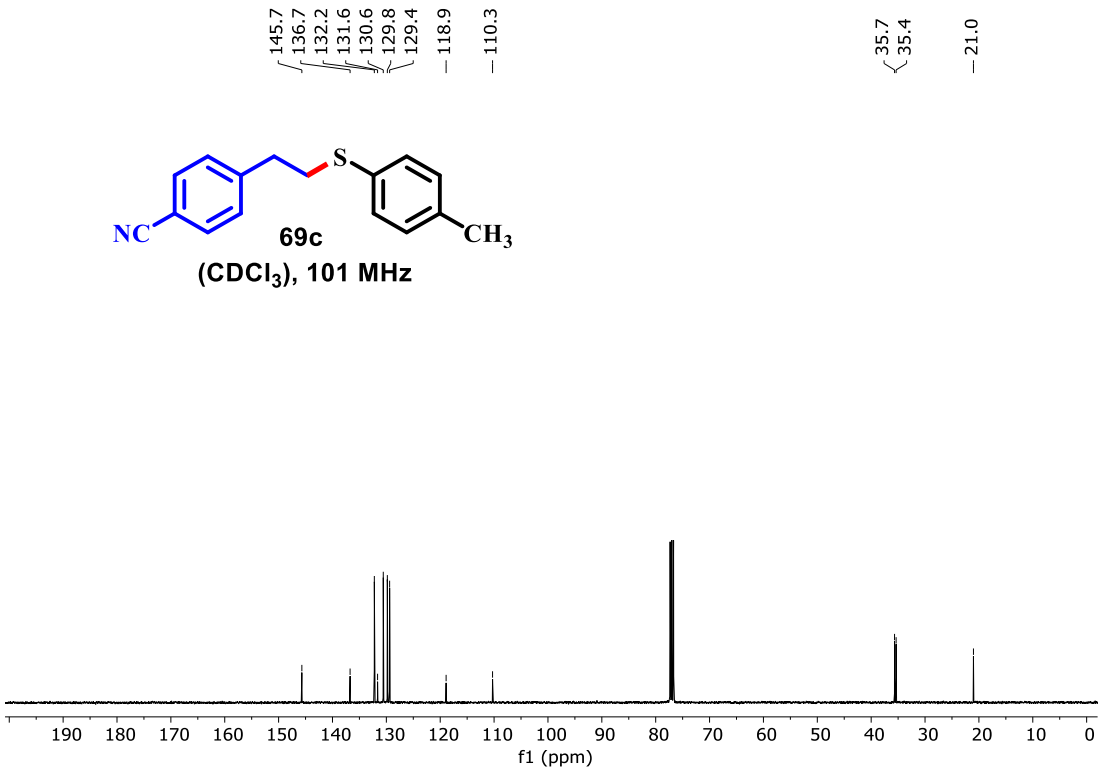

Figure B31: ^{13}C NMR spectrum of compound **69c** (101 MHz, $CDCl_3$).

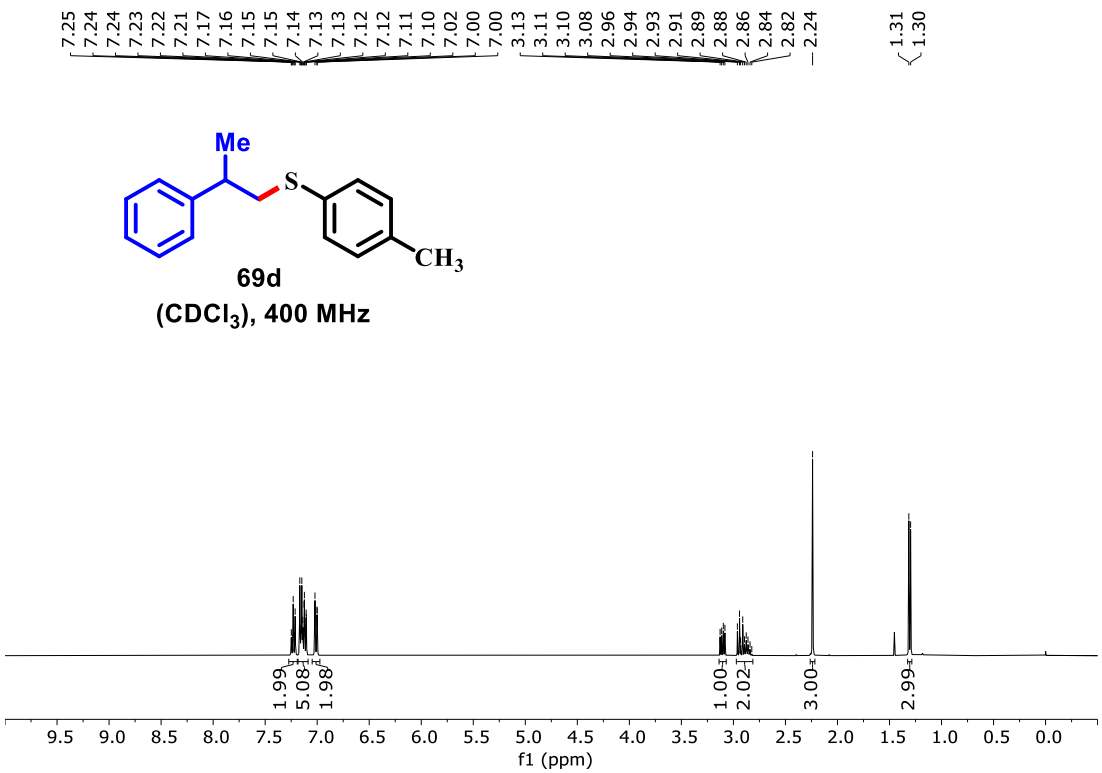

Figure B32: ^{1}H NMR spectrum of compound **69d** (400 MHz, $CDCl_3$).

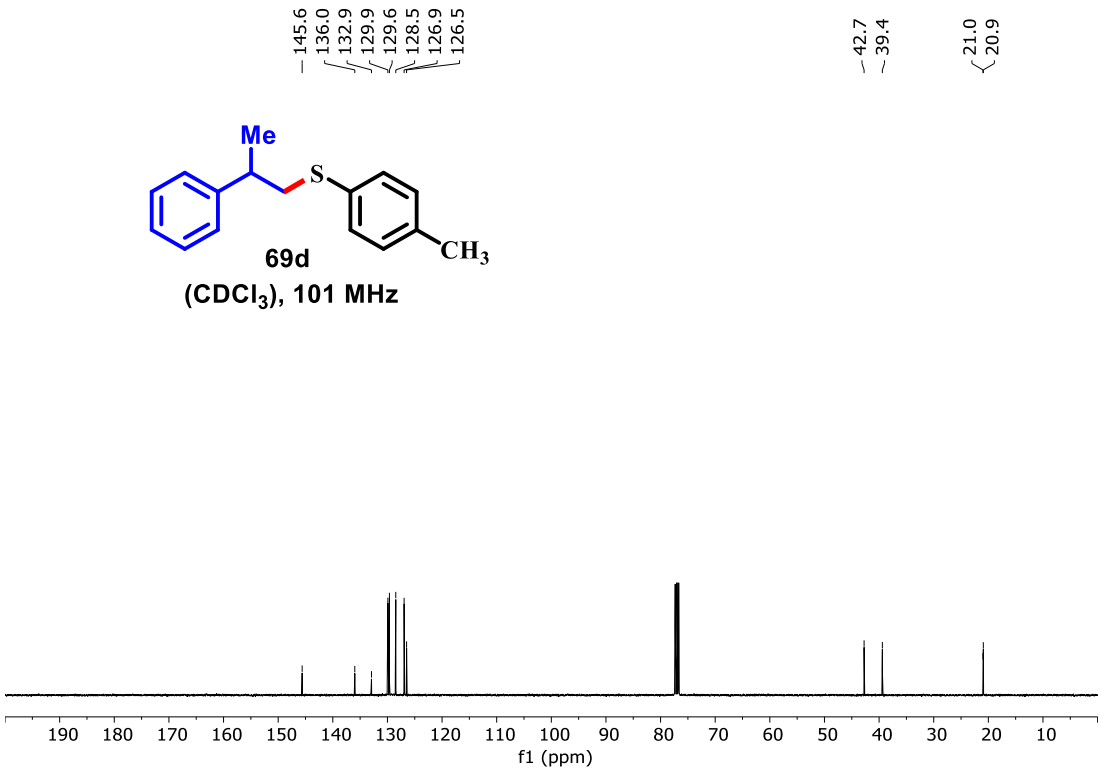

Figure B33: ^{13}C NMR spectrum of compound **69d** (101 MHz, $CDCl_3$).

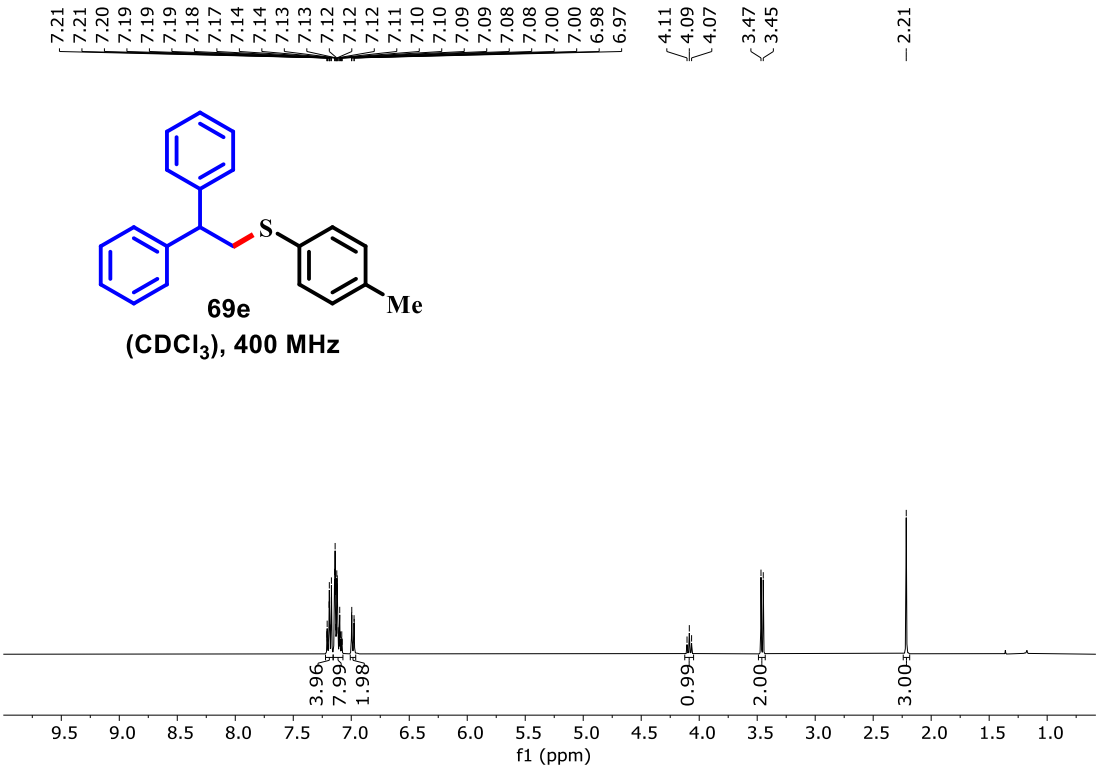

Figure B34: ^{1}H NMR spectrum of compound **69e** (400 MHz, $CDCl_3$).

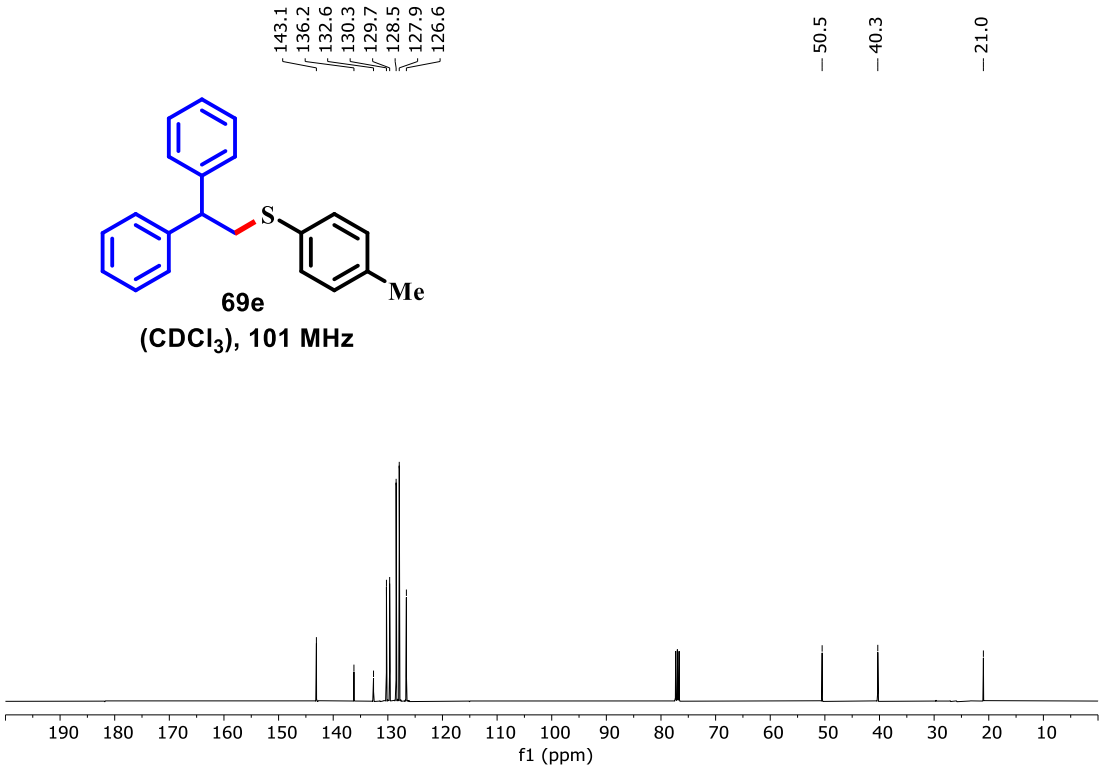

Figure B35: ^{13}C NMR spectrum of compound **69e** (101 MHz, $CDCl_3$).

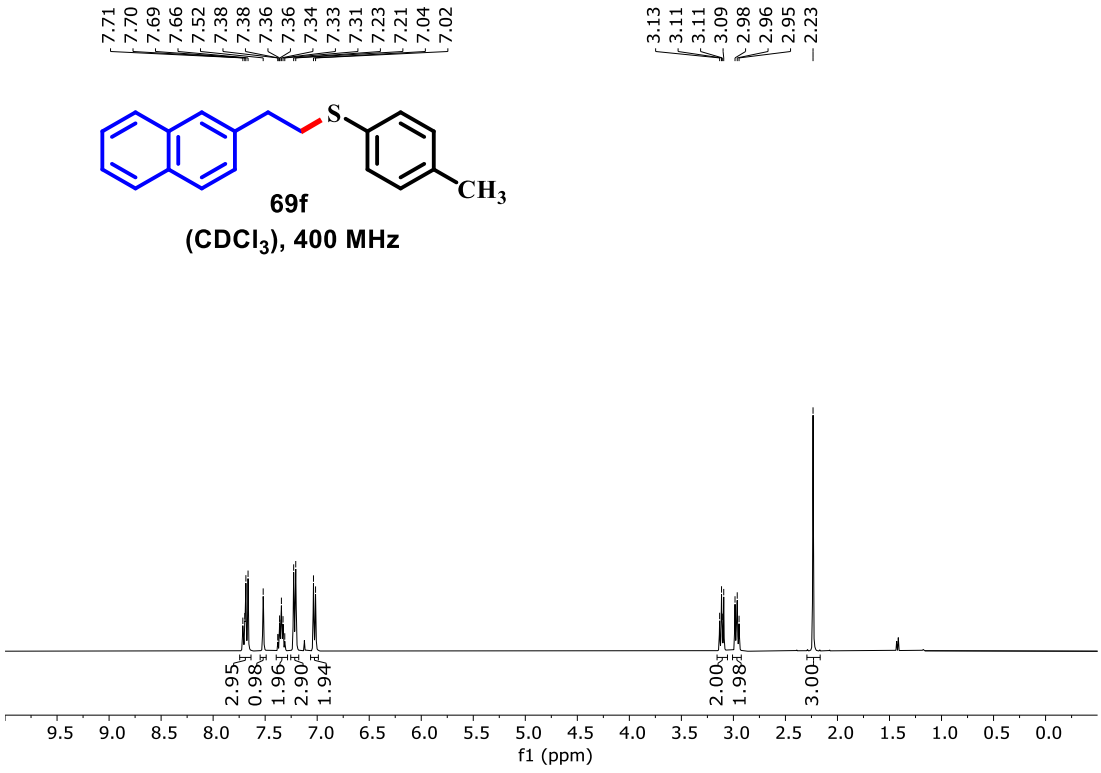

Figure B36: ^{1}H NMR spectrum of compound **69f** (400 MHz, $CDCl_3$).

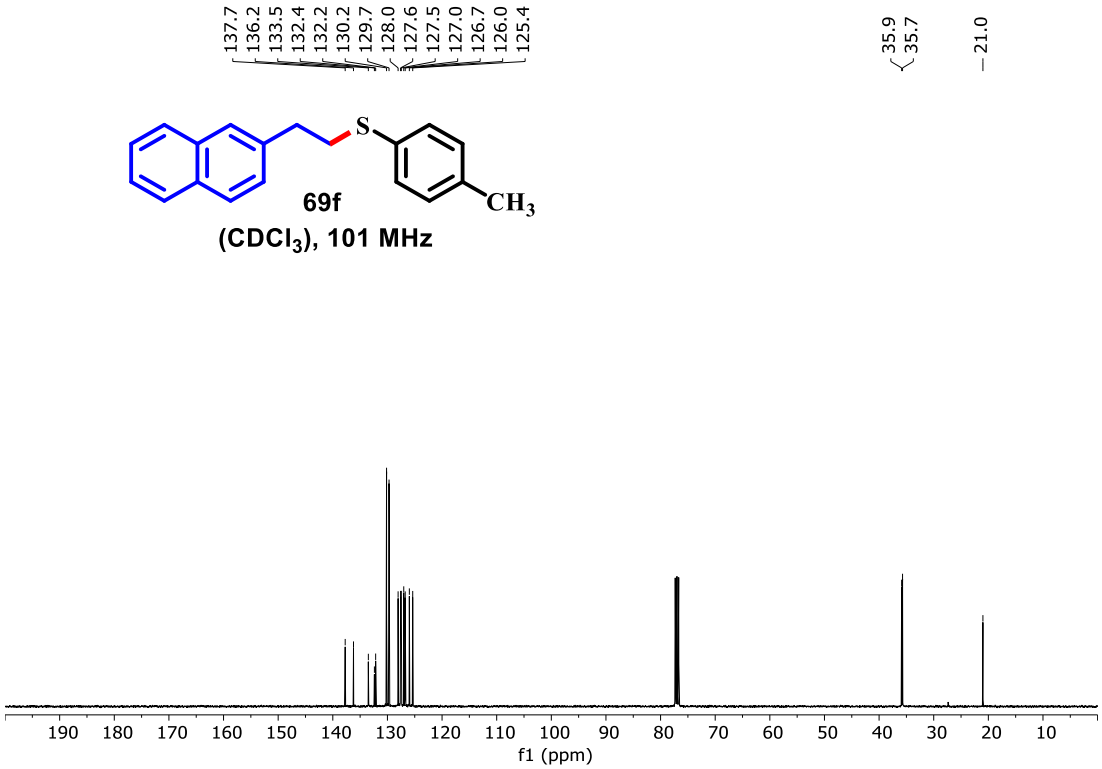

Figure B37: ^{13}C NMR spectrum of compound **69f** (101 MHz, $CDCl_3$).

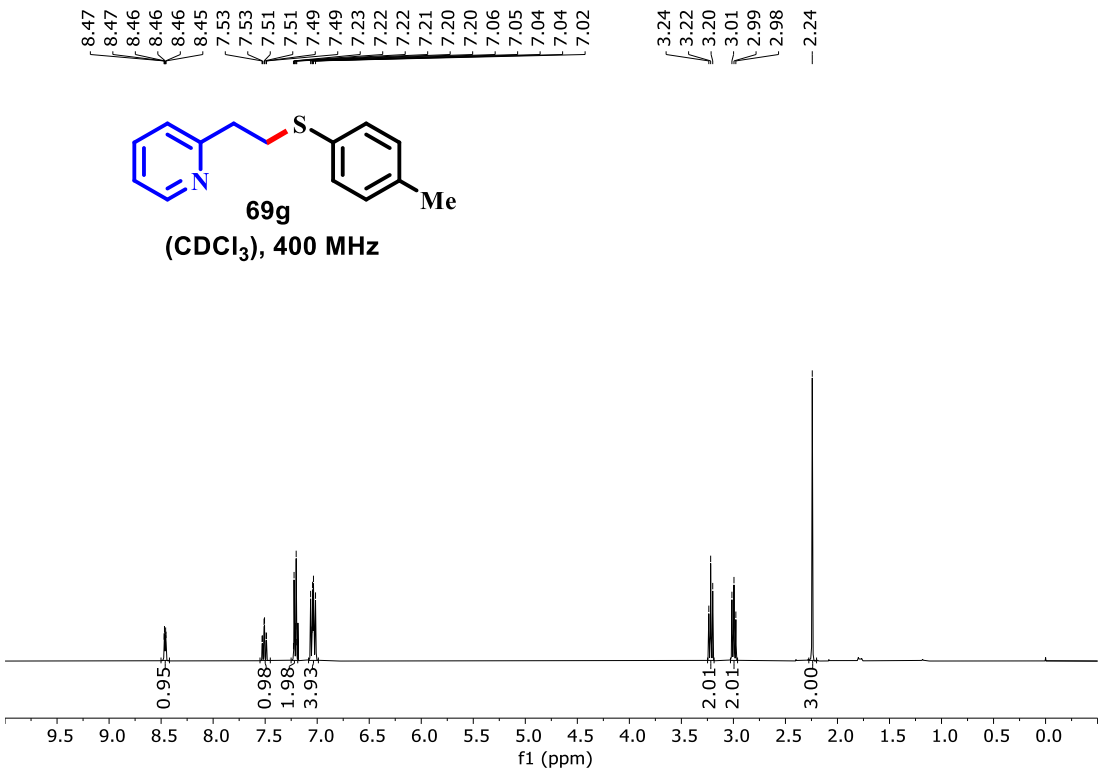

Figure B38: ^{1}H NMR spectrum of compound **69g** (400 MHz, $CDCl_3$).

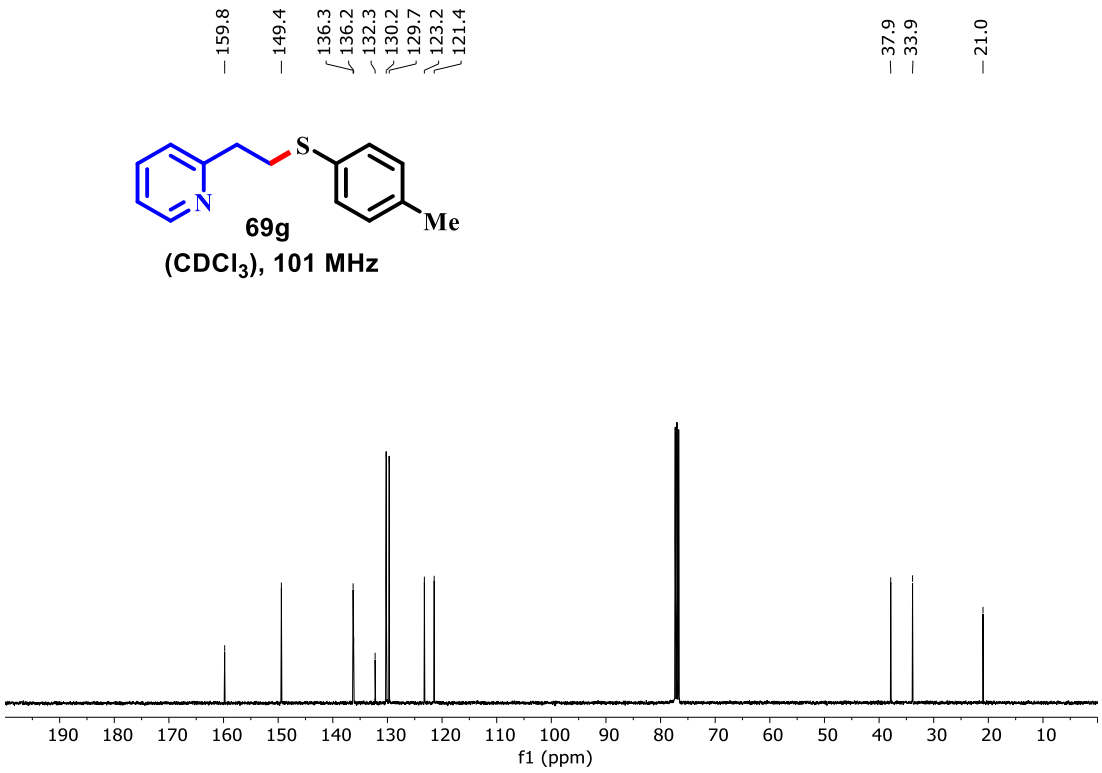

Figure B39: ^{13}C NMR spectrum of compound **69g** (101 MHz, $CDCl_3$).

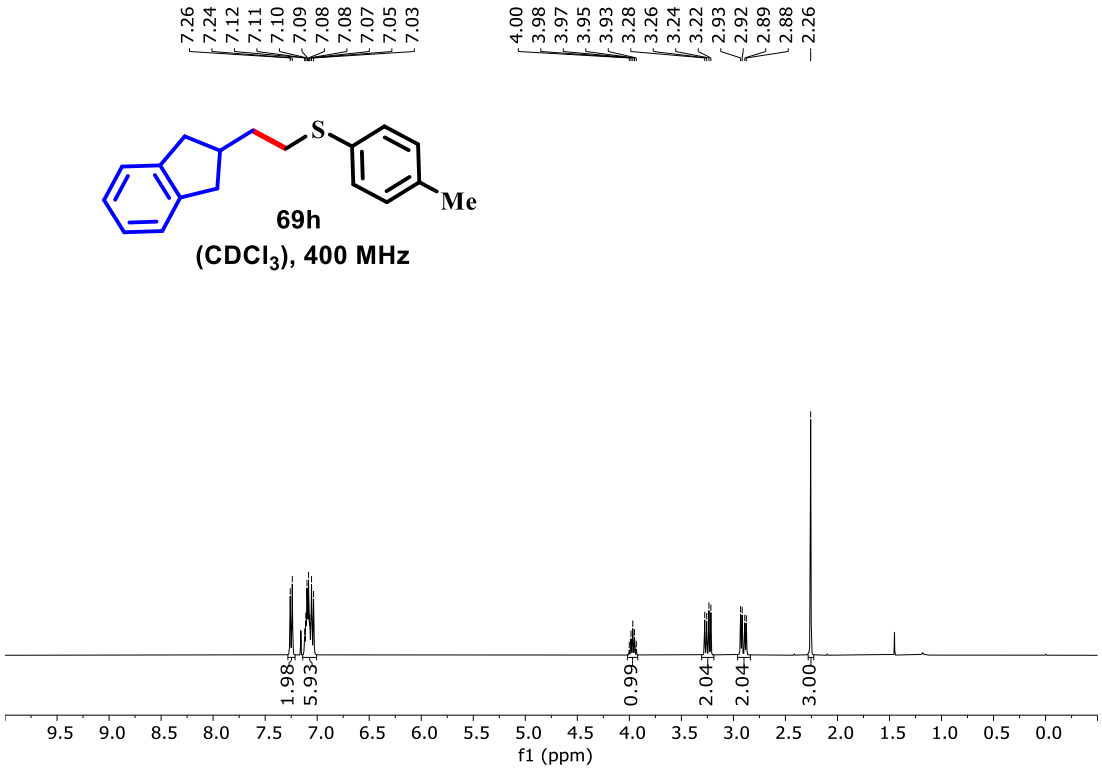

Figure B40: ^{1}H NMR spectrum of compound **69h** (400 MHz, $CDCl_3$).

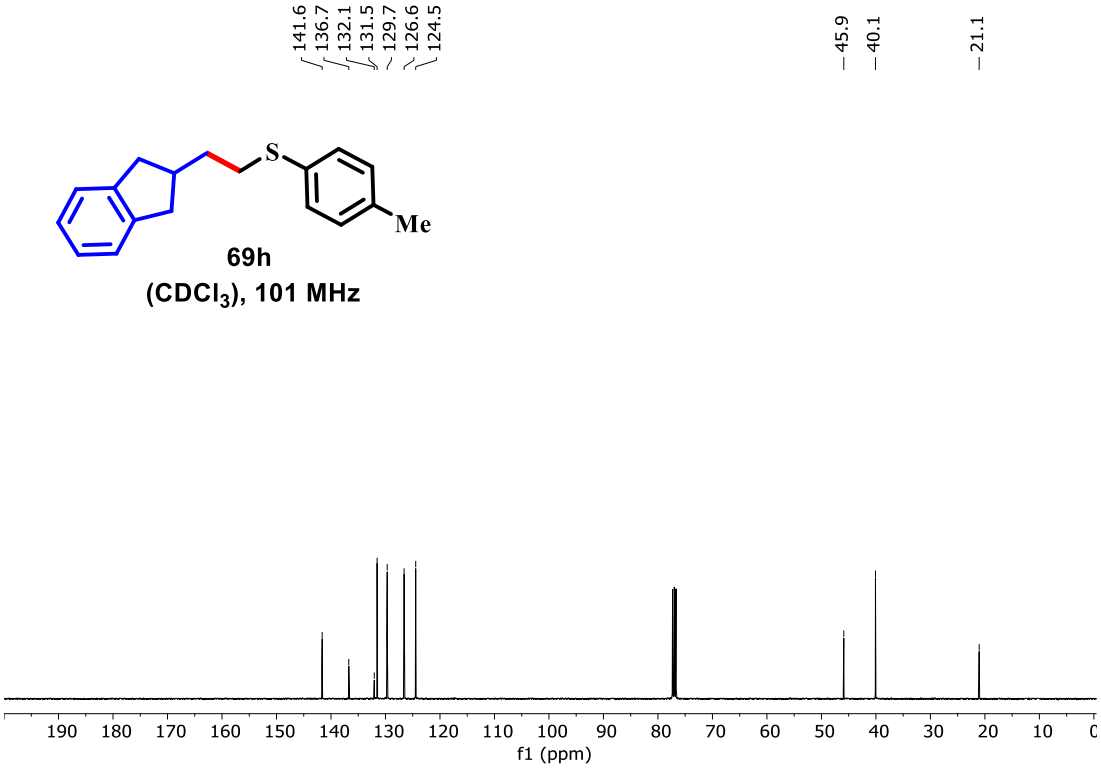

Figure B41: ^{13}C NMR spectrum of compound **69g** (101 MHz, $CDCl_3$).

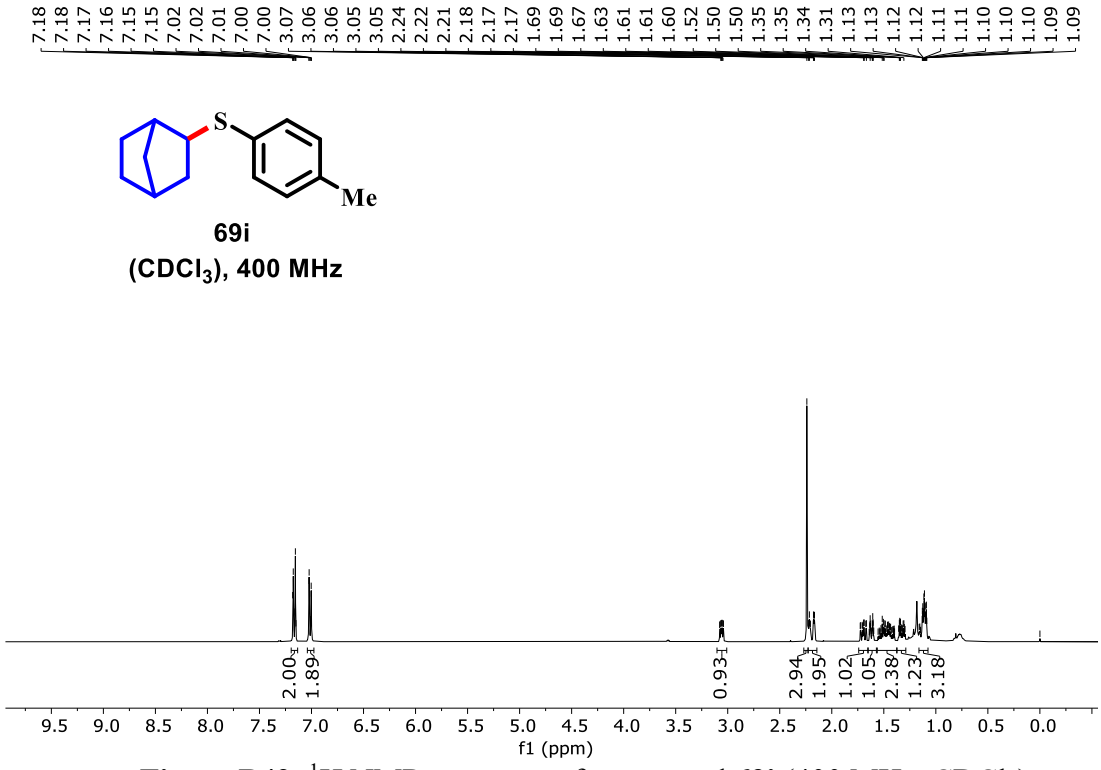

Figure B42: ^{1}H NMR spectrum of compound **69i** (400 MHz, $CDCl_3$).

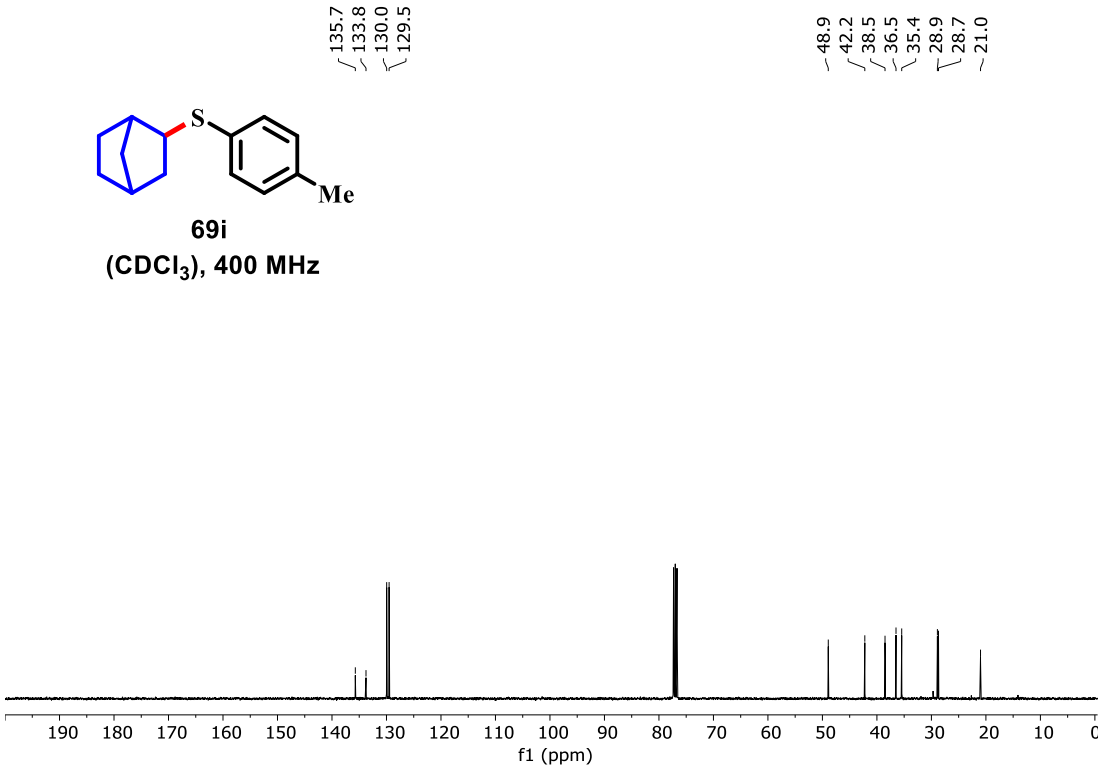

Figure B43: ^{13}C NMR spectrum of compound **69i** (101 MHz, $CDCl_3$).

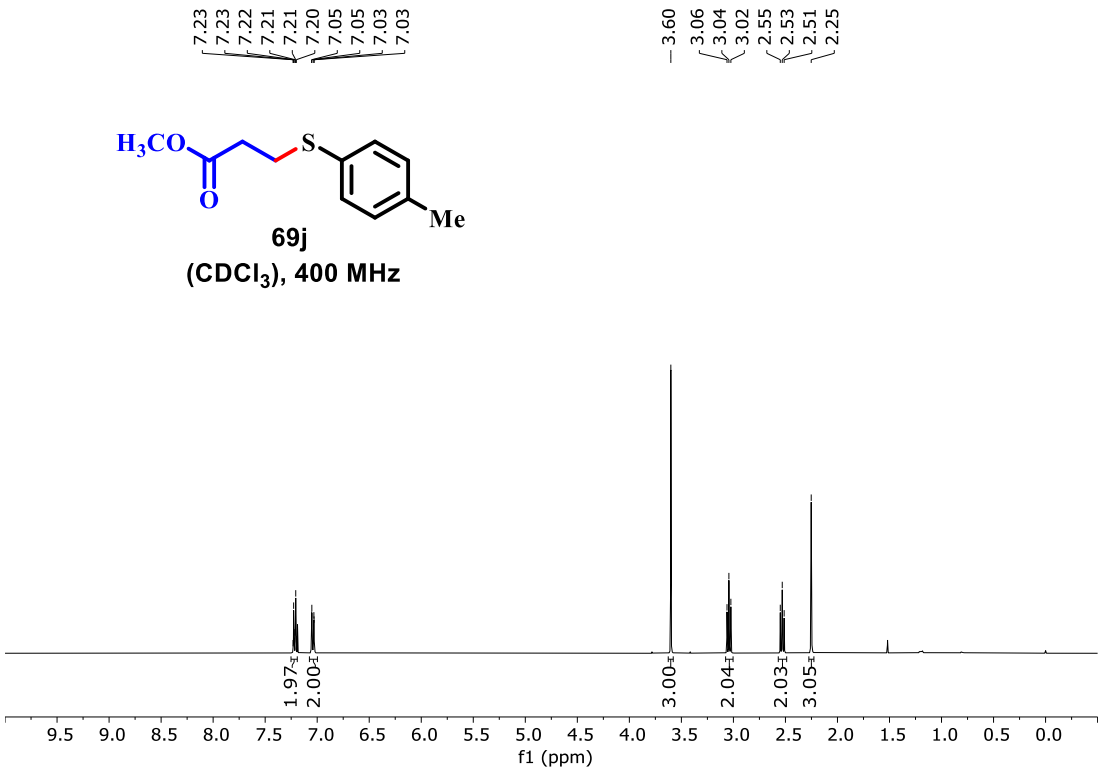

Figure B44: ^{1}H NMR spectrum of compound **69j** (400 MHz, $CDCl_3$).

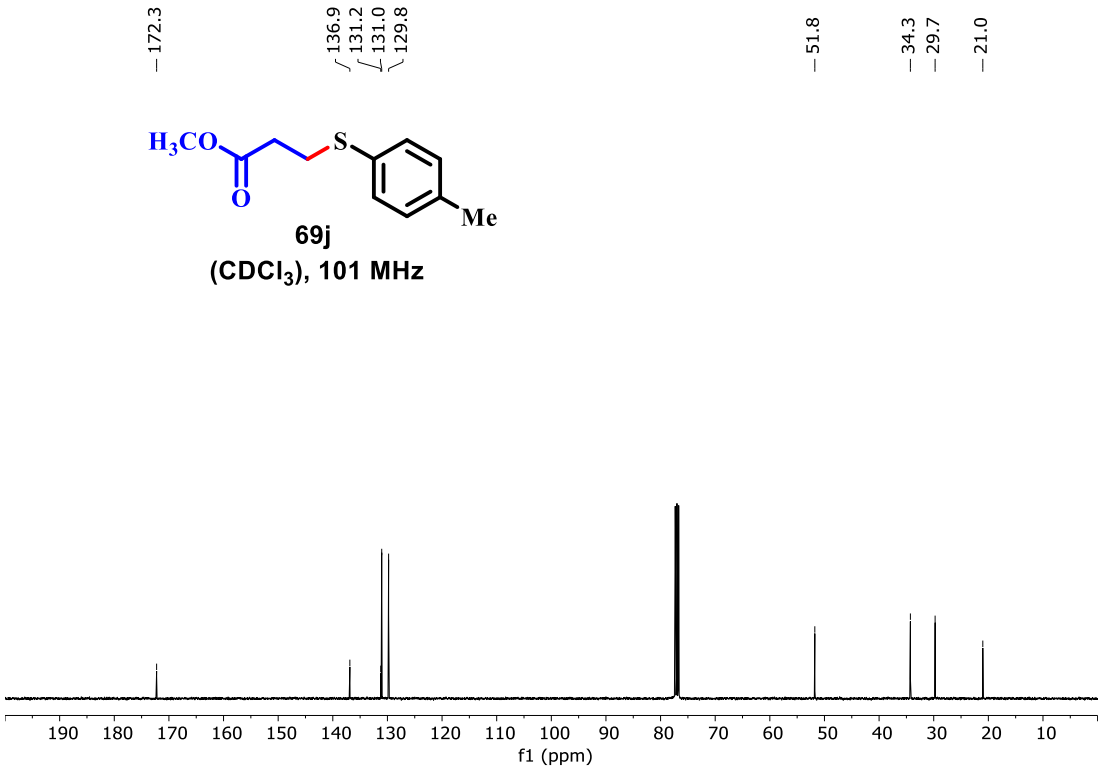

Figure B45: ^{13}C NMR spectrum of compound **69j** (101 MHz, $CDCl_3$).

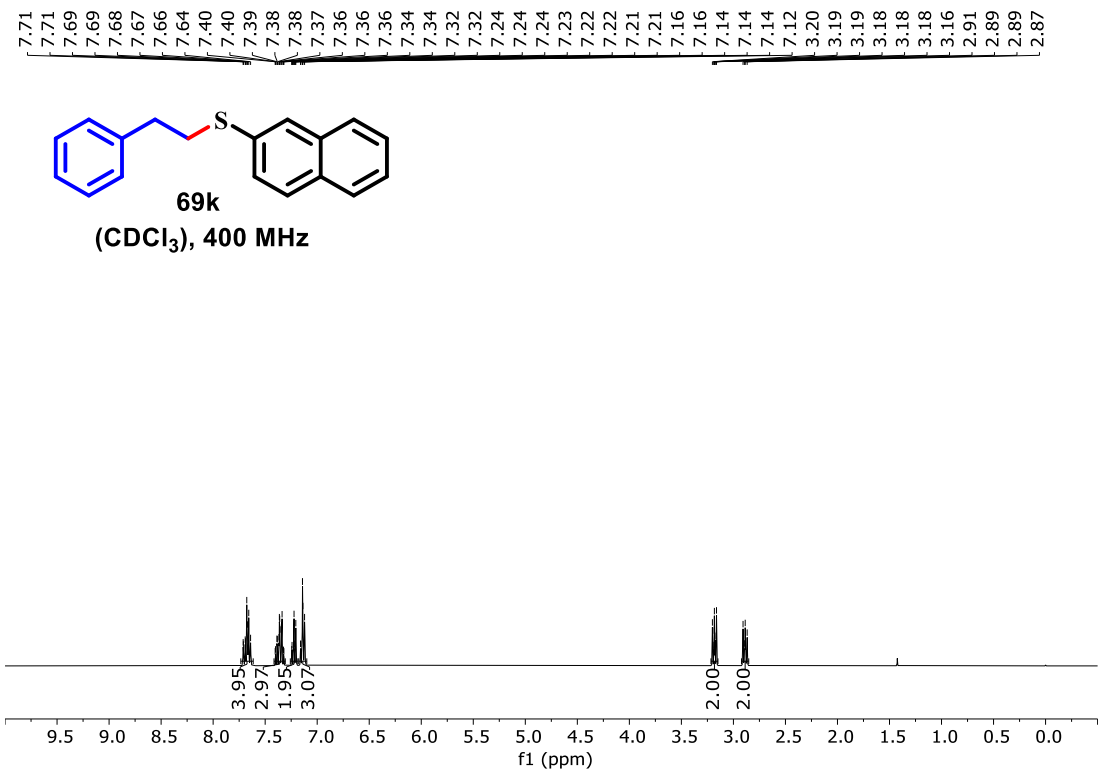

Figure B46: ^{1}H NMR spectrum of compound **69k** (400 MHz, $CDCl_3$).

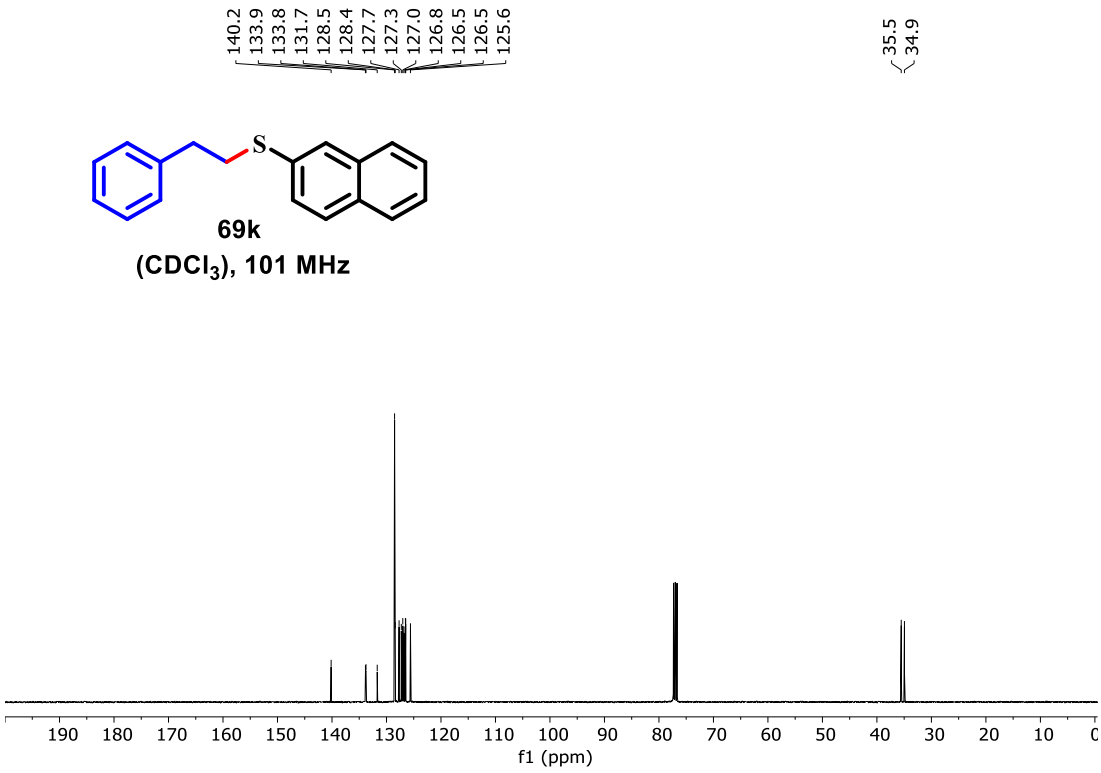

Figure B47: ^{13}C NMR spectrum of compound **69k** (101 MHz, $CDCl_3$).

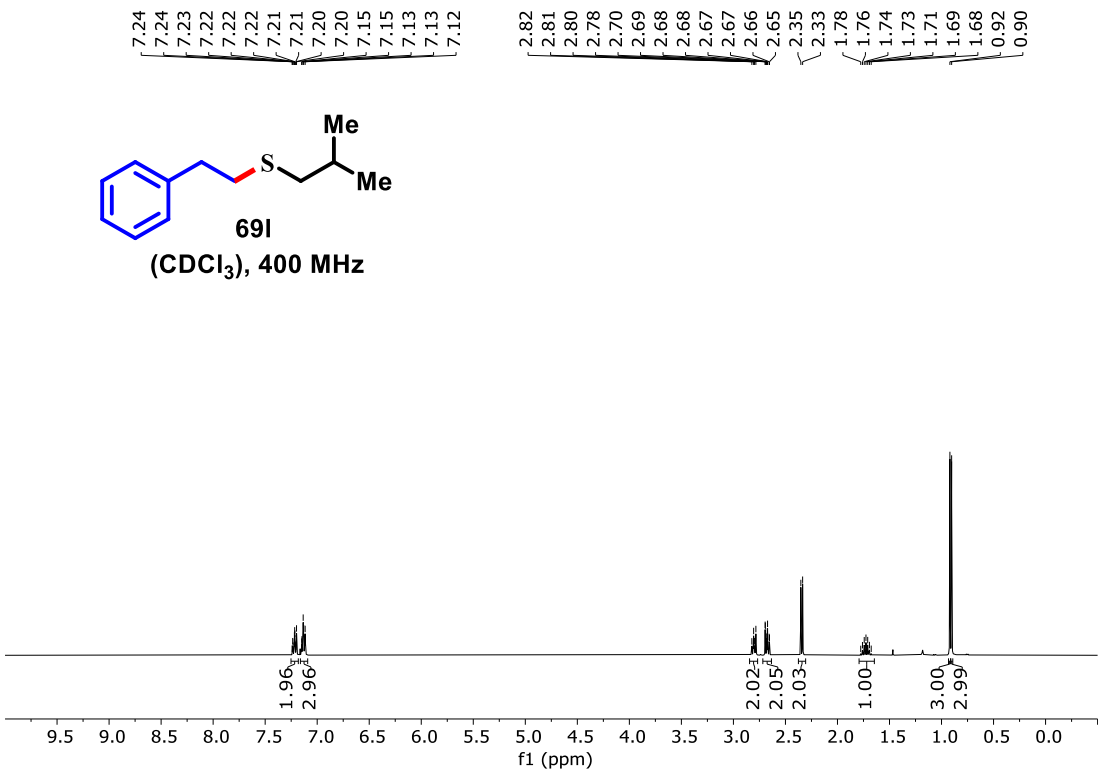

Figure B48: ^{1}H NMR spectrum of compound **69l** (400 MHz, $CDCl_3$).

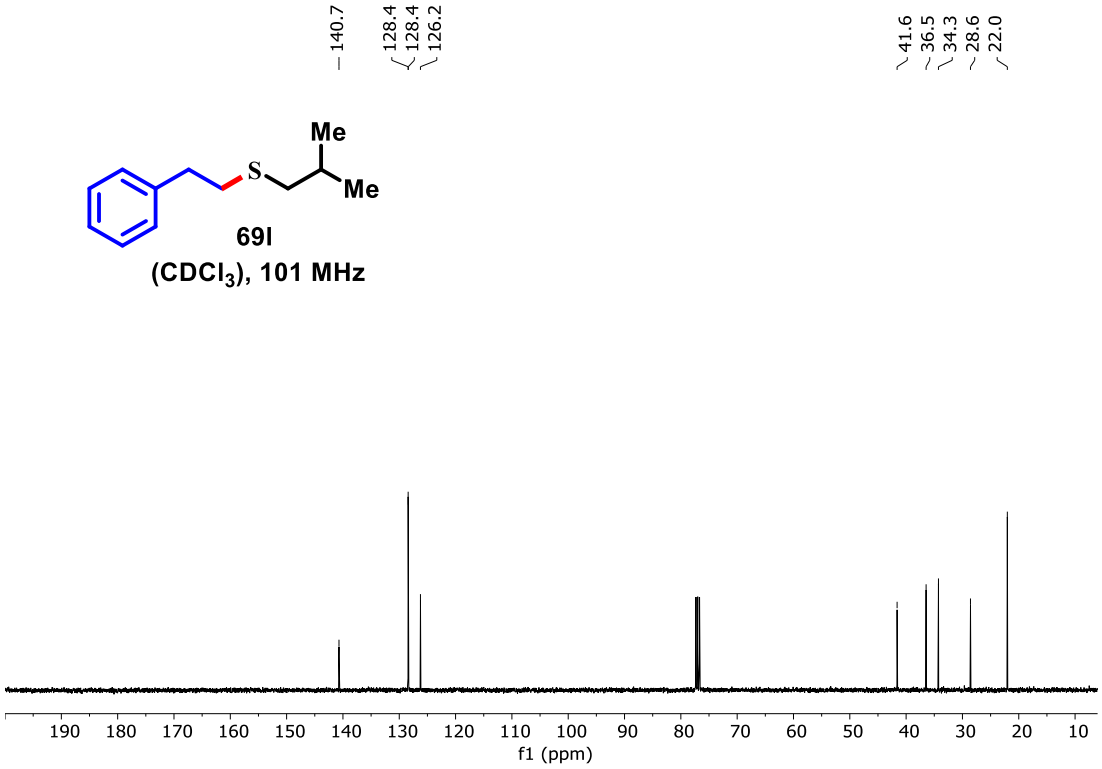

Figure B49: ^{13}C NMR spectrum of compound **69k** (101 MHz, $CDCl_3$).